

PROCEEDINGS



SPIE—The International Society for Optical Engineering

Intense Microwave Pulses IV

Howard E. Brandt
Chair/Editor

7-8 August 1996
Denver, Colorado

AIR FORCE OF SCIENTIFIC RESEARCH (AFSC)
OFFICE OF THE ASSISTANT SECRETARY
This document is approved and is
toprove
is
John S.
STINFO

19961125 196



Volume 2843

REPORT DOCUMENTATION PAGEForm Approved
OMB No. 0704-0188

Public reporting burden for this collection of information is estimated to average 1 hour per response, including the time for reviewing instructions, searching existing data sources, gathering and maintaining the data needed, and completing and reviewing the collection of information. Send comments regarding this burden estimate or any other aspect of this collection of information, including suggestions for reducing this burden, to Washington Headquarters Services, Directorate for Information Operations and Reports, 1215 Jefferson Davis Highway, Suite 1204, Arlington, VA 22202-4302, and to the Office of Management and Budget, Paperwork Reduction Project (0704-0188), Washington, DC 20503.

1. AGENCY USE ONLY (Leave blank)		2. REPORT DATE	3. REPORT TYPE AND DATES COVERED FINAL REPORT 1 Jul 96 - 31 Dec 96	
4. TITLE AND SUBTITLE SPIE'S 1996 CONFERENCE PROGRAM ON MILLIMETER AND MICROWAVE ENGINEERING			5. FUNDING NUMBERS 63726F 4702/XX	
6. AUTHOR(S) Dr Pearson			AFOSR-TR-96 0564	
7. PERFORMING ORGANIZATION NAME(S) AND ADDRESS(ES) International Society for Optical Engineering 1000 20th Street P O Box 10 Bellingham, WA 98227				
9. SPONSORING / MONITORING AGENCY NAME(S) AND ADDRESS(ES) AFOSR/NE 110 DUNCAN AVENUE SUITE B115 BOLLING AFB DC 20332-8080			10. SPONSORING / MONITORING AGENCY REPORT NUMBER F49620-96-1-0237	
11. SUPPLEMENTARY NOTES				
12a. DISTRIBUTION / AVAILABILITY STATEMENT APPROVED FOR PUBLIC RELEASE: DISTRIBUTION UNLIMITED			12b. DISTRIBUTION CODE	
13. ABSTRACT (Maximum 200 words) A conference was held 7-8 August 1996 in Denver, Colorado				
14. SUBJECT TERMS			15. NUMBER OF PAGES	
			16. PRICE CODE	
17. SECURITY CLASSIFICATION OF REPORT UNCLASSIFIED	18. SECURITY CLASSIFICATION OF THIS PAGE UNCLASSIFIED	19. SECURITY CLASSIFICATION OF ABSTRACT UNCLASSIFIED	20. LIMITATION OF ABSTRACT	

DISCLAIMER NOTICE



**THIS DOCUMENT IS BEST
QUALITY AVAILABLE. THE
COPY FURNISHED TO DTIC
CONTAINED A SIGNIFICANT
NUMBER OF PAGES WHICH DO
NOT REPRODUCE LEGIBLY.**



PROCEEDINGS
SPIE—The International Society for Optical Engineering

Intense Microwave Pulses IV

Howard E. Brandt
Chair/Editor

7–8 August 1996
Denver, Colorado

Sponsored and Published by
SPIE—The International Society for Optical Engineering

Cosponsored by
Rome Laboratory



Volume 2843

DTIC QUALITY INSPECTED 3

SPIE is an international technical society dedicated to advancing engineering and scientific applications of optical, photonic, imaging, electronic, and optoelectronic technologies.



The papers appearing in this book comprise the proceedings of the meeting mentioned on the cover and title page. They reflect the authors' opinions and are published as presented and without change, in the interests of timely dissemination. Their inclusion in this publication does not necessarily constitute endorsement by the editors or by SPIE.

Please use the following format to cite material from this book:

Author(s), "Title of paper," in *Intense Microwave Pulses IV*, Howard E. Brandt, Editor, Proc. SPIE 2843, page numbers (1996).

Library of Congress Catalog Card No. 96-68341
ISBN 0-8194-2231-2

Published by
SPIE—The International Society for Optical Engineering
P.O. Box 10, Bellingham, Washington 98227-0010 USA
Telephone 360/676-3290 (Pacific Time) • Fax 360/647-1445

Copyright ©1996, The Society of Photo-Optical Instrumentation Engineers.

Copying of material in this book for internal or personal use, or for the internal or personal use of specific clients, beyond the fair use provisions granted by the U.S. Copyright Law is authorized by SPIE subject to payment of copying fees. The Transactional Reporting Service base fee for this volume is \$6.00 per article (or portion thereof), which should be paid directly to the Copyright Clearance Center (CCC), 222 Rosewood Drive, Danvers, MA 01923. Payment may also be made electronically through CCC Online at <http://www.directory.net/copyright/>. Other copying for republication, resale, advertising or promotion, or any form of systematic or multiple reproduction of any material in this book is prohibited except with permission in writing from the publisher. The CCC fee code is 0-8194-2231-2/96/\$6.00.

Printed in the United States of America.

Contents

vii	<i>Conference Committee</i>
ix	<i>Introduction</i>

SESSION 1

2	Pulse shortening in high-peak-power Reltron tubes [2843-01] R. B. Miller, Titan Advanced Innovative Technologies
14	Model of injection-locked relativistic klystron oscillator [2843-02] J. W. Luginsland, Y. Y. Lau, K. J. Hendricks, P. D. Coleman, Univ. of Michigan
24	Investigation of lower-order mode suppression in a high-current high-voltage gyro-BWO experiment [2843-03] T. A. Spencer, M. D. Stump, K. J. Hendricks, Air Force Phillips Lab.; R. M. Gilgenbach, Univ. of Michigan
30	Cyclotron maser experiment in two-dimensional periodic array [2843-04] L. Lei, E. Jerby, Tel Aviv Univ. (Israel)
38	Rectangular-cross-section high-power gyrotron [2843-05] J. M. Hochman, R. M. Gilgenbach, R. L. Jaynes, J. I. Rintamaki, Y. Y. Lau, J. W. Luginsland, J. S. Lash, Univ. of Michigan; T. A. Spencer, Air Force Phillips Lab.
47	Computer modeling of phase locking in magnetrons [2843-06] X. Chen, M. Esterson, P. A. Lindsay, King's College London (UK)
57	Electromagnetic resonances of an asymmetrically loaded magnetron cavity [2843-07] M. Botton, I. Schnitzer, A. Rosenberg, Rafael (Israel)
69	Pasotron high-power microwave source performance [2843-08] D. M. Goebel, E. S. Ponti, J. R. Feicht, R. M. Watkins, Hughes Research Labs.

SESSION 2

80	Photonic bandgap (PBG) technology for antennae [2843-27] L. J. Jasper, G. T. Tran, Army Research Lab.
90	Gases evolved from the common cold cathode [2843-28] M. S. Litz, D. C. Judy, G. A. Huttlin, C. J. Lazard, Army Research Lab.
96	Bremsstrahlung recoil force on second-order dynamic polarization charge of a relativistic test particle in a nonequilibrium beam-plasma system [2843-29] H. E. Brandt, Army Research Lab.
101	Evolution of spectral power density in grounded-cathode relativistic magnetron [2843-31] I. Schnitzer, A. Rosenberg, C. Leibovitz, I. Cohen, M. Botton, J. Leopold, Rafael (Israel)

- 110 **Mechanism of microwave amplification in relativistic klystron amplifier** [2843-35]
W. Ding, Institute of Applied Physics and Computational Mathematics (China)
- 117 **Study of electromagnetic shock wave in modified MITL** [2843-36]
E. A. Galstjan, L. N. Kazanskiy, A. I. Khomenko, Moscow Radiotechnical Institute (Russia);
A. L. Babkin, V. I. Chelpanov, V. G. Kornilov, V. D. Selemir, V. S. Zhdanov, All-Russian
Research Institute of Experimental Physics
- 123 **Prospect of superlight source application for charged-particle acceleration** [2843-37]
Yu. N. Lazarev, P. V. Petrov, Russian Federal Nuclear Ctr.
- 134 **Harmonic generation in the reflection of microwave radiation from semiconductor surface**
[2843-38]
A. V. Shepelev, M. Y. Glotova, A. V. Shvartsburg, Central Design Bureau for Unique
Instrumentation (Russia)
- 137 **Wide-bandwidth high-power Cerenkov amplifiers: why dielectric slow-wave structures?**
[2843-32]
A. S. Shlapakovskii, Tomsk Polytechnical Univ. (Russia)

SESSION 3

- 144 **Pulse shortening in the magnetically insulated line oscillator (MILO)** [2843-39]
F. J. Agee, S. E. Calico, K. J. Hendricks, M. D. Haworth, T. A. Spencer, Air Force Phillips Lab.;
D. L. Ralph, E. Blankenship, Maxwell Labs.; M. C. Clark, R. W. Lemke, Sandia National Labs.
- 153 **Breakdown at window interfaces caused by high-power microwave fields** [2843-40]
J. C. Dickens, J. Elliott, L. L. Hatfield, M. Kristiansen, H. Krompholz, Texas Tech Univ.
- 160 **Interaction of multipactor and rf circuit** [2843-41]
R. Kishek, Y. Y. Lau, Univ. of Michigan; D. P. Chernin, Science Applications International
Corp.; R. M. Gilgenbach, Univ. of Michigan
- 166 **High-power microwave field measurements using Stark broadening** [2843-42]
T. J. Englert, M. D. Haworth, K. J. Hendricks, F. M. Lehr, D. A. Shiffler, Air Force Phillips Lab.
- 172 **Review of catastrophic electromagnetic breakdown for short pulse widths** [2843-43]
F. J. Agee, D. W. Scholfield, R. P. Copeland, T. H. Martin, Air Force Phillips Lab.; J. J. Carroll,
Youngstown State Univ.; J. J. Mankowski, M. Kristiansen, L. L. Hatfield, Texas Tech Univ.
- 183 **Dependence of drift length on cavity gap voltage in a space-charge-dominated klystron
amplifier** [2843-58]
H. E. Brandt, Army Research Lab.
- 188 **Standard antennas designed with electro-optic modulators and optical fiber linkage** [2843-61]
K. D. Masterson, D. R. Novotny, K. H. Cavecy, National Institute of Standards and Technology
- 197 **Broadband superlight source of high-power microwaves** [2843-57]
Yu. N. Lazarev, P. V. Petrov, Russian Federal Nuclear Ctr.
- 208 **Beam-plasma generators of stochastic microwave oscillations used for plasma heating in
fusion and plasma-chemistry devices and ionospheric investigations** [2843-47]
L. A. Mitin, V. I. Perevodchikov, A. L. Shapiro, M. A. Zavjalov, All-Russian Electrotechnical
Institute; Yu. P. Bliokh, Ya. B. Fainberg, Kharkov Institute of Physics and Technology (Ukraine)

- 219 **Helical Cerenkov effect with very strong magnetic fields [2843-46]**
J. Z. Šoln, Army Research Lab.

SESSION 4

- 228 **Compact source of high-power microwaves [2843-54]**
V. P. Gubanov, S. D. Korovin, I. V. Pegel, V. V. Rostov, A. S. Stepchenko, E. M. Totmeninov,
Institute of High-Current Electronics (Russia)

SESSION 5 POSTER SESSION

- 240 **Beam focusing and plasma channel formation in the Pasotron HPM source [2843-09]**
E. S. Ponti, D. M. Goebel, R. L. Poeschel, Hughes Research Labs.
- 251 **Pulse shortening in high-power backward wave oscillators [2843-10]**
C. Grabowski, J. M. Gahl, E. Schamiloglu, C. B. Fleddermann, Univ. of New Mexico
- 260 **Nonlinear study of mode locking in a quasi-optical gyrotron [2843-11]**
H. Wu, A. H. McCurdy, Univ. of Southern California
- 269 **Multimode linear analysis of plasma Cerenkov masers driven by relativistic electron beams [2843-12]**
M. Birau, Ecole Polytechnique/CNRS (France)
- 280 **Analysis of an electromagnetically pumped free-electron laser with a tapered guide magnetic field [2843-14]**
Y. G. Liu, S. K. Zhang, C. L. Li, National Univ. of Defense Technology (China)
- 287 **Electromagnetic oscillation generation in the virtual cathode triode from the viewpoint of the parametric interaction of electrons with a variable field [2843-16]**
V. P. Grigoryev, T. V. Koval, Tomsk Polytechnical Univ. (Russia)
- 293 **Stabilization of synchronous frequency in a system of strongly coupled microwave oscillators [2843-18]**
S. S. Novikov, S. A. Maidanovskii, S. A. Sulakshin, Tomsk State Univ. (Russia)
- 303 **Intense microwave pulse production from vircators with inductive energy storage [2843-22]**
A. G. Zherlitsyn, G. G. Kanaev, V. I. Tsvetkov, Tomsk Polytechnical Univ. (Russia)
- 307 **Narrowband microwave generation from virtual cathode oscillating inside a resonant cavity [2843-24]**
J. Liu, Y. Zhang, C. Li, G. Chen, Q. Tan, National Univ. of Defense Technology (China)
- 314 **Single-pulse analysis with a 35-GHz optical sampler [2843-59]**
A. Ghis, M. Cuzin, M. Gentet, Ph. Ouvrier-Buffet, LETI/CEA (France); M. Nail, P. Gibert,
D. Husson, DAM/CEA (France); L. Armengaud, M. Lalande, B. Jecko, Univ. de Limoges (France)
- 325 *Addendum*
327 *Author Index*

Conference Committee

Conference Chair

Howard E. Brandt, Army Research Laboratory

Cochair

Ronald M. Gilgenbach, University of Michigan

Introduction

The primary purpose of this conference was to present and critically assess current research on the generation and transmission of intense microwave pulses. The present volume documents all research presented at the conference and is the sequel to *Intense Microwave Pulses III*, Howard E. Brandt, Editor, Proc. SPIE 2557 (1995).

At this year's meeting, the phenomenon of pulse shortening in high-power microwave sources received special attention. Specifically, reports were made on investigations of pulse shortening in the Reltron, the Pasotron, the magnetically insulated line oscillator (MILO), and a long-pulse backward-wave oscillator. Possible causes and remedies were addressed. Related investigations of breakdown phenomena at window interfaces, multipactor discharge in microwave cavities, and explosive cathode emission phenomenology were reported.

Ongoing research on high-power klystron oscillators and amplifiers was also presented. This included: (1) a simple model of an injection-locked relativistic klystron oscillator, (2) an analytical model of electron-beam bunching and gain in a relativistic klystron amplifier (RKA), and (3) an explicit expression showing the dependence of RKA drift length on buncher-cavity gap voltage.

In research on high-power magnetrons, the design, operation, and spectral characteristics were reported for a relativistic magnetron with a grounded cathode. In other work, effects were calculated for asymmetric loading of a magnetron cavity on the resonant frequency and quality factor of various cavity modes. Numerical simulations of magnetron phase locking were also presented.

Work reported on virtual-cathode sources included determination of spectral characteristics of a vircator resonantly coupled to a surrounding cavity, and analysis and experiments on microwave generation by a vircator utilizing inductive energy storage.

In gyrotron research, experiments on long-pulse microwave production by a high-power gyrotron with rectangular cross section were reported. Also presented was work on harmonic multiplication as a possible way to produce high frequency, large bandwidth, and high power in gyrotron oscillators and amplifiers. Results on nonlinear time-dependent multimode calculations of mode locking in quasi-optical gyrotron oscillators were reported. Also presented were experimental results on a novel design for a cyclotron maser having a periodic waveguide consisting of a two-dimensional linear array of metal posts. In addition, research on unwanted-mode suppression in a gyrotron-backward wave oscillator was presented.

A useful model of a Cerenkov maser was presented, together with calculations of dispersion relations, growth rates, and field structure. Also presented was a study of possible advantages of dielectric Cerenkov amplifiers over devices with periodic conducting slow-wave structures for wide-bandwidth high-power microwave production. Theoretical and experimental results on a beam-plasma inertial-feedback amplifier were reported, in which the amplifier served as a stochastic microwave source. The interaction of the stochastic radiation with plasma was also addressed.

Recent Pasotron research was presented, including an investigation of the performance characteristics of the device using various rippled-wall and helical slow-wave structures, and using a repetitive plasma-cathode electron gun. Also, on the basis of experimental studies of the electron-beam dynamics, it was concluded that a new depressed collector configuration for the Pasotron tube may significantly improve the overall device efficiency.

In other work, nonlinear analysis was presented of the dispersion relation, growth rate, and energy conversion efficiency of an electromagnetically pumped free-electron laser with a tapered guide field. Also reported were analysis, together with model experiments, on synchronous frequency stabilization in systems of strongly coupled microwave oscillators utilizing high-Q resonators.

Experimental results were discussed on the formation of electromagnetic shock waves in the magnetically insulated transmission line of an electron-beam generator with a dielectric insert in the cathode. In other work, theory was presented on electromagnetic pulse production by ionizing radiation incident on a photoemissive surface.

In the area of microwave diagnostics, the following research was reported: (1) the measurement of high-power microwave fields by means of the rf Stark effect, and (2) the operation of a standard rf probe with a fiber optic link and a Michelson modulator. Also, very innovative and stimulating analytical and experimental work was presented on the use of photonic bandgap technology in the development of ultrawideband antennas.

This conference evolved from earlier SPIE conferences reporting closely related research which is documented in SPIE Volumes 1061, 1226, 1407, 1629, 1872, 2154, and 2557.

I wish to thank Ronald Gilgenbach of the University of Michigan for his outstanding performance as cochair and session chair of this conference.

Howard E. Brandt

SESSION 1

Pulse-shortening in high-peak-power Reltron tubes

R. B. Miller

TITAN Advanced Innovative Technologies
Albuquerque, NM 87119-9254

ABSTRACT

Most high-peak-power (≥ 100 MW) microwave tubes are seemingly limited to an output RF energy per pulse of about 100 J. While Titan's L-band Reltron tubes have achieved 250 J/pulse, we have also observed pulse-shortening phenomena in both the modulating cavity and output cavity regions. We have examined the effects of construction materials, fabrication techniques, vacuum pressure, and conditioning. We will present data from these experiments and discuss a plausible pulse-shortening hypothesis involving electric-field-induced gas evolution and subsequent ionization.

We believe that our energy-per-pulse limitations are the result of our current tube construction approach which uses explosive emission cathodes, plastic insulators, and grids to define cavity boundaries. While some simple extensions of this approach offer some hope for increasing the energy per pulse to perhaps 500 joules in L-band, we believe that achieving ≥ 1 kJ/pulse will require the use of conventional microwave tube construction techniques, including thermionic cathodes, ceramic insulators, and brazed joining with high-temperature bakeout. We will present the design of an L-band Reltron tube having these features.

Keywords: pulse shortening, microwave tubes, Reltron

1. INTRODUCTION

Pulse-shortening has been observed in all high-power (≥ 100 MW) microwave tubes that have attempted to extend the useful power pulse beyond about 100 ns.¹⁻³ As a result, most experimental L-band tubes, for example, are limited to ≤ 100 joules per pulse. Titan's Reltron tube is notable in that it has produced as much as 250 joules in L-band, but it too suffers from pulse-shortening phenomena.⁴

Prior to describing our detailed experimental observations, we briefly discuss the tube construction, the pulser circuit, and the various diagnostic signals. A schematic diagram of a Reltron tube is shown in Figure 1.⁵ For the purpose of this paper we will limit our discussion to the present design and construction of our high-peak-power Reltron tubes. An electron beam is drawn from a planar velvet cathode via an explosive emission process when voltage is applied to the gun region. The beam becomes modulated through a self-excited oscillator mechanism as it passes through the modulation cavity.⁶ This structure is a three-cavity section of a side-coupled, standing-wave rf linac. The two cavities through which the beam passes are defined by grids, made of either stainless steel wire mesh, or electro-etched molybdenum. The high-voltage vacuum insulators are comprised of stacks of alternating plastic (polystyrene) insulator rings and aluminum grading rings. An external magnetic field is not required; focusing is provided by shaping the electric field in the region of the accelerating gap. The accelerating gap voltage also increases the beam power and reduces the relative kinetic energy spread of the electrons in the bunched beam. Multiple output cavities are used to efficiently extract rf power from the beam, while limiting the peak electric field that appears in any one output cavity. The spent beam is deposited in a beam dump made of either stainless steel or high-density graphite. The vacuum pressure is maintained in the 10^{-5} torr range with a turbo-molecular pump, backed by an oil roughing pump. The linear geometry of this tube provides a convenient test-bed for studying pulse-shortening phenomena. Unlike a magnetron or other cross-field devices, there is no externally applied magnetic field, and the beam generation, bunching, and power conversion processes occur in different regions of the tube. This configuration therefore allows progress to be made in each region, somewhat independently of the other regions.

The pulser used for most of our experiments has been described previously.⁴ It is a conventional Marx generator operated in run-down mode, i.e., a simple RC-decay voltage pulse. The voltages supplied to the accelerating gap and electron gun region of the tube are adjusted with a simple resistive voltage divider. In typical high power operation approximately 200 kV is applied to the gun region, and 800 kV is applied to the accelerating gap. Beam currents are typically 1 kiloampere. A triggered crowbar switch is used to shunt the Marx energy to ground to prevent late-time damage to the tube. Firing of the crowbar switch is adjustable relative to the time of Marx erection; for the experiments reported here, the voltage pulses had a typical duration of 0.5 - 1 microsecond.

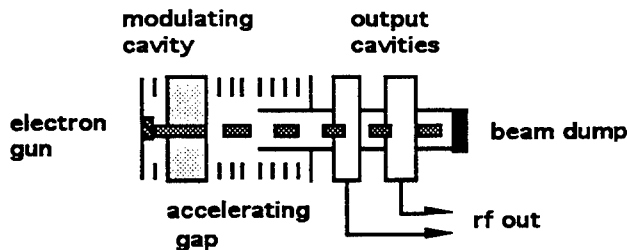


Figure 1. Schematic diagram of a Reltron tube, indicating the electron gun region, the modulating cavity, the accelerating gap, the multiple output cavities and the beam dump.

Our minimal standard diagnostics include resistive voltage monitors for the total Marx voltage and for the voltage applied to the accelerating gap, a B-dot probe situated inside the Marx tank to monitor the modulated beam current propagating through the accelerating gap region, and a B-dot monitor in the anechoic chamber to monitor the radiated microwave power. The beam modulation signal is split with a directional coupler. On one output of the coupler a crystal detector is used to determine the envelope of the beam modulation pulse. The second output of the coupler is sent to a mixer crystal in which the beam modulation signal is heterodyned with the signal from a fixed frequency local oscillator. The resulting intermediate frequency (IF) signal is a measure of the beam modulation frequency. A crystal detector is also used to measure the microwave power from the anechoic chamber B-dot probe. This arrangement of diagnostic signals is important because it allows us to independently monitor the performance of the modulating cavity and the output cavities.

2. EXPERIMENTAL OBSERVATIONS

In the following sections we briefly summarize our experimental observations having relevance for the pulse shortening issue. We begin by discussing an example which illustrates pulse shortening in the output cavity. We then present observations of pulse shortening in both the modulation cavity and output cavities under a variety of conditions.

2.1 Pulse Shortening Example

In Figure 2 we exhibit our best experimental results as of approximately three years ago, in terms of energy per pulse.⁴ After a lengthy pump-down period (a few days), and considerable hot test conditioning (several hundreds of pulses) we were able to obtain 1-GHz operation at a peak power of about 600 MW, with a peak energy per pulse of approximately 250 joules. Note that high-level beam modulation was maintained for the entire duration of the voltage pulse at a very constant frequency; however, the output power pulse began to decay after a few hundred nanoseconds, dropping to essentially zero by the end of the voltage pulse, even though the beam modulation was still quite good. Also note that A-K gap "closure" was not a factor, even for these very long pulses. For our velvet cathodes operating at stress levels of up to several tens of kV/cm, significant impedance collapse was not observed, suggesting that plasma closure velocities must be less than 0.5 cm/ μ sec. In other words, for this particular set of tube conditions, pulse shortening was not observed in the anode-cathode gap or in the modulating cavity, but did occur in the output cavities. If we could have obtained output cavity performance equivalent to the performance of the modulating cavity, we would have been able to produce nearly 500 joules per pulse from this Reltron tube at an operating voltage of about 1.2 MV.

2.2 Modulating Cavity Performance

2.2.1 Conditioning Effects

We have repeatedly observed the beneficial effects of "conditioning" on the performance of both the modulating cavity and the output cavities. As a general comment, we always see a beneficial effect of good vacuum ($\leq 10^{-5}$ torr) and improved results with prolonged tube operation under good vacuum conditions. However, the most dramatic conditioning is that initially observed after a tube has been exposed to air for a few days.

We first discuss the effects of conditioning on the beam modulation pulse. The shot history shown in Figure 3 is fairly typical of the expected performance using new 50 mesh stainless steel grids (50 one-mil wires per inch) in the modulating cavity of our 1.3 GHz Reltron tube. At low initial charge voltage the modulation pulse duration (FWHM) is nearly full (800 ns), but as the voltage is subsequently raised, the pulse duration becomes erratic, and generally shorter for several shots, until the modulating cavity becomes "conditioned" at that particular voltage and pulse duration.

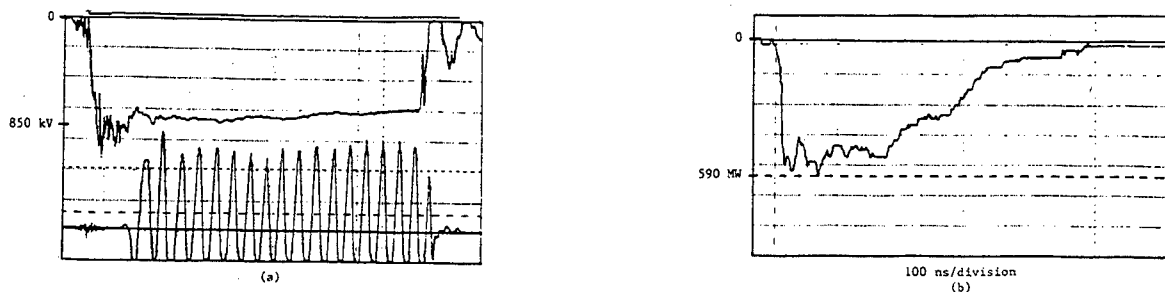


Figure 2. (a) The top trace is the voltage pulse applied to the accelerating gap region; the bottom trace is the intermediate frequency output of a mixer crystal obtained by heterodyning the modulated beam current signal with that of a local oscillator. The beam modulation is essentially fully developed within 80 ns after the Marx voltage reaches its maximum value. Note that there is no frequency chirp over almost 700 ns of beam modulation. The frequency is about 1 GHz. Figure 2. (b) This trace is the output power pulse obtained on the same shot as the signals of 3(a). The power was radiated into an anechoic chamber, sensed by a magnetic loop probe, attenuated, and detected with a crystal detector. The output power pulse remains approximately constant over about 300 ns, but decays to zero by the end of the voltage pulse, even though the beam modulation is still quite good. The peak power is nearly 600 MW and the total rf energy in the pulse is about 250 joules.

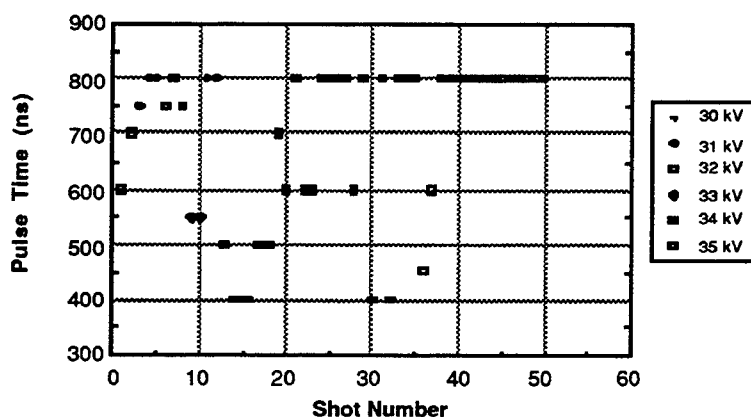


Figure 3. FWHM duration of the beam modulation pulse as a function of shot number, as the voltage is systematically increased.

It is also instructive to examine the variation in modulation frequency when a short pulse results. The waveforms shown in Figure 4 (a) and (b) typify a good beam modulation pulse. The detected signal from the B-dot probe is nearly square, and terminates when the crowbar switch terminates the voltage pulse. The corresponding IF trace from the mixer crystal indicates very little chirp, showing only a slight decrease in frequency as the voltage droops. (This slight decrease in frequency with voltage results from the changing beam loading conditions in the modulating cavity.) On the other hand, the waveforms shown in Figure 4 (c) and (d) typify a short beam modulation pulse, meaning that the beam modulation ceases before the voltage pulse terminates. The corresponding IF trace clearly indicates an increase in the beam modulation frequency prior to the cessation of beam modulation.

2.2.2 Re-Conditioning Effects

During our initial Reltron tube development efforts we did not use a crowbar switch to terminate the voltage pulse.⁶ The resulting late-time arcing of the accelerating gap insulators on almost every shot caused considerable tube damage. Although progress was made, the output rf pulses during periods of arcing were observed to be erratic in both duration and amplitude. After installation of the crowbar switch, progress was much faster, but until the switch was

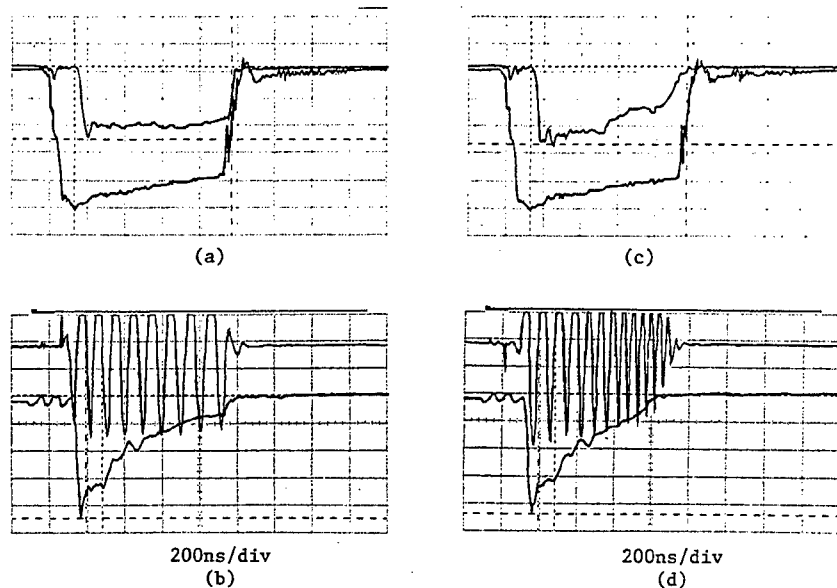


Figure 4 (a) and (b). Reltron waveforms obtained after conditioning of the modulating cavity. (a) The top trace is the envelope of the detected beam modulation signal, while the bottom trace is the voltage applied to the accelerating gap. (b) The top trace is the IF of the beam modulation signal; it is relatively constant over the 800 ns pulse width, displaying only a slight chirp to lower frequency as the applied voltage droops. The bottom trace is the output power pulse; it displays severe pulse shortening.

Figure 4 (c) and (d). Reltron waveforms obtained during conditioning of the modulating cavity. (c) The envelope of the beam modulation signal decreases to zero by the end of the applied voltage pulse. (d) The IF signal indicates a significant chirp to higher frequency. Note that the output power pulse is very similar to that in 5 (b) above, but simply terminates when the beam modulation stops.

perfected we experienced occasional shots for which the switch did not fire, again resulting in arcing of the accelerating gap insulator. Since the switch misfires were relatively infrequent, we did not experience significant tube damage; however, we did note that after almost every insulator arc, the ensuing several shots would exhibit shortening of the beam modulation pulse. It would sometimes take a few tens of shots for re-conditioning of the modulation cavity in this circumstance.

2.2.3 Effects of Grid Construction

We have experimented with several different grid designs and grid construction techniques. Most of our low frequency tubes have used standard stainless steel wire mesh composed of one mil wire woven into a rectangular grid with 50 wires per inch in both dimensions. In early experiments we found that 100 mesh one-mil grids gave even longer pulses, but significantly reduced the output power, presumably because of the reduced transparency. We have also experimented with grid transparencies of nearly 99% using a circular grid with radial spokes made of one-mil molybdenum. After nearly 100 pulses, the beam modulation pulse was still of short duration (400 ns) and low amplitude. Replacing these grids with the standard 50-mesh stainless steel restored tube performance. A tungsten mesh woven with one-mil wire into a rectangular grid with 40 wires per inch does improve performance in comparison with the stainless grids. They appear to condition faster, to give faster turn-on of the beam modulation, and to give higher amplitude beam modulation signals.

2.2.4 Idler Cavity Construction

Most Reltron tubes have been tunable, and we have explored several mechanisms for mechanically varying the cavity dimensions. Our most common approach uses co-moving plungers to vary the resonant frequency of the cavities through which the beam passes, and a tuning screw to vary the gap separation in the re-entrant side-coupler cavity (the idler cavity). For both actuators vacuum integrity is preserved using stainless steel bellows. In the case of the plungers, we have always placed the bellows outside of the modulating cavity structure proper for ease of construction. The idler movement is shown in Figure 5. In an early design the bellows itself formed the re-entrant post in one-half of the idler.

During experimentation we noted that quite good beam modulation pulses were achieved when the the frequency was held constant, but that short beam modulation pulses often occurred for a few shots after the frequency was changed. We subsequently determined that the cause of this behavior was flexing of the idler bellows during the mechanical tuning procedure. Placing this bellows outside the interior of the idler cavity region eliminated this cause of pulse shortening.

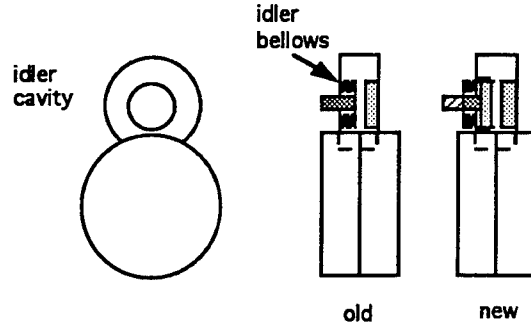


Figure 5 Removing the idler cavity bellows from the cavity interior eliminated pulse shortening as the Reltron operating frequency was varied.

2.2.5 Frequency Effects

Reltron tubes have been built with center frequencies in the range of 0.7-6 GHz. While theory suggests that the peak power of a Reltron tube should be independent of frequency,⁶ it is easier to obtain high power at lower frequencies. Even more dramatic is the reduction of the pulse duration. While the peak power scales no faster than $f^{-1/2}$, the pulse duration appears to scale at least as fast as f^{-1} . Moreover, the pulse shortening observed at S-band and higher is almost always caused by termination of beam modulation. Typical beam modulation and output power waveforms for a high-power S-band Reltron tube are shown in Figure 6. We have been able to obtain pulse durations of greater than one microsecond using our high-peak-power S-band tube design, but only by substantially decreasing the applied voltages. With 60 kV applied to the gun and 90 kV applied to the accelerating gap we have produced an output power of >10 MW at an efficiency of about 35 % (unoptimized). Typical waveforms for these tests are shown in Figure 7.

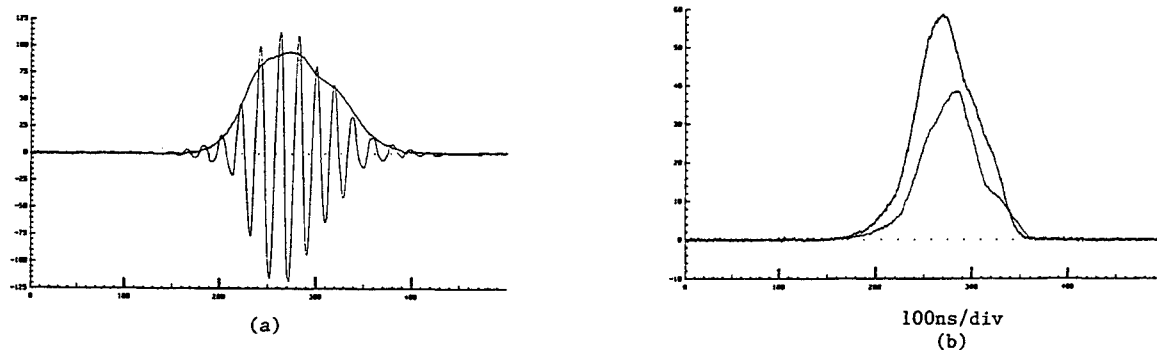


Figure 6 (a) Beam modulation envelope and IF waveforms for an S-band Reltron tube. (b) Corresponding output power pulses from two output sections containing two output cavities each. The peak power from each section is about 80 MW.

2.3 Output Cavity Performance

2.3.1 Effects of Conditioning

Conditioning is also observed in the output cavities, although the results are less dramatic than for the modulating cavity. The results shown in Figure 8 at 1.3 GHz are fairly typical for an output section that has been exposed to air for a few days, then evacuated to a pressure of $\leq 10^{-5}$ torr for a few hours. The Marx charge voltage was held at only 32 kV (about 650 kV total voltage) for these data. For shot #7 there is a sharp power peak (about 120 MW), followed by a rapid decrease in power. By shot #16 the peak power has increased to about 140 MW, and the pulse has lengthened somewhat. From shot #16 to shot #35 the power pulse gradually broadens, without a significant increase in peak power. The total energy in the pulse from this single output section (containing two cavities) is about 40 joules at this low voltage level.

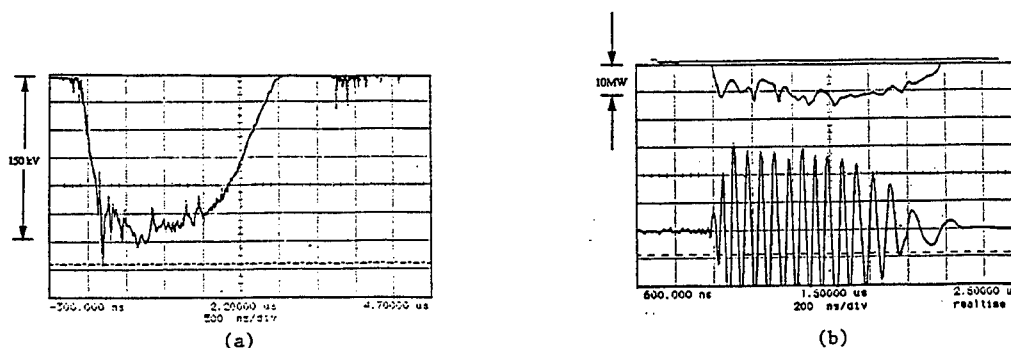


Figure 7 Repetitive pulse (25 Hz max.) waveforms obtained under low power conditions (10-20 MW) with our S-band Relatron tube. (a) the applied voltage from a thyatron-switched PFN/transformer pulser; (b) the top trace is the detected power pulse; the bottom trace is the IF signal. There is no pulse shortening, although the frequency chirp (to lower frequencies) is quite apparent as the voltage droops.



Figure 8. Output cavity conditioning during a series of pulses at 32 kV charge voltage with a well-conditioned modulation cavity. (a) Shot #7 displays a sharp power peak. (b) By shot #16, the power peak has broadened. (c) By shot #35, some additional pulse broadening has occurred, but there is no further increase in peak power. Additional pulsing at this voltage level will produce no further improvement.

2.4 First Extractor Output vs Second Extractor Output

Our standard output cavity design uses rectangular output cavities with inductive irises opening into rectangular waveguide.⁷ The output cavity quality factor is usually of the order of 20, with the resistive shunt impedance chosen according to the modulated beam current, the total beam voltage, and the number of output cavities. The output cavities often have grids also, with the standard being one-mil stainless steel wire with 100 wires per inch. Our 1.3-GHz tube was initially designed with two output extraction sections, with each section containing two cavities. Output pulses from the first extraction section (containing two output cavities) were shown previously in Figure 4 under high power operating conditions. These pulses rather dramatically exhibit the pulse shortening phenomenon. The two-extractor configuration enabled us to examine how the pulse shortening in the first extractor might affect the power pulse from the second extractor. In Figure 9 we present the results from an experiment in which the charge voltage was relatively low (30 kV, for a total voltage of 600 kV), and the cavities of the first extraction section were tuned to extract most of the available rf power. That is, the areas of the inductive iris openings were sufficiently decreased to develop a total stopping voltage approximately equal to the beam voltage when the resonant frequency of the output cavities was adjusted to that of the beam modulation frequency. Under these conditions the output power pulse from the first extractor clearly exhibited pulse shortening. Also, as expected the output power pulse from the second extractor was initially small, but increased dramatically later in the pulse when the power level from the first extractor decreased. Evidently, the pulse shortening mechanism caused the rf electric fields to decrease in the cavities of the first extractor.

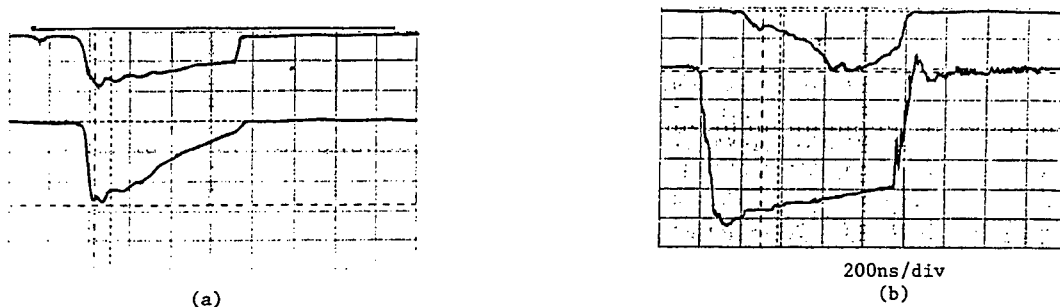


Figure 9 (a) The top trace is the beam modulation envelope. The bottom trace is the output power pulse from the first output extraction section.

Figure 9 (b) The top trace is the output power pulse from the second extraction section. The bottom trace is the voltage applied to the post-acceleration gap.

2.5 Effects of Output Cavity Construction

We have also replaced the standard 100-mesh stainless grids in the output cavity with 50-mesh stainless grids, but have found that they give even shorter pulse durations, with essentially no improvement in peak output power. (The beam kinetic energy in the output section is sufficiently high that the electrons are not stopped by one mil of stainless steel; this is not the case for the grids in the modulating cavity.)

In a recent set of experiments we simply removed the stainless mesh grids from their holders on the entrance and exit sides of the first two-cavity extractor, leaving the center grid in place (to ensure no crosstalk between the two cavities). The resulting output pulse is compared with that obtained with the 100-mesh stainless grids in tact in Figure 10 (a) and (b). The peak amplitude without the grids decreased significantly, but the output pulse was much wider. We subsequently increased the voltage until we obtained an output pulse which had nominally the same peak amplitude as that of Figure 10 (a). This pulse is shown in Figure 10 (c); it clearly has a longer duration than that of Figure 10 (a).

We next replaced the grid holders with plates having a smaller aperture (1.75" dia). Output pulses are shown in Figure 10 (d). Note that the peak power for the same voltage is comparable with the aperture plates replacing the grids, and the pulse durations are significantly longer also. However, as the voltage was raised, the pulse shortening returned, as shown in Figure 10 (e). As the final test in this series, we replaced the grid between the two output cavities with a 1.75" aperture plate, also. With this configuration we were able to increase the charge voltage to 38 kV (about 740 kV), and after some conditioning, we obtained the traces shown in Figure 11. There is no apparent pulse shortening. Although the interaction efficiency with the aperture plates was somewhat decreased, reducing the peak power to about 150 MW, the lack of pulse shortening permitted an extracted energy per pulse of about 120 joules from the first extraction section alone. By implementing this strategy on the second extraction section as well, we were able to obtain a maximum energy per pulse of about 250 joules with a peak output power of about 350 MW at a charge voltage of 40 kV. This represented an improvement in energy per pulse of about a factor of two above our previous best results using our 1.3 GHz tube.

2.7 Repetition Rate Effects

We have operated high-peak-power Reltron tubes in a repetitive mode using PFN-Marx and PFN-transformer pulser configurations at lower voltages (200 kV), and therefore lower rf power (20 MW). At repetition rates up to a few tens of Hz, with voltage pulse durations of $\leq 2 \mu\text{sec}$, we observed rapid tube conditioning, including improved power and pulse duration over the full voltage pulse, provided that the tube pressure did not exceed about 1×10^{-4} torr. If the pressure reached this level, the microwave pulses virtually disappeared in a few tens of shots. In addition, we have operated a sealed Reltron tube which had been baked at a low temperature (200 °C) for a few hours. Although the background pressure was good (1×10^{-7} torr), at repetition rates of a few Hz, rf pulse durations over the full voltage pulse could not be obtained. However, when the repetition rate was increased above about 10 Hz, the output pulses rapidly broadened until rf pulse durations equal to the duration of the voltage pulse (about $2 \mu\text{sec}$.) were achieved. Decreasing the repetition rate again resulted in pulse shortening. This behavior persisted for many days of operation.

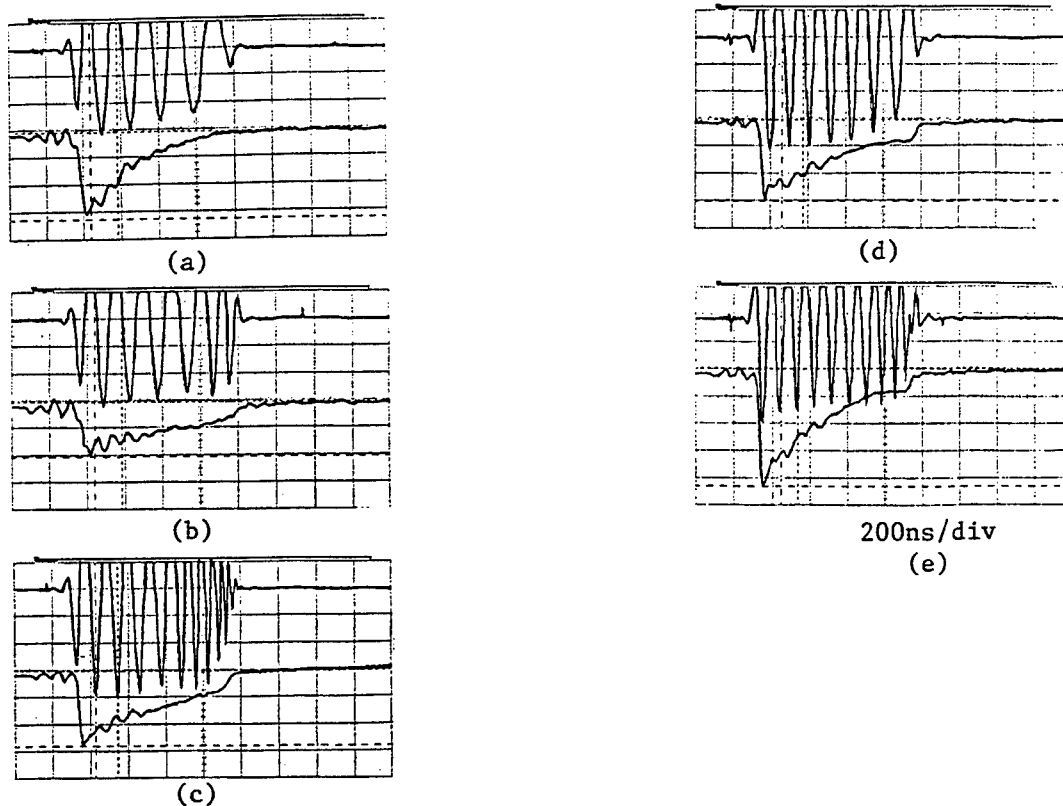


Figure 10 Effects of grid removal on the output power pulse. In (a) through (e) the top trace is the IF signal and the bottom trace is the power pulse from the first of two extraction sections, each of which had two output cavities. (a) Typical output power pulse using 100-mesh grids at a charge voltage of 32 kV. (b) Output power pulse obtained at 32 kV with the entrance and exit grids removed. (c) Output power pulse obtained at 38 kV with the entrance and exit grids removed. (d) Power pulse obtained at 32 kV, with 1.75" aperture plates replacing the entrance and exit grids. (e) Power pulse obtained at 38kV, with 1.75" aperture plates replacing the entrance and exit grids.

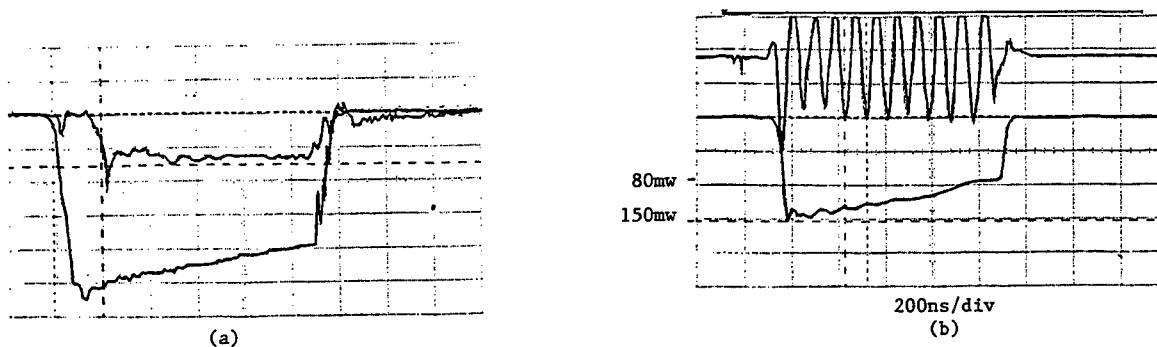


Figure 11. Waveforms from our 1.3-GHz tube at 38 kV charge voltage and 1.2-GHz operating frequency. (a) The top trace is the envelope of the modulated beam current; the bottom trace is the voltage applied to the accelerating gap (about 740 kV). (b) The top trace is the IF signal; the bottom trace is the output power pulse from the first extraction section with all grids replaced by 1.75" aperture plates. The pulse duration exceeds 900 ns, and pulse shortening is not apparent.

3. DISCUSSION

For the parameter ranges in which we have operated our high-peak-power Reltron tubes our experimental observations related to pulse-shortening can be summarized as follows:

1. Anode-cathode gap closure is not a limiting factor. Rather, the pulse shortening that we observe is usually the result of cessation of beam modulation (for our S-band tubes), or "breakdown" in the output cavities (our L-band tubes).
2. Conditioning occurs in both modulation and output cavities. Improved operation is observed with better vacuum, and continuous pumping improves performance, even if there is little improvement in the pressure. Reliable operation ceases if the pressure approaches 2×10^{-4} torr. In one experiment, operation at ≥ 10 Hz dramatically improved the pulse duration.
3. Processes which liberate gas or particles in the vicinity of the modulating cavity, such as arcing, or flexing of the idler bellows in an earlier tube design, often cause shorter pulses and erratic behavior until the surfaces are reconditioned.
4. During modulating cavity conditioning, chirping to higher frequency usually precedes cessation of beam modulation.
5. Grids with higher transparency generally worsen the pulse shortening problem, both in the modulating cavity and in the output cavities. Grids with lower transparency in the modulating cavity decrease the output power.
6. Replacing the grids with apertures in the L-band output cavities eliminated pulse shortening for pulse durations of nearly one microsecond. The interaction efficiency decreased but the energy per pulse improved by about a factor of two.

We believe these observations are the result of gas liberation and ionization in the strong rf electric fields of the modulating and output cavities. Anode-cathode closure is not an issue, and electron interactions with the grids cannot be the controlling mechanism, because lower transparency grids give longer modulation pulses. We first summarize the theory of electrode breakdown for "dirty" electrodes. We then discuss our experimental observations in light of this theory.

3.1 Summary of Electrode Breakdown Theory

It is observed that electrodes formed from ultra-clean metal surfaces that are processed by heating and field desorption in ultra-high vacuum (10^{-8} torr) at temperatures above 1000°C can support electric fields of up to 10 MV/cm without breakdown.⁸ In contrast, bare metal electrodes which are handled in air, cleaned by modest means, and pumped to moderate vacuum pressures (10^{-5} torr) for a short time (few hours) are observed to undergo electric field breakdown processes at electric field intensities of 100 kV/cm.⁹ In the latter case, the electrode surfaces are coated by the natural oxide ($>1\text{ nm}$), by adsorbate layers ($>1\text{ nm}$) and by dust (microparticles larger than 1 micron). For porous oxides of steel and especially aluminum, the larger effective surface area permits large quantities of water and hydrocarbon adsorbates. Thus, typical steel and aluminum electrodes are coated by oxides (5 nm), by adsorbates (10 nm), and by dust. The bonding of the oxygen in the oxides is electronic in nature and so strong that at room temperature an improved vacuum has little effect. Adsorbates are bonded more weakly by definition, so that baking at 300°C will significantly reduce their amount.

All field limitations are due to the transfer of electric field energy to the kinetic energy of electrons and ions. This transfer is dominated by electrons because of their small mass. The generally accepted theory for the observed electric field limitations for breakdown in the case of "dirty" surfaces contains the following elements:⁹ (1) Local electric field enhancement at dust particles or microscopic protrusions gives rise to electron field emission. (2) These electrons are accelerated in the applied field and impact other surfaces, heating these surfaces and generating secondary electrons and photons. (3) These processes result in gas desorption via electronic excitations. (4) The desorbed gas is collisionally ionized. (5) The free electrons and ions are accelerated, absorbing more energy, and causing more gas desorption, more plasma formation, etc., leading to breakdown. The conditioning that is observed using such electrodes is usually attributed to the removal of contaminants (dust) and microscopic protrusions by explosive vaporization, the formation of unsaturated, polymerized hydrocarbon layers, and the desorption of adsorbates. Vaporization of dust and microscopic protrusions reduces the amount of primary electron sources; the conditioned, polymerized hydrocarbon layers have large inelastic electron scattering cross sections which reduce the amount of field emission and secondary electron emission that can occur; and desorption of adsorbates reduces the quantity of gas that can be liberated and ionized.

3.2 Interpretation of Reltron Experimental Observations

We believe that these processes also occur in the modulating cavity and the output cavities of our Reltron tubes, with the primary difference being the alternating polarity of the electric fields. In our cavities cathodes and anodes do not exist; all surfaces are subject to both electron and positive ion impact, although the possible energy gain of ions is limited.

We first calculate the approximate electric field strengths which characterize the modulating cavity and the output cavities of Reltron tubes. The modulating cavity of a Reltron tube is designed to optimize the modulated electron beam current. This condition occurs for a cavity grid spacing approximately given by⁶ $d = v/(3.2 f)$, and an electric field $E_{mc} = V/d$, with $V = 0.8$ times the voltage applied to the gun. The variation of E_{mc} with gun voltage is shown in Figure 12 for $f = 1$ GHz and $f = 3$ GHz. At 1 GHz the average electric fields in the modulating cavity are quite low; however, since the average field strength scales inversely with frequency, the average field stress approaches 100 kV/cm for high-power S-band operation; it was about 36 kV/cm for our low-power S-band Reltron experiment.

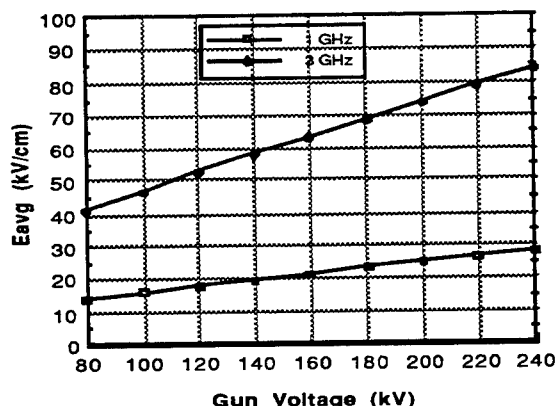


Figure 12. The average electric field in the modulating cavity vs the electron gun voltage for optimized Reltron modulating cavity designs.

The average electric fields in the output cavities can be estimated by first dividing the total applied voltage by the number of output cavities.⁷ The grid spacing is approximately equal to one-fourth the maximum waveguide dimension appropriate for the frequency range of the tube. For the frequency range of 1-1.5 GHz, using WR770 for example, this dimension is 7.7 inches. Assuming four such output cavities and a total tube voltage of 1 MV, then the average field stress in an output cavity is approximately 50 kV/cm, or about twice the field stress in the corresponding modulating cavity. In a similarly constructed S-band output section the average field stress is therefore about 150 kV/cm.

If grids are used we must also consider the field enhancement on the grid wires. An approximate estimate of the field enhancement can be obtained by dividing a unit area by the total surface area of the grid wires onto which electric field lines can terminate. A grid wire of radius r and unit length will have a surface area of $2\pi r$, and roughly half of this area is exposed to the field. Since there are n wires per unit length in both the horizontal and vertical directions, the total grid wire surface area is $2n(\pi r)$, and the field enhancement FE factor is estimated as $FE = [2n(\pi r)]^{-1}$. For our 50-mesh grids $FE = 6.4$, and for our 100-mesh grids, $FE = 3.2$. Therefore, for 100-mesh grids, the peak electric fields in the modulating cavity of our L-band tube will never exceed 100 kV/cm, but will approach 150 kV/cm in the output cavity. On the other hand, 50-mesh grids in L-band will give fields in the range of 150 kV/cm in the modulating cavity and 300 kV/cm in the output cavity. Increasing the frequency by a factor of three increases these field stresses by three, also. For example, 50-mesh grids in the modulating cavity of our S-band tube will result in 450 kV/cm fields under high-power conditions.

From the electric field estimates, it is apparent that the field levels in the cavities of our high-peak-power Reltron tubes are comparable to those in "dirty" electrode breakdown experiments, and the operating vacuum pressure and Reltron handling and construction techniques are also similar. We therefore expect the interior vacuum surfaces to be coated by natural oxides, adsorbates, and dust. During initial pulsing at low voltage, dust particles and microprotrusions are removed by explosive vaporization, and adsorbates are liberated through various surface heating processes, eliminating field emission sites, and reducing the amount of loosely adsorbed gas on the cavity surfaces. Continued pumping and pulsing at successively higher voltage levels further removes contaminants and adsorbed gas, and forms polymerized hydrocarbon layers which further reduce the amount of field emission and secondary electron emission. After a few hours of pulsing at repetition rates of no more than one per minute (limited by the Marx pulser), the modulating cavity surfaces become sufficiently well conditioned that beam modulation pulses of up to one microsecond in duration can be sustained at enhanced electric field strengths of about 150 kV/cm on the grid wires of the modulating cavities. However, such conditioning is not fully observed in the output cavities at similar field levels, although improvements do occur. Apparently, the higher beam current density (area convergence ratio of approximately 16) in the output region prevents conditioning from fully occurring because of direct electron beam interaction with the grids. In our high power S-band tube, full conditioning of the

modulating cavity does not occur. Apparently, the enhanced field strength (450 kV/cm) causes field emission from the grid wires, even after dust and microprotrusions have been vaporized. Long pulses can be realized only for very much reduced power output (10-20 MW), when the modulating cavity field stresses are reduced to the 150 kV/cm level. The observation of severe pulse shortening following an arc is explained by the evolution of significant quantities of gas and particulates during the arc, which loosely adhere to the cavity surfaces. With subsequent pulsing, this material is liberated from the surfaces, resulting in reconditioning.

We speculate that the frequency chirp often observed during the conditioning procedure is the result of changing beam loading conditions due to an expanding plasma in the modulating cavity. To a good approximation, the operating frequency f of a Reltron tube is given by¹⁰

$$f = f_0 [1 + (2 Q_L \tan \theta_g)^{-1}] \quad (1)$$

in which f_0 is the unloaded frequency of the unstable $\pi/2$ mode of the modulating cavity, Q_L is the loaded cavity quality factor, and $\theta_g = 2\pi f_0 d/v$ is the modulating cavity transit angle. d is the spacing between grids, and v is the electron velocity imparted by the gun voltage. For optimized operation, $d = v/(3.2 f_0)$, implying that $\theta_g = \text{const} = 2$, and $\tan \theta_g = -2.2$. When the loaded quality factor parameter is evaluated, the result is a negative frequency shift from the unloaded cavity frequency of typically 1.5%, e.g., from 1 GHz to 985 MHz.

Now suppose there is an expanding plasma on the cavity grids. Then the effective grid spacing d will decrease with time. A 10% decrease in d will cause $\tan \theta_g$ to become more negative (-4.3), resulting in reduced beam loading and an apparent increase in operating frequency, e.g., to 992 MHz for the above example. A 20% decrease in d would nearly eliminate the beam loading effect, but would also quench the instability because of the detuning.

In the case of the repetitive pulse experiment, only a single output section was used. A rough estimate of the electric fields at the 10 MW level again indicated a field strength of about 100 kV/cm. With some enhancement on the nose cones of the apertures, the peak stress probably exceeded 150 kV/cm. Consequently, at low repetition rates field emission led to gas evolution, and the subsequent ionization of this gas quenched the output pulse. As the repetition rate was increased, the output pulses lengthened substantially, although the peak power remained unchanged. The only significant effect of the increased repetition rate was that the temperature on the cavity surfaces became higher. Apparently, at low repetition rate the cavity surfaces cooled rapidly enough that they effectively gettered gas liberated during previous pulses. As the temperature increased, however, the gettering action was impeded, and there was much less loosely adsorbed gas on the surfaces. The minimal field emission was not enough to sustain the avalanche process.

4. REDUCING PULSE-SHORTENING IN RELTRON TUBES

Although our present high-peak-power Reltron tubes suffer from pulse-shortening phenomena, they also have several attractive features, including high power (several hundred MW), good efficiency (40-50%), and good pulse duration and energy per pulse (> 250 joules/pulse in L-band). They also feature a good tuning bandwidth, and excellent frequency stability during the pulse. Finally, they are affordable and nearly indestructible. Routine maintenance operations are routine, relatively simple procedures. An external magnetic field is not necessary, and the vacuum system requirements are modest. While some applications necessarily dictate the use of alternate design and construction techniques, for other applications the affordability and robustness of the present designs are so important that it is useful to consider methods for reducing the impact of pulse shortening. In this section we first examine this question, turning later to questions of implementing more conventional microwave tube technologies into our Reltron tube designs.

Based on our present data base, grids must be eliminated from all output cavities, regardless of frequency. Also, the enhanced electric field stress must be kept below 150 kV/cm. While this is relatively easy to accomplish in L-band using grids at nominal operating parameter levels of 1 MV total voltage and 500 MW of output power, it can only be achieved in S-band with a significant decrease in applied voltage (200 kV), and a corresponding decrease in output power (to tens of MW). To improve performance at the higher frequencies it is necessary to decrease the enhanced electric field stress by either reducing the grid transparency, or by eliminating the grids altogether. Since the first solution results in unacceptable beam interception, we have examined configurations which use a spherical gun design to focus the beam into a gridless modulating cavity. Focusing of the beam after bunching is provided by the accelerating gap fields and the self-magnetic field of the beam as it passes through the focusing grid. The output cavities are also gridless. The field stresses on the nose cones of the modulating cavity apertures are kept below 150 kV/cm. With this approach we believe it should

be possible to achieve 500 joules/pulse in L-band with pulse durations in the range of 1-2 microseconds, and over 100 joules per pulse in S-band with pulse durations of approximately 500 ns.

To realize further improvements, we must incorporate conventional microwave tube technologies into our high-peak-power designs. For example, our high-average-power designs¹¹ already incorporate thermionic cathodes, ceramic insulators, brazed construction, high-temperature (500°C) bakeout, and extensive high-voltage and rf conditioning at hard vacuum (10^{-8} - 10^{-7} torr). The intent of these operations is to eliminate dust and contaminants, eliminate adsorbed gas, form a polymerized hydrocarbon layers, and eliminate significant sources of additional outgassing. A high-peak-power L-band Reltron tube designed in this fashion is shown in Figure 13. We believe this design has the potential for achieving up to 5 kJ per pulse at pulse repetition rates in excess of 100 Hz for burst durations of several seconds.

5. CONCLUSIONS

Pulse-shortening has been observed in all high power microwave (>100 MW) tubes that have attempted to extend the useful power pulse beyond 100 ns; the energy per pulse has been limited to typically 100 joules. While Titan's L-band Reltron tubes have achieved 250 joules/pulse, they too suffer from pulse-shortening phenomena. Our data suggest that a significant lengthening of the rf pulses can be achieved by holding the enhanced electric field stresses below 150 kV/cm. To obtain further improvements we believe that it is necessary to incorporate conventional microwave tube materials and construction techniques into our high-power tube designs. We have developed preliminary designs for such Reltron tubes.

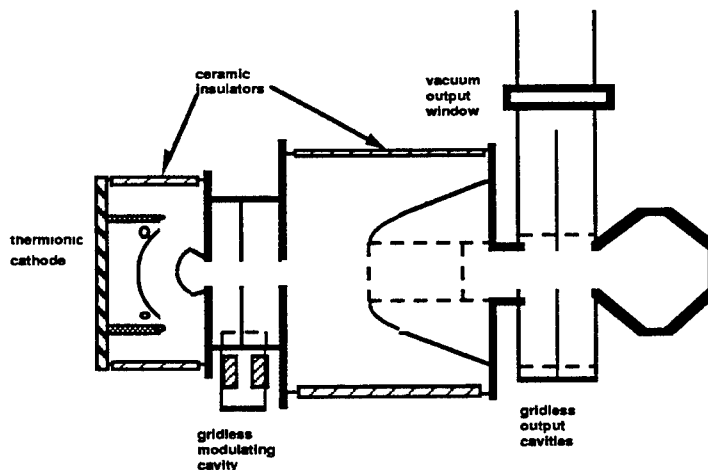


Figure 13. Schematic diagram of a Reltron tube designed for high energy per pulse. All grids have been eliminated from the regions of high rf fields. The tube is bakable, incorporating a thermionic cathode, ceramic insulators, and a ceramic vacuum window.

6. REFERENCES

1. S. Ashby, R. R. Smith, N. Aiello, J. N. Benford, N. Cooksey, D. V. Drury, B. D. Harteneck, J. S. Levine, P. Sincerny, L. Thompson, and L. Schlitt, IEEE Trans. Plasma Sci., 20, 344-350, 1992.
2. M. V. Fazio, W. B. Haynes, B. E. Carlsten, and R. M. Stringfield, IEEE Trans. Plasma Sci., 22, 740-749, 1994.
3. K. J. Hendricks, P. D. Coleman, R. W. Lemke, M. J. Arman, and L. Bowers, Phys. Rev. Lett., 76, 154-157, 1996.
4. R. B. Miller, C. A. Muehlenweg, K. W. Habiger, J. R. Smith, and D. A. Shiffler, Intense Microwave Pulses II, Proc. SPIE, 2154, 99-109, 1994.
5. R. B. Miller, US Patent No. 5101168, 1992.
6. R. B. Miller, W. F. McCullough, K. T. Lancaster, and C. A. Muehlenweg, IEEE Trans. Plasma Sci., 20, 332-343, 1992.
7. R. B. Miller, C. A. Muehlenweg, K. W. Habiger, and J. Clifford, IEEE Trans. Plasma Sci., 22, 701-705, 1994.
8. R. J. Noer, Appl. Phys., A28, 1-25, 1982.
9. J. Halbritter, IEEE Trans. Elect. Sci., EI-20, 671-681, 1985.
10. R. B. Miller, unpublished, 1996.
11. R. B. Miller, K. W. Habiger, W. R. Beggs, Jr., and J. C. Clifford, Intense Microwave Pulses III, Proc. SPIE, 1995.

A Model of Injection Locked Relativistic Klystron Oscillator*

J.W. Luginsland, Y.Y. Lau, K. Hendricks¹, and P. D. Coleman²

Intense Energy Interaction Laboratory

Department of Nuclear Engineering

The University of Michigan

Ann Arbor, MI 48109-2104

Abstract

By the use of a simple model, we explicitly incorporate the coupling between the driver cavity and the booster cavity in a relativistic klystron amplifier (RKA). We show that this RKA configuration may turn into an injection locked oscillator only when the beam current is sufficiently high. Other features revealed by this model include: the downshifted frequency mode ("0" mode) is unstable whereas the upshifted frequency mode ("π" mode) is stable; the growth rate of the "0" mode is relatively mild so that the oscillation can start only in an injection locked mode; the oscillation does not require the presence of reflected electrons; and the separation of the cavities must be sufficiently short. These, and other features, are found to be in qualitative agreement with the recent experiments on the injection locked relativistic klystron oscillator (RKO) that were conducted at the Phillips Laboratory.

*Supported by SDIO/BMD/ONR and MURI managed by AFOSR through Texas Tech University

¹ Permanent address: Phillips Laboratory, Kirtland AFB, NM 87117-5776

² Permanent address: Sandia National Laboratory, Albuquerque, NM 87185

I. Introduction

Current modulation of an intense relativistic electron beam (IREB) remains a challenging and active research problem [1] with applications to high power microwave (HPM) production [2-4], and to some accelerator schemes that use an IREB as a driver [5,6]. Recently, a series of experiments were performed at Phillips Laboratory [7], where an IREB was placed in a relativistic klystron amplifier (RKA) geometry [2-4], with the driver and booster cavities sufficiently close to couple to one another. This cavity coupling caused the structure to oscillate at a frequency different from the driver frequency. This oscillation persisted after the external drive was shut off, but its appearance has always required an input drive and a sufficiently large DC current. Thus, the device operated as an injection-locked relativistic klystron oscillator (RKO). It provided 40% to 60% of current modulation on the DC beam when the gap separation is on the order of only 10 cm, as opposed to 30 cm in a typical RKA geometry with similar frequency (at 1.3 GHz), beam current and drift tube diameter. Another interesting feature is that virtual cathodes did not seem to have been formed for the operation of this RKO. The feedback, therefore, was due only to the electromagnetic coupling among the two cavities, and not to the reflected electrons as in previous works [8].

In this paper, we present a simple analytic model, explicitly including the effect of cavity coupling. The results of this model demonstrate several features that were observed in the RKO experiments mentioned above. They are summarized in the abstract and are discussed further below.

II. Model

Consider an annular intense relativistic electron beam (IREB) with radius r_b propagating in a drift tube of radius r_w and passing by two cavities [Fig. 1]. The first cavity, with gap voltage $A(t)$, is driven by an external source. The second cavity, with gap voltage $B(t)$ and located at a distance d downstream, is driven by the beam. When d is sufficiently small, there would be coupling between A and B even if the drift tube is cutoff to the frequency of operation. In the absence of the beam, the steady state voltages A and B are either in phase ("0" mode) or 180° out of phase ("pi" mode). That is, there is no phase delay between the two cavities, when the beam is absent, because the drift tube is cutoff [9].

To study this effect, we start by writing down the circuit equations of the two cavities, each having a natural frequency ω_o , and quality factor Q . The evolution of the gap voltages A and B is governed by

$$\left[\frac{d^2}{dt^2} + \frac{\omega_o}{Q} \frac{d}{dt} + \omega_o^2 \right] A(t) = \omega_o^2 C B(t) , \quad (1)$$

$$\left[\frac{d^2}{dt^2} + \frac{\omega_o}{Q} \frac{d}{dt} + \omega_o^2 \right] B(t) = -j\omega_o^2 Z I + \omega_o^2 C A(t) , \quad (2)$$

where C ($\ll 1$) is the dimensionless, real constant measuring the degree of coupling between the two gaps when the beam is absent [9], and Z is defined such that ZQ is the impedance (in Ohms) at the second gap. Equation (1) expresses the excitation of the gap voltage A by the gap voltage B as a result of cavity coupling C . Since we are concentrating on the RKO operation, we ignore the external rf drive on the gap voltage A , and we envision the effect of this external drive to enter only as the initial condition on A , at the instant when the external drive is shut off. Equation (2)

describes the excitation of the second gap by the rf current, I , and by the first gap voltage A because of the cavity coupling.

As in the usual klystron theory, the rf current I at the second gap is due to the voltage at the first gap. In the case of an IREB of DC current I_0 , it is given by [1]

$$I = j \left(\frac{A}{R} \right) \sin(k_p d) e^{-j\theta} . \quad (3)$$

In Eq. (3), R is the rf beam impedance (in Ohms), $\theta = \omega d / \beta c$ is the phase delay of the beam mode, and

$$k_p d = \frac{\sqrt{\alpha}}{\beta^2 \gamma} \left(\frac{\omega d}{c} \right) , \quad R = \frac{511 \text{ kV}}{I_0} \gamma^2 \beta \sqrt{\alpha} , \quad (4)$$

$$\alpha = \frac{I_0}{I_s \beta \gamma^3} , \quad I_s = 8.5 \text{ kA} / \ln(r_w / r_b) ,$$

where β and γ are the usual relativistic mass factors associated with the DC beam, and c is the speed of light. Upon inserting Eq. (3) into Eq. (2), we obtain two equations (1), (2) in two unknowns A , B . Assuming $\exp(j\omega t)$ dependence for both A and B , we obtain the dispersion relation for ω which may easily be solved to yield

$$\omega = \omega_0 \left[1 + \frac{j}{2Q} \pm \frac{C}{2} \sqrt{1 + \frac{Z}{CR} \sin(k_p d) e^{-j\theta}} \right] . \quad (5)$$

Equation (5) gives the temporal growth rate of the coupled-cavity RKO in terms of the circuit parameters (ω_0 , Q , C , d , Z) and the beam parameters (R , k_p , θ). In the next section, we present

the numerical results using parameters similar to those in the experiments [7]. We shall also describe the interesting features revealed by the dispersion relation (5).

III. Numerical Results

We shall first establish the numerical values of the parameters from the experiments [7]. In the cold tests, it was observed that when the two cavities are coupled, there was a frequency shift of ± 7 MHz from the natural frequency of 1.27 GHz that was measured for an isolated cavity. Thus, when the beam is absent, $R \rightarrow \infty$ from Eq. (4) and we obtain from Eq. (5) the cold tube coupled-cavity natural frequencies

$$\omega = \omega_0 \left[1 + \frac{j}{2Q} \pm \frac{C}{2} \right], \quad (6)$$

with $\omega_0 = 2\pi \times 1.27$ GHz and $\omega_0 C/2 = 2\pi \times 7$ MHz. This yields the coupling constant $C = 0.0112$. In Eq. (6), the (+) sign corresponds to the " π " mode and the (-) sign corresponds to the "0" mode. Substitution of Eq. (6) into Eq. (1), in which d/dt is replaced by $j\omega$, shows that the gap voltages A and B are 180° out of phase for the " π " mode, and that they are in phase for the "0" mode.

The value of Q to be used is uncertain. There is the cold tube value, in excess of 400 according to measurements [7], and there is the substantially reduced value of the beam-loaded Q , which depends on the beam current. Let us arbitrarily set the beam-loaded Q to be 100, say. The value of Z may be estimated from Eq. (2) which shows that, in the absence of cavity coupling [i.e., $C = 0$], the magnitude of the gap voltage B equals to QZ times the magnitude of the rf current I there. From this definition of Z , we estimate that $Z = 1.6 \Omega$ when Q is assigned to be 100. The

beam parameters R , k_p , and θ , are determined as follows. We set the beam voltage at 400 keV, beam current $I_0 = 12$ kA, with mean beam radius $r_b = 6.85$ cm in a drift tube of radius $r_w = 7.65$ cm. Using these parameters, we find $\gamma = 1.783$, $\beta = 0.828$, $I_s = 77$ kA, $\alpha = 0.033$, $k_p = 0.0398$ cm⁻¹ and $R = 20.4$ Ω . If we set the gap separation at $d = 11$ cm, then $k_p d = 0.437$ and $\theta = 3.55$. Using these parameters in Eq. (5), we find

$$\omega = \omega_0(1.0023 + 0.0127j) \quad \text{"}\pi\text{" mode} \quad (7a)$$

$$\omega = \omega_0(0.9976 - 0.00266j) \quad \text{"0" mode} \quad (7b)$$

Equations (7a) and (7b) show the following.

- A. The " π " mode is stable and the "0" mode is unstable.
- B. For the "0" mode, there is a downshift in frequency from $f_0 = \omega_0/2\pi = 1.27$ GHz, by the amount of 1.27 GHz $\times (1 - 0.9976) = 3.05$ MHz. That is, the mode is upshifted from the cold-tube "0" mode frequency by the amount of 7 MHz - 3.05 MHz = 3.95 MHz, and this upshift is beam induced.
- C. The growth of the "0" mode, according to Eq. (7b), is relatively mild. The total number of e-folds in a time $\tau = 100$ ns is $\omega_i \tau = 2.12$. This mild growth implies that, for an IREB whose pulselength is on the order of 100 ns, the manifestation of RKO behavior may require an external drive so that there is already a significant rf gap voltage by the time this external rf drive is shut off.
- D. The "0" mode is unstable only if the DC beam current is sufficiently high. This is obvious since in the limit of zero current, the mode is damped [cf. Eq. (6)]. Using the parameters given in the paragraph preceeding Eq. (7a), we find that the threshold DC beam current for the onset of growth for the "0" mode is 7.2 kA. Similar levels of threshold current were observed in the experiments.

E. Upon inserting Eq. (7b) into Eq. (1), in which d/dt is replaced by $j\omega$, we find the ratio of the gap voltage to be $|B / A| = 1.43$ using the parameters in the paragraph preceeding Eq (7a).

This number is in reasonable agreement with experimental observations.

Points A - E are features revealed by the experiments [7]. We wish to add the following points which also seem to corroborate the experimental results.

- F. The instability does not require the formation of a virtual cathode. That is, there is no need to invoke reflected electrons to provide the feedback that is usually required for oscillation [8].
- G. The cavity separation must be sufficiently short to provide appreciable coupling between the two cavities.
- H. The operation of this injection-locked RKO is restricted only to a narrow range of gap separation, d , once the other circuit parameters, beam parameters, and the level of rf drive are fixed. There are three reasons for this: (i) The cavity coupling diminishes rapidly with increasing d , as the drift tube is below cutoff. (ii) If d is too small, there is little buildup in the current modulation from the driver cavity to the second one downstream. (iii) The ballistic phase θ that appears in Eq. (5) is proportional to d . Note that (i) is quantified in Eq. (5) through the coupling constant C and (ii) is quantified in Eq. (5) through the factor $\sin(k_p d)$.

IV. Concluding Remarks

While we are able to construct a relatively simple model which appears to be capable of explaining many features observed in the recent injection-locked RKO experiments, it must be kept in mind that there are many uncertainties in the model. Chief among them are the values of Q and the coupling constant C . The beam-loaded Q depends on the current modulation, which depends

not only on the DC current, but also on the level of rf drive and the gap separation d . The value of C is a sensitive function of gap separation, and the one we use in this paper is inferred from the cold tube measurements. There is also uncertainty in the value of the gap impedance Z because the "gap transit time factor", which is significantly affected by the DC space charge effects associated with an IREB, will make the determination of Z far from a trivial matter [10]. Unfortunately, the *conceptually* simple mechanism proposed in this paper may not be easy to verify in particle-in-cell codes. The main reason is that the mild growth envisioned would require a long simulation time. To shorten the simulation time by raising the beam current runs into the possibility of triggering virtual cathode formation. In addition, there may be marked difference between the "numerical Q ", the cold-tube Q , and the hot-tube Q in the experiments. As explained above, our model shows that the threshold current may depend sensitively both on Q and on the gap separation d .

In spite of the great uncertainties in several crucial parameters, we find it remarkable that a reasonable choice of parameters does yield reasonable agreement with observations, based just on the simple analytic model.

V. Acknowledgements

We would like to thank R.M. Gilgenbach, J.P. Holloway, and J.W. Schumer for helpful and stimulating discussions. The support of SDIO/BMD/ONR and AFOSR/MURI is gratefully acknowledged.

References

1. M. Friedman, and V. Serlin, Phys. Rev. Lett. **55**, 2860 (1985); M. Friedman, J. Krall, Y.Y. Lau, and V. Serlin, J. Appl. Phys. **64**, 3353 (1988); M. Friedman et al., Phys. Rev. Lett. **74**, 322 (1995).
2. See, e.g., J. Benford, and J. Swegle, *High Power Microwaves* (Artech House, Norwood, MA, 1992).
3. M. Friedman, J. Krall, Y.Y. Lau, and V. Serlin, Rev. Sci. Instrum. **61**, 171 (1990); Y. Y. Lau, J. Krall, M. Friedman, V. Serlin, IEEE Trans. Plasma Sci. **18**, 553 (1990); M. Friedman and V. Serlin, Proc. SPIE Vol. 1872, p. 2 (1993); M. Friedman et al., Phys. Rev. Lett. **75**, 1214 (1995).
4. G. Bekefi, P. Cateravas, C. Chen and I. Mastovsky, Proc. SPIE Vol. 1872, p. 25 (1993); M.V. Fazio et. al., IEEE Trans. **PS-22**, 740 (1994); J.S. Levine, and B.D. Hartenbeck, Appl. Phys. Lett. **65**, 2133 (1994).
5. M. Friedman, J. Krall, Y.Y. Lau, and V. Serlin, Phys. Rev. Lett. **63**, 2468 (1989).
6. Ya. S. Derbenev, Y.Y. Lau, and R.M. Gilgenbach, Phys. Rev. Lett. **72**, 3025 (1994).
7. K.J. Hendricks et. al., to be published (1995).
8. M. Friedman, V. Serlin, A. Drobot, and L. Seftor, J. Appl. Phys. **56**, 2459 (1984); M. Friedman, V. Serlin, A. Drobot, and A. Modelli, IEEE Trans. **PS-14**, 201 (1986); H. Uhm, IEEE Trans. **PS-22**, 5 (1994).
9. If an electromagnetic wave is allowed to travel between two cavities, there would then be a phase shift between the gap voltages. Models that include this phase delay may be found in D. G. Colombant and Y. Y. Lau, J. Appl. Phys. **72**, 3874 (1992). In the present paper, since the drift tube is cutoff to the electromagnetic waves, a sinusoidal steady state voltage on one gap does not induce a phase shift in the voltage on the other gap, when the beam is absent.
10. D.G. Colombant, and Y.Y. Lau, Phys. Rev. Lett. **64**, 2320 (1990).

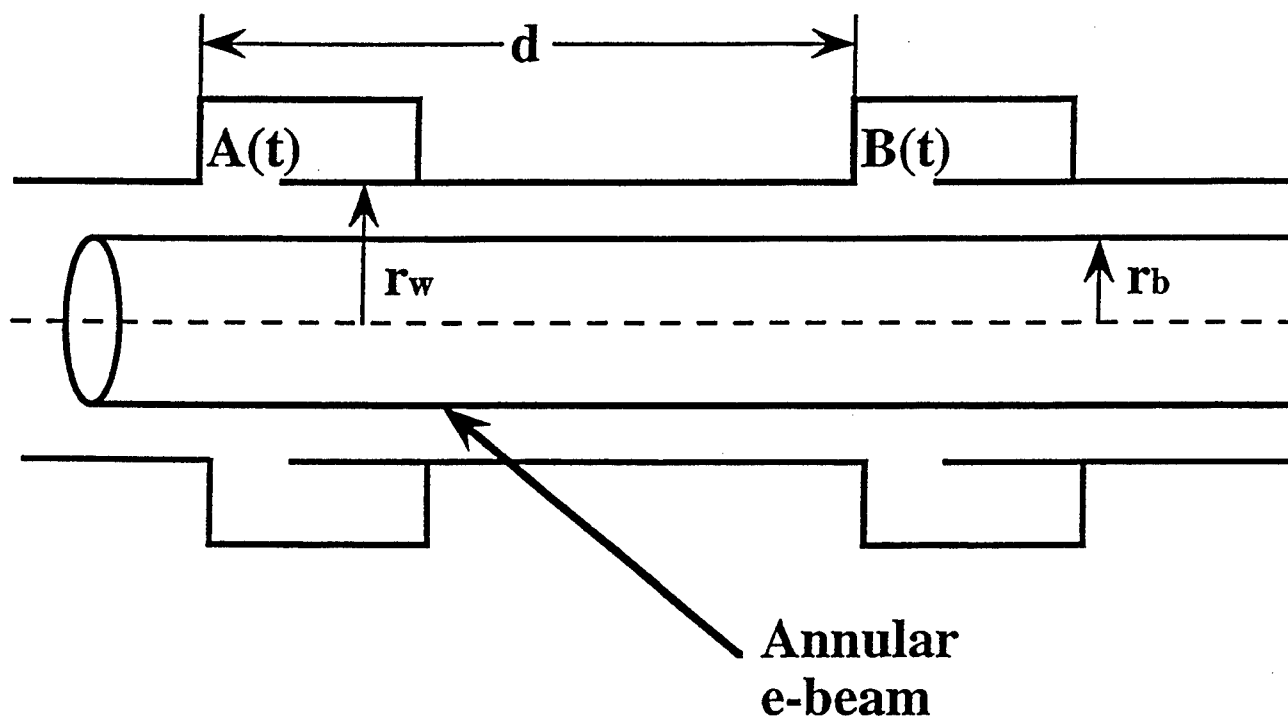


Fig. 1 The model

Investigation of Lower Order Mode Suppression in a High Current, High Voltage Gyro-BWO Experiment

Thomas A. Spencer, Mark D. Stump, Kyle J. Hendricks

The Air Force Phillips Laboratory
PL/WSQN, Bldg. 66071
Narrowband Sources Branch
3550 Aberdeen Ave SE
Kirtland AFB, NM 87117-5776

Ronald M. Gilgenbach

Intense Energy Interaction Laboratory
Nuclear Engin. and Radiological Sciences Dept., Univ. of Michigan
Ann Arbor, MI 48109-2104

ABSTRACT

The Air Force Phillips Laboratory Gyro-BWO experiment is utilizing the RAMBO pulser, with electron beam parameters of: $V_D = 300\text{-}800\text{ kV}$; $I_D = 1\text{-}50\text{ kA}$; pulselength = $1\text{-}3\text{ }\mu\text{s}$. An annular electron beam of $\sim 1\text{-}3\text{ kA}$ is produced by an annular aluminum cathode. The interaction cavity is designed to radiate in the frequency range of $4.2\text{ - }5.5\text{ GHz}$ in a TE_{01} mode. The interaction cavity has a radius of 4.37 cm and a length of 15 cm . Diode and interaction magnetic fields are used together to provide a magnetic compression of the electron beam. C-Band bevel-cut antennas located at the diode end of the experiment are used to extract the backward wave. Experiments have shown evidence of mode competition existing as two different frequency values appearing at the same time. A helical slotted cavity has been designed, in an effort to suppress the TE_{n1} modes, $n \neq 0$. Analysis and numerical simulations from the 3-D code HFSS will be presented, as well as the latest experimental results.

Keywords: Gyrotron, Gyrotron Backward Wave Oscillator, High Power Microwave, Frequency Tunable, Gyro-BWO, Electron Cyclotron Resonance, HFSS, High Frequency Structure Simulator

1. INTRODUCTION

A variety of applications exist, notably high resolution radar, electronic warfare, atmospheric sensors, as well as many others, where both high power and frequency tunability/agility are desirable. The electron cyclotron resonance (ECR) device class answers the frequency tunability problem, in that one may adjust either the applied external magnetic field or the electron voltage and the emitted RF frequency can be shifted either up or down. The main drawback of ECR devices in general is their extreme sensitivity to electron velocity spread¹, thus the necessity of thermal cathodes and the devices being configured as amplifiers. ECR devices being investigated include the standard gyrotron, the peniotron, the cyclotron autoresonance maser (CARM), and other mixed hybrid devices such as the gyro-klystron² and gyro-TWT³. An ECR device that is not as sensitive to electron velocity spread is the Gyrotron-Backward-Wave Oscillator (Gyro-BWO). Gyro-BWOs also tend to be less sensitive to α (the ratio of perpendicular to parallel velocity) spreads, and, since the interaction is located on the negative side of the dispersion curve (see section 2.), a small change in the voltage during any given pulse may not affect the dominant frequency that already exists in the device. Based on this, 'cold-cathode' technology may be employed to produce a

high power oscillator, taking advantage of the backward wave intersection. 'Cold-cathode' technology is necessary to provide the several gigawatt electron beam necessary to produce a high power rf oscillator. Another advantage of the Gyro-BWO device is the fact that no slow-wave structure is needed (as is the case for conventional BWOs), thus giving the device better power handling capabilities.

2. DESIGN

A TE₀₁, 4.2 - 6.0 GHz Gyro-BWO has been designed with the aid of analytical calculations and the computer code MAGIC. The uncoupled dispersion relation⁴ for an electron beam interacting with a waveguide can be obtained by simultaneously solving the waveguide vacuum modes

$$\omega^2 - \omega_{c0}^2 - k_z^2 c^2 = 0 \quad (1)$$

and the beam cyclotron modes,

$$\omega - k_z v_{z0} - s\Omega_r = 0 \quad (2)$$

where ω_{c0} is the cavity cutoff frequency, k_z is the axial wavenumber, c is the speed of light, v_{z0} is the axial velocity of the beam, s is the harmonic number ($s = 1$ is the fundamental mode), and Ω_r is the relativistic cyclotron resonance frequency, $\Omega_r = eB/\gamma m$ where e is the electron charge, B is the magnetic field, γ is the relativistic factor, and m is the mass of the electron. A dispersion curve based on Equations 1 and 2 is shown in Figure 1. The curve is calculated using parameters appropriate for the desired TE₀₁ mode, using a voltage of 400 kV, a magnetic field of 4 kG, a current of 2 kA, a radius of 4.37 cm, and an α (the ratio of perpendicular velocity to parallel velocity) of 0.7.

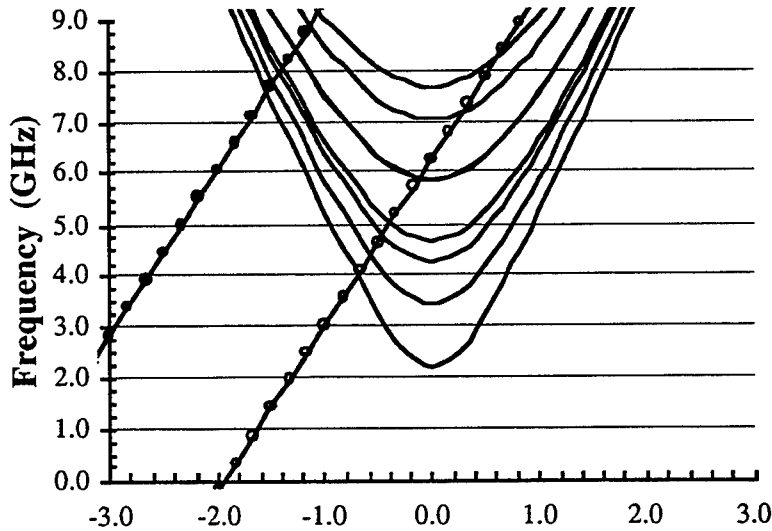


Figure 1. Dispersion curve showing the backward wave intersections for the fundamental (line with open circles) and second harmonics (line with solid circles) for (solid lines from bottom to top) TE₁₁, TE₂₁, TE₀₁, TE₃₁, TE₄₁ (TE₁₂), TE₅₁, and TE₀₂. Note that the TE₄₁ and TE₁₂ are indistinguishable, since the Bessel zeros are 5.3176 and 5.3314, respectively. Parameters: $V=400$ kV, $I = 2$ kA, $B = 4$ kG, $\alpha = 0.7$.

Figure 2 shows the experimental configuration. The electron beam is generated from the diode in a field immersed cathode (the magnetic field is provided by the dc diode coils, variable from 200-2000 G), propagates downstream where it is adiabatically compressed and focused into the interaction cavity by a pair of pulsed Helmholtz configured magnets (variable, from 1-7 kG). By choosing the correct magnetic field obtained from a dispersion curve diagram, an electromagnetic field grows from noise and propagates anti-parallel to the electron beam, and is extracted using one or two C-Band bevel cut waveguide antennas located upstream at the diode end of the experiment. The RF wave is then split using waveguide directional couplers and stripline power dividers. The RF is sent through several different frequency filters with passband of ± 100 MHz. The signal is converted to a voltage signal by using crystal diode detectors, and sent to fast oscilloscopes. All waveguide pieces, cables, power dividers, attenuators and crystal diode detectors are calibrated over a wide frequency range (3.0 - 6.0 GHz) to allow for an accurate extracted power measurement. The electron beam continues down the drift tube and is directed into the sides of the drift tube by a pair of permanent magnets. Rogowski coils are located at both the upstream and downstream end of the interaction cavity to measure the entrance and exit electron beam current. The pulse power machine used was the RAMBO pulser, with maximum diode parameters of 800 kV, 10 Ω , and a pulselength of 1 - 3 microseconds (the pulser is configured as a rundown Marx).

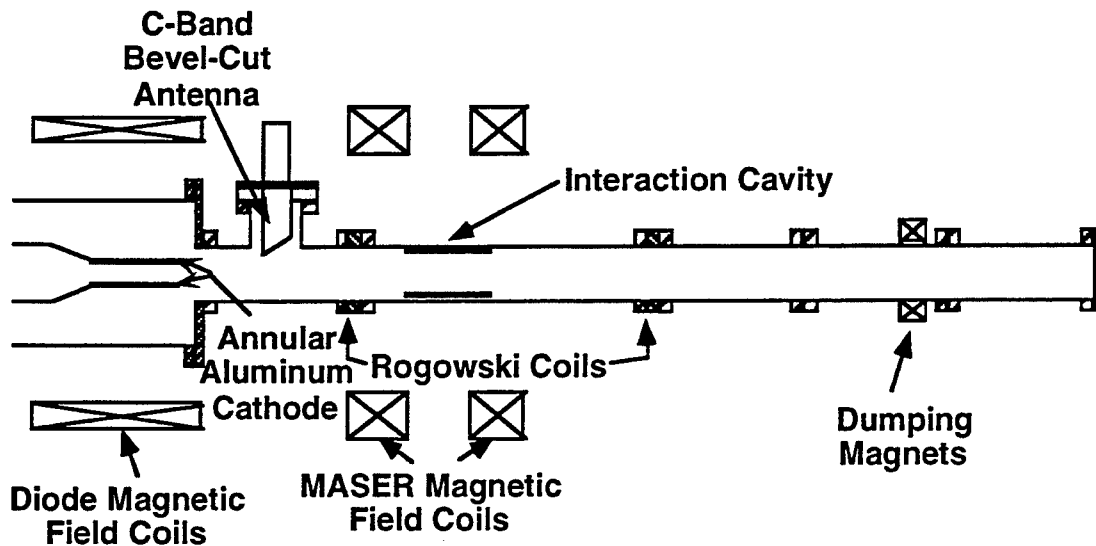


Figure 2. The experimental configuration of the Gyro-BWO device.

3. PAST MEASUREMENTS AND FURTHER INVESTIGATION

Frequency spectrum diagnostics (in particular, a series of narrow-band frequency filters that cover the range of 4.0 - 6.5 GHz, with passband of center frequency ± 100 MHz) have been used to obtain a detailed frequency spectrum measurement for a variety of magnetic fields. Many frequencies exist throughout the voltage pulse, some simultaneously, indicating mode competition. Experimental data has shown two frequencies existing simultaneously, at 4.0 and 5.0 GHz, as demonstrated in Figure 3. Based on dispersion curve calculations, one can show that TE_{11} , TE_{21} , and TE_{01} can exist simultaneously over 4.0 - 5.5 GHz for the given parameters, as well as many other higher order modes (see Figure 1).

One of the difficulties of interpreting this result is the possibility of the C-Band bevel cut extractor being a better coupler to the TE_{21} mode than the TE_{01} , thus giving the appearance of higher power extracted and a major mode competition problem. The computer code High Frequency Structure Simulator (HFSS) was used to model the interaction region and bevel cut extractors, to check the coupling of the different modes. A computer model of the area investigated is shown in Figure 4. During the simulation runs, it was discovered that the drift tube area immediately surrounding the bevel cut extractor was a virtual cavity,

decreasing the extractor efficiency for not only the TE_{01} mode, but for all other modes as well. However, there was not a significant difference in the extractor efficiencies in the TE_{21} and TE_{01} modes, (both between 1-6%, depending on the frequency of operation), and thus it is believed that mode competition is a serious problem in the device. Also, other experimental evidence exists where similar parameters produce long pulses of rf (up to 600 ns) in a single frequency band (4.4 GHz) without evidence of other lower frequencies existing at the same time. This may be due to the interaction being closer to the TE_{01} cutoff and thus having a higher growth rate than any of the other modes. This is still being investigated.

In an effort to suppress the mode competition demonstrated in Figure 3, slotted cavities have been designed and are presently being modeled. A cavity of helical slotted design has been fabricated which should decrease the available axial length for non- TE_{0n} mode oscillation, and will be experimentally tested in the future. HFSS is being used to model the cavity (an example of which is shown in Figure 5) at the present time. Results from these calculations are pending..

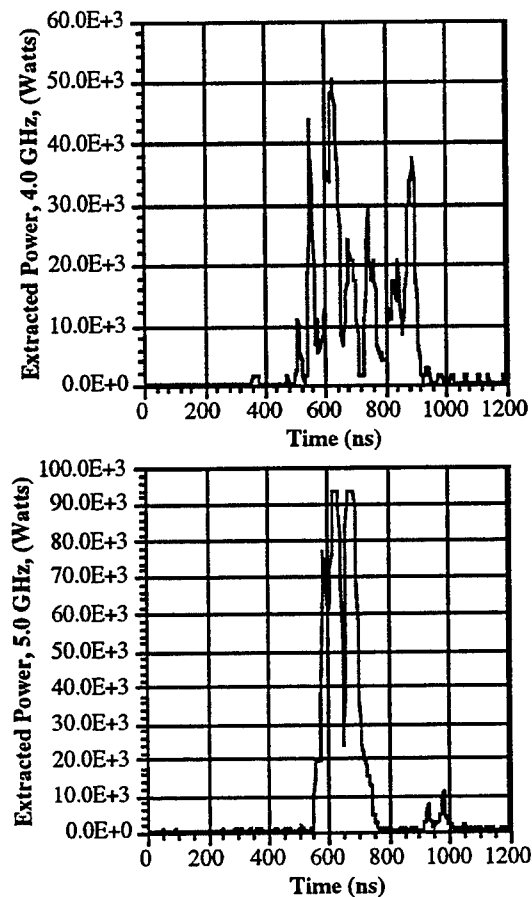


Figure 3. Experimental rf signals showing the existence of both the 4.0 ± 0.1 GHz frequency (upper trace) and the 5.0 ± 0.1 GHz frequency (lower trace) simultaneously.

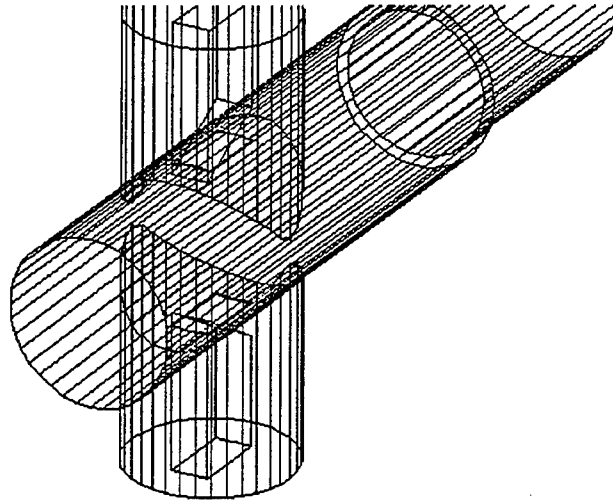


Figure 4. HFSS model of the interaction region and the bevel cut extractors. An rf wave is launched from the downstream end back towards the extractors. S-parameters are measured at the two waveguide exit openings and converted to a measure of the percentage of power extracted.

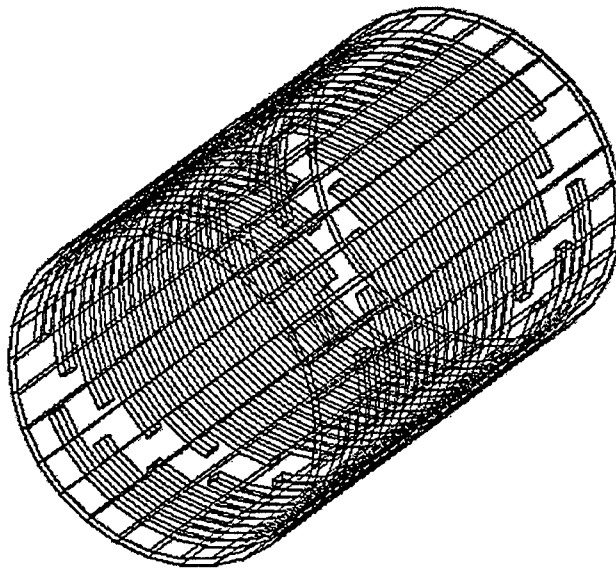


Figure 5. HFSS model of the helical slotted interaction region.

4. ACKNOWLEDGMENTS

The authors would like to thank the Air Force Office of Scientific Research for access to the AFOSR-sponsored MAGIC User's Group, MAGIC and SOS, developed by Mission Research Corp. (MRC), Larry Ludeking of MRC for useful discussions on MAGIC and SOS, and to AFOSR in helping to support this project. The authors would also like to acknowledge Drs. Moe Arman, Kirk Hackett, and Jack Agee, for their helpful suggestions pertaining to both the experiment and simulations.

5. REFERENCES

1. Chen, Zeng-Gui, "Effect of Electron Velocity Spread on Gyro-Peniotron Efficiency," Inter. J. Infrared and MM Waves, Vol. 14, No. 1, pp. 23-33, 1993.
2. Calame, J. P., Cheng, J., Hogan, B., Lawson, W., Striffler, C. D., Latham, P. E., and Irwin, V., "Measurements of Velocity Ratio in a 90 MW Gyrokystron Electron Beam," IEEE Trans on Plasma Science, Vol. 22, No. 4, pp. 476-485, August 1994.
3. Chong, C. K., McDermott, D. B., and Luhmann, Jr., N. C., "Slotted Third-Harmonic Gyro-TWT Experiment," to be published in IEEE Trans on Plasma Science, High Power Microwave Special Issue, June 1996.
4. McNeil, B. W. J., Robb, G. R. M., and Phelps, A. D. R., "Universally scaled cyclotron resonance maser equations," J. Phys. D: Appl. Phys., 27, pp. 1092-1096, 1994.
5. Goplen, B., Ludeking, L., Smithe, D., and Warren, G., The Magic Users Manual, MRC/WDC-R-282, Mission Research Corporation, Alexandria, VA, 1991.
6. Ramo, S., Whinnery, J. R., and Van Duzer, T., *Fields and Waves in Radio Communications*, John Wiley and Sons, New York, 1965.

Cyclotron Maser Experiment in a Two-Dimensional Periodic Array

Li Lei and Eli Jerby *

Faculty of Engineering, Tel Aviv University, Ramat Aviv 69978, Israel.

ABSTRACT

The cyclotron-resonance maser (CRM) interaction is demonstrated in a periodic-waveguide which consists of a two-dimensional array of metal posts. The CRM employs a low-energy electron beam (~ 5 keV, 0.1 A) in an axial magnetic field (~ 3 kG). Microwave output signals are observed in microwave frequencies around 7 GHz. The conversion efficiency is $\sim 10\%$.

Key word: Cyclotron-resonance maser, high-power microwaves, electron-cyclotron maser.

* Correspondence: e-mail: jerby@taunivm.tau.ac.il Fax: +972 3 6423508

1. INTRODUCTION

In previous experiments ^{1,2}, we studied the cyclotron-resonance maser (CRM) interaction in the periodic-waveguide shown in Fig. 1a. The waveguide consists of two columns of metal posts, where the electron-beam flows in between them. This scheme is referred here as a one-dimensional (1D) array. Amplifier ¹ and oscillator ² experiments were operated in this scheme in the microwave X-band (8-12 GHz) with electron-beam energies of ~ 10 keV. Theoretical studies of the periodic-waveguide CRM are presented in Refs. ^{3,4}. The electron-beam is rotated in the uniform axial magnetic field B_0 and interacts with one of the spatial harmonics in the periodic waveguide. The cyclotron resonance satisfies the condition

$$\omega = \omega_c + \beta_n v_z, \quad (1)$$

where ω and β_n are the angular frequency and axial-wavenumber of the em wave, and ω_c and v_z are the electron cyclotron angular frequency and axial-velocity, respectively.

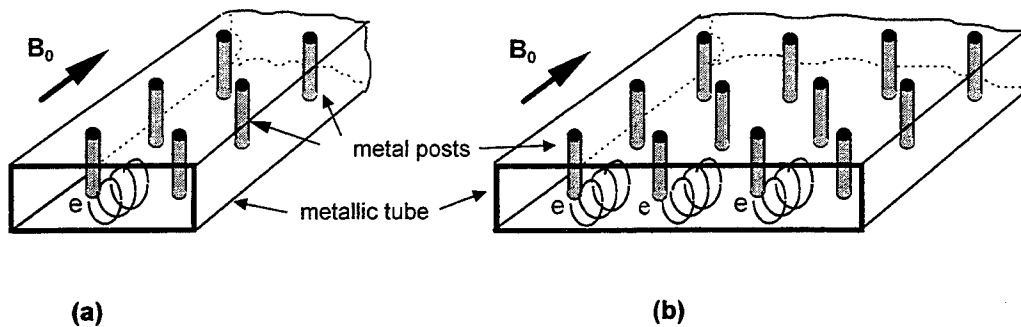


Fig. 1. Schematics of periodic-waveguide CRMs in 1D (a) and 2D (b) arrays.

The 2D multi-beam CRM array, shown in Fig. 1b, was proposed ⁵ as a mechanism for high-power microwave generation in relatively low voltages. The proposed device may consist of tens, and even hundreds, electron beams in a 2D or 3D array. Considering the parameters of the 1D oscillator experiment in Ref. ², the output RF power expected from a 3D array with one thousand electron-beams, $\sim 10\text{keV}/1\text{A}$ each, is above 1 Mega-Watt. Synergistic effects may increase the output power even further. In addition, this device might have an attractive feature of a direct phased-array antenna, incorporated in the multi-beam CRM array ⁵.

This paper describes the results of the first stage of the multi-beam periodic-waveguide CRM project ⁶, in which the device shown in Fig. 1b is realized with a four-column metal-post array, and a single electron-beam (in the center). The operation of this device with two electron-beams is planned for the next stage of the project.

2. EXPERIMENTAL SETUP

A block diagram of the experimental arrangement is shown in Fig. 2. The experimental parameters are listed in Table 1. The CRM device shown in Fig. 1b is immersed in a uniform axial magnetic field ($2.7\text{--}3.0\text{ kG}$) generated by a solenoid. A single electron-beam is emitted from a dispenser thermionic cathode (5 mm diameter). The first row of metal posts acts as an anode. The electron beam is spun up by a small kicker coil. The pulsers used for the e-gun, kicker and solenoid are similar to those described in Ref. ². The electron-beam propagates in a cyclotron motion in the center of the periodic waveguide, which consists of 4×27 metal post array. A waveguide taper is used as a mode converter and also as a collector for the electron beam (its current is measured by means of a $10\ \Omega$ resistor). A small portion of the RF power is sampled by a 20 dB cross-coupler, attenuated, and analyzed by the RF diagnostic setup.

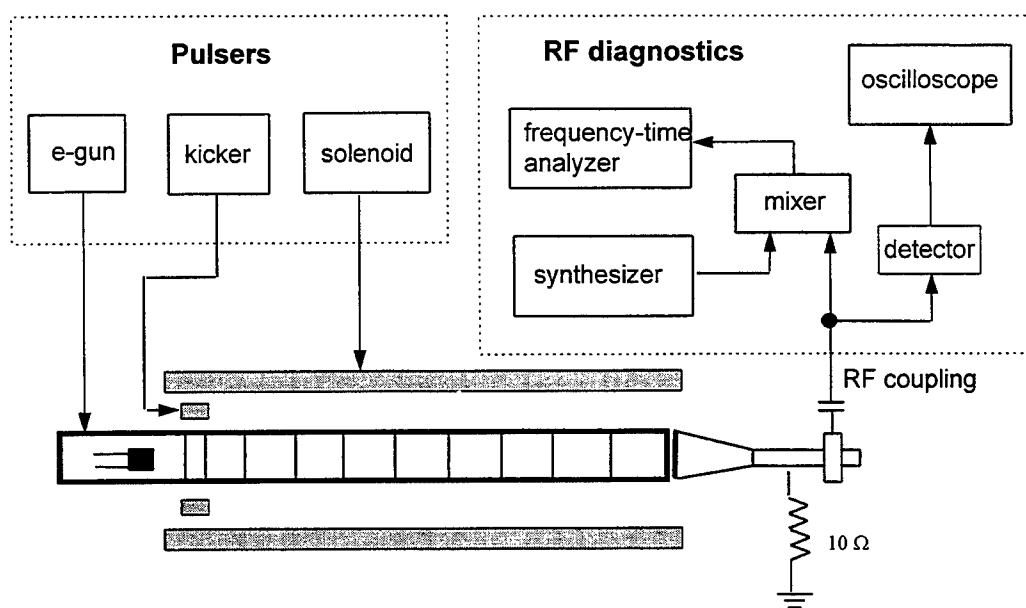


Fig. 2. A block diagram of the experimental setup.

The output coupled RF signal is attenuated and divided into two arms. In one arm, the signal is detected by a crystal detector (HP 424A) and recorded by a digital oscilloscope (Tektronix TDS 540). In the other arm, the signal is fed into a mixer (HP 5364A) and is mixed with a local-oscillator (HP 83752A). The intermediate signal is analyzed by a frequency and time interval analyzer (HP 5372A). The results shows the frequency variation as a function of time. This measurement reveals the CRM frequency shift due to the electron energy variation, and enables the verification of the CRM synchronism condition (1).

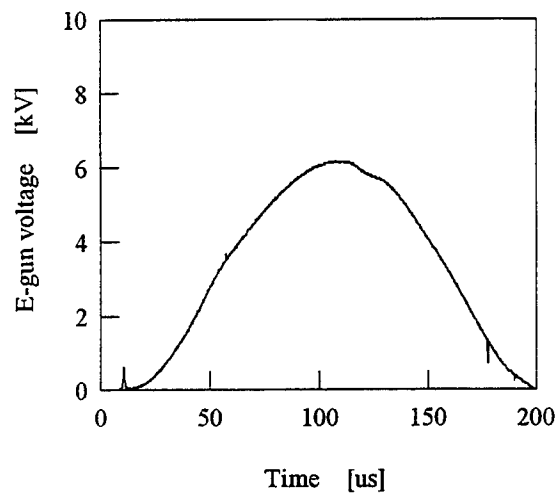
Table 1. Experimental Parameters

Electron beam:	
energy	4.0 - 7.5 keV
current	~ 0.1 A
duration	0.2 ms
Magnetic field:	
solenoid	2.7 - 3.0 kG
kicker	9 kA turns
Periodic waveguide:	
rectangular tube	47.6 X 24.9 mm ²
length	60 cm
post diameter	3 mm
periodicity	20 mm
reflector periodicity	10 mm

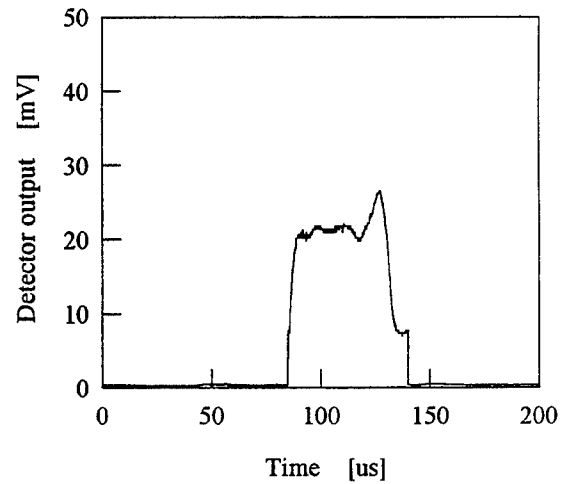
3. EXPERIMENTAL RESULTS

The typical traces presented in Fig. 3 show the electron-gun voltage and current, and the consequence detector output and frequency variation. The axial magnetic field in this run is 3 kG, which corresponds to a cyclotron frequency of 8.31 GHz. The average radiation frequency is 7.51 GHz, hence the device operates in the backward wave regime. In a CRM operation with an electron-energy slightly higher than the optimal value, as shown in Fig. 4, the synchronism condition takes place in the leading and trailing edges of the voltage pulse. This results in a *rabbit-ears* shape of the detector output in Fig. 4c.

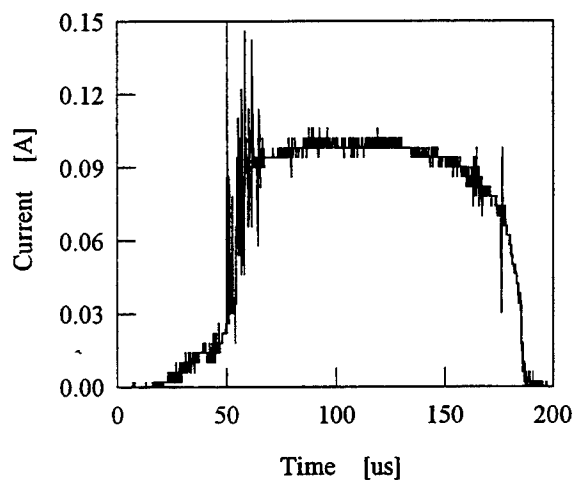
A series of measurements were made in different axial magnetic fields and electron-gun voltages. Oscillations were observed in different frequencies as shown in Fig. 5. In all cases studied, the RF frequency tends to decrease as the electron energy increases. For axial magnetic fields in the range 2.7-3.0 kG, the corresponding wave frequency is 6.88-7.51 GHz,



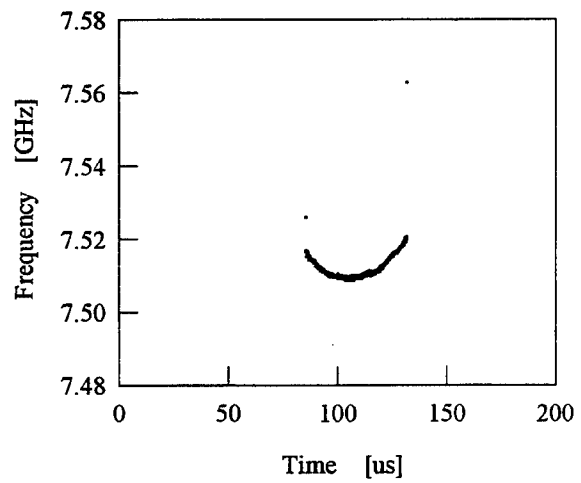
(a)



(c)

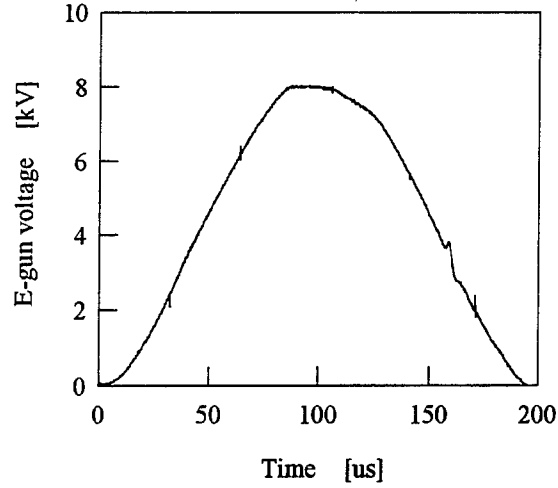


(b)

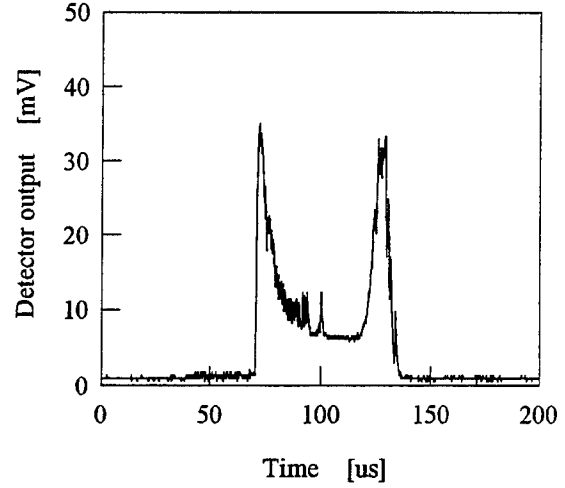


(d)

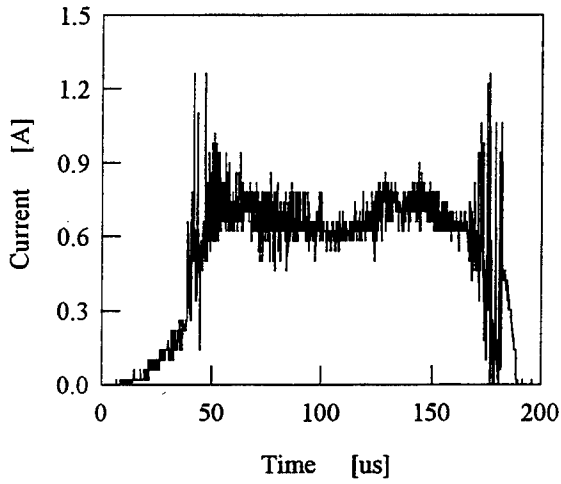
Fig. 3. Typical experimental results of CRM oscillator for $B_0=3$ kG. The electron-gun voltage (a) and current measured in the collector (b). The detector RF output (c) and the frequency vs. time measurement (d).



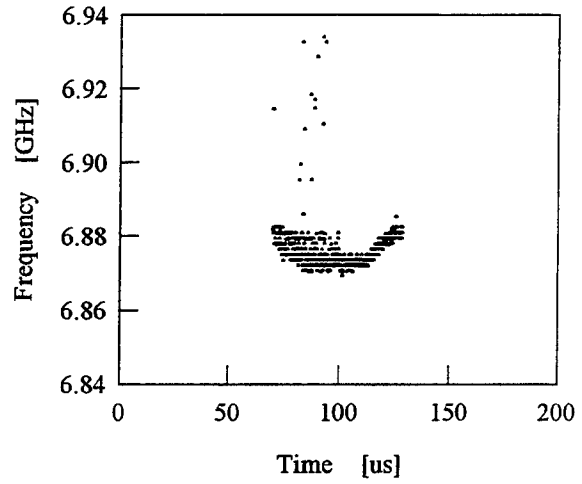
(a)



(b)

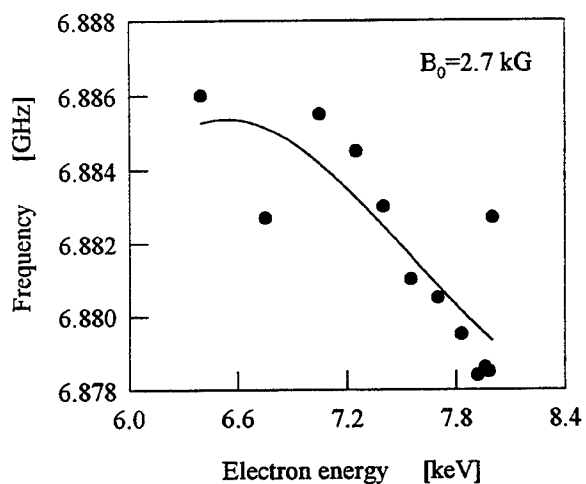


(c)

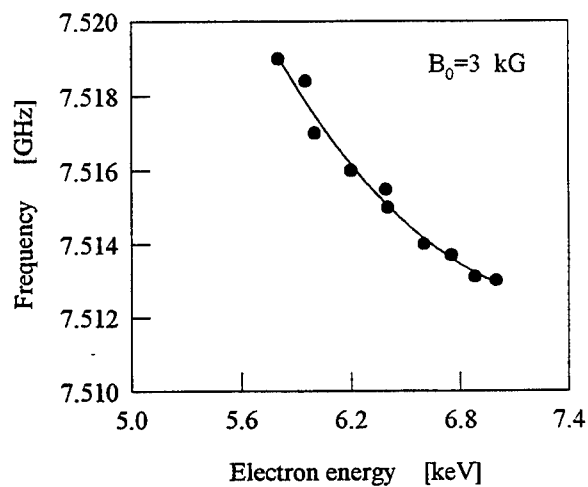


(d)

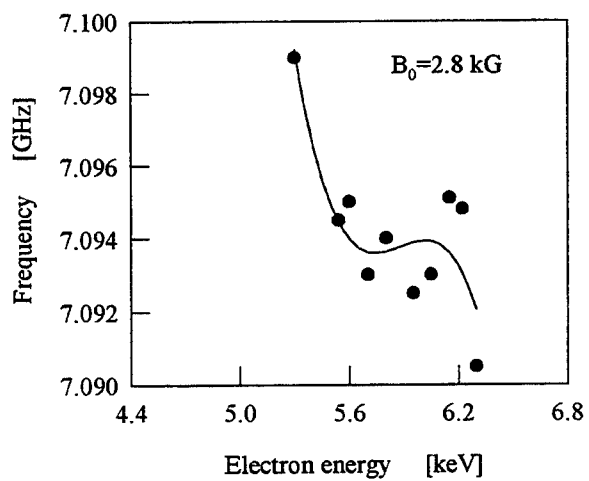
Fig. 4. Typical experimental results of CRM oscillator for $B_0=2.7$ kG. The electron-gun voltage (a) and the current measured in the collector (b). The detector RF output (c) and the frequency vs. time measurement (d).



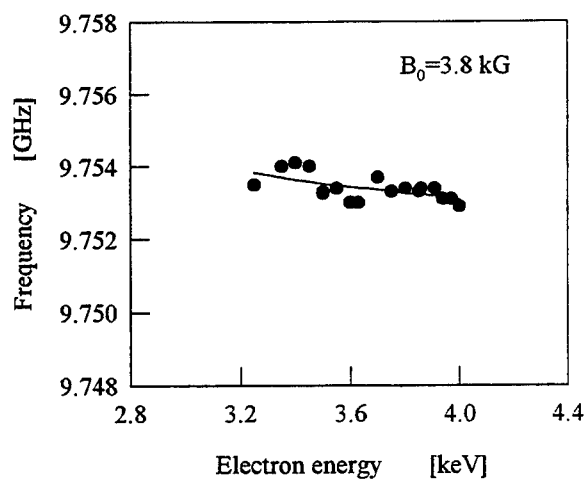
(a)



(c)



(b)



(d)

Fig. 5. CRM tuning characteristics for different values of axial magnetic field.

respectively, in the first passband of the periodic waveguide. For an axial magnetic field of 3.8 kG, the interaction occurs in the second passband, 9.64-9.78 GHz, as shown in Fig. 5d. The output power in the first passband is ~ 25 W and the efficiency is ~ 10 %. In the second passband the efficiency is much smaller, since the interaction occurs mostly with the second-order mode which has a null in the center ⁷. The emission in this case results from the finite width of the electron beam, and from its slightly off-axis propagation.

The CRM tuning conditions observed in this experiment are illustrated in Fig. 6. The Brillouin diagram, measured as in Ref. ², shows the periodic-waveguide dispersion. The electron-beam lines are computed by Eq. (1) according to the experimental parameters for $B_0 = 2.7$ kG and 3.8 kG. The intersection points between the electron-beam lines and the waveguide dispersion curves indicate the em resonance frequencies. The results for the backward-wave interaction are closed to to the experimental results.

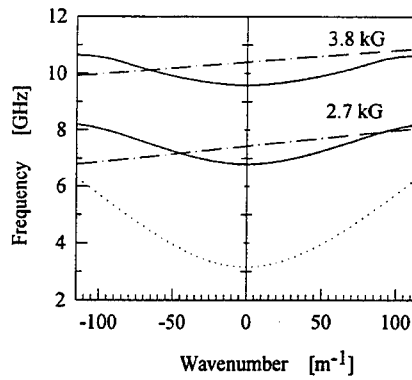


Fig. 6. The CRM tuning diagram. The solid curves show the periodic-waveguide dispersion in the first and second passbands. The dashed lines present the electron-beam lines as result from Eq. (1). The dotted curve is the fundamental mode of the rectangular tube.

4. CONCLUSIONS

The experiment presented in this paper demonstrates the feasibility of a CRM interaction in the two-dimensional array shown in Fig. 1b, with a single electron beam. This result provides the basis for the next stage in the multi-beam CRM study, the operation of the same device with two and three electron beams.

ACKNOWLEDGMENTS

The authors thank A. Shahadi, M. Korol, and V. Dikhtiar for their valuable cooperation. This work is supported by the Israeli Ministry of Energy, the Belfer Center of Energy Research, and the Israeli Academy of Science and Humanities.

REFERENCES

1. E. Jerby and G. Bekefi, "Cyclotron maser oscillator experiments in a periodic waveguide," Phys. Rev. E, Vol. 48, pp. 4637-4641, 1993.
2. E. Jerby, A. Shahadi, V. Grinberg, V. Dikhtiar, E. Agmon, H. Golombek, V. Trebich, M. Bensal, and G. Bekefi, "Cyclotron maser oscillator experiments in a periodically loaded waveguide," IEEE Journal of Quantum Electron., Vol. 31, pp. 970-978, 1995.
3. E. Jerby, "Linear analysis of periodic-waveguide cyclotron maser interaction," Phys. Rev. E, Vol. 49, pp. 4487-4496, 1994.
4. M. Korol and E. Jerby, "Quasi-anomalous Doppler effect in a periodic-waveguide cyclotron maser," to be published in Nuclear Instrum. Methods.
5. E. Jerby, "Multi-beam cyclotron-resonance maser," unpublished.
6. "Cyclotron-resonance maser experiments in periodic-waveguides," Grant # 724/94-2, Israeli Academy of Science.
7. M. Korol and E. Jerby, "Cyclotron resonance maser in a periodic array - a single-mode analysis," to be published.

Rectangular cross-section high power gyrotron

J. M. Hochman, R. M. Gilgenbach, R. L. Jaynes, J. I. Rintamaki, Y. Y. Lau, J. W. Luginsland, and
J. S. Lash

Intense Energy Beam Interaction Laboratory
Department of Nuclear Engineering and Radiological Sciences
The University of Michigan
Ann Arbor, MI 48109-2104

T. A. Spencer
Air Force Phillips Lab
Kirtland AFB, NM

Abstract

Experiments are underway to generate high power, long-pulse microwaves by the gyrotron mechanism in rectangular-cross-section interaction tubes. Long-pulse electron beams are generated by MELBA (Michigan Electron Long Beam Accelerator), which operates with parameters: -0.8MV, 1-10kA diode current, and 0.5-1 microsecond pulselength. Multimegawatt range microwave power levels have been generated. Adjustment of the solenoidal magnetic field is being studied for polarization control. Polarization power ratios up to a factor of 15 have been achieved. Electron beam dynamics, i. e. beam alpha (the ratio of the beam perpendicular velocity to the parallel velocity, $v_{\text{perp}}/v_{\text{par}}$), are being measured by radiation darkening on glass plates. Computer modeling utilizes the MAGIC Code and a single particle orbit code into which are injected a distribution of electron angles or energies. Both small-orbit and large orbit (rotating) e-beams are being investigated.

Keywords: gyrotron, intense microwave pulses, electron beam

I. Introduction

Long-pulse, high power microwave sources have significant applications to radar systems¹, propulsion², and plasma heating³. Different sources have produced power levels in excess of 1 GW, offering a high potential for military applications.⁴ Polarization control for launching high power

microwaves is a challenge. A theoretical study was previously performed of the active-circulator-gyrotron, which operates in an almost square waveguide, inputting a signal of the TE₀₁ form, but outputting a wave in the form of the TE₁₀ mode.⁵ Another approach for polarization control is the rectangular-cross-section (RCS) gyrotron.⁶ The RCS gyrotron allows generation of linearly polarized microwaves, rather than use of a mode converter. Experiments at UM have initially concentrated on an RCS gyrotron oscillator. Both small-orbit and large-orbit devices are currently under investigation, studying polarization control, mode competition, and pulse shortening.⁷ The maximum efficiency of a gyrotron is determined by the electron beam alpha ($v_{\text{perp}}/v_{\text{par}}$). Electron beam alpha measurements by radiation darkening of glass plates have been used for e-beam diagnostics.⁸

In this paper we describe initial RCS gyrotron results, for both small-orbit and large-orbit cases. MAGIC code studies are presented. Results of e-beam diagnostics are also presented.

II. Experimental Configuration

The Michigan Electron Long Beam Accelerator (MELBA) generates an electron beam with the following parameters: beam voltage = -750 to -800 keV, diode current = 1-10kA, and pulselength = 0.5-1.0 microseconds. The experimental configuration of the rectangular-cross-section gyrotron is exhibited in Figure 1. An exposed aluminum circular ring on a glyptal-coated cathode produces an annular electron beam by explosive emission at a radius of 2.25 +/- 0.25 cm. The graphite anode has a 4.55 cm aperture for small-orbit gyrotron measurements, an annular, 3-slotted aperture of radius 2.2 +/- 0.2 cm for large-orbit gyrotron measurements, and eight apertures of 1 mm diameter drilled on a circle of radius 2.25 cm for e-beam diagnostics. Large, magnetic field coils generate approximately 1 kGauss on the diode. The e-beam is extracted through the anode and enters a stainless-steel tube, onto which is wound a solenoid. For the small-orbit gyrotron, the e-beam is adiabatically compressed in the solenoidal interaction region, but for the large-orbit case, the beam is sent through a magnetic cusp prior to the solenoidal interaction region. The beam interacts in a rectangular-cross-section waveguide with dimensions of 7.2 cm by 5.4 cm, which is made by modifying and joining 2 sections of S-band waveguide. Prior to the entrance of the waveguide, a Rogowski coil is placed into the drift tube for transported current measurements. The entrance to the waveguide has a circular aperture of 2.6 cm radius. The exit of the interaction region has removable copper strips (1cm x 7.2cm) at 21cm downstream of the entrance, which are used for varying the cavity Q.

Microwave output is directed through waveguide of the same transverse dimensions as the interaction cavity. The electron beam is dumped to one side after exiting the interaction region. A large

chamber with microwave absorber is located at the end of the waveguide. Two S-band waveguides perpendicular to each other at the end of the chamber are used to collect the high power microwave emissions. The waveguides have thin copper wires across the long dimensions to prevent cross-polarized electric fields from entering the waveguide. Directional couplers and attenuators are used to transmit the microwave signals to a Faraday cage via coaxial cable. Total power measurements are made for both waveguide orientations, and the frequency is diagnosed by a four-channel microstrip filter system (2-2.5, 2.5-3, 3-3.5, 3.5-4 GHz filters).

For beam diagnostics, a glass witness plate is placed in the uniform magnetic field region of the solenoid (interaction cavity removed). The eight beamlets emerging from the apertured anode are spun up adiabatically by the increasing magnetic field for the small-orbit gyrotron as shown in Figure 2, and by the magnetic cusp for the large-orbit case. Radiation darkened patterns are visually analyzed after 15-25 shots.

III. Computer Simulations

Figure 3 shows the cavity geometry for MAGIC Code simulations. Four beamlets initially of radius 0.25cm at a radius of 2.25 cm are used to simulate the annular beam generated by MELBA. MAGIC code models used a beam alpha ($v_{\text{perp}}/v_{\text{par}}$) of 0.3 for the small-orbit model and 1.0 for the large-orbit gyrotron model. The simulation is run for 750 keV and 800 keV flat voltage pulses for 30nsec. The large-orbit case assumes a current of 200 A, while the small-orbit case uses a 1 kA beam current.

For interpretation of beam diagnostic data, a computer code was developed to model single electron trajectories. The code takes an input of an angular distribution of electrons, and the x-y position of each electron is plotted at the axial (z) position which corresponds to the glass plate. Glass plate analysis is also compared with results of the E-gun code.

IV. Experimental Results & Concluding Remarks

Typical waveforms for the small-orbit gyrotron are shown in Figure 4. The first two signals (a and b) come from microstrip filters over a 500MHz range. The signal in the 2.5-3 GHz filter corresponds to a peak power of ~0.4 MW, and the second signal corresponds to a peak of ~0.2 MW for the 3-3.5 GHz filter. The next two signals (c and d) are total power for both horizontal (H) and vertical (V) polarizations. The H-polarization has a peak power of about 2MW, while the V polarization peaks at about 0.5 MW.

All of the microwave pulses demonstrate pulse shortening, an area of ongoing study. The last signal(e) is the MELBA voltage pulse, which is flat for over 0.5 μ sec.

Figure 5 shows the measured polarization ratios of the total power in each waveguide versus magnetic fields for the small-orbit gyrotron case, and Figure 6 exhibits the results of MAGIC simulations for both small and large-orbit gyrotron cases, using a ratio of peak electric fields; Figure 7 is a graph of the polarization ratios for the large-orbit gyrotron case. While the small-orbit case shows more of the emission power is horizontally polarized over the 2-3kGauss range, the large-orbit case shifts from horizontally polarized to vertically polarized below 2 kGauss. Comparison of Figures 6 and 7 shows that MAGIC results agree with the large-orbit case.

A comparison between the computed electron trajectories and a single beamlet's radiation darkened pattern are shown in Figure 8 for a small-orbit gyrotron experiment. While some electrons landed in the center of the plate for the trajectory code, a significantly higher density of electrons landed near the edge where the radiation darkening occurred in the experiment. The code and experimental results agree well, confirming an average α ($v_{\text{perp}}/v_{\text{par}}$) of 0.3. The Larmor radius for the small-orbit gyrotron for the darkest radiation pattern was measured to be approximately 0.6 cm. Egun simulations for the small-orbit gyrotron yielded an α of approximately 0.2. Using the same technique for the large-orbit gyrotron, an average α of approximately 1.0 is measured where the Larmor radius was measured to be approximately 1.4 cm.

V. Acknowledgments

Research supported by the Air Force Office of Scientific Research, DoD-Multidisciplinary University Research Initiative (MURI) administered through Texas Tech University; Phillips Lab, and the AFOSR-sponsored MAGIC Code User's Group, administered by Mission Research Corp.; support from Northrop Grumman Corp. is also acknowledged.

VI. References

1. J. Benford, "Applications of high power microwaves to modification and measurement of the atmosphere," SPIE OE/LASE Conference, Los Angeles, CA, January 1993.
2. J. Benford and R. Dickinson, "Space propulsion and power beaming using millimeter systems," Paper 25, SPIE 2557, San Diego, CA, July 1995 .

3. R. M. Gilgenbach, M. E. Read, K. E. Hackett, et al., "Heating at the electron cyclotron frequency in the ISX-B tokamak," *Phys. Rev. Lett.*, vol. 44, pp. 647-650, 1980.
4. J. Sweigle and J. Benford, "State of the art in high-power microwaves: an overview," presented at "Lasers '93", Lake Tahoe, CA, December 1993.
5. Y. Y. Lau, L. R. Barnett, and J. M. Baird, "An active circulator-gyrotron traveling-wave amplifier," *IEEE Trans. Elect. Dev.* ED-31, pp. 337-347, March 1984.
6. D. J. Radack, K. Ramaswamy, W. W. Destler, and J. Rodgers, "A fundamental mode, high-power, large-orbit gyrotron using a rectangular interaction region," *J. Appl. Phys.* 73, pp. 8139-8145, February 1993.
7. R. M. Gilgenbach, J. M. Hochman, R. Jaynes, M. T. Walter, J. I. Rintamaki, J. S. Lash, Y. Y. Lau, J. W. Luginsland, and T. A. Spencer, "Rectangular interaction structures in high power gyrotron devices," *Proc. of Infrared and Millimeter Waves Conference*, Orlando, FL, December 1995.
8. J. J. Choi, R. M. Gilgenbach, T. A. Spencer, P. R. Menge, and C. H. Ching, "Measurement of long-pulse relativistic electron beam perpendicular-to-parallel velocity ratio by Cerenkov emission and radiation darkening on a glass plate," *Rev. Sci. Instr.* 63 (2), pp. 1671-1675, February 1992.

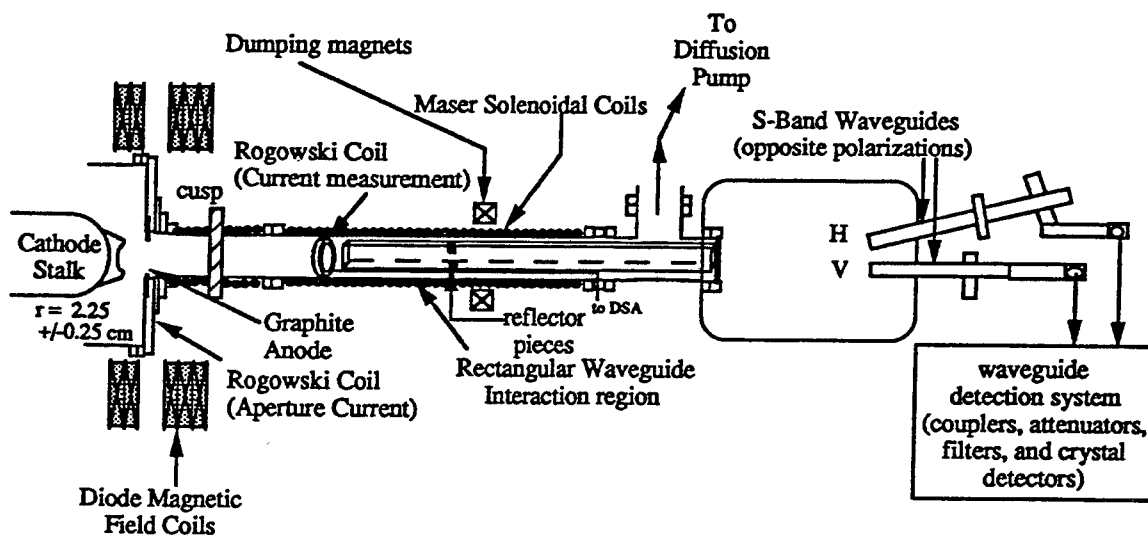


Fig. 1. Experimental configuration for rectangular-cross-section gyrotron.

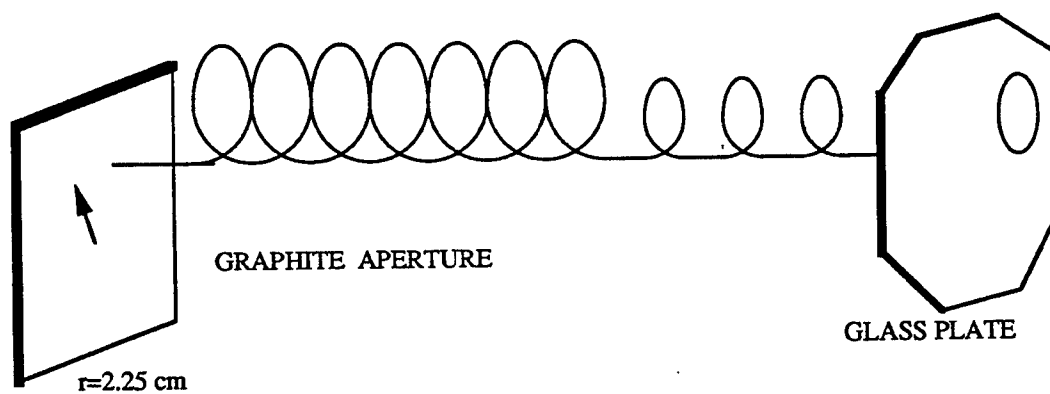


Fig. 2. Small-orbit gyrotron electron beam diagnostic for alpha measurements.

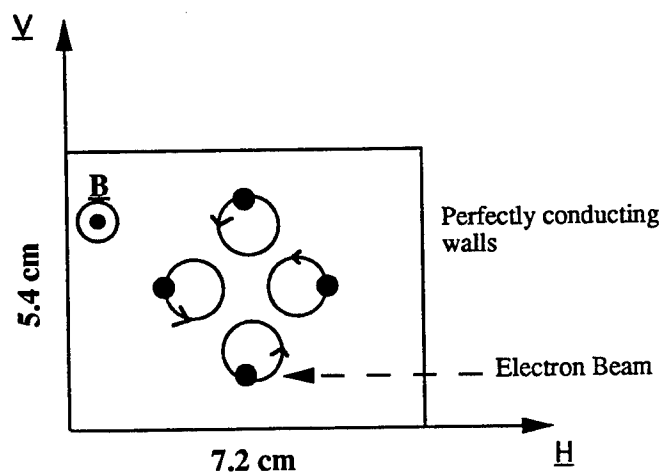


Fig. 3. Cavity geometry for MAGIC code simulations. The voltage is held constant at either 750 keV or 800 keV for 30 nsec. Large-orbit gyrotron uses an alpha of 1.0, and the small-orbit case uses an alpha of 0.3.



Fig. 4. MELBA experimental shot at 2.2kGauss for the small-orbit gyrotron.
 (a) signal from 2.5-3.0GHz microstrip filter with peak power corresponding to ~0.4MW. (b) signal from 3.0-3.5 GHz microstrip filter with peak power ~0.2MW.
 (c) total power measured from horizontally polarized signal, peak power corresponding to ~2MW. (d) vertically polarized signal, peak corresponds to ~0.5MW.
 (e) Voltage monitor signal (620 keV/div).

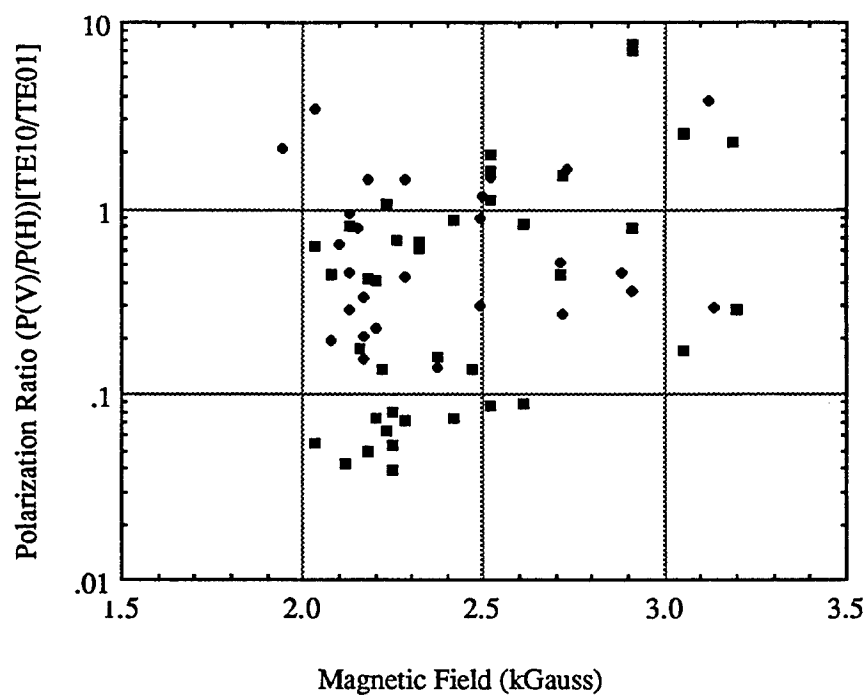


Fig. 5. Measured polarization power ratio versus magnetic field for the small-orbit gyrotron.

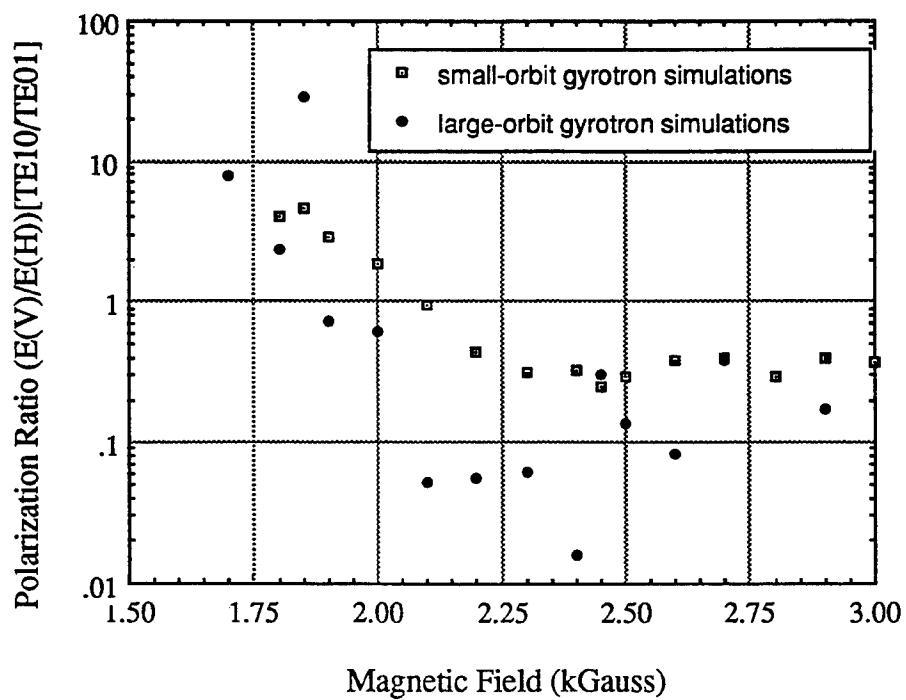


Fig. 6. MAGIC simulation results showing the ratio of electric fields of the lowest two TE modes for the RCS cavity geometry.

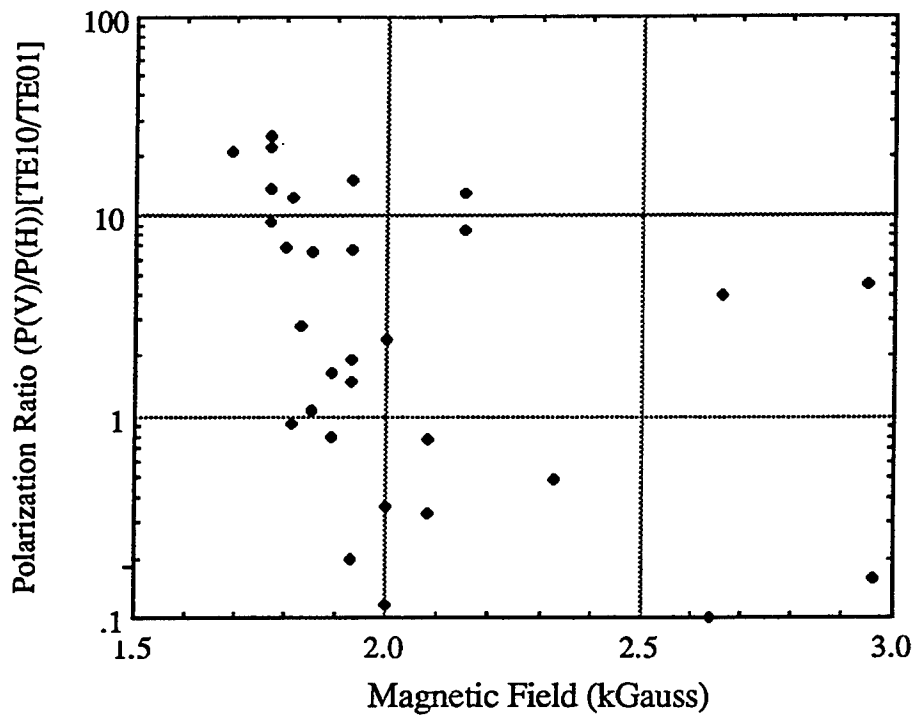


Fig. 7. Measured polarization power ratio versus magnetic field for the large-orbit gyrotron.

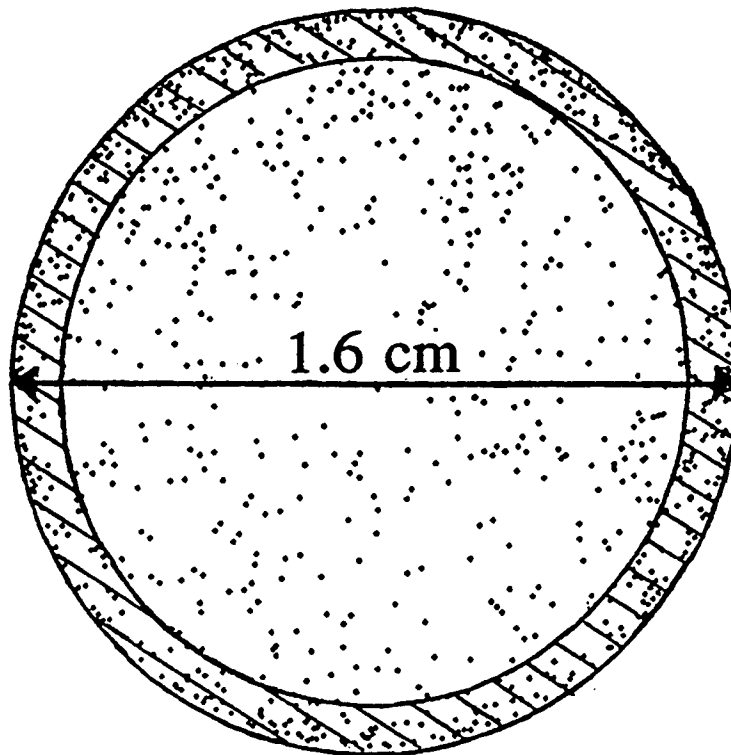


Fig. 8. Comparison between radiation darkened glass plate pattern of a single beamlet (outlined and cross-hatched) and the computed electron trajectories.

Computer Modelling of Phase Locking in Magnetrons

X. Chen, M. Esterson and P.A. Lindsay

Dept. of Electronic and Electrical Eng., King's College London
London WC2R 2LS, UK

ABSTRACT

The phase locking in a rising-sun, L-band, 100 MW pulsed magnetron has been investigated using a powerful computer program called MAGIC. It has been shown that in the process of phase locking the injection signal eliminates the initial space-charge noise and consequently speeds up the start of oscillations. Also small-signal results for the locking bandwidth have been extended to nonlinear regime of operation. The modelling of the system to the voltage pulse jitter is still being investigated. In the process an accurate phase measuring technique has been developed.

Keywords: magnetrons, phase locking, nonlinearity, computer modelling

1. INTRODUCTION

The process of phase locking of high power microwave oscillators, for example magnetrons, was being investigated for various reasons since the end of World War II¹⁻⁵. However, the simple theory, initially developed by Adler² and David³ some forty years ago, is based on a form of small signal approximation and therefore is *linear*. In spite of its early successes in explaining many experimental observations it was felt that, in view of the inherent *nonlinearity* of the phase locking process, further investigations based on computer modelling would be desirable.

In the past we would use a powerful 2-D particle-in-cell (PIC) code, called MAGIC⁶, in successfully modelling transient effects in a typical magnetron⁷. The code proved to be ideal for investigating the transition from noise to large amplitude oscillations, including the related mode dynamics, the space charge playing a crucial role in this process. Therefore we felt it would be a natural extension of the MAGIC code, if we used it for modelling the phase locking process, where an injected control signal influences, with the help of space charge, the mode of oscillation of the tube.

Using MAGIC, we have now been able to obtain some interesting results concerning noise generation and phase locking. In this connection a new computing technique has

been developed which clearly reveals the dynamical behaviour of frequency and phase during the phase locking process. It is the object of our communication to describe this technique and to consider its application to the problem of phase locking in a magnetron of our choice. In particular, we propose to describe the effect of space charge noise and voltage pulse jitter on the ultimate phase of a phase-locked signal, and to consider the influence of the amplitude of the injected signal on the locking bandwidth. We thus hope to show that our technique, based on the use of MAGIC, can be developed to act as a design tool when the phase locking of magnetrons has to be considered.

2. THE MODELLING PROCEDURE

The magnetron we have chosen for our model is an experimental, rising-sun, EEV L-band tube shown in Fig. 1(a). The most important characteristics of the tube are listed below:

Table 1

Number of cavities	$N=10$
Vane angle (radial vanes)	$\theta = 18^\circ$
Anode radius	$r_a = 50 \text{ mm}$
Cathode radius	$r_c = 25 \text{ mm}$
Back wall radius (big cavities)	$r_b = 110 \text{ mm}$
Back wall radius (small cavities)	$r_s = 80 \text{ mm}$
Operating voltage	$V_{DC} = 170 \text{ kV}$
Magnetic field	$B_0 = 0.09 \text{ T}$

We began our investigations by modelling the start of oscillation and its dependence on the rate of rise of the DC anode voltage, the results of these investigations being available elsewhere⁷. There the DC voltage was chosen to vary in an exponential fashion governed by the following function: $V_{DC} = V_0\{1-\exp(-t/\tau)\}$, where the amplitude V_0 and the rate of rise τ could be varied independently. At a proper rate of rise of the DC voltage, the tube would first generate random noise, then it would pick up a frequency corresponding to the π -mode and finally it would burst into oscillations at full power. This process is illustrated in Fig. 1(b), which is a plot of time history of the RF voltage as measured between the ends of two adjacent vanes. Although in the program there is no direct assignment of a load or of a dissipative element in the system, the algorithm governing the field computation continuously dumps a percentage of the RF energy, a

process which is equivalent to the existence of an axial load. This is the reason why the oscillations settle down at a fix level instead of growing indefinitely. Based on the information provided by MAGIC, the following values for the relevant parameters have been obtained:

$$\begin{aligned} \text{Oscillating frequency:} & \quad f_0 = 1.130 \text{ GHz} \\ \text{Loaded quality factor:} & \quad Q_L = 126. \\ \text{Output power:} & \quad P_{\text{out}} = 608.7 \text{ MW/m} \end{aligned} \tag{1}$$

The phase locking arrangement is in the form of a master (injected signal) driving one or more slave magnetrons; in our model we only have a single tube. The RF control signal is injected into the magnetron with the help of a dipole placed in one of its cavities, as shown in Fig. 2(a). In order to assess the rate at which the control signal energy is being fed into the system (P_{in}), a computation equivalent to a 'cold test' has been carried out by feeding the control signal and at the same time suppressing the emission of electrons from the cathode. The actual phase-locking process has been modelled using an injected signal of varying frequency and amplitude. Fig. 2(b) shows a typical time history of the RF voltage when the phase locking has been achieved. Comparing with the results shown in Fig. 1(b), it is clear that in the presence of phase locking the oscillations start much earlier and there is no sign of an initial noisy transient. This can be further illustrated by viewing the electron cloud in Figs 1(a) and 2(a); in the former at 80 nsecs the electrons are just in the process of developing five bulky spokes (π -mode), and in the latter at 40 nsecs, ie much earlier, the electrons have already developed five well defined spokes.

At this point one ought to consider some of the physics associated with the use of MAGIC. In the modelling of phase locking the external parameters are kept constant so that the injected signal can only affect the space charge, ie the equivalent reactance of the system; this in turn influences the frequency and phase of the output signal (frequency pushing). The ability of the code to handle frequency pushing has been tested independently since it is essential in our investigation.

3. PHASE MEASUREMENT AND PHASE LOCKING

The time dependence of the RF voltage provided by MAGIC and shown in Fig. 2(b) gives us a qualitative description of the process of phase-locking as it occurs in a magnetron. In practice it is necessary however to develop a more detailed technique for monitoring the dynamics of phase locking, for example by obtaining a quantitative

relationship between control and output signals. This is achieved by a continuous phase comparison over a period of time, preferably until the system is finally phase locked. Since in the process of phase-locking the output signal is not necessarily sinusoidal, its phase cannot be directly deduced from an inverse sine function. Instead, we have to measure the phase difference by observing the position of alternative nodes, ie the points at which the RF signal crosses the time axis. The phase difference between these nodes and the corresponding nodes of the reference signal are then measured, as shown in Fig. 3.

When the power of the injected signal is not sufficiently high as is shown in Fig. 4 where $P_{in} = 0.024P_{out}$, the ultimate phase of the output drifts upwards during the whole observation period of 560 nsecs. This indicates that phase locking has failed to occur. In Fig. 5, where the power of the injected signal is substantially higher, $P_{in} = 0.072P_{out}$, after a short transient the phase of the output signal settles down to a fixed value, indicating that phase locking has been achieved. It is clear that without developing our technique of phase measurement we could not have reached the above conclusions by merely observing the output signal shown in Fig. 2(b), however interesting the figure may be in its own right.

We are now in a better position to consider an important aspect of phase locking, viz. the locking bandwidth. According to Adler's linear theory², the locking bandwidth is given by:

$$\Delta f = \frac{f_0}{2Q} \sqrt{\frac{P_{in}}{P_{out}}} \quad (2)$$

where $\Delta f = f_i - f_0$.

The results obtained from (2) and from our nonlinear model are compared in Table 2;

Table 2

f_i (GHz)	1.127	1.128	1.129	1.131	1.132	1.133
$\Delta f = f_i - f_0$ (MHz)	-3	-2	-1	+1	+2	+3
Theoretical P_{out}/P_{in} (db)	3.5	7.0	13.0	13.0	7.0	3.5
P_{in} - control signal (MW/m)	85.7	64.2	42.8	42.8	64.2	85.7
P_{out} - output signal (MW/m)	440	514	613	594	560	500
Calculated P_{out}/P_{in} (db)	7.1	9.0	11.6	11.4	9.4	7.6

they are also summarised in Fig. 6, where the dashed and solid curves respectively represents the results obtained from (2) and from our computations. It can be seen that there is a noticeable difference between the two sets of curves. For the same locking bandwidth, the dashed curves are everywhere steeper than the solid curves; thus the maximum locking bandwidth shown in Fig. 4 requires a power ratio P_{out}/P_{in} of approx. 3 db according to (2), but about 7 db according to our computations. Therefore our results suggest that less injected power is needed to achieve phase locking, especially at the far end of the bandwidth. A likely explanation is that (2), being based on a small signal theory, tends to predict less well when the control frequency is far away from the central frequency. The situation is somewhat reversed for small bandwidths, where the agreement between (2) and the computed results is much better.

Another aspect of phase locking to be studied is that of the DC voltage pulse jitter. In our model this can be simulated by starting the applied voltage at different phases of the control signal. This will be the subject of an additional paper.

4. CONCLUSIONS

1. Without the injected control signal the start of oscillations is preceded by a weak and noisy output lasting for a period of time equivalent to some 50 - 100 cycles. In the presence of the injected signal the noise output is almost completely eliminated, the oscillations beginning to build up almost immediately, the tube delivering full power after some 20 - 30 cycles.
2. When the injected signal is sufficiently strong to achieve phase locking, the locking bandwidth is substantially greater than that obtained from the small signal theory; thus in practice a greater locking bandwidth is obtained using a weaker control signal. Clearly in the case of phase locking it is advisable to take the nonlinear behaviour of the system into account.
3. Since during phase locking the output is quite complex, it is unsafe to assume for purposes of phase assessment that it can be represented by a simple sine wave. A technique of phase measurement based on the time of alternative crossings of the time axis by the output signal has been developed in order to obtain an accurate measure of the phase difference between the injected control signal and the output signal of the tube.

5. ACKNOWLEDGEMENTS

The above work has been mostly carried out using the version of the Mission Research Corporation's MAGIC code which was provided under the AFOSR-sponsored MAGIC User's Group. The authors would also like to thank the Defence Research Agency for their support of the above investigations.

6. REFERENCES

1. W. Bostick, E. Everhart and M. Labitt, RLE Technical Report No. 14, 1946.
2. R. Adler, "A study of locking phenomena in oscillators", Proc. IRE, vol. 34, pp.351-357, June 1946.
3. E.E. David,Jr., "RF phase control in pulsed magnetrons", Proc. IRE, vol. 40 pp.669-685, June 1952.
4. J. Benford, H. Sze, W. Woo, R. Smith and B. Harteneck, "Phase locking of relativistic magnetrons", Phy. Rev. Lett., vol. 62, pp.969-971, February 1989.
5. T.A. Treado, R. Bolton and et al, "High-power, high efficiency, injection-locked, secondary-emission magnetron", IEEE Trans. on PS, vol. 20, pp.351-359, June 1992.
6. B. Goplen, L. Ludeking, J. Mcdonald, G. Warren, and R. Worl, *MAGIC User's Manual*, MRC/WDC-R-310, Mission Research Corporation, VA 22122, 1993
7. P.A. Lindsay, J. Watkins and X. Chen, "Simulation of some transient effects in a magnetron using the MAGIC code", MUGshots -- MAGIC User's Group Newsletter, vol. 3, pp.1-5, February 1995.

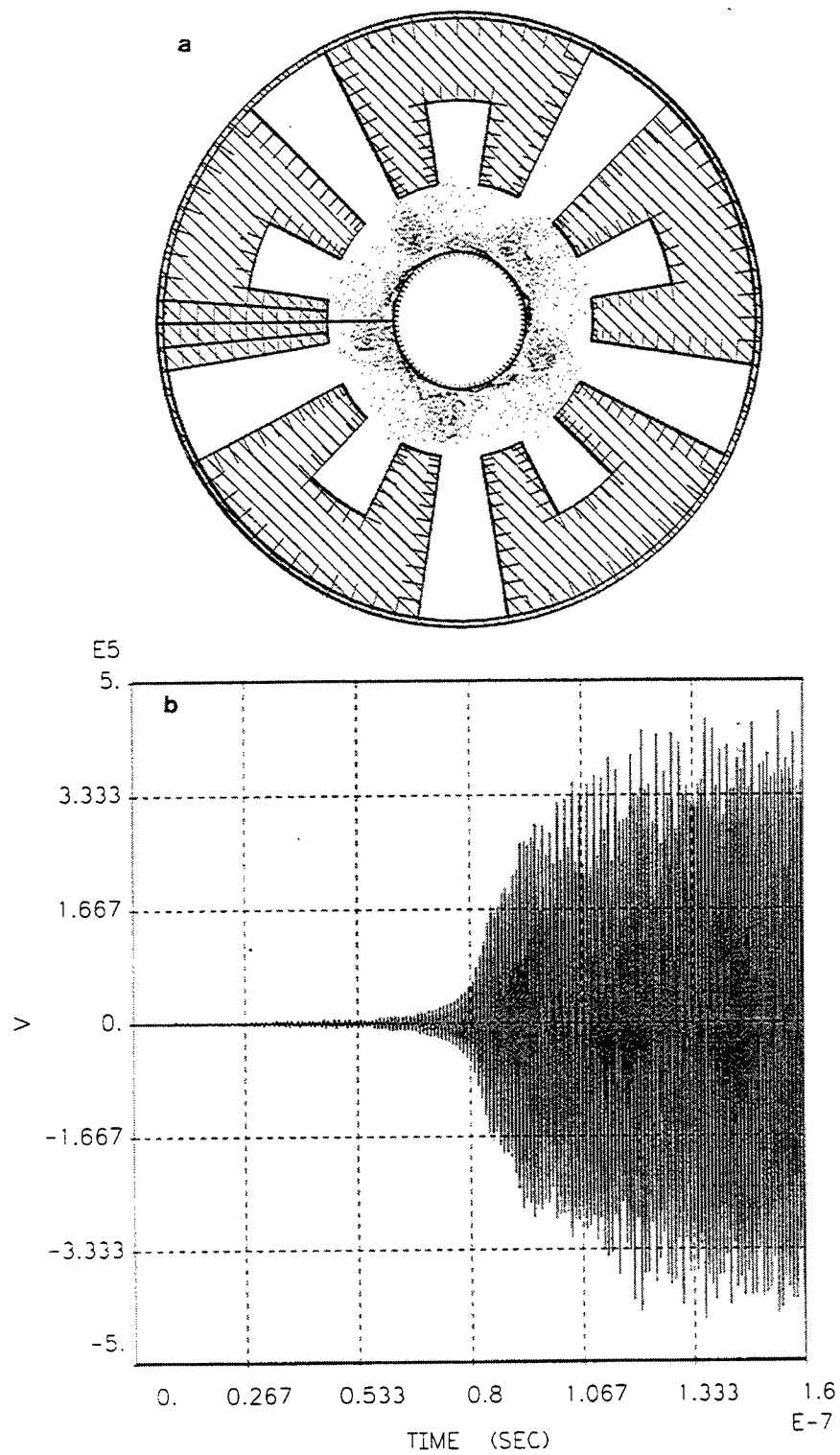


Fig. 1 The free-running magnetron: (a) the geometry and the electron cloud;
(b) the time history of the RF voltage on the anode.

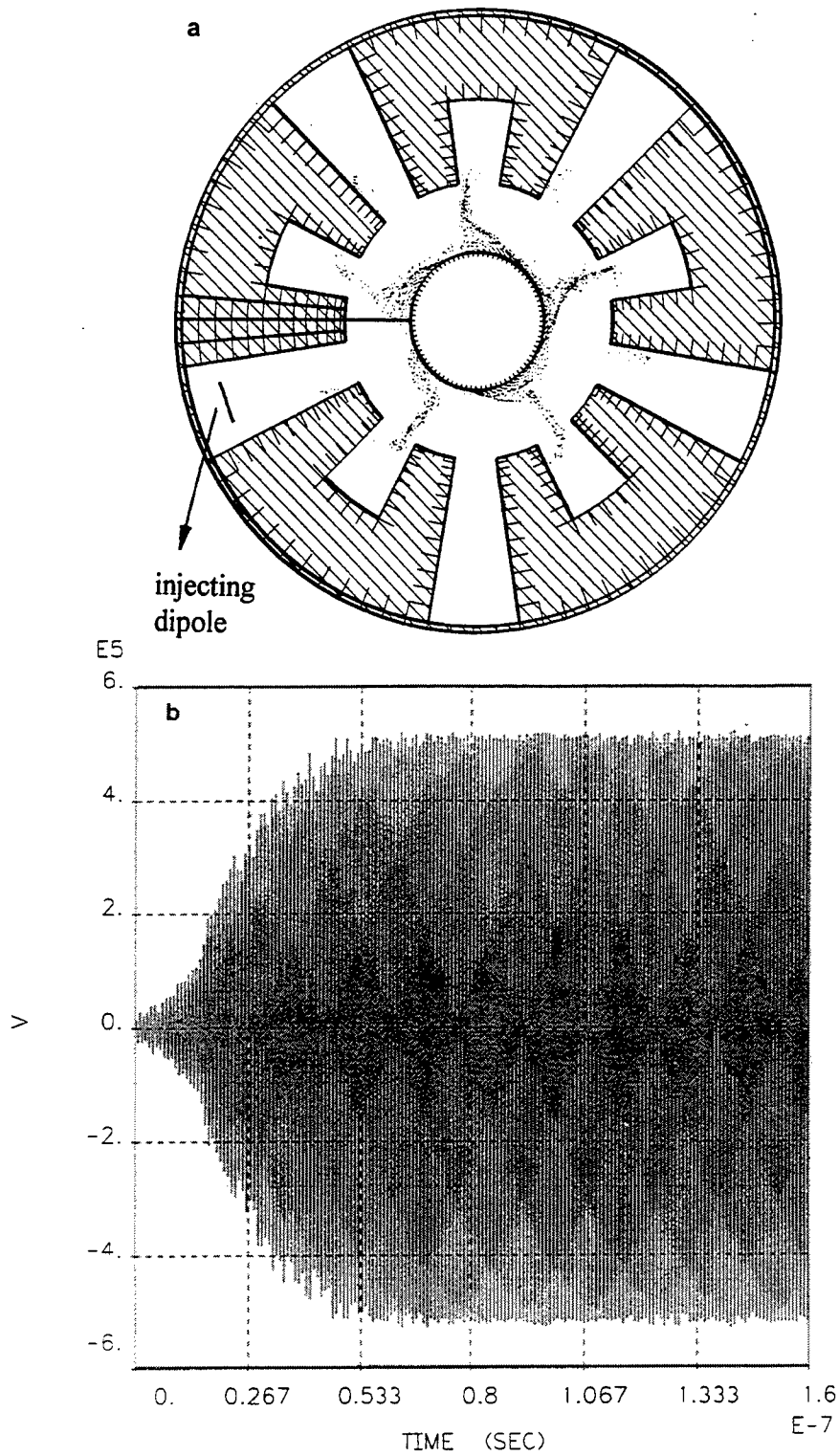


Fig. 2 The magnetron with injection: (a) the geometry and electron cloud; (b) the time history of RF voltage on the anode.

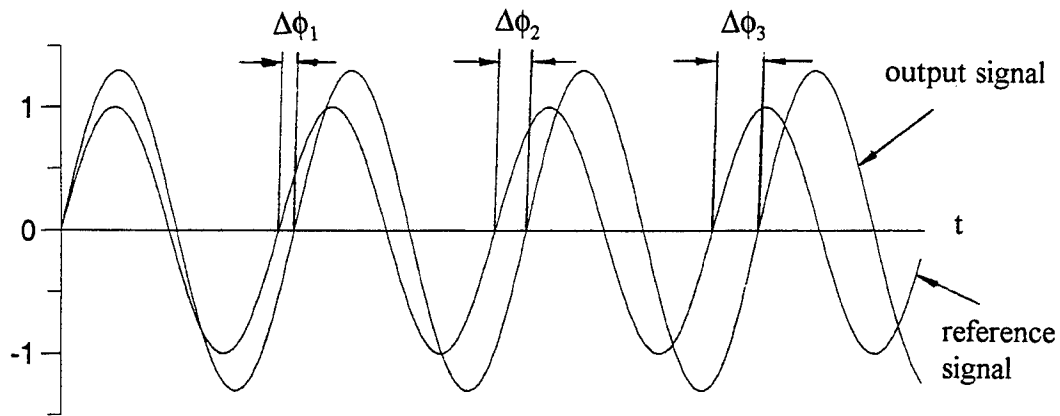


Fig. 3 The scheme for calculating the phase difference.

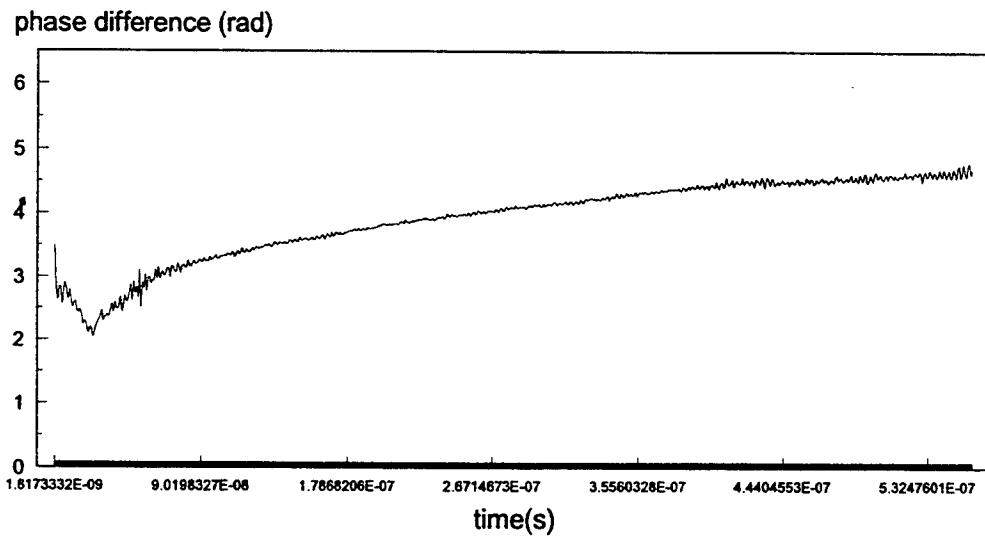


Fig. 4 The phase difference curve when $P_{in} = 0.024P_{out}$ and $f_i = 1.131\text{GHz}$.

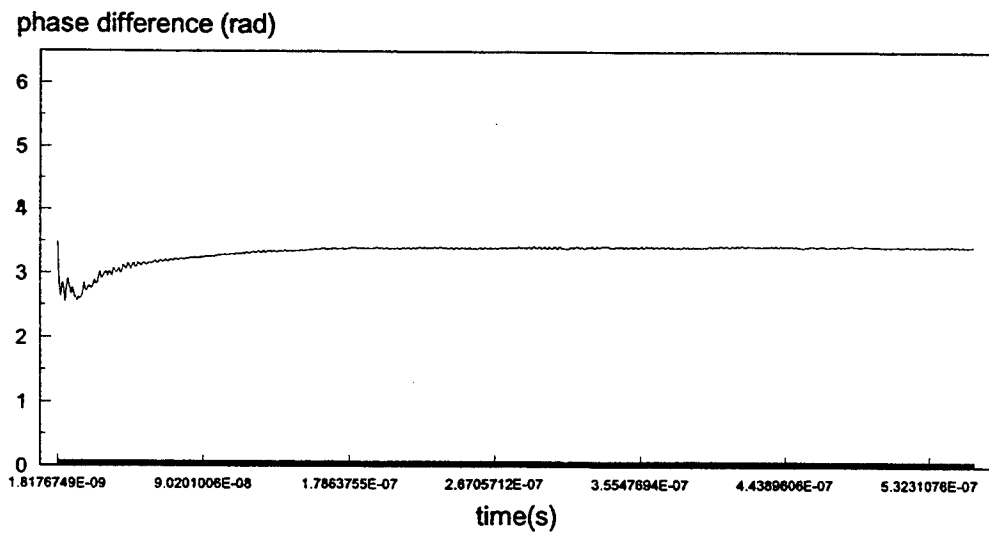


Fig. 5 The phase difference curve when $P_{in} = 0.072P_{out}$ and $f_i = 1.131\text{GHz}$.

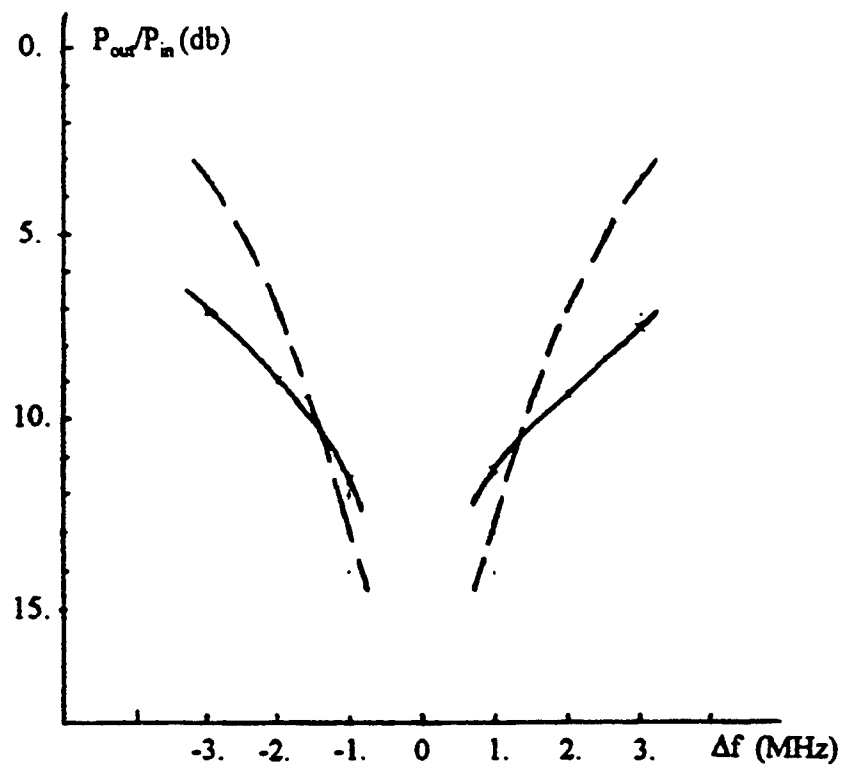


Fig. 6 Locking bandwidth vs injection ration

Electromagnetic resonances of an asymmetrically loaded magnetron cavity

M. Botton, I. Schnitzer, A. Rosenberg

RAFAEL, P. O. Box 2250, Haifa 31021, ISRAEL

ABSTRACT

We present an analysis of the electromagnetic fields and "cold" resonance modes of a loaded magnetron cavity. The loading violates the assumption of all identical side resonators and hence affects the pattern of the fields and resonance frequencies. Depending on the angular loading scheme, the coupling of the modes also changes. The analysis is expected to be useful for future design of magnetron cavities.

keywords: magnetron cavity, cold modes, cavity loading

1. INTRODUCTION

The Electromagnetic energy in high power relativistic magnetrons is usually extracted by means of waveguides coupled through slots to the side resonators of the anode block¹⁻³. The heavy loading conditions, which are common in such systems, break the similarity between loaded and unloaded side resonators, and hence change the electromagnetic properties of the cavity. Sze et. al.⁴ have experimentally studied the effects of different loading schemes on the operation characteristics of the magnetron. They have found that for the A6 configuration the optimal loading is with three open side resonators, a structure that preserves the symmetry for the π mode, while under other loading schemes (e.g. one open side resonator), the extracted power level is lower. Furthermore, the frequency characteristics of the emitted pulse depend on the loading scheme. In most of the cases however, the design of the anode block does not take into considerations of the loading (e.g. Refs. 5,6), *all* the side resonators are assumed to be identical and the resonance frequencies are computed using the classical way, known since the forties⁷. As the fast developing field of relativistic magnetrons approaches maturity, a more detailed analysis of the electromagnetic resonances is called for in order to improve the performance of the system.

In this work we present a theoretical analysis of the electromagnetic fields in a magnetron cavity considering the loading and the resulting symmetry properties. In many cases, the loading of the side resonators depends on the fine details of the extraction scheme. For clarity of presentation, we use a phenomenological model, namely represent the coupling of the side resonators as a slot in a radial waveguide, and calculate an equivalent reflection

coefficient. This model facilitates the analysis and preserves the major properties of the real coupling schemes. We then determine the symmetry properties of the fields in the central region of the cavity, according to the loading set-up (namely the number of loaded side resonators and the angular arrangement), and obtain a dispersion equation for the resonance frequencies and quality factors of the various modes. We show that different angular loading arrangements may lead to different dispersion equations, and hence different resonance frequencies and quality factors even for the same extraction scheme (i.e. slot width). The angular loading scheme also affects the conditions for resonant interaction between the electrons and the fields (the Bunneman-Hartree condition), as it changes the phase velocity of the waves.

The organization of this work is as follows: In the next section we present an analysis of the electromagnetic fields in the magnetron cavity and derive the dispersion equation. In section 3, we solve the dispersion equation for several examples of angular loading schemes. Finally, in section 4 we discuss the results, including possible effects of the angular loading schemes on the Bunneman-Hartree resonance condition.

2. FIELD ANALYSIS

Consider a magnetron cavity with N side resonators, r_a is the inner radius of the anode, and r_c the cathode radius (see Fig. 1). The angle subtended on axis by a side resonator is ψ , its outer radius is r_v , and it is terminated by a slot of angle θ through which the electromagnetic energy is extracted. We assume that all the resonators have the same opening angle ψ , and outer radius r_v , however, the slot angle θ may vary from one resonator to another, reflecting thus a possible different level of energy extraction from each side resonator. We further assume that the axial length of the cavity is much larger than any other dimension, hence we neglect axial variations of the fields, and solve the two dimensional case using a cylindrical coordinate system (r, α) . The electromagnetic field comprises three components, namely E_r, E_α, H_z which satisfy Maxwell's equations (c.g.s. units and harmonic time dependence $\exp(-i\omega t)$ are used):

$$(1) \quad \left\{ \begin{array}{l} \frac{1}{r} \frac{\partial H_z}{\partial \alpha} = -i \frac{\omega}{c} E_r \\ \frac{\partial H_z}{\partial r} = i \frac{\omega}{c} E_\alpha \\ \frac{1}{r} \frac{\partial}{\partial r} (r E_\alpha) - \frac{1}{r} \frac{\partial E_r}{\partial \alpha} = i \frac{\omega}{c} H_z \end{array} \right.$$

where c is the speed of light in vacuum and ω the circular frequency.

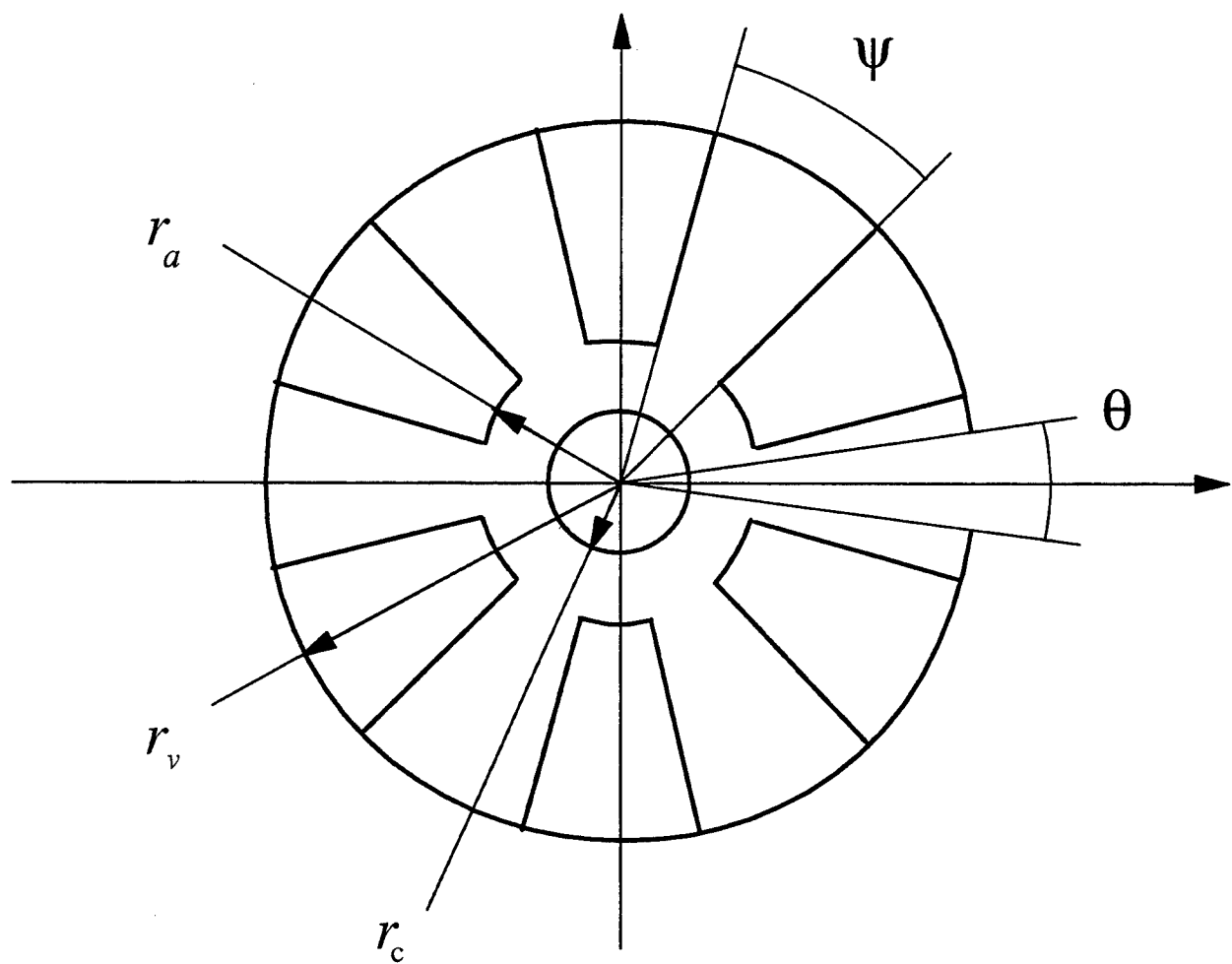


Figure 1: The magnetron cavity.

From these equations we obtain the wave equation for the magnetic field component:

$$(2) \quad \frac{1}{\rho} \frac{\partial}{\partial \rho} \left(\rho \frac{\partial H_z}{\partial \rho} \right) + \frac{1}{\rho^2} \frac{\partial^2 H_z}{\partial \alpha^2} + H_z = 0$$

where we defined the normalized variables $\rho = r\omega/c$. The solution of the wave equation in the central region of the cavity ($\rho \leq \rho_a \equiv r_a \omega/c$) with the boundary condition on the surface of the cathode is:

$$(3) \quad \begin{cases} H_z = \sum_l d_l Z_l(\rho) \exp(il\alpha) \\ E_\alpha = \sum_l -id_l Z'_l(\rho) \exp(il\alpha) \\ E_r = \sum_l \frac{l}{\rho} d_l Z_l(\rho) \exp(il\alpha) \end{cases}$$

and

$$Z_l(\rho) = H_l^{(1)}(\rho) - \frac{H_l^{(1)'}(\rho_c)}{H_l^{(2)'}(\rho_c)} H_l^{(2)}(\rho), \quad Z'_l(\rho) = H_l^{(1)'}(\rho) - \frac{H_l^{(1)'}(\rho_c)}{H_l^{(2)'}(\rho_c)} H_l^{(2)'}(\rho)$$

where $H_l^{(1)}(\rho), H_l^{(2)}(\rho)$ are the Hankel functions of the first and second type and order l , $\rho_c = r_c \omega/c$ is the normalized cathode radius, prime means differentiation with respect to the argument, and the sum over l reflects the angular periodicity of 2π . The fields in the p 's side resonator satisfy the boundary conditions:

$$E_r(r, \alpha) = 0, \quad \alpha - 2\pi(p-1)/N = 0, \psi$$

and therefore the fields are:

$$(4) \quad \begin{cases} H_z = \sum_n b_{pn} (H_{nv}^{(1)}(\rho) + \chi_{pn} H_{nv}^{(2)}(\rho)) \cos(nv\alpha_p) \\ E_\alpha = \sum_n -ib_{pn} (H_{nv}^{(1)'}(\rho) + \chi_{pn} H_{nv}^{(2)'}(\rho)) \cos(nv\alpha_p) \\ E_r = \sum_n -i \frac{nv}{\rho} b_{pn} (H_{nv}^{(1)}(\rho) + \chi_{pn} H_{nv}^{(2)}(\rho)) \sin(nv\alpha_p) \end{cases} \quad 0 < \alpha_p < \psi$$

where $v = \pi/\psi > 1$, and $\alpha_p = \alpha - 2\pi(p-1)/N$. Here χ_{pn} represents the possible different loading scheme for each side resonator and its value (amplitude and phase) depends on the exact details of the coupling section. For brevity, we use a simplified description of the coupling, i.e. a slot in a radial waveguide which has the same angular opening as the side resonators, but extends to $\rho > \rho_v$. With this model we find that the fields are (noting that in most cases $v \gg 1$):

$$(5) \quad \begin{cases} H_z \cong b_{p0} (H_0^{(1)}(\rho) + \chi_{p0} H_0^{(2)}(\rho)) + \sum_{n>0} b_{pn} J_{nv}(\rho) \cos(nv\alpha_p) \\ E_\alpha \cong -ib_{p0} (H_0^{(1)'}(\rho) + \chi_{p0} H_0^{(2)'}(\rho)) - i \sum_{n>0} b_{pn} J_{nv}'(\rho) \cos(nv\alpha_p) & 0 < \alpha_p < \psi \\ E_r \cong -i \sum_{n>0} \frac{nv}{\rho} b_{pn} J_{nv}(\rho) \sin(nv\alpha_p) \end{cases}$$

$$\chi_{p0} = -\frac{H_1^{(1)}(\rho_v)}{H_1^{(2)}(\rho_v)} \left(1 - \frac{1}{1 - i\xi \rho_v} \right), \quad \xi = \frac{-\ln\left(\sin\left(\frac{\pi}{2}\varepsilon\right)\right)}{v(1 - 2/e)}, \quad \varepsilon = \frac{\theta}{\psi}$$

Equations (3) and (5) are our results for the electromagnetic fields in the two different regions of the cavity and they must be continuous on the inner radius of the anode:

$$(6) \quad \begin{cases} \sum_l d_l Z_l(\rho_a) \exp(il\alpha) = b_{p0} (H_0^{(1)}(\rho_a) + \chi_{p0} H_0^{(2)}(\rho_a)) + \sum_{n>0} b_{pn} J_{nv}(\rho_a) \cos(nv\alpha_p) \\ \sum_l d_l Z_l'(\rho_a) \exp(il\alpha) = f(\alpha) \end{cases}$$

where

$$(7) \quad f(\alpha) = \begin{cases} E_{\alpha p} & 0 < \alpha - 2\pi(p-1)/N < \psi \\ 0 & \text{otherwise} \end{cases}$$

At this point, we wish emphasize the importance of the function f , which contains the angular loading scheme of the magnetron, and therefore describes the symmetry properties. Using Equations (6) and (7) we can eliminate the coefficients d_l , b_{pn} and obtain the dispersion equation for the resonance frequencies of the cavity.

3. DISPERSION EQUATION

To obtain the dispersion equation, we eliminate the angular dependence in the continuity condition of the magnetic and electric field:

$$(8) \quad \begin{cases} b_{p0} (H_0^{(1)}(\rho_a) + \chi_{p0} H_0^{(2)}(\rho_a)) = \\ \sum_i d_i Z_i(\rho_a) \exp\left(i l \left((p-1) \frac{2\pi}{N} + \psi \right) \right) \text{sinc}(l\psi) \\ d_i Z'_i(\rho_a) = \frac{1}{2\pi} \int_0^{2\pi} f(\alpha) \exp(-il\alpha) d\alpha \end{cases}$$

and $\text{sinc}(l\psi) \equiv \sin(l\psi)/l\psi$. Further simplification of Eq. 8 requires the detailed specification of the angular loading scheme of the magnetron, as it determines the form of the function f . Out of the many possible loading schemes, we chose to analyze the following three important cases:

- A. N Equal side resonators
- B. $(N/2)$ Separated equal side resonators
- C. 2 Opposing equal side resonators

Note however that the form of Eq. 8 enables the analysis of other cases as well (e.g. N different side resonators).

A. N equal Side Resonators

In this case we assume that the energy extraction from all the side resonators is the same, namely $\chi_1 = \chi_2 = \dots \chi_N$ (the opening angle of the slot is equal). Accordingly, the fields in two resonators differ only in phase but not in amplitude and f has the following symmetry:

$$(9) \quad f\left(\alpha + \frac{2\pi}{N}\right) = \exp\left(i \frac{2\pi q}{N}\right) f(\alpha) \quad q = 0, 1, \dots, N-1$$

where q is the mode number. Using Eq. 9 in 8, we find the dispersion equation:

$$(10) \quad \begin{aligned} & (H_0^{(1)}(\rho_a) + \chi_0 H_0^{(2)}(\rho_a)) + \frac{N}{2v} (H_1^{(1)}(\rho_a) + \chi_0 H_1^{(2)}(\rho_a)) \times \\ & \sum_m \frac{Z_{q+mN}(\rho_a)}{Z'_{q+mN}(\rho_a)} \text{sinc}^2(\psi(q+mN)) = 0 \end{aligned}$$

The zeros of Eq. 10 are the resonance frequencies of the magnetron with N open side resonators. As this assumption of equal side resonators lies also at the basis of the

conventional theory, the form of the equation we get here, is similar to the conventional one (see Ref. 7 eqs. 29,37). In the present case, however, we include the loading of the cavity via the reflection coefficient χ_0 hence the zeros are complex numbers representing the resonance frequency and the quality factor of the cavity.

Fig. 2 shows the solutions of Eq. 10 for the A6 cavity ($r_c = 1.58\text{cm}$, $r_a = 2.11\text{cm}$, $r_v = 4.11\text{cm}$, $\psi = 20^\circ$), as a function of the opening angle ratio ($\varepsilon \equiv \theta/\psi$) of the slot in each side resonator (the resonance frequency in fig. 2a and the quality factor in fig. 2b). The frequency of all the modes is changed by the loading, and they are coupled out. The order of the modes, however, remains unchanged, a fact that we explain by noting that the basic symmetry properties of the cavity are not different from the un-loaded cavity. At this point we wish to emphasize that the exact amount of frequency shift and the magnitude of Q are *sensitive* functions of the coupling model, therefore to obtain a better quantitative estimate of these values a more accurate model of the coupling section is required.

B. N/2 Separated Equal Resonators

In this case we assume that alternate side resonators are equal, namely $\chi_1 = \chi_3 = \dots \chi_{N-1}$, $\chi_2 = \chi_4 = \dots \chi_N$, (e.g. one is open while its neighbor is closed). As a result, the fields in two adjacent resonators differ not only in phase, but also in amplitude, hence the basic symmetry is not valid, and the periodicity properties of f are:

$$(11) \quad f\left(\alpha + 2\frac{2\pi}{N}\right) = \exp\left(i\frac{4\pi}{N}q\right)f(\alpha) \quad q = 0, 1, \dots, N-1$$

Hence, the dispersion equation that we get is a 2x2 determinant, which reflects the fact that there are two different types of side resonators:

$$(12) \quad \det_2 \left\{ \left(H_0^{(1)}(\rho_a) + \chi_{0p} H_0^{(2)}(\rho_a) \right) \delta_{pp'} + \frac{N}{4v} \left(H_1^{(1)}(\rho_a) + \chi_{0p'} H_1^{(2)}(\rho_a) \right) \times \right. \\ \left. \sum_m \frac{Z_{q+mN/2}(\rho_a)}{Z'_{q+mN/2}(\rho_a)} \sin^2 \left(\psi \left(q + \frac{mN}{2} \right) \right) \exp \left(i \left(q + \frac{mN}{2} \right) \frac{2\pi}{N} (p - p') \right) \right\} = 0$$

Here p, p' are the indices of the two side resonators, and $\delta_{pp'} = 1$ for $p = p'$ and 0 for $p \neq p'$. Fig. 3 shows the solutions of eq. 12 for the A6 cavity with three open side resonators (3a resonance frequency and 3b quality factor) as a function of the slot opening angle ratio (ε). The symmetry change clearly affects the various modes differently. For example, the resonance frequency of the $n=1$ mode changes by a far smaller amount than in the previous case, and the same is the quality factors. It is interesting to note that for this loading scheme we can group every two adjacent side resonators and analyze the system as a cavity with basic $N/2$ symmetry like the rising sun magnetron.

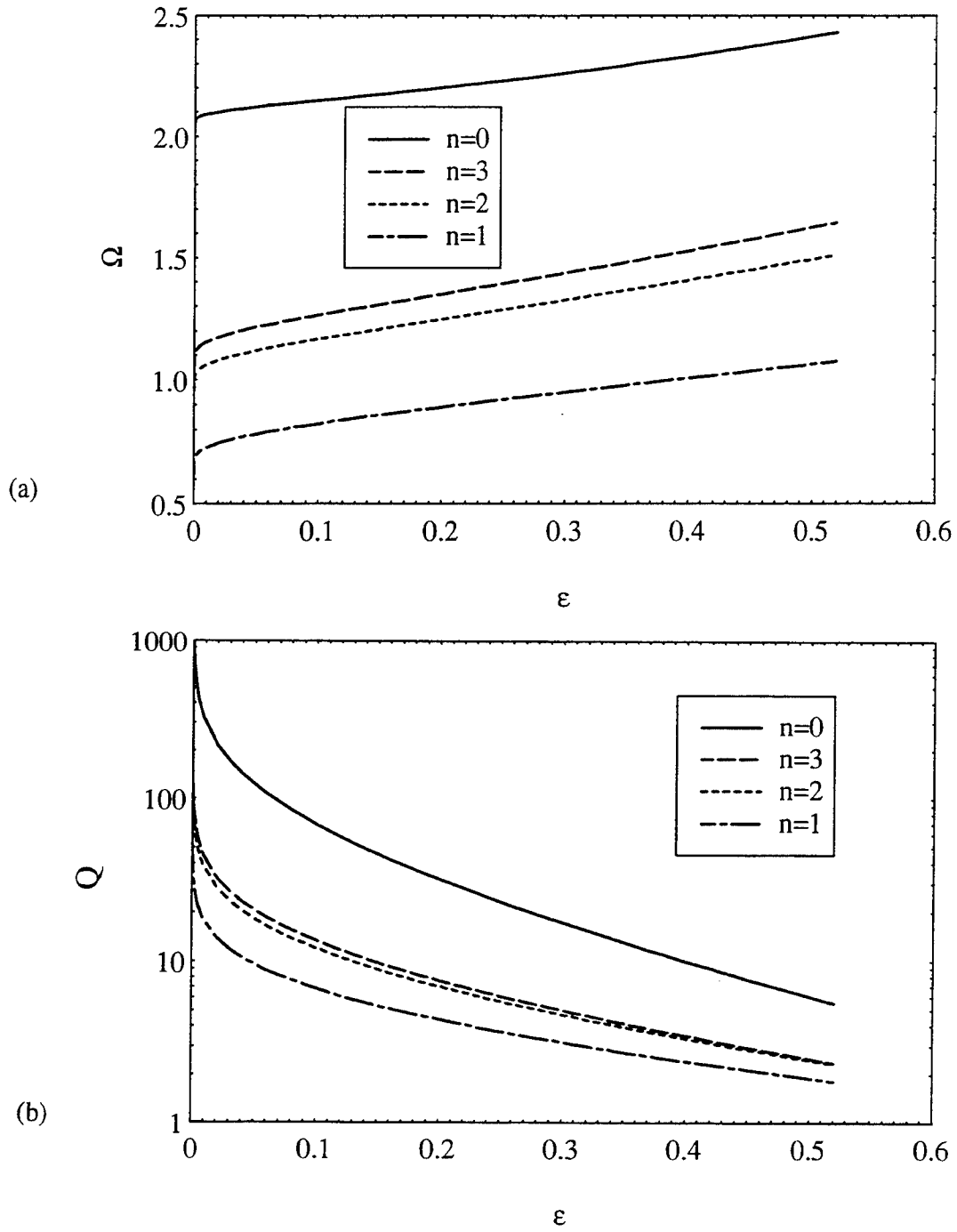


Figure 2: The normalized resonance frequency (a) and quality factor (b) as a function of opening angle ratio ϵ for the lowest four modes of the A6 magnetron ($r_c = 1.58\text{cm}$, $r_a = 2.11\text{cm}$, $r_v = 4.11\text{cm}$, $\psi = 20^\circ$). The angular loading scheme is of six equally loaded side resonators.

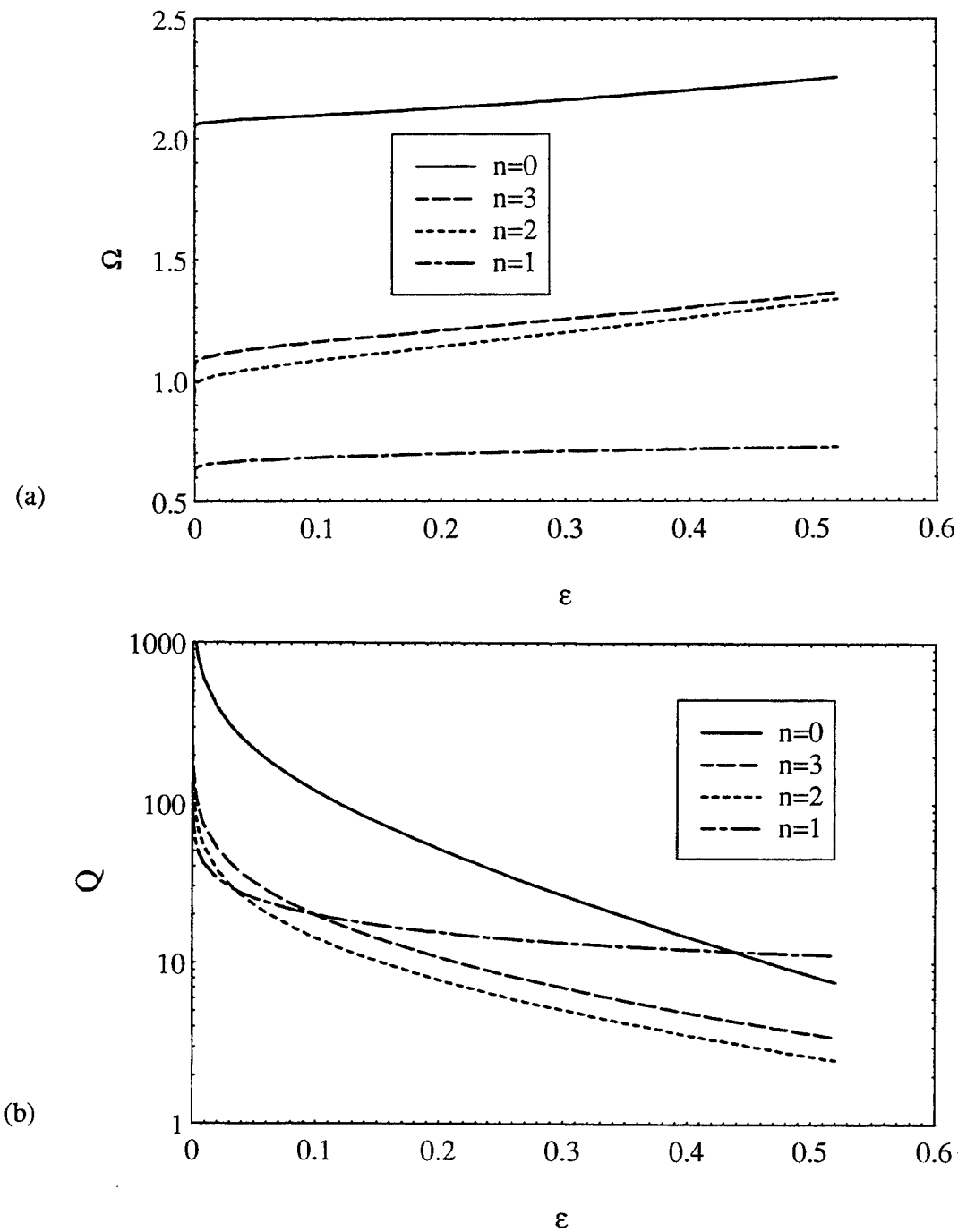


Figure 3: The normalized resonance frequency (a) and quality factor (b) as a function of opening angle ratio ε for the lowest four modes of the A6 magnetron ($r_c = 1.58\text{cm}$, $r_a = 2.11\text{cm}$, $r_v = 4.11\text{cm}$, $\psi = 20^\circ$). The angular loading scheme is of three equally loaded side resonators, and alternating three closed side resonators.

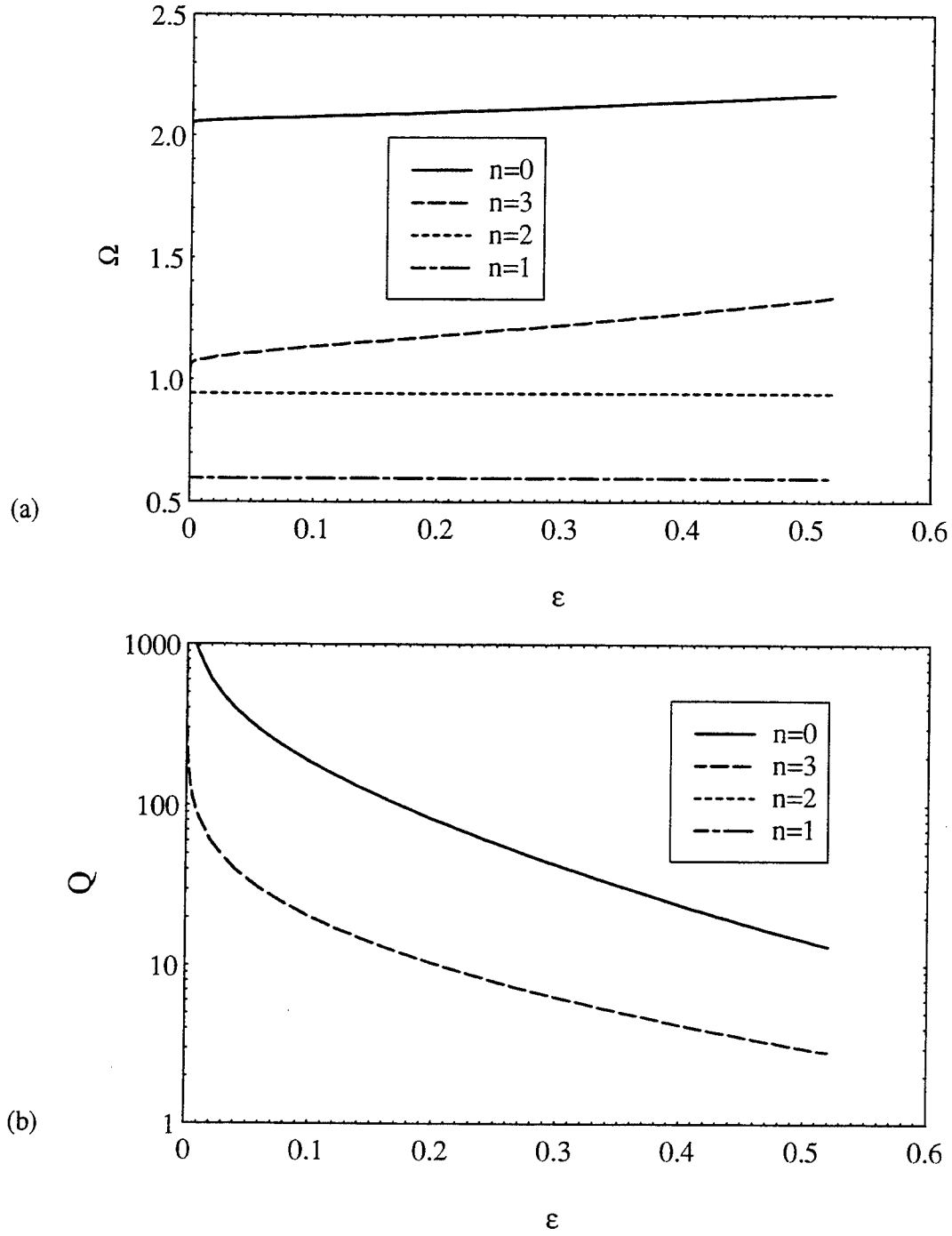


Figure 4: The normalized resonance frequency (a) and quality factor (b) as a function of opening angle ratio ϵ for the lowest four modes of the A6 magnetron ($r_c = 1.58\text{cm}$, $r_a = 2.11\text{cm}$, $r_v = 4.11\text{cm}$, $\psi = 20^\circ$). The angular loading scheme is of two equally loaded side resonators oppsite of each other and four closed side resonators.

C. 2 Opposite Equal Resonators

The last case we present in this work is of a cavity in which every two opposite side resonators are the same, namely $\chi_1 = \chi_{N/2}$, $\chi_2 = \chi_{N/2+1}$, ..., so that the symmetry properties of f are:

$$(13) \quad f\left(\alpha + \frac{N-2\pi}{2N}\right) = \exp(iq\pi) f(\alpha) \quad q = 0, 1, \dots, N-1$$

The dispersion equation is now a $N/2 \times N/2$ determinant reflecting the fact that there are $N/2$ different types of resonators:

$$(14) \quad \det_{\frac{N}{2}} \left\{ \left(H_0^{(1)}(\rho_a) + \chi_{0p} H_0^{(2)}(\rho_a) \right) \delta_{pp'} + \frac{1}{v} \left(H_1^{(1)}(\rho_a) + \chi_{0p'} H_1^{(2)}(\rho_a) \right) \times \right. \\ \left. \sum_m \frac{Z_{q+2m}(\rho_a)}{Z'_{q+2m}(\rho_a)} \sin c^2(\psi(q+2m)) \exp\left(i(q+2m) \frac{2\pi}{N} (p-p') \right) \right\} = 0$$

Fig. 4 shows the solutions of this equation for the A6 cavity where there are only two open side resonators (resonance frequency in 4a and quality factor in 4b) as a function of the slot opening angle ratio (ϵ). This case demonstrates the important influence of the symmetry properties on the various modes. The changes in the $n=1$ and $n=2$ modes are very small, while the changes in the $n=3$ (π mode) are far more prominent. We can explain this by noting that the angular loading scheme now has a basic symmetry of π and therefore this will be the most affected mode.

4. DISCUSSION

The examples clearly demonstrate the effects that the loading has on the resonance frequency and quality factor of the various magnetron modes. The analysis shows that different angular arrangement of the loading with a given coupling scheme (i.e. the slot opening angle) will result in different frequency shifts and decay rates for the magnetron modes. Moreover, the different symmetry properties of the cavity affect also the phase velocity of the waves, and hence change the condition for synchronization between the waves and the electrons, namely the Bunneman-Hartree condition. When all the side resonators are equal (regardless of the exact loading scheme) the phase velocity is $v_p = r_a \omega / q$ (q is the mode number). However, other symmetry properties change this velocity, e.g. for $N/2$ symmetry (case B. above) the phase velocity of the wave is $v_p = 2r_a \omega / q$ as the wave propagates twice the distance during the same time. This fact has a direct implications on the Bunneman-Hartree lines and therefore on the possible interaction between the electrons and the magnetron modes. However, it is important to

note that the analysis of the cold modes can not stand by itself, and must be supported by a study of the effects due to the electronic loading. Furthermore, three dimensional effects and more accurate accounting of the coupling schemes are required in order to have a precise quantitative predictions of the loading effects.

5. ACKNOWLEDGMENTS

We wish to thank Dr. J. Shiloh and Dr. J. Leopold for stimulating discussions during the preparation of this work.

6. REFERENCES

1. A. Palevsky and G. Bekefi, "Microwave emission from pulsed, relativistic e-beam diodes. II The multiresonator magnetron", *Phys. Fluids*, **22**(5), 986-996, (1978).
2. V. L. Granatstein and I. A. Alexeff, Ed., *High Power Microwave Sources*, Ch. 9-10, pp. 309-396, Artech House, New York, (1987).
3. J. Benford and J. Swegle, *High Power Microwaves*, Ch. 5, Artech House, Boston, (1992).
4. H. Sze, B. Harteneck, J. Benford and T. S. T. Young, "Operating characteristics of a relativistic magnetron with a washer cathode", *IEEE Trans. Plasma Sci.*, **PS-15** (3), 327-334, (1987).
5. S. T. Spang, D. E. Anderson, K. O. Busby, K. D. Claborn, S. P. Manning, A. K. Milakovic, J. J. Prochazka, D. M. Rexroad, E. P. Scannel, T. K. Seybold, R. J. Williams Jr. and D. A. Woodyard, "Relativistic magnetron development for use in a lightweight repetitively pulsed portable HPM transmitter", *IEEE Trans. Plasma Sci.*, **PS-18** (3), 586-593, (1990).
6. R. S. Smith, J. Benford, B. Harteneck and H. Sze, "Development and test of an L-band magnetron", *IEEE Trans. Plasma Sci.*, **PS-19** (4), 628-631, (1991).
7. N. Kroll, "The unstrapped resonant system", *Microwave magnetrons*, G. B. Collins, Ed., pp. 49-77, McGraw-Hill, New York, (1948)

PASOTRON™ high-power microwave source performance

Dan M. Goebel, Elmira S. Ponti, Jon R. Feicht, Ron M. Watkins
Hughes Research Laboratories
3011 Malibu Canyon Rd., MS RL 58
Malibu, CA 90265

ABSTRACT

The PASOTRON (Plasma Assisted Slow-wave Oscillator) high-power microwave source utilizes a unique plasma-cathode electron gun and self-generated plasma channel to inject a long-pulse electron beam into a variety of slow-wave structures for microwave generation. The plasma-channel beam transport eliminates the need for an externally-applied axial magnetic field to confine the beam, which results in a very compact, low weight HPM source compared to conventional technologies. The Pasotron has been configured as both a backward-wave oscillator (BWO) and a traveling-wave amplifier, and has produced up to 20-MW of peak power and ≥ 500 Joules per pulse during operation as a BWO. In this paper, we will present the performance of the Pasotron device for a variety of rippled-wall and helix slow-wave structures. The advantages of each slow-wave structure will be discussed, and the output couplers and mode-converters used with each structure to obtain TE-mode outputs are described. The device configurations used for operation in C-band and in L-band will be shown. Long-pulse ($\approx 100 \mu\text{sec}$), plasma-cathode electron-guns operating at 30-to-200 kV and currents of 50-to-1000 A will also be described. Finally, we will present and discuss pulse shortening that has been observed in these plasma-filled devices.

Keywords: PASOTRON, microwave source, plasma

1. INTRODUCTION

PASOTRON high power microwave (HPM) sources are unique devices designed to eliminate one of the major components that contribute to size and weight in conventional linear HPM sources; namely, the solenoid that generates the applied axial magnetic field. Electron beam propagation through a variety of different slow-wave structures (SWS) is accomplished by the self-generation of a plasma channel by the beam. The electron beam is operated in the ion-focused, self-pinched regime where the beam-produced plasma filling the SWS neutralizes the majority of the space charge forces in the beam and permits the self-pinch force to compress the beam for injection into the SWS. The PASOTRON also utilizes a long-pulse, high-perveance, multi-aperture electron gun which employs a low-pressure plasma discharge to provide a stable, high current-density electron source that can withstand the backstreaming ion bombardment from the plasma transport channel.

PASOTRON sources been built as high power backward-wave oscillators¹ (BWO) and traveling-wave amplifiers². Rippled-wall waveguide (RWG), helix, and ring-bar SWS have been used to produce radiation in the L, S, C and X-bands. The devices typically use an electron beam with energies of 50-to-150 kV, beam currents of 50-to-500 A, and pulsewidths of about 100 μsec . RF power in the range of 1 to 5 MW has been obtained from the BWOs, depending on the beam parameters and gas fill, with an electron-beam to microwave-radiation power-conversion efficiency typically ranges from 15 to 25%. One high power PASOTRON source utilized an electron gun capable of operating at 240 kV and over 1 kA to produce a peak microwave power of up to 20 MW.

In this paper, we will present an overview of the PASOTRON device design and performance for the different SWSs just discussed. The C-Band, L-Band RWG, L-Band helix tube performance will be described. Each SWS utilizes different output couplers and mode-converters to obtain TM and TE-mode radiation. The peak power output and energy per pulse obtained from this source is discussed, and pulse shortening observations made.

2. C-Band RWG PASOTRON

The original C-band tube¹, shown schematically in Figure 1, utilized a rippled-wall waveguide SWS designed to operate as a backward-wave oscillator. Radiation in the TM_{01} and TE_{n1} modes could be directly produced in the RWG depending on the parameters and dynamics of the injected electron beam. The operating mode was diagnosed by a series of axial and azimuthal E_r probes, and the power measured by a calibrated side-wall hole coupler. The radiation was

coupled directly out of the system through a low-gain antenna and ceramic dome, which also acted as the vacuum interface. RF power in the range of 1 to 5 MW was obtained, depending on the beam parameters and gas fill, and RF pulsewidths of over 100 μsec were achieved at up to 2-Hz pulse-repetition-rate. The electron-beam to microwave-radiation power-conversion efficiency for this type of device typically ranges from 15 to 25%.

Electron-beam pulses for this PASOTRON source were obtained from a Hollow-Cathode-Plasma (HCP) electron gun.³ The HCP gun provides high-current density ($>50 \text{ A/cm}^2$) and long-pulse operation without gap closure by generating a controlled plasma discharge which acts as the electron source. A low-pressure glow discharge generated between the hollow cathode of the gun and the discharge anode produces a uniform and stable plasma. The plasma density in the hollow cathode, and subsequently the beam current density, is controlled by a discharge pulser circuit. The cold-cathode discharge requires no filament heater power, and can be operated at high pulse-repetition rates. The anode of the discharge acts as the first grid, or "cathode", of a high-perveance, multi-aperture electron accelerator. The second grid of the accelerator (the beam anode) has apertures aligned with the first grid. A dc high-voltage power supply connected between the grids accelerates electrons that arrive at the apertures from the plasma, while the low-voltage discharge pulser modulates the beam current to generate arbitrary pulse waveforms. The voltage of the electron beam is controlled by the dc voltage level, while the beam current, pulse width, and pulse repetition frequency are independently controlled by the low-voltage ($< 5 \text{ kV}$) pulser circuit. A low current ($<10 \text{ mA}$) "keep-alive" discharge is continuously maintained in the background gas to reduce the turn-on jitter during initiation of the cold-cathode discharge. Typical electron beam energies up to 100 kV, beam currents of up to 300 A, and pulsewidths of about 100 μsec were used with this device.

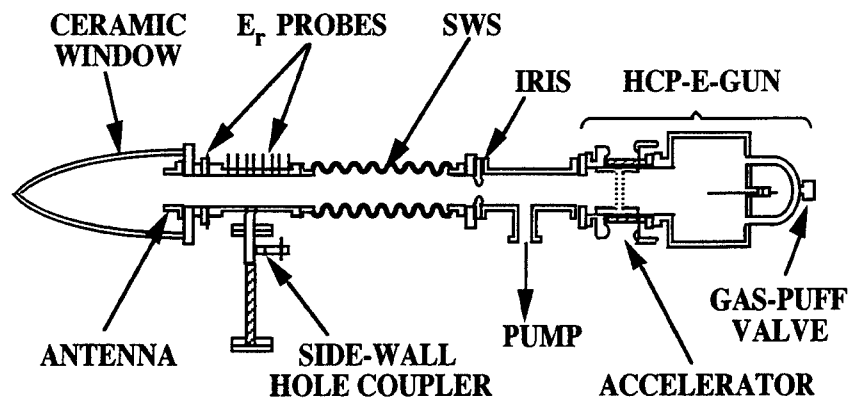


Figure 1. Schematic diagram of a ripples waveguide SWS C-Band PASOTRON Oscillator.

The gas pressure required to produce the glow discharge plasma inside this electron gun is in the range of 5 to 50 mTorr of helium. For HPM generation with the PASOTRON SWS, a transient helium gas-puff system is used to supply an adequate pressure inside the hollow cathode to strike the glow discharge, and provide a reduced gas pressure in the SWS that enhances beam propagation and microwave generation. An electromagnetic gas-puff valve is triggered prior to the plasma discharge switch to provide the gas puff to the hollow-cathode chamber. Our present puff valve is capable of operation up to 10 Hz, and operation at PRF of typically 0.2-to-0.5 Hz is used. It was found that the efficiency of the PASOTRON source could be increased under most beam conditions by adjusting the time between the gas puff pulse and the plasma discharge pulse to optimize the neutral gas pressure both in the gun and the SWS, and also backfilling the SWS with a low-pressure gas typically consisting of xenon at a pressure of about 2×10^{-5} Torr. Formation of the plasma channel and propagation of the electron beam is discussed elsewhere.⁴

Typical output power levels for the C-band RWG PASOTRON are illustrated in Figure 2. As the electron beam voltage and current are varied, the device turns-on at different frequencies corresponding to different waveguide modes, and also exhibits regions with no microwave production. Each operating voltage that produced radiation was observed to have an optimum maximum beam current, which is indicated in the figure. Within an operating voltage range, the optimum current increased with beam voltage. On a dispersion diagram, this corresponds to the system maintaining operation at a fixed frequency and wave-number for a given radiation mode in the RWG. This characteristic operation

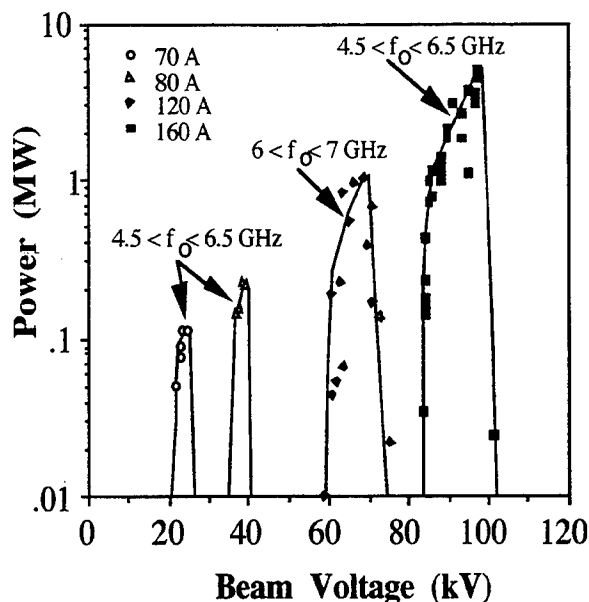


Figure 2. Output from the C-Band PASOTRON oscillator.

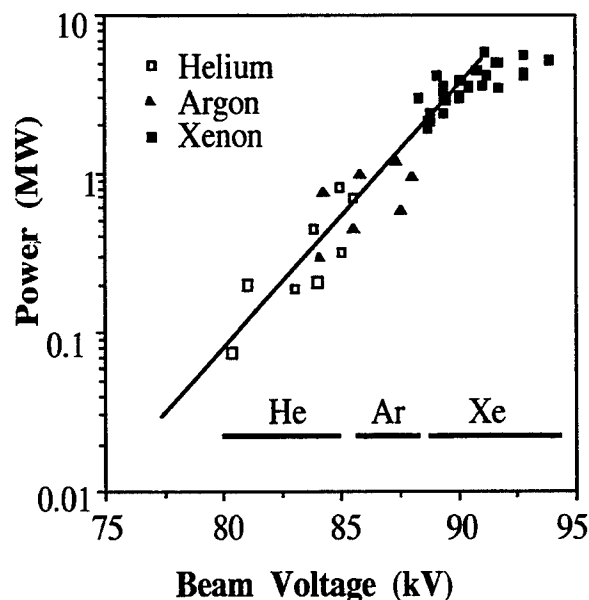


Figure 3. RWG PASOTRON power output versus beam voltage effect of using heavy ion masses.

at a single frequency as the beam voltage changes results from the balancing of the electron energy as the voltage increases with the depression of the beam line due to the slow space-charge wave as the current increases. The frequency at which the device produces the maximum output power occurs where the gain of the system is a maximum, which is a function of system length and end reflections.^{5,6} Adjusting the beam parameters such that the frequency corresponds to this maximum gain of the SWS produces the highest system efficiency and output power. In fact, the PASOTRON RWG SWS was usually made so short (8-to-12 ripples) in an attempt to reduce the system length that the device would only oscillate at the points of maximum gain.

It should be emphasized that low gain systems with significant end reflections have large output power variations and "stop bands" with no radiation when the beam current and voltage move away from the optimum gain. This can have the same appearance as pulse shortening occurring toward the end of the pulse, but is simply de-tuning of the system efficiency with voltage droop or current variations that can occur within the beam pulse. Pulse shortening that occurs at nearly constant beam current and voltage are caused by different effects, and will be discussed later.

Another characteristic of the RWG PASOTRON was the improvement in efficiency and output power as the mass of the fill gas used to make the plasma channel was increased. Figure 3 shows an example of the maximum power that could be produced by the device at any beam current as a function of beam voltage for the three fill gases indicated. Operation in xenon in the range of 10^{-5} -to- 10^{-4} Torr provided the highest output powers, and the performance shown in Figure 2 was with a xenon backfill. This improved performance with heavier gases is believed to be due to a suppression of beam hydrodynamic instabilities. Oscillations observed in the output power had characteristic frequencies that decreased as the square-root of the ion mass. The frequency and growth rate of hose instabilities evaluated for our beam parameters decreases with ion mass, which is consistent with these results in that the instability has difficulty growing within the 100- μ sec pulse duration in xenon. Probe data from this system with a smooth wall also showed the presence of a kink instability under certain beam parameters and gas fill pressures. Suppression of the beam instabilities was observed to maximize the peak output power and rf pulse duration.

3. L-Band RWG PASOTRON

In an attempt to produce higher peak powers and higher energy per pulse, the voltage and current capabilities of the gas-puff electron gun used in the PASOTRON system were increased. At the same time, the RWG SWS was redesigned to operate in L-Band. Figure 4 shows a schematic drawing of the L-Band RWG PASOTRON HPM source. The HCP electron gun was designed to operate at 2000 A and 240 kV by scaling the active grid area up to 482 cm² and the cathode area up to about 10,000 cm². The SF₆-insulated, 17- μ perv E-gun utilized the gas-puff injection system from the C-band device. The gun was connected to a 10- μ F, 200-kJ capacitor bank that could be charged up to 240 kV by a 10-kW power supply, and the beam current modulated by an ignitron discharge pulser that turned the plasma in the HCP E-gun on and off.

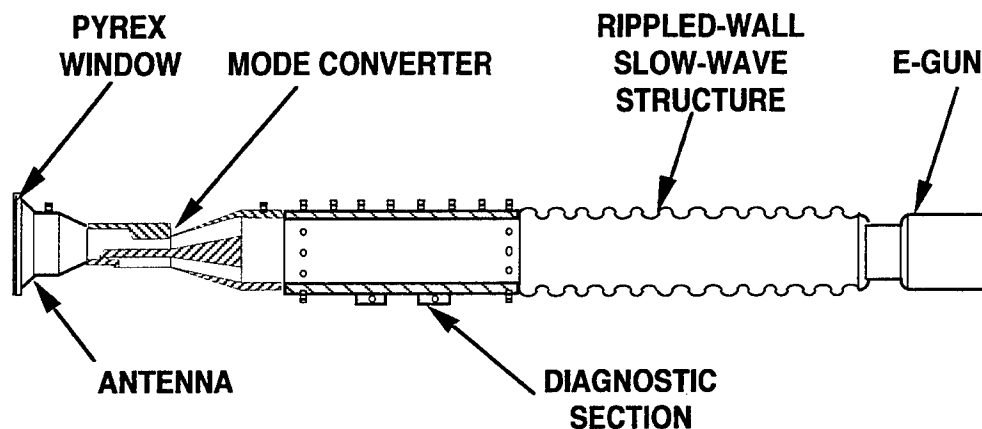


Figure 4: Schematic diagram of the high voltage L-Band RWG PASOTRON.

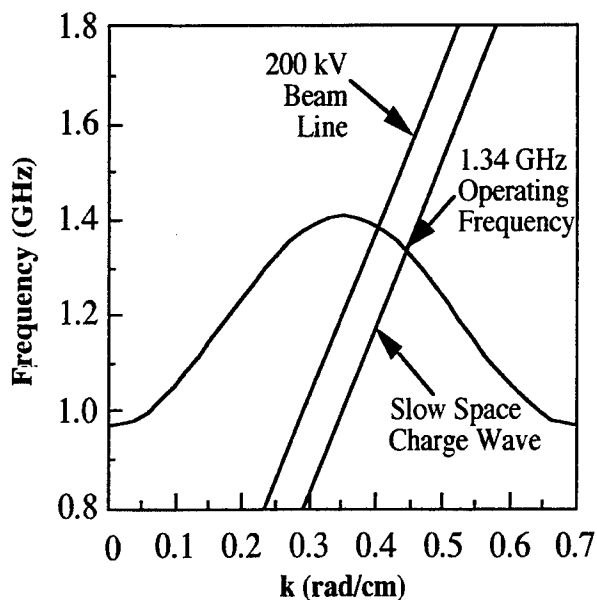


Figure 5: Dispersion diagram for the high voltage L-Band showing the 1.34 GHz operating frequency.

The RWG SWS was designed with an inside diameter of the ripples of 18.3 cm, an outside diameter of the ripples of 28.5 cm, a ripple pitch of 8.6 cm, and a total of 12 ripples. The dispersion diagram for this structure is shown in Figure 5, where the designed operating frequency of 1.34 GHz for the fundamental TM₀₁ waveguide mode is indicated. The SWS was fabricated by machining a large aluminum mandrel, electrodepositing \approx 3-mm of copper on the mandrel, and then chemically etching the mandrel away. UHV flanges were attached to straight sections at the end of the ripples. The structure was designed such that irises of various diameters and cylindrical-waveguide sections of various lengths could be added to optimize the magnitude and phase of the reflections at the ends of the SWS for maximum output power.

The SWS was attached to a 122-cm long diagnostic section of straight cylindrical aluminum waveguide. Sidewall E_r probes were installed in axial and azimuthal arrays on the cylinder to measure the VSWR and operation mode in the device. In addition, two side-wall hole couplers were installed

and calibrated to determine the power level in the waveguide. The diagnostics section was connected directly to a mode converter, shown in Figure 6, to transform the output power from the TM_{01} to the TE_{11} cylindrical waveguide mode. The mode converter is designed such that the TM_{01} mode is converted to TEM by a tapered axial-conductor section, which bends at 90° to launch a TE_{01} mode in rectangular waveguide. The rectangular waveguide is tapered up to the original diameter cylindrical waveguide carrying the TE_{11} mode, and attached to a 13-dB gain antenna. Insertion loss measurements indicated that less than 0.5 dB loss was obtained over a 30% bandwidth. Several E_r probes were inserted in the output cylindrical section to measure the output power from the mode converter in waveguide. A pyrex window was then attached directly to the end of the antenna, and the power radiated into a large load. In addition, an array of calibrated probes was installed into the load to measure the radiated power levels.

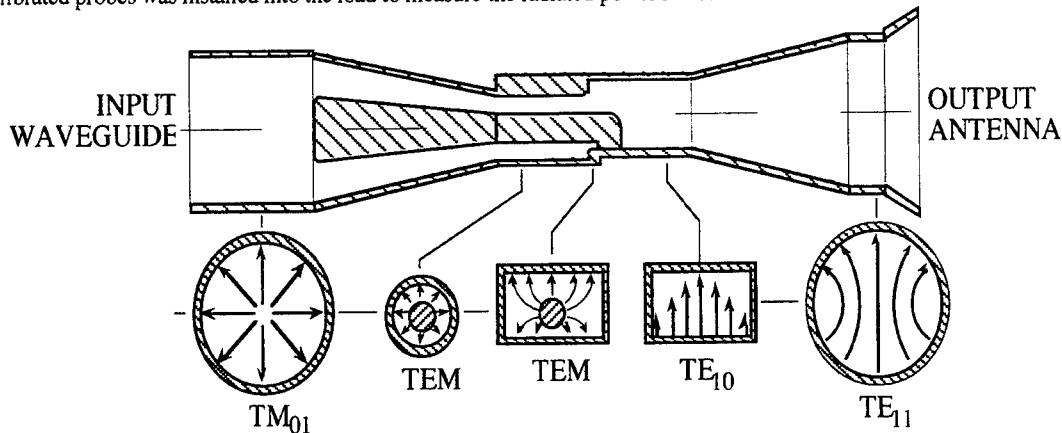


Figure 6: Schematic drawing of the low insertion loss mode converter for launching the TE_{11} mode.

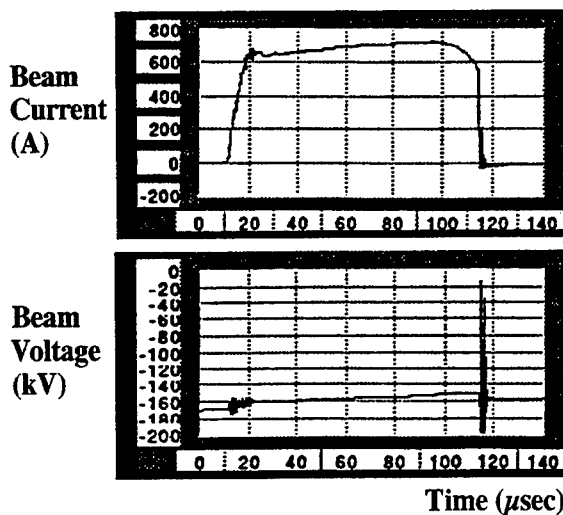


Figure 7: Typical E-gun current pulse and voltage showing beam currents of about 700 A at voltages of 160 kV for pulse times of over 100 μ sec.

A typical waveform from the electron gun is shown in Figure 7. Beam pulses in excess of 700 A at up to 200 kV were routinely generated at pulse lengths of 100 μ sec, and peak currents of over 1 kA at voltage of over 225 kV were obtained. Representative microwave generation in the TM_{01} mode in this device is illustrated in Figure 8. In Fig. 8a, operation at 350 A and 150 kV produced a peak power of just under 10 MW, with radiation lasting for the full duration of the beam pulse. As the beam current is increased in Fig. 8b to 500 A, the >10 MW peak-power pulse is found to terminate after about 40 μ sec, even though the beam pulse ran stably for 100 μ sec. Finally, increasing the beam current to 1 kA in Fig. 8c causes the pulse to terminate in a few microseconds before the peak power level even approached that achieved in Fig. 8a. Termination of the pulse in the case of Fig. 8b was found to correspond to device changing modes to the TE_{n1} mode, which is reflected by the mode converter. However, complete suppression of the microwave generation in any mode was also observed for the beam current and voltage case of Fig. 8b, and as the beam power was increased, as shown in Fig. 8c.

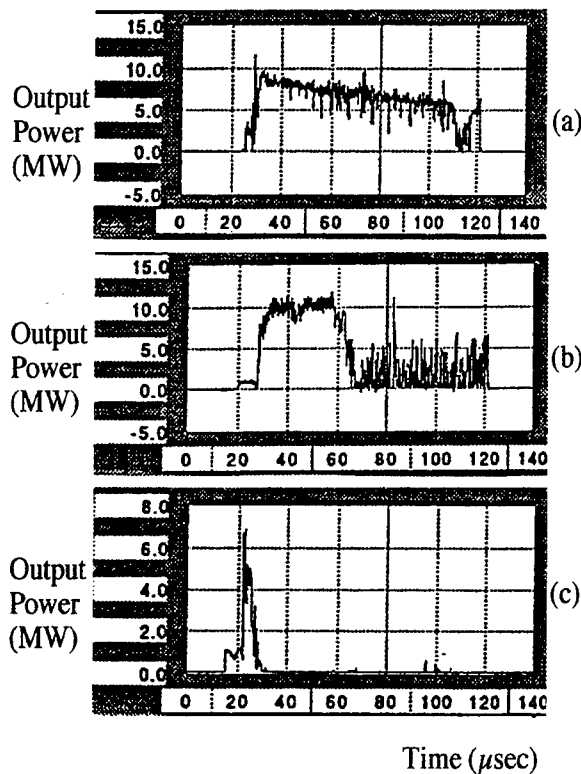


Figure 8: Sequence of pulses at (a) 350 A, 150 kV, (b) 500 A, 160 kV, and (c) 1 kA, 170 kV showing pulse shortening evolution as the beam current is increased.

inversely with frequency. Operation in L-band requires a RWG SWS to have a diameter in excess of 20-cm. The finite length of each of these large-diameter ripples then leads to a physically long structure and a large system size and weight. This problem can be alleviated by using a helical SWS. To first order, the helical structure operates in a co-axial TEM mode that does not depend strongly on diameter. The diameter and length of the device are then determined primarily by other considerations such as the desired operating voltage, beam diameter, and gain.

There are two major factors that have historically limited the power output from microwave sources that utilize helical SWSs. The first is overheating of the helix structure and subsequent "power-fade" due to direct beam interception on the helix or joule-heating from the rf currents. The second factor is electrical breakdown in the output coupler at the high fields characteristic of HPM sources. The helix-PASOTRON source uses a water-cooled copper helical SWS and a unique, high-power output coupler to generate high-power (>1 MW) microwave radiation and transport it out of the device to a load or antenna.

The helix-PASOTRON geometry is shown schematically in Figure 9. The electron beam is generated by the HCP E-gun discussed above. The electron beam is injected into the gas-filled vessel, where the beam interacts with the helical SWS to produce microwave energy at the desired frequency from the BWO interaction. The beam propagates through the SWS without the use of confining magnetic fields due to the self-generated plasma channel. The unused electron beam is collected on a carbon beam dump located beyond the downstream output coupler, and on the helix and barrel of the tube. The microwave radiation is coupled out of the system by a co-axial transformer to quarter-height waveguide, shown in Figure 10, and matched to full-height waveguide by a stepped-transition region. The output radiation in full height waveguide is diagnosed by a directional loop-coupler and transported in the waveguide to a recirculating water-load or an antenna. The system is pumped out to a base pressure in the 10^{-8} Torr range by either a vac-ion pump or a

Removal of the mode converter and operating the device such that TE_{n1} modes were directly generated¹ in the SWS was not successful in increasing the peak power or energy per pulse capability of the device. Similar pulse shortening with increasing beam current was observed during generation of TE_{11} and TE_{21} modes, indicating that mode-competition can cause pulse shortening if there are components in the system such as our mode-converter that limit the output of the favored mode. Optical photo-detectors located at the entrance and exit of the SWS indicated that the pulse shortening occurred for all rf modes at nearly the same light intensity, corresponding to a critical plasma density. Higher beam currents caused this critical plasma density to be reached earlier in the pulse, which produced the progressive reduction in pulse length with increasing beam current shown in Fig. 8. Increasing the background gas pressure produced the same effect as increasing the beam current, which correlates with an ionization rate dependence on the rf pulse length. This pulse shortening effect limited the peak power produced in all rf modes in this device to less than 20 MW and the energy in the pulses to less than 1 kJ. Additional information about pulse shortening in PASOTRON devices is presented in the following sections.

4. L-Band Helix-PASOTRON

A major disadvantage of the RWG PASOTRON source is that the electromagnetic mode in the device that interacts with the beam is either TM_{01} or TE_{n1} . These waveguide modes cause the waveguide diameter required to propagate the microwave energy to scale

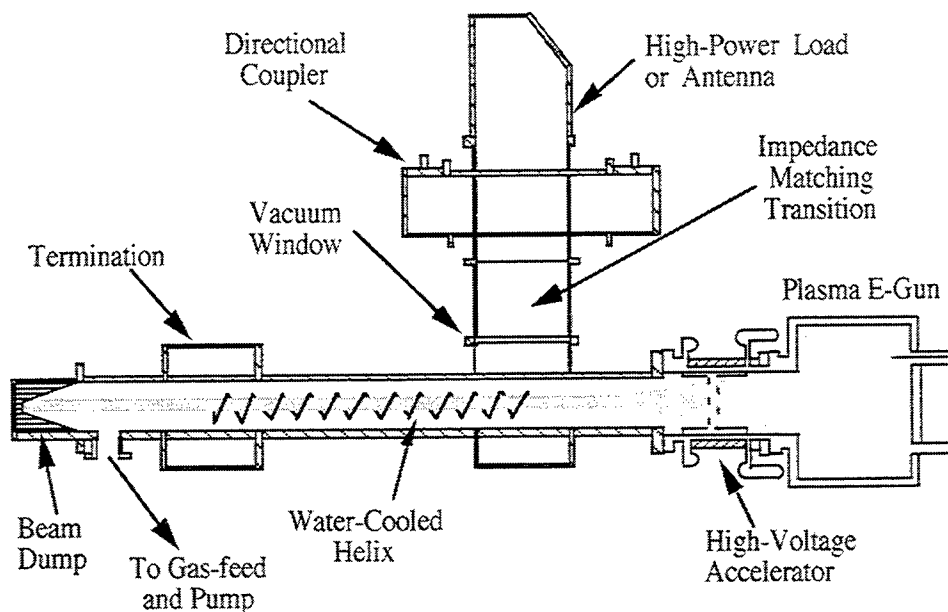


Figure 9. Schematic drawing of the helix-PASOTRON HPM source.

turbomolecular pump, and filled with gas by either a gas puff of helium from the gun or by a back-fill of xenon with a static pressure of 1-to- 4×10^{-5} Torr.

To fabricate the helix in the L-Band PASOTRON, a 0.64-cm diameter copper tube was wound under tension on an aluminum mandrel such that a helix was formed with a 5-cm nominal diameter and a 2.2-cm diameter pitch. The tube has a barrel inside diameter of 10 cm. The RF radiation generated in the system is extracted at the upstream end of the helix through the side-wall output coupler shown in Fig. 10. The TEM mode excited on the copper conductor passes

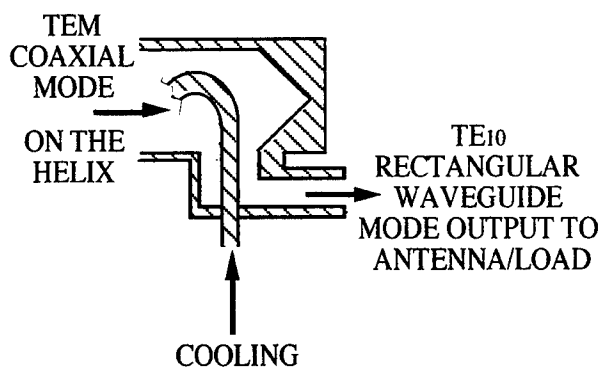


Figure 10. Output mode converter for transforming the TEM mode on the helix end into TE_{10} rectangular waveguide mode.

through the side-wall aperture and launches a TE_{10} mode in the quarter-height rectangular waveguide. The copper conductor is electrically terminated on the opposite wall of the waveguide, and water cooling is injected into the tube at this location to cool the helix. The quarter-height waveguide is transitioned by a series of steps to full height waveguide. The RF radiation is then monitored by a directional coupler in the full-height waveguide section. A portion of the sampled rf signal is directed to a calibrated detector for absolute power measurements, and another portion is directed to several diagnostics (tuned receiver, time-domain analyzer, and heterodyne system) for frequency and bandwidth measurements. After passing the RF diagnostic section, the high-power microwave pulse is deposited in a high-power waveguide load, or can be directed via waveguide to an antenna and radiated into high power absorber.

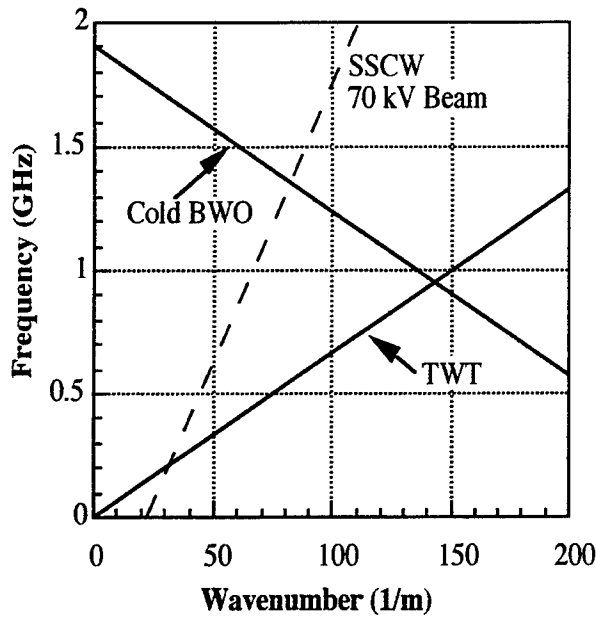


Figure 11. Cold dispersion for the Helix-PASOTRON showing the BWO, TWT, and slow space charge wave for the 70 kV electron beam.

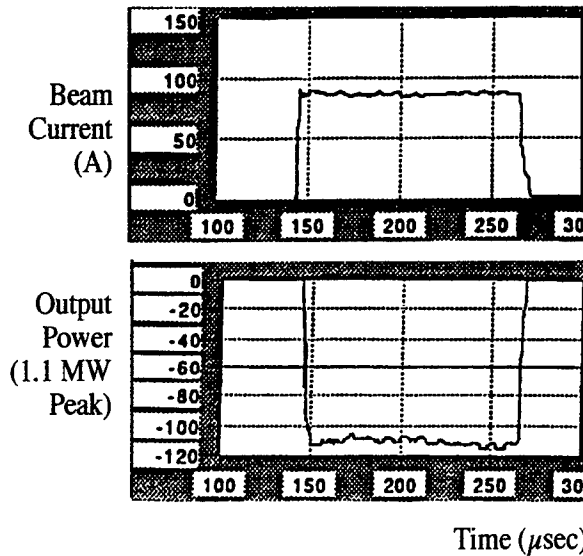


Figure 11. Beam current and typical microwave output pulse from the helix-PASOTRON.

neutralization fraction approaches or even exceeds 1, and the beam is fully pinched to its Bennett equilibrium diameter.⁷ Subsequent ionization further increases the plasma density with time during the pulse. If the plasma frequency is significant compared to the BWO frequency, then the output frequency will chirp (increase with time) due to plasma generation and beam pinch processes that cause the dispersion curve to shift upward with time.

The backward wave frequency at which this helix structure can operate, to first order in the absence of plasma in the SWS, is given by

$$\omega = -\frac{k c p}{\pi d} + \frac{2 c}{d},$$

where ω is the angular frequency, k is the wave number, c is the speed of light, p is the pitch of the helix, and d is the nominal diameter of the helix. The system will oscillate when this frequency matches the slow-space charge wave (SSCW) frequency on the beam, given by $\omega = v_b k - \omega_b$, where v_b is the beam velocity and ω_b is the beam plasma frequency. A plot of the dispersion relationship based on these two equations is shown in Fig. 11. The BWO and forward-wave (TWT) lines ($n = \pm 1$ spatial harmonics) are shown with the SSCW line for an 80-A beam at 70 kV. If the beam voltage and/or current is changed, the slope of the beam-SSCW and the frequency changes. This feature provides the frequency tuning with beam voltage for which BWOs are known.

Typical beam current and output power pulses from the L-Band Helix-PASOTRON are shown in Figure 12. At a beam current of 80-A and a voltage of 70 kV, corresponding to the conditions shown in the dispersion diagram of Fig. 11, a calibrated output power of 1.1 MW is measured. This example corresponds to an efficiency of about 20%. The L-band radiation lasts for the full duration of the beam pulse ($>100 \mu\text{sec}$), and the power output is fairly constant during the pulse. The maximum output power for this L-Band helix system that lasted the full duration of the 100- μsec beam pulse was about 2 MW, and efficiencies approaching 30% have been observed.

The plasma inside the helix that confines and transports the beam also changes the dispersion of the system. The dispersion relationship for this case is

$$\omega^2 = \left(-\frac{k c p}{\pi d} + \frac{2 c}{d} \right)^2 + \omega_p^2,$$

where ω_p is the characteristic frequency of the plasma inside the SWS. As the beam ionizes the background gas, the plasma density in the SWS increases and the beam starts to pinch. This process increases the background plasma density with time until the

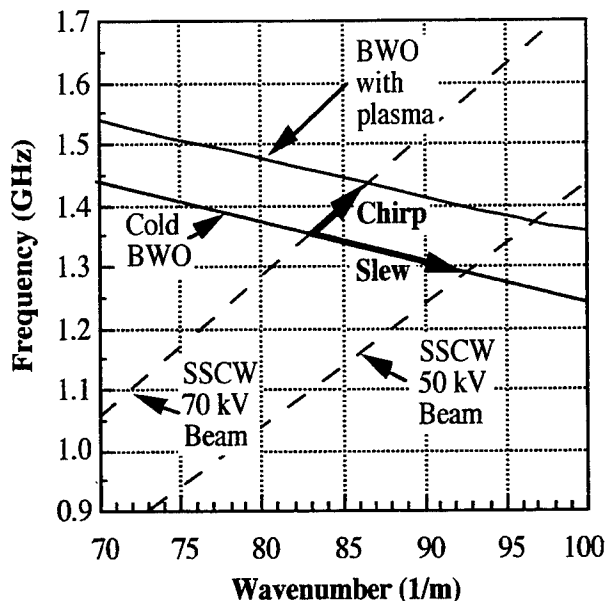


Figure 13. Hot dispersion relationship for the L-Band Helix-PASOTRON showing the displacement of the dispersion curve with plasma in the SWS and the effect of voltage variations during the pulse.

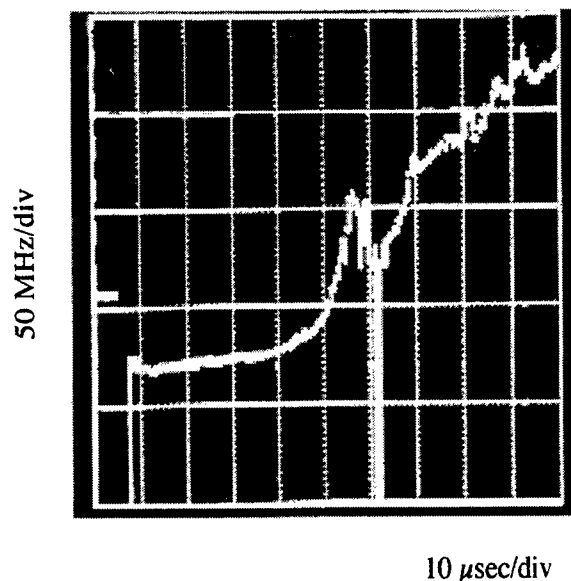


Figure 14. Frequency versus time for the Helix-Pasotron with a xenon gas fill of 2×10^{-5} Torr. Frequency starts at 1.22 GHz, steps down and then chirps up.

Another possibility is that the beam voltage may sag during the pulse due to finite output capacitance or poor regulation of the beam power supply. This causes the oscillation frequency to slew (decrease with time) during the pulse. Finally, if the beam current changes during the pulse due to the power supply or gun perveance changes, the slope of the beam line will change due to variations in the beam plasma frequency, and the oscillation frequency will again change. When all of these effects occur in a normal laboratory environment, and become significant compared to the cold BWO frequency, then the actual oscillation frequency may be very dynamic with time within the pulse.

Demonstration of this effect of output frequency variation within the pulse length is shown in Fig. 14. In this photograph of the display of a time domain analyzer monitoring the L-Band Helix PASOTRON output pulse, the frequency is shown versus time. The system starts oscillating a frequency of 1.22 GHz, and as the beam current increases at the start of the pulse the frequency steps down to the characteristic operating frequency. This frequency is fairly stable for nearly 30 μ sec, but eventually the frequency starts to chirp and vary significantly near the end of the pulse. During the frequency chirp, the output power typically decreases somewhat (10-to-50%), and then in this case dropped dramatically to nearly zero after 60 μ sec. The magnitude of the chirp decreases with conditioning of the system, corresponding to the reduction in impurities that are easily ionized by the beam. In this example of a poorly conditioned system, the frequency chirps about 150 MHz over the 100- μ sec pulse. After about 1000 shots, this increase in frequency is typically less than 20 MHz for this system, and the output power is roughly constant during the majority of the pulse.

The magnitude of the chirp in helix-PASOTRON sources is determined by the neutral gas fill pressure, the beam current and voltage, and the impurity level (conditioning and cleanliness). This is clearly an ionization rate effect that shifts the dispersion curve and beam line with time as the plasma density in the helix increases. This ultimately results in pulse shortening, because higher ionization rates associated with trying to increase the output power by raising the beam current causes the frequency to chirp up out of the band of the output couplers. The pulse cuts off because of significant reflection back from the output coupler. In addition, the gain of the system

again depends on the frequency due to end reflections, which affects the output power during the chirp. Plasma generation in the helix SWS produces self-detuning of the helix system similar to the strong beam-voltage induced RWG detuning shown in Fig. 2. The fact that this is an ionization rate effect indicates that self-detuning of the system away from optimum gain and output coupling is a major cause of pulse shortening observed in both the RWG and helix SWSs.

5. CONCLUSIONS

The PASOTRON HPM source is a unique device capable of peak powers of up to 20 MW and energy per pulse of nearly 1 kJ (to date). The plasma-channel transport of the electron beam through the SWS in this device eliminates the requirement for an applied magnetic field to confine the beam, which results in a significantly smaller HPM source compared to conventional technology. Various SWSs have been used to produce radiation in C and L band, and novel output couplers have been developed to provide waveguide output in the TE_{10} mode for routing the rf to high power loads or antenna structures. The finite length of the SWS and the presence of end reflections in these devices cause the gain and efficiency to depend strongly on the operating voltage and frequency. The dynamic plasma parameters inside the SWS due to beam ionization of the background gas also affect the operating frequency of the oscillator by shifting the dispersion curves and beam lines. Variations in the output power during the pulse and premature termination of the rf output power is characteristic of "pulse shortening" in some cases, and simple tuning of the sensitive beam-structure system in other cases.

Pulse shortening in the L-band PASOTRON sources was found to be caused by mode competition, beam instabilities (hose instabilities), and plasma generation which caused frequency changes and gain variations. Standard causes for pulse shortening associated with arcing in the system have also been observed, but these decrease rapidly with time as the surfaces become conditioned. The changes in operating frequency within a pulse (from the plasma upshifting the dispersion curves) cause pulse shortening by driving the oscillation frequency out of the bandwidth of the rf components in the device, which causes power to be reflected back into the system and mode/gain competition to occur. In finite length system with end reflections, this frequency change also strongly affects the gain and efficiency. The advantage in size and weight of the system won by using plasma to transport the beam carries the complexity of dealing with a dynamic plasma density in the SWS in simultaneously achieving high peak powers and long pulse lengths. Designing high bandwidth components and controlling the plasma generation rate have been found to be crucial to minimize pulse-shortening effects in PASOTRON sources.

6. ACKNOWLEDGMENTS

This work was supported by Hughes Research Laboratories internal research and development funds. The authors would like to acknowledge the technical contributions of R. Schumacher, J. Santoru, R. Kates, P. Sumner, R. Robson, J. Butler and J. Hyman, Jr. to this work.

7. REFERENCES

1. D.M. Goebel, J.M. Butler, R.W. Schumacher, J. Santoru, and R.L. Eisenhart, "High-power microwave source based on an unmagnetized Backward-Wave Oscillator", IEEE Transactions on Plasma Science, **22**, No. 5, pp. 547-553 (1994).
2. E.S. Ponti, D.M. Goebel, J. Feicht, J. Santoru, "PASOTRON amplifier experiments", Proc. SPIE Conf., Los Angeles, CA, 1995.
3. D.M. Goebel, R.W. Schumacher, and R.M. Watkins, "Long-pulse plasma cathode E-gun", Conference on High Power Particle Beams, Washington, DC, May 25-29, 1992, pp. 1093-1098.
4. E.S. Ponti, D.M. Goebel, R.L. Poeschel, "Beam focussing and plasma channel formation in the PASOTRON HPM source," these proceedings.
5. B. Levush, T.M. Antonsen, Jr., A. Bromborsky, W.R. Lou, and Y. Carmel, "Theory of relativistic backward-wave oscillators with end reflections," IEEE Trans. Plasma Sci., **20**, 1992, pp.263-280.
6. L.D. Moreland, E. Schamiloglu, and R.W. Lemke, "Effects of end reflections on the performance of relativistic backward wave oscillators," to be published in IEEE Trans. Plasma Sci., Special Issue on HPM, 1996.
7. W.H. Bennett, Phys. Rev., **45**, pg. 890 (1934).

SESSION 2

Photonic band gap (PBG) technology for antennas

L. J. Jasper and G. T. Tran

Army Research Laboratory
2800 Powder Mill Rd., Adelphi, MD 20783-1197

ABSTRACT

Using the new and powerful technology of photonic band gap (PBG) engineering to produce planar format antennas allows designers to shape antenna characteristics and improve their functional capabilities. In this paper, we describe both analytical and experimental work performed to develop ultra-wideband (> octave) PBG antennas, and to characterize frequency/bandwidth-agile PBG substrates. We also highlight new and interesting PBG concepts that should offer additional capabilities and applications, once they have matured and are commercially viable.

Keywords: photonic band gap, lattice, phased-array, dielectric substrate, photoconductors, antennas

1. INTRODUCTION

Photonic band gap (PBG) structures have pass and stop bands with respect to electromagnetic (EM) radiation. A one-dimensional (1-D) PBG structure has dielectric layers with an index of refraction that alternates between a high and low value. PBG structures are designed to have overlapping (forbidden range of frequencies) band gaps in each direction of propagation. A two-dimensional (2-D) PBG structure forbids EM propagation at frequencies within the band gap for all directions in a 2-D lattice. A three-dimensional (3-D) PBG forbids EM propagation at frequencies within the band gap in all directions in a 3-D lattice. The first experimental validation of this concept was published by Yablonovitch and Gmitter [1], and the first correct theoretical model was developed by Leung [2].

Planar antennas fabricated on conventional dielectric substrates have evoked tremendous interest because of their compatibility with integrated-circuit technology, and because they can be attached flush with the outside of a vehicle or ordnance. However, it is well known that such antennas are highly inefficient radiators. This inefficiency is due primarily to the fact that the antennas radiate much more efficiently into the dielectric substrate than into air. Energy radiated into the substrate is lost to surface-wave and leaky-wave excitation, which causes coupling to other components of the circuit and generates cross-talk and noise. A PBG substrate is an excellent planar antenna substrate, since radiation is not allowed to couple into the substrate over the band gap, leading to a significant enhancement in radiation efficiency. This concept has been demonstrated previously for time-harmonic operation using a bow-tie antenna on a 3-D PBG substrate [3].

In this paper, we describe our investigative techniques for producing PBG structures with ultra-wideband (UWB) characteristics and frequency/bandwidth agility. We examine several new types of PBG structures with distinctive band-gap properties that make them well-suited for UWB and high-intense radiation antennas. We introduce a new technique for producing a quasi 3-D PBG structure using the property of a Luneberg lens for directing (channeling) EM propagation inside a PBG structure. (We suggest a Luneberg PBG structure in conjunction with internal emitters as a means for microwave generation, power enhancement, and radiation directivity.) Finally, we examine several phased-array schemes in which PBG technology will play a major role.

1.1. Design and characterization of a 2-D PBG structure and a PBG-backed antenna

The Army Research Laboratory (ARL) sponsored a program with Polytechnic University with the objective of demonstrating a UWB 2-D PBG structure for use as a substrate for a planar antenna. For this study, we took EM measurements in order to characterize PBG structures, and to examine their utility for producing highly efficient UWB planar antennas.

We performed the experiments through the optical switching of planar antennas fabricated on a photoconductive material [4]. A mode-locked, pulse-compressed, frequency-doubled Nd-YLF laser produced green pulses with 200 mW average power, 4 ps duration, and 527 nm wavelength. We used oxygen-bombarded silicon-on-sapphire (SOS) photoconductors [4] for the work presented here.

We measured the pass and stop bands of several 2-D PBG structures using transmitting and receiving coplanar-strip horn antennas [5]. We designed PBG structures with stop bands greater than an octave bandwidth by combining two PBG structures with overlapping band gaps. Figure 1 shows the frequency-domain results from transmission measurements that we performed on three different PBG structures consisting of dielectric rods ($\epsilon_r = 12.7$) arranged in 2-D rectangular lattices. One structure has 1.66-mm diameter rods with 4.49-mm interrod spacing; another structure has 1.11-mm rods with 3-mm interrod spacing; and the third structure consists of each of these two structures assembled back-to-back to constitute a single hybrid 2-D PBG structure. As shown in Figure 1, the composite structure has a stop band extending from about 22 to 50 GHz. We calculated the frequency-domain results by performing a Fourier transform on the measured time-domain data.

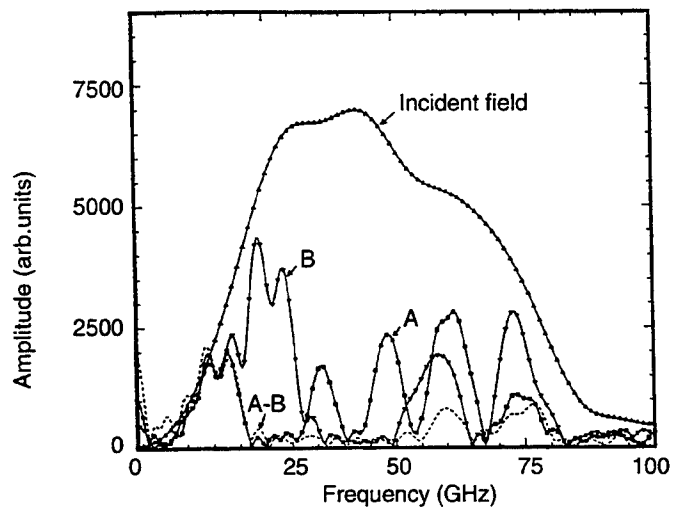


Figure 1. Dispersion curves for two different PCBs (A and B), and structure A and B placed back to back (A-B).

Another set of our experiments investigated the utility of using PBG structures for achieving highly efficient planar antennas. We used a spiral circuit placed on a 1-D PBG structure as the transmit antenna, and a coplanar strip horn antenna as the receiver. Optical fiber guides the optical light (for photoconductive switching) to the transmitting and receiving antennas. The 1-D PBG structure has 0.613-mm-thick $\epsilon_r = 12.7$ dielectric layers alternating between 0.615-mm air gaps [6]. It has a stop band from approximately 40 to 50 GHz. The spiral antenna with two aluminum arms was designed to be operational over the 10- to 90-GHz bandwidth, and it was fabricated on an SOS wafer. We used the silicon side of the 0.5-mm-thick SOS as the photoconductor. We charged the two arms of the spiral antenna with respect to one another using a dc battery, and switched the antenna photoconductively in the center of the antenna. We examined three different antenna structures: an aluminum conductor-backed spiral antenna; the 1-D PBG-backed spiral antenna; and the spiral antenna with no backing. We saw that the PBG structure enhanced the radiated field significantly over a wide frequency range (Fig. 2). The results from the 1-D PBG substrate were not as good as we would have expected from 2-D and 3-D PBG substrates—the 1-D PBG allowed deleterious surface-wave excitation at angles perpendicular to the periodicity. The 3-D PBG does not allow radiation in all directions into the substrates, and only permits radiation into air.

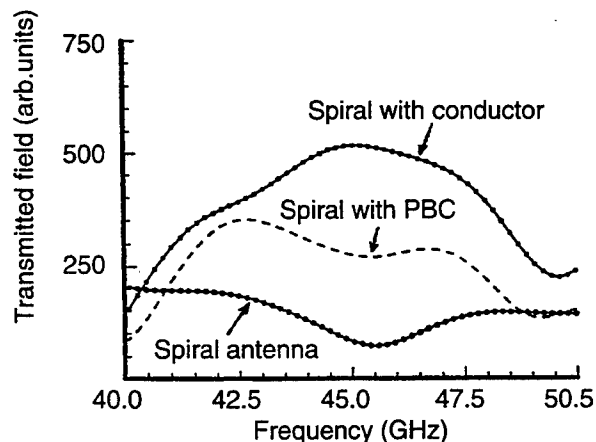


Figure 2. Comparison of radiated field strengths for three different spiral antenna configurations.

At lower microwave frequencies, we would expect to obtain higher radiation efficiencies for the PBG-backed antenna when the thickness of the SOS wafer is much smaller than the wavelength. This was not the case at the 40- to 50-GHz range. The conductor-backed antenna also gave good results, but this technique has several problems. If the dielectric substrate is made sufficiently thin, the conductor on the back of the substrate shorts out the antenna, reducing and, ultimately, eliminating the radiated field. Furthermore, the conductor significantly increases the number of surface waves supported by the structure at a given frequency. Another problem with conductor-backed planar antennas is that the substrate is too thin and mechanically fragile for good operation at high microwave (millimeter wave) frequencies.

1.2. Design and characterization of a 3-D PBG structure

The Army Research Office (ARO) and ARL sponsored a program with the Lincoln Laboratory with the objectives of determining the feasibility of producing UWB 3-D PBG structures, and of demonstrating a UWB 3-D PBG structure that operated from 1 to 2 GHz [7]. A composite structure was made by stacking monoperiodic sections of the (111)-oriented Lincoln Lab face-centered-cubic (fcc) crystal, as shown in Figure 3. Because of its similarity to semiconductor heteroepitaxial structures made from semiconductors with different band gaps, the resulting structure was called a photonic-crystal heterostructure. By making a discrete change in the lattice constant between adjacent monoperiodic sections, the net stop bandwidth can be increased well beyond that of a given section.

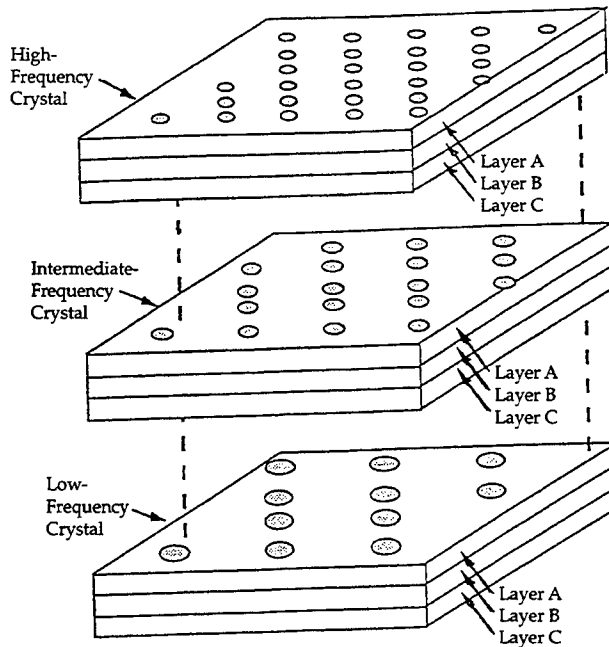


Figure 3. Composite photonic crystal consisting of monoperiodic sections of fcc crystal having different lattice constants [7].

The Lincoln Laboratory fcc crystal was constructed and tested in the range of 15 to 26 GHz. Each section was made from Stycast. The description of the fabrication of the component fcc PBG structures is found in [8]. Figures 4(a) through (d) show the experimental transmission at normal incidence through the heterostructure, the high-frequency component crystal, the middle-frequency component crystal, and the low-frequency component crystal. The heterostructure has a maximum rejection of approximately 48 dB at 22.5 GHz, a minimum rejection of approximately 7 dB at 17.9 GHz, and a stop band that extends from 16 to at least 25 GHz. The low rejection at approximately 18 GHz occurs from too little overlap between the component stop bands seen in Figures 4(c) and (d). In Figure 4(d), there is a higher-order stop band at about 22.5 GHz that contributes to the average UWB stop band. The rejection of the heterostructure around 22.5 GHz is being assisted by the second stop band of the low-frequency crystal; the fact that it is much deeper than the first stop band is typical for the Lincoln Lab fcc crystal. The experimental data given above is not ideal, but it was the first attempt to make a UWB 3-D PBG structure by stacking component structures in tandem. We determined that the stacking sequence is critical and that crystals with overlapping band gaps must also be in intimate contact with one another to avoid cavity modes.

We also produced a 1- to 2-GHz 3-D PBG structure under this project. The structure was too bulky for our application, and we determined that the technique of using a heterostructure to obtain a UWB structure is probably not the optimum structure for microwave frequencies below C-band. The tandem stacking of two or more PBG structures tripled both the weight and volume of the UWB structure; therefore, the metalodielectric photonic crystal (MDPC) concept was originated [8]. This structure requires just one repeat unit of the fcc crystal to obtain an octave bandwidth, and has a high rejection-per-unit constant. We discuss the MDPC later in this paper.

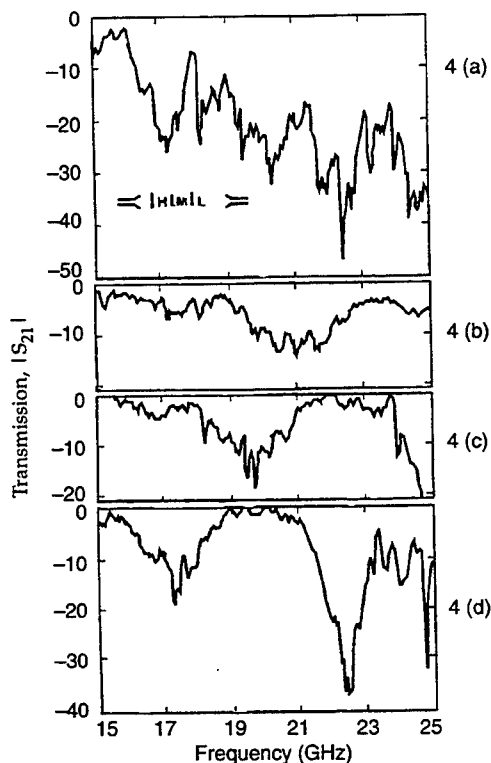


Figure 4. Transmission through photonic-crystal heterostructure made from three monopieric fcc structures having slightly different lattice constants [8].

1.3. New PBG concepts for antennas

The trend toward high-density circuit integration and reduced power per operation has made electronics circuits more susceptible to interference, upset, and damage from radio frequency (RF) overstress; therefore, it is important to protect sensitive components downstream from the antenna. System-hardening methodologies require that a system must successfully perform its mission in and out of the threat environment—the hardening technique utilized must not degrade system performance to unacceptable levels. The antenna is the first line of defense against unwanted RF signals that could enter the system from the front door.

PBG technology offers an immense potential for creating a whole new class of antennas that can perform multiple functions, while protecting against unwanted RF transients. Functions such as frequency selectivity, bandwidth tunability, and real-time filtering are required for RF protection. A picosecond-response-time shutter that opens only during the time duration of the transmit/receive pulse and, in addition, is both time- and frequency-agile would give the needed front-door protection from fratricide and electromagnetic interference (EMI), and would also raise the stakes for an adversary deploying a dedicated directed energy weapon (DEW) against our systems.

Below, we discuss new antenna concepts that use PBG techniques. Some of these concepts have already been demonstrated, others are under development, and some others are awaiting the development process.

1.4. Ferroelectric PBG antenna substrate

The ARL and Polytechnic University conducted a preliminary investigation into the feasibility of incorporating ferroelectric material into a PBG structure for producing narrow band (NB) transmit/receive windows that may be tuned electronically across a UWB gap (octave or greater). A composite ferroelectric 2-D PBG is made up of a stack of four different subcrystals. Each subcrystal has a thickness of six layers, and a square unit cell containing a single dielectric (ferroelectric) rod with a square cross-section. The rods have a dielectric constant of $\epsilon_r = 22$. The lattice spacing is: a (for subcrystal 1 and 2) and b (for sub-crystal 3 and 4), where $b = 4a/3$. The widths of the dielectric rods are: $w_1 = 0.062a$, $w_2 = 0.089a$, $w_3 = 0.062b$, and $w_4 = 0.089b$.

The computer-generated transmission amplitude spectrum of this composite PBG is shown in Figure 5. There is a forbidden frequency band gap that extends from 0.73 GHz to 1.3 GHz. However, if ϵ_2 is changed from 22 to 26 (an 18 percent change), for example, by applying a dc voltage across the ferroelectric rods of subcrystal 2, we see that the spectrum (as shown by the solid curve) still has this forbidden band gap, except for a narrow transmission peak centered at about 1.17 GHz. Transmission peaks centered at different locations within the original forbidden band gap occur when the voltages are applied at different frequencies within the composite crystal. For example, transmission peaks centered at 0.95 GHz (double-dotted) or 0.85 GHz (dotted) occur when ϵ_3 or ϵ_4 is increased by the same amount. These computer data indicate that it is possible to design composite PBG structures with transmission/receive peaks at various frequencies across a reasonably wide forbidden band gap. Low-loss ceramic ferroelectric material exists with ϵ_r having both low and high (>1000) values, and for which ϵ_r can be varied up to 50 percent by applying a bias voltage. The design of a ferroelectric PBG substrate could,

perhaps, use these materials to make a compact crystal with continuous frequency selectivity across an octave bandwidth.

One drawback to the ceramic ferroelectric materials is that large electric fields (on the order of a volt per micrometer) are required to produce reasonable dielectric constant tunability. This implies large bias voltages for operation at low microwave frequencies where ferroelectric rods would have a thickness of a few millimeters. A potential problem for use with high average power is that ferroelectrics are temperature-sensitive—they degrade with heat. This property may limit their use for low average power antenna systems.

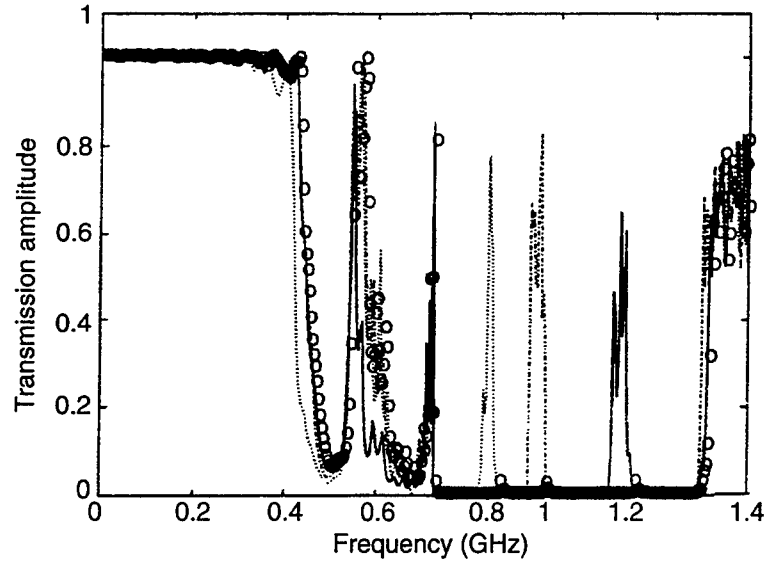


Figure 5. Amplitude spectra for PBG, where ϵ_r is varied.

We made some dielectric constant measurements with an applied electric field on single crystal barium titanate. Figure 6 compares the results for ceramic barium titanate (BaTi) and single-crystal BaTi. The single-crystal BaTi has a factor of almost 100 reduction in the applied electric field, as compared to ceramic BaTi, to produce the same percentage change in the dielectric constant. The single-crystal BaTi is more suitable for low-bias voltage operation.

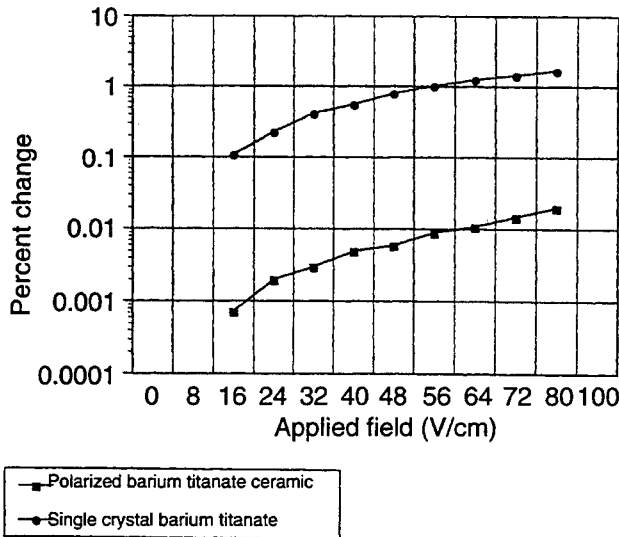


Figure 6. Dielectric constant versus applied field for single crystal and ceramic barium titanate (measured at 10 MHz, along c-axis for the single crystal and along the polarization axis for the ceramic).

1.5. Metallodielectric photonic crystal (MDPC) antenna substrate

The 3-D UWB antenna using the heterostructure previously described tends to be bulky, since multiple PBG structures are required to achieve the UWB. Also, care must be taken in aligning component stop bands, since cavity modes can exist between the component crystals. The antenna's design is complicated by the necessity to overlap the stop bands and allow each substrate to have intimate contact with one another to avoid cavity modes.

The MDPC is another type of PBG structure that can also achieve UWB, but is more compact because stacking of multiple PBG crystals is not required to achieve UWB. The MDPC is a name given to this type of PBG structure because the stop band characteristics depend strongly on the size of metal spheres used in its construction, as well as the support material dielectric constant. The MDPC was first introduced by Brown [9]. In his paper, Brown describes a MDPC with metal spheres

in adjacent layers arranged in a fcc format and not physically touching each other. Teflon and Stycast were the dielectric materials used in several of Brown's MDPCs. An important characteristic of the MDPC is that it has an octave bandwidth. Its compactness and UWB characteristics are attractive features for planar UWB antenna applications. Millimeter (mm) wave frequencies will probably be the upper limit for the MDPC, because of the electrical losses associated with metals at those frequencies.

Another type of MDPC is the 3-D wire mesh structure developed by Yablonovitch [10]. This structure is very interesting for high intense radiation antennas because: it is light weight; it is simple to construct (i.e., the filling ratio—which is the volume ratio of metal to dielectric—is, typically, very small); and, most importantly, it should be capable of handling large average power when low-loss dielectric materials are used.

Figure 7 is a pictorial view of the 3-D wire mesh, which forms a diamond lattice when the zigzag pieces are joined together. The dominant feature of this structure is that it has a deep and wide stop band that extends from dc up to a frequency corresponding to about one-half of the spatial periodicity of the wires. For high-power microwave (HPM) applications, you can generate a stop band from dc up to C-band, which is a range of interest for many applications. Due to compactness considerations, it is desirable to operate this wire mesh structure at a mesh spacing much smaller than a vacuum wavelength, λ_0 . The condition that $a \ll \lambda_0$ defines a new regime for PBG crystals, where a is the length of the unit cube of the diamond lattice. For the conventional dielectric PBG crystal, $a \sim \lambda_0$ (same order of magnitude). The condition $a \ll \lambda_0$ plays a major role in the generation of the wire mesh structure; we will show later that the same condition is dominant for a Luneberg dielectric lens. In this new operating regime, the EM wave penetrates the wire mesh; therefore, it is not a true 3-D structure, but a quasi 3-D structure. A band gap within this band gap structure can be realized by creating resistive, capacitive, and inductive defects, such as by cutting wires and filling gaps with ϵ and μ materials.

1.6. Luneberg metallodielectric PBG structure

A Luneberg lens is a dielectric structure with an index of refraction that varies with distance from the center so that a beam of parallel rays incident on one face of the structure is focused to a point on the opposite surface. Dolgin [11] gives a novel design of a spherical Luneberg lens. The lens is assembled out of thin sheets of dielectric that have an array of holes with a "daisy wheel" pattern on the outer circumference (Figure 8).

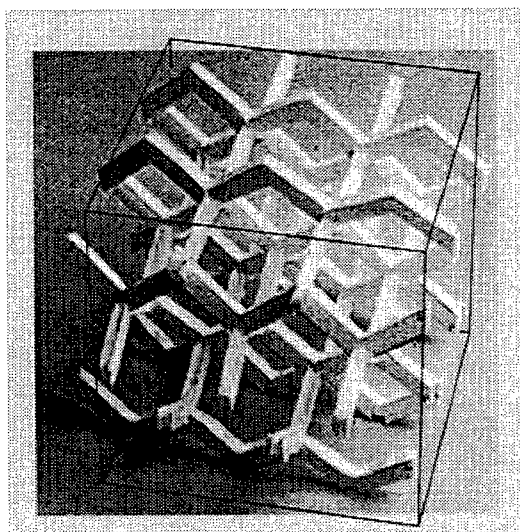


Figure 7. 3-D diamond lattice, wire mesh PBG structure.

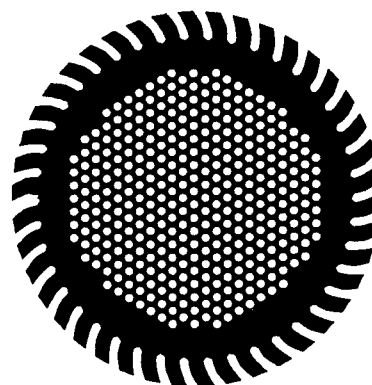


Figure 8. One sheet of a Luneberg spherical dielectric lens containing holes and slots. (Multiple sheets are assembled in tandem.) [12]

Each sheet has a unique array of holes and daisy wheel; the sheets are stacked in tandem to form the lens. Several conditions are required to achieve the required spatial variation of permittivity. First, each hole or slot must be much smaller than a wavelength. This condition is, basically, the same condition required for the metal wire mesh PBG structure. Second, the holes and slots in adjacent layers must not be concentric or parallel to each other. This condition is not as stringent as for a fcc PBG crystal, since adjacent layers are stacked so that the holes of a given layer lie directly above the center of a triangular unit cell. These similar conditions of the Luneberg lens and the metallodielectric (wire mesh) PBG structure indicate that perhaps the metallodielectric PBG can also be designed to be a Luneberg lens structure. We investigated this concept by comparing the localized volume fraction (volume ratio of holes and dielectric) for the Luneberg lens single-drilled pattern [11] with the PBG (low-frequency scalar approximation). The volume fraction of the Luneberg lens is, $V_1 = (\pi D^2)/(2L^2\sqrt{3})$, where D equals the diameter of the holes and L equals the distance between holes. The volume fraction for the PBG crystal is approximately $V_p = (4\pi r^2 h)/(2L^3\sqrt{2})$, where h is the sheet thickness, r is the hole radius, and $h/L = \sqrt{2/3}$. Substituting $h/L = \sqrt{2/3}$ into the above equation shows that the localized volume fraction of the Luneberg lens is, essentially, the same as that for the PBG crystal for the scalar approximation. Note that L is not a constant for the Luneberg lens. It seems reasonable that a Luneberg metallodielectric PBG structure could be designed. In the following text, we describe a new emitter concept that uses a Luneberg metallodielectric PBG structure.

1.7. Luneberg metallodielectric PBG emitter array

Scalora et al [12] numerically investigated dipole emission rates in 1-D PBG structures and found that the total power is enhanced near the photonic band edge by a factor of nearly 15 over the free-space radiation rate. They also found that, for frequencies inside the photonic band gap, emitter power can be suppressed by nearly three orders of magnitude, with respect to free space. Figure 9 [12] shows the steady-state power output as a function of the normalized dipole oscillation frequency. The power output is normalized with respect to the power output in a vacuum. The structure studied was a 1-D PBG structure consisting of dielectric layers alternating between a high and low index of refraction. The model used a collection of point-radiating dipoles arbitrarily located inside the finite PBG structure. Figure 9 gives the power output for a thin emitting dipole layer near the center of the structure and in the center of a high-index region. The dipole radiation profile outside the PBG structure will have a spatial distribution over the face of the structure, and the distribution will be a function of the internal location of the emitter dipole array. We suggest that it may be possible to concentrate the dipole radiation profile outside the PBG structure by placing the emitter dipoles inside a Luneberg PBG structure. To our knowledge, dipole emission rates in 3-D PBG structures have not yet been investigated as related to emission rates near the photonic band edge. We would, however, expect to observe similar dipole emission rates to the 1-D PBG structure and, perhaps, with enhanced emission rates.

An interesting technique is to place an array of photoconducting diodes inside a Luneberg metallodielectric PBG structure to achieve a power gain with radiation directivity (a compact pulser/radiator). Presently, directivity can only be achieved for frequencies that are in the stop band through the technique of creating defects in the PBG crystal. Defects can be made that will confine the radiation to a given path length (waveguide).

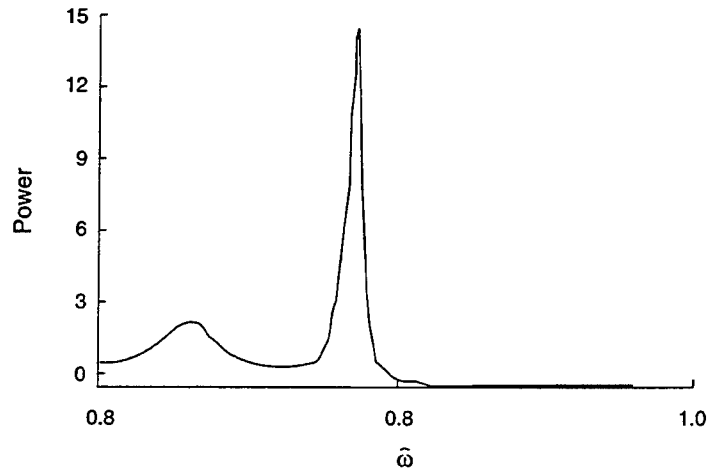


Figure 9. Normalized radiated power ($P_{\text{PBG}}/P_{\text{vac}}$) as a function of normalized frequency $\hat{\omega} = \omega/\omega_{cg}$ and ω_{cg} is the frequency at the center of the band gap [12].

Another technique that we suggest to achieve power gain and directivity is to use a dielectric PBG structure with internal emitter diodes that are tuned to the diode frequency at the band's edge. A separate dielectric Luneberg lens is then stacked against the power output face of the PBG structure to achieve the desired directivity. This technique is more straightforward in that it allows more flexibility in the design and type PBG structure (e.g., 1-D, 2-D, 3-D, dielectric, metallodielectric), but it will add more weight and volume, since two structures are required.

1.8. PBG technology for phased array antennas

It is possible to radiate high-power pulses by synchronizing an array of radiators. Since a large number of radiators are required to obtain high microwave power levels, it is more cost-effective to use planar monolithic technology. As we discussed earlier, a planar antenna that has a dielectric substrate is an inefficient radiator. Also, energy that radiates into the substrate is lost to surface-wave and leaky-wave excitation, which can contribute to cross-talk and noise among the phased-array radiators. Another problem typically encountered at high microwave (mm wave) frequencies is that thin substrates are required for good antenna operation, and these substrates are too fragile mechanically.

The following text describes two phased-array techniques in which PBG technology offers considerable performance improvements to the antenna.

1.9. Tapered slot antenna on a PBG substrate

Ellis and Gabriel [13] observed dramatic improvements in the radiation properties of tapered slot antennas (TSAs) when integrated on a 2-D, fcc, PBG structure. The TSA launches a traveling wave (end-fire) and radiates along the substrate, thereby interacting with the substrate over $2-5\lambda$. (Figure 10 shows the TSA.) The measured directivity of a 10-GHz TSA on the PBG substrate was improved 237 percent, as compared to the same TSA on a dielectric substrate. Similar results were obtained for a 30-GHz TSA. The significance of the PBG substrate TSA is that a conventional TSA has an effective substrate thickness that must be very thin for good operation at high microwave frequencies. The PBG substrate enables the designer to dramatically increase (i.e., triple or quadruple) the substrate thickness for good operation and mechanical stability. This upgrade may have viable commercial and military applications for phased arrays and satellite communications systems. Integration of the end-fire antenna on PBG substrates with GaAs as the host material will yield a low-cost design. Work is ongoing at the University of Michigan [13] to optimize TSA performance, and to measure its radiation characteristics.

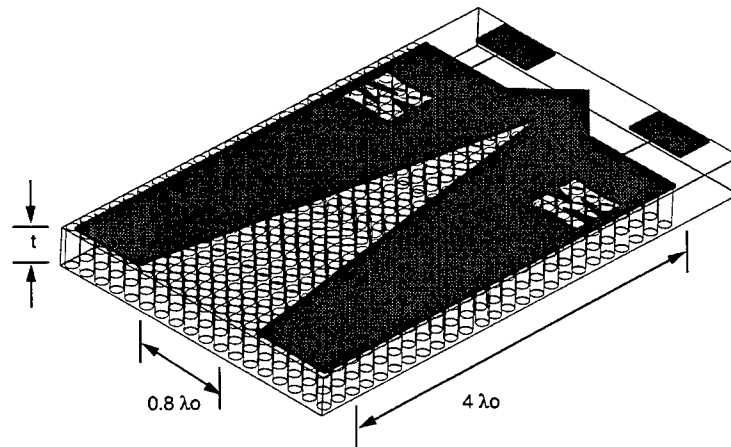


Figure 10. Micromachined tapered slot antenna (TSA) [13].

Integration of the end-fire antenna on PBG substrates with GaAs as the host material will yield a low-cost design. Work is ongoing at the University of Michigan [13] to optimize TSA performance, and to measure its radiation characteristics.

1.10. Photoconductive (PC) switching for coherent power combining of UWB pulsed radiation

An approach under development at ARL is to exploit the jitter-free nature of photoconductive switching to radiate high peak powers [14]. When operated at modest hold-off voltages, GaAs and Si PC switches exhibit jitter-free (sub-picosecond) operation, with respect to a laser trigger pulse. Therefore, it is possible to radiate high-power pulses by synchronizing an array of radiators, each driven by an individual PC switch. The electric field from each of the synchronized radiators adds together in free space, giving a peak power that scales as N^2 ,

where N is the number of radiating elements. This approach allows each PC switch to be operated at safe power levels, where the performance of the PC switch is not expected to degrade over time. Furthermore, this technique allows the creation of a UWB phased array, whereby the antenna array radiation pattern can be controlled by adjustment of the arrival time of the optical pulse, which triggers each element (true time delay). We conducted feasibility experiments at ARL using three identical bowtie antennas fabricated on copper-clad glass/epoxy circuit boards with a thickness of 1.55 mm by the use of a standard photo-sensitized etching technique. The antennas were designed to radiate an approximately 250-ps FWHM pulse in response to step-function electrical excitation. In one of four experiments, each of the three elements was triggered with a relative delay of 160 ps between adjacent elements; the fields from each of the elements added together in free space at 30° to produce a signal at the field probe three times as large and, therefore, received peak power nine times as large. In the actual experiment (Fig. 11), the charge voltage V_a dropped when additional elements were added, because of the high output impedance of the pulser. Therefore, the peak signal received is scaled by a factor of 2.3 over that obtained by a single element, rather than by a factor of 3.

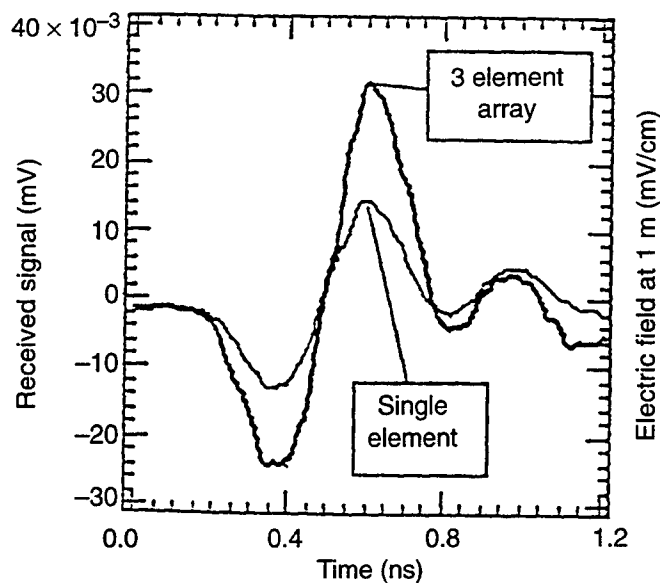


Figure 11. CMA response showing received waveforms at $\theta = 30^\circ$ and relative delay of 160 ps between adjacent elements. Optical trigger is blocked to all but one of bowtie antenna elements (single element), and all three antennas are simultaneously activated (array).

In another experiment, we demonstrated beam steering by adjusting the delay between radiating elements [14]. The implementation of an N -element jitter-free array for free-space power combining to increase the radiated power is a viable solution to power scale-up. The array provides beam-steering capabilities not available from a single switch/antenna system. The UWB pulses are radiated in complete synchronization with the optical pulse train, a property that can be exploited in the design of coherent receivers.

PBG technology is expected to benefit this coherent power-combining technique by dramatically increasing the radiation efficiency of each of the radiation elements. PBG technology is now available at microwave frequencies for implementation into this power-combining technique. It is also expected that PBG technology at the IR and optical frequencies will become available in the near term (3 to 5 years) to produce compact PBG waveguides with programmable laser beam delays for real-time beam steering.

2. ACKNOWLEDGMENTS

The authors would like to acknowledge the work on 2-D photonic band gap crystals by Polytechnic University; Lincoln Laboratory for their contributions on 3-D photonic band gap crystals; Drs. Eric Funk and Stephen Sadow of ARL for their contributions on photoconductive switching for high-power radiation and beam steering; and Mr. Philip Brody of ARL for the BaTi dielectric constant measurements.

3. REFERENCES

1. E. Yablonovitch and T. J. Gmitter, "Photonic Band Structure: The Face-Centered-Cubic Case," *Journal of Optical Society of America B*, Vol. 7, p. 1792, 1990.
2. E. Yablonovitch, T. J. Gmitter, and K. M. Leung, "Photonic Band Structure: The Face-Centered-Cubic Case Employing Nonspherical Atoms," *Physical Review Letters*, Vol. 67, p. 2295, 1991.
3. E. R. Brown, C. D. Parker, and E. Yablonovitch, "Radiation Properties of a Planar Antenna on a Photonic Crystal Substrate," *Journal of Optical Society of America B*, Vol. 10, p. 404, 1993.
4. L. Carin, D. R. Kralj, M. R. Melloch, and J. M. Woodall, *IEEE Microwave and Guided Wave Letters*, Vol. 2, p. 339, 1993.
5. D. Kralj and L. Carin, *IEEE Transaction of Microwave Theory Tech.*, Vol. 42, p. 553, 1994.
6. L. Carin, K. Agi, K. M. Leung, and B. A. Garetz, *Quantum Elect.*, 1993.
7. K. Agi, E. R. Brown, O. B. McMahon, C. Dill III, and K. J. Malloy, "Design of Ultra-wideband Photonic Crystal for Broadband Antenna Applications," *Electronics Letters*, Vol. 30, No. 25, p. 2166, 1994.
8. E. Brown, "Wideband Photonic Crystal," Lincoln Laboratory report, ARO-157-94, July 1995.
9. E. R. Brown and O. B. McMahon, "Large Electromagnetic Stop Bands in Metallodielectric Photonic Crystal," *Applied Physics Letters*, Vol. 67, No. 15, p. 2138, 1995.
10. D.F. Sievenpiper, M.E. Sickmiller, and E. Yablonovitch, "3D Wire Mesh Photonic Crystals," *Physical Review Letters*, Vol. 76, No. 14, P. 2480-2483, 1 April 1996.
11. B. P. Dolgin, "Perforated-Layer Implementation of Radio-Frequency Lenses," NASA's Jet Propulsion Laboratory paper, NPO-19217, January 1996.
12. M. Scalora, J. P. Dowling, M. Tocci, M. J. Bloemer, C. M. Bowden, and J. W. Haus, "Dipole Emission Rates in One-Dimensional Photonic Band Gap Materials," *Appl. Phys. B* 60, S57-S61, 1995.
13. T. J. Ellis and G. M. Rebeiz, "Improvements in Tapered Slot Antennas on Thick Dielectric Substrates Using Micromachining Techniques," *IEEE Transactions on Antennas & Propagation*, July 1996.
14. E. E. Funk, S. E. Sadow, L. J. Jasper, and C. H. Lee, "Time Coherent Ultra-wideband Pulse Transceiver and Applications," *GOMAC*, March 1996.

Gases evolved from the common cold cathode

Marc S. Litz, Daniel Judy, George Huttlin, Carl Lazard
Army Research Laboratory
Adelphi, MD 20783

ABSTRACT

One of the contributing factors to rf pulse shortening in long-pulse high-power microwave sources is gas evolution from the cathode surface during the explosive emission process. Theory of ecton formation,¹ models of expanding arc plasmas,² and high-speed diagnostics³ are leading to a better understanding of the contributing factors to the cold-cathode emission processes. While technological leaps often result from applications of new materials, it is worthwhile to characterize and understand the effects of existing cathode materials commonly used in pulsed power systems. This paper describes the use of a residual gas analyzer (RGA) to measure the atomic mass spectrum and total pressure of the background gas evolved from the cathode surface in a repetitively-pulsed electron beam vacuum chamber.

Cathode materials studied include carbon fiber, velvet, copper, and stainless steel. The increase in the background pressure and the constituents of the background pressure are catalogued for the four cathode material samples. The simultaneous narrowing of voltage-pulse width with increase in background pressure is also measured. The carbon fiber cathode contributes least to the background pressure, and maintains the most stable and repeatable diode impedance.

Keywords: cold cathodes, carbon fiber, velvet, rf pulse-shortening, industrial processing

2. INTRODUCTION

Two technologies are driving these investigations. The first is the increasing number of industrial applications for electron-beam sources. These include the elimination of flue gas contaminants, ion implantation, x-ray lithography and material surface modification. Secondly, the problem of rf pulse shortening in high-power microwave devices motivates this work. The most significant source of pulse shortening is often device dependent. However a common curse is the generation of background plasma in the anode/cathode (AK) gap region due to gas evolved from the cathode surface during the explosive-whisker emission process.

The approach taken in these investigations is to vary the cathode material with a set of commonly used materials. These include 1) carbon fiber (CF), 2) velvet, 3) copper (Cu), and 4) stainless steel (SS). Voltage and current diagnostics monitor the macroscopic electrical characteristics. These signals indicate the timing and amplitude of the machine voltage and current. In addition, the vacuum-chamber is monitored with a residual gas analyzer (RGA) which measures the partial pressure of the background gas as a function of atomic mass units (AMU).

3. EXPERIMENTAL APPARATUS

3.1 Modulator

A resonantly charged, five-stage, 70-ohm, Blumlein pulse forming line (PFL) is triggered by a thyatron. The E-type Guilleman network configuration of identical capacitors and variable inductance along the line permits voltage pulse shaping for varying load impedance of the experimental electrical load. The 100-kV, 1- μ s pulse-width PFL output is delivered to the load over a 25' length of RG-8 cable.⁴

The 25-cm-diameter coaxial vacuum vessel is 50 cm long. The negative 100-kV pulse is applied to the center conductor of the cylindrical vacuum chamber. The cathodes are mounted on the end of the center conductor. A planar AK gap of 1.6 cm is realized between the flat-circular cathode and the 15.2 cm-diameter titanium (Ti) wire-mesh anode.

3.2 Cathodes

Four types of cathode are compared in this study. Each type is 5.08 cm diameter ($\sim 20 \text{ cm}^2$), the diameter of the center conductor. The first type is a carbon fiber brush cathode fabricated from 3- μm -diameter carbon fibers attached to an aluminum base with an epoxy-resin mix. The density of carbon fibers is $\sim 10^6 \text{ fibers/cm}^2$. In addition to the CF cathode, a velvet, copper and stainless steel cathode are also investigated. The velvet is attached to an aluminum base using a spray adhesive, and the Cu and SS are machined from rod stock.

3.3 Diagnostics

Several voltage and current probes are located along the path of energy flow from the PFN to the vacuum chamber. A 1000:1 resistive voltage divider and a 40:1 current transformer are co-located at the output of the PFN. A capacitive voltage divider and a B-dot loop are co-located in the vacuum chamber. The two sets of voltage and current diagnostics provide corroborating measurements of the electrical pulse characteristics.

A residual gas analyzer (RGA) measures the ratio of mass-to-charge in a gas sample. The mass spectrum is calculated in a three stage process that includes ionization, mass separation, and detection.⁵ Unambiguous identification of an AMU with a particular molecule (ie. CO vs. N_2) is performed by matching the mass spectrum with the empirically determined cracking patterns. Fragments of original molecule are created when molecules of a gas are struck by electrons whose energy can cause ionization. The ratio of fragments (cracking pattern) forms a fingerprint of the gas constituents.

4. EXPERIMENT

Each experimental series followed similar data-taking procedures. The cathode sample was mounted on the end of the cylindrical center conductor. The cryogenic vacuum system pumped overnight on the chamber, establishing equilibrium within the vacuum chamber. The typical base pressure achieved was 9×10^{-6} Torr. The RGA was turned on at least one hour before firing the modulator in order to get a baseline on the partial pressures. Three single shots were fired so that voltage and current baseline data could be acquired (before a shot series).

EMI during a shot sequence precluded operation of the RGA during shooting of the 100 kV modulator. After the shot sequence (i.e. 1000 shot series), three additional single shots were fired for voltage and current data, and the RGA was turned back on for another hour (though equilibrium was reached usually within 20 minutes).

Diode impedance was calculated from the voltage and current traces acquired both before and after the shot series. The RGA scans taken every 2 minutes both before and after the shot series were compared for amplitude differences. More important than the absolute pressure values recorded by the RGA, is the change in pressure before and after the shot series. The reference subtracted data clearly shows the partial pressure variations that quantify plasma evolved from the cathode surface. In addition, the percentage change was calculated to quantify natural fluctuations as differentiated from contributions in gas evolved from the surface of the cathodes. Another discriminating factor between noise fluctuations and gas evolved is the observation of the return to equilibrium of the partial pressure.

5. RESULTS

5.1 Voltage and Current Diagnostics

The change in the width of the voltage pulse before and after a 1000 shot series is an indication of the change in plasma density in the AK gap region. As the background pressure (or local plasma density) increases the electron beam dynamics (i.e. beam charge neutralization, ion flow across the gap) are modified. While identification of the specific effect requires diagnostics beyond what was available for this experimental series, the variations calculated from voltage and current are real indications of the increase in local plasma density.

The width of the voltage pulse results from emission threshold and the plasma closure associated with the various cathode materials. After 1000 shots the emission threshold does not change. However, the plasma closure time decreases as a result of the gas evolved from the cathode surface. This is clearly evident in the difference between voltage pulse width before and after a shot series shown in figure 1. The voltage pulse width is reduced by 120 ns for the velvet, and only 30 ns reduction for the carbon fiber.

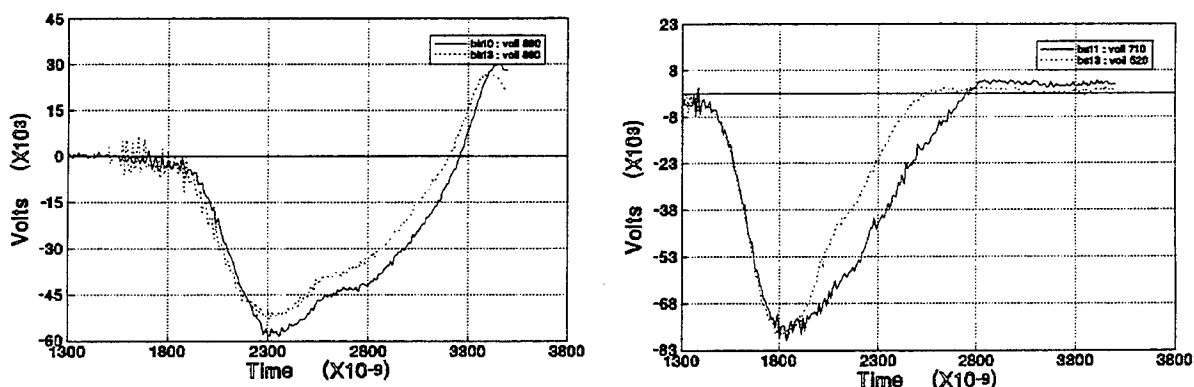


Figure 1. Voltage pulse-width reduction after 1000 shots for a) carbon fiber and b) velvet.

5.2 Residual Gas Analysis

A scan of the partial pressure as a function of AMU is shown in figure 2. The peaks are labeled by molecule. For these experiments, the best indication of the composition of the gas evolved from the surface of the cathode is the change in background pressure spectrum after the shot series. The fact that the background spectrum returns to its pre-shot appearance indicates that the appearance of the spectrum immediately after the shot sequence is a result of the shot sequence and not the result of spurious events in the vacuum system.

The return to equilibrium is easily identifiable. An RGA scan before the shot series is subtracted as a reference from those scans that occur after the shot series. These difference traces taken at two minute intervals are then displayed sequentially in figure 3. The peaks in figure 3 are evidence of the gas emitted from the sequence of 1000 pulses. It is clear from the figure that the gas has returned to the pre-shot mixture within 20 minutes. The percentage change for each AMU in the spectrum is also calculated because 1) large changes in less dominant AMU lines are of interest to catalogue, and 2) changes of 10% in Ti are barely visible (10^{-8}) when compared directly with the 1% changes (10^{-6}) of N_2 . Preliminary analysis does not permit us to correlate mass with time to closure at this writing.

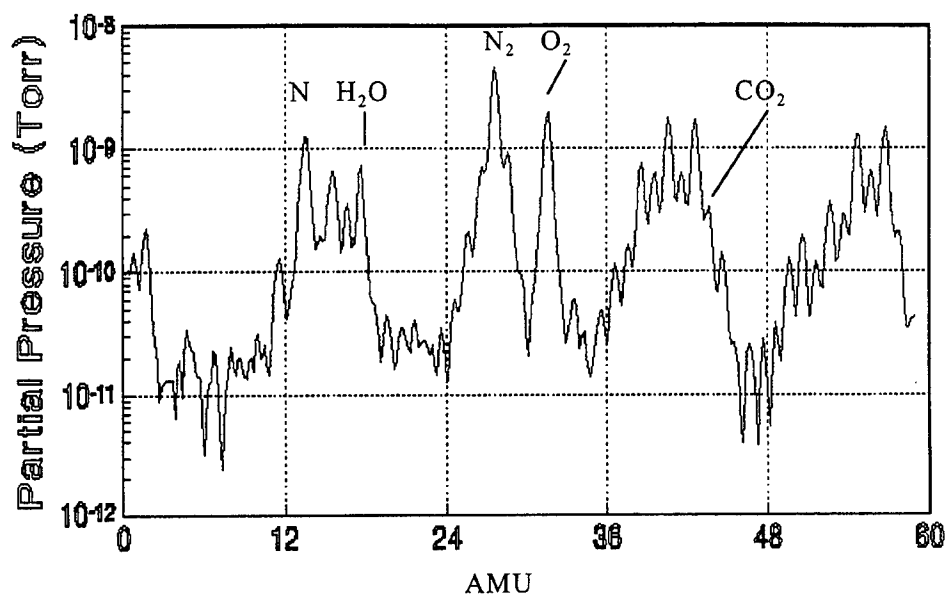


Figure 2. RGA output scan for copper.

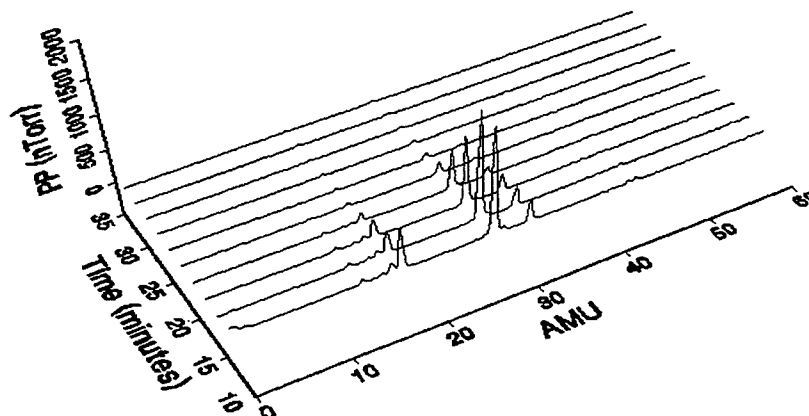


Figure 3. Difference (scan minus reference) plotted every 2 minutes following the shot sequence.

Using the ideal gas law approximation ($PV=NkT$) to determine the number of molecules liberated from the cathode surface we find that a pressure change of $1 \mu\text{Torr}$ corresponds to 6.5×10^{14} molecules generated in the vacuum chamber or 32×10^{12} molecules emitted per cm^2 of the cathode surface. Changes of $1 \mu\text{Torr}$ are significant given that baseline fluctuations are limited to the order of 10^{-11} Torr.

A summary of the significant results are shown in table 1. First, the change in pressure resulting from several hundred shots on each cathode clearly shows that the CF cathode minimizes changes in the background pressure by a factor of 2 over the velvet cathode. The largest contribution to the pressure comes from N_2 , which is one of the dominant line present in the background gas with velvet generating three times greater number of nitrogen molecules than the CF cathode.

Cathode Material	number of shots	total pressure change (10 ⁻⁶ Torr)	partial pressure change as a function of AMU							pulse-width change (ns)	Current peak (1) (Amps)
			14 N	18 H ₂ O	28 N ₂	32 O ₂	44 CO ₂	48 Ti	41,43,55,57 pump oil		
<u>CF</u>	1000	1.5	0.03		0.34	0.04	0.02			-30	800
<u>Velvet</u>	1000	3		0.12	0.9	0.1	0.02			-120	1200
<u>Copper</u>	300	4.5	0.1	0.2	1.5	0.22		0.001	0.05	—(2)	800
<u>St. St.</u>	500	5	0.08	0.25	1.1	0.2				—(2)	1500

(1) peak may occur after diode voltage shorts

(2) lack of stability does not permit determination

Table 1. Summary of significant results.

6. DISCUSSION

The lack of stability in the turn-on times for the Cu and SS cathodes suggests that the electric field threshold for emission for Cu and SS is too close to the peak applied field for these two materials to turn-on uniformly across the cathode surface. The comparatively robust turn-on of the CF and velvet cathodes as seen in the present data is consistent with the relatively low (compared with the 47-kV/cm gap field) turn-on fields of 10 and 35 kV/cm reported elsewhere.⁴ Anode damage with the Cu and SS cathodes shows that these cathodes turn on preferentially at their edges. This explains the lack of stability observed in the voltage and current traces for the Cu and SS. The pressure values recorded by the ion gauge and RGA are not effected by the turn-on instability because of the time-integrated nature of these diagnostics.

This investigation focused on measuring the gas evolved from the surface of cold cathodes during the explosive whisker emission phase and the effects of the gas on pulse length. Another important issue arises from the effects on pressure from electron bombardment of the chamber surfaces and the anode in particular. Using solid anodes of a variety of materials, changes in the background pressure due to electron bombardment may be investigated.

Further studies following similar procedures, would reduce the AK gap to 1 cm and the cathode diameter to 2.5 cm. These two changes would permit repetitive operation in an impedance range consistent with the original modulator design of 70 ohms. Also the change would provide the higher electric field for more stable turn-on of Cu and SS cathodes. The reduced AK may produce gap closure before the 1 μ s voltage pulse-width, however this scenario would assure a uniform cathode surface turn-on.

7. CONCLUSIONS

The gas evolved from the cathode surface during whisker emission is minimized with the use of carbon fiber cathodes. The gas contribution affecting the voltage pulse-shortening observed in these experiments is also minimized with the use of the CF cathodes. Carbon fiber cathodes present an ideal solution for low-voltage modulators where 1) low a E-field threshold is required for emission, 2) a spacially uniform beam is needed, and 3) a stable diode impedance is desired.

Gas evolved during a single shot may not be sufficiently significant to affect beam dynamics, but it is shown here that the effects from multiple shots do build up to significant levels. The gas evolved from single shots in sealed systems (or hard tubes) that maintain pressures of 10⁻⁸ or 10⁻⁹ could be subject to

changes in pulse-width from cathode gases evolved during the explosive whisker emission process that occur in common cold cathodes.

8. REFERENCES

1. G. A. Mesyats, "Ecton mechanism of the vacuum arc cathode spot," IEEE Trans. On Plasma Science, Vol. 23, No. 6, p. 879, 1995.
2. F. Schwirtzke, "Vacuum breakdown on metal surfaces," IEEE Trans. On Plasma Science, Vol. 19, No. 5, p. 690, 1991.
3. P. Siemroth, T. Schulke, T. Witke, "Microscopic high speed investigations of vacuum arc cathode spots," IEEE Trans. On Plasma Science, Vol. 23, No. 6, p. 919, 1995.
4. M. Litz, J. Golden, "Repetitive explosive whisker emission cathode investigation," Proc. SPIE 1994, Vol. 2154, p. 110.
5. J. F. O'Hanlon, "A User's Guide to Vacuum Technology," Wiley, 1980.

Bremsstrahlung recoil force on second-order dynamic polarization charge of a relativistic test particle in a nonequilibrium beam-plasma system

Howard E. Brandt

Army Research Laboratory, Adelphi, MD 20783-1197

ABSTRACT

The recoil force on the second-order dynamic polarization charge of a relativistic test particle participating in collective bremsstrahlung in a nonequilibrium beam-plasma system is calculated. Contributions arise both from terms involving direct interaction of the field of the test particle in second order with its own induced dynamic polarization, and from interaction of the field scattered by the dynamic polarization with the dynamic polarization itself.

Keywords: radiative instability, bremsstrahlung, beam-plasma systems, electron beams

1. INTRODUCTION

For a relativistic nonequilibrium beam-plasma system, an expression was obtained previously^{1,2} for the recoil force on the second-order dynamic polarization charge of a relativistic test particle participating in collective bremsstrahlung. This expression resulted from adding Eq. (62) of Ref.1 and Eq. (25) of Ref.2 to obtain Eq. (26) of Ref.2. However, these equations can be further reduced, and this will be accomplished in the present work. The resulting expression will be convenient for future discussions. To avoid extensive repetition, we employ the notations, definitions, and equations of Refs.1 and 2. For this purpose, we designate Eq. (N) of Ref.1 by Eq. (I-N), and Eq. (N) of Ref.2 by Eq. (II-N).

2. MATHEMATICAL REDUCTION OF THE FORCE

For the contribution to the force given by Eq. (I-62) to be of the bremsstrahlung form,^{3,4} the factor $\delta(\omega - \vec{k} \cdot \vec{v}_\alpha + (\vec{k} - \vec{k}_1) \cdot \vec{v}_\beta)$ must appear, where \vec{k} is the momentum transfer from the test particle of species α to the scattering particle of species β . However, what does appear explicitly in Eq. (I-62) is $\delta(\omega + \omega_1 - (\vec{k} + \vec{k}_1) \cdot \vec{v}_\alpha)$. An additional factor $\delta(\omega_1 - \vec{k}_1 \cdot \vec{v}_\beta)$ is needed, for then one notes that

$$\delta(\omega + \omega_1 - (\vec{k} + \vec{k}_1) \cdot \vec{v}_\alpha) \delta(\omega_1 - \vec{k}_1 \cdot \vec{v}_\beta) = \delta(\omega_1 - \vec{k}_1 \cdot \vec{v}_\beta) \delta(\omega - (\vec{k} + \vec{k}_1) \cdot \vec{v}_\alpha + \vec{k}_1 \cdot \vec{v}_\beta). \quad (1)$$

Renaming the variable $\vec{k} + \vec{k}_1$ as \vec{k} causes Eq. (1) to become

$$\delta(\omega + \omega_1 - (\vec{k} + \vec{k}_1) \cdot \vec{v}_\alpha) \delta(\omega_1 - \vec{k}_1 \cdot \vec{v}_\beta) = \delta(\omega_1 - (\vec{k} - \vec{k}_1) \cdot \vec{v}_\beta) \delta(\omega - \vec{k} \cdot \vec{v}_\alpha + (\vec{k} - \vec{k}_1) \cdot \vec{v}_\beta), \quad (2)$$

which contains the needed factor. In Eq. (I-62), the needed factor of $\delta(\omega_1 - \vec{k}_1 \cdot \vec{v}_\beta)$ can only arise from the imaginary part of $G_{jv}(k_1)$ or $\tilde{C}_{ij1}^{(s)}(k, k_1)$. Also one notes that, for complex numbers $z_n = x_n + iy_n$,

$$\begin{aligned} \text{Im}[z_1 z_2 z_3] &= \text{Im}[(x_1 + iy_1) z_2 z_3] = y_1 \text{Re}(z_2 z_3) + x_1 \text{Im}(z_2 z_3) \\ &= y_1 \text{Re}(z_2 z_3) + x_1 x_2 \text{Im} z_3 + x_1 x_3 \text{Im} z_2, \end{aligned} \quad (3)$$

or

$$\text{Im}[z_1 z_2 z_3] = \frac{1}{2}(\text{Im } z_1)(z_2 z_3 + z_2^* z_3^*) + \text{Re } z_1 \text{ Re } z_2 \text{ Im } z_3 + \text{Re } z_1 \text{ Re } z_3 \text{ Im } z_2 . \quad (4)$$

Then, letting $z_1 = G_{jv}(k_1)$, $z_2 = e_{ki}^\sigma e_{kn}^{\sigma*} \Lambda_{vn}^{(\alpha)*}(k, k_1) G_{1m}^*(k + k_1) (\omega + \omega_1 - i\delta)^{-2} (\omega_1 + i\delta)^{-2}$, and $z_3 = \tilde{C}_{ijl}^{(s)}(k, k_1)$, and in Eq. (I-62) defining

$$Q_1 = B \text{ Im} \left[e_{ki}^\sigma e_{kn}^{\sigma*} \frac{G_{jv}(k_1) G_{1m}^*(k + k_1) \Lambda_{vn}^{(\alpha)*}(k, k_1) \tilde{C}_{ijl}^{(s)}(k, k_1)}{(\omega_1 + i\delta)^2 (\omega + \omega_1 - i\delta)^2} \right] , \quad (5)$$

one has

$$\begin{aligned} Q_1 = B & \left[\frac{1}{2} \text{Im } G_{jv}(k_1) \left[e_{ki}^\sigma e_{kn}^{\sigma*} \frac{\Lambda_{vn}^{(\alpha)*}(k_3, k_1) G_{1m}^*(k + k_1)}{(\omega_1 + i\delta)^2 (\omega + \omega_1 - i\delta)^2} \tilde{C}_{ijl}^{(s)}(k, k_1) \right. \right. \\ & \left. \left. + e_{ki}^{\sigma*} e_{kn}^\sigma \frac{\Lambda_{vn}^{(\alpha)}(k, k_1) G_{1m}(k + k_1)}{(\omega_1 - i\delta)^2 (\omega + \omega_1 + i\delta)^2} \tilde{C}_{ijl}^{(s)*}(k, k_1) \right] \right. \\ & \left. + \text{Re } G_{jv}(k_1) \text{ Re} \left[e_{ki}^\sigma e_{kn}^{\sigma*} \frac{G_{1m}^*(k + k_1) \Lambda_{vn}^{(\alpha)*}(k, k_1)}{(\omega_1 + i\delta)^2 (\omega + \omega_1 - i\delta)^2} \right] \text{Im } \tilde{C}_{ijl}^{(s)}(k, k_1) \right. \\ & \left. + \text{Re } G_{jv}(k_1) \text{ Re } \tilde{C}_{ijl}^{(s)}(k, k_1) \text{Im} \left[e_{ki}^\sigma e_{kn}^{\sigma*} \frac{G_{1m}^*(k + k_1) \Lambda_{vn}^{(\alpha)*}(k, k_1)}{(\omega_1 + i\delta)^2 (\omega + \omega_1 - i\delta)^2} \right] \right] . \quad (6) \end{aligned}$$

The B operation on the last term of Eq. (6) yields zero since that term does not contain the needed imaginary part. Then Eq.(6) can be written

$$\begin{aligned} Q_1 = B & \left[\frac{1}{2} \text{Im } G_{jv}(k_1) \left[e_{ki}^\sigma e_{kn}^{\sigma*} \frac{\Lambda_{vn}^{(\alpha)*}(k, k_1) G_{1m}^*(k + k_1)}{(\omega_1 + i\delta)^2 (\omega + \omega_1 - i\delta)^2} \tilde{C}_{ijl}^{(s)}(k, k_1) \right. \right. \\ & \left. \left. + e_{ki}^{\sigma*} e_{kn}^\sigma \frac{\Lambda_{vn}^{(\alpha)}(k, k_1) G_{1m}(k + k_1)}{(\omega_1 - i\delta)^2 (\omega + \omega_1 + i\delta)^2} \tilde{C}_{ijl}^{(s)*}(k, k_1) \right] \right. \\ & \left. + \text{Re} \left[\frac{1}{2} e_{ki}^\sigma e_{kn}^{\sigma*} [G_{jv}(k_1) + G_{jv}^*(k_1)] \frac{G_{1m}^*(k + k_1) \Lambda_{vn}^{(\alpha)*}(k, k_1)}{(\omega_1 + i\delta)^2 (\omega + \omega_1 - i\delta)^2} \right] \text{Im } \tilde{C}_{ijl}^{(s)}(k, k_1) \right] , \quad (7) \end{aligned}$$

where the relation $\text{Re } z_1 \text{ Re } z_2 = \text{Re}[(\text{Re } z_1)z_2] = \text{Re}[(z_1 + z_1^*)z_2/2]$ has been used. For

a nearly nonabsorptive and spatially isotropic background, one has approximately³

$$\frac{G_{j\nu}^*(k_1)}{\omega_1 - i\delta} = \frac{G_{\nu j}(k_1)}{\omega_1 + i\delta} = \frac{G_{j\nu}(k_1)}{\omega_1 + i\delta} \quad (8)$$

Using Eq. (8) in Eq. (7) gives

$$\begin{aligned} Q_1 = B & \left[\left(e_{ki}^\sigma e_{kn}^{\sigma*} \frac{G_{lm}^*(k+k_1) \Lambda_{\nu n}^{(\alpha)*}(k, k_1)}{2(\omega_1 + i\delta)^2 (\omega + \omega_1 - i\delta)^2} \vec{C}_{ijl}^{(s)}(k, k_1) \right. \right. \\ & + \left. e_{ki}^{\sigma*} e_{kn}^\sigma \frac{G_{lm}(k+k_1) \Lambda_{\nu n}^{(\alpha)}(k, k_1)}{2(\omega_1 - i\delta)^2 (\omega + \omega_1 + i\delta)^2} \vec{C}_{ijl}^{(s)*}(k, k_1) \right) \text{Im } G_{j\nu}(k_1) \\ & + \left. \text{Re} \left[e_{ki}^\sigma e_{kn}^{\sigma*} \frac{G_{j\nu}(k_1) G_{lm}^*(k+k_1) \Lambda_{\nu n}^{(\alpha)*}(k, k_1)}{(\omega_1 + i\delta)^2 (\omega + \omega_1 - i\delta)^2} \right] \text{Im } \vec{C}_{ijl}^{(s)}(k, k_1) \right] \quad (9) \end{aligned}$$

Substituting Eqs. (5) and (9) in Eq. (I-62) results in

$$\begin{aligned} \langle \vec{F}_{dp}^{(1a)} \rangle = & - \frac{Be_\alpha^2}{(2\pi)^3} \int \frac{dk dk_1}{\omega^2} |E_k^{\sigma(0)}|^2 \delta(\omega + \omega_1 - (\vec{k} + \vec{k}_1) \cdot \vec{v}_\alpha) \\ & \times \left[v_{\alpha m} \left(e_{ki}^\sigma e_{kn}^{\sigma*} \frac{G_{lm}^*(k+k_1) \Lambda_{\nu n}^{(\alpha)*}(k, k_1)}{2(\omega_1 + i\delta)^2 (\omega + \omega_1 - i\delta)^2} \sum_s e_s \vec{C}_{ijl}^{(s)}(k, k_1) \right. \right. \\ & + \left. e_{ki}^{\sigma*} e_{kn}^\sigma \frac{G_{lm}(k+k_1) \Lambda_{\nu n}^{(\alpha)}(k, k_1)}{2(\omega_1 - i\delta)^2 (\omega + \omega_1 + i\delta)^2} \sum_s e_s \vec{C}_{ijl}^{(s)*}(k, k_1) \right) \text{Im } G_{j\nu}(k_1) \\ & + \left. \sum_s e_s \text{Re} \left[e_{ki}^\sigma e_{kn}^{\sigma*} \frac{v_{\alpha m} G_{j\nu}(k_1) G_{lm}^*(k+k_1) \Lambda_{\nu n}^{(\alpha)*}(k, k_1)}{(\omega_1 + i\delta)^2 (\omega + \omega_1 - i\delta)^2} \right] \text{Im } \vec{C}_{ijl}^{(s)}(k, k_1) \right] \quad (10) \end{aligned}$$

Eq. (11) below is produced as follows: in the first term of Eq. (10), dummy indices (m, ν) are renamed as (ν, m), and Eq. (8) is used; in the second term, dummy indices (m, ν, n, i, j) are renamed as (ν, j, i, n, m), and Eq. (8) is used; in the third term, Eq. (8) is used; and the imaginary part of pure frequency denominators is ignored:

$$\begin{aligned}
\langle \vec{F}_{dp}^{(1a)} \rangle = & - \frac{Be_\alpha^2}{(2\pi)^3} \left[\frac{dk dk_1}{\omega^2 \omega_1^2} |E_k^{\sigma(0)}|^2 \delta(\omega + \omega_1 - (\vec{k} + \vec{k}_1) \cdot \vec{v}_\alpha) \right. \\
& \times \left[e_{ki}^\sigma e_{kn}^{\sigma*} \frac{v_{\alpha v} G_{1v}(k + k_1)}{2(\omega + \omega_1)^2} \sum_s e_s \vec{C}_{ijl}^{(s)}(k, k_1) \Lambda_{mn}^{(\alpha)*}(k, k_1) \right. \\
& + \Lambda_{ji}^{(\alpha)}(k, k_1) \left. \left[\frac{v_{\alpha v} G_{1v}(k + k_1)}{2(\omega + \omega_1)^2} \sum_s e_s \vec{C}_{nml}^{(s)}(k, k_1) \right]^* \right] \text{Im } G_{jm}(k_1) \\
& \left. + \sum_s e_s \frac{v_{\alpha m}}{(\omega + \omega_1)^2} \text{Re} [e_{ki}^\sigma e_{kn}^{\sigma*} G_{jv}(k_1) G_{ml}^*(k + k_1) \Lambda_{vn}^{(\alpha)*}(k, k_1)] \text{Im } \vec{C}_{ijl}^{(s)}(k, k_1) \right] . \quad (11)
\end{aligned}$$

According to Eq. (49) of Ref.5, one also has:

$$\delta(\omega + \omega_1 - (\vec{k} + \vec{k}_1) \cdot \vec{v}_\alpha) \Lambda_{vn}^{(\alpha)}(k, k_1) = \delta(\omega + \omega_1 - (\vec{k} + \vec{k}_1) \cdot \vec{v}_\alpha) \Lambda_{nv}^{(\alpha)*}(k_1, k) . \quad (12)$$

If one ignores Cerenkov resonance, then according to Eq. (I-8), $\Lambda_{vn}^{(\alpha)}(k, k_1)$ is effectively real, which, together with Eq. (8), makes $G_{jv}(k_1) G_{ml}^*(k + k_1) \Lambda_{vn}^{(\alpha)*}(k, k_1)$ in the last term of Eq. (11) effectively real, and then $\text{Re}(e_{ki}^\sigma e_{kn}^{\sigma*})$ can be factored out of that term. Doing so and using Eq. (12) in Eq. (11) results in

$$\begin{aligned}
\langle \vec{F}_{dp}^{(1a)} \rangle = & - \frac{Be_\alpha^2}{(2\pi)^3} \left[\frac{dk dk_1}{\omega^2 \omega_1^2} |E_k^{\sigma(0)}|^2 \delta(\omega + \omega_1 - (\vec{k} + \vec{k}_1) \cdot \vec{v}_\alpha) \right. \\
& \times \left[e_{ki}^\sigma e_{kn}^{\sigma*} \frac{v_{\alpha v} G_{1v}(k + k_1)}{2(\omega + \omega_1)^2} \sum_s e_s \vec{C}_{ijl}^{(s)}(k, k_1) \Lambda_{nm}^{(\alpha)}(k_1, k) \text{Im } G_{jm}(k_1) \right. \\
& + e_{ki}^\sigma e_{kn}^{\sigma*} \frac{\Lambda_{ij}^{(\alpha)*}(k_1, k)}{2} \left[v_{\alpha v} \frac{G_{1v}(k + k_1)}{(\omega + \omega_1)^2} \sum_s e_s \vec{C}_{nml}^{(s)}(k, k_1) \right]^* \text{Im } G_{jm}(k_1) \\
& \left. + \frac{v_{\alpha m}}{(\omega + \omega_1)^2} \sum_s e_s \text{Re}(e_{ki}^\sigma e_{kn}^{\sigma*}) \text{Re}[G_{jv}(k_1) G_{ml}^*(k + k_1) \Lambda_{nv}^{(\alpha)}(k_1, k)] \text{Im } \vec{C}_{ijl}^{(s)}(k, k_1) \right] . \quad (13)
\end{aligned}$$

Substituting Eqs. (II-25) and (13) in Eq. (I-23) and ignoring zero-frequency resonances, one obtains

$$\begin{aligned}
\langle \vec{F}_{dp}^{(1)} \rangle = & - \frac{Be_\alpha^2}{(2\pi)^3} \int \frac{dk dk_1}{\omega^2 \omega_1^2} |E_k^{\sigma(0)}|^2 \delta(\omega + \omega_1 - (\vec{k} + \vec{k}_1) \cdot \vec{v}_\alpha) \\
& \times \left[e_{ki}^\sigma e_{kn}^{\sigma*} \frac{v_{\alpha\nu} G_{1\nu}(k + k_1)}{2(\omega + \omega_1)^2} \sum_s e_s \vec{C}_{ijl}^{(s)}(k, k_1) \Lambda_{nm}^{(\alpha)}(k_1, k) \text{Im } G_{jm}(k_1) \right. \\
& + e_{ki}^\sigma e_{kn}^{\sigma*} \frac{\Lambda_{ij}^{(\alpha)*}(k_1, k)}{2} \left[v_{\alpha\nu} \frac{G_{1\nu}(k + k_1)}{(\omega + \omega_1)^2} \sum_s e_s \vec{C}_{nml}^{(s)}(k, k_1) \right]^* \text{Im } G_{jm}(k_1) \\
& + \frac{v_{\alpha m}}{(\omega + \omega_1)^2} \sum_s e_s \text{Re}(e_{ki}^\sigma e_{kn}^{\sigma*}) \text{Re}[G_{j\nu}(k_1) G_{ml}^*(k + k_1) \Lambda_{nv}^{(\alpha)}(k_1, k)] \text{Im } \vec{C}_{ijl}^{(s)}(k, k_1) \\
& + \frac{v_{\alpha m} v_{\alpha \mu}}{(\omega + \omega_1)^4} \sum_{st} e_s e_t \text{Im}[e_{ki}^\sigma e_{kn}^{\sigma*} G_{j\nu}(k_1) G_{lm}^*(k + k_1) G_{q\mu}(k + k_1) \\
& \times \sigma_{\nu nq}^{(t)}(k_1, -k, k + k_1) \vec{C}_{ijl}^{(s)}(k, k_1)] \Big] . \tag{14}
\end{aligned}$$

3. SUMMARY

Equation (14) (or Eq. (II-26) is the time and stochastic average of the bremsstrahlung recoil force due to the total electromagnetic field acting on the second-order nonlinear dynamic polarization charge of a test particle. The tensor $\vec{C}_{ijl}^{(s)}(k, k_1)$ is given by Eq. (I-60) in terms of the second-order nonlinear conductivity tensor. This force will be further reduced elsewhere, after it is combined with other components of the recoil force on the test particle.

4. REFERENCES

1. H. E. Brandt, "Reduction of bremsstrahlung recoil force on the second-order nonlinear dynamic polarization charge of a relativistic test particle," in Intense Microwave Pulses II, Howard E. Brandt, Editor, Proc. SPIE 2154, pp. 247-261, 1994
2. H. E. Brandt, "Bremsstrahlung recoil force on the second-order nonlinear dynamic polarization charge of a relativistic test particle," in Intense Microwave Pulses III, Howard E. Brandt, Editor, Proc. SPIE 2557, pp. 122-129, 1995.
3. H. E. Brandt, "On nonlinear bremsstrahlung in nonequilibrium relativistic beam-plasma systems," in Intense Microwave and Particle Beams II, Howard E. Brandt, Editor, Proc. SPIE 1407, pp. 326-353, 1991.
4. H. E. Brandt, "On the form of the collective bremsstrahlung recoil force in a nonequilibrium relativistic beam plasma system," Harry Diamond Laboratories, HDL-TR-2026, January 1984.
5. H. E. Brandt, "Nonlinear force on an unpolarized relativistic test particle to second order in the total field in a nonequilibrium beam-plasma system," Harry Diamond Laboratories, HDL-TR-1995, August 1983.

Evolution of spectral power density in grounded cathode relativistic magnetron

I. Schnitzer, A. Rosenberg, C. Leibovitz, I. Cohen, M. Botton, and J. Leopold

Rafael, Department #23, P.O.Box 2250, Haifa 31021, Israel.

FAX: +972-4-897-5315. E-mail: Schnit@Netvision.Net.il

ABSTRACT

A novel, rep-rated, relativistic magnetron design is demonstrated. Unlike other relativistic magnetrons, the high voltage pulse is positively charged, feeding the anode block, while the cathode is grounded. Moreover, the anode-cathode interaction space is centered in a larger *buffer* cavity that serves as an electric insulator and electromagnetic impedance matching between the anode block and the exit waveguide(s). The grounded cathode geometry eliminates the axial current (improving efficiency) and enables the use of compact, CW, U-shaped electromagnet. It may also be utilized for frequency tunability through the buffer cavity in a way similar to coaxial magnetrons. Operation with peak power of 50MW (100MW) and pulse length of 150ns (70ns) has been achieved. Employing metal-dielectric cathodes led to repetitive operation up to 10Hz. The analysis emphasizes time-resolved spectral power density of both in-cavity and emitted microwaves in regard to the undesirable occurrence of pulse shortening.

Keywords: relativistic magnetron, high-power microwaves, metal-dielectric cathode, time-frequency distribution, pulse shortening, magnetron cavity design

1. INTRODUCTION

Since the first landmark by Bekefi et al.,¹ announcing the A6 relativistic magnetron, substantial improvements accomplished peak power levels of several gigawatts. However, pragmatic considerations emphasized repetitive mode of operation and longer pulse duration (i.e., higher average power) at the expense of peak power. Repetition rate of about 200pps with peak power levels around 600MW and pulse lengths 30ns (~20J/pulse) were achieved by Physics International, USA,^{2,3} and 360MW/60ns (~22J/pulse) by the Institute of Nuclear Physics, Tomsk, Russia.^{2,4}

Further progress seems to be impeded by the following two facts: *i)* Both of these leading groups, which employ versions of the A6 resonator geometry, confront with an underlying limitation of the pulse energy, also known as *pulse shortening*. *ii)* The required magnetic field coils are either too large for numerous applications (PI's at CW operation), or, if suitably smaller, can be operated only in short bursts.⁴

At *Rafael*, we recently initiated a relativistic magnetron program that emphasizes compactness and repetitive operation at longer pulse duration ($\sim 200\text{ns}$) with pulse energy $> 20\text{J}$. To fulfill these requirements we explore a new design, named hereafter as the *grounded cathode magnetron*. This paper presents the design considerations of the new geometry, some preliminary results, and physical interpretations of the measured time-resolved spectral power density.

2. DESIGN

2.1 Grounded Cathode Geometry

Our magnetron design (Patent pending) is fundamentally different from the above mentioned relativistic magnetrons. As shown in Figure 1, the cathode is grounded and the positive high-voltage

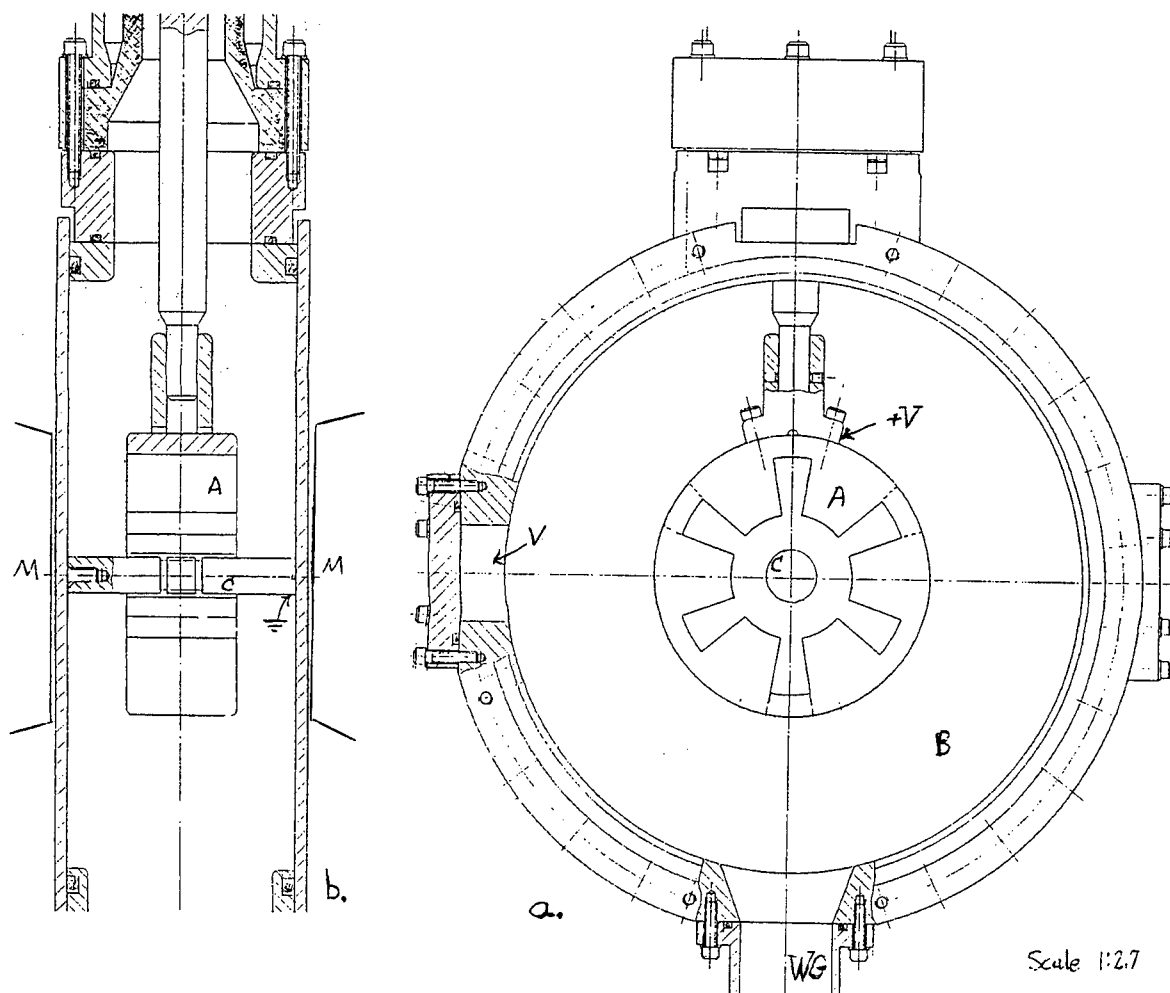


Figure 1. Grounded Cathode Magnetron design, top view is (a) and side view (b). Note the anode block (A), the cathode (C), the buffer cavity (B), the electromagnet poles (M), the waveguide exit (WG), the pumping port (V), and the ceramic interface (darkened) with the transmission line.

(H.V.) pulse is injected to the anode block (essentially, an A6 resonator). The anode block is centered in a cylindrical cavity, the *buffer cavity*, which isolates the positively charged anode from the buffer cavity walls, the exit waveguide, and the transmission line. Note that the buffer cavity diameter is 210mm and **84mm wide** (90mm externally) accommodating an A6 resonator operating around 2.5GHz.

Injecting a positive pulse through a buffer cavity has the following major advantages:

1. The H.V. transmission line is connected perpendicularly to the DC magnetic field axis. Such a configuration enables the use of a compact U-shaped electromagnet instead of the large Helmholtz coils that are often used in relativistic magnetrons. See the side view in Figure 1.
2. There are no axial currents in the grounded cathode geometry since both the surrounding walls and the emitter are at the same potential. The elimination of the axial current component improves the electronic efficiency since all the electrons fall to the anode block.
3. The external cavity functions as a buffer between the anode-cathode (A-K) interaction region and the output waveguide. In other words, the buffer cavity can be regarded as an electromagnetic impedance matching element that reduces the stored energy density for the same output power.
4. The grounded cathode magnetron may be tunable through the buffer cavity in a way similar to coaxial magnetrons. Alternatively, broad tunability range may be achieved by a mechanical change of the **grounded** cathode dimensions in a way similar to the anode regulation implied by the PI group.⁵
5. The grounded cathode scheme is most suitable for the employment of more sophisticated and innovative, long lifetime, emitters such as plasma cathodes. The option of timed cathode excitation by another low (-) voltage trigger electrode seems very promising.
6. There is an inherent advantage in transmitting a positively charged H.V. pulse as opposed to a negatively charged pulse. Generally speaking, it allows for tighter lines for equivalent charging.

One disadvantage of the grounded cathode geometry is the control of electrons ejected from the buffer cavity walls toward the anode block and feed line, and of positive ions traversing the buffer cavity. Another difficulty is the electromagnetic cavity design which is generally more demanding because of the crucial role played by the external (buffer) cavity and its coupling to both the A-K resonator and the waveguide. These drawbacks are presently contemplated as will be described later.

2.2 Metal-Dielectric Cathode

We have attempted many of the conventional cathode designs including edge-enhanced metallic cathode, velvet cathode, and graphite. However, none of these were found suitable for **repetitive**, relatively **low voltage** (<300kV), and **large gap** (14mm) as imposed by our magnetron design. They were either emission limited or rep-rate limited.

Introducing compound cathode design, particularly the metal-dielectric cathode (MDC), yield significant improvements. In MDC, best described by Mesyats and Proskurovsky,^{6,7} the surface microexplosive process that develops into a self-sustained explosive electron emission (EEE) is initiated in the so called **triple points** (metal-dielectric-vacuum interface). This emission mechanism, enhanced

by the dielectric material ($\epsilon > 1$) presence, was known for a long time as a clean (in terms of vacuum integrity), high current density, low voltage, and long lifetime source.

So far we have used uncontrollable MDC schemes. The emissive section of a typical cathode is 20mm long, centered at the mid-plane of the 40mm thick anode. It consists of alternating disks of metal and dielectric materials. Some of the metallic disks are floating (electrically) and their diameter, thickness, sharpness, and composition are varied in order to optimize the emission characteristics. In this scheme, capacitive links through adjacent metallic disks result in strong surface fields at the triple points which later develop to surface plasma over the dielectric disks from which electrons are being extracted by the positively charged anode.

Although such simple MDC seem promising, we feel that there is still a lot to improve. It is both technologically valuable and physically interesting to master the dimensions and material science that determines emission time scale, uniformity, and cathode longevity. We are presently looking to contract the apparent emission delay ($> 20\text{ns}$) which lowers the overall efficiency. In the future, we may include controllable MDC by a special trigger electrode (-5kV , roughly) to initiate the surface plasma prior to the H.V. pulse.

3. OPERATION

3.1 Diagnostics

We use several field probes, simultaneously. Typically a far-field probe/antenna, one small loop in the buffer cavity, and one at the exit waveguide. Each of these RF signals is attenuated and split into three channels: one into a Schottky diode detector (power envelope), and two are being mixed with local oscillators (LO) set at two different frequencies (upper LO & lower LO). The diode current and voltage traces are recorded as well. Other diagnostic tools, such as Ne lamp arrays and open shutter photography (time integrated), are also valuable.

All this data has been recorded for several cathode types and different anode and buffer cavity designs. Here we only emphasize the study of the emitted spectral power density as a diagnostic tool.

3.2 Time-Resolved Spectral Power Density

Typical pulse length is about 200ns, as shown in Figure 2. Sampling of these pulses at rates of 1Gs/second, as we do, can reveal not only their spectral content but also their time evolution with acceptable resolution. The temporal evolution of the trace from Figure 2 is shown in Figure 4.

The most natural thing to do is to divide the signal into overlapping segments and to find the spectral power density of each segment (temporal window). That procedure is known as *running window*, or *Gabor transformation*. When squared to yield the power density it is known as *spectrogram*. Mathematically, the time resolved spectral power density, of the signal $S(t)$ is given by⁸

$$P_{SPEC}(t, \omega) = \left| \int \exp(-i\omega t') S(t') h(t'-t) dt' \right|^2$$

where $h(t)$ is a carefully chosen smoothing window function. This relatively simple transformation was found to be problematic for signals whose frequency varies significantly within each time segment. It also tends to peak artificially at the window center. Consequently, we were looking for more sophisticated time-frequency distributions using adaptive window size that is optimized to the temporal signal behavior. In particular, the class of *Orthonormal Shift-Invariant Trigonometric Decomposition*.⁹ We have learned that none of these linear transformation gave reliable picture of the time-resolved spectral power.

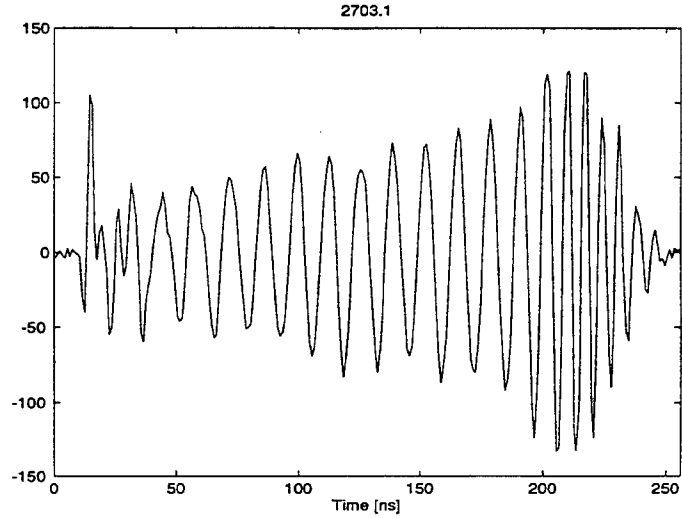


Figure 2. Heterodyne signal sampled at 1GS/s (RF - LO)

However, it was found that Cohen's class smoothed distributions are more reliable for these short pulses. Of these, the most known is the *Wigner* distribution defined as

$$P_W(t, \omega) = \int S^*(t - \tau/2) \exp(-i\omega\tau) S(t + \tau/2) d\tau.$$

The main disadvantage of such bilinear transformation is the artificial cross terms resulting from interfering distinct components in the time-frequency plane. That problem was minimized by a proper smoothing function with an acceptable loss of T-F resolution. The data which is presented here was processed by the following *Smoothed Pseudo Wigner* distribution (SPW).

$$P_{SPW}(t, \omega) = \int \sqrt{\alpha\beta} \exp\left[-\alpha(t - t')^2 - \beta(\omega - \omega')^2\right] P_W(t', \omega') dt' d\omega'$$

where the smoothing parameters α and β were optimized for the type of measured traces that we have and remain unchanged throughout the analysis.

3.3 Mode Competition and Chirping

Figure 3 presents the time-resolved spectral density for a magnetron operated with a velvet cathode in a single-shot mode with $B_{axial} = 2.1$ kG. In 3a, the averaged diode voltage (on the plateau) and current were $V = 220$ kV and $I = 0.7$ kA, and the emitted peak power was 50 MW. (In all cases the radiation was emitted through a circular waveguide into a conical antenna and measured with a calibrated antenna placed in the far field.). In 3b we measured $V = 180$ kV, $I = 1.4$ kA, and the emitted peak power was 100 MW.

The two central frequencies, or modes, in Figure 3 seem quite reasonable in light of the fact that the computed¹⁰ eigenfrequency of the $2\pi/3$ mode and the π mode are 2.424 GHz and 2.518 GHz, respectively. Moreover, it looks as if the $2\pi/3$ mode builds up faster due to the higher voltage at the

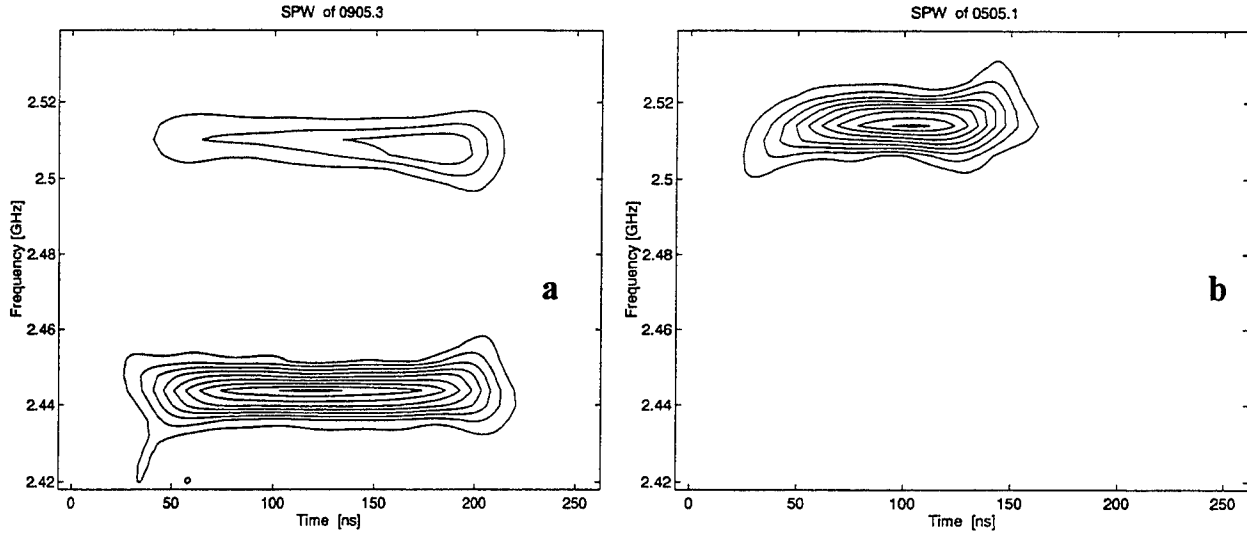


Figure 3. Time-resolved spectral density from the magnetron. Details are given in the text above.

beginning of the pulse and then, as the impedance (and voltage) drops, the electron drift velocity tends to synchronize with the π mode. This mode competition reduces the efficiency which otherwise is expected to be as high as 50% in the absence of axial currents.

At slightly higher charging, and perhaps more effective, under different vacuum conditioning, we managed to reduce the diode impedance to about 120Ω (matched to the generator), as in 3b. Indeed, under these conditions we see single mode (π) efficient operation, in accordance with the Hull/Bunneman-Hartree V - B plane. However, the microwave pulse terminates after about 70ns. In fact, when examining the evolution of the in-cavity spectral density we find it to be pronounced in the $2\pi/3$ mode just prior to the build up of the externally emitted π mode. Such perplexing observations are quite common but were not quantified because of the unknown coupling of each mode to the internal field probe. They attest, however, on the existence and timing of other modes in the buffer cavity.

As a last example of this section we examine the temporal evolution of the spectral power density obtained with a preliminary design of MDC. The emission dynamics of this cathode is noticeably different from the previously described velvet cathodes, as shown in Figure 4. Instead of specific mode signature we observe frequency **chirping** (not always with a knee shape, in some cases it evolves along diagonal lines in the T-F plane). It is believed that the chirp develops due to cathode

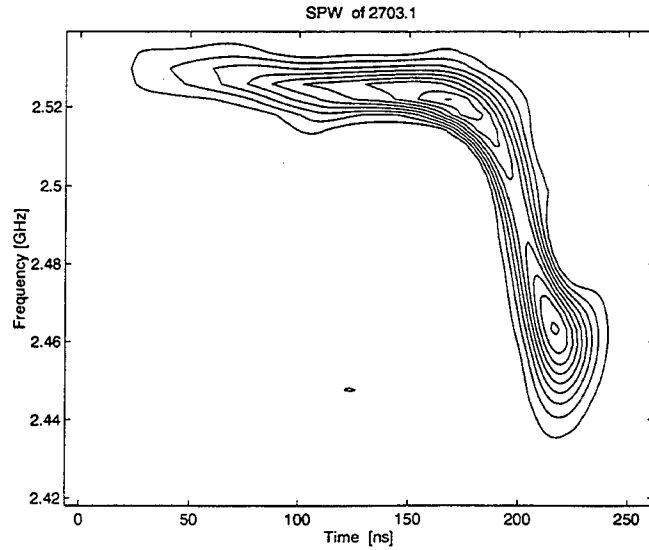


Figure 4. Chirped magnetron emission with MDC.

plasma motion outward which effectively increases the cathode diameter. Calculation shows that as the cathode radius expands from 8mm to 13mm, the π mode frequency changes from 2.518 GHz to 2.465 GHz for anode inner and outer radii of 22mm and 42mm, respectively, as we have.

3.4 Pulse Shortening

At this point we note the following observations with regard to the pulse shortening: *i)* Square 150ns flat top pulses with single mode frequency of 2.52 GHz were routinely observed, but in these cases the peak power was under 36 MW. *ii)* In all cases of pulse shortening (Figure 3b. and 5b. below) the emitted power was single moded, within the emission band width of about 15 Mhz. *iii)* Open shutter photography through the exit waveguide, vacuum window, and the anode coupling slot, did not reveal any specific record of pulse shortening (internal breakdowns are clearly evident).

Of the possible explanations that we have considered, it seems that plasma gap closure, either anode or cathode plasmas, is unlikely due to the steady spectral content of these pulses. The plasma motion should change the RF boundary and thereby chirp the resonant frequency as shown in Figure 4. Excluding RF breakdown as the cause for pulse shortening, based on our in-cavity photography, is less certain. However, the mere fact that we also experience pulse shortening at lower power density compare to other groups indicate that it is of a more universal nature and should be looked for elsewhere.

In light of the above mentioned observations, the fact that our magnetron impedance is typically larger than that of the generator's, and the predominant role of the cathode emission mechanism, we believe that **impedance mismatch** is to be blamed for pulse shortening. The term impedance mismatch should be taken in a generalized manner to include both the electrical impedance and the electromagnetic impedance since they are strongly coupled. In an oscillator, the load conductance (RF out-coupling) determines the electrical load, which in turn determines the voltage, the electrical power, pulls the frequency (or pushes for purely resistive load), and so on, in a self consistent manner. This interplay is governed by the cavity Q factors, out-coupling factor, and through the specific dependence of the diode complex impedance on the applied voltage. In magnetron theory, it is customary to present this interplay in Rieke diagrams in which contours of constant power and of constant frequency are drawn in the load admittance plane. Such Rieke diagrams,¹¹ can explain how impedance mismatch may lead to pulse shortening.

3.5 Repetitive Operation

At first, the MARX-PFN generator was upgraded to produce nearly square pulses of up to 300kV on matched impedance of 120 Ω at the rate of 10pps. The magnetron was then operated using a metal-dielectric cathode (MDC-1) as mentioned above in relation to Figure 4. Although, repetitive operation was successful, the cathode emission was poor. In order to improve the emission (and reduce the cathode plasma), the design was revised (MDC-2) as described in 2.2 above. These new cathodes are thicker than the former and therefore lower resonant frequency are expected.

Figure 5 presents two examples of pulse bursts as analyzed by a spectrum analyzer (note, power is measured in dBm). In the first case (5a), a burst of about 250 pulses at 5pps and peak power around 40MW was scanned for 50 seconds with 2MHz band width. As expected the main frequency is indeed lower. However, this shift is much too large and is excused, for the moment, by structural asymmetry. Note that coexist with the main emission frequency at 2.28GHz is the component at 2.518 GHz, about 6dB lower. Note also that the density of lines implies that misfire is rare if not absent.

Figure 5b is similar but was recorded at full charging voltage for a shorter time (20s). The rate was 5pps as well and the peak power around 65MW. The main difference between the two bursts is, however, the absence of the higher frequency component in the second burst. We should point out that pulses from the more intense burst were short, about 70ns, while those shown in Figure 5a varied in pulse lengths between 70ns to 150ns. Similarly, we recorded the spectra from the internal field probe and found it to resemble the emitted one in both cases.

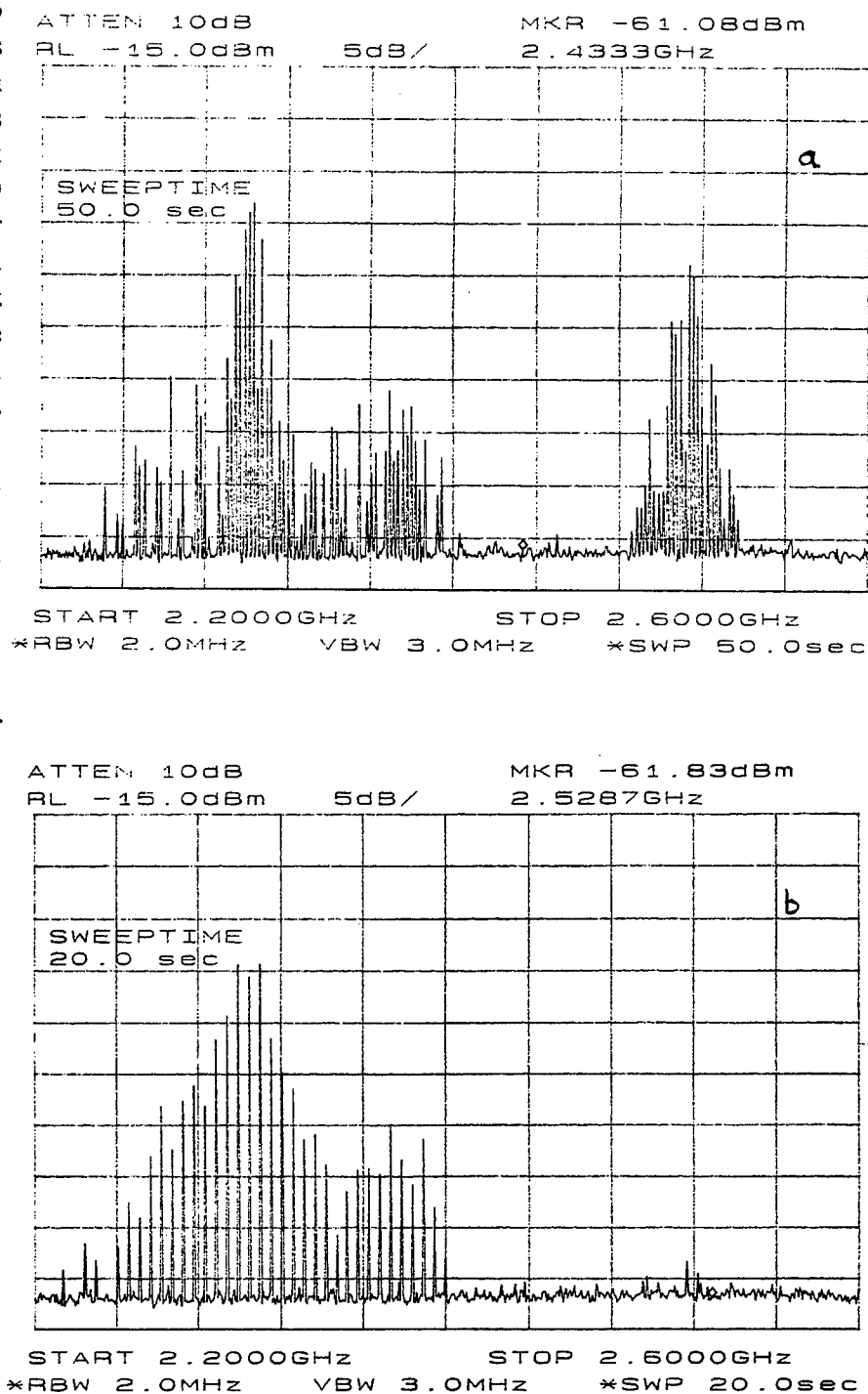


Figure 5. Burst mode operation of the magnetron at 5pps as recorded by a spectrum analyzer at 2MHz band with for 50 second (a. on top) and for 20 seconds (b. on the bottom). In both cases the emitted main frequency is 2.3GHz, and peak power is 40MW in a and 60 MW in b. Note the absence of the higher frequency component in the more intense burst.

4. SUMMARY

We have described a novel relativistic magnetron design which is fundamentally different from other relativistic magnetrons. The *grounded cathode* geometry eliminates axial current, allows the use of a more compact electromagnet, incorporates a buffer cavity to achieve better adaptivity (and complexity) to intense RF fields, and is more permissible to advanced rep-rated cathode designs.

We emphasized the capacity of time-resolved spectral analysis as an important diagnostic tool. It led us to the conclusion that pulse shortening is most likely due to impedance mismatch. We believe that it should be challenged by adapting the diode impedance characteristics (cathode dynamics) to the electromagnetic load. Presently, we are in the process of full 3D electromagnetic simulation (EMA3D code, Electromagnetic Applications, Inc., Denver) of the complete structure including the resonators, the buffer cavity, and the exit waveguide.

Metal-dielectric cathodes were found to be promising for such low voltage, rep-rated, relativistic magnetron. They performed almost as good as the simple (single shot) velvet cathodes at rates of 10pps. We feel that there is still a lot to improve in MDC design. With the *grounded cathode* it is also tempting to think of more innovative cathode schemes for better impedance matching.

5. REFERENCES

1. A. Palevsky and G. Bekefi, "Microwave emission from pulsed, relativistic E-beam diodes," *Phys Fluids*, **22**, 985, (1979), and G. Bekefi and T. J. Orzechowski, *Phys. Rev. Lett.* **37**, 379 (1976).
2. J. Benford and J. Swegle, *High-Power Microwaves*, Artech house, 1992.
3. R. Smith, J. Benford, N. Cooksey, N. Aiello, J. Levine, and B. Harteneck, "Operation of an L-band relativistic magnetron at 100Hz," *Intense Microwave & Particle Beams II*, ed H. Brandt, *SPIE*, **1407**, 83 (1991).
4. V. V. Vasil'yev, I. I. Vintizenko, A. N. Didenko, Y. I. Lukonin, A. S. Sulakshin, G. P. Femenko, and E. G. Furman, "Relativistic magnetron operating in the mode of a train of pulses," *Sov. Tech. Phys. Lett.*, **13**, 762, (1987).
5. J. S. Levine, B. D. Harteneck, and H. D. Price, "Frequency agile relativistic," *Intense Microwave Pulses III*, ed H. E. Brandt, *SPIE*, **2557**, 74 (1995).
6. A. Mesyats, "Physics of electron emission from metal-dielectric cathodes," *BEAMS '94* pp. 93-99.
7. A. Mesyats and D. I. Proskurovsky, *Pulsed Electrical Discharge in Vacuum*, Springer Series on Atoms & Plasmas, Springer-Verlag, Berlin, 1989.
8. Cohen, "Time-frequency distribution - a review," *Proceedings of the IEEE* **70**, 941-981 (1989)
9. Cohen, S. Raz, and I. Schnitzer, "Best basis algorithm for orthonormal shift-invariant trigonometric decomposition," *Proc. IEEE Digital Signal Processing Workshop*, Loen, Norway 9/1996.
10. J. B. Collins, *Microwave Magnetrons*, New York: McGraw-Hill, 1948.
11. J. Slater, *Microwave Electronics*, Princeton: Van Nostrand, 1950, (Particularly section 9.3).

Mechanism of microwave amplification in relativistic klystron amplifier

Wu Ding

Institute of Applied Physics and Computational Mathematics
P.O.Box 8009, Beijing 100088, China

ABSTRACT

In this paper, the electron beam prebunching in the modulation cavity and shift tube of the relativistic klystron amplifier is studied analytically; a self-consistent equation of radiation generated by the prebunched electron beam in the radiation cavity is derived for the first time by using the field method of particle-wave interaction instead of the circuit method, and from the equation a gain formula in the linear regime is obtained.

Keywords: amplification mechanism, prebunching, field method, radiation equation

1. INTRODUCTION

The relativistic klystron amplifier(RKA) is one of two types of the high power microwave device (the other is the multiwave Cerenkov generators) with power at 10 GW and energy at 1KJ level, and the device has the potential of generating high average power. In order to make full use of its advantages and improve on the engineering design of the device it is necessary to deeply understand its mechanism of microwave amplification. In this paper, we will analyze the RKA mechanism of microwave amplification using the field method of particle-wave interaction instead of the circuit method.

2. PREBUNCHING OF THE ELECTRON BEAM

2.1 Velocity modulation of the electron beam in the modulation cavity

RKA, as shown in Fig.1, consists of the following main parts: the cathod, modulation cavity (typically there are two), shift tube, radiation cavity and microwave output window. In addition, there are still the input rf source, guiding magnetic field and electron collector.

Modulation of the modulation cavities on the electron beam is achieved by gaps between the cavity and the shift tube. The ac voltage at the first gap excites the slow and fast space-charge waves on the electron beam, these waves make the voltage and current of the electron beam modulated. The second gap is equivalent to feed a structure of impedance Z_c to the electron beam. Based on above understanding, the voltage modulation of the electron beam through two cavities is given by using the transmission line theory in reference¹:

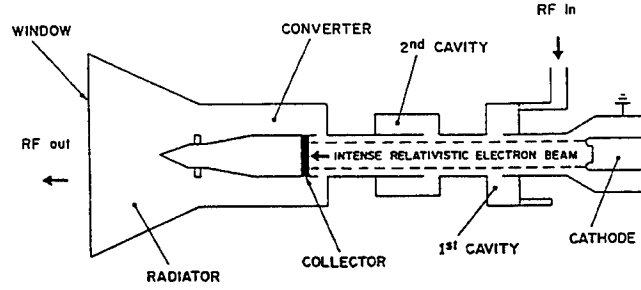


Figure 1. Schematic of the NRL Relativistic Klystron Amplifier.

$$\tilde{V}_1' = V_{10} \left\{ \cos(\alpha\mu\theta_1) + i \left(\frac{R_s}{Z} + \zeta \right) \sin(\alpha\mu\theta_1) \right\} e^{i(\omega t - \theta_1)} \quad (1)$$

$$\theta_1 = \frac{\omega \delta z_1}{c \beta_0} \quad (\delta > 1) \quad (2)$$

In deriving the expression(1), it is assumed that the first gap is at $z = 0$, the second gap is at $z = z_1$, the structure of impedance Z_c is a resonant cavity, $Z_c = R_s$, R_s is the resistance. The symbols of the physical quantities used in the expression (1) and the other physical quantities in this paper are the same as in the reference¹, except additional illustrations.

The relation of the velocity modulation with the voltage modulation of the electron beam can be obtained as follows:

$$m_0 c^2 (\gamma_{inj} - 1) = |e| V \quad (3)$$

$$\gamma_{inj} = \gamma_0 + \frac{I_0}{I_s \beta_0} \quad (4)$$

$$m_0 c^2 \frac{\partial \gamma_{inj}}{\partial \gamma_0} \frac{\partial \gamma_0}{\partial \beta} \Delta \beta = |e| \Delta V \quad (5)$$

$$\therefore \Delta \beta = \frac{|e| \delta}{m_0 c^2 \gamma_0^3 \beta_0} \Delta V \quad (6)$$

$$\begin{aligned} \Delta V = \tilde{V}_1' + c.c = V_{10} & \left[\cos^2(\alpha\mu\theta_1) + \left(\frac{R_s}{Z} + \zeta \right)^2 \sin^2(\alpha\mu\theta_1) \right]^{\frac{1}{2}} \\ & \cdot \cos \left[\tan^{-1} \frac{\left(\frac{R_s}{Z} + \zeta \right) \sin(\alpha\mu\theta_1)}{\cos(\alpha\mu\theta_1)} + \omega t - \theta_1 \right] \end{aligned} \quad (7)$$

Assuming that the guiding magnetic field is strong enough, then we only consider the motion in the axial direction, i.e. $v = v_z$, and time t in formula (7) is given by the following approximation:

$$t = t_0 + \int_0^{z_1} \frac{dz}{c\beta} \approx t_0 + \frac{z_1}{c\beta_0} \quad (8)$$

$$\text{Let } \frac{(\frac{R_s}{Z} + \zeta) \sin(\alpha\mu\theta_1)}{\cos(\alpha\mu\theta_1)} = -ctg \left[\frac{(\delta-1)\omega z_1}{c\beta_0} \right] \quad (9)$$

$$\text{then } \Delta\beta(z_1, t_0) = \frac{|e|\delta V_{10}}{m_0 c^2 \gamma_0^3 \beta_0} \left[\cos^2(\alpha\mu\theta_1) + \left(\frac{R_s}{Z} + \zeta\right)^2 \sin^2(\alpha\mu\theta_1) \right]^{\frac{1}{2}} \cdot \sin(\omega t_0) \quad (10)$$

where t_0 is the Lagrangian time coordinate of the electron, $\Delta\beta(z_1, t_0)$ is the magnitude of velocity modulation as the electron beam passes through two modulation cavities.

2.2 Dispersion of the electron beam in the shift tube

We assume that the shift tube connected the second gap is long enough, so the velocity modulation of the electron beam is transformed into its density modulation, i.e. phase modulation as the electron beam freely shifts in it²:

$$\Delta\Psi = \frac{\partial\Psi}{\partial\gamma} \Delta\gamma = \frac{\omega}{c\beta_0^2} \int_0^{L_d} \Delta\beta(z_1, t_0) dz \quad (11)$$

where $\Delta\Psi$ is the phase modulation of the electrons. In consequence, we can obtain the prebunching factor:

$$\begin{aligned} \frac{f(t_0)}{n_b} &= \exp\{-i\Delta\Psi\} = \exp\left\{-i\frac{\omega}{c\beta_0^2} \int_0^{L_d} \Delta\beta(z_1, t_0) dz\right\} \\ &= \sum_l (-1)^l J_l \left\{ \frac{\omega L_d \beta_{10}}{c\beta_0^2} \left[\cos^2(\alpha\mu\theta_1) + \left(\frac{R_s}{Z} + \zeta\right)^2 \sin^2(\alpha\mu\theta_1) \right]^{\frac{1}{2}} \right\} \cdot e^{i\omega t_0} \end{aligned} \quad (12)$$

$$\beta_{10} = \frac{|e|\delta V_{10}}{m_0 c^2 \gamma_0^3 \beta_0} \quad (13)$$

where $L_d = z_2 - z_1$ is the length of the shift tube, J_l is Bessel function of the first kind with order l .

3. RADIATION OF THE PREBUNCHED ELECTRON BEAM IN THE RADIATION CAVITY

3.1 Radiation equation

We consider that the interaction of the prebunched electron beam with the TM modes of the radiation cavity leads to generate radiation as the electron beam enters the radiation cavity next to the second modulation cavity. The electromagnetic field for one transverse mode in the radiation cavity can be written:

$$\vec{E}(\vec{x}, t) = [\vec{E}_p(\vec{x}, k) \varepsilon(z, t) + \vec{E}_{sc}(\vec{x}, t, k)] e^{i(kz - \omega t)} + c.c \quad (14)$$

$$\vec{B}(\vec{x}, t) = [\vec{B}_p(\vec{x}, k) \varepsilon(z, t) + \vec{B}_{sc}(\vec{x}, t, k)] e^{i(kz - \omega t)} + c.c \quad (15)$$

Where c.c is the conjugate complex, k is the "Floquet wavenumber", $k = \frac{\delta\omega}{c\beta_0}$, inside the electron beam, and it

is the propagation wavenumber of the radiation wave outside the electron beam in the waveguide, which is determined by the boundary conditions; $\vec{E}_{sc}(\vec{x}, t, k)$ and $\vec{B}_{sc}(\vec{x}, t, k)$ are the space-charge wave field from the electron beam; $\varepsilon(z, t)$ is the slow varying complex amplitude of the radiation field; $\vec{E}_p(\vec{x}, k)$ and $\vec{B}_p(\vec{x}, k)$ are the eigenfunctions of the radiation cavity loaded the electron beam, which are found by the following procedure: dividing the radiation cavity into 3 regions which correspond to $0 < r < r_b$, $r_b < r < r_b + \Delta$ and $r_b + \Delta < r < R$, the solutions of each region are determined by Maxwell's equations without source and the boundary conditions. Where R is the radius of the radiation cavity, and it has been assumed that the cross section of the electron beam is a ring with the radius r_b and width Δ , and $\Delta / r_b < 1$.

Following reference³, the evolution equation of the slow varying complex amplitude of the radiation wave can also be derived by using Maxwell's equations with source for an axisymmetric smooth waveguide:

$$\begin{aligned} \frac{\partial \varepsilon}{\partial t} + v_g \frac{\partial \varepsilon}{\partial z} &= -\frac{1}{U} \int_{z-\frac{1}{2}}^{z+\frac{1}{2}} dz' \int_0^R 2\pi r dr \vec{E}_p^* \cdot \vec{j} e^{-i(kz' - \omega t)} \\ &= -\frac{1}{U} \int_{z-\frac{1}{2}}^{z+\frac{1}{2}} dz' \int_0^R 2\pi r dr E_{pz}^* j_z e^{-i(kz' - \omega t)} \end{aligned} \quad (16)$$

$$v_g = \frac{c}{4\pi} \int_{z-\frac{1}{2}}^{z+\frac{1}{2}} dz' \int_0^R 2\pi r dr \hat{z} \cdot \frac{[\vec{E}_p \times \vec{B}_p^* + \vec{E}_p^* \times \vec{B}_p]}{U} \quad (17)$$

$$U = \frac{1}{4\pi} \int_{z-\frac{1}{2}}^{z+\frac{1}{2}} dz' \int_0^R 2\pi r dr \left[|\vec{E}_p|^2 + |\vec{B}_p|^2 \right] \quad (18)$$

Where v_g is the group velocity for the electromagnetic wave; U is the electromagnetic energy per $|\varepsilon|^2$ contained in one period of the wave, $\lambda = \frac{2\pi c}{\omega}$; j_z is the current density of the prebunched electron beam, which can be represented by

$$j_z = -|e|cn_b \int 2\pi r_0 dr_0 \int \beta_0 c dt_0 \frac{f(t_0)}{n_b} \beta \frac{\delta(r - r_e(r_0, t_0, t))}{2\pi r} \cdot \delta(z - z_e(r_0, t_0, t)) \quad (19)$$

Where r_0 is the Lagrangian radial coordinate of electron, and (r_e, z_e) are the orbit of the electron.

From reference⁴, expanding the phase of the electrons

$$\Psi = kz - \omega t \approx kz - \frac{\omega z}{c\beta_0} - \omega t_0 + \frac{\omega}{c\beta_0^2} \int_0^z \Delta\beta(r, z, t_0) dz \quad (20)$$

and substituting (19) and (20) into (16), we obtain

$$\frac{\partial \varepsilon}{\partial t} + v_z \frac{\partial \varepsilon}{\partial z} = \frac{|e|c\beta_0 n_b}{U} \int_{z-\frac{1}{2}}^{z+\frac{1}{2}} c\beta_0 dt_0 \int_0^z 2\pi r_0 dr_0 E_{pz}^* \frac{f(t_0)}{n_b} e^{-i\Delta kz + i\omega t_0} F(r_0, z, t_0) \quad (21)$$

$$\Delta k = \frac{(\delta - 1)\omega}{c\beta_0} \quad (22)$$

$$F(r_0, z, t_0) = \exp \left\{ -i \frac{\omega}{c\beta_0^3 \gamma_0^3} \int_0^z \Delta\gamma(r_0, z', t_0) dz' \right\} \quad (23)$$

$$\left(\frac{\partial}{\partial t} + v_z \frac{\partial}{\partial z} \right) \Delta\gamma = -\frac{1}{2} \frac{|e|}{mc^2} v(E_{pz} \varepsilon + E_{scz}) e^{i(kz - \omega t)} + c.c \quad (24)$$

$$\frac{i\omega}{c} E_{scz} \simeq \frac{4\pi}{c} j_z e^{-i(kz - \omega t)} \quad (25)$$

Where γ is the relativistic factor of the electron; $F(r_0, z, t_0)$ is referred as a self-bunching factor. Eqs.(12), (21)–(25) are the self-consistent ones described radiation emitted by the prebunched electron beam in the radiation cavity.

3.2 Gain in the linear regime

Assuming that the electron beam is long enough, we can neglect the nonsteady-state performance of the system. When linear approximation for Eqs.(20),(23),(24) and (25) are made, to the first power of the radiation field $E_{pz}\varepsilon$, we have

$$\Psi = \Delta kz - \omega t_0 \quad (26)$$

$$\Delta\gamma = -\frac{1}{2} \frac{|e|}{mc^2} \int_0^z dz (E_{pz} \varepsilon + E_{scz}) e^{i(\Delta kz - \omega t_0)} + c.c \quad (27)$$

$$F(r_0, z, t_0) = 1 - \frac{i\omega}{c\beta_0^3 \gamma_0^3} \int_0^z \Delta\gamma(r_0, z, t_0) dz \quad (28)$$

$$E_{scz} = \frac{\frac{\omega_b^2}{\gamma_0^3 (kv_0 - \omega)^2}}{1 - \frac{\omega_b^2}{\gamma_0^3 (kv_0 - \omega)^2}} E_{pz} \varepsilon \quad (29)$$

where ω_b is the plasma frequency of the electrons, the expression (29) is derived from Eq.(25) by using the first order approximation $-|e|[n_b \delta v + v_0 \delta n_b]$ of the modulated current density $j_z e^{-i(kz - \omega t)}$ and equations which govern the perturbed momentum $\delta p = m\gamma_0^3 \delta v$ and density δn_b of the electrons.

Substituting (26)–(29) into (21), we finally obtain

$$\frac{\partial \varepsilon}{\partial z} = SJ_1(\eta) e^{-i\Delta k z} + iG_0 J_0(\eta) e^{-i\Delta k z} \int_0^z dz_1 \int_0^{z_1} dz_2 e^{i\Delta k z_2} \varepsilon(z_2) \quad (30)$$

$$S = \frac{|e|c\beta_0 n_b}{v_g} \cdot \frac{\lambda \int_0^R 2\pi r_0 dr_0 E_{pz}^*}{U} \quad (31)$$

$$G_0 = \frac{\omega_b^2 \omega}{8\pi c^2 v_g \beta_0^2 \gamma_0^3} \frac{\lambda \int_0^R 2\pi r_0 dr_0 |E_{pz}|^2}{U} \frac{1}{1 - \frac{\omega_b^2}{\gamma_0^3 (kv_0 - \omega)^2}} \quad (32)$$

$$\eta = \frac{\omega L_d \beta_{10}}{c\beta_0^2} \left[\cos^2(\alpha\mu\theta_1) + \left(\frac{R_s}{Z} + \zeta \right)^2 \sin^2(\alpha\mu\theta_1) \right]^{\frac{1}{2}} \quad (33)$$

It is seen from Eq.(30) that superradiance due to prebunching and stimulated radiation due to self-bunching are contained in radiation emitted by the prebunched electron beam in the radiation cavity, which correspond to the first and second term on the right side of Eq.(30), respectively.

$$\text{Let} \quad \varepsilon = \varepsilon_0 e^{i\varphi z + \Gamma z} \quad (34)$$

Where Γ and φ are the rate of the amplitude and phase growth of the radiation field, respectively. Substituting (34) into (30) and taking into account the condition

$$e^{-\Gamma z} < 1 \quad (35)$$

we can find that

$$\Gamma = \frac{\sqrt{3}}{2} (G_0 J_0(\eta))^{1/3} \left[1 - \left(\frac{\Delta K}{3(G_0 J_0(\eta))^{1/3}} \right)^2 \right] \quad (36)$$

$$\varphi = \frac{1}{2} (G_0 J_0(\eta))^{1/3} \left[1 - 4 \frac{\Delta K}{3(G_0 J_0(\eta))^{1/3}} \right] \quad (37)$$

4. CONCLUSION

Using the field method of particle-wave interaction, we have studied the prebunching of the electron beam in RKA; and derived out a set of self-consistent equations of radiation generated by the prebunched electron beam and the gain formula in the linear regime from the equations.

5. REFERENCE

1. M.Friedman, J.Krall, Y.Y.Lau and V.Serlin, "Externally modulated intense relativistic electron beams", *J.Appl.Phys.*, Vol.64, No.7, pp3353-3379, 1988.
2. Wu Ding, "Superradiance in an optical klystron", *Nucl.Instr. and Meth.*, A318, pp588-591, 1992.
3. Baruch Levush, Thomas M.Antonsen, Alan Bromborsky, Wei-Ran Lou, and Yuval Carmel, "Theory of relativistic backward-wave oscillators with end reflections" , *IEEE Trans.Plasm.Sci.*, Vol.20, No.3, pp263-280, 1992.
4. Min Yu, "On the longitudinal modes of FEL", *High power laser and particle beams*, Vol.3, No.2, pp127-135, 1991.

Study of electromagnetic chock wave in modified MITL

Eugene A.Galstjan, Lev N.Kazanskiy, Alex I.Khomenko

Moscow Radiotechnical Institute of Russian Academy of Sciences
Warshawskoe Shosse 132, Moscow 113519, Russia

A.L.Babkin, V.I.Chelpanov, V.G.Kornilov, V.D.Selemer, V.S.Zhdanov

All-Russian Research Institute of Experimental Physics,
607200 Arzamas-16, Russia

ABSTRACT

Modified magnetically insulated transmission line (MITL) has a dielectric filled break in the cathode part. Propagation of electromagnetic energy along this line is defined by the dielectric flashover and is inherently shock electromagnetic wave - the TEM - wave with a transverse current leakage. As a result of the evolution of this intricate process, high-power ($1 - 10^4$ GW) electron beam/electric pulse may be generated in the time range of 0.1 - 1 nsec.

The purpose of this presentation is to show new experimental results gained from continuing study at the ZET accelerator in MRTI and at essentially different accelerator facility - the linear induction accelerator I-3000 (3-MeV, 20-kA, 20-ns) - in ARRIEP. Newly, in both cases, REB's front shortening from 10 - 15 ns up to a value less than 1 ns has obtained.

Besides experimental investigation, also theoretical studying of the process has been under way, for beginning, in the framework of the "telegraph equations".

Keywords: relativistic electron beam, high-power MW pulse generation, electromagnetic shock wave, flashover

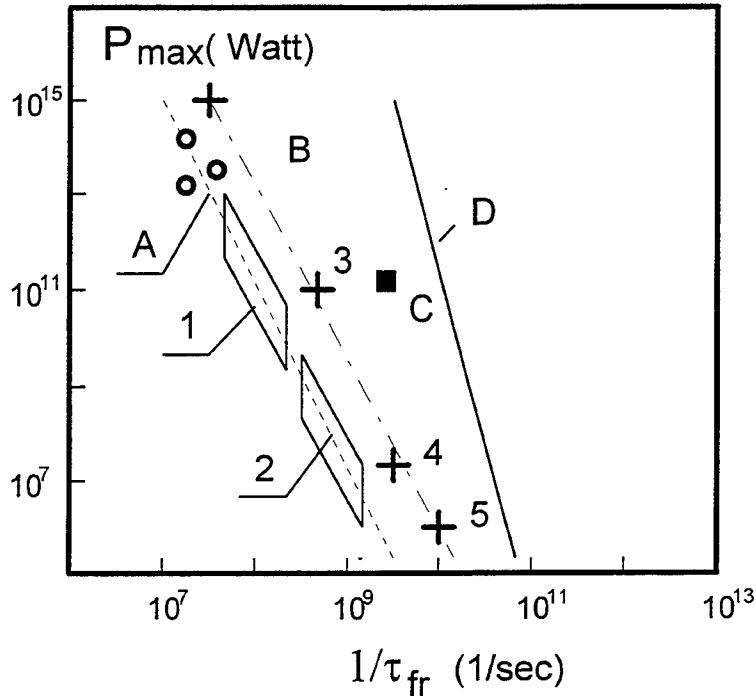
1. INTRODUCTION

The paper is devoted to the area of physics of high power high-current electron beams with usual parameters: energy 0.5 - 10 MeV, current 1 - 1000 kA, power 0.5 GW - 10 TW. For many applications current rise time is "lost" time, in the best case, because of the needed value is the maximum one. Sometimes, too long rise time leads to problems, for instance, in high power MW generation. So, high-power high-current electron beams with very short rise time (the shorter, the better) are needed for many applications. Why physicists have not built so kind of accelerators? The diagram on the next page shows that a rise of power of an accelerator or a generator is accompanied by increase of pulse rise time. There are some physical restrictions. We have proposed a physical method of production of high-power high-current electron beams with very short rise time or pulse duration - generation of a shock electromagnetic wave in a self-magnetically insulated transmission line. Is this method well known in physics? Yes, but the shortest rise time is about 4 ns. We propose modification of this method tested in preliminary experiments.

Modified magnetically insulated transmission line (MITL) has a dielectric filled break in the cathode part. Propagation of electromagnetic energy along this line is defined by the dielectric flashover and is inherently shock electromagnetic wave - the TEM - wave with a transverse current leakage. As a result of the evolution of this intricate process, high-power ($1 - 10^4$ GW) electron beam/electric pulse may be generated in the time range of 0.1 - 1 nsec. At the present time, so kind of power electron beams have the pulse duration in the range of 3 - 30 nsec. The assumption that it is possible to shorten the front of high-power REB up to a sub-nanosecond value was borne out by the preliminary experiments¹⁻³. A 1.5-MeV, 15-kA, 90-ns, 20-GW electron beam with a front duration of 0.5 ns was generated by using MITL with an inner dielectric insert.

The purpose of this presentation is to show new experimental results gained from continuing study at the ZET accelerator in MRTI and at essentially different accelerator facility - the linear induction accelerator I-3000 (3-MeV, 20-kA, 20-ns) - in ARRIEP.

**Correlation between Peak Power and Pulses Rise Time
of High Power Generators and High Current Particle
Beam Accelerators**



A. High Power High-Current Particle Beam Accelerators
(PBFA-II, Hermes-III, Aurora and so on).

1. Typical Accelerators.
2. Special compact short pulse Accelerators.

B. High Power Electric Pulse and EMP Generators.

3. Super Power EMP Generators.
4. Typical EMP Generators.
5. Semiconductor Generators.

C. Preliminary experiments in MRTI.

D. Our Hypothesis (the MITL with dielectric insert)

2. COLLABORATION WORK

Absence of financial support of our work has forced us to be looking for a collaboration with some physicist in Russia and abroad. After publication of our results a few groups of physicists have shown an interest to be in this collaboration in the frame of a project for the International Science and Technology Center. Now our foreign collaborators are as follows: Texas Tech University (Lubbock, USA) - Prof. M. Christiansen; Los Alamos National Laboratory (Los Alamos, USA) - Dr. Michael V. Fazio; California University (Irvine, USA) - Prof. Norman Rostoker; Imperial College of Science (London, GB) - Prof. Jeremy P. Chittenden. The collaboration shall consist of intensive exchange of results of the investigations and other information.

The MRTI Research Group in collaboration with the ARRIEP Research Group proposed to make investigation of a shock electromagnetic wave in a quite short modified magnetically insulated transmission line connected with a diode of a high-power electron accelerator. The program of investigations is as follows:

- High-current relativistic electron beam (20 - 30 kA, 2.5 - 3.0 MeV) with sub-nanosecond front duration has to be generated in this structure as a result of a shock electromagnetic wave excitation.
- Both experimental and theoretical studies of an influence of an insert material, a structure geometry and an external pulse magnetic field are suggested.
- To do this would require a pick up and monitoring system for signals in the range of picoseconds.
- Once the experiments have been provided in the single mode regime at the accelerator "ZED", they are repeated in the repetitive mode at the "Sinus-Luch" with a repetitive rate 10 - 50 Hz.

Besides experimental investigation, also theoretical studying of the process has been under way, for beginning, in the framework of the "telegraph equations". The "telegraph equations" model can give the main parameters - current, voltage, electron leakage value and its distribution. This model takes into account the space inhomogeneity of the line.

As a first step of so kind of collaboration we decided to test our main results at ARRIEP. At the ZET accelerator mainly an influence of location of the dielectric insert with respect to cathode region was investigated.

3. EXPERIMENT

Accelerator facility I-3000⁴ has been used as an electron beam generator to test a possibility of electron beam front sharpening by means of dielectric insert. The accelerator I-3000 was created on the basis of two accelerating modules of the LIA-10 facility and vacuum transmission line ($Z=43$ Ohm) of 2 m length. The line is formed by grounded electrode with the inner diameter of 51 cm and high voltage electrode 24 cm in diameter. It generates a 2.5-MeV, 10...15-kA, 20 -ns electron beam with the pulse duration about of 20 ns for the study of high-power MW generators. One of the methods of voltage increase, generating by a series of inductors, is connecting to their output the transmission line with high wave resistance. The load - electron beam - is switched on at the moment when the second accelerating voltage pulse of 2τ duration has come to the transmission line output of τ electric length. In the case of optimization of the transmission line wave resistance, the output voltage may rise up to the value of $1.85U_0$. It is just this method which is used in the accelerator facility I-3000.

To provide test experiments minimum modification of the facility was made. An additional vacuum chamber ($Z=95$ Ohm) was connected to the transmission line and a polyethylene rod (25 cm) was inserted in cathode (See Fig.1). So, the same modified MITL was studied at widely different accelerator with an additional diagnostic - x ray detector.

Typical oscillograms of the output current and the x-ray detector signal without dielectric insert are shown on Fig.2. In this case the pulse front duration is about of 10 ns.

In the case of the front sharpening experiments the additional vacuum chamber with the wave resistance of 95 Ohm was connected to the main transmission line with the wave resistance of 43 Ohm. At the end of the main transmission line the polyethylene rod (25 cm in length and 3.5 cm in diameter) was inserted. This part of the line has the wave resistance of about 160 Ohm. The dielectric rod was continued by a cathode tube of the same diameter and 35 cm in length, the final cathode - anode gap was equal to 5.5 cm. The thin (0.4 mm) tantalum target was used as a collector and ($e^- - \gamma$) converter. The diode current was measured by the self-integrating Rogowski coil and the X-ray radiation was picked up by pin-diode SPPD3. Schematic of the experimental set up is shown on Fig.1.

Newly, in both cases, REB's front shortening from 10 ns up to a value of 1 - 1.5 ns has obtained (Fig.3). Unlike the current signals, the signals from the X-ray detector have shown only slight oscillations at the top of the pulse. The first part of the current oscillograms demonstrate a response of the Rogowski coil to the start signal. Next slow-rise part of the current signal is due to emission from the triple point (exactly it should say triple ring). On this stage a conductivity along the dielectric rod get origin an slowly rise. In about of 10 ns a surface conductivity rise as an avalanche and the current is doubled in a time period less than 2 ns. Duration of next stage of the current, in the case of dielectric insert, is sufficiently more than without dielectric. It is due to plasma motion.

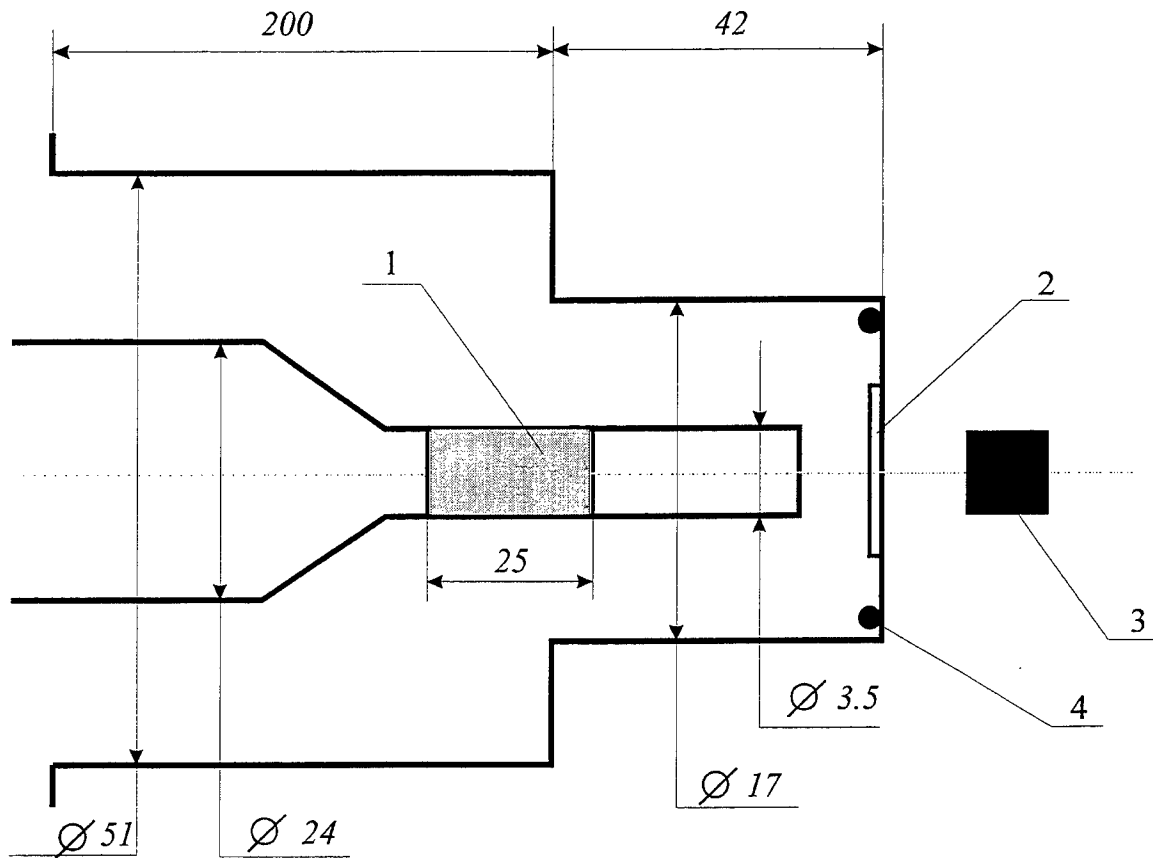
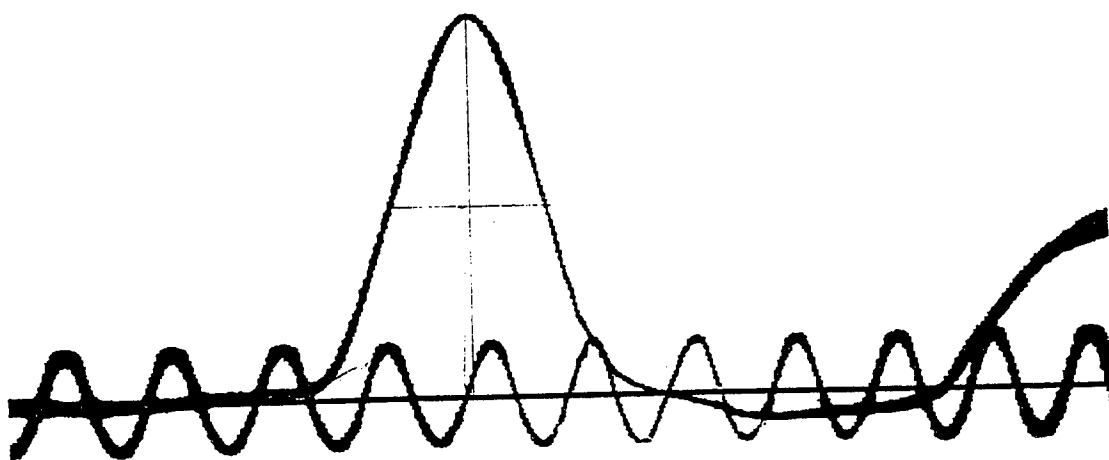


Fig. 1. Schematic of the experimental set up at the accelerator facility I-3000 in ARRIEP.
1 - dielectric insert, 2- the collector, 3 - the x-ray detector, 4 - the self-integrating Rogowski coil.
All dimensions are given in cm.

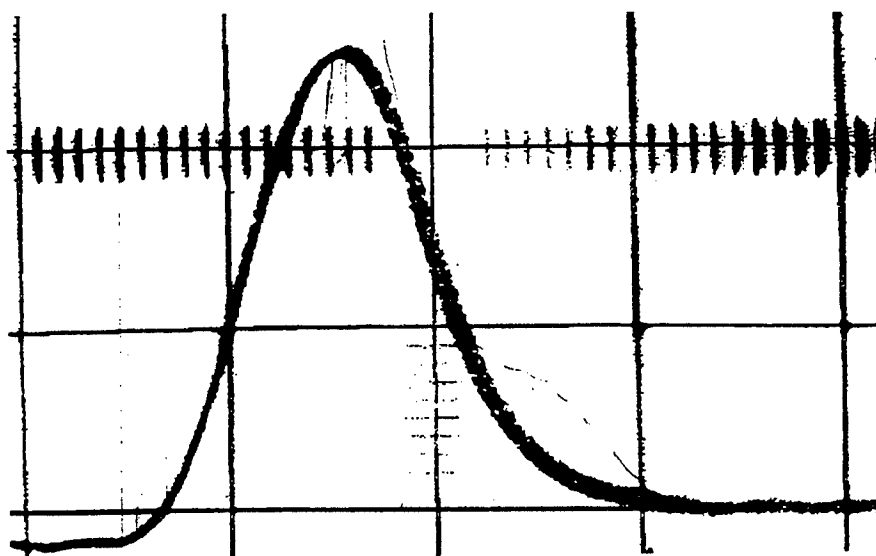
These experiments have demonstrated also the possibility to sharp the front duration of high power relativistic electron beam by means of a long dielectric insert in a transmission line. It should be mentioned that the experiments was carried out practically without special arrangements and there was a lot of disadvantages in the set up. For the transmission line was sufficiently non uniform, the leakage currents may be of the order of the main diode current and a part of non sharpened current from the triple point may be measured by the Rogowski coil.

4. CONCLUSIONS

It has been known that a quite sharp electron beam rise time (up to 4 ns) may be achieved by using of the electromagnetic shock wave formation phenomenon taking place in long enough (~ 10 m) magnetically insulated transmission lines. To reduce the MITL length and to achieve an extremely sharp wave front (less 1 ns) it has been suggested to build into the cathode line a sufficiently long dielectric insert. Efficiency of the shock wave formation has been assumed to grow owing to a dependence of its front velocity on the speed of the flashover front propagation. To test this hypothesis, experimental investigations were performed at MRTI and at ARRIAP accelerator facility, in both cases, REB's front shortening from 10 - 15 ns up to a value of 1 - 1.5 ns has obtained.



1



2

Fig.2. Typical oscillograms of the output current (1) and the X-ray signal (2) without a dielectric insert.

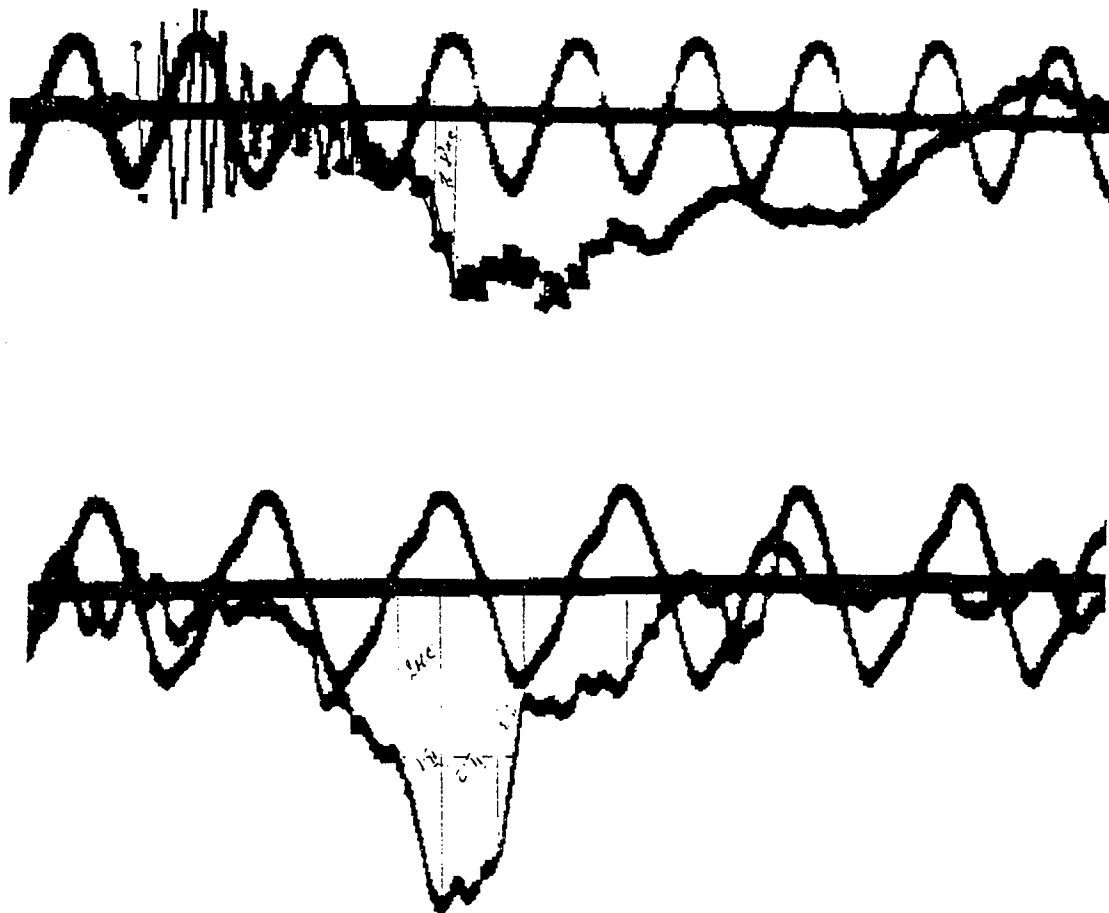


Fig.3. Typical oscillograms of the output current and the X-ray signal with the dielectric insert.

REFERENCES

1. E.A.Galstjan and L.N.Kazanskiy in *Proceedings of Intense MW Pulses III*, Vol. SPIE 2557, p.516G, 1995.
2. E.A.Galstjan and L.N.Kazanskiy in *Proceedings of 10-th Intern. Conf. on High Power Particles Beams*,
3. E.A.Galstjan in *Proceedings of 10-th Intern. Conf. on High Power Particles Beams*,
4. A.I.Pavlovky, V.D.Selemir, V.V.Ivanov et al., *Proceedings of 9-th Intern. Conf. on High Power Particles Beams*, Vol.2, pp. 1655-1660, edited by D.Mosher and G.Cooperstain, NRL, Washington, DC, 1992.

Prospect of superlight source application for charged particle acceleration

Yuri Lazarev and Peter Petrov

Russian Federal Nuclear Center - All-Russian Institute of Technical Physics, Department of Theoretical Physics and Applied Mathematics, 456770 Snezhinsk, Chelyabinsk Region, Russia

ABSTRACT

A possibility to use the microwave superlight source for an electromagnetic wave focusing, a conceptual sketch and expected parameters of compact, charge particle accelerator with accelerating gradient of order of 10 GeV per meter and more on the basis of such device are considered. Investigation results of electromagnetic field space-time distribution near the focus and the process of charged particle acceleration are presented.

Keywords: microwaves, superlight source, charged particle accelerator.

1. INTRODUCTION. QUALITATIVE CONSIDERATION. SIMPLE ESTIMATIONS

As is known, the simplest superlight source is a current pulse propagating along some plane conducting surface with superlight velocity. Such current pulse occurs, in particular, when obliquely incident plane flux of ionizing radiation illuminates a plane metallic surface^{1,2}. The arrangement of the emission current over the surface constitutes an antenna with phased excitation such that the radiated wave is emitted in the direction corresponding to specular reflection of the ionizing radiation. Consequently, if the illuminated surface is the focusing mirror for the incident radiation, then electromagnetic wave energy may be focused. Further, it is suggested that the illuminated surface has the form of paraboloid.

Unfortunately, it turns out that, the superlight source under consideration generates the high power microwaves only if the power of the ionizing radiation source is also very high. Estimations show that in order for an electric field near the focus of order of atomic to be obtained a gamma radiation source, for example, should have the power of about 10^{15} W and the longer the ionizing radiation wave length the higher the power of the ionizing radiation source should be. Such high power ionizing radiation source do not exist or are not widely available. However, this difficulty may be resolved. It will suffice to separate the process of electron emission from energy pumping.

Let us imagine, that a plane flux of rather low-frequency radiation, for example - light, irradiates a paraboloid surface of photoemission material and sufficiently strong electric field is created close to paraboloid surface.

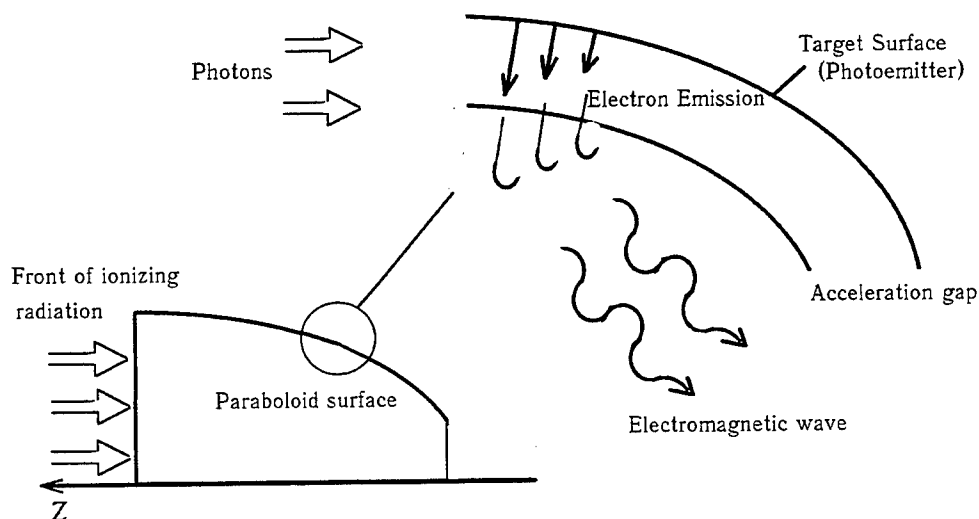


Figure. 1. Schematic model of super strong electric field generation.

Emitted electrons are accelerated in this field and their final energy may be about 1 Mev. Outside the accelerating gap as well as in the previous case a phased-radiating dipole layer is formed. But now the required power of ionizing radiation source is sufficiently lower - of order of $10^{10} \sim 10^{11}$ W. Light sources of such power exist, for example - lasers, and are not unique.

Because electromagnetic energy flux nearby paraboloid surface and nearby focus should coincide:

$$E_0^2 r_0^2 \sim E^2 \lambda^2 \quad (1)$$

then the following estimation for field amplitude in the focus is true

$$E \sim E_0 \frac{r_0}{\lambda} \quad (2)$$

where E is the electric field in the paraboloid focus, E_0 is the electric field of the emitted wave nearby paraboloid surface, r_0 is paraboloid radius in the focal plane, $2\pi\lambda$ is the dominant wavelength of the electromagnetic wave.

As is known^{2,3}:

$$E_0 \sim \frac{4\pi}{c} \dot{D} \quad (3)$$

where \dot{D} is the first time derivative of the dipole moment surface density D , c - velocity of light.

$$\dot{D} \sim \frac{c}{\lambda} D, \quad D = \frac{\varepsilon_f}{2\pi e}, \quad (4)$$

e - the charge of electron.

It follows that

$$E_0 \sim \frac{\varepsilon_f}{e\lambda}, \quad (5)$$

and, consequently,

$$E \sim \frac{\varepsilon_f}{e\lambda} \frac{r_0}{\lambda}. \quad (6)$$

If, it is assumed, that a charged particle with charge e and mass M (electron or proton) is accelerated in this electric field, then at the end of the acceleration it would have the impulse P :

$$P \sim eE \frac{\lambda}{c} \sim \frac{\varepsilon_f}{c} \frac{r_0}{\lambda} \quad (7)$$

and energy ε_a :

$$\varepsilon_a \sim \begin{cases} \varepsilon_f \frac{r_0}{\lambda}, & \frac{P}{Mc} > 1, \\ \frac{\varepsilon_f^2}{Mc^2} \left(\frac{r_0}{\lambda} \right)^2, & \frac{P}{Mc} < 1. \end{cases} \quad (8)$$

The values of $\varepsilon_f \sim 1\text{Mev}$, $\lambda \approx 0.1 \div 1\text{cm}$, $\frac{r_0}{\lambda} \sim 10^2 \div 10^3$ seem really achievable and, consequently, electron and proton energy after acceleration may be of order of 1 GeV under relatively small size of accelerator - about several meters. The accelerating length is of order of several λ , so the accelerating gradient would be of order of 10 GeV per meter or greater.

To check the obtained results the rigorous consideration of the problem was performed on the base of the analytical approach and computer simulation. The results are presented in the next sections.

2. ANALYTICAL RESULTS

2.1. Electron acceleration.

One may obtain an analytical expression for an electric field nearby paraboloid focus:

$$E = -\frac{1}{c} \frac{\partial \bar{A}}{\partial t} - \nabla \varphi, \quad (9)$$

using retarded potentials:

$$\varphi = \int d\vec{r} \frac{\rho\left(t - \frac{|R - \vec{r}|}{c}\right)}{|R - \vec{r}|}, \quad (10)$$

$$\bar{A} = \int d\vec{r} \frac{\vec{j}\left(t - \frac{|R - \vec{r}|}{c}\right)}{|R - \vec{r}|}$$

and Lorentz condition

$$\text{div}(\bar{A}) + \frac{1}{c} \frac{\partial \varphi}{\partial t} = 0 \quad (11)$$

Because nearby focus $R \ll r$, then assuming emission current to be directed normally to paraboloid surface one may obtain the following relation for field component along paraboloid axis:

$$E_z = -\frac{1}{c^2} \int \frac{dv}{r} \cdot \sin \alpha \cdot \cos \frac{\alpha}{2} \cdot \frac{\partial j_{\perp}}{\partial t} \quad (12)$$

where α - the angle \vec{r} vector makes with the z-axis.

Using the dipole approximation, applicable in this case:

$$E_z = \frac{r_0 D_0}{\lambda^2} \int_0^{2\pi} d\varphi \int_{\omega_0}^{\omega_k} d\omega \frac{1+\omega}{1-\omega} f\left(\tau + \frac{Z}{\lambda} \omega + \frac{Y}{\lambda} \sqrt{1-\omega^2} \cos \varphi\right), \quad \omega = \frac{z}{z+r_0} \quad (13)$$

where $\omega_0 = \frac{z_0}{z_0 + r_0}$, $\omega_k = \frac{z_k}{z_k + r_0}$, $\lambda = c \cdot T_0$

z is the component of \vec{r} vector,

z_0, z_k - coordinates of the beginning and the end of paraboloid,

Z, Y - cylindrical components of \vec{R} vector,

D_0 - the amplitude of the dipole moment per unit area,

$\tau = \frac{t}{T_0}$, T_0 - the characteristic time of dipole moment variation,

r_0 - paraboloid radius in the focal plane,

$f(\tau) = \frac{dF}{d\tau}$ - dimensionless function of the order of 1, approximately³ :

$$f(\tau) = \begin{cases} 0, & \tau < 0 \\ 2.17 \cdot \frac{d}{d\tau} (\tau^2 \cdot \exp(-\tau)), & \tau \geq 0 \end{cases} \quad (14)$$

In (13) it is taken into account that a current density is a function of $t + \frac{r}{c}$ and r :

$$\vec{j} = \vec{j}(t + \frac{r}{c}, r)$$

Along the paraboloid axis:

$$E_z = \frac{2\pi r_0 D_0}{\lambda^2} \int_{\omega_0}^{\omega_1} d\omega \frac{1+\omega}{1-\omega} f\left(\tau + \frac{Z}{\lambda} \omega\right) \quad (15)$$

The introduced variable ω varies from -1 to +1 moving over the paraboloid surface (see table 1):

Table 1.

$\frac{z}{r_0}$	1	2	3	4	5	6	9
ω	0.5	0.67	0.75	0.8	0.83	0.87	0.9

It can be seen from the relation (1) that the fixed value of the field phase propagates at the velocity $\frac{c}{\langle \omega \rangle} > c$, because

$$\frac{\omega}{\lambda} \cdot \frac{dZ}{dt} + \frac{d\tau}{dt} = 0 \Rightarrow \frac{dZ}{dt} = \frac{c}{\omega} \quad (16)$$

It is clear that the closer is the particle velocity to the phase velocity the more effective is the acceleration process. Therefore the set of paraboloids with $|\omega| \approx 1$ are of the most interest. Because of integrand factor $\frac{1+\omega}{1-\omega}$ in the relation (15) the utilizing of paraboloids with $\omega \sim 1$ is more preferred. In physical sense this statement is rather evident- the amplitude of dipole radiation field peaks in the plane normal to dipole axis and a dipole doesn't radiate along its axis. An angle which the axis of the dipole situated in this point makes with the direction to the focus tends to 0 under $\omega \rightarrow -1$ and to $\frac{\pi}{2}$ under $\omega \rightarrow 1$.

In this connection let us next consider only paraboloids with $\omega_0, \omega_k \approx 1$. Then for the points nearby focus with

$$\frac{Z}{\lambda}(\omega_k - \omega_0) < 1 \quad (17)$$

the further simplification of the relation for the electric field along paraboloid axis is possible:

$$E_z \cong \frac{2\pi r_0 D_0}{\lambda^2} f\left(\tau + \frac{Z}{\lambda} \bar{\omega}\right) \cdot \left(\frac{1+\bar{\omega}}{1-\bar{\omega}}\right) \cdot (\omega_k - \omega_0). \quad (18)$$

For ω_k not too close to 1 ($\omega_k < 0.95$)

$$\left(\frac{1+\bar{\omega}}{1-\bar{\omega}}\right) \approx \frac{1+\bar{\omega}}{1-\bar{\omega}}, \bar{\omega} = \frac{\omega_k + \omega_0}{2}. \quad (19)$$

Actually ω_k , which are in close proximity to 1, are of no practical interest. The reason is that the power which a light radiation source should have is inversely proportional to the sine of flashout angle. Under $\omega \rightarrow 1$ the sine reduces and the power increases as $\frac{1}{\sqrt{1-\omega}}$. Besides a significant difference between ω_k and ω_0 (lengthy paraboloid) leads to irradiation nonuniformity and wave emanation point coordinate dependence of λ (characteristic wave length).

Let us consider the process of electron acceleration. Letting an electron be a relativistic one, then its velocity is close to the light velocity $v \approx c$, and we can represent the trajectory equation as follows:

$$z = z_i + c(t - t_i) = z_i + \lambda(\tau - \tau_i). \quad (20)$$

Application of this relation allows us to obtain an equation which determines the variation of the accelerated electron impulse:

$$\frac{dP_z}{dt} = \frac{2\pi e r_0 D_0}{\lambda^2} \cdot (\omega_k - \omega_0) \cdot \left(\frac{1+\bar{\omega}}{1-\bar{\omega}}\right) \cdot f\left((1-\bar{\omega}) \cdot (\tau - \tau_i)\right), \quad (21)$$

It follows that,

$$P_z(\tau) = P_z(\tau_i) + \frac{2\pi e r_0 D_0}{c\lambda} \cdot \frac{(1+\bar{\omega})}{(1-\bar{\omega})^2} \cdot (\omega_k - \omega_0) \cdot F\left((1-\bar{\omega}) \cdot (\tau - \tau_i)\right), \quad (22)$$

where $F(\tau)$ was defined by expression (14)

The relation (22) has been obtained under the assumption

$$\frac{Z}{\lambda} \cdot (\omega_k - \omega_0) < 1 \quad (23)$$

consequently, within the limits of this approximation the following inequality is to be

$$(\tau - \tau_i) \cdot (\omega_k - \omega_0) < 1 \quad (24)$$

This inequality determines the time interval throughout which one may examine acceleration process in approximation formulated above.

The function $F(\tau)$ has a wide maximum at $\tau=2$ and therefore accelerated electron will be increasing its power up to the instant of time - τ_{\max} :

$$\tau_{\max} - \tau_i \approx \frac{2}{1-\bar{\omega}} \quad (25)$$

In this case according to (24) the following inequality is to be correct:

$$\frac{2}{1-\bar{\omega}} \cdot (\omega_k - \omega_0) < 1 \quad (26)$$

If this is not the case, as a τ_{\max} we should use the time defined by (24).

The set of parabolooids, defined by (25), is nonempty one which is confirmed by the figure 2 stated below

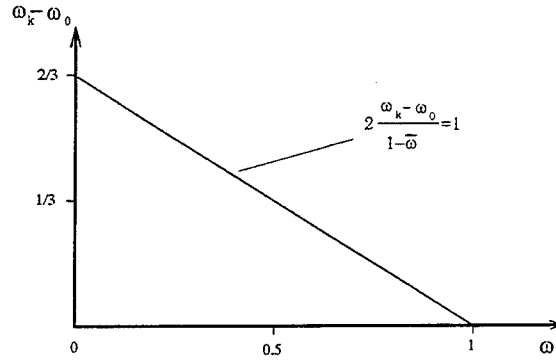


Figure 2.

Thus we may consider that $F = F_{\max} = 1$ and therefore in the process of relativistic electron acceleration its impulse may reach the value of P_{\max} .

$$P_{\max} = P_i + \frac{2\pi e r_0 D_0}{c\hbar} \cdot \frac{1+\bar{\omega}}{(1-\bar{\omega})^2} \cdot (\omega_k - \omega_0) . \quad (27)$$

Because

$$\frac{1+\bar{\omega}}{(1-\bar{\omega})^2} (\omega_k - \omega_0) \approx 2 \cdot \frac{\Lambda}{r_0}, \quad \Lambda = z_k - z_0 \quad (28)$$

and

$$D_0 = \frac{\varepsilon_f}{2\pi e}, \quad (29)$$

then

$$\frac{P_{\max}}{m_e c} \approx \frac{P_i}{m_e c} + 2 \frac{\Lambda}{\lambda} \cdot \frac{\varepsilon_f}{m_e c^2}. \quad (30)$$

Under conditions

$$\frac{\varepsilon_f}{m_e c^2} = \gamma_f - 1 \sim 1, \quad \frac{P_i}{m_e c} \sim 1, \quad \frac{\Lambda}{\lambda} \gg 1, \quad (31)$$

we have

$$\frac{P_{\max}}{m_e c} \approx 2 \frac{\Lambda}{\lambda} \cdot \frac{\varepsilon_f}{m_e c^2}, \quad (32)$$

that is

$$(\gamma - 1)_{\max} \approx 2 \frac{\Lambda}{\lambda} \cdot (\gamma_f - 1). \quad (33)$$

It follows that accelerated electron energy will be of the order of 1 GeV when $\frac{\Lambda}{\lambda} \sim 10^3$.

Yet we considered a relativistic electron acceleration. If an electron is nonrelativistic one, but

$$\frac{\Lambda}{\lambda} \cdot (1 - \bar{\omega}) \gg 1, \quad (34)$$

then all the obtained results also hold correct in the value order in this case.

When an accelerated particle moves out of phase with accelerating field (it is just the case which takes place at nonrelativistic velocities $v \ll c$) the acceleration time decreases in proportion to $1 - \bar{\omega}$. But if the equation (34) is correct, then an electron becomes relativistic one very quickly and the process takes place as in the case discussed above.

2.2. Proton Acceleration.

An electron and a proton have opposite charges. Because of this proton velocity, phase velocity of accelerating field and accelerating force directions will coincide under $\tau > 2$, when the field changes its sign. A proton is approximately 1840 times more massive than an electron, then it would appear reasonable that the proton would remain nonrelativistic one during acceleration process. We have no prior knowledge of proton position varying in time, but this is not needed for estimations. It is sufficient to solve formally the equation of motion.

$$z = z_i + \int_{\tau_i}^{\tau} d\tau' \cdot \frac{v}{c} \cdot \lambda = z_i + \bar{\lambda} \cdot \frac{\bar{v}(\tau)}{c} \cdot (\tau - \tau_i), \quad \frac{\bar{v}(\tau)}{c} \ll 1 \quad (35)$$

Substituting a proton moving coordinate in the expression for field phase we can obtain

$$\tau + \frac{z}{\bar{\lambda}} \bar{\omega} = \tau + \frac{z_i}{\bar{\lambda}} \bar{\omega} + \bar{\omega} \frac{\bar{v}}{c} (\tau - \tau_i) = \left(1 - \frac{\bar{v}}{c} \bar{\omega}\right) (\tau - \tau_i) \approx \tau - \tau_i, \quad \left(\frac{z_i}{\bar{\lambda}} = -\tau_i\right). \quad (36)$$

Now it is easy to obtain the solution of proton impulse equation

$$P \approx P_i + \frac{2\pi e r_0 D_0}{c\lambda} \cdot \left(2 \ln \left(\frac{1-\omega_0}{1-\omega_k} \right) - \omega_k + \omega_0 \right) \cdot F(\tau - \tau_i). \quad (37)$$

It follows that

$$\frac{P_{\max}}{Mc} \sim \frac{r_0}{\lambda} \cdot \frac{m_e}{M} \cdot (\gamma_f - 1), \quad \left(\frac{P_i}{Mc} \ll 1 \right), \quad (38)$$

and under $\frac{r_0}{\lambda} \sim 10^3$, $\gamma_f - 1 \approx 1$, it would be $\frac{P_{\max}}{Mc} \approx 0.5$, it means that proton can be accelerated up to the energy of the order of 100 MeV.

3. EXPECTED CHARACTERISTICS AND ACCELERATOR CONFIGURATION.

3.1. Electron accelerator

The obtained results allow to make an impression on accelerator configuration and its component parameters which are to be possessed.

In fact the condition $\frac{\Lambda}{\lambda} = 10^{-3}$ defines system sizes. Evidently we may consider $\lambda \approx 0.15$ cm as an actually attained value of λ .

In this case under $\gamma_f \approx 3$ an accelerating gap L is to be about 0.1 cm. It follows that paraboloid length is to be 0.75 m ($\Lambda = 0.75$ m). If we assume that $\omega_k = 0.83$ and $\omega_0 = 0.75$ then paraboloid radius in focal plane is to be 0.375 m ($r_0 = 0.375$ m), maximum radius of paraboloid - 1.125m, paraboloid surface area $S \approx 5.6$ m².

The accelerating length is approximately $\frac{2}{1-\omega} \lambda = 1.5$ cm. So the accelerating gradient is ≈ 70 GeV/m.

It is not difficult to estimate:

-quantity of energy which is accumulated in accelerating gap nearby paraboloid surface

$$U \sim 116 \frac{(\gamma_f - 1)^2}{L} \cdot S \text{ (J)} \approx 26 \text{ (kJ)}$$

-power of a laser providing electron emission from paraboloid surface

$$J \sim 4 \cdot 10^7 \frac{(\gamma_f - 1)^{\frac{3}{2}}}{YL^2} S \text{ (W)} \approx 310^{11} \text{ (W)}, \quad (Y \approx 0.2).$$

Laser energy ≤ 3 (J).

An accelerator is represented schematically in Fig.3.

It is obvious that an accelerator with acceleration energy less than 1 GeV would be smaller in sizes.

Let be $r_0 = 3.75$ cm., $\omega_k = 0.83$, $\omega_0 = 0.75$ then the total length from the focus to the end of paraboloid is 18.75 cm and $\Lambda = 7.5$ cm. If we assume as in the previous case that $\lambda = 0.15$ cm then it is evident that all the parameters of the accelerator under consideration should be 100 times less in comparison with the previous case: $S \approx 0.056$ m², $J \sim 310^9$ W, $U \sim 260$ J. As for the energy ε_a , derived by an electron owing to acceleration then it is only 10 times less: $\varepsilon_a \sim 100$ MeV.

The total accelerator length including laser with optical system will be approximately 1 m.

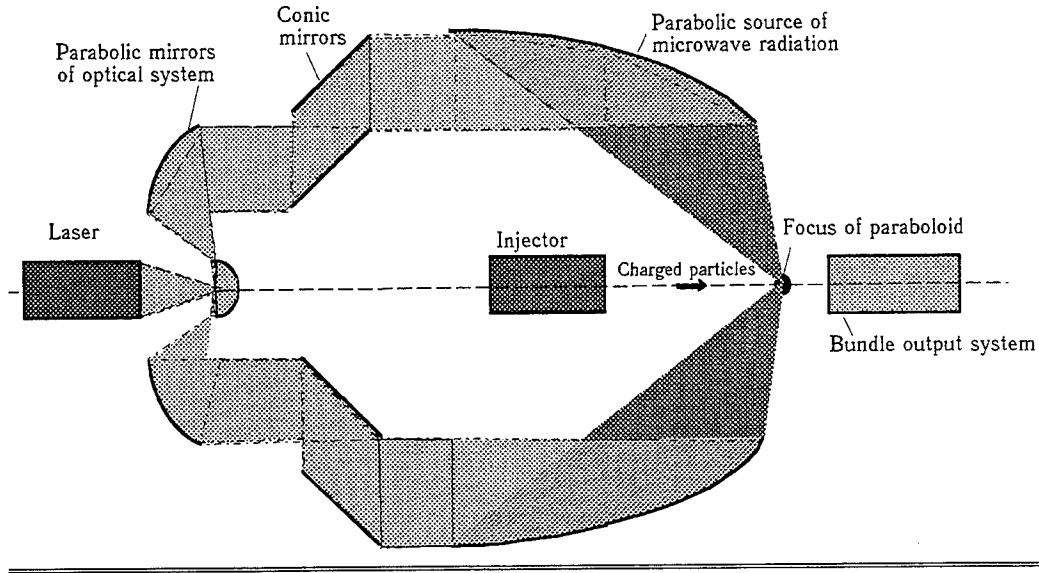


Figure 3. Schematic of accelerator model.

3.2. Proton accelerator

The proton energy ε_a will be about 1 GeV under $P_{\max} \approx 18 Mc$. As in the previous case let be $\gamma_f = 3$, $\lambda = 0.15 cm$.

Assuming that $\omega_k = 0.67$, $\omega_0 = 0$ and using (37) one can obtain:

$$\frac{P_{\max}}{Mc} \approx 1.66 \cdot 10^{-3} \frac{r_0}{\lambda}$$

and consequently

$$r_0 \approx 1.08 \cdot 10^3 \lambda \approx 162 m$$

The length of paraboloid is to be 3.25m, maximum radius - $\approx 3.63m$.

It is pertinent to note that in this case the accelerated energy $\varepsilon_a = 100 MeV$ may be reached under $r_0 = 0.43m$, paraboloid length - 0.85m, maximum radius $\approx 0.95m$.

4. NUMERICAL RESULTS.

Two-dimensional electrodynamic FDTD code EMC2D was used for numerical investigations of an electric field distribution nearby paraboloid focus.

For simulation of superlight current pulse excited by radiation on the interior surface of paraboloid

$$z_{\text{paraboloid}} = \frac{\rho^2}{2r_0}, \quad 0.85 < \frac{z}{r_0} < 1.15 \quad \text{with } r_0 = 100 \text{ cm an electron current density directed normal to the surface was defined in the}$$

layer $\Delta z = 0.15 \text{ cm}$ thick:

$$\vec{j}(t, z, \rho) = J\left(t - \frac{z_{\max}}{c} + \frac{z}{c}\right) \cdot \vec{n}, \quad \vec{n} = \left(1 + \frac{\rho^2}{r_0^2}\right)^{-1/2} \left\{-\frac{\rho}{r_0}; 1\right\}$$

where $J(t) = 2.17 \cdot (t / T_0)^2 e^{-t/T_0} \eta(t / T_0) (\eta(z_{\text{paraboloid}} + \Delta z) - \eta(z_{\text{paraboloid}}))$, η - step function,

$T_0 = 5 \cdot 10^{-11}$ s, $\lambda = cT_0 = 1.5$ cm,

$T_{\max} = t(\max_{t, z=z_f}(E_z)) = 5.55$ nsec.

Figures 4-8 show the design geometry and the simulation results of electromagnetic wave focusing.

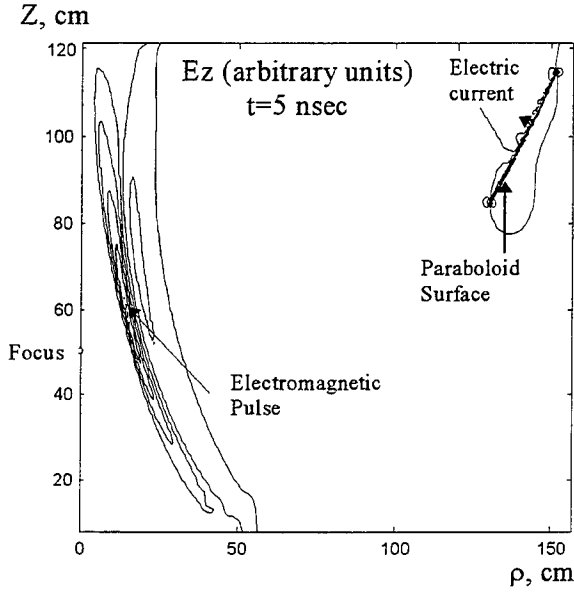


Figure 4. Electric field E_z level lines.

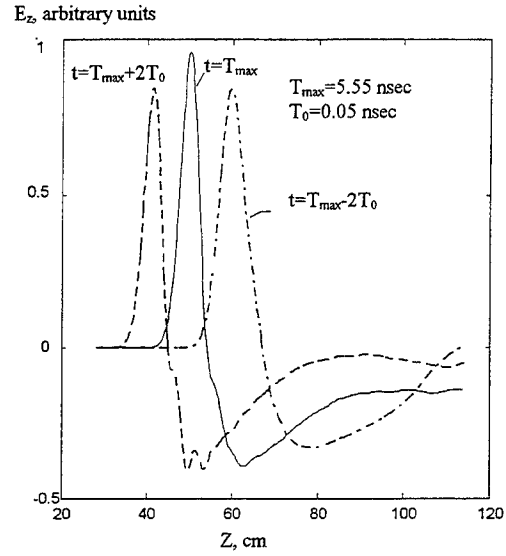


Figure 5. Electric field E_z in $\rho=0$. vs. z at various times

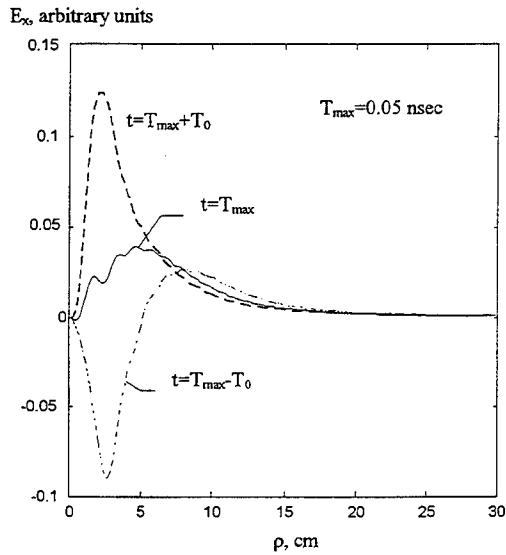


Figure 6. Electric field E_ρ in $z=z_f$. vs. ρ at various times.

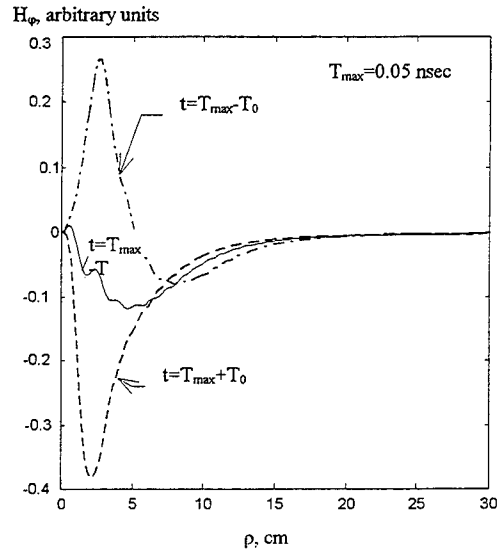


Figure 7. Magnetic field H_ϕ in $z=z_f$. vs. ρ at various times.

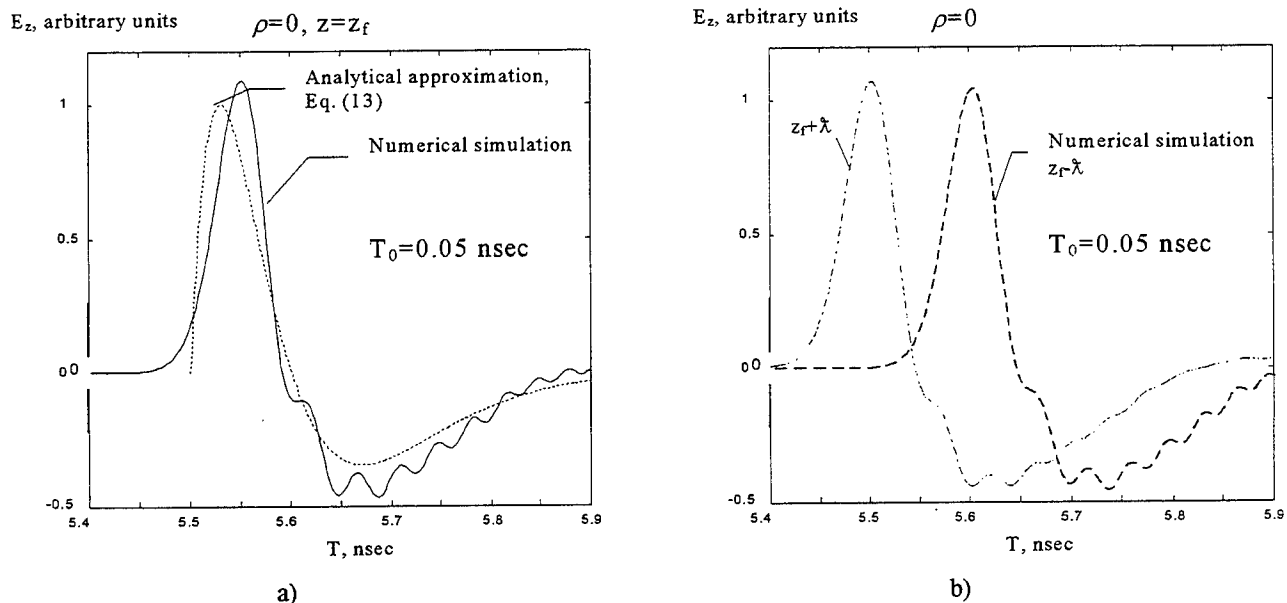


Figure 5. Time history of electric field E_z near the focus.

As a whole numerical simulation data confirmed the possibility of superstrong electric field generation in focal region of paraboloid.

5. CONCLUSIONS.

Investigation results presented in this report show that superlight sources utilizing for charged particle acceleration is theoretically possible. Accelerators on the basis of superlight sources of microwave radiation would provide charged particle acceleration up to energy of the order of hundreds-thousands MeV and be of compact sizes in comparison with linear accelerators. Because characteristics of devices providing such accelerator operation are not unique, then it is quite possible that such accelerator production will present no problems in practice if superlight source of microwave radiation are produced.

6. ACKNOWLEDGMENTS

This research was supported by the International Scientific and Technology Center, Grant No. 299-95.

7. REFERENCES

1. V. L. Ginzburg. Theoretical Physics and Astrophysics [in Russian], (Nauka, Moscow), 1981.
2. N. J. Carron, C.L. Longmire. Electromagnetic Pulse Produced by Obliquely Incident X-rays, IEEE Trans. on Nucl. Sci., Vol. NS-23, No.6, pp.1897-1902, 1976.
3. N. J. Carron, C.L. Longmire. Scaling Behavior of The Time-Dependent SGEMP Boundary Layer, IEEE Trans. on Nucl. Sci., NS-25, No.6, pp.1329-1335, 1978.

Harmonic generation in the reflection of microwave radiation from semiconductor surface

A. V. Shepelev, M. Y. Glotova, A. V. Shvartsburg

Central Design Bureau for Unique Instrumentation, Russian Academy of Sciences
Butlerov Street 15, Moscow, 117342, Russia

ABSTRACT

Nonlinear reflection of radiation in the range of 0.3-5mm from semiconductor surfaces is analyzed. When external field (including wave field) influences the semiconductor charge carriers, the carriers temperature increases in comparison with the lattice one. As a result, the time interval of the pulse relaxation and, consequently, the dielectric constant varies. Thus, the heating of the carriers by the microwave radiation field leads to the dependence of reflection coefficient on the field, i.e., to the generation of harmonics.

Analytical and numerical estimations of the harmonic generation efficiency are carried out. An interesting effect of the generation efficiency decrease under the wave amplitude increase is discovered. This is explained by the fact that the wave frequency is close to the resonant frequency of the plasma free carriers.

Keywords: microwave, nonlinear interaction, semiconductor surface, harmonic generation.

The interaction between the microwave radiation, reflected from the semiconductor surface, and the gas of free carriers results in emergence of radiation harmonics. The external electric field of the incident wave E causes the variation of the carriers distribution, so their mean energy, i.e., the carriers temperature, changes: $T_e = T_e(E)$. This leads to the change of the relaxation time τ ($\tau = \tau(T_e)$), and, as a consequence, to the variation of the dielectric constant $\varepsilon = \varepsilon(\tau)$. Thus, the dielectric constant depends on the amplitude of the electric field of the incident wave and can be developed as a series in powers of the field:

$$\varepsilon(E) = \varepsilon(0) + \chi_1 E + \chi_2 E^2 + \chi_3 E^3 + \dots \quad (1)$$

$\chi_1, \chi_2, \chi_3, \dots$ are the nonlinear susceptibilities, provided by this dependence of ε on the external field.

The carriers temperature may be introduced in case of quasiequilibrium carriers distribution only. That is why the period of the wave must be more than the relaxation time: $T \gg \tau$ or $\omega\tau \ll 2\pi$. (If this condition is not valid, another method of calculation of the harmonics generation has to be applied.)

The dielectric constant of a semiconductor in the microwave range may be written as¹:

$$\begin{aligned} \varepsilon &= \varepsilon_1 + i\varepsilon_2, \\ \varepsilon_1 &= \varepsilon_0 \left(1 - \frac{\omega_p^2}{\omega^2 + \tau^{-2}}\right), \\ \varepsilon_2 &= \varepsilon_0 \omega^{-1} \tau^{-1} \left(\frac{\omega_p^2}{\omega^2 + \tau^{-2}}\right), \end{aligned} \quad (2)$$

where $\omega_p = \left(\frac{4\pi N e^2}{m^* \varepsilon_0}\right)$ is the plasma frequency, N - carriers concentration, e - electron charge, m^* - carriers mass, ε_0 - dielectric constant of the lattice, accounting all the process besides of the polarization of the gas of free carriers.

The ratio of carriers temperature to the lattice temperature is equal to²

$$T_e / T = \frac{1}{2} \left\{ 1 + \left[1 + \frac{3\pi}{8} \left(\frac{\mu_0 E}{c_s} \right)^2 \right]^{1/2} \right\}, \quad (3)$$

where μ_0 is the initial mobility, c_s - the sound velocity.

The main contribution to the process of the relaxation of the carriers pulse makes their interaction with the ionized lattice impurities. The well-known Conwell-Weisskopf relation determines the relation between the relaxation time and the carriers temperature:

$$\tau \approx \tau_0 \left(\frac{T_e}{T} \right)^{3/2}. \quad (4)$$

The substitution of (2),(3),(4) into (1) allows to calculate the nonlinear susceptibilities χ_1, χ_2, \dots . But the direct application of the Fresnel's reflection coefficient is more convenient in the calculation of the efficiency of the reflected harmonics generation.

In case of the normal incidence this coefficient is equal to

$$R = \frac{(n-1)^2 + \kappa^2}{(n+1)^2 + \kappa^2}, \quad (5)$$

n and κ being defined from the expression $\varepsilon = \varepsilon_1 + i\varepsilon_2 = (n + i\kappa)^2$, that leads to

$$n = \left[\frac{1}{2} (\sqrt{\varepsilon_1^2 + \varepsilon_2^2} + \varepsilon_1) \right]^{1/2};$$

$$\kappa = \left[\frac{1}{2} (\sqrt{\varepsilon_1^2 + \varepsilon_2^2} - \varepsilon_1) \right]^{1/2}. \quad (6)$$

If $\omega_p \approx \omega$, the expression (6) and the law of dispersion (2) result in the relation

$$n(E) = \left[\frac{\varepsilon_0}{2} \frac{\sqrt{\omega^2 \tau^2(E) + 1} + 1}{\omega^2 \tau^2(E) + 1} \right]^{1/2};$$

$$\kappa(E) = \left[\frac{\varepsilon_0}{2} \frac{\sqrt{\omega^2 \tau^2(E) + 1} - 1}{\omega^2 \tau^2(E) + 1} \right]^{1/2}. \quad (7)$$

For the weak external field the relations (3) and (4) allow to find the dependence of the relaxation time on the field:

$$\tau(E) = \tau_0 \left[1 + \frac{4\pi}{64} \left(\frac{\mu_0 E}{c_s} \right)^2 \right] \quad (8)$$

By substituting (7) and (8) into the expression for the Fresnel's reflection (5), one can define the dependence of the reflection coefficient R from the incident wave field. The field amplitude of the reflected wave E_R can be developed in powers of the external field E :

$$E_R = E \cdot R(E) = R_1 E + R_3 E^3, \quad (9)$$

where

$$R_1 = \frac{\sqrt{\varepsilon_0} - 1}{\sqrt{\varepsilon_0} + 1} \left(1 + \frac{\sqrt{\varepsilon_0} (3 + \varepsilon_0)}{4(\varepsilon_0 - 1)^2} \omega^2 \tau_0^2 \right),$$

$$R_3 = \frac{\sqrt{\varepsilon_0} - 1}{\sqrt{\varepsilon_0} + 1} \frac{\sqrt{\varepsilon_0} (3 + \varepsilon_0)}{4(\varepsilon_0 - 1)^2} \omega^2 \tau_0^2 \frac{9\pi}{32} \left(\frac{\mu_0}{c_s} \right)^2, \quad (10)$$

that leads to $R_3 \approx \tau_0^2 \mu_0^2 \approx \tau_0^4$. Since usually the relaxation time increases when the carrier concentration decreases, the value of R_3 grows sufficiently for hyperpure semiconductors. If the external field is monochromatic, $E = E_0 \sin \omega t$, the reflected field is equal to

$$E_R = \{E_0 R_1 + \frac{3}{4} R_3\} \sin \omega t + \left\{ \frac{1}{4} E_0^3 R_3 \right\} \sin 3\omega t. \quad (11)$$

The coefficient R_3 is the efficiency of the third harmonic generation. The amplitude of the third harmonic is proportional to the third degree of the incident amplitude wave. For the typical semiconductor $\varepsilon_0 \approx 10$, $\omega_p = 10^{12} \text{ Gz}$, $\tau_0 = 10^{-13} \text{ s}$, $\mu_0 = 300 \text{ cm}^2 \text{ V}^{-1} \text{ s}^{-1}$, $c_s = 3000 \text{ m} \cdot \text{s}^{-1}$, so when the amplitude of the incident wave is equal to 10^2 V/cm , the amplitude of the third harmonic is of order of 10^{-5} of the first harmonic amplitude.

The analytical expressions (10), (11) are received for the case of the normal incidence. In case of the arbitrary angle of incidence the tedious calculations, based on Fresnel's formulas, make it inadvisable to deduce analytically the relations for the nonlinear reflection. The numerical calculations were carried out to determine the third and the fifth harmonic generation efficiency. Fig.1 reprints the dependence of the energetic reflection coefficient R^2 from the parameter $(\omega\tau)^{-1}$ for the incidence angle 75° . (Remember, that the relaxation time τ depends on the external field according to (8))

The general formula of the Furrier analysis was used for the calculation of Furrier harmonics amplitudes:

$$E_k = \frac{\omega}{\pi} \int_{-\pi/\omega}^{\pi/\omega} ER(E) \sin k\omega t dt,$$

where $E = E_0 \sin \omega t$ - the field of the incident wave, $k=1,2,\dots$ - the harmonic number. The dependence $R(E)$ is determined by the curve in Fig.1.

The relative intensities of harmonics $(E_k / E_0)^2$ as functions of the incident wave amplitude are presented in Figs.2,3. The relative intensity of the first harmonic (Fig.2) has a minimum at the certain value of the incident wave amplitude; this fact is due to dispersion law (7). The same is seen in the third harmonic intensity dependence, presented in Fig.3: the intensity can decrease when the intensity of the incident wave increases.

Such unusual behavior can be explained by resonance phenomena under the proximity of the three frequencies: the external field frequency, the incident wave one and the frequency of the carriers collisions. If the reflection coefficient would be independent on the external field, the harmonics in the reflected radiation would be absent. This is observed in the minimum of the reflection coefficient dependence on the parameter $(\omega\tau)^{-1}$. So, if the parameter $(\omega\tau)^{-1}$, being dependent on the external field amplitude, has a value corresponding to the minimal reflection at some external field amplitude, then the intensity of harmonics would decrease.

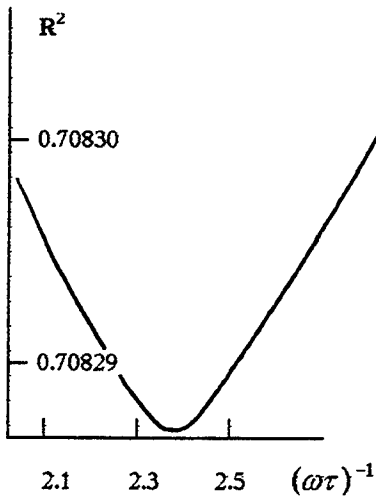


Fig.1

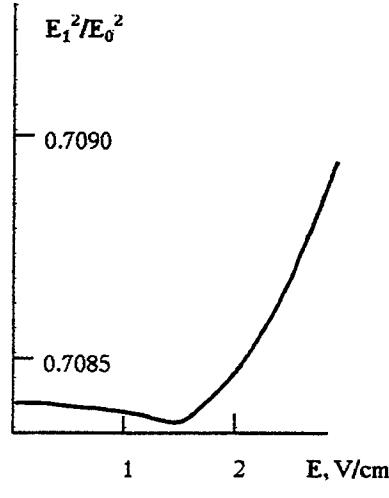


Fig.2

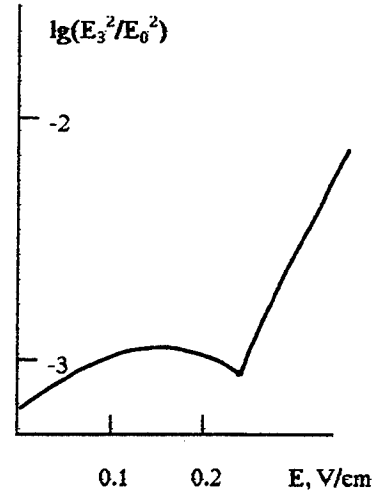


Fig.3

REFERENCES

- 1.A.B.Shvartsburg, *Nonlinear Pulses in Integrated and Waveguide Optic*, Oxford Univ. Press, 1993.
- 2.S.M.Sze, *Physics of Semiconductor Devices*, A Wiley-Interscience Publication, John Wiley & Sons, 1981.
- 3.E.Conwell, V.F.Weisskopf. *Phys.Rev.*, Vol.77, p.388,1950.

Wide-bandwidth high-power Cherenkov amplifiers: why dielectric slow-wave structures?

A. S. Shlapakovskii

Institute of Nuclear Physics of Tomsk Polytechnical University,
P. O. Box 25, Tomsk, 634050 Russia

ABSTRACT

Dielectric and conducting periodic slow-wave structures are compared for achievable values of relativistic amplifier bandwidths. It was shown earlier that a dielectric Cherenkov maser is capable of very large -3 dB bandwidths; on the other hand, in the case of conducting structures, there are no disadvantages caused by dielectric presence. Despite of stopband existence, a periodic waveguide may have rather wide passband and weak dispersion at relativistic phase velocities if its parameters are properly choosed. For comparison, a simplified model is employed neglecting the space harmonics of a periodic waveguide. The -3 dB bandwidth values have been determined from the numerical solution of the dispersion relation. It turns out that periodic structures, even at weaker dispersion, can not compete with dielectric-lined waveguides for wide-bandwidth amplifier operation. The reasons and consequences of that are discussed.

Keywords: Cherenkov maser, relativistic electron beam, wide-bandwidth microwave amplifier, dielectric-lined waveguide, periodic slow-wave structure

1. INTRODUCTION

At present, many various kinds of high-power microwave sources driven by relativistic high-current electron beams have already been developed and are under development and investigations. There is, however, a class of devices which remains practically unexplored. Those are wide-bandwidth amplifiers capable of hundreds MW power level and, at the same time, allowing frequency tuning over a range of up to an octave. Recently, it has been shown that rather wide (40-50%) -3 dB bandwidth can be achieved in the dielectric Cherenkov maser (DCM) amplifier.¹ As a smooth slow-wave structure, a dielectric-lined waveguide does not have stopbands, and a liner of a small to moderate dielectric constant may provide it with rather weak dispersion over a very wide frequency range at relativistic values of phase velocities. A DCM is a good candidate for a high-power wide-bandwidth amplifier, however, presence of a dielectric causes significant problems connected with charging a surface, RF breakdown along it, etc. This is a serious drawback of DCMs.

In the case of conducting periodic slow-wave structures (such as corrugated or ridged waveguides), there are no such problems. Relativistic Cherenkov oscillators with corrugated waveguides reliably operate in rep-rate regime and are already investigated as emitting units of radars.² Despite of the fact that periodic waveguide passband is always limited, it may be, nevertheless, rather wide; and weak dispersion at relativistic phase velocities is possible as well. For this, the period of the structure should be much less than the depth of corrugation or ridges and the depth, in its turn, should be much less than the operating wavelengths. The question arises: could the amplification band due to the beam-wave interaction in such waveguides be so wide as achievable in DCMs?

Let us consider the simplest model of a circular ridged waveguide of infinitely small period, i. e., not taking the space harmonics into account. Such a simplification will result in the wider amplification band than in reality as it results in wider waveguide passband. One can make certain conclusions concerning periodic structure potential to provide broad amplification band even from the analysis of no-beam system dispersion.

2. COMPARISON OF NO-BEAM SYSTEMS

For symmetric TM-modes of ridged waveguide, under assumption of infinitely small period, the dispersion relation is following³

$$\frac{I_1(qa)}{I_0(qa)} = \frac{q F_1(ka, kb)}{k F_0(ka, kb)}, \quad (1)$$

where $F_0(x, y) \equiv J_0(x)Y_0(y) - J_0(y)Y_0(x)$, $F_1(x, y) \equiv J_1(x)Y_0(y) - J_0(y)Y_1(x)$, $k = \omega/c$, $q^2 = h^2 - k^2$, ω and h stand for frequency and longitudinal wavenumber, a, b are inner and outer radii of ridges, respectively, c is the speed of light, $J_{0,1}$, $Y_{0,1}$, $I_{0,1}$ are Bessel functions. In Fig.1, phase velocity vs frequency obtained from Eq.(1) is plotted for various geometries. For comparison, the curve is presented in Fig.1 illustrating dispersion of circular dielectric-lined waveguide lowest TM_{01} mode at parameters providing an X-band DCM amplifier with wide bandwidth for 600 keV electron energy level.¹

One can see the very significant difference. There is rather weak dispersion for a dielectric-lined waveguide where the dielectric fills the substantial portion of the waveguide cross-section (inner to outer liner radius ratio $a/b = 0.5$). For ridged waveguide with $a/b = 0.5$, dispersion is very strong (curve 1). It becomes weaker as the degree of waveguide filling reduces (at increased waveguide radius, in order to have phase velocities of 0.8-0.9c in the X-band), and becomes so weak as for dielectric-lined waveguide only at very small filling ($a/b = 0.9$, curve 3).

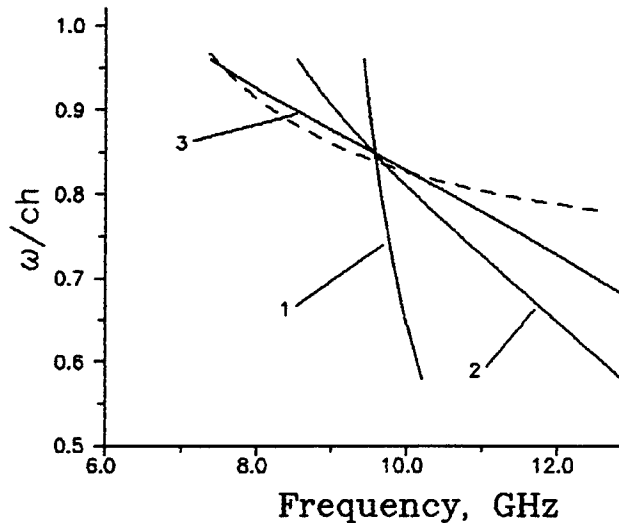


Fig. 1. Phase velocity vs frequency for various ridged waveguide geometries (solid curves).
1 - $a/b = 0.5$, $b = 1.3$ cm;
2 - $a/b = 0.8$, $b = 2$ cm;
3 - $a/b = 0.9$, $b = 3.3$ cm.
Also plotted (dashed curve) is dielectric-lined waveguide TM_{01} mode dispersion (dielectric constant $\epsilon = 2$, $a/b = 0.5$, $b = 2$ cm).

Meantime, it was noted in the work¹ that substantial filling with a dielectric is the important condition for obtaining a wide bandwidth in a DCM amplifier. Otherwise, the wave field is strongly evanescent, and the beam-wave coupling exponentially decreases as the frequency increases restricting the amplification

band. Fig.1 shows that for ridged waveguides, substantial filling the cross-section is not compatible with the requirement of weak dispersion, the main condition necessary for wide-bandwidth amplifier operation. Therefore, one can expect not so large bandwidth values in that case.

3. RESULTS OF DISPERSION RELATION ANALYSIS

To determine actual quantitative values, let us derive the dispersion relation for the system with a hollow electron beam assuming it to be infinitely thin, monoenergetic, and fully magnetized. In linear consideration, the jump of the radial derivative of the longitudinal electric field component E_z at the beam surface can be written as

$$\left\{ \frac{dE_z}{dr} \right\}_{r=r_b} = -\frac{2I_b}{\beta\gamma^3 I_A} \frac{q^2}{(k - \beta h)^2} \frac{E_z(r_b)}{r_b}, \quad (2)$$

where r_b is the beam radius, β is the dimensionless beam velocity, $\gamma = (1 - \beta^2)^{-1/2}$ is Lorentz factor, I_b denotes the beam current, $I_A = mc^3/e = 17$ kA. Matching the solutions of the wave equation for electrical Hertz vector in various regions and taking Eq.(2) into account, one can finally obtain the following dispersion relation:

$$\left[\frac{I_1(qa)}{I_0(qa)} - \frac{q}{k} \frac{F_1(ka, kb)}{F_0(ka, kb)} \right] (k - \beta h)^2 = \frac{2q^2 I_b}{\beta\gamma^3 I_A} \frac{I_0(qr_b)}{I_0(qa)} \left[\mathcal{F}_1(qa, qr_b) - \frac{q}{k} \frac{F_1(ka, kb)}{F_0(ka, kb)} \mathcal{F}_0(qa, qr_b) \right]. \quad (3)$$

Here, $\mathcal{F}_0(x, y) \equiv I_0(x)K_0(y) - I_0(y)K_0(x)$, $\mathcal{F}_1(x, y) \equiv I_1(x)K_0(y) + I_0(y)K_1(x)$, $K_{0,1}$ are Bessel functions. One can prove that Eq.(3) is the particular of more general equation of the work⁴ where the space harmonics and also the finite ridge thickness and electron energy spread were taken into consideration.

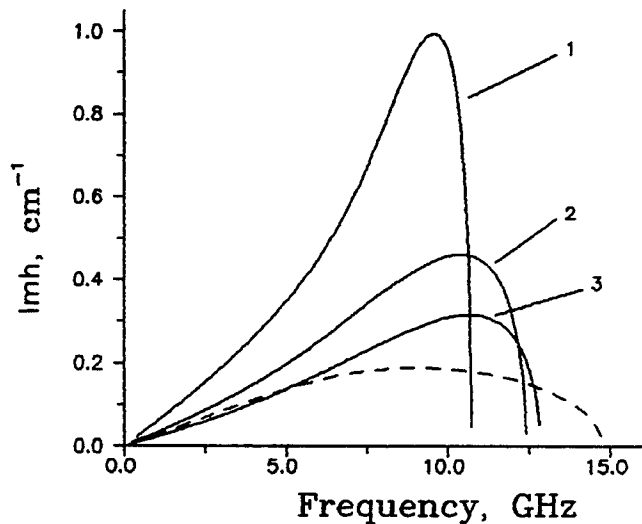


Fig. 2. Spatial growth rates vs frequency for various geometries of the system with a hollow beam. Ridged waveguide (solid curves) and dielectric-lined waveguide (dashed curve) parameters are the same as in Fig.1. For all curves, the beam parameters are: $\gamma = 2.2$, $I_b/I_A = 0.4$, $r_b = a - 2$ mm.

In Fig.2, the results of the Eq.(3) numerical solution are presented for the same parameters as in Fig.1 at fixed values of beam current, electron energy and distance to the ridges. The solution of the DCM dispersion relation¹ is also presented here. One can see that for the case of dielectric-lined waveguide (dashed curve) the spatial growth rate dependence on frequency is much more slightly sloping than for ridged waveguides. At substantial filling and small radius of the ridged waveguide (curve 1), the beam-wave

coupling is very strong, and the dependence maximum is quite sharp. At small filling and larger radius, the growth rate approach the maximum more gently from the low frequency side, however, at the high frequency side, it drops drastically as expected.

The most direct comparison is the comparison of -3 dB bandwidth values which can be determined from growth rate vs bandwidth dependences for given peak gain G . If the gain is large, the traveling wave tube theory formulas⁵ yield

$$\frac{\Delta(I_m h)}{(I_m h)_m} \approx \frac{3}{G[dB] + \alpha}, \quad (4)$$

where $\Delta(I_m h)$ is the difference between the maximum growth rate $(I_m h)_m$ and the growth rate corresponding to -3 dB power level, and α equals to 9.5 dB for the single-particle (Compton) regime or 6.0 dB for the collective (Raman) regime. Using formula (4), the curves are obtained plotted in Fig.3 as -3 dB bandwidth vs beam current dependences for the same other parameters as in Fig.2 and $G = 40$ dB. They demonstrate differences between amplifiers employing dielectric-lined and periodic waveguides as slow-wave structures. Qualitatively, for ridged waveguides, there is a saturation in the bandwidth vs current dependence, in difference of a maximum in DCM case. It is naturally explained by the stopband existence resulting in the limited frequency upshift in the collective regime. For DCMs, the amplification band shifts to higher frequencies as the current increases without any limit so that the beam-wave coupling decreases somewhere enough for bandwidth narrowing. And the main difference is, of course, the quantitative difference. Maximum achievable bandwidth values for periodic structures (at weak dispersion) are only of the level of 20% whereas for dielectric-lined waveguides, they approach 50% at the same parameters of the electron beam.

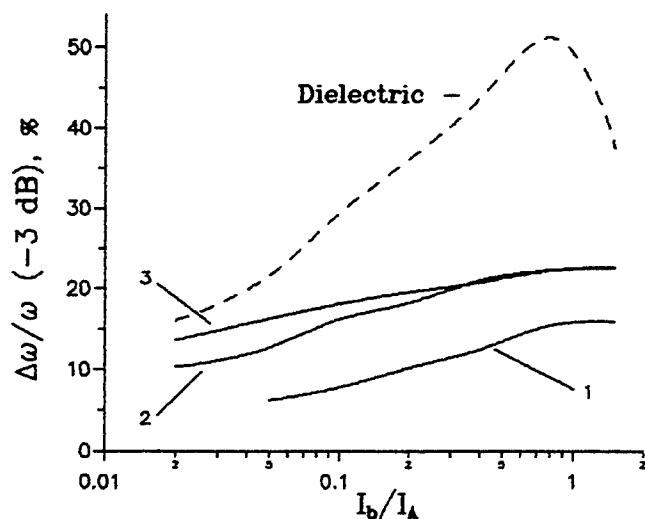


Fig. 3. -3 dB bandwidth vs beam current for periodic (solid curves) and dielectric (dashed curve) structures. For all curves, parameters are the same as in Fig.2. The peak gain $G = 40$ dB.

4. CONCLUSIONS

In summary, periodic conducting slow-wave structures, even at weaker dispersion, can not compete with dielectric-lined waveguides for wide-bandwidth relativistic traveling wave tube operation. The reason is in the fact that the requirements of weak dispersion at relativistic phase velocities and substantial filling the waveguide cross-section are not compatible for periodic waveguides so that the synchronous wave field significantly reduces as the frequency increases. It means, therefore, that the demands of the development of

high-power superwide-bandwidth amplifiers will motivate future researches on high-current DCMs aiming, in particular, to overcome problems caused by dielectric presence in order to explore the long-pulse and repetition-rate modes of operation.

5. ACKNOWLEDGEMENT

The author is grateful to Dr. S. D. Korovin for the stimulating discussion.

6. REFERENCES

1. A. S. Shlapakovskii and K. A. Chirko, "Dielectric Cherenkov masers as powerful amplifiers with superwide bandwidth," *IEEE Trans. Plasma Sci.*, Vol. 22, no. 5, pp. 544-546, 1994.
2. B. V. Bunkin, A. V. Gaponov-Grekhov, A. S. Eltchaninov *et al.*, "Nanosecond radar system based on repetitive pulsed relativistic BWO", *BEAMS 92. Proc. 9th Int. Conf. High-Power Particle Beams*, Eds., David Mosher and Gerald Cooperstein, Volume I, pp. 195-202, Washington, DC, 1992.
3. L. A. Vainshtein, *Electromagnetic waves (in Russian)*, Radio i sviaz, Moscow, 1988.
4. H. E. Brandt and H. S. Uhm, "Sensitivity of a relativistic backward wave oscillator to Budker's parameter," *IEEE Trans. Plasma Sci.*, Vol. 13, no. 6, pp. 553-558, 1985.
5. V. N. Shevchik and D. I. Trubetskov, *Analytical methods in microwave electronics (in Russian)*, Sovetskoye radio, Moscow, 1970.

SESSION 3

Pulse shortening in the magnetically insulated line oscillator (MILO)

Forrest J. Agee, Steve E. Calico, Kyle J. Hendricks, Mike Haworth,
and Tom Spencer

USAF Phillips Laboratory
Kirtland AFB, NM 87117

Dale Ralph and Earl Blankenship

Maxwell Laboratories
Kirtland AFB, NM 87117

M. Collins Clark and Raymond W. Lemke

Sandia National Laboratories
Albuquerque, NM 87119

ABSTRACT

The Magnetically Insulated Line Oscillator (MILO) is a cross field tube that has been studied analytically and experimentally by researchers in several laboratories. The tube is remarkable in that it requires no externally imposed magnetic field, but rather it can be designed to provide a sufficient self field in the relativistic electron beam to guide the electrons. The MILO can be made to operate at high power in the power range above 100 MW. It has been observed that the tube experiences a diminution in pulse width when operated at successively higher powers. This phenomenon, called variously pulse shortening or pulse tearing is also observed in conventional tubes designed for lower power. The process of conditioning commercial tubes is a costly part of the production of high power tubes for applications including particle accelerators. In the case of high power microwave tubes operating in excess of 100 MW, it presents a limitation on the energy that can be extracted from these tubes. This paper describes work performed at the Phillips Laboratory on a relatively high power MILO and discusses the phenomena that may account for this behavior.

KEYWORDS

1. Magnetically insulated line oscillator, 2 Cross field device, 3. MILO,
4. Narrowband tubes, 5. High power microwave sources, 6. Intense RF sources

1. INTRODUCTION

The Magnetically Insulated Line Oscillator (MILO) has been studied theoretically and experimentally at the Phillips Laboratory and has been shown to be an impressive source of intense RF power. In early work on the MILO, somewhat less than 100 MW of peak power and some theoretical understanding of the device were achieved.^{1,2,3} More recently, we have again pursued the MILO with the goal of achieving higher power and energy from the device. The MILO is an attractive device for a number of reasons, one being that it does not require an external magnetic field for it to operate, which offers the

possibility of a light weight, portable RF source of relatively modest complexity. The MILO, like other high power microwave tubes exhibits the phenomenon of pulse shortening, in which a number of different kinds of sources exhibit an ability to generate intense power, sometimes in excess of 1 GW for short periods of time (ten to a hundred nanoseconds) at high power or pulses for much longer periods, a microsecond or more, but only at lower power. This has the effect of limiting the energy available in the pulse, and makes the high power microwave power available unsuited to many applications. In the accelerator industry, for example, the ability to replace tubes that provide 50 to 100 MW with tubes at much higher power could revolutionize accelerator design, replacing accelerator stages counted in the hundreds by tens of them. This would enable many industrial applications including deep welding in heavy industry, as well as making physics accelerators more affordable. This problem is one that is being studied in a number of government, university and industrial laboratories. In the United States, the Air Force Phillips Laboratory and the Air Force Office of Scientific Research are pursuing a coordinated effort⁴ that is looking at a number of sources that exhibit pulse shortening with a goal of understanding the governing physics and developing ways to lengthen the pulses and increase the energy in the pulses.

2. PROGRESS IN THE MILO

The Phillips Laboratory has conducted an extensive program of optimization and has made much progress in understanding the MILO, which has been shown to be capable of producing axially extracted radiation with power in excess of 1 GW. A number of important technical issues must be properly considered in order to obtain this level of performance. These include the provision of a suitable choke at the pulsed power end of the tube, arranged to provide constructive reinforcement of the forward going wave with the reflected backward going wave. The four cavity MILO (Figure 1) operates in the π mode, with 180 degree phase difference between adjacent cavities, which appears from our observations to give the best performance. Other configurations with more cavities were not as efficient or operationally stable. Details of the beam dump and microwave extraction cavity are also important. The dimension of the last vane controls the efficiency of coupling of the energy out of the slow wave structure. The device will operate over a wide range of voltage at a fixed frequency. The MILO is a robust and repeatable device. Our experience is that it can be taken apart, reassembled, and it will operate as it did before this treatment. It is not particularly efficient, about 5% under good conditions. We have been able to operate the MILO in a repetitively pulsed mode⁵ using the Phillips Laboratory Rep-Rate Pulser, which is optimized for low impedance operation and which can be reconfigured to provide a number of impedances.⁶ The tube represents a source that is an interesting one for a number of reasons, and it has been extensively characterized and improved in performance in the recent work on it.^{5, 6, 7, 8}

3. PULSE SHORTENING IN THE MILO

The magnetically insulated line oscillator exhibits classical pulse shortening. It is unusual in that it can operate in a stable fashion over a wide range of voltages, which is usually not the case for microwave tubes. However, it can produce the highest power only for a relatively short fraction of the available current and voltage pulse length. At reduced voltage, and power, it can generate longer pulses of RF energy, as shown in Figure 2. The pulse shapes for two voltages and power levels are shown in Figure 3. The variation in pulse length for two power levels is shown in Figure 3. The left waveform has 850 MW peak power and a pulse width twice that of the right waveform at 1.5 GW. This is typical of pulse shortening in high power microwave sources, which tends to hold constant the

energy as the power increases. Figure 4 shows three microwave pulses compared to the current waveform of the available pulsed power driving the tube. Only a small portion of the current pulse contributes to RF production for all three microwave pulses. The effect of pulse shortening is dramatically displayed by comparing the pulse widths of the three RF pulses.

4. HARD TUBE MILO

In order to further investigate the pulse shortening phenomena, we have conducted additional experiments using a second pulsed power system at another facility at Kirtland AFB in Sandia Area IV. The IMP pulser was selected to allow uninterrupted experimentation, and as a site for investigating the role of high vacuum on the effects observed to date. For the latter investigation, we have arranged to make another MILO that has many of the features of conventional hard tubes such as klystrons in the way the tube is made and assembled. Whereas we have used flanges and o-ring seals typical of high power microwave experiments using powerful electron beams in previous work, the new "hard tube MILO" is assembled with brazed joints that make a close approximation to the kind of tubes that are commercially produced. A strong contrast with conventional tube technology is the cathode, which is velvet, and cannot be baked with the rest of the tube. We are very interested in exploring alternate cathodes that can give the same current performance and can be sealed up permanently inside the tube, be baked, etc. This will be a continuing area of research. Ideally, we would like to have a cathode with the same emissivity as velvet, but a much more durable, bakeable, and high vacuum friendly material. The initial stage of our work at the IMP pulser was to take the MILO reported on previously^{5,6,7,8} to the new facility to try it using the new pulser. New diagnostics were also added to enable measurements of the power inside the vacuum as well as inside the cavities and outside the output window and antenna.

A brief series of MILO/IMP pulser experiments were conducted in Sandia National Laboratories Technical Area IV to allow baseline comparison with the MILO experiments using the ETDL pulser. We wanted to establish that the IMP pulse power did not alter the operation of the basic MILO. Briefly, the pulse shortening previously reported was observed, as was the level of the radiated RF power. However, it was also observed that the pulse shortening inferred from the RF magnetic fields in the MILO cavities and the radiated power may be misleading. We added a vacuum RF monitor which showed that the MILO still produced power even after the cavity B-dots indicated no signal. This shows that the B-dot probes were arcing due to seeing too much RF magnetic field in the cavities.

The above observation is not to be confused with the pulse shortening due to plasma loss in the vacuum interface/bell jar. We have also observed the same arcing or plasma flares in the main lobe of the antenna pattern as previously reported, even though we now have an additional 30 feet of vacuum pipe. Figure 8 shows that there is more RF energy inside the vacuum than is getting past the output window. The arcing is much more intense than anything previously seen while using the PL injection locked relativistic klystron oscillator at higher power.^{8,9} This means there is an arcing mechanism inherent in the MILO which generates the arcing, whose source has not been identified. An additional piece of information is that a 3000 ASA, 4 inch by 5 inch piece of Polaroid film was attached to the air side of the bell jar, positioned to be in the maximum of the antenna pattern. The film showed a fully exposed frame indicating x-rays produced from the electrons of the plasma arc. The source of these electrons is still under investigation.

The above data was obtained to better compare the experimental performance of the MILO on the two different pulsers, however the new experiment with the Hard Tube MILO

(HTMILO) is to investigate improving the MILO by employing many techniques employed by the conventional microwave tube manufacturers. Toward that goal we brazed the RF choke section, MILO section, and fabricated an extractor/beam dump supported by $1/4$ wavelength legs (Figure 5). The brazing and a review and assistance with the design of the hard tube MILO was accomplished with the assistance of the staff of Stanford Linear Accelerator, who are collaborating with the Phillips Laboratory under a MURI grant administered by AFOSR.

As a preliminary comparison we used a Residual Gas Analyzer (RGA) to obtain a mass spectrograph of the constituent components of the vacuum base pressure in the original MILO and the HTMILO, prior to all conditioning. The mass spectra from the old MILO, shown in Figure 6 and for the hard tube MILO, shown in Figure 7 show dominant contributions from water, atomic oxygen, atomic hydrogen, molecular hydrogen, molecular oxygen, and molecular nitrogen. These are not unexpected results for vacuums above 10^{-6} Torr for the old MILO and somewhat less for the HTMILO. As we go through conditioning the HTMILO by bakeout at 300°C and RF discharge cleaning we anticipate that the magnitudes of these constituent gases will be reduced. At that point we can determine if the generic MILO class device operates better with improved vacuum or if the MILO class devices are essentially unchanged by the vacuum level.

5. CONCLUSIONS

The magnetically insulated line oscillator has demonstrated high power and other features that make it an attractive source of high power microwave RF energy. It suffers from pulse shortening, and the work reported here is a progress report on investigations as to the causes and possible remedies. Measurements made recently indicate breakdown both at probes in the cavities and at the output window of the tube. These phenomena will be further studied to better define the cause and possible remedies. The present course will also explore the reduction of pressure through vacuum improvements to the tube to investigate a new parameter space that may have an effect upon pulse shortening. Future directions will include studies of improved cathodes to enable exploration of even higher vacuum regimes, with an eventual goal of a true hard tube MILO.

6. REFERENCES

1. R. W. Lemke and M. C. Clark, "Theory and simulation of high-power microwave generation in a magnetically insulated transmission line oscillator," *J. Appl. Phys.*, Vol. 62, No. 8, 3436-3440, 15 October, 1987.
2. R. M. Lemke, "Linear stability of relativistic space-charge flow in a magnetically insulated transmission line oscillator," *Proc. of the SPIE* Vol. 1061, 112 - 124 (1989).
3. V. I. Kurilko, V. I. Kuchurov, A. O. Ostrovskii, and Yu. V. Tkach, "Stability of a relativistic electron beam in a periodic cylindrical waveguide," *Sov. Phys. Tech. Phys.* 24 (12), 1451 (1979).
4. R. J. Barker and F. J. Agee, "National University Consortium on Microwave Research (NUCOMR)," *Proc. of the SPIE* 2557, 300 - 309 (1995).
5. S. E. Calico, F. J. Agee, M. C. Clark, R. W. Lemke, and M. C. Scott, "Rep-rate operation of a magnetically insulated line oscillator (MILO) in *Proc. of the First International Workshop on Crossed-Field Devices*, University of Michigan, Ann Arbor, MI, August, 1995.

6. S. E. Calico and M. C. Scott, "Performance enhancement of the Phillips Laboratory Rep-Rate Pulser with a triggered output switch," in *Conference Record of the 1994 Twenty-First International Power Modulator Symposium*, 56-59, June, 1994.
7. S. E. Calico, M. C. Clark, R. M. Lemke, and M. C. Scott, "Experimental and theoretical investigations of a magnetically insulated line oscillator (MILO), *Proc. of the SPIE* Vol. 2557, 50 - 59 (1995).
8. F. J. Agee, "Current Issues in High Power Microwaves," in *Proc. of the 1996 Twenty-Second International Power Modulator Symposium*, 1996 (to be published).
9. K. J. Hendricks *et al*, "The Extraction of RF Power from an Injection Locked Relativistic Klystron Oscillator," *Phys. Rev. Lett.* **76**, 154 (1996).

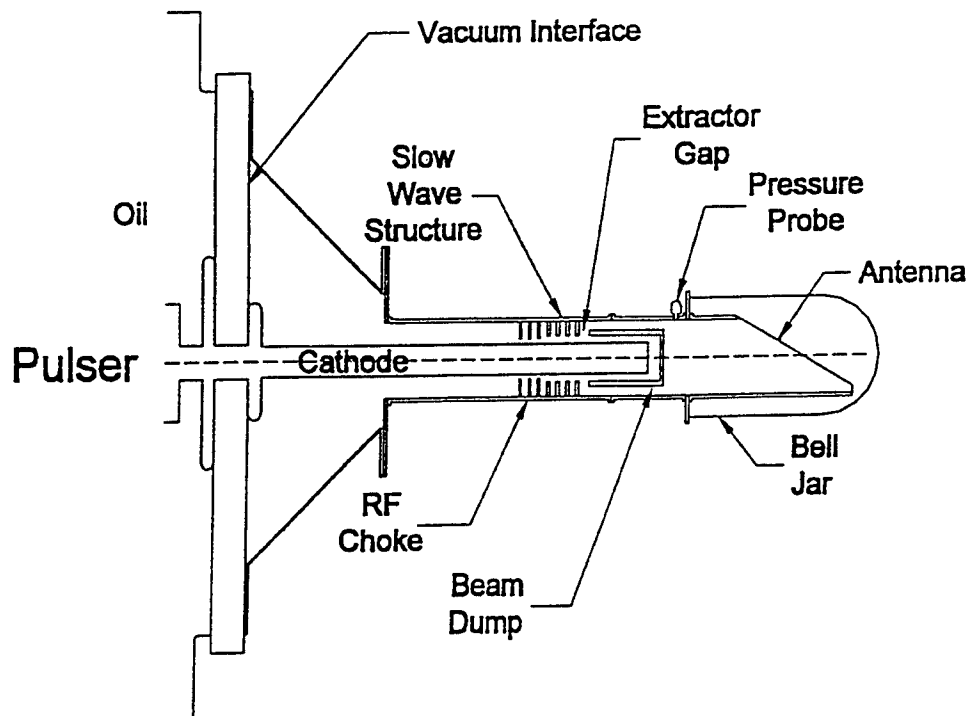


Figure 1. Schematic diagram of the MILO.

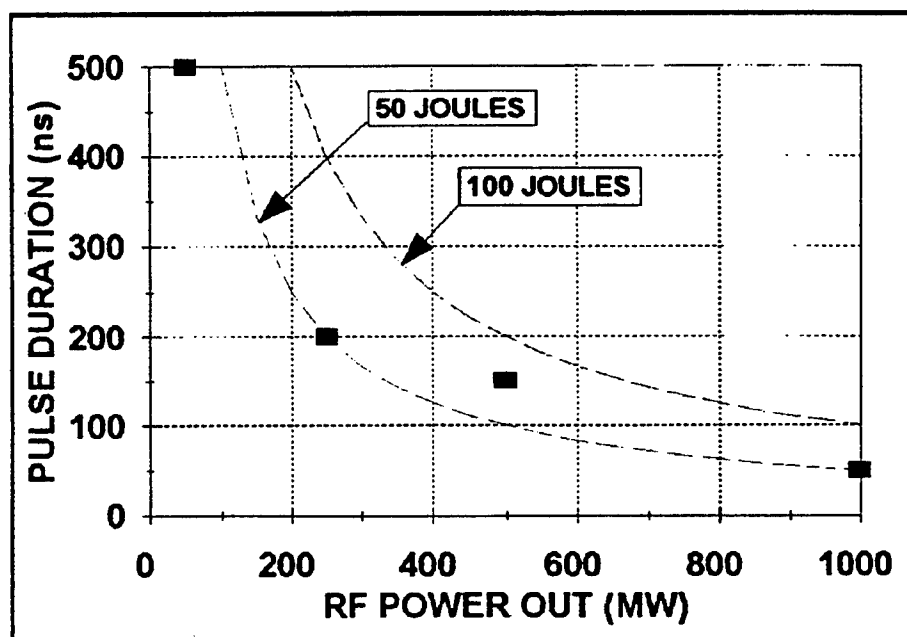


Figure 2. Pulse shortening in the MILO - wide range of power and pulse duration.

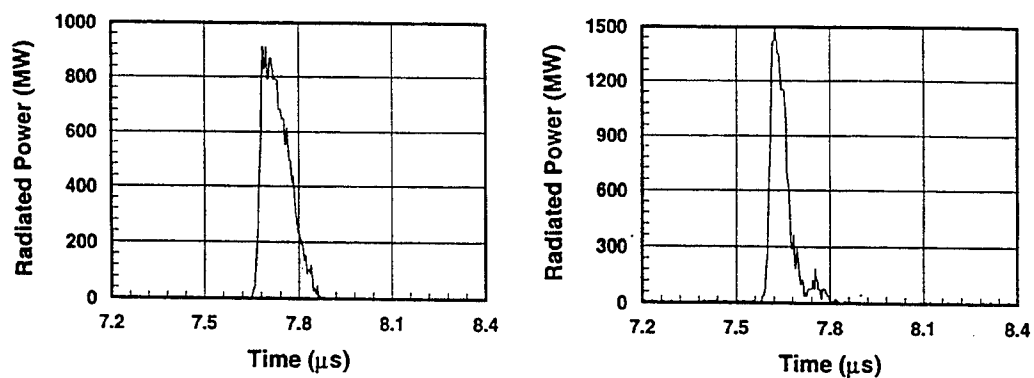


Figure 3. Two pulses from the MILO show the constant energy aspect of pulse shortening.

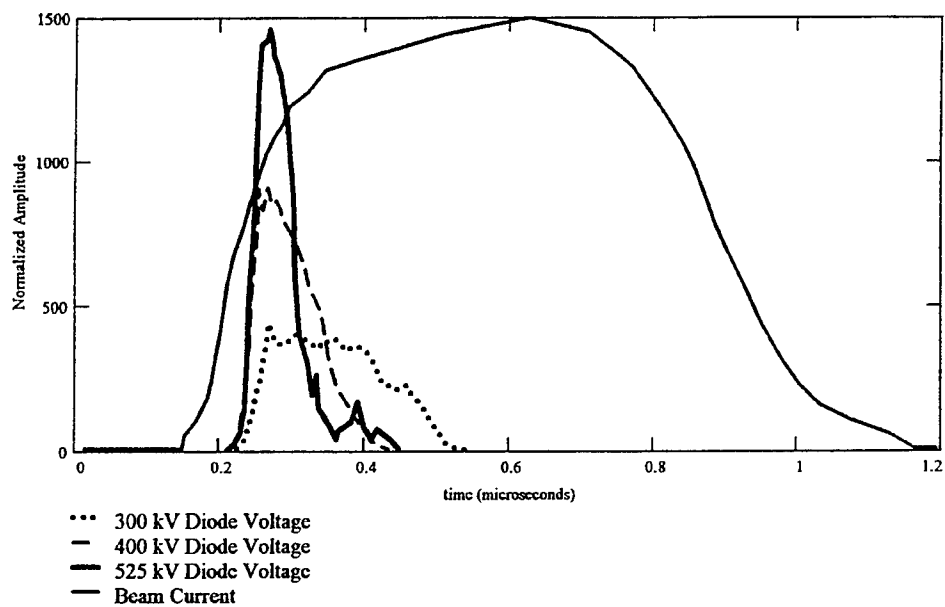


Figure 4. RF pulses from MILO compared to current pulse width available.

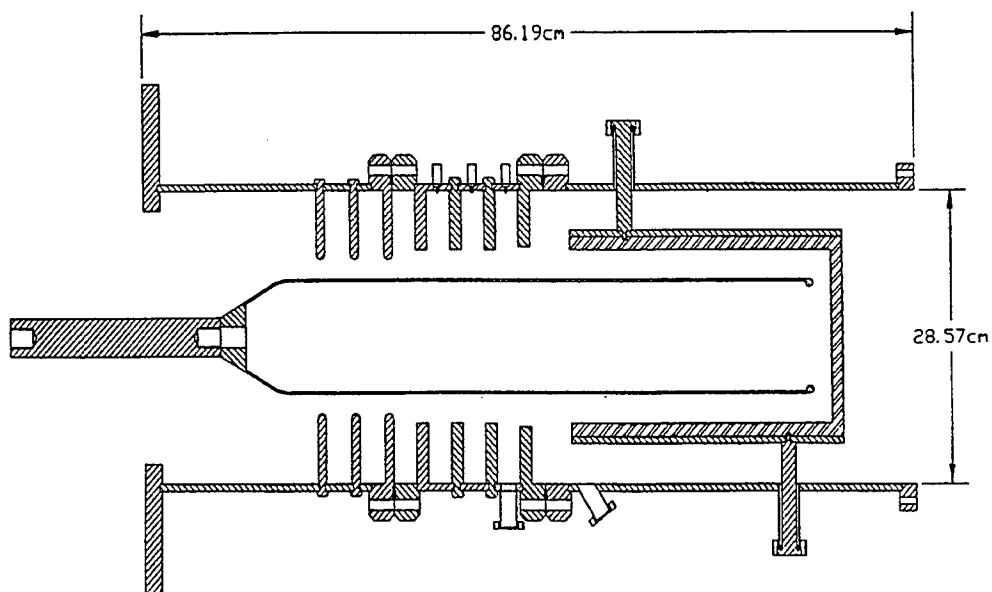


Figure 5. Hard Tube MILO offers access to higher vacuum regime.

Dycor Quadrupole Gas Analyzer

July 24, 1996 14:08:07

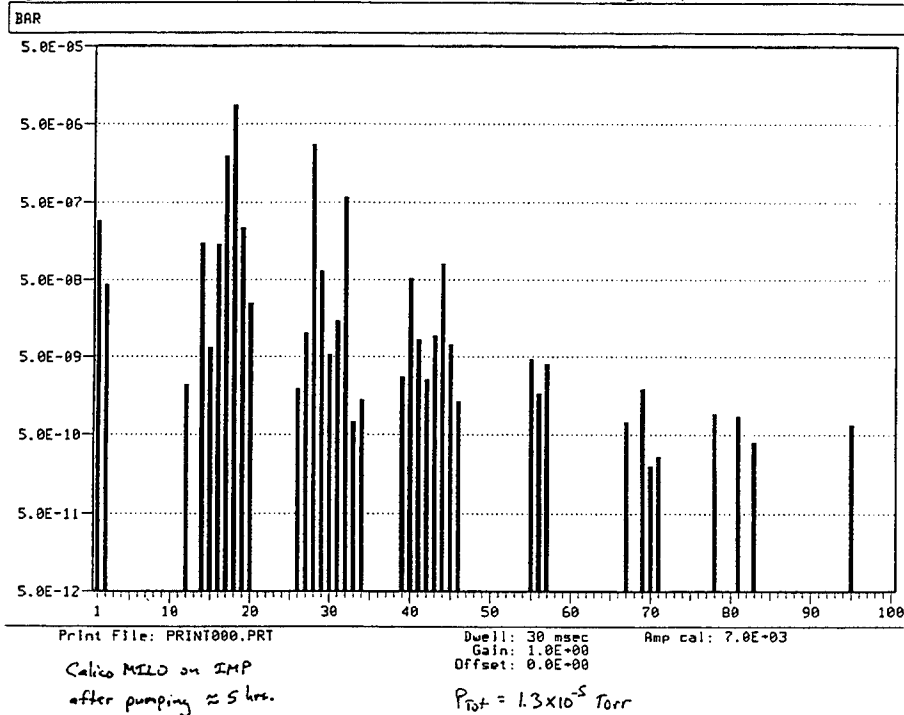


Figure 6. Gas chromatograph of old MILO shows constituents of gas pressure.

Dycor Quadrupole Gas Analyzer

July 26, 1996 11:23:49

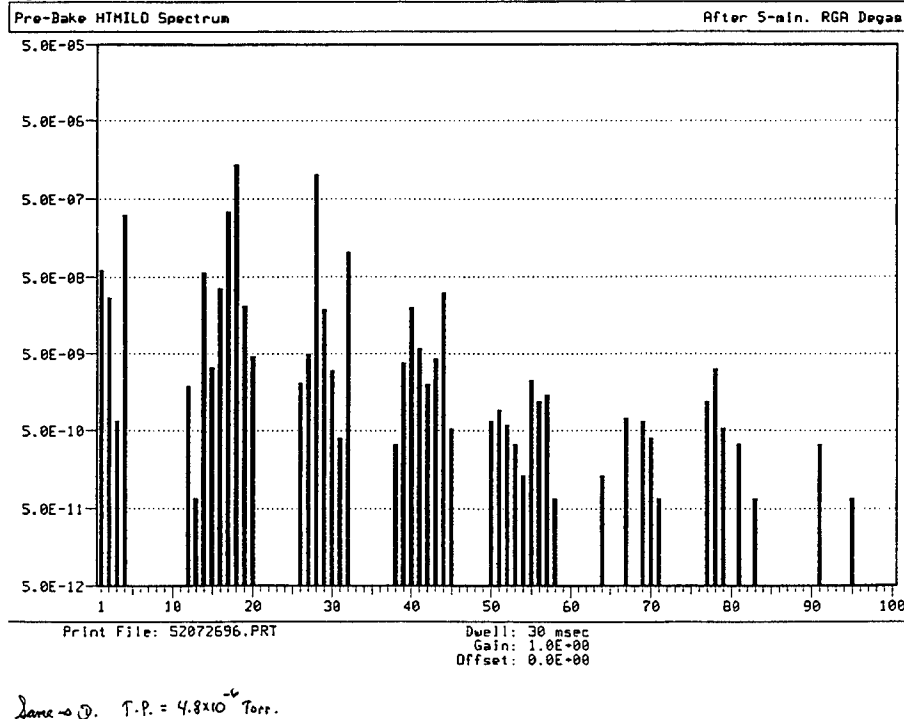


Figure 7. Gas chromatograph of hard tube MILO shows some improvement even before baking.

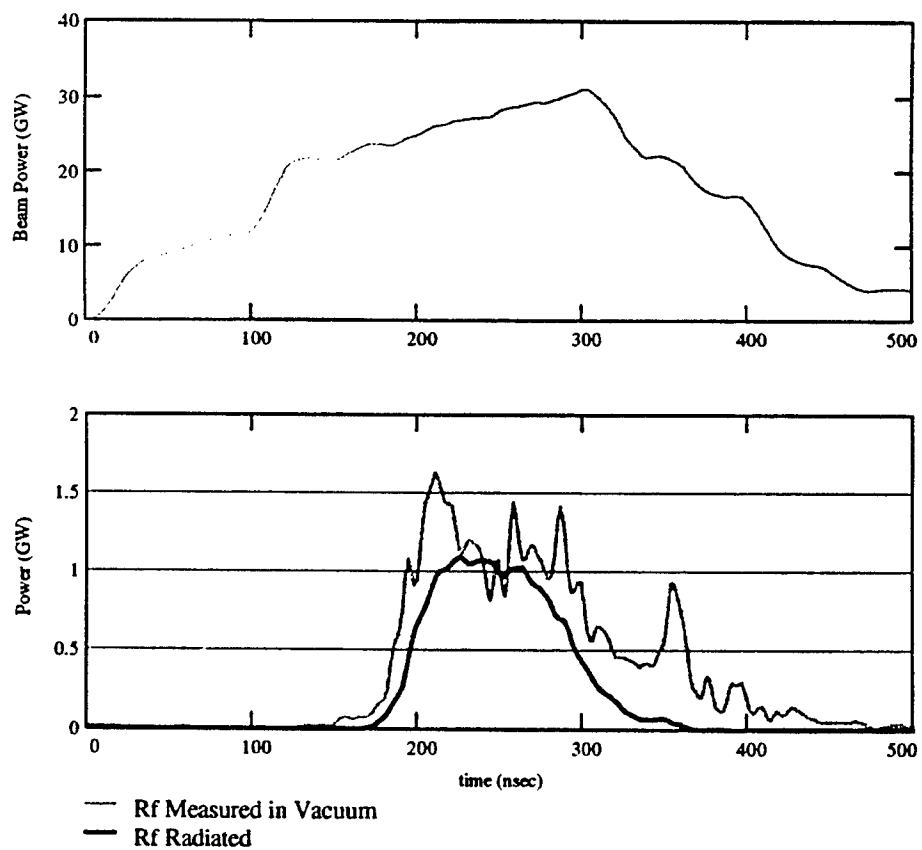


Figure 8. Beam power and RF power for MILO on IMP pulser. RF data show longer RF waveform in vacuum before window than after emission from tube into air.

Breakdown at Window Interfaces Caused by High Power Microwave Fields

J.C. Dickens, J. Elliott, L.L. Hatfield, M. Kristiansen and H. Krompholz
Pulsed Power Laboratory
Departments of Electrical Engineering and Physics
Texas Tech University
Lubbock, TX 79409-3102

ABSTRACT

Breakdown phenomena at window interfaces are investigated for microwave power levels of up to 100 MW. The test stand utilizes a 3 MW magnetron operating at 2.85 GHz, coupled to an S-band traveling wave resonant ring. Various configurations of dielectric windows (i.e. vacuum-air, or vacuum-vacuum), in various geometries (standard pillbox geometry, or windows filling the S-band waveguide cross section) can be investigated. Diagnostics include the measurement of transmitted and reflected microwave power, luminosity from the discharge plasma, x-ray emission from initially free electrons, and electric field probes. All these quantities are measured with high amplitude and high temporal (0.2...1 ns) resolution. Goals are to determine the physical mechanisms - such as the dominant electron multiplication process - leading to flashover. The knowledge gained from these experiments will be used to investigate and design methods to increase the power density which can be transmitted through windows. In addition, parametric studies are planned, in which window material, profile, and surface coatings are varied. The basic system and the diagnostics methods will be expanded for the investigation of microwave cavity breakdown as well.

2. INTRODUCTION

Different breakdown mechanisms limit generation and transport of high power microwaves. The most important breakdown forms are:

- (1) Internal breakdown in high power microwave generators, often in the presence of plasma and UV radiation,
- (2) Breakdown in cavities, usually caused by a multipactor mechanism [1]
- (3) Surface breakdown at interfaces, with the most common type occurring on the air-side of a vacuum/air interface [2].

Furthermore, these breakdown phenomena might play a role in pulse shortening mechanisms in all types of high power microwave generators [3].

The aim of the present paper is to clarify the physical mechanisms leading to breakdown for a variety of conditions. These mechanisms can be roughly categorized into two parts: the generation of starting electrons, and amplification or avalanche mechanisms leading to a build-up of a high electron density plasma, which inhibits microwave propagation. Knowledge of these physical processes is a prerequisite to develop ways to increase breakdown thresholds. Up to now, mainly empirical methods have been used, such as selection of materials, surface coatings, and the choice of proper geometries to avoid macroscopic field enhancement areas. Another promising way to increase breakdown thresholds is the

use of low amplitude insulating magnetic fields, which has been successful in increasing the hold-off voltage for unipolar surface flashover [4].

To explore the physical mechanisms leading to breakdown, we employ high speed real-time diagnostics of easily accessible phenomena, such as measuring the forward and reflected microwave power, x-ray emission by initially free high energy electrons, and luminosity of either the developing discharge plasma or luminescence of window materials. The combined results of these measurements yield a comprehensive phenomenological picture of the events leading to breakdown, and they serve as starting points to develop methods for increasing breakdown thresholds.

3. EXPERIMENTAL SETUP

To reach microwave power densities on the order of 10^7 Wcm^{-2} at a frequency of 2.85 GHz, a magnetron in combination with a traveling wave resonant ring [5] is used (Fig. 1). The magnetron, a Varian type VMS1143B, has a nominal output power of 3.2 MW and a pulse duration of 3 μs . With a 14.6 dB directional coupler, a ring loss per pass of 0.22 dB and a phase shifter matching the traveling and incoming phases, a stored power of 60 MW with a risetime of 0.9 μs and a pulse duration (FWHM) of 1.5 μs is obtained. The system is operated at a maximum pressure of 10^{-6} Pa . Various breakdown test objects, such as a single window with vacuum on both sides, two windows with a high pressure region in between, or waveguide/cavity sections with field enhancement can be inserted.

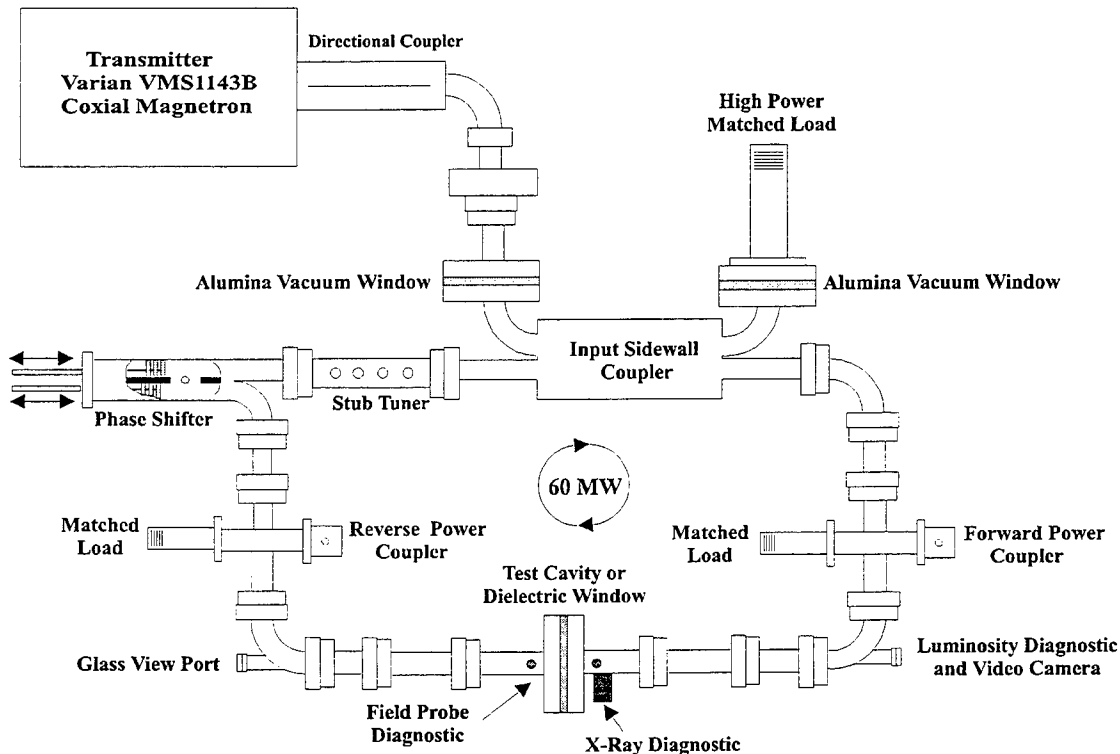


Figure 1. Traveling wave resonator.

Directional couplers with 56 and 46 dB, respectively, measure forward and reverse power in the ring, where rectifying diodes (HP-8474B) provide a temporal resolution of 200 ps. Short antenna local field probes are located close to the test object and provide information on the local power with similar

temporal resolution. The luminosity is measured with photomultiplier tubes (Hamamatsu R 4703) with a risetime of 0.8 ns, S-20 spectral characteristics, and a sensitivity of 2×10^4 A/W. Typical detectable threshold powers for the optical setups used are on the order of several 10 's μ W. X-ray emission measurements are accomplished with plastic scintillator (NE 111) photomultiplier (Amperex XP 2020) combinations, with a risetime of 1.3 ns. Aluminum foils with different thickness (10 to 200 μ m) in front of the scintillator provide shot to shot information on the x-ray energy distribution. The detectable threshold for x-ray emission measurements has been estimated to be on the order of about 10^5 electrons per nanosecond, where electrons with an energy of 10 keV producing Bremsstrahlung in a copper target have been assumed. All time resolved signals are measured with Tektronix 7104 oscilloscopes (risetime 350 ps), or, in some cases, with Tektronix SCD 5000 digitizers (risetime 80 ps). The accuracy of the temporal correlation between signals is estimated to be less than 1 ns, where PMT transit times, cable delays, etc., have been considered. Time integrated recordings of the visible light emission are taken with a video camera.

The diagnostics system will be extended by a pinhole camera to get information on the time-integrated structure of x-ray sources, a streak camera (Hamamatsu C 979) to measure the dynamics of luminescence and luminosity, and by spectroscopic methods to analyze visible emission phenomena, and to distinguish between window material luminescence and plasma luminosity. Furthermore, a laser beam deflection system is available to quantitatively measure gas and plasma development. This system provides a temporal resolution of 5 ns, and minimum detectable line densities for the expected density structures are on the order of 10^{15} cm^{-2} for gas, and 10^{14} cm^{-2} for plasma [6].

4. FIRST TESTS AND RESULTS

First system tests have been performed, using a window configuration shown in Fig. 2, a planar alumina window in a circular enclosure ("pill-box"). The pressure was less than 10^{-6} Pa on both sides of the window. For this case, the microwave power was measured on both sides of the window at a distance of 5 cm. Time integrated pictures were taken and luminosity and x-ray emission were recorded as shown in Fig. 3. The spectral sensitivity of the x-ray measurement is determined by the absorption of a 10 μ m aluminum foil, which provides a "flat" response starting at a quantum energy of approximately 3 keV.

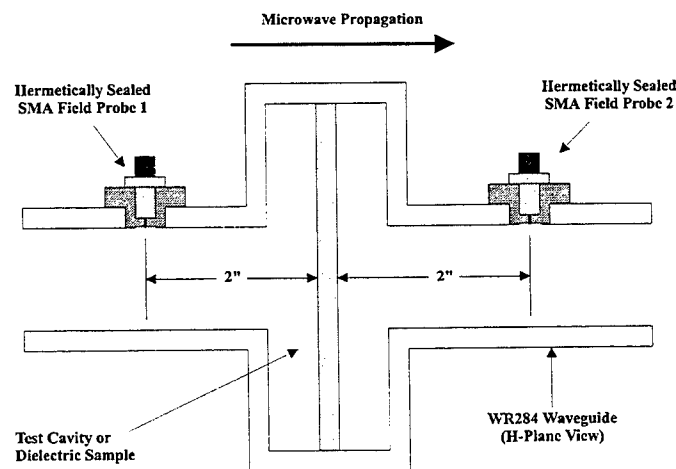


Figure 2. Test window configuration.

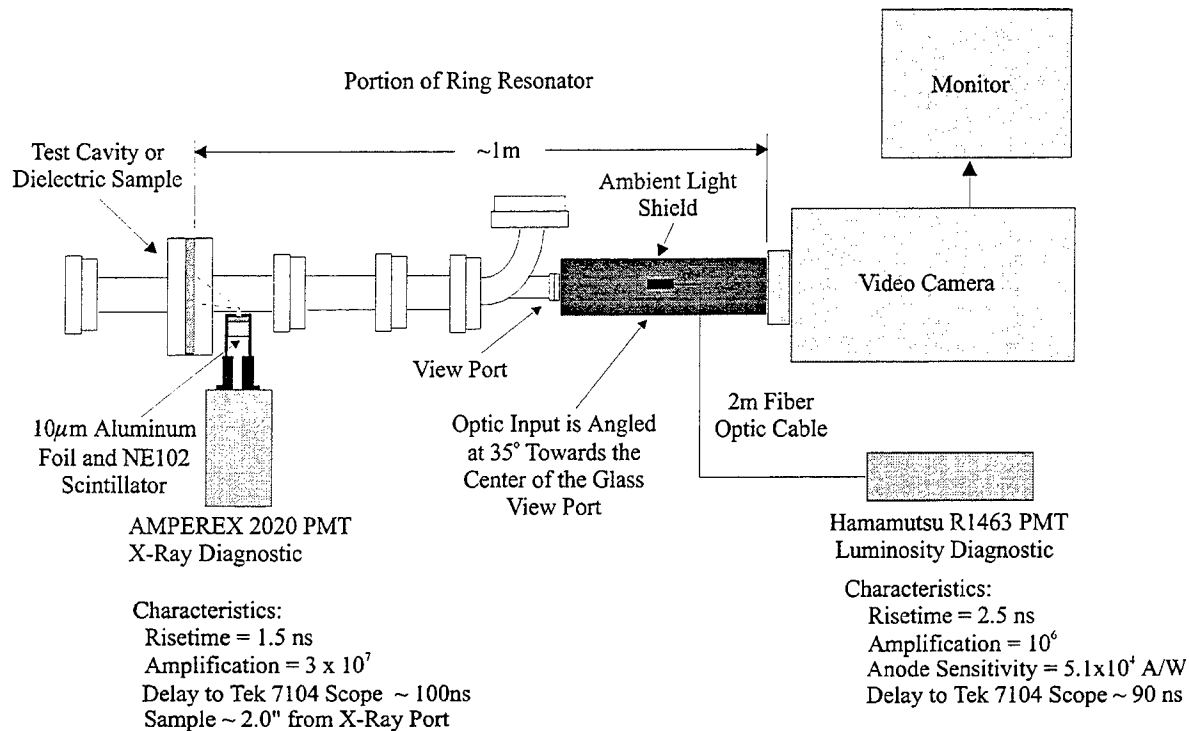


Figure 3. Diagnostics for window breakdown.

Field plots for this geometry, i.e., a transition from rectangular geometry to circular geometry, and back to rectangular geometry, have been obtained using the "Maxwell Eminence" program by Ansoft Corp (Fig. 4). At a time of maximum field enhancement at the edges of the rectangular waveguide, tangential fields across the window are almost zero, and the normal field at the window shows two maxima 5 cm apart. At a phase of 90 degrees later, no field enhancements at the waveguide edges are observed, but a tangential field at the window with a maximum at the center.

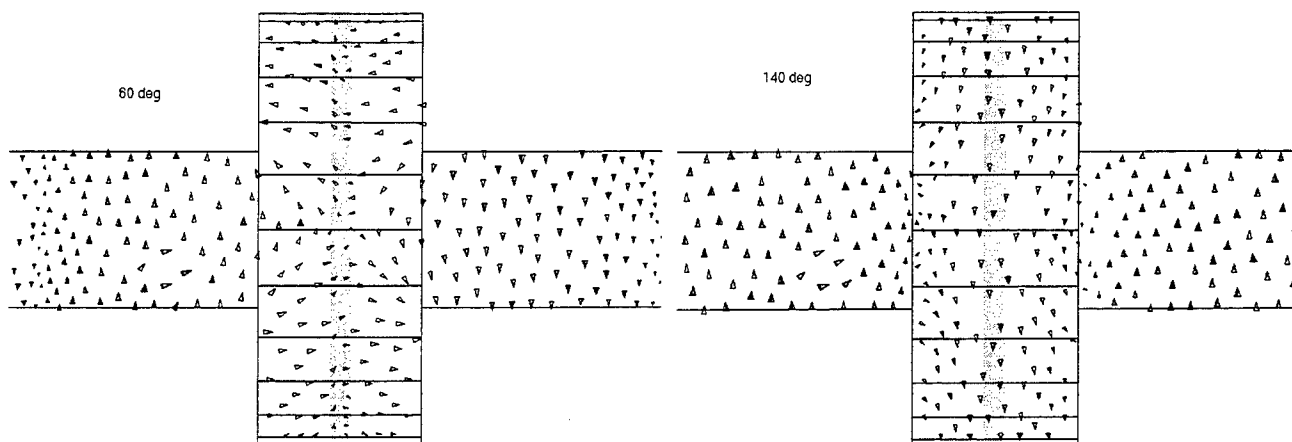


Figure 4. E-field vector at window from simulation.

From this field configuration we expect a multipactor-like discharge from the waveguide edge to the two normal field maxima at the window, combined with a surface discharge along the window, connecting the two normal field maxima. These expectations are confirmed by the visible time-integrated appearance of the discharge, as seen in Fig. 5. Superimposed are a number of small luminous spots surrounding the two normal field maxima.

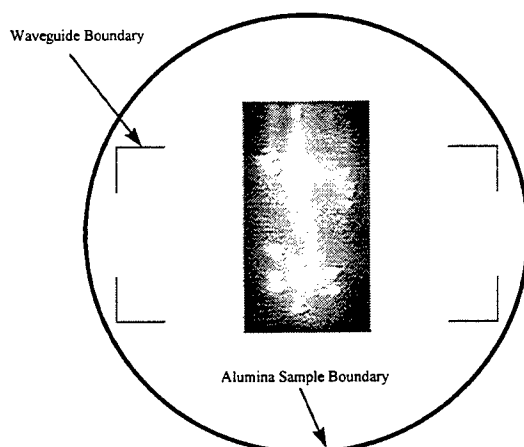


Figure 5. Time-integrated photo of window discharge.

The complexity of this discharge phenomenon is also seen in the time-resolved signals (Fig. 6). The structure of the x-ray signal, for instance, consists mainly of single spikes with a spacing equal to the transit time of the ring. During the early stage, obviously only a small amount of power is absorbed, and the power in the ring is almost constant. After 100 ns, a main discharge is developing with large x-ray emission, which is associated with an almost full absorption of the available power, i.e., a decrease of the two microwave probe signals. The behavior of the luminosity is qualitatively similar to the behavior of the x-ray emission (except for a much longer decay time), but it is not possible at this time to distinguish between luminescence from the window material due to electron bombardment, and luminosity from the developing plasma.

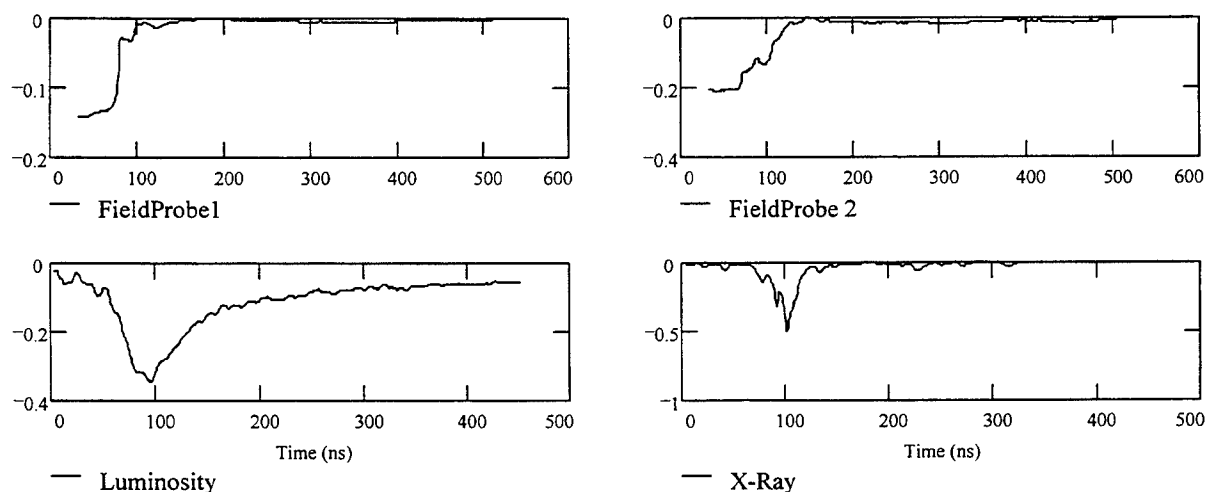


Figure 6. Waveforms of diagnostic signals for standard window.

Time resolved signals for a simpler case are depicted in Fig. 7. Field enhancement points at the window surface (at the positions of the normal field maxima) cause a pure surface discharge as seen in a distinct luminosity channel connecting the two normal field maximum points. No other components of the time integrated luminosity have been observed for this case. The power threshold for this discharge type is by a factor of two smaller than the one described above. At a power level of approximately 10 MW, the luminosity signal starts and reaches a peak after 100 ns. X-ray emission is delayed with respect to this light signal. After the main x-ray peak, the luminosity rises again to a higher level, and decays after that with a time constant of 0.6 μ s. The appearance of this discharge type, i.e., x-ray emission followed by light emission, is very similar to the phenomena occurring in unipolar surface discharges [7]. Here, initially free electrons producing the x-ray emission cause electron induced outgassing, which leads to a Paschen-type breakdown in the developing gas cloud above the surface. In this gas cloud, electrons are collision dominated, and the x-ray emission stops. Increasing plasma density is associated with increasing luminosity during this phase.

5. CONCLUSIONS

The combination of a 3-MW magnetron and the traveling wave resonator is a versatile instrument to study breakdown phenomena caused by high power microwaves. High speed diagnostic methods (microwave power, visible light emission, and x-ray emission) provide the necessary information to describe the breakdown process. Knowledge of the breakdown mechanism will be the starting point to develop methods to increase the breakdown threshold. Our first results using a combination of cavity and window in vacuum show a complex discharge behavior with several competing discharge types. Field enhancement points can be used to favor specific discharge types resulting in a simpler appearance, which opens the way to access the physical phenomena involved.

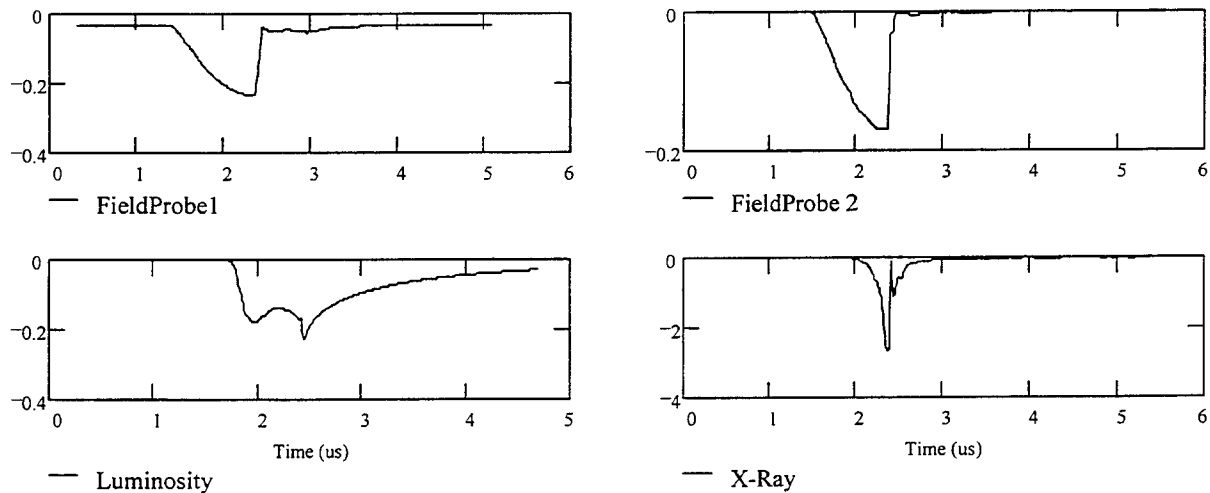


Figure 7. Waveforms of diagnostic signals for window with field enhancement.

6. ACKNOWLEDGMENTS

This work was supported by the AFOSR/DoD Multidisciplinary University Research Initiative on "High Energy Microwave Sources", and we like to thank R. Fowkes, G. Caryotakis, J. Siambis (SLAC), and J. Agee and J. O'Loughlin (Phillips Laboratory) for providing equipment.

7. REFERENCES

- [1] R. Kishek and Y.Y. Lau, "Interaction of Multipactor Discharge and RF Circuits", *Phys. Rev. Lett.* **75**, 1218 (1995).
- [2] M.D. Haworth et. al., "L-Band Vacuum Window Design for Gigawatt-Level Single-Pulse Microwave Sources," IEEE ICOPS June 3-5, Boston, MA, 1996.
- [3] J. Benford, "Pulse Shortening in High Power Microwave Sources," IEEE ICOPS June 3-5, Boston, MA, 1996, and Proceedings of BEAMS '96, Prague, Czech Republic, June 10-14, 1996.
- [4] M. Lehr, R. Korzekwa, H. Krompholz, M. Kristiansen, "Magnetic field effects on vacuum insulator flashover," *Appl. Phys.* **71**, 389 (1992).
- [5] L.J. Milosevic, R. Vautey, "Traveling Wave Resonators," *Inst. Radio Engrs. Transactions on Microwave Theory and Techniques* **6**, 136 (1958).
- [6] G. Masten, T. Mueller, F. Hegeler, H. Krompholz, "Plasma development in the early phase of dielectric surface flashover," *IEEE Transactions on Plasma Science* **22**, 1034 (1994).
- [7] F. Hegeler, G. Masten, H. Krompholz, and L.L. Hatfield, "Current, Luminosity, and X-ray Emission in the Early Phase of Dielectric Surface Flashover in Vacuum," *IEEE Transactions on Plasma Science* **21**, 223 (1993).

Interaction of Multipactor and RF Circuit

R. Kishek, Y. Y. Lau, D. Chernin⁺, and R. M. Gilgenbach
Department of Nuclear Engineering and Radiological Sciences
University of Michigan, Ann Arbor, MI 48109-2104

Tel: (313)764-5122 FAX: (313)763-4540 email: yylau@umich.edu

⁺SAIC, 1710 Goodridge Drive, McLean, VA 22102

Abstract A simple model is constructed to analyze the temporal evolution of a multipactor discharge in an rf cavity. The multipactor current may, transiently, reach a level comparable to the wall current that is needed to sustain the rf field. It saturates at a much lower level in the steady state, primarily by its loading of the cavity; the space charge force associated with the multipactor electrons plays a relatively minor role. At saturation, the electron impact energy equals the lowest value that gives unity in the secondary electron yield curve. We also discovered a new phase focusing mechanism, whereby the leading edge of the multipactor discharge grows at the expense of the trailing edge, in spite of the mutual repulsion among the electrons. This phase focusing mechanism may shape the steady state multipactor discharge in the form of a very tight bunch of electrons.

Multipactor is a well known resonant phenomenon of rf breakdown in microwave cavities, windows, satellite rf payloads, and accelerator structures. Its persistence requires, at the minimum, stability in the phase of the electron orbit with respect to the rf cycle^{1,2}. Most of the studies omit the important processes of loading and detuning of the rf cavities as the multipactor current grows. Moreover, as the space charge builds up, Vaughan's phase focusing¹ may be destroyed by the mutual electrostatic repulsion among the multipactor electrons. It is often conjectured that the multipactor current may saturate when the electrostatic repulsion is about to overcome the phase focusing that is obtained from the consideration of single particle orbit. Here, we use a simple model to address these issues, the analysis of which yields interesting information on the multipactor saturation level, the saturation mechanism, the time scale over which multipactor evolves, and possibly the drastic transient growth of multipactor current before the steady state solution is reached³. We also find the surprising result⁴ that the electrostatic repulsions among the space charges do not lead to saturation of the multipactor current. On the contrary, the mutual repulsion leads to a new phase focusing mechanism which shapes the steady state multipactor discharge in the form of a very tight bunch of electrons.

For simplicity, we shall use a one dimensional model where the multipactor occurs inside a planar gap [Fig. 1]. The gap separation is D and the gap voltage is $V_g(t)$. We shall first consider a single electron sheet of surface density σ to model the multipactor electrons which move across this gap. Upon impact on a gap surface, a new electron sheet is generated by secondary emission. We assume that the voltage V_g that drives the multipactor is provided by an rf cavity. This cavity is modelled by an RLC circuit [Fig. 1], with a corresponding quality factor Q and characteristic frequency $\omega_0 = 1/\sqrt{LC}$. As the multipactor electron sheet moves inside the gap, it induces a wall current, $I_m(t)$, which loads the RLC circuit. Thus, the present model allows for the progressive loading and detuning of the cavity as the multipactor current builds up [Fig. 1]. This loading in turn modifies the electron's energy and phase at impact.

Hereafter, we shall use dimensionless quantities with the following normalization scales: D for distance, ω_0 for frequency, $1/\omega_0$ for time, $v = \omega_0 D$ for velocity, $U = mv^2$ for energy, $V = U/e$ for voltage, $E = V/D$ for electric field, $\Sigma = \epsilon_0 E$ for surface charge density, V/Z for current. Here, m is the electron mass, $e = 1.602 \times 10^{-19}$ Coulomb, ϵ_0 is the free space permittivity, and $Z = \sqrt{L/C}$ is the intrinsic impedance of the RLC circuit. The RLC circuit is driven by the normalized ideal current source $I_d(t) = I_{d0} \sin(\omega t + \phi)$ and by the multipactor current I_m . We set $\omega = 1$ (i.e., resonantly driven), $\delta_{\max} = 1.2$, and $E_{\max} = 0.36$ in the secondary yield curve [Fig. 2]. In dimensional units, if the rf cavity has a natural frequency of 1 GHz, and a gap separation of 0.22 cm, over which multipactor occurs, these parameters correspond to an ideal rf driver current exactly at 1 GHz, the first cross-over point $E_1 = 166$ eV, and δ reaches a maximum value of 1.2 when the impact energy is $E_{\max} = 400$ eV.

The normalized multipactor current I_m is given by

$$I_m(t) = -\sigma(t) \frac{dx(t)}{dt}, \quad (1)$$

where σ is always positive, by convention. Equation (1) accounts for the induced current as a result of the motion of the electron sheet within the gap, $0 < x < 1$. It is this term that is solely responsible for the non-linear beam loading and frequency detuning of the cavity by the multipactor, as readily seen from Fig. 1.

During its transit across the gap, the electron sheet is accelerated according to the normalized force law,

$$\frac{d^2x}{dt^2} = V_g + \sigma \bullet \left(x - \frac{1}{2}\right), \quad (2)$$

where the first term on the right hand side represents the force due to the gap voltage and the second term the force due to the image charge (of the multipacting electron sheet) on the plates.

Figure 3a shows the multipactor current, monitored at impact, in units of the driver current amplitude I_{d0} , for $Q = 1, 10, 100, 1000$. The very low value of Q , e.g., $Q = 1$, is included in our study to show the trend of multipactor in a non-resonant structure — one that is relatively immune to beam loading, such as a window. In all of these runs, we fix the peak rf gap voltage at a value of 0.3 prior to $t = 0$. The fraction of rf power consumed by the multipactor, $\langle -V_g I_m \rangle / \langle V_g I_d \rangle$, is shown in Fig. 3b. Here $\langle \rangle$ denotes the average over the transit time of an electron. Note that in a high Q cavity, transiently, the multipactor current may reach a level higher than the drive current I_d [Fig. 3a], and at the same time draw much of the power provided by the external source [Fig. 3b]. Alternatively, the rf energy stored in a high Q cavity is capable of driving the multipactor current to a large amplitude when the condition becomes favorable. In this regard, it is interesting to recall the well-known fact¹ that multipactor can deposit considerable energy into a tiny spot, and, as a result, causes significant damage to the surface.

The fact that the curves for the multipactor current [Fig. 3a] follow the corresponding ones for power dissipation [Fig. 3b] suggests that a multipactor discharge

behaves a lot more resistively than reactively, even during its nonlinear, transient interaction with the rf circuit. Note, however, that the equivalent resistance is a function of time, since the multipactor current may change over a wide range, as shown in the $Q = 1000$ case in Fig. 3a, while the gap voltage remains relatively constant during the buildup of the multipactor current [Fig. 4a]. For each curve displayed in Fig. 3, a steady state is indeed reached after a sufficiently long time (longer than that shown in Fig. 3 for the $Q = 100$ and $Q = 1000$ cases). In these runs, regardless of the values of Q , the steady state multipactor current ranges between 5 to 10 per cent of the driver current. Thus, if 20 watts of rf power would be required to maintain a steady gap voltage on the order of 300 volts, the steady state multipactor would consume about 2-4 watts. However, for a high Q cavity, all 20 watts of the external power may transiently go to the multipactor. If the spatial extent of the multipactor region is very small, the power density delivered to the gap surface by the multipactor electrons could be very high.

Throughout the transient development of the multipactor, the peak rf gap voltage in each cycle changes relatively little, for either the $Q = 1$ case or the $Q = 1000$ case [Fig. 4a]. The secondary emission coefficient δ also stays around unity [Fig. 4b], in fact, in the vicinity of the first cross-over point (E_1) in Fig. 2. A simple physical argument shows that only the first cross-over point E_1 in Fig. 2 gives the stable steady state solution⁶. Our numerical results show that the impact energy indeed approaches E_1 asymptotically in time. We have spot-checked that the steady state values of the gap voltage, of the electron impact phase in the rf cycle, and of the surface charge density, are all in good agreement with those obtained from our analytic formulation⁷.

In the present formulation, multipactor affects its own evolution in two ways: through its "beam loading" of the cavity [described by I_m in Eq. (1)] and through the image space charge force [described by the last term in Eq. (2)]. It turns out that as long as $Q \gtrsim 10$, the beam loading effect is far more important than the space charge force in determining the saturation level of the multipactor current. The disparity of their relative importance becomes increasingly more pronounced as Q increases, as high Q cavities can be more readily loaded by a multipactor current. This also explains the sensitivity in the high Q cavities, as exhibited in Fig. 3. This figure gives the tantalizing clue that, in reality, the rf energy stored in high Q cavities may relax via a multipactor discharge, albeit transiently in time, and locally in space.

The single sheet model [Fig. 1] given above may readily extended to two electron sheets so as to investigate the effect of mutual interaction among the multipactor electrons⁴. We consider two electron sheets, of surface density σ_1 and σ_2 , located respectively at x_1 and x_2 inside a planar gap. Figures 5a and 6a exhibit the case where both sheets are launched with the same initial charge density, $\sigma_{01} = \sigma_{02}$, with sheet 1 launched slightly ahead of sheet 2 at time $t = 0$ (sheet 1 is leading). Figure 5a shows that although both sheets start out with almost the same impact energy and the same secondary electron yield, sheet 2 always has a lower yield. As the charge densities increase, beam loading sets in to reduce the secondary yields of both sheets to near unity (drop in gap voltage leads to lower impact energies). After some time, the repulsion by sheet 1 forces sheet 2 further and further away from the fixed phase, and the secondary yield for sheet 2 decreases below unity [Fig. 5a]. Figure 6a shows that σ_1 increases rapidly, while σ_2 increases at a slower rate, then drops. Eventually, the charge density σ_2 on sheet 2 becomes so low it can be ignored, and the model reduces to the single sheet model of Fig. 1. By the same token, a model consisting of N electron sheets (N large) will have its leading sheets growing faster than the trailing sheets, eventually quenching

them one-by-one, until only two sheets, then one, is left⁴. Thus, steady state multipactor, if it exists, may be adequately described by a single sheet to model the sharp bunch that is observed in the steady state⁹.

The above cannibalism mechanism is still operative even if the trailing sheet is initially much stronger than the leading sheet. In Figs. 5b and 6b, the trailing sheet 2 is launched with 50 times the initial charge density of the leading sheet 1. Although the charge density on sheet 2 grows to a relatively high level for some time, sheet 1 dominates in the end. This arises as the yield for sheet 2 is forced to be below unity [Fig. 5b], and σ_2 rapidly diminishes [Fig. 6b]. Hence the above process of cannibalism holds, regardless of initial conditions⁸. These features are also observed for δ_{\max} [Fig. 2] as high as 5. Note however that the initial conditions and space charge forces do affect the timing of the multipactor. A slab of a finite width may reach the steady state more rapidly than a single, infinitesimally thin sheet.

The above rudimentary analysis provides only some quantifications on the temporal evolution of multipactor. Other theoretical issues involving the accessibility of the steady state multipactor solutions and the possible conversions from the first order to higher order multipactors are addressed elsewhere⁷. It must also be remembered that multipactor is known to depend a great deal on the geometry, on the processing and conditioning of the rf structure, on the cleanliness and condition of the surface, on the duration and power level of the rf pulse, and on the external magnetic field, etc. Nevertheless, our simple model does yield the following conclusions: (a) Steady state multipactor discharge occurs when the rf voltage is of the order of the first cross-over energy (E_1 , in Fig. 2), confirming the prevailing notion that multipactor is a low to medium voltage phenomenon. (b) It saturates in an rf cavity as a result of loading; the space charge force of the multipacting electrons is insignificant to alter the phase condition or the saturation condition whenever $Q \gtrsim 10$. (c) The rf energy stored in a high-Q cavity may lead to a large build-up of multipactor current in a transient manner. (d) There are two phase focusing mechanisms in multipactor - one described in by Vaughan and Riyopoulos et al. and the other one described above. These phase focusing mechanisms may shape the steady state multipactor in the form of a very tight bunch⁴. (e) The peak gap voltage need not be appreciably reduced during the buildup of the multipactor current.

We have benefited from many useful conversations with Spilios Riyopoulos. This work was supported by NRL/ONR, MURI, and NSWC/CRANE.

References

1. J. R. M. Vaughan, IEEE Trans. ED-35, 1172 (1988).
2. S. Riyopoulos, D. Chernin, and D. Dialetis, Phys. Plasmas 2, 3194 (1995).
3. R. Kishek and Y. Y. Lau, Phys. Rev. Lett. 75, 1218 (1995).
4. R. Kishek and Y. Y. Lau, Phys. Plasmas 3, 1481 (1996).
5. It is shown by Riyopoulos et al [Ref. 2] that the inclusion of the initial velocity of the secondary electrons does not qualitatively change their steady state solutions.
6. If the impact energy E_i is greater (less) than the first cross-over point E_1 , more (fewer) electrons will be released by secondary emission. As a result, more (less) energy will be drained from the cavity as it accelerates more (fewer) secondary

electrons. This leads to a lower (higher) gap voltage which makes E_i closer to E_1 in subsequent cycles. Thus E_1 is a stable steady state solution. A similar argument shows that the second cross-over point, E_2 in Fig. 2, is unstable.

7. R. Kishek, D. Chernin, and Y. Y. Lau, Phys. Plasmas, to be published (1996).
8. A spread in the emission velocities of the secondary electrons, and the time delays in secondary emission, may weaken (or even destroy in extreme cases) the phase focusing mechanism.

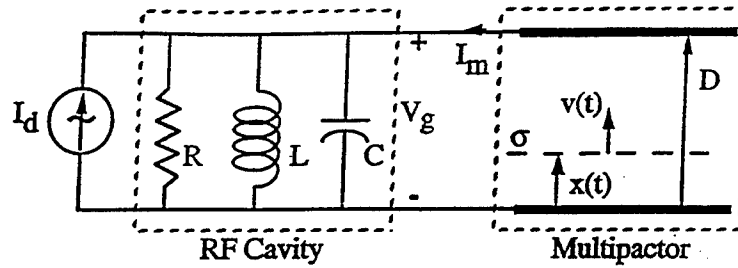


Fig. 1: Model of interaction between rf cavity and multipactor discharge.

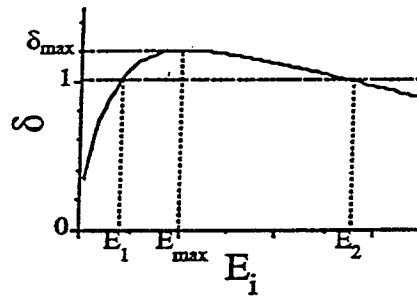


Fig. 2: Secondary electron yield, δ , as a function of impact energy E_i .

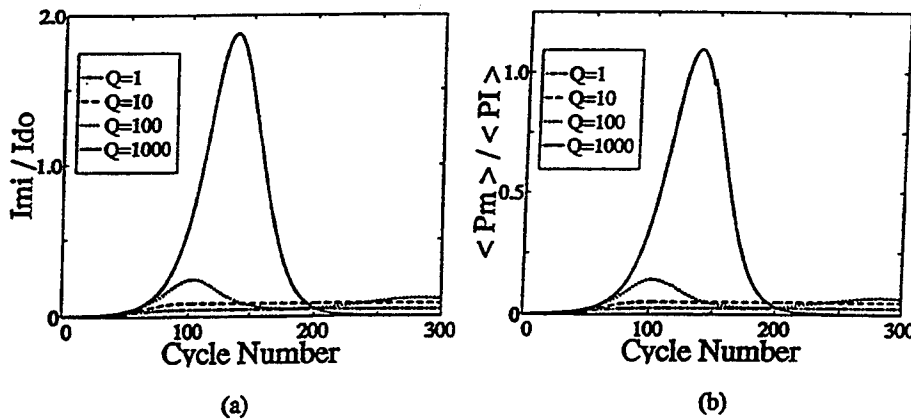


Fig. 3: (a) Transient evolution of multipactor current at impact, in units of the drive current amplitude I_{d0} , for various values of quality factor, Q .

(b) Time history of the power consumed by multipactor, in units of the input power, at various values of Q .

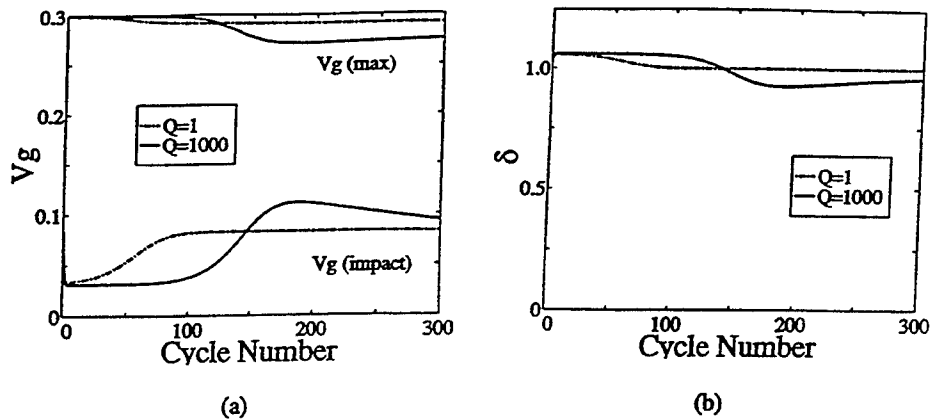


Fig. 4: (a) Evolution of the peak gap voltage, $V_g(\text{max})$, and of the gap voltage at the instant of electron impact, $V_g(\text{impact})$, for $Q = 1$ and $Q = 1000$.
(b) Evolution of the secondary electron yield, δ .

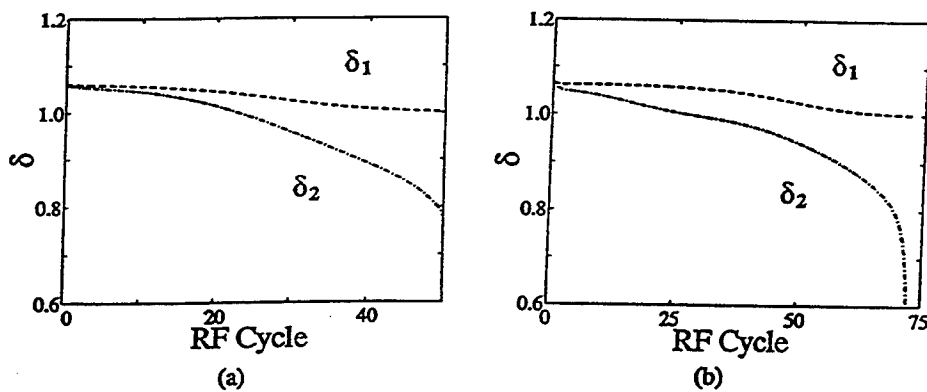


Fig 5: Secondary electron yield (δ_1 , δ_2) for sheets 1 and 2 as a function of time:
(a) $\sigma_{a2} = \sigma_{o1}$, (b) $\sigma_{a2} = 50 \sigma_{o1}$.

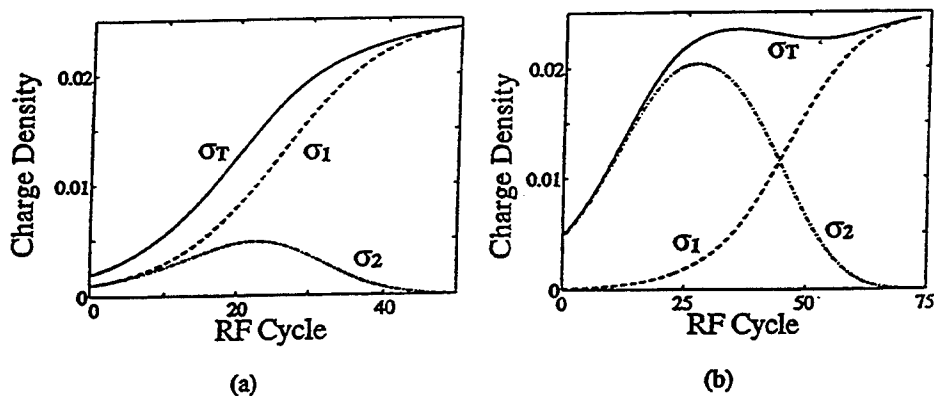


Fig 6: Charge density (σ_1 , σ_2) on sheets 1 and 2 and the total charge density $\sigma_T = \sigma_1 + \sigma_2$:
(a) $\sigma_{a2} = \sigma_{o1}$, (b) $\sigma_{a2} = 50 \sigma_{o1}$.

High-power microwave field measurements using Stark broadening

Thad J. Englert, Mike Haworth, Kyle Hendricks, F. Mark Lehr, and Donald Shiffler

Phillips Laboratory
Kirtland AFB, NM87117-6008

ABSTRACT

High power microwave sources driven by intense relativistic electron beams have been a subject of much research over the last decade. In the course of research upon the issues of RF breakdown, we have developed a diagnostic capable of measuring high RF power levels in high electric field regions. This diagnostic takes advantage of the RF Stark effect. To investigate the effect, a hydrogen-filled glass tube is placed in a region of high RF power. When an RF pulse impinges on the tube, the gas in the tube is excited. By spectral observations of the decay of the gas back to the ground state, the Stark splitting of the atomic states can be measured. This splitting is proportional to both the RF electric field amplitude and frequency. In this paper we present results from a series of experiments performed at the Phillips Laboratory on the relativistic klystron. Spectral measurements were performed in the near field of the radiating antenna using an optical multi-channel analyzer with a half-meter spectrograph. These experiments demonstrate that Stark broadening can be a useful diagnostic in high field environments.

Keywords: Stark effect, high-power microwaves

1. INTRODUCTION

Advances in the sophistication of pulsed microwave sources have increased power outputs significantly in the past decade. One of the problems incurred in such devices is the pulse shortening which is often associated with electrical breakdown induced by the large RF fields. The initial motivation of the work reported here was to identify the constituents of the plasma created during breakdown and to make estimates of the electric field associated with the breakdown. It is at best difficult to measure field amplitudes under these conditions without causing severe perturbations of the RF pulse due to the presence of the probe. Earlier works have dealt with the concept¹⁻³ of RF-induced broadening, which we have utilized in measurements of the hydrogen alpha (H_α) line (6562.8 angstroms) to infer the electric field strength in RF discharges. Although more susceptible to broadening, the hydrogen beta (H_β) line (4861.3 angstroms) is much less intense and does not provide adequate signal-to-noise in these experiments. In this paper, we describe the experimental technique and present data and modeling for RF-modulated Stark broadening.

2. EXPERIMENTAL ARRANGEMENT

A simple, commercially available, hydrogen Geisler tube is allowed to reside in the RF field environment. The capillary section of the tube is nominally 15 cm long and the over-all length is 20 cm with electrodes at both ends. Alignment of the Geisler tube was parallel to the RF electric field. Open shutter photographs showed no sign of arcing from the electrodes. Pressure in the tube is 0.5 milli Torr⁴. Some attempts at biasing the tube were made, however RF power was typically sufficiently high to cause the gas to glow without external bias. Grounding of one end of the tube was found to be beneficial, giving greater intensity in the emitted light. An optical fiber with a 100 micron silica core was used to transmit light to an Optical Multichannel Analyzer (OMA) system utilizing a pulsed vidicon detector. No focusing optics were used to launch light into the fiber whose numerical aperture is approximately 0.2. With the fiber tip placed in close proximity (a few millimeters) to the tube, the sampled region is small enough that field amplitude variations within the view should be negligible. Output light from the fiber was fed into a

half-meter spectrograph housing a grating with 1180 grooves/mm. Figure 1 depicts the experimental setup.

Careful measurements of the instrumental broadening were made using helium-neon laser light and H_{α} light from the unperturbed Geisler tube in situ. Pearson profiles were determined to give best fit for unperturbed lines by using commercially available spectroscopic software. Typical FWHM of the unperturbed line was ~ 1.5 - 2.0 angstroms. An unperturbed line is shown in a later section describing samples of acquired data.

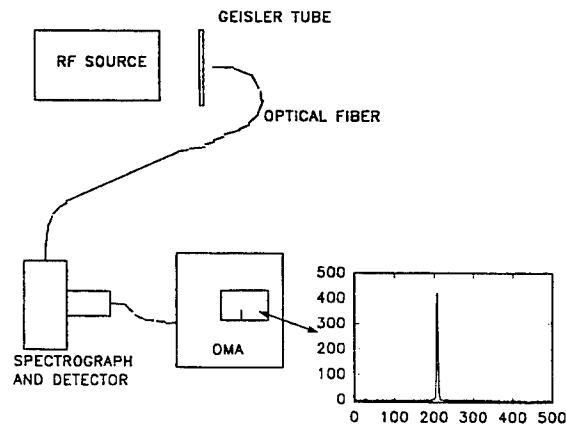


Figure 1. Diagram depicting experimental arrangement for data acquisition.

3. CALIBRATION AND EXPERIMENTAL DATA

For purposes of calibration, and to provide a controlled environment for comparison with theory, a waveguide was driven by a 5 MW magnetron, operating in the S-band at 2.7 GHz. The waveguide is designed with a half-taper to provide a maximum field of 27 kV/cm and the tube inserted at the apex of the taper so that the exposed length was parallel to the electric field. Power through the waveguide was monitored down stream and calibration measurements on the waveguide provided determination of absolute RF power. A qualitative appreciation of the broadening effect is seen in Figure 2 which shows typical broadened H_{α} lines and corresponding RF power in the waveguide. A linear fit of the full width at half maximum (FWHM) vs RF power gives $\text{FWHM} = 0.128P + 2.05$ angstroms. The fitted value of FWHM extrapolated to zero power is 2.0 angstroms which agrees with the measured FWHM of 1.97 angstroms for the unperturbed H_{α} line. Pearson profiles were used in all instances. Although the FWHM gives a qualitative indication of the broadening, it does not provide detailed information regarding the shape, nor the constituent peaks, of the wings.

Measurements were conducted on the Phillips Laboratory Annular Beam Amplifier (ABA)⁵ which operates at 1.27 GHz. Here the Geisler tube is placed 27 cm from the plane of the Vlasov antenna used on the ABA and parallel to the electric field. The dimensions of the RF radiation were such that the Geisler tube electrodes were exposed to the radiation near the edge of the pattern but no evidence of severe beam perturbation was noted. The beam divergence from the Vlasov antenna was measured to be $\pm 13^\circ$. Figure 3 shows the H_{α} line recorded during a shot which radiated approximately 500 MW for 100 ns. The profile seen here represents the average during the duration of the RF output, however we believe that significant light output from the Geisler tube does not occur until at, or near, peak RF power. Verification of this conjecture will be made at a later time by using a microchannel plate camera. Timing limitations on the OMA do not reliably allow for time windows shorter than 100 ns. For the L-band device, the RF pulse is on the order of 100 ns to 200 ns long. Although the modeling, described in a later section, does

not yet include the H_β line, it is of some interest to include a sample of the acquired spectrum. The data shown in Figure 4 were obtained by removing the slit from a quarter-meter spectrograph housing a 600/mm grating used early on in the project. The spectrograph was focused to image the bare fiber tip onto the OMA detector in order to gather more light since intensities were rather minimal at the outset.

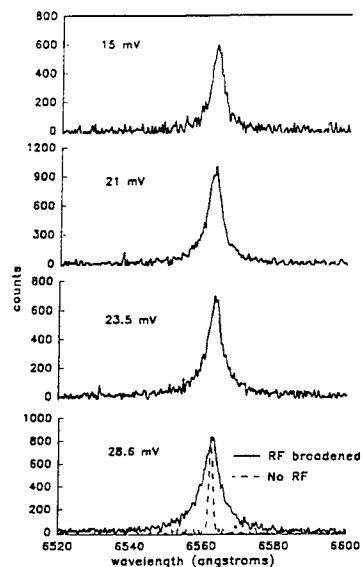


Figure 2. Series of spectra taken from Geisler tube placed in 2.7 GHz half-tapered waveguide showing increase in broadening of H_α line with RF power. Bottom trace shows unperturbed line superimposed on experimental data. Inset numbers show the RF power.

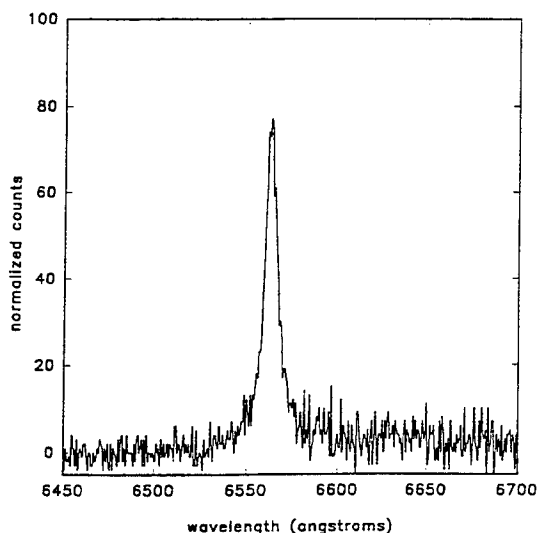


Figure 3. Typical H_α line recorded from Geisler tube in beam of ABA for 500 MW RF pulse.

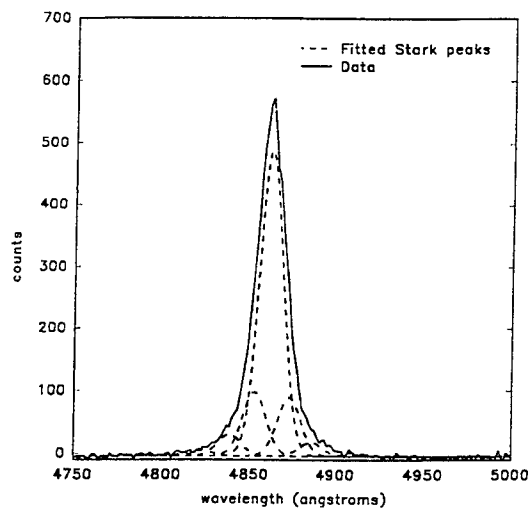


Figure 4. Broadened H_β line from Geisler tube in beam of ABA. Over lay shows set of satellites required to fit data.

Fitted constituent peaks shown are determined by assuming the overall profile is made up of Stark transitions and the shape of the peak for individual transitions determined by the instrumental broadening as measured from the unperturbed H_β line. Satellite structure symmetric about the central peak can be seen, even with the limited resolution provided with this coarse grating. The constituent peaks shown in Figure 4 are likely not an accurate representation of the satellites discussed in the next section, but give a qualitative appreciation of the structure of the wings.

4. MODELING AND COMPARISON WITH DATA

Use of the term "Stark effect", for the purposes described herein, may be somewhat misleading since the majority of past measurements based on the Stark effect have dealt with static or quasistatic fields⁶. The situation here requires the treatment of a quantum system (atom) emerged in a time varying field and, although the frequency of the perturbation is small compared to the frequency of the radiation emitted from the atom, the effect may be pronounced. The model used in the analysis of data presented here is based on the excellent works by E. Oks³. The solution of the Schrodinger equation for a hydrogen-like system, perturbed by a sinusoidal potential, results in the summation of Bessel functions of increasing order. The argument of the Bessel functions contains the ratio of the field amplitude to the perturbing field frequency (E_0/ω). Summation of the Bessel functions results in "satellite" peaks symmetrically located about the central line. Locations of the satellites, relative to the central line (ω_0), occur at integral multiples ($\omega_0 + p\omega$) of the perturbing field frequency. Satellite intensities, $I(p, \epsilon)$, are given by³

$$I(p, \epsilon) = [f_0 \delta_{p0} + 2 \sum_k f_k J_p^2(X_k \epsilon)] (f_0 + 2 \sum_k f_k)^{-1}, \quad (1)$$

where the summations are taken over the lateral Stark components, f_k is the intensity of the lateral Stark component, f_0 is the summation of the Stark intensities, $X_k = n(n_1 - n_2) - n'(n_1' - n_2')$ which are quantum numbers as described by Bethe and Salpeter⁷, and $\epsilon = (3\hbar E_0)/(4\pi m_e \omega)$. Total spectral intensity, calculated by the model, then becomes the summation of all calculated $I(p, \epsilon)$. Line shape and instrumental broadening is applied to each satellite, based on the assumption that Stark transitions have the same shape as the unperturbed line. The modeled spectrum is then generated by summing Pearson profiles whose amplitudes are given by Eq. 1 and whose Pearson coefficients are determined from the unperturbed line shape.

Our earliest attempts at modeling have used commercially available mathematical software and up to and including $J_{100}(X\epsilon)$. We now believe that higher order Bessel functions are necessary to adequately fit the data as may be seen in Figure 5. The data was acquired from the ABA experiment, which operates at a frequency of 1.27 GHz. Field calculations, based on the measured power output, give a peak field of $E_0 = 16.5$ V/cm. Figure 5 (a) shows the results of the 100th-order fit which clearly truncates and does not adequately fit the wings of the measured line. Figure 5 (b) shows the results of model fitting of the broadened line, the model contains 300 orders of Bessel functions and gives a best fit for $\epsilon = 23.8$. "Best fit" is determined by minimizing the sum of squares of the difference between experimentally acquired data and model values at each point of the normalized spectrum. Using the frequency of the perturbing field, 1.27 GHz, we obtain $E_0 = 16.1$ kV/cm, in good agreement with the calculated value noted above.

It remains to validate the technique by applying the model to the series of spectra shown in Figure 3, from the Geisler tube in the S-band, 2.7 GHz device. Commercially available mathematical software has been used but requires excessively long run times. Programming is in progress to alleviate this problem.

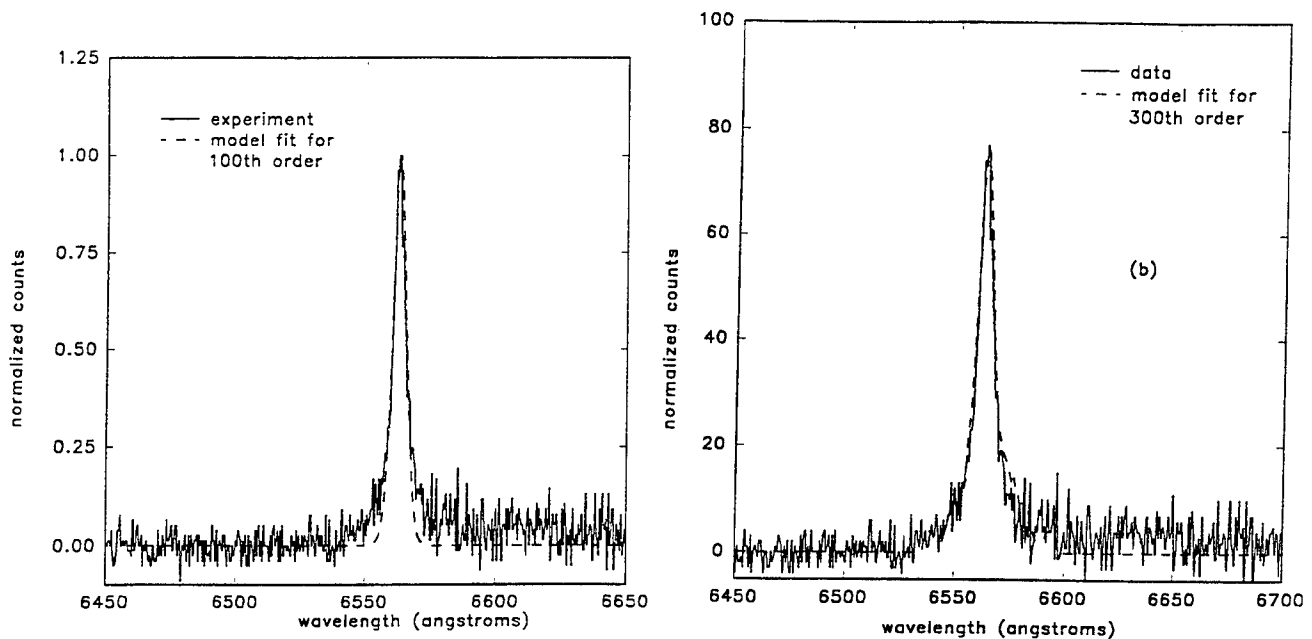


Figure 5. (a) Fit of model to broadened H_{α} line (Fig. 2) by using $J_0(X\epsilon)$ through $J_{100}(X\epsilon)$. Note truncation of model in the wings.
 (b) Fit of model to broadened H_{α} line (Fig. 2) by using $J_0(X\epsilon)$ through $J_{300}(X\epsilon)$. Fit gives 16.1 kV/cm for peak RF field.

5. CONCLUSIONS AND DISCUSSION

Agreement between the model and field calculations shows that the RF-modulated Stark model is a viable means of measuring the electric fields in high-power microwave radiation. Furthermore, the technique is relatively unobtrusive and requires inexpensive, "off-the-shelf" components for the probe. The accuracy of the fit between model and data is primarily dependent on the statistics of the counts, however, even signal-to-noise values of 10:1 are found to yield good results.

The question of Stark broadening contribution due to electrons should be considered briefly. Separate measurements were made on H_{α} and H_{β} lines, with conditions of RF output on the ABA apparatus nominally the same for each measurement. Figure 6 shows the spectrum, adjusted for detector response at the two central wavelengths. Electron temperature is estimated from the line intensity ratio⁶ to be $1.0 \text{ eV} < T_e < 1.5 \text{ eV}$. The gas pressure in the Geisler tube of 0.5 mTorr would at most yield $\sim 3 \times 10^{13}$ electron/cm³. At this temperature we would expect less than total ionization yielding a Stark broadening of the H_{α} line on the order of, or less than, 0.1 angstroms. Admittedly these estimates assume an equilibrium state which may not be entirely suitable for the experiments described here. It seems reasonable, however, to claim that Stark broadening due to plasma effects is negligible in these experiments.

Future work will include modeling the H_{β} line for RF-modulated Stark broadening and comparison with observation in those cases where adequate light intensity is available. Programming of the model for expeditiously obtaining fitted results is in progress. It would be especially convenient to be able to model broadening of spectral lines from elements present in breakdown arcs. In such instances it would not be necessary to introduce a "probe" which, in general, is difficult due to space limitations.

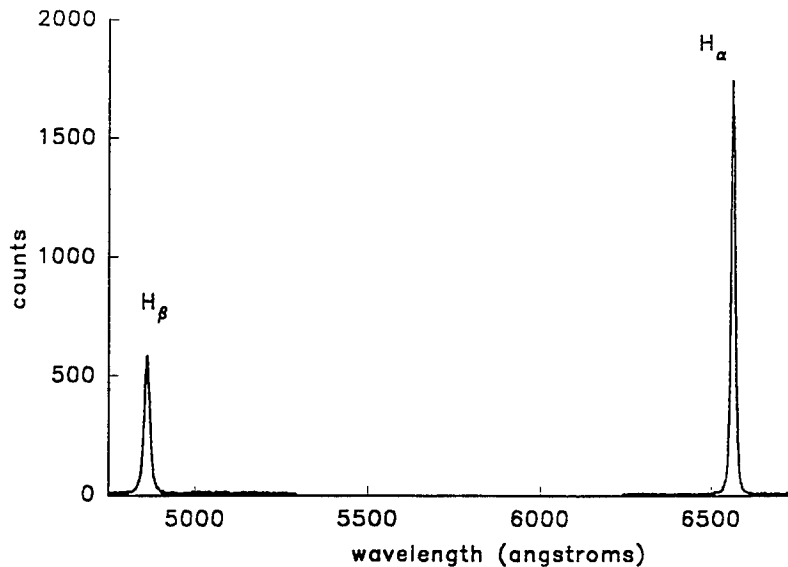


Figure 6. Spectra, corrected for detector response only, used to estimate electron temperature of the gas in the Geisler tube. This data was acquired by placing the tube in the ABA beam during a ~500MW RF pulse.

6. ACKNOWLEDGEMENTS

The authors wish to express their gratitude to Miguel Sena and Rudy Sedillo of Maxwell Labs for the technical support during these experiments, and to Sgt Vern Mimms and Sgt Ralph Peredo for retrieving the S-band transmitter from a remote site. Our gratitude is also extended to Dr. Tom Spencer for his assistance in design of the half-tapered waveguide. Special thanks is due to Dr. Kirk Hackett for the many fruitful discussions and constructive criticisms, and for not being too sceptical at the notion of using Bessel functions to 300th order.

7. REFERENCES

1. R.E. Shefer and G. Bekefi, Stark broadening by the intense electric field of a pulsed relativistic magnetron, *Phy. Fluids*, **22**, No. 8, pp 1584-1586, August, 1979.
2. A. Kamp and G. Himmel, *Appl. Phys. B*, **47**, 177 (1988).
3. E. Oks, *Plasma Spectroscopy: The Influence of Microwaves and Laser Fields*, Springer-Verlag, 1995.
4. Private communication, Edmund Scientific Company technical staff,
5. Kyle J. Hendricks, P. Dale Coleman, Raymond W. Lemke, J.J. Arman, and Les Bowers, Extraction of 1 GW of RF power from an injection locked relativistic klystron oscillator, *Phys. Rev. Lett.*, **76**, No. 1, pp 154-157, January, 1996.
6. Hans R. Griem, *Plasma Spectroscopy*, McGraw-Hill Book Company, 1964.
7. H.A. Bethe and E.E. Salpeter, *Quantum Mechanics of One- and Two-Electron Atoms*, Springer-Verlag, 1957.

A review of catastrophic electromagnetic breakdown for short pulse widths

Forrest J. Agee, David W. Scholfield, Richard P. Copeland and T. H. Martin

USAF Phillips Laboratory
High Energy Sources Division
Kirtland AFB, NM 87117

James J. Carroll

Youngstown State University
Department of Physics and Astronomy
Youngstown, OH 44555

John J. Mankowski, M. Kristiansen, and Lynn L. Hatfield

Texas Tech University
Pulsed Power Laboratory
Department of Electrical Engineering
Lubbock, TX 79409

ABSTRACT

This paper reviews the experimental research accomplished to date relating to catastrophic electromagnetic breakdown in certain media that are interesting for high voltage, short temporal pulse width pulsed. The authors begin with the classic work of Felsenthal and Proud and follow experimental results into the present day. The paper considers not only the experimental results of short pulse radio frequency breakdown but also the relationship with long pulse RF breakdown. The paper presents some recent measurements as well as reviewing the previous work performed in our laboratories and elsewhere.

KEYWORDS

1. Electrical breakdown, 2. RF breakdown, 3. High-power microwave, 4. Short pulse ultra-wide band, 5. Electrical discharge

1. INTRODUCTION

The research and development of novel sources of ultra-wideband RF radiation has made substantial progress over the past thirty years. The technology was driven in the 1960s and 1970s by interest in the simulation of nuclear electromagnetic pulse effects. The focus in those days was the radiation of electromagnetic pulses with rise times of the order of 5 - 10 ns and pulse widths of the order of 600 ns. Clever designs for simulators evolved at Physics International, Maxwell Laboratories, Air Force Weapons Laboratory, Harry Diamond Laboratories, and elsewhere that made specific use of the practical implications of the fact that the speed of light is about a foot per nanosecond, and pulsed power was advanced to deliver multi-megavolt pulses onto antenna structures without losing the rise time of the pulses. This required some equally clever designs to avoid flashover of the antenna feeds, within the pulser, and at the interface of the pulser, often filled with SF₆, and air.

The present interest in ultra-wide band emitters¹ is in a different temporal regime that corresponds to microwave frequencies rather than the HF to UHF frequencies characteristic of EMP. The higher frequencies contained in the pulses provide opportunities for applications that include novel radar systems to provide more information than just range and bearing. A side effect is that this development moves some of the same problems encountered earlier in pulser, antenna feeds, and antennas into a new parameter space in which there is relatively little published data on RF and electrical breakdown. Some of the new sources, including the Phillips Laboratory Hindenberg series of hydrogen gas switched pulsers have hydrogen at hundreds of atmospheres of pressure at the switch. These must be designed to transmit sub-nanosecond pulses to an antenna at atmospheric pressure without distortion of the pulse parameters, in particular the rise time of the pulse. A research effort is underway at the Phillips Laboratory and at a number of universities related to research problems in high power microwaves and sponsored by the Air Force Office of Scientific Research. This paper reviews the situation as we know it for RF and electrical breakdown in the short pulse regime characteristic of ultra-wide band high power microwave sources. We anticipate that the data in this regime will increase as the technology advances, and as other researchers become aware of our interest in it.

This paper is subdivided into two major sections. The first section presents empirical data of catastrophic electromagnetic breakdown in gases, liquids and solids. The majority of data on behavior in pulsed conditions is presently found to be for gases and liquids. The authors begin with the classic works of Felsenthal and Proud, and T. H. Martin and follows experimental results into present day for the gases and liquids typically considered in breakdown processes. The discussion presents some recent measurements as well as reviewing the previous work performed in our laboratories and a selection of that found elsewhere.

The second section briefly describes theoretical approaches and issues of experimental instrumentation. Included are discharge models in different media and diagnostic techniques such as capacitive probes.

2. CATASTROPHIC ELECTROMAGNETIC BREAKDOWN

2.1. Gasses

The archetype for studies of the breakdown behavior of gasses in the nanosecond regime is that of Felsenthal and Proud.² Their results are given in Fig. 1 for nitrogen and shows plots of the product of pressure and pulse duration (abscissa) versus the electromagnetic field normalized for pressure (ordinate). This graph is similar to the traditional Paschen Curve. The bottom-most curve of the figure extends from approximately 1×10^{-6} Torr-s to approximately 1×10^{-8} Torr-s. Additional investigations by later researchers tended towards monofrequency electromagnetic energy of increasingly higher frequency, and ever decreasing pulse length. This trend is represented in the figure by the experiments of Ali and Coffey³ as shown by the two midrange curves which extend from approximately 1×10^{-5} Torr-s to approximately 1×10^{-7} Torr-s. The upper-most curves represent Ali and Coffey's results for 10 GHz and 3 GHz microwaves in air, respectively. Generally, higher frequencies reside closer to the upper right-hand corner of Fig. 1, due to the effect of frequency on the calculation of the effective electric field.

Since the mid 80's there has been increasing emphasis on intense electromagnetic transient events. This has necessitated a reconsideration of the Paschen Curve, which has typically been utilized to summarize a monofrequency perspective. Electromagnetic transient events of sufficiently short length have bandwidths which make selection of a single frequency for generation of the Paschen Curve problematic, at best. This issue was addressed by one of these authors⁴ with a theoretical derivation and experimental confirmation of a Paschen Curve suitable for consideration of a nanosecond electromagnetic transient in nitrogen. That work is also represented in Fig. 1 as the curve which begins at 1×10^{-5} Torr-s, traverses to 1×10^{-9} Torr-s, and then proceeds vertically. The rotated square symbols annotate the experimentally obtained data. Classical theory and experimental data suggest that a collisional frequency limit exists at approximately 1×10^{-9} Torr-s. The results of the investigation imply that an intense electromagnetic pulse of arbitrary magnitude may be transmitted through a gaseous medium without breakdown occurring if the parameter of the pulse length multiplied by the pressure does not exceed 1×10^{-9} Torr-s.

Another of these authors⁵ has developed a macroscopic gas breakdown relationship which estimates the breakdown threshold independent of the species of gas being investigated. This relationship is shown in Fig. 2 which gives a plot of the product of density and pulse duration (abscissa) versus the electromagnetic field normalized for

density (ordinate). The legend describes the investigations of Felsenthal and Proud ² (F&P), Wells and Martin ⁶ (W&M), Martin ⁷ (JCM-AIR), Udo ⁸ (UDO-AIR), Guenther ⁹ (P&G LTS N/A) and Martin ¹⁰ (SHKUROPAT).

Additional data have recently been reported by Mankowski. ¹¹ Figure 3 shows normalized breakdown vs. the product of gas density and breakdown time for various gasses. Unlike the low pressures in the work of Fig. 2, gas pressures as high as 2,000 PSI were examined.

2.2. Fluids

The macroscopic gas breakdown relationship developed by T. H. Martin has been applied to transformer oil data by J. Wells. ¹² As opposed to the Paschen Curve for gases shown in Fig. 2, in Fig. 4 the density of the oil has been removed from both the abscissa and the ordinate. This was done because the density represented a constant. As noted in the legend, the solid line represents the calculated breakdown of oil based upon the work of T. H. Martin in gaseous media, the diamond symbol represents an accumulation of Sandia National Laboratory oil breakdown data acquired through out their years of pulsed power experiments, the dashed curve represents oil breakdown data acquired utilizing the Phoenix pulser at the Phillips Laboratory, and the plus symbol represents a datum obtained by Zheltov. ¹³ The square symbol represents the experimental results obtained by the Hindenberg Device Group for oil breakdown. There is a pronounced deviation from the macroscopic relationship developed by T. H. Martin beginning at the nanosecond region of Fig. 4. This is indicative of a region in which a different set of physical properties dominate.

Breakdown strength of transformer oil in the one to hundreds of nanosecond regime has been reported by Vorobyov. ¹⁴ The experimental setup consisted of a breakdown gap between two spherical electrodes. A rectangular pulse voltage of 0.2 - 1 MV was applied for 3 to 300 ns. Other data on the transformer oil breakdown have been gathered by Zheltov. ¹³ These data were obtained with bell-shaped voltage pulses with amplitudes ranging from 0.4 - 1.4 MV and risetimes of 1.5 - 7 ns. The results of these two groups are shown in Fig. 5. Notice that the electric field breakdown strength versus time to breakdown is linear in two regions, between 1.5 - 6 ns and greater than 6 ns. In the region of 1.5 - 6 ns, the breakdown strength increases approximately 2.5 times with a 10 times decrease in exposure to the applied voltage. It is the breakdown time region less than 6 ns that is of interest.

Recent data on liquid dielectric breakdown has been reported by Mankowski. ¹⁵ Liquids under investigation were filtered and unfiltered transformer oil, castor oil, and freon 12. The setup consisted of a 250 kV, 1 ns risetime, 4 ns pulsewidth delivered to a gap consisting of hemispherical electrodes all in a coaxial geometry. Figure 6 shows the findings for peak electric field versus time to breakdown for these four liquids. The clean

transformer oil is filtered down to 1 micron particles. An improvement in breakdown performance of the filtered transformer oil versus the unfiltered is obvious from the figure.

2.3 Solids

The dielectric properties and breakdown characteristics of a wide range of solid materials have been studied for many years. However, the vast majority of that work was conducted in either the DC regime or for pulses having durations in the microsecond range or longer. Recently, attention has focused on the behavior of solid dielectric materials when subjected to short-duration pulses. Harjes¹⁶ discusses the possibility of employing laminates of solid dielectric materials in magnetic switches. Such materials include Mylar, polycarbonate (Lexan), Kapton etc. The issues primarily addressed in that work concentrate on deposition and coating techniques and the management of heat production within the laminates during switch operation.

Yamada and Fujiwara¹⁷ have developed an instrument designed for low-noise measurements of pre-breakdown currents in liquid or solid dielectric materials. The goal was to provide time-resolved precision data sufficient to serve as the basis for new theoretical approaches. Rectangular voltage pulses with magnitudes ranging from 30 - 50 kV were used in that work. The rise time of the pulses was 20 ns and the pulse width was 760 ns. In the work of Ref. 16 materials tested using this technique included polymethylmethacrylate (PMMA). The data indicated a substantial delay in the appearance of pre-breakdown current on the order of 20 ns after the arrival of the voltage pulse, and a delay of 740 ns from arrival to total breakdown. Those authors extended the studies¹⁸ to polypropylene and found a similar behavior to that observed for liquid nitrogen as a calibrator.

3. MISCELLANEOUS ISSUES

3.1. Instrumentation diagnostic considerations

Pulses in the nanosecond regime and with amplitudes of hundreds of kilovolts to several megavolts along transmission lines require measurement with the help of wide-band dividers. The characteristics of such dividers are attenuation levels of up to -100 dB and a bandwidth of several gigahertz with a smooth passband. The primary type of divider used is the capacitive divider. Another requirement is a wide bandwidth transient recorder. The type presently in use have bandwidths of up to 4.5 GHz. As pulse risetimes shorten to less than a hundred picoseconds, wider bandwidth recorders will become necessary. These diagnostic techniques were employed in the work of Refs. 11 and 15.

3.2. Theoretical approaches

The area of theory is greatly lacking regarding the breakdown of dielectric materials due to nanosecond pulses. An empirical approach of considerable utility is that Martin.¹⁰ mentioned previously. Another theory was suggested by Leiker¹⁹. The latter approach was proposed to explain the small numbers of secondary electrons measured at the interface between dielectric materials and metals. Pulse lengths of several microsecond were employed in that work. Solid dielectrics employed included Lexan, Lucite, polyethylene, Macor, quartz, alumina and an alumina epoxy. The theory considers a loss of secondary electrons at the interface due to collisions which delays the breakdown of the dielectric by retarding the pre-breakdown current. However, as other authors have pointed out, there remains no commonly accepted theory which permits a widely applicable explanation of the breakdown process for solids.

4. CONCLUSIONS

The above brief review demonstrates the need for improved models and new experiments to understand the breakdown characteristics of dielectric materials when subjected to high-voltages pulses of nanosecond and smaller pulsewidth. This information is needed by those seeking to advance the art in ultra-wide band sources of RF energy. The Phillips Laboratory and Texas Tech University have a substantial interest and activity in this area of research.

5. REFERENCES

1. F. J. Agee, D. W. Scholfield, W. Prather, J. W. Berger, "Powerful Ultra-wide Band RF Emitters: Status and Challenges," Proc. SPIE 2557, 98 (1985).
2. P. Felsenthal and J. M. Proud, "Nanosecond Pulse Breakdown in Gasses," 139, 1796 (1965).
3. A. W. Ali and T. Coffey, Naval Research Laboratory Memorandum No. 4320, (1980) unpublished.
4. D. W. Scholfield, J. M. Gahl, and B. W. Mullins, "Investigation of the Paschen Curve of Nitrogen via the Application of Nanosecond Pulsed Electromagnetic Radiation," J. Appl. Phys. 76, 1469 (1994).
5. T. H. Martin, "A Macroscopic Gas Breakdown Relationship," in Gaseous Dielectrics VI, (Plenum, New York, 1991) p. 349.
6. J. Wells, M.S. Thesis in Electrical Engineering, Univ. of New Mexico (1987) unpublished.
7. J. C. Martin, "Dielectric Strength Notes," 15, 1967. First printed as SSWA/JCM/697/71, AWE internal publication.
8. T. Udo, IEEE Trans. Power Apparatus and Systems, PAS-84, 304 (1965).
9. A. H. Guenther, J Phys. D: Appl. Phys. 11, 1577 (1978).
10. T. H. Martin, "An Empirical Formula for Gas Switch Breakdown Delay," Proceedings of the 7th IEEE Pulsed Power Conference, Monterey, CA. 1989. IEEE Catalog Number 89CH2678-2, p. 73.
11. J. J. Mankowski, M. Kristiansen and L. Hatfield, "High voltage gas breakdown at nanosecond pulsewidths," Proceedings of AMEREM '96, May 27, 1996, Albuquerque, NM.
12. J. Wells, J. Eggbert, M. Usher, and R. Copeland, "Development of a Low Loss Liquid Load Solution for Termination of High Power Broadband Pulses," Proceedings of the AMEREM 1996, May 27, 1996, Albuquerque, NM.
13. K. A. Zheltov, "Picosecond High Current Electron Accelerators," in *Energoatomizadat* (Moscow, 1991).

14. A. A. Vorobyov, V. Ya. Ushakov and V. V. Bagin, "Electrical strength of liquid dielectrics at voltage pulses of a nanosecond duration," *Electrotechnika* 7 (1971).
15. J. Mankowski, M. Kristiansen and L. Hatfield, "Nanosecond breakdown of liquid dielectrics," Proceedings of BEAMS '96, June 3, 1996, Prague, Czech Republic.
16. M. C. Harjes, D. J. Sharp, G. A. Mann, F. A. Morgan and W. C. Yelton, "Investigations into the use of dielectric coatings in magnetic switches," Sandia National Laboratory Report SAND-90-0415C (1990).
17. H. Yamada and T. Fujiwara, "Low-noise high-response pre-breakdown current measurement system," *Rev. Sci. Instrum.* 64, 3641 (1993).
18. H. Yamada, T. Fujiwara and Y. Suzuoki, "Electrical breakdown time delay and breakdown propagation velocity in polypropylene under a highly non-uniform field condition," *J. Phys. D: Appl. Phys.* 26, 3128 (1993).
19. G. R. Leiker, Ph.D. Thesis, Texas Tech University (1988) unpublished.

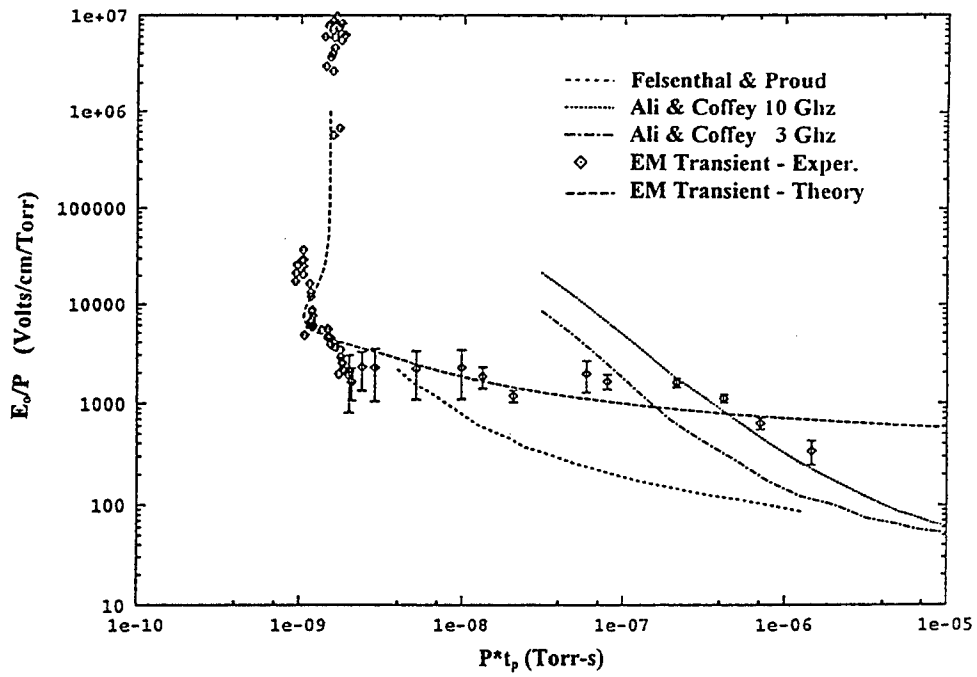


Figure 1. Gaseous Paschen Curves normalized for pressure.

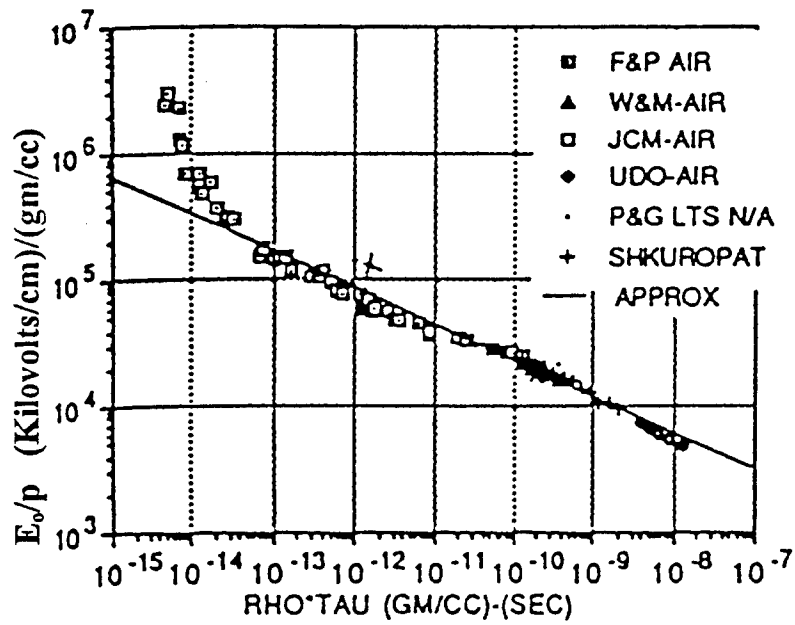


Figure 2. Gaseous Paschen Curves normalized for density

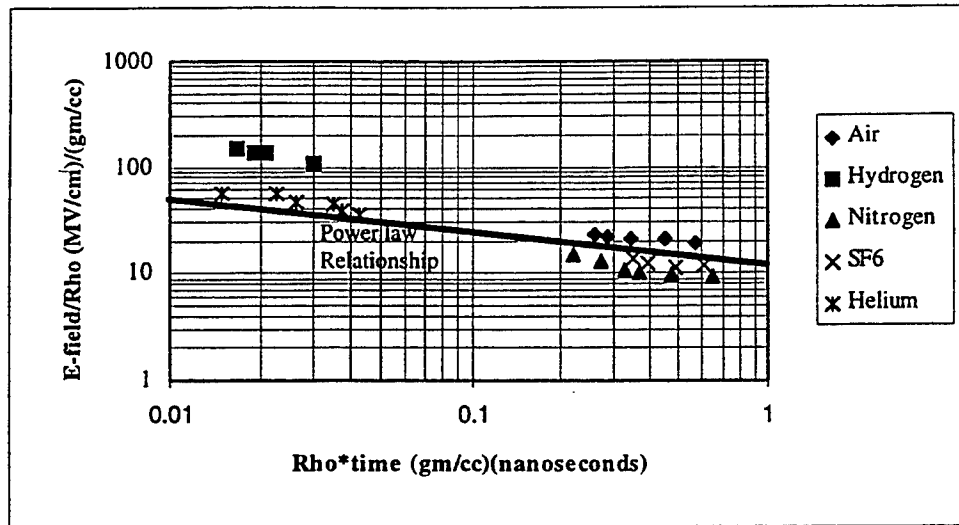


Figure 3. Time-averaged E field vs. time to breakdown with gas density scaling.

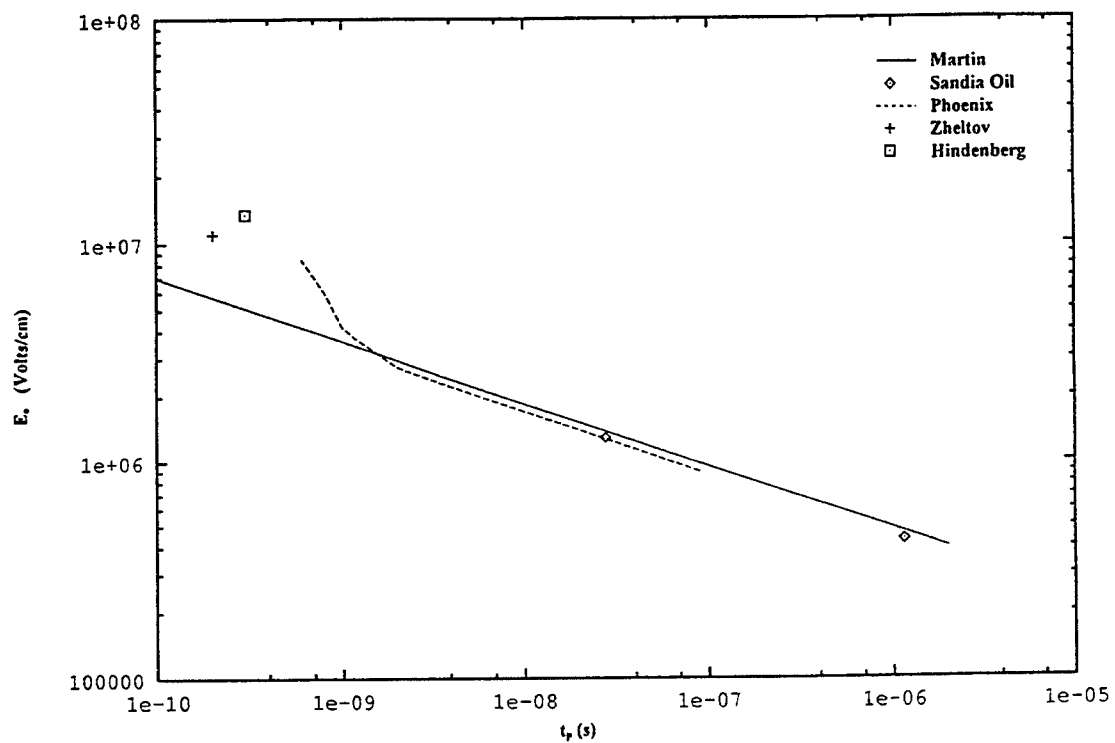


Figure 4. Oil breakdown curves.

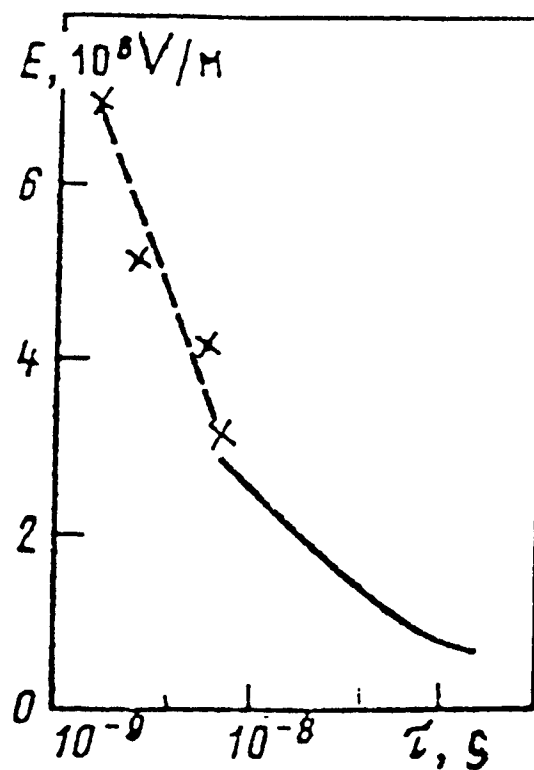


Figure 5. Dependence of electric field strength of transformer oil on the time of action of the voltage.

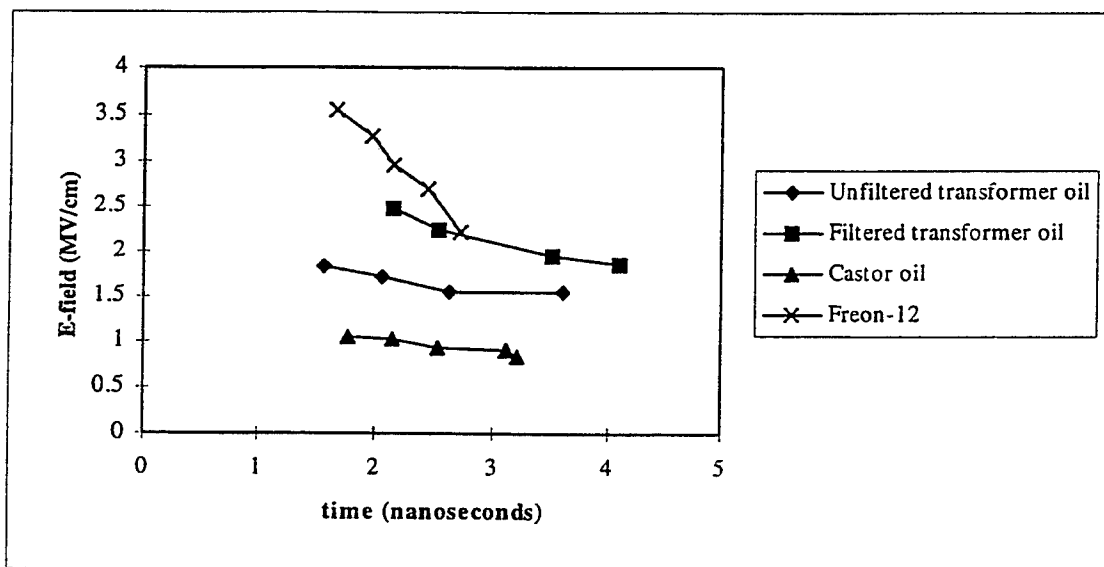


Figure 6. Time-averaged E field vs. time to breakdown for various liquid dielectrics.

Dependence of drift length on cavity gap voltage in a space-charge-dominated klystron amplifier

Howard E. Brandt

Army Research Laboratory, Adelphi, MD 20783-1197

ABSTRACT

Recently, an expression was obtained for the drift distance to the point of maximum current modulation in a space-charge-dominated klystron amplifier. An explicit dependence on gap voltage was obtained. In the present work, we show in detail how this expression results from the solution to an appropriate cubic equation. We also verify that the solution satisfies the well-known extreme space-charge limit.

Keywords: klystron amplifiers, microwave sources, current modulation, electron beams

1. INTRODUCTION

For a relativistic klystron amplifier with a space-charge-dominated beam, the drift distance from the modulating gap of the buncher cavity to the point of maximum current modulation is approximated by^{1,2}

$$z = \frac{\beta_b mc^3 \gamma_b (\gamma_b^2 - 1)}{e\omega(\Delta\phi)} \xi, \quad (1)$$

where the normalized drift distance ξ satisfies the cubic equation

$$\xi^3 + \frac{3}{4} \xi^2 - \kappa = 0. \quad (2)$$

Here β_b is the ratio to the velocity of light c of the beam entering the gap, m is the rest mass of the electron, e is the charge of the electron, ω is the cavity driving frequency arising from the rf input into the buncher cavity, and $\Delta\phi$ is the maximum voltage across the gap of the buncher cavity. Also,

$$\gamma_b = (1 - \beta_b^2)^{-\frac{1}{2}}, \quad (3)$$

and

$$\kappa = \frac{3\gamma_b}{2(\gamma_b^2 - 1)S} \left(\frac{e\Delta\phi}{mc^2} \right)^2, \quad (4)$$

where

$$S = 2\nu[1/4 + \ln(R_c/\bar{a})], \quad (5)$$

in which ν is Budker's parameter, \bar{a} is the beam radius, and R_c is the radius of the drift tube downstream from the buncher cavity. To obtain an explicit expression for the drift length, we must solve the cubic equation, Eq. (2), and substitute the solution ξ in Eq. (1). The result was simply stated without proof in Refs. 1 and 2. In the present work we show in detail how the drift length results from the solution to the cubic equation (2), and also that the solution satisfies the known extreme space-charge limit.

2. ROOTS OF GENERIC CUBIC EQUATION

For a generic cubic equation,

$$y^3 + py^2 + qy + r = 0 \quad , \quad (6)$$

in which p , q , and r are constants, the solution is obtained as follows.³ By substituting for y the value,

$$y = x - p/3 \quad , \quad (7)$$

we transform Eq. (6) into

$$x^3 + ax + b = 0 \quad , \quad (8)$$

where

$$a = \frac{1}{3}(3q - p^2) \quad , \quad (9)$$

and

$$b = \frac{1}{27}(2p^3 - 9pq + 27r) \quad . \quad (10)$$

The three complex solutions to Eq. (8) are given by

$$x = A + B \quad , \quad (11)$$

$$x_+ = -\frac{1}{2}(A + B) + \frac{1}{2}(A - B)\sqrt{-3} \quad , \quad (12)$$

$$x_- = -\frac{1}{2}(A + B) - \frac{1}{2}(A - B)\sqrt{-3} \quad , \quad (13)$$

where

$$A = (-b/2 + (b^2/4 + a^3/27)^{1/2})^{1/3} \quad , \quad (14)$$

and

$$B = (-b/2 - (b^2/4 + a^3/27)^{1/2})^{1/3} \quad . \quad (15)$$

If $(b^2/4 + a^3/27) > 0$, there is one real root, and two conjugate imaginary roots. If $(b^2/4 + a^3/27) = 0$, there are three real roots, of which at least two are equal. If $(b^2/4 + a^3/27) < 0$, there are three unequal real roots.

3. SOLVING FOR THE DRIFT LENGTH

We proceed to solve Eq. (2) by using Eqs. (6)-(15). Comparing Eqs. (2) and (6), we identify

$$p = 3/4 \quad , \quad q = 0 \quad , \quad r = -\kappa \quad , \quad (16)$$

and possible solutions to Eq. (2) then follow from Eqs. (7), (11)-(15), namely,

$$\xi = \begin{cases} x - p/3 = x - 1/4 \\ x_+ - 1/4 \\ x_- - 1/4 \end{cases} \quad . \quad (17)$$

Using Eqs. (9), (10), and (16), we obtain

$$a = -3/16 \quad (18)$$

and

$$b = 1/32 - \kappa \quad (19)$$

and therefore

$$b^2/4 + a^3/27 = -(1/16 - \kappa)\kappa/4 \quad (20)$$

For $\kappa < 1/16$, Eq. (20) yields $(b^2/4 + a^3/27) < 0$, and there are three real and unequal roots given by Eqs. (11)-(13). Substituting Eqs. (9) and (10) in Eqs. (14) and (15), one obtains

$$A = (\kappa/2 - 1/64 + i[(1/16 - \kappa)\kappa/4]^{1/2})^{1/3} \quad (21)$$

and

$$B = A^* \quad (22)$$

where A^* denotes the complex conjugate of A . Then substituting Eqs. (21) and (22) in Eqs. (11)-(13), one obtains

$$x = A + A^* = 2\operatorname{Re} A \quad (23)$$

and

$$x_{\pm} = -\operatorname{Re} A \mp \sqrt{3}\operatorname{Im} A \quad (24)$$

We next define the quantity

$$z_0 \equiv (\kappa/2 - 1/64) + i((1/16 - \kappa)\kappa/4)^{1/2} \quad (25)$$

appearing in Eq. (21). Then Eq.(21) becomes

$$A = z_0^{1/3} \quad (26)$$

We next write z_0 in terms of its amplitude $|z_0|$ and phase ϕ_0 , namely,

$$z_0 \equiv |z_0|e^{i\phi_0} \quad (27)$$

where

$$|z_0| = [(\operatorname{Re} z_0)^2 + (\operatorname{Im} z_0)^2]^{1/2} \quad (28)$$

and

$$\phi = \tan^{-1}(\operatorname{Im} z_0/\operatorname{Re} z_0) \quad (29)$$

If we use Eq. (25) in Eqs. (28) and (29), it follows that

$$|z_0| = 1/64 \quad (30)$$

$$\phi_0 = \tan^{-1}\{8[\kappa(1 - 16\kappa)]^{1/2}/(32\kappa - 1)\} \quad (31)$$

and Eq. (27) becomes

$$z_0 = \frac{1}{64} \exp \left[i \tan^{-1} \{ 8[\kappa(1 - 16\kappa)]^{\frac{1}{2}} / (32\kappa - 1) \} \right] . \quad (32)$$

Here it is to be understood that the value of the inverse tangent ranges between 0 and π . Next, substituting Eq. (32) in Eq. (26), we obtain

$$A = \frac{1}{4} \exp \left[\frac{i}{3} \tan^{-1} \{ 8[\kappa(1 - 16\kappa)]^{\frac{1}{2}} / (32\kappa - 1) \} \right] . \quad (33)$$

If we substitute Eq. (33) in Eq. (23), the latter becomes

$$x = \frac{1}{2} \cos \left[\frac{1}{3} \tan^{-1} \{ 8[\kappa(1 - 16\kappa)]^{\frac{1}{2}} / (32\kappa - 1) \} \right] , \quad (34)$$

and Eqs. (34) and (17) yield

$$\xi = \frac{1}{2} \cos \left[\frac{1}{3} \tan^{-1} \{ 8[\kappa(1 - 16\kappa)]^{\frac{1}{2}} / (32\kappa - 1) \} \right] - \frac{1}{4} , \quad \kappa \leq 1/16. \quad (35)$$

For $\kappa = 1/16$, Eq. (35) reduces as follows:

$$\xi|_{\kappa=1/16} = \frac{1}{2} \cos \left[\frac{1}{3} \tan^{-1} 0 \right] - \frac{1}{4} = \frac{1}{2} \cos(0) - \frac{1}{4} = \frac{1}{4} . \quad (36)$$

The remaining two roots corresponding to x_+ and x_- for $\kappa \leq 1/16$ are real but result in negative values for z , and since we are interested only in a positive drift length, we ignore those roots.

In the extreme space-charge limit (large Budker's parameter), one has, according to Eqs. (4) and (5), $\kappa \rightarrow 0$, and Eq. (35) becomes

$$\xi \approx \frac{1}{2} \cos \left[\frac{1}{3} \tan^{-1} (-8\kappa^{\frac{1}{2}}) \right] - \frac{1}{4} = \frac{1}{2} \cos \left[\frac{1}{3} (\pi - 8\kappa^{\frac{1}{2}}) \right] - \frac{1}{4} . \quad (37)$$

If we use the trigonometric identity for the cosine of the sum of two angles, Eq. (37) becomes

$$\xi = \frac{1}{2} [\cos(\pi/3)\cos(8\kappa^{\frac{1}{2}}/3) + \sin(\pi/3)\sin(8\kappa^{\frac{1}{2}}/3)] - \frac{1}{4} . \quad (38)$$

Therefore, in the limit of $\kappa \rightarrow 0$, one obtains

$$\xi \xrightarrow{\kappa \rightarrow 0} \frac{2\sqrt{3}}{3} \kappa^{\frac{1}{2}} . \quad (39)$$

Substituting Eqs. (4) and (39) in Eq. (1), one obtains in the extreme space-charge limit,

$$z \xrightarrow{\kappa \rightarrow 0} \frac{\beta_{bc}}{\omega} [2\gamma_b^3 (\gamma_b^2 - 1)/S]^{\frac{1}{2}} . \quad (40)$$

Equation (40) is the known expression for the klystron drift length in the case of an extreme space-charge-dominated klystron.⁴

We next consider the case $\kappa > 1/16$, for which, according to Eq. (20), one has $(b^2/4 + a^3/27) > 0$, and there is one real root and two conjugate imaginary roots. Then Eqs. (14) and (15) become

$$A = \frac{1}{4} \{32\kappa - 1 + 8[\kappa(16\kappa - 1)]^{\frac{1}{2}}\}^{\frac{1}{3}}, \quad (41)$$

$$B = \frac{1}{4} \{32\kappa - 1 - 8[\kappa(16\kappa - 1)]^{\frac{1}{2}}\}^{\frac{1}{3}}. \quad (42)$$

In this case, the only real root is given by Eqs. (11) and (17), namely,

$$\xi = \frac{1}{4} \left[\{32\kappa - 1 + 8[\kappa(16\kappa - 1)]^{\frac{1}{2}}\}^{\frac{1}{3}} + \{32\kappa - 1 - 8[\kappa(16\kappa - 1)]^{\frac{1}{2}}\}^{\frac{1}{3}} - 1 \right], \quad \kappa \geq 1/16. \quad (43)$$

We note that

$$\xi|_{\kappa=1/16} = 1/4, \quad (44)$$

which agrees with Eq. (36), as it must.

Finally combining our solutions, Eqs. (35) and (43), with Eq. (1), we obtain

$$z = \frac{mc^3 \beta_b \gamma_b (\gamma_b^2 - 1)}{e\omega \Delta\phi} \begin{cases} \frac{1}{2} \cos \left[\frac{1}{3} \tan^{-1} \left(\frac{8(\kappa(1-16\kappa))^{\frac{1}{2}}}{32\kappa-1} \right) \right] - \frac{1}{4}, & \kappa \leq 1/16 \\ \frac{1}{4} \left[(32\kappa-1+8(\kappa(16\kappa-1))^{\frac{1}{2}})^{\frac{1}{3}} + (32\kappa-1-8(\kappa(16\kappa-1))^{\frac{1}{2}})^{\frac{1}{3}} - 1 \right], & \kappa \geq 1/16 \end{cases}. \quad (45)$$

Equation (44) is the result announced previously without proof.^{1,2}

4. REFERENCES

1. H. E. Brandt, "Uhm's laws of current modulation in klystron amplifiers," in Intense Microwave Pulses III, Howard E. Brandt, Editor, Proc. SPIE 2557, pp.32-38, 1995.
2. H. E. Brandt, "Current modulation in relativistic klystron amplifiers," to appear in IEEE Trans. Plasma Science, June, 1996.
3. Charles D. Hodgman, Editor, C.R.C. Standard Mathematical Tables, Eleventh Edition, p. 344, Chemical Rubber Publishing Company, Cleveland, 1957.
4. H. S. Uhm, "A self-consistent nonlinear theory of current modulation in relativistic klystron amplifiers," Phys. Fluids B 5, 190, 1993.

Standard antennas designed with electrooptic modulators and optical-fiber linkage

Keith D. Masterson, David R. Novotny, and Kenneth H. Cavecy

National Institute of Standards and Technology
Electromagnetic Fields Division
Boulder, CO 80303

ABSTRACT

We describe the design of standard reference antennas that uses an electrooptic transducer together with optical-fiber linkage to preserve the amplitude and phase information of the received signal. They will be used over a range from 10 MHz to 2 GHz at our open area test site in order to reduce measurement uncertainties attributable to the ambient electromagnetic spectrum. The transducer consists of an optical-fiber directional coupler with unbalanced legs and LiNbO_3 phase modulators. The output signal is processed to servocontrol the wavelength of the laser and maintain the optimal optical bias point in changing environments. The complementary rf signals are subtracted to provide common mode noise rejection. The output signal is modeled to determine the design and operating parameters required for good repeatability and accuracy. The results show that spurious reflections in the modulator legs need to be < -50 dB in order to obtain the desired stability.

Keywords: Active bias control, Michelson interferometer, radio frequency, standard antenna

1. BACKGROUND

Antenna calibrations on NIST's open area test site (OATS) are done by the standard reference antenna method.¹ In this method, the signals from the antenna under test are compared to the signals from a standard reference antenna in the same incident field. This is necessary because various environmental effects make it difficult to establish a well known standard field with day-to-day repeatability. We use resonantly tuned, half-wave dipoles of small radius for our standard antennas because the effective length and hence the open circuit voltage generated across the dipole gap can be calculated accurately.^{2,3} In current practice, this voltage is rectified by a Schottky diode and transmitted over nonmetallic, high-resistance leads to a high-impedance dc voltmeter that provides a dc output signal. This configuration provides a favorable high shunt impedance ($>100\text{ M}\Omega$) for the dipole, reduced perturbation of the field by the signal leads, and reduced susceptibility to common mode pickup and other sources of interference. Although tuned dipoles are most sensitive at the resonant frequency, they respond strongly enough to the broad spectrum of ambient fields to produce a measurable background in the dc signal and an accompanying uncertainty in the calibration. Our current measurement uncertainties are about ± 1 dB.¹

We observe increasing levels of ambient electromagnetic fields at our OATS facility. This is due to the increasing use of wireless communication products such as dispatch radios and cellular phones.

Contribution of the U.S. Government, not subject to copyright in the United States.

Commercial radio and TV also contribute substantially to the background. This leads to increased uncertainties in our antenna calibrations. The uncertainties due to the ambient fields can be reduced by detecting the signals from the reference antenna and the antenna under test in a narrow frequency band with a high-quality rf receiver that can filter the out-of-band signals. This also allows calibrations to be done within frequency bands where the ambient field is low. Until recently, this required an electrically conducting, coaxial cable for the signal link. Unfortunately, such links are susceptible to electromagnetic interference and common mode pickup, and perturb the test field, all of which are major contributors to a calibration uncertainty. The technology of optical-fiber communication systems now provides the components that mitigate these problems and still maintain the phase and amplitude of the signal from the reference antenna over a broad bandwidth. By coupling the optical fibers to passive electrooptic modulators placed across the dipole gap, we can maintain the desirable high shunt impedance without the need of a power source at the reference antenna.

2. APPROACH

We have previously demonstrated photonic probes with the sensitivity required to provide adequate signals from a 10 V/m standard field when using nonresonate dipoles.^{4,5} Depending on construction, they are capable of frequencies from near dc to above 50 GHz. For the standard reference antennas, we use existing optical fiber technology and develop a feedback control strategy which will stabilize the signal output against drift and noise caused by environmental stress.

The principal components of the system are shown in Fig. 1. The details of the electrooptic modulator are shown in Fig. 2. We use an optical-fiber directional coupler together with guided-wave, LiNbO_3 phase modulators. The configuration is that of a Michelson interferometer. The complementary outputs can be subtracted to provide common mode noise rejection and a 3 dB gain in rf signal. Also, since the physical path lengths of the two modulator legs differ by about 1 mm, the bias point of the interferometer is wavelength dependent. We compare the two low frequency outputs to determine the optical bias point and then use the result to control the laser wavelength in order to maintain an optimal setting. An optical-fiber directional coupler was used because the coupling ratio is more stable than generally is achievable in a guided-wave LiNbO_3 coupler.

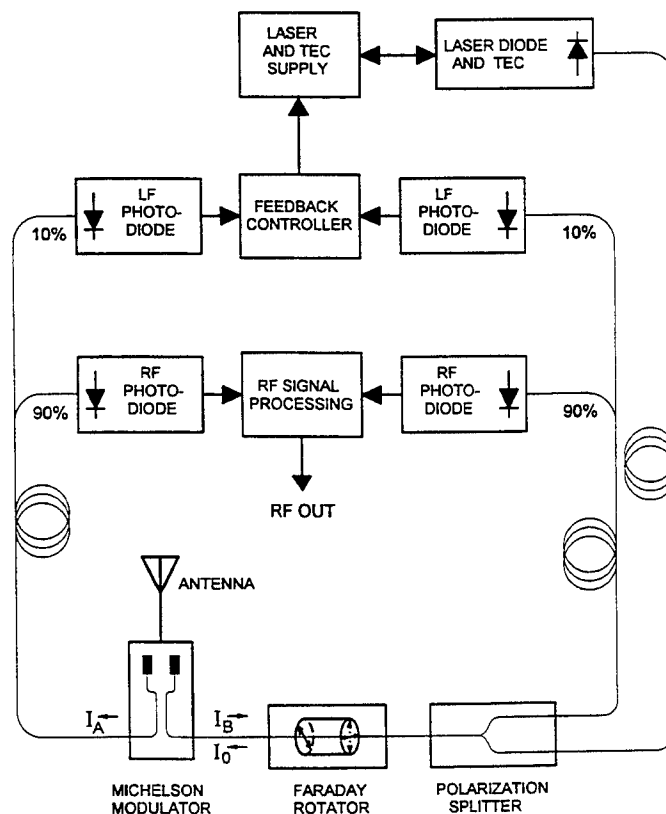


Figure 1. Major components of the rf standard antenna system.

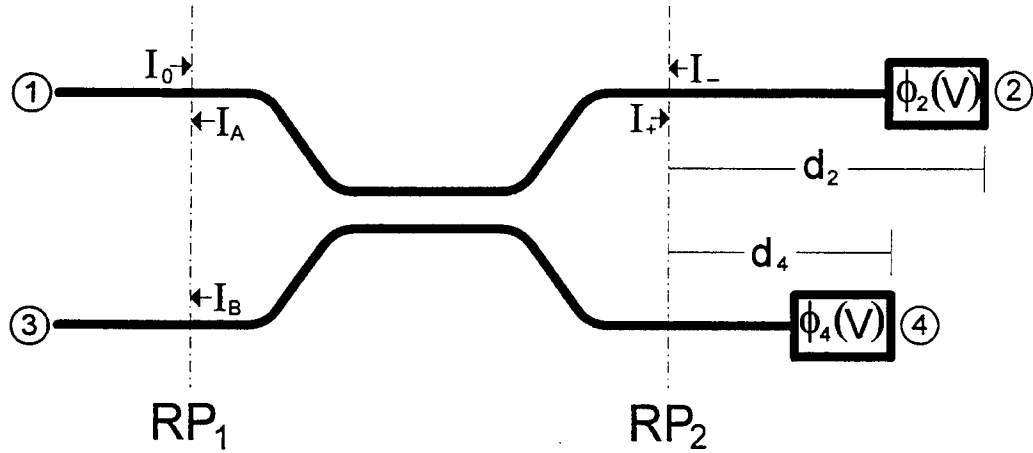


Figure 2. Detail of the electrooptic modulator.

A distributed feedback laser with a 40 MHz line width is used as the source. The laser wavelength is tuneable over a few nanometers by controlling the temperature of the thermoelectric cooler (TEC). The Faraday rotator and polarization splitting, optical-fiber coupler are used to efficiently separate one of the modulator's output signals into a separate downlink fiber. Polarization-maintaining, high-birefringence Panda fiber is used in the uplink and the directional couplers.

3. THEORY

The optical intensities from fibers A and B that are incident on the photodetectors are

$$\begin{aligned} I_A &= T_A (A_2 + A_4)(A_2 + A_4)^* , \\ I_B &= T_B (B_2 + B_4)(B_2 + B_4)^* , \end{aligned} \quad (1)$$

where A_i and B_i are phasors that represent the lightwaves which arrive at the reference plane RP_1 in fibers A and B from phase modulators at 2 and 4. The $T_{A,B}$ are the transmittances from the reference plane RP_1 to the photodetectors. The four phasors are

$$\begin{aligned} A_2 &= \sqrt{I_0} S_{12} r_2 S_{21} \exp [i(\omega t + \phi_2 + \pi V/V'_\pi)], \\ A_4 &= \sqrt{I_0} S_{14} r_4 S_{41} \exp [i(\omega t + \phi_4 + \pi V/V''_\pi)], \\ B_2 &= \sqrt{I_0} S_{12} r_2 S_{23} \exp [i(\omega t + \phi_2 + \pi V/V'_\pi)], \\ B_4 &= \sqrt{I_0} S_{14} r_4 S_{43} \exp [i(\omega t + \phi_4 + \pi V/V''_\pi)]. \end{aligned} \quad (2)$$

I_0 is the optical intensity incident at the reference plane RP_1 from the uplink fiber. The r_i are the ratios of the amplitudes of the plus and minus traveling waves at reference plane RP_2 . They account for the insertion losses of the phase modulators. These losses are due to the mode mismatch at the pigtail, absorption and scattering in the modulator, and the reflectance at the back surface of the modulator. The ϕ_i are the phase changes over the optical path lengths of the two modulator legs with no applied voltage, V is the voltage applied to the modulators' electrodes, and the V_π are the voltages required on each modulator for a π phase shift in an optical carrier of angular frequency ω . The S_{ij} are the elements of the scattering matrix which describes the coupler. For a 4-port, symmetric directional coupler the scattering matrix is ⁶

$$S = \begin{bmatrix} 0 & \alpha & 0 & \beta \exp(i\pi/2) \\ \alpha & 0 & \beta \exp(i\pi/2) & 0 \\ 0 & \beta \exp(i\pi/2) & 0 & \alpha \\ \beta \exp(i\pi/2) & 0 & \alpha & 0 \end{bmatrix} \quad (3)$$

where α and β are the coupling coefficients for the amplitudes of the outputs. By substituting Eqs. (2 and 3) back into Eq. (1), we obtain the more familiar form for the optical intensities arriving at receivers A and B,

$$\begin{aligned} I_B &= I_0 T_B (K_B - K_C \cos(\phi_0 + \pi V/V_\pi)) , \\ I_A &= I_0 T_A (K_A - K_C \cos(\phi_0 + \pi V/V_\pi)) , \end{aligned} \quad (4)$$

where $K_A = (r_2 \alpha^2)^2 + (r_4 \beta^2)^2$; $K_B = (r_2^2 + r_4^2) \alpha^2 \beta^2$; $K_C = r_2 r_4 \alpha^2 \beta^2$;

$$\phi_0 = \phi_2 - \phi_4; \text{ and } 1/V_\pi = (1/V'_\pi) + (1/V''_\pi).$$

The bias phase ϕ_0 due to the difference in the optical path lengths in the modulator arms is

$$\phi_0 = 2\pi \frac{n(d_2 - d_1)}{\lambda} , \quad (5)$$

where n is the index of refraction for the fiber, the d_i are the physical lengths of the two arms and λ is the laser wavelength. In our interferometer, the physical lengths differ by about 1 mm to give a mode spacing of about 0.5 nm at a wavelength of 1.3 μm .

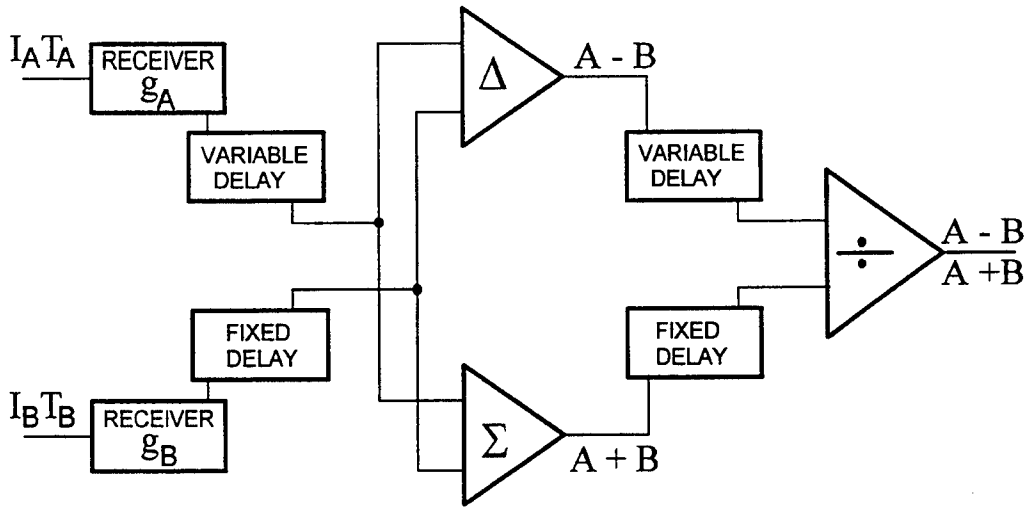


Figure 3. Block diagram for rf signal processing.

The optical intensities are converted to electrical signals in optical receivers that have transfer coefficients g_i which include the photodiode quantum efficiencies and amplifier gains. To complete the signal recovery, the electrical outputs from the receivers are split, routed to sum and difference amplifiers, and then ratioed as shown in Fig. 3. Analytically, the resulting normalized signal N emerging from the processing electronics is

$$N = N_0 \frac{g_A I_A - g_B I_B}{g_A I_A + g_B I_B} \quad (6)$$

$$= N_0 \frac{g_A T_A K_A - g_B T_B K_B - (g_A T_A + g_B T_B) K_C \cos(\phi_0 + \pi V/V_\pi) + OS_A/I_0}{g_A T_A K_A + g_B T_B K_B - (g_A T_A - g_B T_B) K_C \cos(\phi_0 + \pi V/V_\pi) + OS_B/I_0},$$

where N_0 is a constant from the divide function and the OS_i are small residual signals added to account for offsets in the sum and difference circuits. Except for the offsets, the output is independent of the uplink optical intensity. By adjusting the receiver gains so that $g_A T_A = g_B T_B$ and the signal channels are balanced, we can eliminate the cosine term from the denominator. The dependence on the offsets can be greatly reduced by adding compensating offsets and operating with fairly high optical power. This configuration provides a normalized, stable output signal and reduces common mode noise. The input optical signal is a function of time since it contains laser noise as well as slower drifts in intensity. The signal processing gives independence from the high frequency fluctuations only if the time delays in each of the channels are matched.

We obtain both an rf signal and a dc signal in the output. The rf signal amplitude N^r is given by the derivative of Eq. (6) with respect to the input voltage. When the gains are adjusted so that the signal channels are balanced, this becomes

$$N^r = N_0 \frac{2K_C \sin(\phi_0)}{K_A + K_B + OS_B/I_0} \frac{\pi V^r}{V_\pi}. \quad (7)$$

The dc signal is

$$N^{dc} = N_0 \frac{K_A - K_B - 2K_C \cos(\phi_0) + \langle OS_A/g_A T_A I_0 \rangle}{K_A + K_B + \langle OS_B/g_A T_A I_0 \rangle} \quad (8)$$

where $\langle \rangle$ is the average value of the enclosed quantity. We use the dc signal for the feedback control by adjusting the laser temperature and hence its wavelength until ϕ_0 is an odd multiple of $\pi/2$, the cosine is zero, and the rf signal gives the best sensitivity and linearity.

4. ANALYSIS OF SPURIOUS REFLECTIONS

An interferometer constructed as shown in Fig. 2 will have reflections at the interfaces between the optical fibers and LiNbO_3 phase modulators. If light from these reflections couples back into the waveguides and mixes with the modulated signal, distortion will result. We modeled the extent of the distortion by adding amplitudes A_i' for these reflected amplitudes to the terms in Eq. (1). We also reduced the original A_i to account for the losses due to the reflection. The resulting intensity out of fiber A is

$$I_A = T_A (A_2 + A_4 + A_2' + A_4') (A_2 + A_4 + A_2' + A_4')^* , \quad (9)$$

and was evaluated numerically. The results are shown in Figs. 4 and 5. Figure 4 shows that for a -14.5 dB back reflection typical of the fiber- LiNbO_3 interface, the optical intensities to the detectors no longer exhibit the desirable simple sinusoidal dependence on the laser wavelength that is shown by the dashed curve. Deviations of this size would severely limit the ability of the control system to maintain the proper bias level by changing the laser wavelength. Figure 5 shows that the transfer function for voltage applied to the modulator is also severely affected. Although these curves do not show the jagged nature of those in Fig. 4, the amplitudes and the slopes differ between neighboring modes. Since the control scheme does not identify which interferometer mode it is referencing, this would lead to unacceptably large uncertainties in the rf signal amplitude. The reflectance of -34 dB that is used for the second set of curves corresponds to a single-layer antireflection coating of aluminum oxynitride (ALON) between the fiber and the crystal.

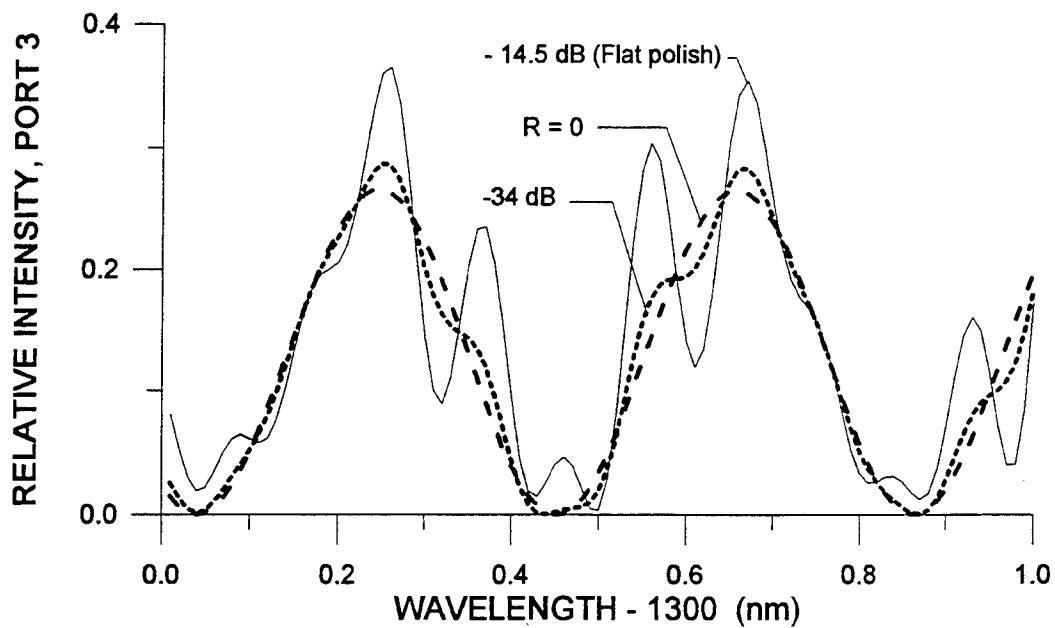


Figure 4. Effect of fiber-LiNbO₃ reflection on the intensity out fiber A as a function of laser wavelength. The dashed line is for the ideal case of zero reflection. The dotted line is for a single-layer antireflection coating of ALON. Solid line is for a flat polish with no coating.

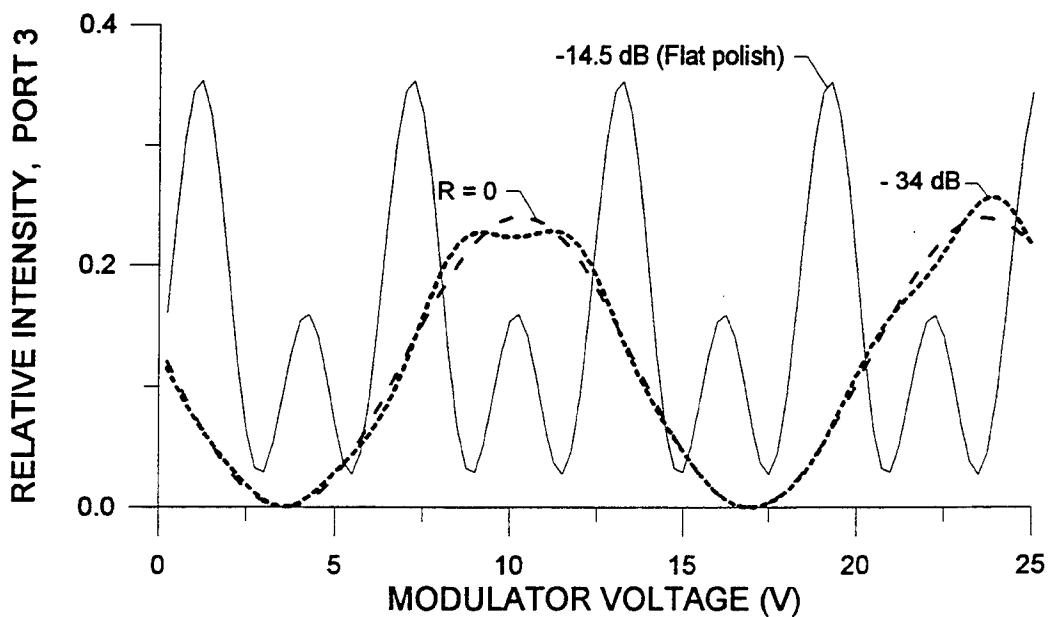


Figure 5. Effect of fiber-LiNbO₃ reflection on intensity out fiber A as a function of applied voltage. The dashed line is for the ideal case of zero reflection. The dotted line is for a single-layer antireflection coating of ALON. Solid line is for a flat polish with no coating.

The index of refraction of this material (1.7687 at $\lambda = 1.31 \mu\text{m}$)⁷ is the closest match to the ideal index of 1.815 , which would give zero reflectance, that we could find in a preliminary search of the literature. Our analysis indicates that back reflections < -50 dB are necessary for acceptable performance. Although this can be achieved in theory with a multilayer coating, it is also obtainable by angle-polishing the fiber ends and modulator edges so that the light reflected at the interface will not couple back into the waveguides.

5. IMPLEMENTATION

We separated the electronics for the bias control and feedback from those for the rf detection and signal processing. This allowed us to use designs and components which optimize the performance of each function and to place them in separate shielded enclosures to reduce cross talk and noise. We used 10 dB optical-fiber splitters at the receiver end of the optical link to separate the signals isolate the inputs.

Traditionally, microwave and rf processing is accomplished through heterodyne techniques to obtain lower frequency signals. These techniques fail to realize the full noise reduction capabilities that would be available by implementing the indicated functions with broadband components. However, a complete implementation of broadband processing is a difficult task. Instead, we use a 180° -hybrid rf coupler for the rf difference function. Its 2 MHz-2 GHz bandwidth is sufficient for our application. Although there is no gain in such a device, the rf coupling eliminates the dc offset. Its simplicity, ruggedness and inherent long term stability are ideal for standards activities. A tuneable delay line is incorporated to adjust the timing between the A and B signals before the subtraction.

A broadband divide function to optimize the rejection of laser noise in the signal normalization is more difficult to achieve. Furthermore, the response of the hybrid coupler does not extend to low enough frequencies to provide a sum signal that will give an effective normalization for slow drifts in optical intensity. Therefore, in our present system we implemented the divide function by attenuating the rf difference signal by an amount proportional to the sum signal from the lower frequency feedback-control circuit. The sum signal is put through a logarithmic amplifier, digitized, and then applied to a digital step attenuator. If linearity requirements can be met, an analog, voltage-variable attenuator to implement this function could extend the upper frequency for the noise rejection in the divide circuit.

6. CONCLUSIONS

We have designed an antenna system that uses optical-fiber technology to transfer the rf signal from the gap between the dipole elements to an rf receiver. It uses a feedback system to control the wavelength of the optical link and stabilize the bias point of the electrooptic modulator against temperature fluctuations characteristic of an outdoor test site. The system performance was modeled and analyzed to show appropriate signal processing to reduce noise and to establish the proper operating parameters. This analysis also showed the necessity to reduce the reflection at the fiber-modulator interface to < -50 dB, a level achievable by angle polishing the optical fiber and modulator ends. Although the system is in the final stages of construction and is yet to be thoroughly characterized, it is expected to have the stability and repeatability necessary for a standard reference antenna and to reduce the uncertainties in our antenna calibrations due to ambient electromagnetic fields.

7. REFERENCES

1. D.B. Camel, E.G. Larsen, and J.E. Cruz, "NBS Calibration Procedures for Horizontal Dipole Antennas (25 to 1000 MHz)," *Nat. Bur. Stand.(U.S.) Tech. Note 1309*, 1987.
2. S.A. Schelkunoff, and H.T. Friis, *Antennas, Theory and Practice*, Wiley, p. 333 and pp. 431-452, 1952.
3. E.C. Jordan and K.G. Balmain, *Electromagnetic Waves and Radiating Systems, 2nd ed.*, Prentice-Hall, Inc., New Jersey, pp.351-353, 1968.
4. K.D. Masterson and L.D. Driver, "Broadband, isotropic, photonic electric-field meter for measurements from 10 kHz to above 1 GHz," *High Bandwidth Analog Applications of Photonics, II*, B. Neyer, ed., Proc. SPIE 987, pp. 107-118, 1988.
5. M. Kanda and K.D. Masterson, "Optically Sensed EM-Field Probes for Pulsed Fields," *Proc. IEEE*, Vol. 80, No. 1, Special Issue on Antennas, p. 209, Jan.1992.
6. F.E. Gardiol, *Introduction to Microwaves*, Artech House, Inc., Dedham MA p. 275, 1984.
7. W.J. Tropf, M.E. Thomas, and T.J. Harris, "Properties of Crystals and Glasses," *Handbook of Optics, 2nd ed. Vol.2*, McGraw Hill, New York, p. 33.61, 1994.

Broadband Superlight Source of High Power Microwaves.

Yuri Lazarev and Peter Petrov

Russian Federal Nuclear Centre - All-Russian Institute of Technical Physics, Department of Theoretical Physics and Applied Mathematics, 456770 Snezhinsk, Chelyabinsk Region, Russia

ABSTRACT

The superlight source is the source moving with the superlight velocity. In particular, the electron current pulse propagating along some plane surface with $v_{ph} > c$ is such a source. It is proposed to use the superlight source for high power microwave generation. The properties of the superlight source are investigated theoretically. It is shown that radiated microwave pulse is broadband and directed, may have the pulse duration $\sim 10^{-12}$ sec and pulse power $> 10^9$ W.

Keywords: high power microwave, superlight current pulse, directed radiation.

1. INTRODUCTION.

Several technological advances directly depend on development of compact, lightweight microwave devices capable of generating a directed, ultrashort, high power microwaves. The pulse length T_p would be of order $10^{-12} \div 10^{-10}$ s. and power of order of 10^9 W and more. This task is very difficult if at all possible to realize for conventional pulse technology. One of the primary obstacles to raising the generated radiation power in conventional pulse technology is the small pulse length T_p which limits the size of the energy-storage region to value $\sim cT_p$, where c is the light velocity, and as the result, the power of generated radiation is decreased with the decreasing of the pulse length. Understandably, achieving a significant increase in the power and the total energy of the electromagnetic pulse will require developing devices of a completely new type, capable of overcoming this obstacle.

In the report it is demonstrated that superlight source of electromagnetic radiation can meet the requirement's listen above and, consequently, it just represents the needed new type of microwave device.

2. QUALITATIVE CONSIDERATION. SIMPLE ESTIMATIONS

2.1 Superlight source in free space.

The simplest case of superlight source is observed when an electron current pulse propagates with superlight velocity along plane metallic surface¹. Such current pulse occurs, when obliquely incident plane flux of ionizing radiation illuminates this surface (Fig. 1)². The arrangement of the emission current over the surface constitutes an antenna with phased excitation such that radiated wave is emitted in the direction corresponding to specular reflection ($\alpha = \psi$) of the ionizing radiation. Consequently if the illuminated surface is the focusing mirror for the incident ionizing radiation then the radiated electromagnetic (EM) wave energy may be focused.

It is easy to see that in any point over the surface the ensemble of electrons ceases to radiate if the current density in this point equals to zero. Hence it follows that the electromagnetic pulse length T_p is determined by the dynamics of the space charge formation. In the case $T\omega_{Le} \gg 1$ (the most interesting case) the space charge is produced during time of order of ω_{Le}^{-1} ,

where ω_{Le} - is the electron Langmuir frequency, T - is the ionizing radiation pulse length³. So $T_p \sim \frac{2\pi}{\omega_{Le}} \sim \frac{10^{-4}}{\sqrt{n_e}}$. Electron

density n_e increases together with increasing of ionizing radiation intensity and may be of order of 10^{12} cm^{-3} and more. As the result microwave pulse length may be very small - of order of 10^{-10} s and less.

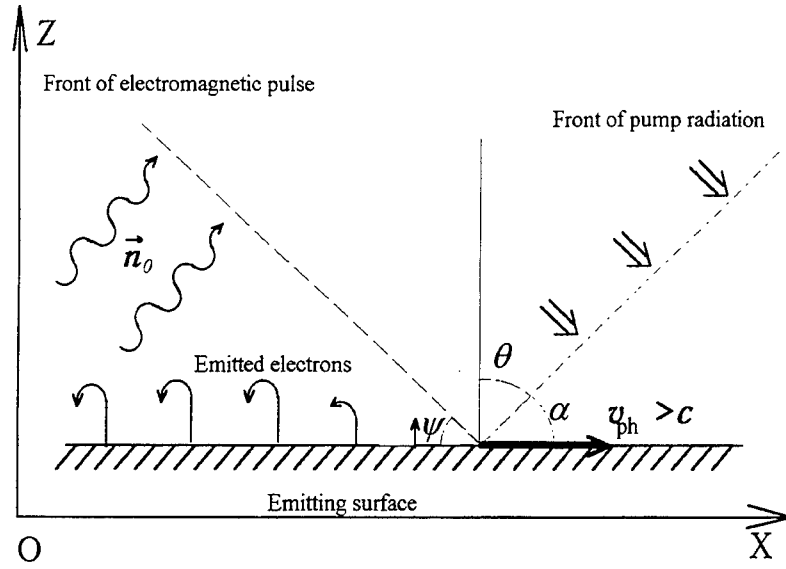


Fig. 1. Principle of the generation of an electromagnetic pulse by a superlight electron-current pulse.

As previously noted, all emitted electrons radiate coherently and at sufficiently large distance R (in wave zone) in the direction of electromagnetic pulse propagation the illuminated surface will radiate as a point dipole with dipole moment equal to the sum of dipole moments of electrons. It immediately follows that

$$E \sim H \sim \frac{\ddot{P}S}{c^2 R} \sim \frac{4\pi^2 PS}{c^2 T_p^2 R} \quad (1)$$

where E, H - electric and magnetic field;

$\ddot{P} \sim \frac{4\pi^2 P}{T_p^2}$ - second time derivative of the dipole moment surface density, $P = \frac{\varepsilon}{2\pi e}$;

S - surface area;

ε, e - electron kinetic energy and charge.

Using (1) one can obtain the estimation of the radiated power Q and energy U :

$$\begin{aligned} Q &\sim 2 \cdot 10^{12} (\gamma - 1)^2 \frac{S}{\lambda^2}, \quad (W) \\ U &\sim 70 \cdot (\gamma - 1)^2 \frac{S}{\lambda^2}, \quad (J) \end{aligned} \quad (2)$$

where $2\pi\lambda = cT_0$, $\gamma = 1 + \frac{\varepsilon}{m_e c^2}$, m_e - electron mass, $[S] = m^2$, $[\lambda] = cm$.

For $S = 10^{-2} m^2$, $\lambda = 0.1 cm$, $\gamma - 1 = 0.7$ equation (2) offers $Q \sim 10^{12} (W)$, $U \sim 3.5 (J)$.

2.2 Superlight source in waveguide.

Another interesting and simple example of superlight source takes place when electron current pulse propagates with the superlight velocity $v_{ph} \gg c$ along one of the surfaces (OX) of the plane waveguide with the width a (Fig.2). As is known, the

radiated field amplitude near the radiated surface is proportional to the first time derivative of the dipole moment surface density²:

$$E \sim H \sim \dot{P}(t) \quad (3)$$

For example, in the case of the plane superlight source:

$$H = \frac{4\pi}{c} \frac{\dot{P}}{\sin \alpha}, \quad \cos \alpha = \frac{c}{v_{ph}}. \quad (4)$$

If the dipole moment surface density oscillates with frequency ω_0 which is a multiple of the waveguide cutoff frequency $\frac{\pi c}{a}$:

$$\omega_0 = \frac{\pi c}{a \sin \alpha} k, \quad k = 1, 2, \dots \quad (5)$$

then amplification of radiated field is observed and, as it is easy to see that possible length of amplification L_0 is equal to $cT_0 \cos \alpha$, where $T_0 = \frac{2\pi}{\omega_0}$ - the duration of the dipole surface density oscillations. But

$$L_0 = cT_0 \cos \alpha \quad (6)$$

only if during amplification the field of the generated electromagnetic wave is less than space charge field.

When the wave field along OZ E_{wz} becomes of order of the space charge field E_{ch} :

$$E_{wz} \sim E_{ch} \sim 4\pi n_e \lambda_D \approx \frac{2\varepsilon}{e\lambda_D}, \quad \text{where } \lambda_D - \text{Debye length} \quad (7)$$

its action on dipole layer formation is not negligible and causes the decreasing of dipole moment surface density and the increasing of oscillation frequency. As a consequence the conditions (5) is broken and the amplification is discontinued.

It is pertinent to note that only case $E_{wz} \geq E_{wx}$ (id est $\cos \alpha \sim 1$) is considered to obviate the difficulties.

The relation $E_{wz} \leq E_{ch}$ imposes the restriction on the length of waveguide amplifier:

$$\frac{L}{\lambda} \leq \frac{4}{\sin \alpha} \frac{\gamma}{\sqrt{\gamma^2 - 1}}, \quad \lambda = 2\pi \tilde{\lambda}. \quad (8)$$

With this results it can be shown that the following estimations are true for radiated power Q and energy U per unit area of the waveguide aperture

$$\begin{aligned} Q &\sim \frac{\pi}{2} m_e c^2 \left(\frac{mc^2}{e^2} \right) (\gamma - 1)^2 \left(\frac{L}{\lambda} \right)^2 \frac{\sin^2 \alpha \cdot \cos \alpha}{\lambda^2} \stackrel{\alpha \approx 45^\circ}{\sim} 2 \cdot 10^9 \cdot \frac{(\gamma - 1)^2}{\lambda^2} \left(\frac{L}{\lambda} \right)^2, \quad \left(\frac{W}{cm^2} \right); \\ U &\sim \frac{\pi}{6} m_e c^2 \left(\frac{mc^2}{e^2} \right) (\gamma - 1)^2 \left(\frac{L}{\lambda} \right)^3 \frac{\sin^4 \alpha}{\lambda} \stackrel{\alpha \approx 45^\circ}{\sim} 2.4 \cdot 10^{-2} \cdot \frac{(\gamma - 1)^2}{\lambda} \left(\frac{L}{\lambda} \right)^3, \quad \left(\frac{J}{cm^2} \right). \end{aligned} \quad (9)$$

For $\gamma - 1 = 0.5$, $\frac{L}{\lambda} = 4$, $\lambda = 0.1 \text{ cm}$ the relations (9) gives the values $Q \sim 10^{12} \left(\frac{W}{cm^2} \right)$, $U \sim 4 \left(\frac{J}{cm^2} \right)$.

So, it is shown, that superlight radiation sources can generate high power and ultrashort pulses but, unfortunately, it requires the high power ionizing radiation source with power of order of 10^{15} W and more at an energy of quantum of order of 1 MeV. The smaller the quantum energy the greater the power of ionizing radiation source should be.

Such high power and widely available ionizing radiation sources do not exist, at least up to now. But the situation is not hopeless and a way out is rather obvious.

It is necessary to divide the processes of current formation into two stages: electron emission and energy pumping.

Let us imagine, that a plane flux of rather low-frequency radiation, for example, light radiation irradiates a plane surface of photoemission material and sufficiently strong electric field is created by acceleration gap near irradiated surface. Emitted low energy electrons are accelerated in this field and their final energy may be reasonably high - of order of hundreds or thousands keV. Outside an acceleration gap as well as on the illuminated plane surface a phased-radiating dipole layer is formed. But now the required power of the ionizing radiation source is significantly lower - of order of 10^{10} W. Light sources of such power exist, for example lasers with not unique characteristics (Fig. 3).

Thus, if our theoretical views are correct the superlight radiation sources open up new possibilities for high power microwave generation.

Rigorous analytical researches and computer simulations were performed to check all of the preceding.

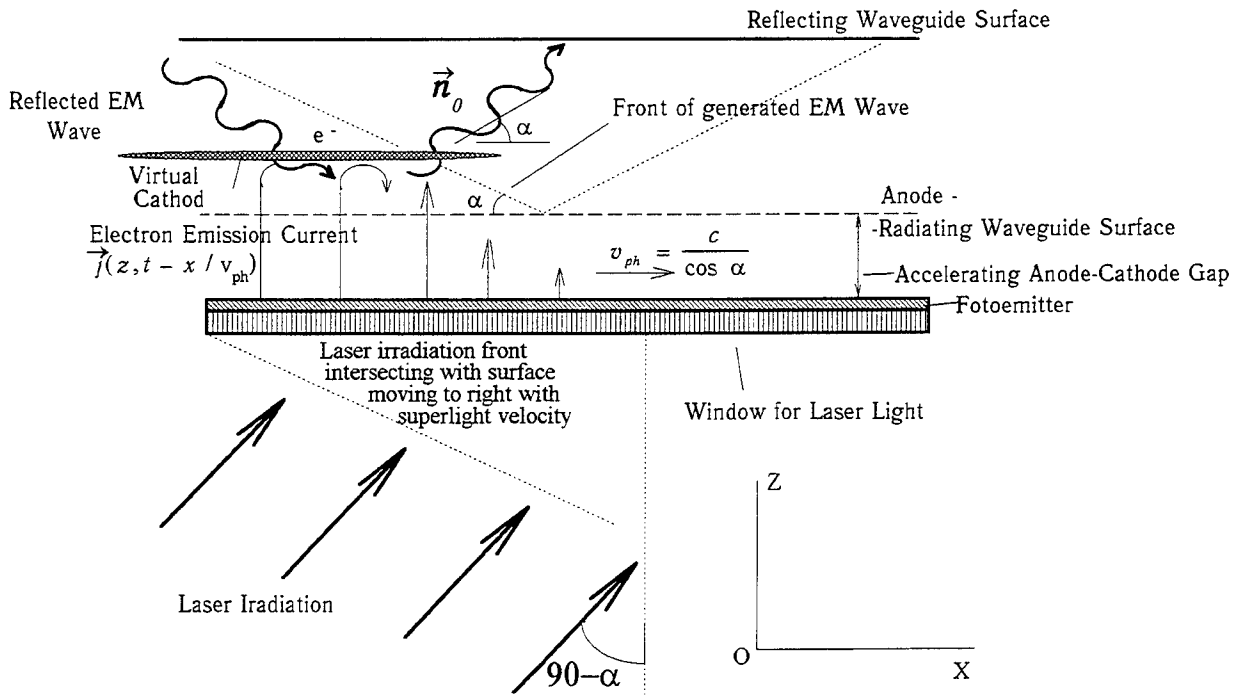


Fig.2 Conceptual sketch of high power microwave waveguide generator-amplifier, driven by virtual-cathode oscillator phased by superlight photoemission current.

axis (Fig.1). The motion of the electrons occurs in the electric fields of the plane, the space charge, and the electromagnetic wave that is formed.

This problem should be examined on the basis of a joint solution of Maxwell's and Vlasov's equations. However, if we assume that the current distribution along the surface is given, and if we also assume that the components of the electromagnetic field depend on the variables x and t in the same combination as for the exciting current, then Maxwell's equations for the nonvanishing field components, namely E_x , E_z and H_y , have the following form:

$$\begin{aligned}\frac{\partial E_x}{\partial \tau} &= -4\pi j_x - c \frac{\partial H_y}{\partial z}; \\ \frac{\partial E_z}{\partial \tau} &= -4\pi j_z - \frac{c}{v_{ph}} \frac{\partial H_y}{\partial \tau}; \\ \frac{\partial H_y}{\partial \tau} &= -c \frac{\partial E_x}{\partial z} - \frac{c}{v_{ph}} \frac{\partial E_z}{\partial \tau}.\end{aligned}\quad (10)$$

with the next boundary and initial conditions

$$\begin{aligned}E_x|_{z=0} &= 0, \quad E_x|_{z \rightarrow \infty} \rightarrow 0 \\ E_x = E_z = H_y|_{\tau=0} &= 0.\end{aligned}\quad (11)$$

From equations (10-11) one can derive the analytic solution:

$$\begin{aligned}E_x(\tau, z) &= \frac{2\pi}{v_{ph}} \left(\int_0^z dz' j_z \left(\tau - \frac{z-z'}{c} \sqrt{1 - \frac{c^2}{v_{ph}^2}}, z' \right) + \int_0^\infty dz' j_z \left(\tau - \frac{z+z'}{c} \sqrt{1 - \frac{c^2}{v_{ph}^2}}, z' \right) - \right. \\ &\quad \left. - \int_z^\infty dz' j_z \left(\tau - \frac{z-z'}{c} \sqrt{1 - \frac{c^2}{v_{ph}^2}}, z' \right) \right).\end{aligned}\quad (12)$$

We assume that the conditions for the applicability of the dipole approximation are satisfied. There are the conditions that the emitted electrons are nonrelativistic ($\bar{v}_e \ll c$, where \bar{v}_e is the average electron velocity) and that the emission current is localized near the emitting surface, in a region of size

$$\Delta z \sim \bar{v}_e T_p < T_p \frac{c v_{ph}}{\sqrt{v_{ph}^2 - c^2}}, \quad (13)$$

where $T_p \approx T_0$ is a time scale of the space charge variation (this condition holds in the case of a space-charge-limiting current). Under these conditions, at $z \gg \Delta z$, we have

$$E_x(\tau, z) \cong \frac{4\pi}{v_{ph}} \dot{P} \left(\tau - \frac{z}{c} \sqrt{1 - \frac{c^2}{v_{ph}^2}} \right), \quad H_y(\tau, z) \cong \frac{4\pi}{\sqrt{v_{ph}^2 - c^2}} \dot{P} \left(\tau - \frac{z}{c} \sqrt{1 - \frac{c^2}{v_{ph}^2}} \right). \quad (14)$$

Here P is the surface density of the dipole moment, and

$$\dot{P} \equiv \frac{dP}{dt} = \int_0^\infty dz' j_z(t, z, z') \quad (15)$$

$$E_x(\tau, z) \cong \frac{4\pi}{v_{ph}} \dot{P}(\tau - \frac{z}{c} \sqrt{1 - \frac{c^2}{v_{ph}^2}}), \quad H_y(\tau, z) \cong \frac{4\pi}{\sqrt{v_{ph}^2 - c^2}} \dot{P}(\tau - \frac{z}{c} \sqrt{1 - \frac{c^2}{v_{ph}^2}}). \quad (14)$$

Here P is the surface density of the dipole moment, and

$$\dot{P} \equiv \frac{dP}{dt} = \int_0^\infty dz' j_z(t, z, z') \quad . \quad (15)$$

It can be seen from these expressions that the radiated electromagnetic propagates along the direction $\vec{n}_0 = (\cos\theta, 0, \sin\theta)$, which makes an angle $\alpha = \pi/2 - \theta$ with the OZ axis. We also see that the amplitude of this wave is proportional to the rate of change of the dipole moment, which is created by emitting particles.

3.2 Effects of finite plane sizes

In the case of a surface with finite dimensions $\sim L$ along the X and Y axes, expressions (12) and (14) are valid only within the Frenel zone. In the wave zone, the expressions for the components of the electromagnetic field can be calculated in terms of retarded potentials. If the observation point, at a distance R from the generator, lies in the $y=0$ plane, we find the following results for the directions \vec{n} , which are close to the wave emission direction \vec{n}_0 , working in the dipole approximation:

$$H_y \approx \frac{2\sin(\theta)}{c^2 R} \int_s dx' dy' \ddot{P}(t - \frac{R}{c} + \frac{x' \cos(\theta)}{c} \vartheta), \quad \cos(\vartheta) = \vec{n} \cdot \vec{n}_0 \cong 1. \quad (16)$$

It follows that the diffraction angle and the boundary of the Frenel zone are determined by

$$\psi_d = \frac{2cT_p}{L \cos(\theta)}, \quad R_f \sim \frac{L^2 \cos(\theta)}{8cT_p}. \quad (17)$$

Correspondingly, under the condition $\vartheta \ll \psi_d$, we have

$$H_y \approx 2 \frac{L^2 \cos(\theta) \ddot{P}(t - R/c)}{c^2 R} \quad (18)$$

The expressions derived for the amplitude of the electromagnetic wave in the wave zone, (5) and (7), show that the radiation intensity is

$$I \approx \frac{c}{4\pi} H_y^2 \quad (19)$$

and that, correspondingly, the power of the microwave source associated with it is determined by the dimensions of the irradiated surface and by the rate of change of the dipole moment \ddot{P} .

3.3 Numerical results.

Our simulation results confirm the generation of high power directed electromagnetic wave. The numerical results represented on Fig.3-4 were obtained with three dimension electrodynamical and two dimensional particle-in-cell codes for metallic plane with the $L=50$ cm and electron emission current defined as $j_z(t) \propto \eta(t - \frac{x}{c} \cos(\alpha))$, $\alpha = \pi/4$, η – step function .

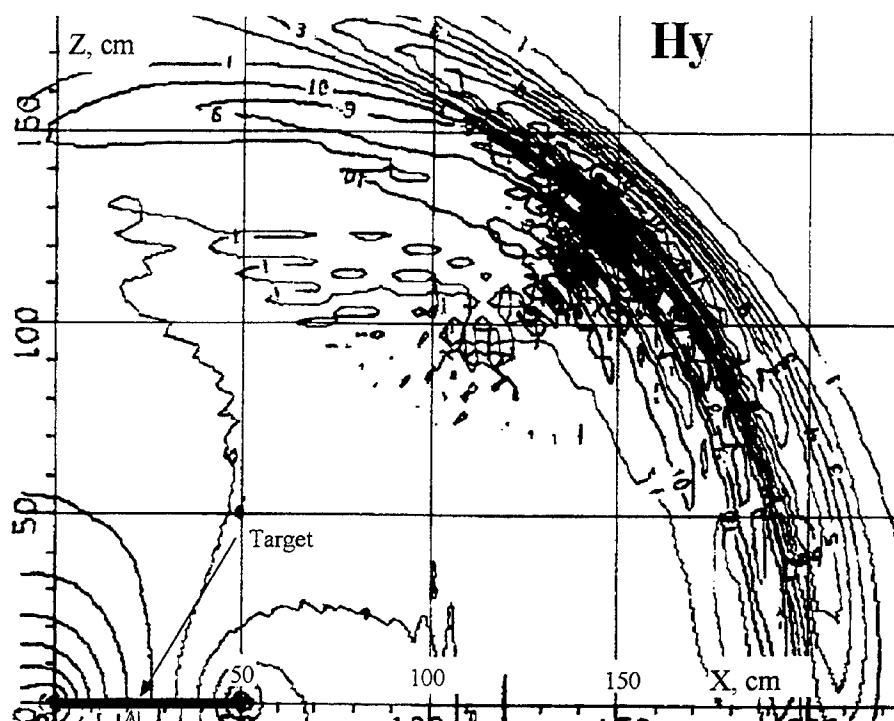


Fig.3. Contour lines of magnetic field generated by electron current moving along surface at the velocity $\sqrt{2}c$.

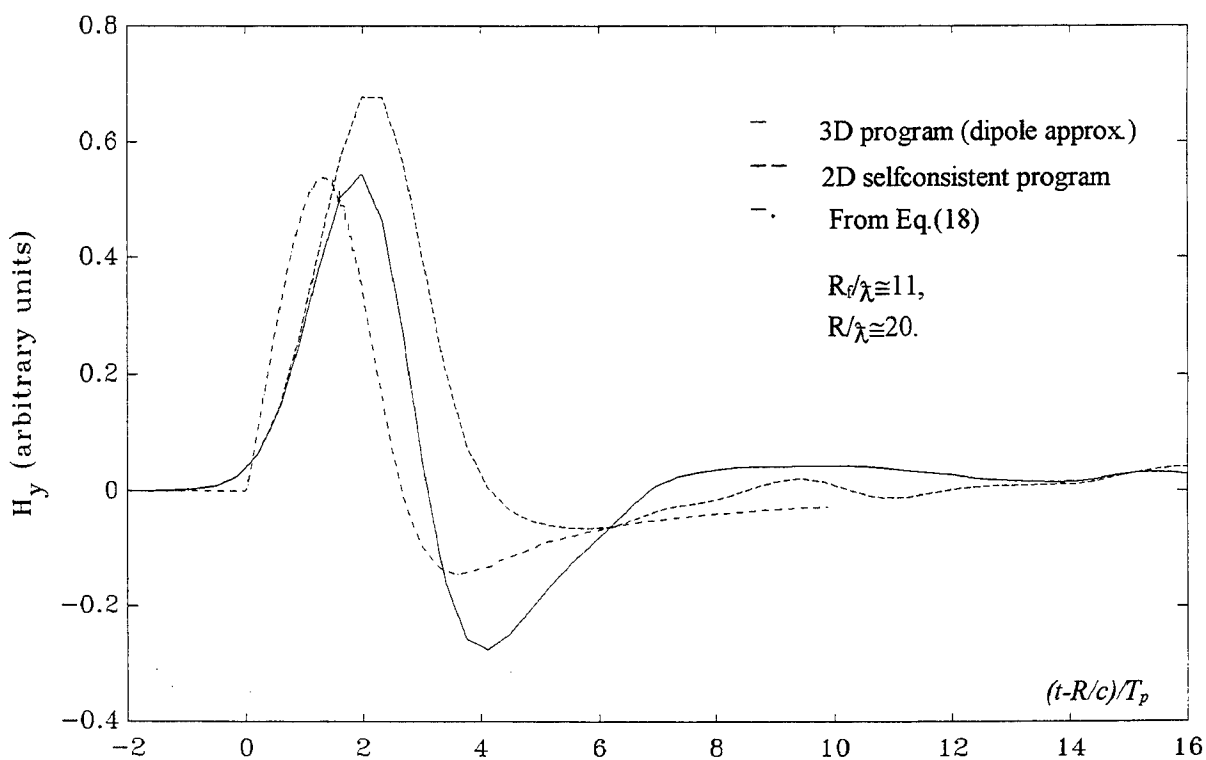


Fig.4. Magnetic field H_y in Frenel zone vs. time.

4. SUPERLIGHT SOURCE IN PLANE WAVEGUIDE

4.1 One-dimensional solution.

Let us suppose that the current pulse of density $j_z = j_z(\tau)$ such as in previous section propagates along the OX axis on internal surface of plane metal waveguide ($Z=0$) (Fig.2) with the width a . The evolution of electromagnetic field in waveguide is defined by equations (10) with boundary conditions

$$E_x|_{z=0, z=a} = 0. \quad (20)$$

and may be obtained in analytic form, which in dipole approximation (13) are given by

$$E_x(z, \tau) \approx \frac{4\pi}{v_{ph}} \sum_{n=0}^{\infty} \int_0^z dz' \left(j_z \left(z', \tau - \frac{2na+z}{c} \sin \alpha \right) - j_z \left(z', \tau - \frac{2(n+1)a-z}{c} \sin \alpha \right) \right) \xrightarrow{z \gg \lambda_d} \frac{4\pi}{v_{ph}} \sum_{n=0}^{\infty} \left(\dot{P} \left(\tau - \frac{2na+z}{c} \sin \alpha \right) - \dot{P} \left(\tau - \frac{2(n+1)a-z}{c} \sin \alpha \right) \right) \quad (21)$$

$$H_y(z, \tau) \xrightarrow{z \gg \lambda_d} \frac{4\pi}{\sqrt{v_{ph}^2 - c^2}} \sum_{n=0}^{\infty} \left(\dot{P} \left(\tau - \frac{2na+z}{c} \sin \alpha \right) + \dot{P} \left(\tau - \frac{2(n+1)a-z}{c} \sin \alpha \right) \right) \quad (22)$$

$$E_z(z, \tau) \xrightarrow{z \gg \lambda_d} -\frac{c}{v_{ph}} H_y$$

From this expressions we find that amplification of generated EM field is observed only if oscillations of the dipole moment are correlated with the waveguide cutoff frequency by equation (5). If the conditions (5,8) are satisfied along the waveguide length L , then amplitude and intensity of the generated EM wave propagates down the waveguide will be increased:

$$\begin{aligned} H_y(z, L) &\cong N \cdot H_0, H_0 = \frac{4\pi}{c \cdot \sin \alpha} \left(\dot{P} \left(\tau - \frac{z}{c} \sin \alpha \right) + \dot{P} \left(\tau - \frac{2a-z}{c} \sin \alpha \right) \right); \\ E_x(z, L) &\cong N \cdot E_0, E_0 = \frac{4\pi}{c} \cos \alpha \cdot \left(\dot{P} \left(\tau - \frac{z}{c} \sin \alpha \right) - \dot{P} \left(\tau - \frac{2a-z}{c} \sin \alpha \right) \right); \\ I_x &= \frac{c}{4\pi} H_y E_z \approx S_0 N^2, I_0 = \frac{c}{4\pi} H_0^2 \cos \alpha. \end{aligned} \quad (23)$$

where $N = \left[\frac{L}{L_0} \right]$, and operator $[]$ means the integral part.

The time dependence of dipole moment surface density is defined by emission current time dependence and electron energy spectrum. We consider the case of $j_z(t) = \text{const}$ for $0 < t < T \gg \omega_{Le}^{-1}$ and two cases of electron spectrum :

- the emission spectrum from the surface is taken to be monoenergetic $E = \bar{E}$ with electrons emitted normal to the surface;
- the emission spectrum is taken to be a constant up to $2\bar{E}$ with electrons emitted normal to the surface.

The numerical simulations results are presented at Fig.5:

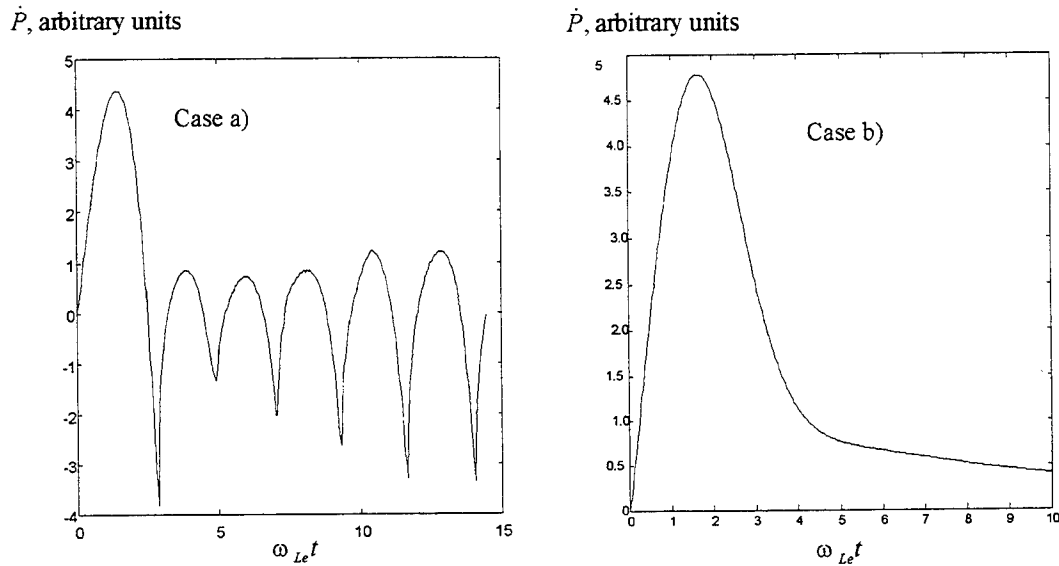


Fig.5. Time derivative of dipole moment vs. time

Numerical simulations show that stable oscillations occur only if the electron emission spectrum is a monoenergetic distribution⁴. Such distribution may be realized if initial energy of emitted electrons is low and final energy electrons are obtained in accelerating gap with the constant voltage.

This phenomena is similar to well known oscillations of virtual cathode⁵.

By this means amplification EM waves in waveguide driven by superlight current may be obtained if virtual cathode oscillations defined by Eq.(5) will be realized.

4.2 Two-dimensional simulation.

To test the validity of the amplification opportunity the 2D electrodynamic code was used for simulation of EM wave propagation in waveguide ($a \approx 4$ cm) driven by superlight ($v_{ph} = \sqrt{2}c$) prescribed electron current with the time dependence displayed in Fig.5(a) which was localized near the waveguide surface ($z=0$) in 0.1λ thick layer. Figures 6 shows the time dependence of magnetic field in fixed distance from the beginning of waveguide which confirms the analytical dependence Eq.(23).

More general simulation was performed with two dimensional particle-in-cell code self consistently solving Vlasov and Maxwell equations. In this case the boundary layer oscillation at the frequency ~ 5 GHz is formed by monoenergetic electrons with $E=500$ kev. Figure 7 shows the increasing of intensity of EM wave as a function of distance from the beginning of waveguide.

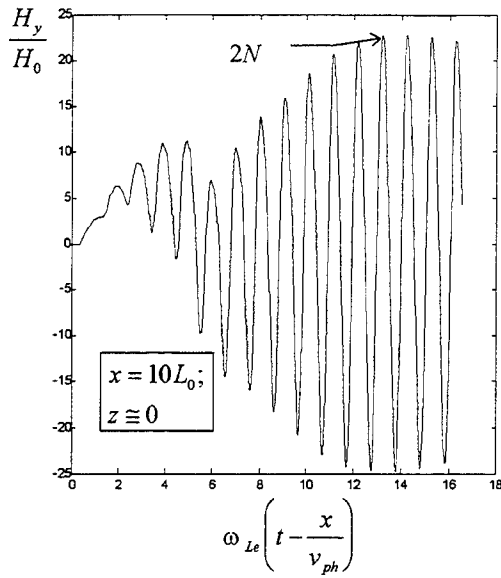


Fig.6. Magnetic field in waveguide vs. time

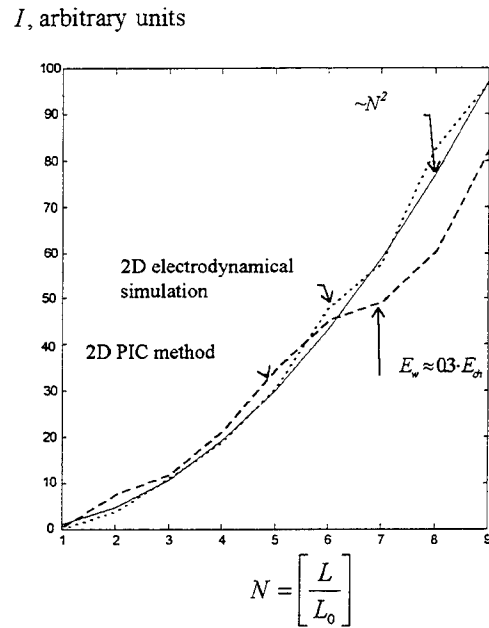


Fig.6. Intensity of generated EM wave vs. distance from the beginning of waveguide.

5. CONCLUSIONS.

A superlight current pulse is formed when the incident plane flux of ionizing radiation illuminates the surface which have photoemission properties. Once a superlight source of electromagnetic radiation has formed, it may be used to generate high power microwaves.

First, the superlight source can generate a directed high power ($\sim 10^9$ W) electromagnetic pulse with ultrashort duration ($10^{-12} \div 10^{-10}$ s). The power of such source increases with decreasing radiated wavelength in contrast to existing microwave devices.

Second, the high power generator - amplifier can be designed on the basis of waveguide driven by the superlight source. Amplification of microwaves can be realized if the superlight current pulse initiates a formation of virtual cathode oscillating with frequency correlated to cutoff frequency of waveguide.

The superlight sources of electromagnetic radiation open new way for designing of high power microwave devices in the short wavelength region.

6. ACKNOWLEDGMENTS

We would like to acknowledge A. Vronskiy and E. Dyankova who helped us to perform numerical simulations.

7. REFERENCES

1. L. Ginzburg. Theoretical Physics and astrophysics [in Russian], (Nauka, Moscow), 1981.

2. N. J. Carron, C.L. Longmire. Electromagnetic Pulse Produced by Obliquely Incident X-rays, IEEE Trans. on Nucl. Sci., Vol. NS-23, No.6, p.1897-1902, 1976.
3. N. J. Carron, C.L. Longmire. Scaling Behavior of The Time-Dependent SGEMP Boundary Layer, IEEE Trans. on Nucl. Sci., NS-25, No.6, p.1329-1335, 1978
4. R. Stettner, Adiabatic Oscillations of the One-dimensional SGEMP Boudary Layer, IEEE Trans. on Nucl. Sci., Vol. NS-24, No.6, p.2461-2466, 1976.
5. J. Benford, J. Swegle, *High Power Microwaves*, Chapter 9, (Artech House, Boston, MA),1991

BEAM - PLASMA GENERATORS OF STOCHASTIC MICROWAVE
OSCILLATIONS USING FOR PLASMA HEATING IN FUSION
AND PLASMA - CHEMISTRY DEVICES AND IONOSPHERIC
INVESTIGATIONS

L.A.Mitin, V.I.Perevodchikov, A.L.Shapiro, M.A.Zavjalov

State Science Center "All-Russian Electrotechnical Institute",
Russia, 111250, Moscow, Krasnokazarmennaja 12

Yu.P.Bliokh, Ya.B.Fainberg

National Science Center "Kharkov Institute of Physics and Technology",
Ukraine, 310108, Kharkov, Academicheskaja 1

ABSTRACT

The results of theoretical and experimental investigations of generator of stochastic microwave power based on beam-plasma inertial feedback amplifier is discussed to use stochastic oscillations for heating of plasma.

The efficiency of heating of plasma in the region of low-frequency resonance in the geometry of "Tokamak" is considered theoretically. It is shown, that the temp of heating is proportional the power multiplied by spectra width of noiselike signal.

KEYWORDS: generator of stochastic microwave power, beam-plasma inertial feedback amplifier, heating of plasma, temp of heating.

1. STOCHASTIC MICROWAVE OSCILLATORS BASED ON HYBRID BEAM-PLASMA SYSTEMS

The high-power beam-plasma generators of stochastic microwave signals are considerable interest for both pure and applied research. On the one hand, they can contribute to the study of fundamental problems of the stochastic dynamics of nonlinear dynamic systems with distributed parameters. On the other hand, they have wide applications in controlled nuclear fusion (as a radiation source for stochastic plasma heating), in nonequilibrium plasma chemistry (stochastic microwave discharge techniques), in charged particle stochastic acceleration, etc.

The nonlocality of the electron beam interactionh in traveling wave systems in conjunction with the nonequilibrium and broad-band character of this interaction leads to an unstable system behavior in the presence of a delayed feedback circuit. At certain nonequilibrium parameter values, the system instability regarding automodulation processes at the nonlinear interaction stage can result in a stochastization of the

microwave oscillations accompanied by the formation of broad noise-type spectra. Numerous papers were devoted to the purely physical and applied aspects of this problem [1-6]. The generator of stochastic microwave oscillations based on a hybrid beam-plasma amplifier with an external delayed feedback circuit belongs to such systems.

In [3], the evolutionary partial differential equations pertaining to the nonstationary model of the electron beam-wave interaction were reduced to an integral equation of the form

$$F(\tau + \theta) = \psi\{|G_0 F(\tau)|, \nu(\tau)\} \cdot \exp\{\arg(G_0 F(\tau))\} \quad (1)$$

Here, F represents the dimensionless complex signal amplitude; τ denotes the dimensionless time; θ is the delay time; G_0 is a difference kernel operator:

$$G_0 F(\tau) = \int_{-\infty}^{\tau} G(\tau - \tau') F(\tau') d\tau',$$

which defines the interaction linear stage; and $\psi\{|GF(\tau)|, \nu\}$ is a nonlinear function describing the nonlinear stage and depending on the instantaneous values of signal level $x = |GF(\tau)|$ and frequency $\nu(\tau)$ at the end of the linear interaction stage. Equation (1) explicitly defines the generator signal current value according to the totality of past signal values, i.e., it transforms the solution process into a certain functional mapping iteration. This equation, in contrast to the partial differential equations, can be analytically analyzed for stability rather easily. The disruption of monochromatic regimes [1-6] followed by automodulation and signal stochastization occurs (for example, at some point of beam current growth) if either of these conditions is satisfied:

$$|a(\nu)| \left| \frac{\partial}{\partial x} |\psi| \right| > 1, \quad (2)$$

$$\frac{d^2}{d\nu^2} |a(\nu)| - |a| |\psi| \frac{d^2}{d\nu^2} \arg(a) - \arg(\psi) > 0. \quad (3)$$

Here, $a(\nu)$ represents the device frequency response in a linear amplification regime and is equivalent to the Fourier transform of function $G(\nu)$. The first condition connects the disruption of monochromatic generation regimes with a steepening of the dropping part of the amplifier amplitude characteristic. The second condition is related to the amplifier frequency response. Therefore, the first mechanism of stability loss is called the amplitude mechanism, and the second, the phase mechanism.

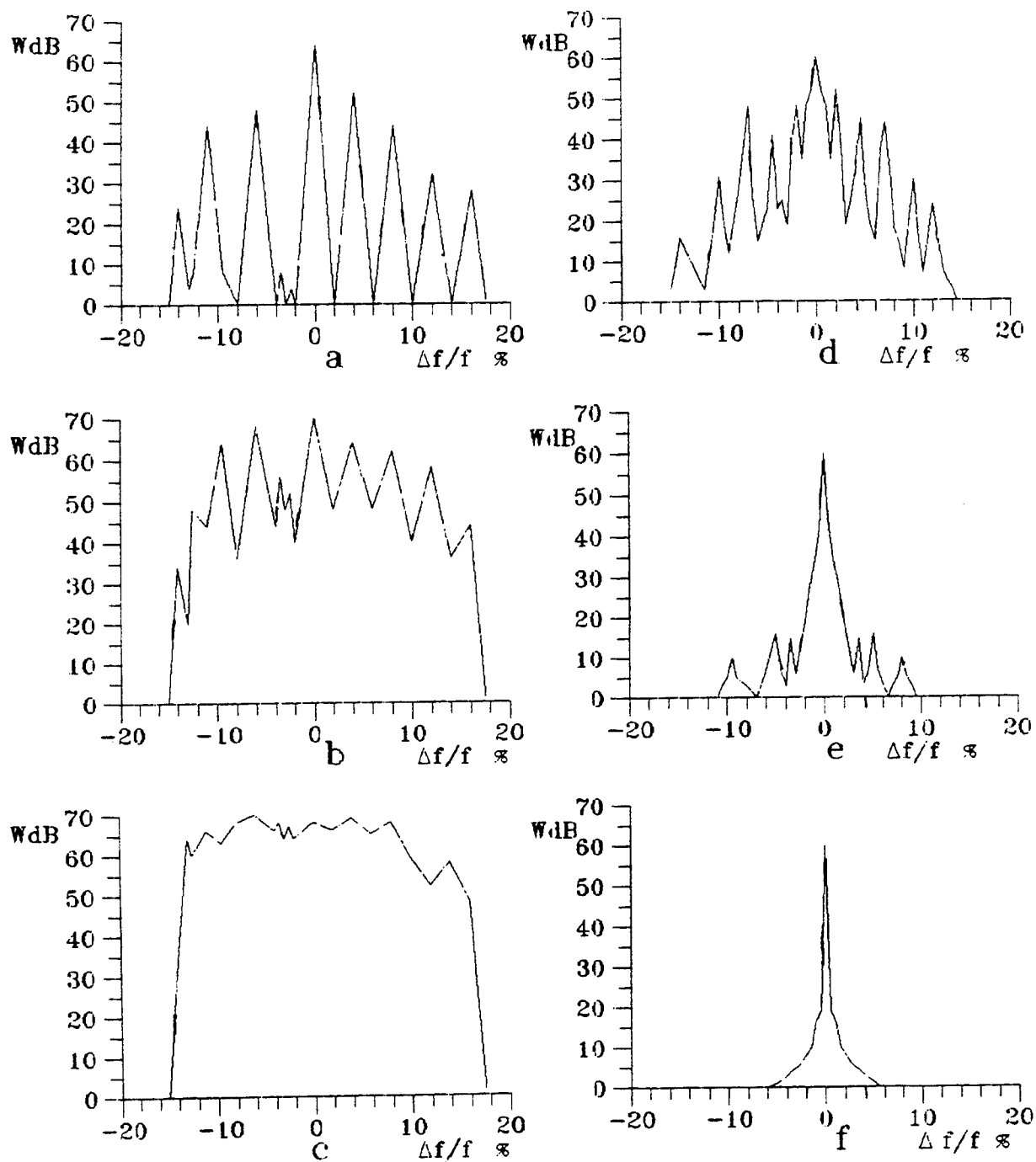


Fig.1. Oscillation spectra for different power levels of feedback circuit signal: (a) 0.5, (b) 0.8, and (c), 1.2 mW; (d), (e), and (f), in the presence of control signal of 0.2, 0.8, and 1.2 mW, respectively.

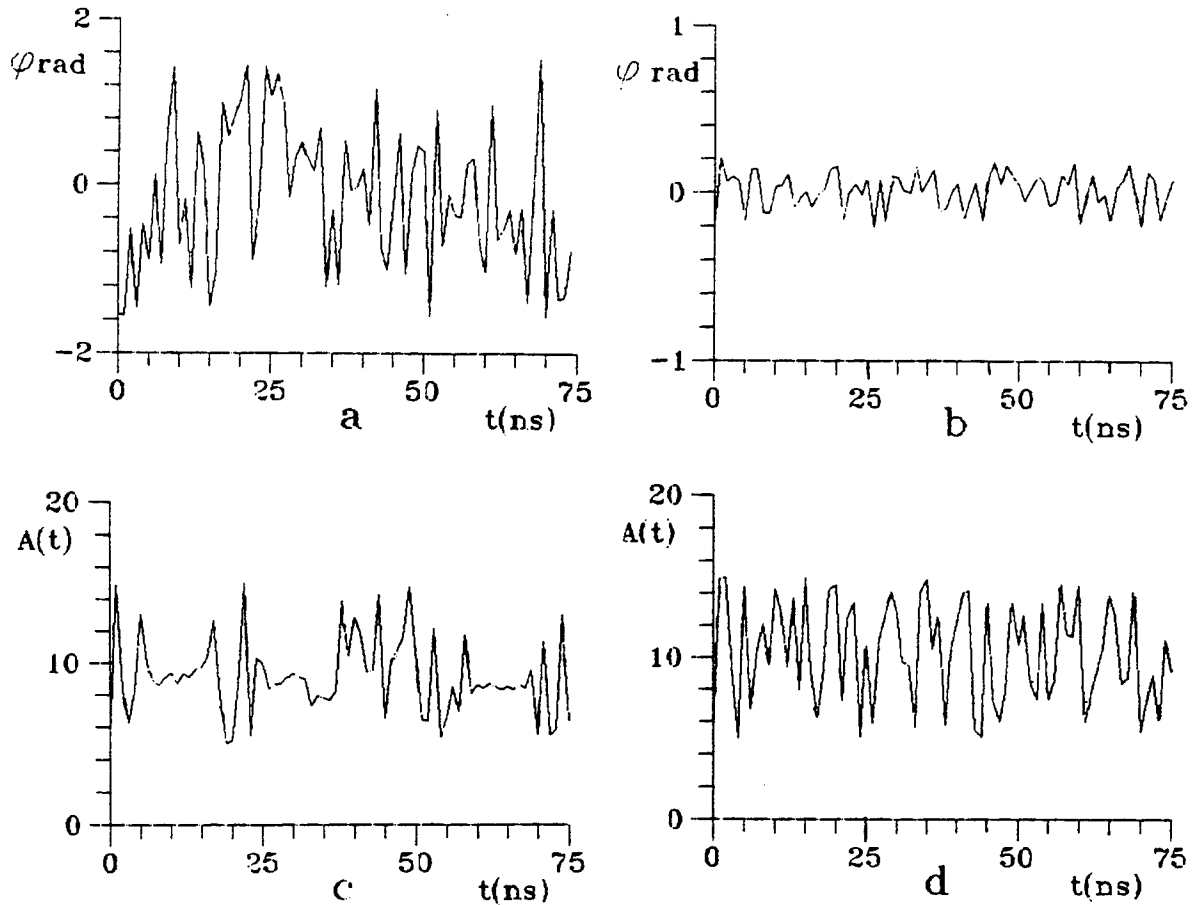


Fig.2. Time dependence of (a) phase of stochastic signal with a wide frequency bandwidth, (b) phase of output signal in the spectrum compression regime, (c) output signal amplitude at 1.8 A electron beam current, (d) output signal amplitude at 3 A electron beam current.

The identification of the mechanism responsible for the oscillation stochasticization is very important, because it determines the signal spectral characteristics and the scenario of the transition from a regular to a stochastic generation mode. Here are the characteristic features of the amplitude mechanism: transition via a chain of period doubling bifurcations; and low probability of large signal amplitudes, and, consequently, a rather small electron efficiency. The phase mechanism involves an intermittent turbulence and a high electron efficiency when the amplitude nonlinearity is weak.

As shown above, the deep amplitude nonlinearity mode involves a significant current deposition onto the slow-wave structure, which is undesirable in high-power CW devices.

The noted advantages of the phase stochastization mechanism were decisive in our choice of our stochastic oscillator scheme.

The experiments were carried out for the same electron beam parameter set, as before, in the amplification regime. Figures 1a-1c present the generated oscillation spectra at various power levels of the feedback signal. As the feedback signal increased, the system passed through a multifrequency generation regime toward stochastic oscillation spectra covering the whole bandwidth defined by the dispersion characteristic. The maximal output power obtained in this regime was 20 kW. In a 30% relative frequency bandwidth, the spectrum of oscillations was flat within 3 dB. Figures 2a, 2d show the signal phase and amplitude (signal envelope) as functions of time. One sees that in the wide-band generation regime the signal is random character both in oscillation amplitude and phase. The phase mechanism of transition to a stochastic behavior is confirmed by the signal realizations recorded at different beam currents (Figs. 2c and 2d). One clearly discerns quasi-monochromatic zones peculiar to the intermittent turbulence regime. They disappeared when the electron beam current was increased.

The wide-band generation mode is hard to control. In addition, it is energetically unprofitable. Therefore, it is not desirable in many applications, unless one needs wide microwave oscillation spectra. In this connection, we realized and studied the regime of frequency spectrum compression by means of an external control signal. The control signal was fed to the input of the traveling wave tube, being a part of the feedback circuit. Figures 1d-1f present the dependence of the generated spectra on the control signal power. For a 1 mW signal power at the traveling wave tube input (100 W at the beam-plasma amplifier input), the spectrum bandwidth was reduced by two orders of magnitude. At the same time, the integral output microwave power remained unchanged at the level of 20 kW. Figure 2b presents the time dependence of the signal phase in the spectrum compression mode. Note that the signal is still a noiselike one, although the phase dispersion is small. It was possible to retune the generated frequency over a bandwidth of about 25%, where the spectrum nonuniformity was within 3 dB.

2. THE PLASMA HEATING AND THE ARTIFICIAL IONIZED LAYER (AIL) CREATION BY STOCHASTIC ELECTROMAGNETIC RADIATION

By way of example, consider the Earth's ionosphere plasma heating by stochastic electromagnetic radiation. The interaction of the powerful electromagnetic radiation with the Earth ionosphere is one of few accessible methods of active influence on the

space plasma. Among different effects connected with powerful electromagnetic radiation on the local thermal instability is one of the essential because it leads to the most marked changing of ionospheric parameters. The efficiency of plasma heating by monochromatic electromagnetic radiation is determined by electron collision frequency ν , which in the ionosphere is rather small ($\sim 10^3 \text{ s}^{-1}$ on the height about 300 km).

In the case of stochastic signal, as it was shown in [7,8], the efficiency of energy transference to plasma electron component is determined by the reciprocal correlation time τ^{-1} . Its value may be much larger than collision frequency ($\tau^{-1} \gg \nu$). It allows to reduce the radiation source power and to increase the frequency. The latter makes accessible on influence all ionosphere, including the region above F-layer.

In [9,10] was shown that the growth rate of particle average kinetic energy is determined by following expression:

$$\frac{d}{dt} \left(\frac{m |V|^2}{2} \right) = \frac{e^2}{m} \frac{(|E|^2)}{(\omega^2 + \tau^{-2})\tau}, \quad (4)$$

where ω is the carrier frequency of a electromagnetic radiation.

As follows from comparison (4) with the analogous formula for plasma heating by monochromatic radiation [11], the role of collision frequency in (4) plays the value τ^{-1} . It means, that the efficiency of the plasma heating by stochastic radiation is greater than heating by monochromatic radiation in ratio of $1/\nu\tau$. In ionosphere the value $1/\nu\tau$ may be very large and it allows to use signals with $\omega \gg \omega_{pm}$ (ω_{pm} is the maximal value of plasma frequency in the region of F-layer), which can warm thoroughly the whole width of the ionosphere. For this case the dependence of heating rate and the electron steady temperature as functions of height will be discussed further.

Taking into account the angular diverging and the loss of energy it is possible to obtain the following expression for dependence of steady electron temperature T_e on height:

$$\frac{\Delta T}{T_e} \equiv \frac{T_e - T_0}{T_0} \sim \frac{e^2 P_{eff} \Delta f}{mc\omega^2 h^2 \nu(h) \delta T_0(h)} \cdot \exp\left(-\frac{3}{4} \frac{\Delta f}{c} \int_0^h dh' \frac{\omega_{p0}^2(h')}{\omega^2}\right). \quad (5)$$

Here T_0 is ionospheric heavy component temperature, $\delta \sim m/M \cdot 10^{-3} - 10^{-4}$ is the part of energy losses due to collisions of electrons with ions or neutrals, P_{eff} is an effective power of the radiation source, Δf is radiation spectrum width: $\Delta f \sim \tau^{-1}$.

Let us consider as an example the ionospheric plasma heating by stochastic electromagnetic radiation with following parameters: $F = 1 \text{ GHz}$, $\Delta f = 10\%$, antenna amp.

$$\text{coefficient} \approx 10^3$$

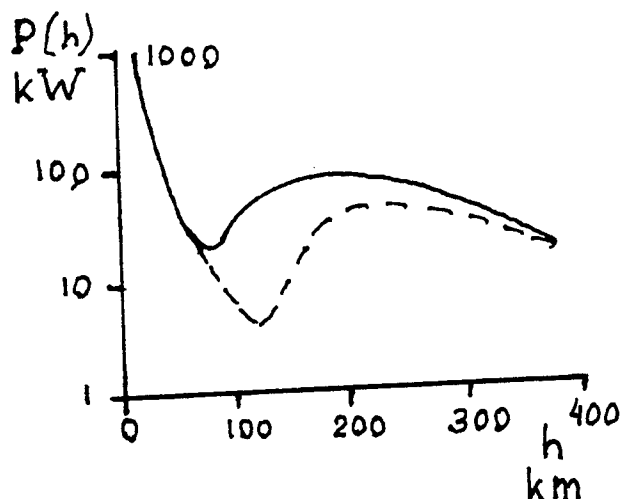


Fig.3. The dependence $P(h)$ of ground-based radiation source power that is necessary for AIL creation on the height h . The carrier frequency is chosen about 1 GHz, the spectrum width is 10% and the antenna growth coefficient is 10^3 . Solid and dotted lines correspond to day and night ionosphere.

To height about 1000 km the loss of power may be neglected and dependence $T_e(h)/T_h$ is determined by function $\varphi(h) = h^2 \nu(h)$ which has a sharp maximum on the height of F-layer. It means that the largest value of the relative temperature growth is to be expected on the heights more and less than F-layer height. This fact illustrates the essential difference between heating by monochromatic and stochastic signals.

The value $\Delta T/T_h$ for above mentioned parameters is about 1 on the height 200 km and higher. The transition time to a steady state is about 10 s.

Formula (5) allows to assess radiation power $P_{eff}^{(i)}$, which is necessary for neutral component ionization. Dependence $P_{eff}^{(i)}$ is determined by function $\varphi(h)$. The minimal power $P_{eff}^{(i)}$ is essential for an AIL creation on the height 150-250 km. The dependence of assessed for AIL creation power $P(h)$ of ground-based source of electromagnetic radiation, that was obtained using standard Earth's ionosphere parameters, is shown on Fig.3. If the radiation power is not very large than changed in a random manner wave amplitude exceed threshold of gas discharge only during short time intervals. In this case the discharge has pulse character that is favourable for ozone production. The point is that in the stationary air discharge the ozone formation is intensive only during initial stage. After that the ozone formation is decreased and some unhealthy nitrogen compounds appear [12]. High efficiency of ionosphere heating and pulse character of discharge make possible to use stochastic electromagnetic radiation for ozone reproduction, for example, in the regions of ozone "holes" that appear during space missiles launching.

The stochastic radiation can be used for long-distance transporting of electromagnetic radiation in the ionosphere. High efficiency of plasma heating make possible to use sources with relatively small power for wave-guide channel creation, where plasma density drop prevent the wave beam divergence. As an example, for the stochastic

tic radiation with carrier frequency ~ 1 GHz and spectrum width ~ 100 MHz the power that is necessary for wave-guide channel creation in the F-layer region is about some kW. Corresponding power of monochromatic radiation with frequency ~ 1 GHz is about 10^5 kW. Such high difference between powers is connected with very low collision frequency in the ionosphere ($\nu \sim 10^3 \text{ s}^{-1}$) that make non-effective heating by monochromatic radiation.

3. THE HEATING IN THE FIELD OF STOCHASTIC POTENTIAL WAVE IN MAGNETIZED PLASMA

In the homogeneous waves fields the heating rate is determined only by their correlation time τ_c . But in the case of non-homogeneous wave created, for example, by localized source (antenna), the heating of plasma electrons is defined not only by temporary but by space correlation characteristics as well. In the dispersive media which plasma is, this characteristics change according to removal from radiation source. The plasma heating efficiency changes according to this one. Below the magnetized plasma heating by localized source of stochastic potential waves is considered. The interest to this wave type is connected with investigation of possibility of stochastic radiation sources using for plasma additional heating in Tokomaks. In the presence the regular low and high hybrids waves are applied particularly. The results about stochastic signal propagation, which are described in this report, can represent also a special interest for Earth's ionosphere physics and removal sensing.

The dispersion of potential magnetized plasma waves connects frequency with direction of wave propagation only. In [13] was shown that on large distance from localized source (antenna) of such waves the correlation time τ determines only a wave beam width, but not the correlation parameters in it. The correlation length in transversal direction and correlation time in a wave beam do not depend on τ .

The constancy of transverse to wave beam direction correlation length l_\perp when mean beam radius increases is a consequence of specific property of considered wave in anisotropic media: their frequency determines only direction of the wave vector but not its modulus. Therefore each spectral harmonic, which propagates at corresponding angle with respect to anisotropy direction (magnetic field), "carries" the source image as a whole. Because in the stationary stochastic processes the spectral components are statistically independent, the space correlation vanishes when two points of observation are separated one from another at distance greater than source size a . So, on the great distance from antenna the transverse correlation length is determined by source dimension only: $l_\perp \sim a$.

The independence of correlation time τ in the wave beam on τ may be explained by following. The signal harmonics from source with a size a may come to the removal observation point only if they are contained in frequency interval $\Delta \omega \sim a/z$ (z is the distance between observation point and antenna). If $\Delta \omega \ll \tau^{-1}$ then signal spectrum in the observation point is much smaller than initial spectrum width τ^{-1} . The media at issue

acts as a frequency filter, which bandwidth decreases as τ^{-1} when z increases. The correlation time τ_* of stochastic signal which passes through narrow - band filter is determined not by initial correlation time τ , but by frequency band width $\Delta\omega$: $\tau_* \sim \Delta\omega$.

Now we shall estimate the electron heating rate. The field that acts on a moving electron has a correlation time τ_e which is determined by expression:

$$\tau_e^{-2} \sim \frac{\nu_0^2}{l_z^2} + \tau_*^{-2}. \quad (6)$$

First term in the right part of (6) connects with transversal stochastic space structure of wave beam, and the second one - with stochastic time variations of the field. According to (3) the temperature T grow rate is described by the following expression:

$$\frac{dT}{dt} \sim \frac{e^2 (E^2)}{m \omega^2 \tau_*} \sim \frac{e^2 (E^2)}{m \omega^2} \sqrt{\nu_0^2 / l_z^2 + \tau_*^{-2}}.$$

A particle crosses the region with dimension R during the time interval $\Delta t \sim R/\nu_0$, so the total particle energy charge¹ during one pass through whole wave beam is

$$\Delta T \sim \frac{e^2 (E^2)}{m \omega^2} \sqrt{\nu_0^2 / l_z^2 + \tau_*^{-2}} \cdot \frac{R}{\nu_0}. \quad (7)$$

As it following from (7), the slow particles acquire greater energy during one crossing of a wave beam than fast ones. This circumstance may be very important, because such "priority" of slow particles prevent the formation of high-energy "tails" in the electron distribution function and it leads to more uniform energy distribution in the plasma electron component.

Let us compare now the expression for ΔT with similar ones for monochromatic signal². In this case the particle energy changing occurs only at the moment when particles cross a beam boundary³, and the value ΔT is determined by the squared oscillation

¹It is assumed here that energy change is small: $\Delta T \ll T$.

²Here only stochastic mechanism of energy exchange between regular wave and particles is considered. Resonance interaction may be more effective but it affects only small group of particles.

³It is assumed that the electron collision frequency ν in a media is small enough: $\nu \ll \nu_0/R$.

velocity in the wave field:

$$\Delta T \sim \frac{e^2 (E^2)}{m \omega^2} . \quad (8)$$

Note, that the expression (5) is the upper boundary for ΔT value and is satisfied for beams with sharp boundaries and uniform intensity distribution across the beam. If the intensity smoothly decreases toward boundary then the particle energy increasing may be much smaller.

In the considered media the radiation of antenna represents the conic shell with axis that is parallel to anisotropy direction. Let us define D as a diameter of cone and R as a shell width in the observation point (for regular radiation $R \ll a$ in the considered approximation). The formulas (7) and (8) expressed in terms of radiation source power P may be rewrite in the form:

$$\Delta T_s \sim \frac{e^2 P}{m c D \omega^2 a} \sqrt{1 + a^2 / (v^2 \tau_e^2)} , \quad (9)$$

$$\Delta T_r \sim \frac{e^2 P}{m c D \omega^2 a} , \quad (10)$$

where $\Delta T_{s,r}$ are the particle energy changing for stochastic and regular radiations corresponding.

As it follows from comparison (9) and (10), the heating efficiency for "slow" electron in the stochastic wave beam's field exceeds the heating efficiency by regular wave with the same power and created by the same source, and for "fast" particles these efficiencies are equal.

4. CONCLUSION

As it was shown mentioned above examples, the stochastic radiation interaction with plasma may be in some conditions more strong as for regular one. It is possible to say that in the ogeneral case the stochastic heating is more effective than heating in the regular fields if the collision frequency is smaller compare to reciprocal correlation time τ_e . Such condition may be fulfilled in the plasma with low density (Earth's ionosphere) or in the high temperature plasma (thermonuclear plasma).

5. REFERENCES

1. V.Ya.Kislov, Lektsii po Elektronike SVCh i Radiofizike (Lectures on Microwave Electronics and Radiophysics), Saratov: Saratov. Gos. Univ., 1980, vol.5, p.78.
2. N.S.Ginzburg and S.P.Kuznetsov, Relyativistskaya Vysokochastotnaya Elektronika (Relativistic High-Frequency Electronics), Gor'kii: Inst. Prikl. Fiz., Akad. Nauk SSSR, 1981, p.104.
3. S.P.Kuznetsov, Izv. Vyssh. Uchebn. Zaved., Radiofizika, 1982, vol.25, p.101.
4. V.S.Anishchenko, Slozhnye Kolebaniya v Prostyykh Sistemakh (Complex Oscillations in Simple Systems), Moscow: Nauka, 1990.
5. A.S.Dmitriev and V.Ya.Kislov, Stokhasticheskie Kolebaniya v Radiofizike i Elektronike (Stochastic Oscillations in Radiophysics and Electronics), Moscow: Nauka, 1989.
6. Yu.P.Bliokh, A.V.Borodkin, M.G.Lyubarskii, et al., Izv. Vyssh. Uchebn. Zaved., Prikladnaya Nelineinaya Dinamika, 1992, vol.1, p.34.
7. F.G.Bass, Ya.B.Fainberg, V.D.Shapiro, Sov. Phys. "JETP", v.49, p.329, 1965.
8. Yu.P.Bliokh, Ya.B.Fainberg, M.G.Lyubarskii, V.O.Podobinskii, Sov. J. "Plasma Phys.", v.19, N 3, 1993.
9. Yu.P.Bliokh, Ya.B.Fainberg, E.A.Kornilov, L.A.Mitin, Plas. Phys. Rep., v.20, N 9, 1994.
10. Ya.B.Fainberg, Yu.P.Bliokh, M.G.Lyubarskii, P.I.Markov, I.N.Onistchenko, G.V.Sotnikov, Plasma Phys. Rep., v.20, N 9, p.681-689, 1994.
11. The Thermal Nonlinear Phenomenon in Plasma, Gorky: Inst. App. Phys., 1979.
12. A.L.Vikharev, A.M.Gorbachev, O.A.Ivanov, A.L.Kolisko, A.G.Litvak, Phys. Letters A, 179, p.122-126, 1993.
13. Yu.P.Bliokh, Plasma Phys. Rep., v.21, N 8, 1995.

Helical Cerenkov effect with very strong magnetic fields

Josip Šoln

Army Research Laboratory
AMSRL-SL-CM
Aberdeen Proving Ground
Edgewood, Maryland 21010-5423

ABSTRACT

The helical Cerenkov effect results from the helical electron motion in a medium with a rather strong magnetic field B . However, at the same radiation angle and the same frequency at which the helical Cerenkov effect is observed one will see harmonic radiation if the parallel (with respect to the magnetic field B) electron velocity components are above and below the helical Cerenkov effect threshold. Increase in the strength in B decreases the number of harmonics at both sides of the helical Cerenkov effect threshold. The radiation frequency dependent asymptotic limit is achieved, by definition, when the number of harmonics, regardless whether occurring below or above the helical Cerenkov effect threshold, is reduced to just the first one. In the visible spectrum and for silica aerogel as a medium such an asymptotic limit already happens at $B \cong 100$ T. There is also a universal frequency dependent asymptotic limit when, regardless of the medium and the radiation angle, no harmonic radiation can occur and only the helical Cerenkov radiation should exist. In the visible spectrum, we argue, this should happen at $B \cong 10^4$ T. For magnetic fields that are even stronger than this, as for example the ones that can be found in neutron stars (pulsars), $B < 10^8$ T, not only that harmonic radiation does not appear but the helical Cerenkov effect degenerates into a form of the ordinary Cerenkov effect, whose angular dependence, however, is determined with respect to the direction of the magnetic field rather than the initial electron velocity.

Keywords: helical Cerenkov effect, dielectric medium, harmonics

1. THE HELICAL CERENKOV EFFECT AND HARMONIC RADIATION ABOVE AND BELOW HELICAL CERENKOV THRESHOLD

When electrons are moving in a medium on helical trajectories under the influence of the uniform magnetic field which, for simplicity, is defined as $\vec{B} = \hat{z}B$ [1,2], generally the helical Cerenkov radiation and the harmonic radiation above and below helical Cerenkov effect threshold may occur. Kinematically they can be described, respectively as follows:

$$l = 0: \quad 1 - n(\omega) \beta_z(0) \cos \theta_0 \cong 0; \quad (1a)$$

$$l = -b \leq -1: \quad \omega[n(\omega) \beta_z(-b) \cos \theta_{-b} - 1] \cong b\omega_c(-b) > 0; \quad (1b)$$

$$l = a \geq 1: \quad \omega[1 - n(\omega) \beta_z(a) \cos \theta_a] \cong a\omega_c(a) > 0; \quad (1c)$$

where l is the harmonic index and $v_z(l)$ denotes the parallel component of the electron velocity with respect to \vec{B} ; here and in what follows, $\beta = v/c$, $\beta_z = v_z/c$, $\beta_\perp = v_\perp/c$

with v_{\perp} being the perpendicular component of the electron velocity with respect to \vec{B} and $v^2 = v_z^2 + v_{\perp}^2$. One notices that v_z is also the velocity of the electron guiding center.

Furthermore, θ_l is the radiation angle associated with harmonic index l , ω is the angular radiation frequency, $n(\omega)$ is the frequency dependent index of refraction, and $\omega_c(l) = eB/M\gamma(l)c$ is the relativistic angular electron cyclotron frequency, with M being the mass of the electron, $\gamma(l)$ the electron relativistic factor, and c the velocity of light.

One should contrast these with the ordinary Cerenkov effect whose kinematics is simply:

$$l \equiv C: \quad 1 - n(\omega) \beta(C) \cos \theta_C \equiv 0, \quad (1d)$$

and which explains why (1a) is called the helical Cerenkov effect.

From now on we shall assume the index of refraction n is independent of ω .

Next, with L denoting the interaction length, to each of the three kinematics regimes (1a,b,c,d) we can evaluate the number spectrum per unit path length,

$d^2 N(\omega; l)/dL d\omega \equiv N(\omega; l)$, as [3]

$$l = 0: \quad N(\omega; l = 0) = \frac{\alpha}{c} \left\{ \left[\sin \theta_0 J_0(\xi_0) \right]^2 + \left[\frac{v_{\perp}(0)}{v_z(0)} J_1(\xi_0) \right]^2 \right\}, \quad (2a)$$

$-l = b = 1, 2, \dots$:

$$\begin{aligned} & N(\omega; -b) \\ &= \frac{\alpha}{c} \left\{ \left[\sin \theta_{-b} J_b(\xi_{-b}) + \left(\frac{v_{\perp}(-b)}{v_z(-b)} \right) \cos \theta_{-b} \left(\frac{J_{b+1}(\xi_{-b}) + J_{b-1}(\xi_{-b})}{2} \right) \right]^2 \right. \\ & \quad \left. + \left(\frac{v_{\perp}(-b)}{v_z(-b)} \right)^2 \left(\frac{J_{b+1}(\xi_{-b}) - J_{b-1}(\xi_{-b})}{2} \right)^2 \right\}, \end{aligned} \quad (2b)$$

$l = a = 1, 2, \dots$:

$$\begin{aligned} & N(\omega; a) \\ &= \frac{\alpha}{c} \left\{ \left[\sin \theta_a J_a(\xi_a) - \left(\frac{v_{\perp}(a)}{v_z(a)} \right) \cos \theta_a \left(\frac{J_{a+1}(\xi_a) + J_{a-1}(\xi_a)}{2} \right) \right]^2 \right. \\ & \quad \left. + \left(\frac{v_{\perp}(a)}{v_z(a)} \right)^2 \left(\frac{J_{a+1}(\xi_a) - J_{a-1}(\xi_a)}{2} \right)^2 \right\}, \end{aligned} \quad (2c)$$

$$l \equiv C: \quad N(\omega; C) = \frac{\alpha}{c} \sin^2 \theta_C. \quad (2d)$$

Here J_l are the Bessel functions and $\xi_l = (n\gamma(l)\beta_{\perp}(l)\sin\theta_l) \frac{\omega(Mc/e)}{B}$.

We are interested in the number of photons per unit path length emitted into the natural angular frequency interval $\Delta\omega$ defined as

$$\Delta\omega = \omega_I - \omega_{II} = \omega_0, \quad \omega_{I,II} = \frac{\sqrt{5} \pm 1}{2} \omega_0, \quad \omega_0 = \frac{\omega_{II} + \omega_I}{\sqrt{5}}, \quad (3)$$

with ω_0 being the central angular radiation frequency. One can see easily that these definitions are numerically very close to what one uses in practice [5]. Furthermore, one also has that $\Delta\omega = 2\pi c/\Delta\lambda$. For latter references the following approximate expression will be found very useful:

$$\sqrt{5} \cong \frac{e+1}{e-1}. \quad (4)$$

With little work, as long as $B \leq 100$ T, we obtain for the HCE in the visible spectrum the expression [3]:

$$\frac{dN(\omega_0, \Delta\omega; l=0)}{dL} = N_{eff}(\omega_0; l=0) \omega_0 \ln(\omega_I / \omega_{II}) \cong N_{eff}(\omega_0; l=0) \omega_0, \quad (5a)$$

$$N_{eff}(\omega; l=0) = \frac{\alpha[(n\beta(0))^2 - 1]}{c\pi\xi_0(n\beta_z(0))^2}. \quad (5b)$$

As far as the harmonic radiation is concerned we simply have,

$$\frac{dN(\omega_0; \Delta\omega; \{a\})}{dL} = \sum_a N(\omega_a; a) \omega_a, \quad (6a)$$

$$\frac{\sqrt{5}-1}{2} \omega_0 \leq \omega_a \leq \frac{\sqrt{5}+1}{2} \omega_0; \quad (6b)$$

$$\frac{(\sqrt{5}-1)\omega_0(1-n\beta_z(a)\cos\theta_a)}{2\omega_c(a)} \leq a \leq \frac{(\sqrt{5}+1)\omega_0(1-n\beta_z(a)\cos\theta_a)}{2\omega_c(a)}; \quad (6c)$$

$$\frac{dN(\omega_0; \Delta\omega; \{-b\})}{dL} = \sum_b N(\omega_{-b}; -b) \omega_{-b}, \quad (7a)$$

$$\frac{\sqrt{5}-1}{2} \omega_0 \leq \omega_{-b} \leq \frac{\sqrt{5}+1}{2} \omega_0, \quad (7b)$$

$$\frac{(\sqrt{5}-1)\omega_0(n\beta_z(-b)\cos\theta_{-b}-1)}{2\omega_c(-b)} \leq b \leq \frac{(\sqrt{5}+1)\omega_0(n\beta_z(-b)\cos\theta_{-b}-1)}{2\omega_c(-b)}, \quad (7c)$$

where approximately $(\sqrt{5} \pm 1)/2 \cong 1.62, 0.62$. Here $\{a\}$ and $\{-b\}$ denote all the a 's and b 's for which relations (6b,c) and (7b,c) hold, respectively; that is for those $\omega_{a,-b}$'s falling within the interval $\Delta\omega$. In practice the number of a 's and b 's that contribute to relations (6b,c) and (7b,c) are finite.

For the monoenergetic beam in the uniform magnetic field and the dielectric medium either the HCE or one of the harmonic radiation can occur. If, however, the beam is non-monoenergetic, the HCE, the harmonic radiation above and below the HCE threshold may occur. Here, by definition, the overall number of photons per unit path length is the superposition over the beam velocities of the emitted total number of helical Cerenkov effect photons per unit path length and the total number of photons per unit path length into the harmonics above and below the helical Cerenkov threshold.

2. INCREASING STRENGTHS OF MAGNETIC FIELDS AND ASYMPTOTIC REGIMES

As the magnetic field B increases the absolute values of Bessel function arguments $|\xi_l|$, $l = 0, a, -b$, become smaller. In general, when $B \rightarrow \infty$, $\xi_l \rightarrow 0$, $l = 0, a, -b$, and both $N(a)$ and $N(-b)$, respectively, decrease first to their values at $a, b = 1$; after that they go to zero as the supports for $a, b = 1$ vanish (compare with relations (6) and (7)). Clearly, depending on other parameters, this process may be achieved already at moderate values of B . For example, in the visible spectrum, where $B \leq 100$ T, we shall show that $N(a)$ and $N(-b)$ are already zero at $B \cong 40$ T.

In any case, how abruptly $N(a)$ and $N(-b)$ go to zero with increasing B depend also on respective beam velocities $\beta_z(a)$ and $\beta_z(-b)$, respective radiation angles θ_a and θ_{-b} , etc. The simplest way to see when the harmonic radiation does not appear is to see for which B 's in relations (1b) and (1c) $a, b \geq 1$ do not appear. Denoting these B 's with B_a and B_{-b} from (6) and (7) we have:

$$B_a \geq \frac{\sqrt{5}+1}{2} \omega_0 \left(\frac{Mc}{e} \right) \gamma(a) (1 - n\beta_z(a) \cos \theta_a) , \quad (8a)$$

$$B_{-b} \geq \frac{\sqrt{5}+1}{2} \omega_0 \left(\frac{Mc}{e} \right) \gamma(-b) (n\beta_z(-b) \cos \theta_{-b} - 1) . \quad (8b)$$

These relations, need not be satisfied simultaneously. Respectively, however, they mean that there is no harmonic radiation below or/and above the HCE threshold. The real value of relations (8) comes when they are applied to a beam with an energy spread and when the angle of observation is the same for harmonic radiation and the HCE. Let $\gamma(a)$ and $\gamma(-b)$ correspond to the lower and upper values of the electron energy within the beam, then, for $\theta_0 = \theta_a = \theta_{-b}$ the larger of the two B 's in relations (8) is the B for which harmonic radiation ceases to exist and only the HCE radiates. Compactly we write this as

$$\theta_0 = \theta_a = \theta_{-b} ; \gamma(a) = \text{Min} \gamma, \gamma(-b) = \text{Max} \gamma;$$

$$B = \text{larger of } B_a, B_{-b} :$$

$$\frac{dN(\omega_0; \Delta\omega; \{a\})}{dL} = \frac{dN(\omega_0; \Delta\omega; \{-b\})}{dL} = 0, \quad \frac{dN(\omega_0; \Delta\omega; 0)}{dL} \neq 0 . \quad (9)$$

As mentioned earlier, relations (9) may be actually satisfied already at moderate values of B . In fact, for the visible light with $\omega_0 \cong 4 \times 10^{15} \text{ s}^{-1}$, the medium of silica aerogel with $n = 1.075$, and taking the beam parameters and angles to be

$$\theta_0 = \theta_a = \theta_{-b} \cong 5^\circ ; \beta_\perp(0) = \beta_\perp(a) = \beta_\perp(-b) = 0.3 , \quad (10a)$$

$$\beta_z(a) = 0.9336 \quad [\beta(a) = 0.9806, \gamma(a) = 5.1037] , \quad (10b)$$

$$\beta_z(-b) = 0.9342 \quad [\beta(-b) = 0.9812, \gamma(-b) = 5.1799] , \quad (10c)$$

the equalities in equations (8) will be satisfied with the following values for magnetic fields:

$$B_a \geq 37.35 \text{ T}, B_{-b} \geq 37.61 \text{ T}, \quad (11)$$

where it is useful to notice that $(Mc/e) \cong 5.56 \times 10^{-12} \text{ sT}$. Therefore, according to relation (9), for $B \cong 37.61 \text{ T}$ we observe only the HCE at $\theta_0 \cong 5^\circ$. This magnetic field is even presently achievable in the laboratory [4]. Relations (5) yield

$$\frac{dN(\omega_0; \Delta\omega; 0)}{dL} = 0.4 \text{ cm}^{-1}. \quad (12)$$

Hence, at the end of the 3 cm silica aerogel we have $N(\omega_0; \Delta\omega; L = 3\text{cm}) = 1.2$ photons. with B as long as $B \leq 100 \text{ T}$.

Finally, we see that relations (8a) and (8b) will have maxima for $\theta_a = \pi$ and $\theta_{-b} = 0$, respectively. Hence, regardless of the radiation angle, no harmonic radiation exists when $B = \frac{\sqrt{5}+1}{2} \omega_0 \left(\frac{Mc}{e} \right) \gamma (n\beta_z + 1)$. Just from $\omega_0 (Mc/e) \cong 10^4 \text{ T}$ we see that in the visible spectrum for $B \cong 10^5 \text{ T}$ and larger the HCE will dominate and no harmonic radiation occurs essentially at any radiation angle. This we call the universal frequency dependent asymptotic regime.

Once we have such large values for B that $|\xi_l| \ll 1$ we may expand the Bessel functions around $\xi_l = 0$ and keeping only terms of $O(\xi_l)$ one has:

$$J_0(\xi_l) \cong 1; J_1(\xi_l) \cong \frac{\xi_l}{2}; J_n(\xi_l) \cong 0, n \geq 2. \quad (13)$$

From relations (2), neglecting terms of $O(\xi_l^2)$, we obtain

$$N(\omega; l=0) = \frac{\alpha}{c} \sin^2 \theta_0; \quad (14a)$$

$$N(\omega; a=1) = \frac{\alpha}{c} \left\{ \left(\frac{v_\perp(1)}{2v_z(1)} \right)^2 [1 + \cos^2 \theta_1] - \frac{\xi_1 v_\perp(1) \sin 2\theta_1}{4v_z(1)} \right\},$$

$$N(\omega; a=2) = 0, \dots; \quad (14b)$$

$$N(\omega; b=1) = \frac{\alpha}{c} \left\{ \left(\frac{v_\perp(-1)}{2v_z(-1)} \right)^2 [1 + \cos^2 \theta_{-1}] + \frac{\xi_{-1} v_\perp(-1) \sin 2\theta_{-1}}{4v_z(-1)} \right\},$$

$$N(\omega; b=2) = 0, \dots. \quad (14c)$$

where one should remember that in order that kinematically $N(\omega; a=1, b=1) \neq 0$, $a=1$ and $b=1$ still have to satisfy relations (6c) and (7c), respectively.

The equations (14) are quasiclassical and, as one can also see from the expression for ξ_l , for the visible spectrum, $\omega_0 \cong 4 \times 10^{15} \text{ s}^{-1}$, they are valid for $B \geq 10^4 \text{ T}$; this is consistent with the onset of the general asymptotic regime at $B \cong 10^5 \text{ T}$ where not even $a=b=1$ are kinematically allowed.

However, if we disregard the wavelength of the radiation (that is regardless whether we are in the asymptotic regime or not) there should be a general physical limit on B for which our quasiclassical theory should be valid. We postulate that our quasiclassical expressions are generally valid as long as the R_l , the electron gyroradius, is larger than the Compton electron wavelength:

$$R_l = \frac{v_{\perp}(l)}{\omega_c(l)} > \frac{\lambda_c}{2\pi} = \frac{\hbar}{Mc} = 3.86 \times 10^{-11} \text{ cm} . \quad (15)$$

This means that the quasiclassical theory of the HCE and the accompanying harmonic radiation holds for B satisfying the inequality,

$$\frac{B}{\beta_{\perp}(l)\gamma(l)} < 4.32 \times 10^9 \text{ T} . \quad (16)$$

Next we look at the meaning of $\xi_l < 1$ for which expressions (14) are valid:

$$l = 0, a, -b: n \sin \theta_l \beta_{\perp}(l)\omega < \omega_c(l) . \quad (17)$$

Now from the practical point of view we can go as high in the radiation frequency as near ultraviolet; after that n is mostly smaller than one [6] and radiation either by the ordinary or the helical Cerenkov effects are forbidden. Hence, for large magnetic fields for which $\omega \ll \omega_c$, relations (6c) and (7c) tell us that no harmonic radiation can occur. In the situation like this only $N(\omega; l = 0)$ exists, and we have simply that the HCE degenerated into the ordinary Cerenkov effect. Since here it is the electron guiding center rather than the electron itself that is causing the Cerenkov radiation, we call this the degenerate HCE (DHCE).

Hence, for the radiation from a neutron star with a dielectric medium, if it exists, where magnetic fields can reach 10^8 T [7], the observed Cerenkov radiation is most likely to be the degenerate helical Cerenkov radiation. Now, for the sake of argument, let us assume that in the supernova with a magnetic field of $B \cong 10^8 \text{ T}$ an electron beam is radiating through a medium with $n \cong 1.075$ a near-ultraviolet radiation of, say, $10^{15.5} \text{ Hz}$ in frequency [6]. Because the magnetic field is so strong no harmonic radiation will occur so that the DHCE will dominate. Assuming that an electron has $\beta_{\perp}(0) \cong 0.3$ and $\beta_z(0) \cong 0.95$, the radiation angle θ_0 turns out to be about 12° . Hence using relations (14a) and

$$\frac{dN(\omega_0, \delta\omega = \omega_0, l)}{dL} = N(\omega_0; l)\omega_0$$

we estimate that for $\omega_0 \cong 10^{15.5} \text{ s}^{-1}$ the number of photons per unit path length is

$$\frac{dN}{dL} \cong 32 \text{ cm}^{-1} .$$

This is a rather large number; particularly if one takes into account that n is actually small index of refraction.

The difference between this DHCE and the ordinary Cerenkov effect is the fact that with the nonmonoenergetic beam for the DHCE all the radiation angles are measured with respect to the direction of the magnetic field \vec{B} . From this example we see that on general grounds the HCE can be used to detect media with strong magnetic fields.

3. DISCUSSION AND CONCLUSION

Clearly, the most significant results when the magnetic field is strong are the asymptotic regimes. Even for the moderate magnetic fields there are beam energies and observation angles where harmonic radiation is negligible and the HCE is dominant; this, of course, is important when one wants to observe the HCE alone. For the extreme values of the magnetic field, say $B \cong 10^8 \text{ T}$, which can be found in supernova, the HCE totally

dominates in a sense that it degenerates into the ordinary Cerenkov effect, the DHCE, where now the gyroradia are so "small" that classically only the Cerenkov radiation essentially is coming from the "straight line" of the electron guiding center.

Of course, as the strengths of magnetic fields increase even beyond these values, the quantum mechanics will start playing important role as now the gyroradia will become quantized because of the existence of electron Landau energy levels. This, while being beyond the scope of this paper, should nevertheless be studied so that, at least in principle, the complete description of the HCE in the semiclassical and the Landau quantum regime is given.

4. REFERENCES

- [1] J. Soln, Phys. Rev. A 46, 5138-5148 (1992).
- [2] J. Soln, IEEE Trans. Plasma Science 22, 526 (1994).
- [3] J. Soln, In Preparation.
- [4] G. Boebinger, A. Passner, and J. Bevk, "Building World-Record Magnets," Scientific American, June 1995, pp. 58-66.
- [5] See, for example, B. R. Martin and G. Shaw, *Particle Physics* (John Wiley & Sons, New York, 1993), pp. 69-71.
- [6] J. V. Jelley, "Cerenkov Radiation and Its Applications" (Pergamon Press, New York, 1958).
- [7] See for example, F. Schwabl, "Quantum Mechanics" (Springer-Verlag, New York, 1990) pp. 138-9.

SESSION 4

ABSTRACT

This paper deals with the theoretical and experimental study of BWO using a high current electron beam. The dependencies of start length and the oscillation increments on the space charge parameter are obtained from the numerical analyze of the linear stage of transient process. For the actual experimental parameters in X-band, the duration of linear stage may be about 2 ns. The established oscillations in the nonlinear stage are steady-state over a wide range of beam current (varied by factor of 20). The further increase of current results in non-sinusoidal self modulation. The efficiency of the generator rises monotonously with the current and reaches ~25%. In the experiment, a compact nanosecond generator with the cathode voltage of up to 350 kV was used capable of operation at a repetition rate of up to 1,000 p.p.s. The pulsed magnetic system in which the coaxial magnetically insulated diode and the BWO slow wave structure are placed can be operated at 1 p.p.s.. The microwave power was ~200 MW with the pulse duration of ~1 ns.

Keywords: nanosecond radar, Backward Wave Oscillator, BWO, transient process, space charge, pulse repetition rate

1. INTRODUCTION

The generation of short powerful microwave pulses became of point of interest during the last years because of wide capabilities of nanosecond radio location¹. A radar with the nanosecond microwave pulse possesses high contrast of object recognition and the spatial resolution² as high as ~15 cm. The most important parameter of a radar is the power pulse of emitter which determines the maximum range of location. In this paper, a possibility to generate nanosecond pulses with the power of ~10⁸ W with the use of a compact high current electron accelerator built on the base of Tesla transformer and the fast-response Backward Wave Oscillator (BWO) is presented.

The relativistic BWO was a subject of numerous theoretical studies. At the same time, the theory of transient process in the BWO gains some special features in the case of intense space charge of high current electron beam³. As is known⁴, the BWO start current tends to increase in this case. The stability of oscillations in terms of self-modulation improves, and the generation keeps steady state over a wider range of (beam current)/(start current) ratio. Therefore, it is definitely important to use the time-dependent linear theory with the space charge to determine the basic parameters of the generator. If the beam current pulse duration t_b is small, the generation establishment time t_u becomes important. Actually, in the previous experiments, the beam pulse duration in the relativistic X-band BWO's exceeded 10⁻⁸ s and the condition $t_u \ll t_b$ was valid. For example, as it follows from the paper⁵, the excitation time of $\tau_u \sim 3$ ns can be achieved only if the beam current significantly exceeds the start current: $I_b \gg I_{st}$. In the limit case of small t_b , the decrease of excitation time practically means the possibility to choose the high voltage source with minimum pulse duration.

2. LINEAR APPROXIMATION

2.1. Formulation of the problem

The analyze of linear phase of transient process in the BWO allows to estimate its excitation time. The hydrodynamic model³ was extended to account the self space charge of the electron beam. If a thin-wall tubular electron beam with a radius of r_b is transported in an uniform magnetic field through a section of corrugated waveguide of length L with the mean radius r_0 , then the first temporal harmonics of the space charge field is expressed as

$$E_{z,b} = -\operatorname{Re} \left\{ \frac{2I_b kT(r_b, r_0)}{c(\gamma_0^2 - 1)} e^{i\theta} J(z, t) \right\} \quad (1)$$

Here I_b is the beam current, c is the speed of light, $k = \omega_0/c$, ω_0 is the frequency of exact synchronism between the beam electrons and the (-1)st spatial harmonics of backward wave, $\theta = \omega_0(t - z/V_0)$, v_0 is the electron velocity at $z = 0$, $\gamma_0 = (1 - V_0^2/c^2)^{-1/2}$, and J is the linearized high frequency current

$$J(z, t) = -\frac{1}{\pi} \int_0^{2\pi} g e^{-i\theta_0} d\theta_0, \quad (2)$$

where $g = \theta - \theta_0 \ll 1$ describes the dynamic shift for the electron the phase of which was equal to θ_0 at $z = 0$. The function $T(r_b, r_0)$ describes the depression of space charge by the metal boundary of the waveguide. It is expressed through modified Bessel's and McDonald's functions⁶. In the most practically important cases, the condition $r_b \gg (\gamma_0^2 - 1)^{1/2} k^{-1}$ is valid and therefore $T = [1 - \exp(-a(r_0 - r_b)/r_b)]/a$ where $k = \omega_0/c$ and $a = 2kr_b(\gamma_0^2 - 1)^{1/2}$. Only the first term is kept in the Fourier series for the space charge field since it is most important during the linear stage of oscillations.

Note that we use an important assumption that the amplitude of the electromagnetic wave changes slowly in time in comparison with the oscillation period $T = 2\pi\omega_0^{-1}$. Assuming also that the section of slow wave structure is matched at both edges get the system of time-dependent linear BWO equations

$$\begin{cases} \frac{\partial^2 J}{\partial \zeta^2} = -F - \alpha J \\ \frac{\partial F}{\partial \tau} - \frac{\partial F}{\partial \zeta} = iJ \end{cases} \quad (3)$$

$$J|_{\zeta=0} = 0, \dots, \frac{\partial J}{\partial \zeta}|_{\zeta=0} = 0, \dots, F|_{\zeta=\zeta_k} = 0, \dots, F|_{\tau=0} = F^0(\zeta). \quad (4)$$

Here, as well as in the paper³, dimensionless variables are used

$$\tau = \frac{\omega_0 C t}{1 + \frac{V_0}{V_g}}, \dots, \zeta = \frac{\omega_0 C z}{V_0}, \dots, \zeta_k = \frac{\omega_0 C L}{V_0}, \dots, C = \left(\frac{e I_b Z}{2 m c^2 \gamma_0^3} \right)^{1/3}. \quad \text{The latter is the modified amplification parameter}$$

in which e, m are the electron charge and mass, $Z = |E_{z,-1}(r_b)|^2 / 2k^2 P$ is the coupling impedance, $E_{z,-1}(r_b)$ is the amplitude of (-1)st spatial harmonics of the wave carrying the power P , and V_g is the wave group velocity. The parameter σ describes the relative participation of the space charge field:

$$\sigma = \frac{2 I_b T(r_b, r_0)}{I_A C^2 \gamma_0^2 (\gamma_0^2 - 1)^{3/2}},$$

where $I_A = mc^3/e$. For typical experiments with a high current electron beam, $\sigma \sim 1$. The physical meaning of this value becomes more clear in terms of plasma-beam instability⁷ the frequency of which may be expressed as $\omega_p = \sigma^{1/2} C \omega_0$.

Find the solution of (3), (4) by the separation of variables: $J = J(\zeta) e^{-iu\tau}$, $F = F(\zeta) e^{-iu\tau}$. For the functions F, J get the boundary problem

$$\begin{cases} \frac{\partial^2 J}{\partial \zeta^2} = -F - \sigma J \\ \frac{\partial F}{\partial \zeta} = -iuF - iJ \end{cases} \quad (5)$$

$$J|_{\zeta=0} = 0, \dots, \frac{\partial J}{\partial \zeta}|_{\zeta=0} = 0, \dots, F|_{\zeta=\zeta_k} = 0. \quad (6)$$

Generally, the complex value u appears as a solution of the system

$$\begin{vmatrix} e^{-ip_1\zeta_k} & e^{-ip_2\zeta_k} & e^{-ip_3\zeta_k} \\ (p_1 - u) & (p_2 - u) & (p_3 - u) \\ (p_1^2 - u^2) & (p_2^2 - u^2) & (p_3^2 - u^2) \end{vmatrix} = 0 \quad (7)$$

where $p_{1,2,3}$ are the roots of the cubic equation $(p^2 - \sigma)(p - u) - 1 = 0$. The number of solutions $u^{(n)}$ and corresponding modes of oscillations depends on the choice of ζ_k .

2.2. Start conditions

Consider a particular case when $u^{(n)}$ are real. Then, each of $u^{(n)}$ determines the deviation of corresponding oscillation mode $\omega_k = \omega_0(1 - u^{(n)C}/(1 + V_0/V_{gr}))$ from the exact synchronism. Each of $u^{(n)}$ has its corresponding value of $\zeta_k^{(n)}$, and this couple of eigenvalues determines the start condition for the n -th mode of oscillation. Enumerate them by the increase of the start length ζ_k . The Figure 1 illustrates the dependence of start conditions for the main ($n = 1$) mode on the space charge parameter. A polynomial interpolation of numerical solution of the equation (7) results in

$$\zeta_k^{(1)} = 1,974 (1 + 0,07\sigma + 0,01\sigma^2 + 0,01\sigma^3) \quad (8)$$

with the error of $<1\%$ for $\sigma \leq 2$. At large space charge parameters $\sigma \gg 1$ this interpolation is not valid. In this case⁴, the interaction between the electromagnetic wave and the slow space charge wave is responsible for the generation in the BWO and the start length rises as $\sigma^{1/2}$.

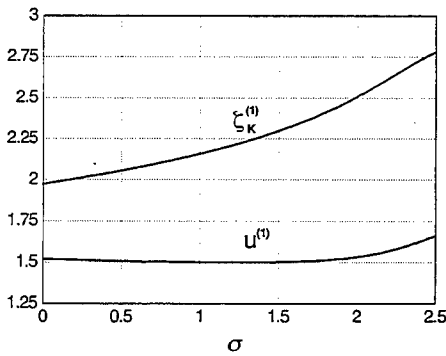


Fig. 1. Start conditions for the main oscillation mode in dependence on the space charge parameter

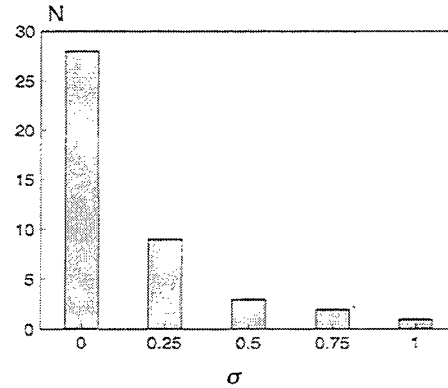


Fig. 2. Number of eigenmodes as a function of the space charge parameter ($\zeta_k=15$)

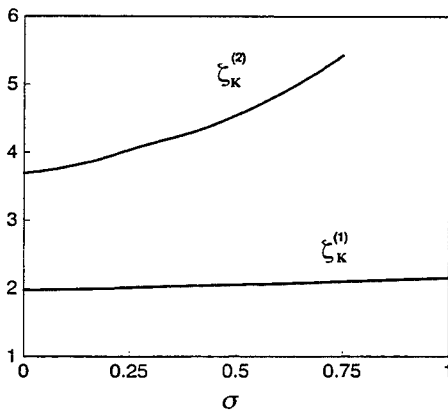


Fig. 3. Start length of the two first oscillation modes as a function of the space charge parameter

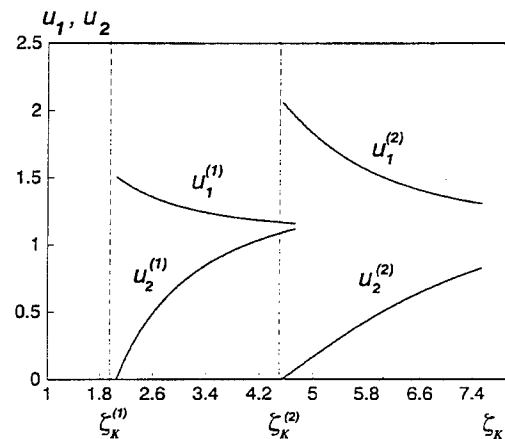


Fig. 4. The eigenvalues for the first two modes as a function of dimensionless length, at $\sigma=0.5$

A principally important effect of the space charge onto the linear processes in BWO is the increased separation of the main oscillation mode ($n = 1$) from its neighbors. This is illustrated in the Figures 2 and 3. Thus, as the parameter σ decreases, the number N of eigenvalues decreases for a BWO which is wittingly long ($\zeta_k = 15$) at $\sigma = 0$ (Fig. 2), and the value $\zeta_k^{(2)}$ increases faster than $\zeta_k^{(1)}$ (Fig. 3).

2.3. Oscillation increments

In the case of non steady-state generation at $\zeta_k > \zeta_k^{(1)}$ the main mode becomes rising. If $u = u_1 + iu_2$ is defined, then, at a fixed dimensionless device length ζ_k the real numbers u_1 and u_2 may be considered as eigenvalues of the problem (5, 6). The latter was solved in consequent approximations with a small step in ζ_k , by integration of the equation (5) and minimization of two-dimensional function $|F(u_1, u_2)|_{\zeta=\zeta_k}$. In the Fig. 4, the behavior of u_1 and u_2 for the first two modes is shown in dependence on ζ_k at $\sigma = 0.5$. As it follows from this figure as well as from the analyze of possible solutions, the values $u_2^{(n)}$ are positive for any n , and for the chosen method of eigenvalue numeration the increment of the main mode is maximum. The following approximation is valid with the error of less than 2%:

$$u_2^{(1)} = (1.84 - 0.38\sigma) \left[1 - \left(\frac{\zeta_k^{(1)}}{\zeta_k} \right)^{1.5} \right] \quad (9)$$

The maximum error of the expression (9) was estimated from the comparison with the numeric results for $0 \leq \sigma \leq 1.5$, $\zeta_k^{(1)} \leq \zeta_k \leq (\zeta_k^{(1)} + 1, 2 + \sigma)$. At $\sigma = 0$, this expression turns into the corresponding expression in the paper³ with the same accuracy of the constant factor. In the case of $\sigma \gg 1$, the increment and eigenvalues in the BWO problem can be found analytically. Thus, using the formula in⁴, it can be written in our definitions:

$$u_2^{(1)} = \left(\frac{2}{\sigma} \right)^{1/2} \operatorname{ctg} \left[\frac{\pi}{2} \left(\frac{\zeta_k^{(1)}}{\zeta_k} \right)^{3/4} \right].$$

Note, however, that this dependence is obtained under the approximation that the current slowly exceeds the start current or $\zeta_k \approx \zeta_k^{(1)}$ which is the same.

The duration of the linear stage of transient process in the BWO can be determined by the expression

$$t_l = \frac{(1 + V_0/V_{gr})}{\omega_0 C u_2^{(1)}} \ln \left| \frac{F_f}{F_0} \right|, \quad (10)$$

where F_0 and F_f are the normalized field amplitudes at the initial and final moment of linear stage at $z=0$. In the most interesting cases, the rise time of the current does not exceed the characteristic time of the feedback $L(1/V_0 + 1/V_{gr})$, and the initial noise in the system appears at the front of electron beam current having a wide spectrum covering, in particular, the synchronism band: $\Delta\omega \cong C\omega_0$. Then $|F_f| \sim 1$ and

$$\left| \frac{F_f}{F_0} \right| \approx \frac{4\pi(1 + V_0/V_{gr})}{C}. \quad (11)$$

Actually, another sources of noise can exist, for example, the cyclotron radiation near the cathode. Also, the current emitted from an explosive-emission cathode shakes with a typical times of $\leq \omega_0^{-1}$. Since the ratio $|F_f/F_0|$ is included in the expression (10) under the logarithm sign, estimate only the value of (11). In the typical experiments with high current electron beams, $C \sim 0.1$. Substituting $\sigma=1$ and $V_0/V_{gr}=2$ into (9, 10, 11), for an X-band BWO get

$$t_u \approx t_l \approx \frac{2}{\left[1 - (I_{st}/I_b)^{0.5} \right]} \text{ (ns)}. \quad (12)$$

Here I_{st} is the start current of the generator determined by the condition $\omega_0 CL/V_0 = \zeta_k^{(1)}$. Thus, the time of oscillation establishment in the generator t_u can range few nanoseconds if $I_b \gg I_{st}$.

3. NONLINEAR STAGE OF TRANSIENT PROCESS IN THE BWO

3.1. Common remarks

The numerical solution of nonlinear BWO problem is important to find out the laws of nonlinear stage of the transient process and the conditions of effective excitation of short electromagnetic pulses.

The common picture of behavior of the relativistic BWO with an intense space charge has been numerically studied till now on the base of the model with infinitely wide electron beam and with the account of only one or few temporal harmonics of the space charge field. The generality of consideration was limited also by the nature of hydrodynamic approach used since it does not allow to describe the stop and the reflection of particles in the electron flow. However, the following information was collected:

- (1) As the space charge increases, the region of the parameter $s \equiv I_b/I_{sr}$ is widen in which the generation is steady-state (no self modulation). For example, $s^{max} = 3,25$ at $\sigma=0$, and $s^{max} \approx 20$ at $\sigma > 0,87\sqrt{\zeta_k}$ (see the papers^{3,7}).
- (2) The maximum efficiency of BWO corresponds to some optimum space charge parameter. The more is the contribution of highest harmonics of space charge in the interaction process the higher is the optimum space charge parameter⁸. The BWO efficiency as a function of space charge parameter has a maximum⁹, and the efficiency can be significantly higher⁷ than at $\sigma=0$.
- (3) The increase of efficiency results from the compensation of overbunching which is typical for the BWO without space charge⁹. In other words, the phasing of the first harmonics of high frequency current along the interaction space is improved¹⁰.

In this paper, basically the results obtained with the use of a simple 1D Particle-In-Cell BWO model are described. The merit of this model is the capability of separate consideration of different physical processes. Note, however, that the axisymmetric version of fully electromagnetic 2.5 and 3D PIC-code KARAT¹¹ has been intensively used to simulate various actual configurations of BWO-based devices.

3.2. One-dimensional BWO PIC-model

The basic assumptions used in the model are as follows. The electron beam is interacting only with one waveguide mode having a fixed transverse structure. As a rule, only the interaction with the (-1)st spatial harmonics of backward wave is accounted but the fundamental harmonics of forward wave may be also simulated by determining the corresponding phase velocity and coupling impedance (for simplicity, not included in the description below). Other non-synchronous waves are not considered. Infinitely strong axial magnetic field is applied and, consequently, the transverse motion of beam electrons is absent. The electron beam is hollow with an infinitely thin wall.

Under these conditions, the only field effecting the electrons is the field of z -component of (-1)st spatial harmonics of the wave. To determine this field, use the general approach based on the waveguide excitation equation, as in the paper³. Express the electric field at the beam trajectory as:

$$E_z(z, r_b, t) = \text{Re} \left\{ A(z, t) Z \exp[i(\omega t - h_{-1} z)] \right\}.$$

Here, $A(z, t)$ is the complex amplitude, Z is the coupling impedance, $h_{-1} = h_0 - \bar{h}$ is the longitudinal wave number of the harmonics, $\bar{h} = 2\pi/d$, and d is the period of the slow wave structure. Generally, a longitudinally-nonuniform profiles of the coupling impedance and the phase velocity may be considered. The dependence of $A(z, t)$ is described by the time-dependent waveguide excitation equation:

$$\frac{\partial A}{\partial t} - |V_{gr}| \frac{\partial A}{\partial z} = |V_{gr}| Z J_\omega(z, t) \exp(ih_{-1} z) \quad (13)$$

where $J_\omega(z, t) = \frac{\omega}{\pi} \int_{t-T}^t I(z, t') \exp(-i\omega_0 t') dt'$ is the amplitude of the 1st Fourier harmonics of beam current at the frequency ω_0 (below, the index ω is passed). Approximate the equation (13) with the 4-point finite-difference scheme:

$$\frac{A_i^j - A_i^{j-1}}{V_{gr} \tau} = \frac{A_{i+1}^{j-1} - A_{i-1}^{j-1}}{2\Delta z} + \frac{A_{i+1}^{j-1} - 2A_i^{j-1} + A_{i-1}^{j-1}}{2\Delta z^2} V_{gr} \tau + F_i^j$$

Here Δz is the spatial and τ is the temporal integration step. The superscripts mean the number of temporal, and subscripts - of the spatial layer, and

$$F_k^j = \sqrt{Z_k} J_k^j \exp\left(i\Delta z \sum_{l=1}^k h_{-1,l}\right)$$

where $J_k^j = \frac{2}{N_f} \sum_{l=0}^{N_f-1} j_k^{j-l} \exp\left(-2\pi i \frac{l}{N_f}\right)$ is the Fourier component of current. Here N_f is the number of time steps in one oscillation period. The scheme is of second-order accuracy and converges at $\tau V_{gr} < \Delta z$.

The traditional PIC-method is used to describe the electron flow, with linear weighting of charge and current densities and the electric field. The relativistic ballistic equations are solved with use of the "leap-frog" method.

The initial (pre-oscillation) noise within the BWO appears, in the framework of this model, as a result of temporal perturbations of beam current density taking place on the fronts of beam current. Also, some high-frequency noise may appear as the shot noise due to finite number of macro particles representing the electron flow. However, usually, the frequency of these vibration significantly exceeds the BWO operation frequency and the noise does not effect the generation. Nevertheless, to decrease the shot noise, uniform positioning of injected particles is used. An invariable number of particles is injected at every time step, and the charge of each particle is proportional to the actual value of injection current.

Considering the space charge field in the BWO, account only its potential component $\mathbf{E} = -\nabla\Phi$ where the potential Φ satisfies the Poisson equation $\Delta\Phi = -4\pi\rho$. Here, $\rho(z)$ is the charge density of the electron beam. Since the external magnetic field is assumed infinitely strong, only the z -component of electrostatic field is important. The comparison with the results of fully electromagnetic simulations indicate that this simplification when the non-potential fields are neglected still allows to describe the basic effects of the space charge. At the same time, the simulation becomes much easier and faster.

It is difficult to use the Fast Fourier Transformation method to solve the Poisson equation for the slow wave structure of relativistic BWO because of its deep corrugation. Integral methods are more convenient in this situation. When using the Green function formalism, the electrostatic potential may be represented as

$$\Phi(\mathbf{r}) = \int_V \rho(\mathbf{r}') G(\mathbf{r}, \mathbf{r}') d\mathbf{r}'.$$

The Green function should satisfy the Poisson equation with the singular right part

$$\Delta_{\mathbf{r}} G(\mathbf{r}, \mathbf{r}') = -4\pi\delta(\mathbf{r} - \mathbf{r}').$$

Calculate the array of Green functions $G(r, z; r', z')$ for the couples of points $(r_b(z), z; r_b(z'), z')$ situated in the beam trajectory and store it to use at each time step of simulation. No recalculation of Green functions is required for a series of runs with the same geometry of slow wave structure and the beam trajectory.

Using the relationship between the spatial ρ and the linear ξ charge densities

$$\rho(\mathbf{r}) = \frac{\xi(z)}{2\pi r_b(z)} \delta(r - r_b(z))$$

get the expression for the potential:

$$\Phi(r_b(z), z) = \int_0^L \xi(z') G[r_b(z), z; r_b(z'), z'] dz'.$$

The physical sense of the function $G(\mathbf{r}, \mathbf{r}')$ is the potential at the point \mathbf{r} , created by the charge situated at the point \mathbf{r}' , with the account of the total charge induced in the system (corresponding to the given boundary conditions). In the case of axial symmetry, these charges are infinitely thin rings of radius r . To calculate their interaction, use the Newton's potentials:

$$\Phi(\mathbf{r}) = - \int_S \frac{\Psi(\mathbf{r}')}{|\mathbf{r} - \mathbf{r}'|} da' - \int_V \frac{\rho(\mathbf{r}')}{|\mathbf{r} - \mathbf{r}'|} d\mathbf{r}'.$$

The spatial charge distribution Ψ is caused by the electron beam. The surface charges are induced on the metal boundary of the electrodynamic system.

Split the surfaces of both the slow wave structure and the beam into infinitely thin charged rings (nodes). The potential at the i -st node is

$$\Phi_i = \sum_{j=1}^{N_b} Q_j G_{ij}$$

where Q_j are the charges at the "beam" nodes, N_b is the their number and the Green functions G_{ij} , are determined as

$$G_{ij} = \sum_{k=1}^{N_s} q_k \alpha_{ik} + \alpha_{ij}$$

where N_s is the number of "metal" nodes and q_k are the charges induced at them. The latter are determined, in their turn, by the condition $\Phi_j=0$ on the metal surface the corresponding system of linear algebraic equations is

$$\sum_{k=1}^{N_s} q_k \alpha_{jk} = \alpha_{ij} - \Phi_j = \alpha_{ij}$$

where the coefficients α_{ij} are the elliptic integrals of 1st kind for $i \neq j$ and for $i=j$ they are determined by inputting of finite thickness of the electron beam wall.

3.3. Simulation results

The parameters of actual BWO experiment were used in numerical simulation. The coupling impedance was $Z=1.5$ Ohm, the length was 16 cm and the kinetic energy of the electrons at the anode was 300 keV. The beam current was varied in a wide range and its rise time was 1 ns. In Fig. 5a, the temporal dependencies of microwave power at the cathode edge of the device are shown obtained without the space charge. Under this approximation, $I_{st} \approx 0.15$ kA.

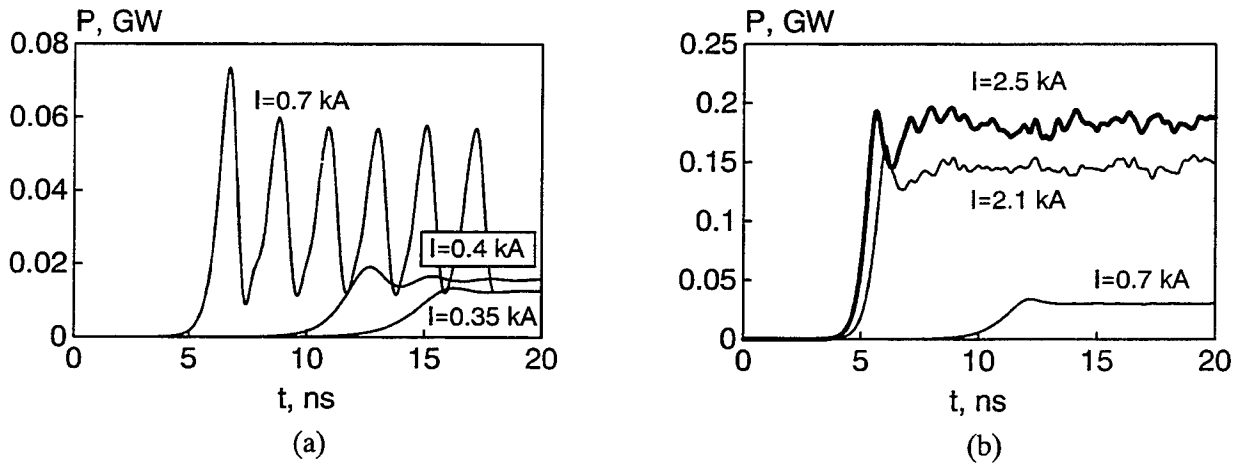


Fig. 5. The results of BWO numerical simulation (a) without and (b) with the account of the space charge

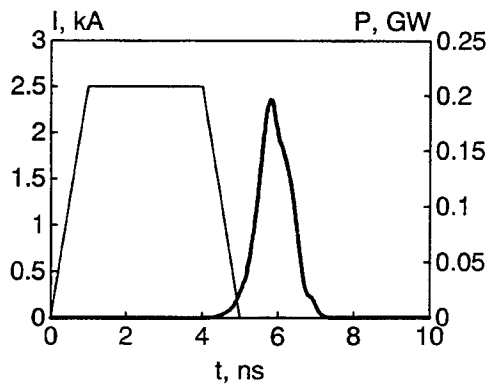


Fig. 6. Simulated output pulse of BWO driven by a trapezoidal beam pulse

The BWO dynamics changes significantly when the space charge is accounted (Fig. 5b). The self-modulation threshold moves to the current of ~ 2.5 kA. The electron efficiency increases approximately as $I^{1/2}$ reaching $\sim 25\%$. In the Fig. 6, the microwave power pulse of BWO driven by a trapezoid current pulse (4 ns FWHM) is shown. The pulses are shifted by 2 ns corresponding to the time of transit of the electron beam and the wave through the device. Generally, the results of numerical simulation indicated that it is possible to realize a short transient process if the work current significantly exceeds the start value (by one order or more). The excitation time observed in the numerical experiment is in good agreement with the predicted from the linear theory (12).

4. HIGH CURRENT NANOSECOND ACCELERATOR

A monopolar pulse generator design was chosen using a coaxial forming line and a Tesla transformer with high coupling coefficient^{2,5}. The forming line with the built-in Tesla transformer is placed in a cylindrical case filled with transformer oil. The parameters of the forming line are listed in Table 1.

Length	34 cm
Outer diameter	12 cm
Electric length	3,5 ns
Wave impedance	30 Ohm
Capacitance	70 pF
Maximum charge voltage - U_2^{max}	450 kV
Charge voltage at 200 p.p.s.	350 kV
Charging time for U_2^{max}	6 μ s
Efficiency of Tesla transformer	50 %

Table 1. Parameters of the high voltage generator

To discharge the forming line, a two-electrode gas switch filled with nitrogen is used. The breakdown voltage (U_k) is varied by changing the gas pressure (0÷30 Atm) and electrode gap (0.5÷1.2 cm). At repetition rates exceeding 10 p.p.s., gas is circulated across the gap. The gas flow system includes a gas filter and cooler. The transmission line serves to deliver the generated high voltage pulse to the load. The double transit time of transmission line exceeds the pulse duration. In the BWO experiments, the impedance of the transmitting line was nonuniform reaching 80 Ohm at the diode edge. In course of testing of the generator, the active load was placed at the output of the transmission line.

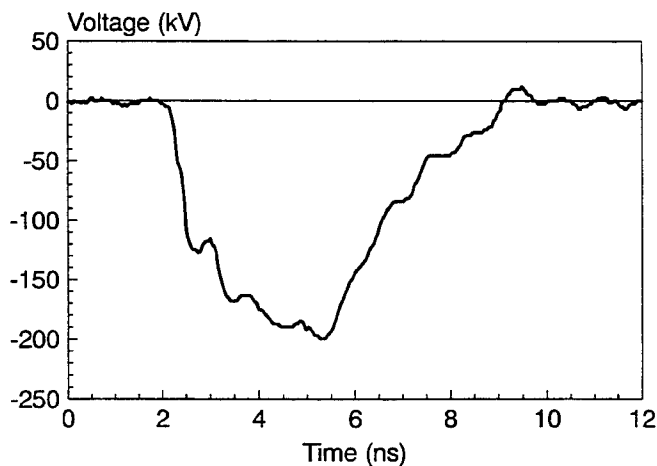


Fig. 7. Pulse of cathode voltage of the nanosecond accelerator

In the experiments, the shape of the generated high voltage pulses, their amplitude U_{max} and pulse-to-pulse instability have been monitored. Capacitive divider was used to measure the parameters of the nanosecond pulses, established at the entrance of the transmission line. In Fig. 7, a typical trace of the voltage pulse measured using a high speed oscilloscope is shown. The instability has been determined as the relative mean-square deviation of U_{max} around its average. Usually, about 1000 pulses were used for averaging.

Measurements of instability for various gas flow rates and its dependence on pulse repetition rate have been made over a wide range of gas pressures in the switch. In Fig. 8, the dependencies of instability of U_{max} on pulse repetition rate are shown for three values of gas velocity ($V_1 > V_2 > V_3$). For a given gas velocity, a limit value of repetition rate exists above which the instability rises steeply.

The maximum repetition rate of the gas switch operation at a given gas velocity depends on its geometry and rises with a decrease in the electrode radius. The gas velocity in the gap was not measured but is estimated to be ~10 m/s for $P \sim 10$ Atm which is in agreement with earlier results.

As the experiments indicate, a significant change in instability occurs in the range of electric field in the gap from 300 to 500 kV/cm. This effect is possibly caused by explosive emission occurring on electrode surfaces during the breakdown process.

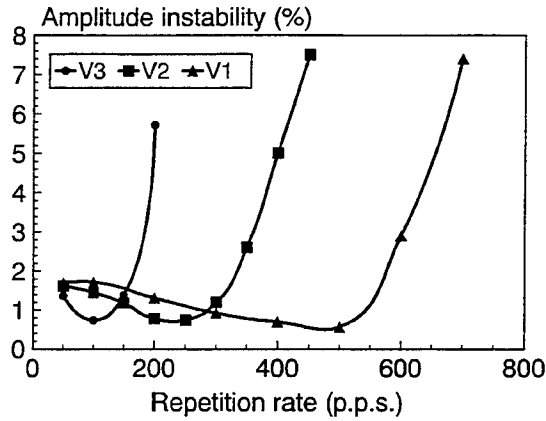


Fig.8. Measured instability of the voltage pulse for different speeds of gas circulation

5. HIGH POWER X-BAND OSCILLATOR

A nanosecond electron beam accelerator with a coaxial vacuum diode and X-band BWO based on the high voltage nanosecond generator described above has been investigated.

The pulsed solenoid in which the vacuum diode and the BWO electrodynamics system were placed produced a magnetic field as strong as 2 T with pulse repetition rate of 1 p.p.s..

In the experiments, the slow wave structure was used designed for TM_{01} operation. It consisted of the rings with 3 mm deep ripples and 30 mm mean diameter. The total structure length was varied. With the use of high voltage generator described above, the pulses of tubular electron beam have been formed with the current of up to 2.5 kA at the beam acceleration voltage 350 kV. In Fig. 9, the signal from microwave detector (vacuum RF diode) is shown. The temporal resolution was about 0.5 ns limited by signal distortion in the 15 m cable and the oscilloscope TDS644A.

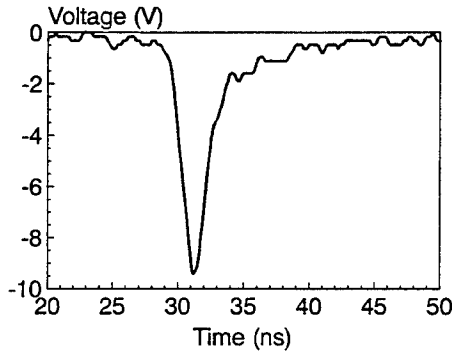


Fig. 9. The shape of microwave pulse measured by the detector

The high electric strength of construction allowed to charge the forming line to ~450 kV at repetition rate of up to 10 p.p.s.. The stored energy therewith was ~ 7 J, and the power in the load was ~1.5 GW. At repetition rates exceeding 10 p.p.s., the elements of the primary circuit are cooled, as well as the gas within the switch, and the maximum charge voltage of the forming line was decreased. The trials showed that the generator equipped with the cooling system is capable of continuous operation at a charge voltage of ~350 kV and pulse repetition rate ~200 p.p.s.. In this case, the power in the pulse is $P_p = U^2/R$ ~ 1 GW, and the average power of generated pulses is $P_{av} \sim P_p \tau f \sim 1$ kW where τ is the pulse duration and R is the load resistance.

The radiation pulse power was estimated to 150 MW (spatial integration of radiation power pattern was made). At the device length shorter than 12 cm, no microwave emission was observed. The minimum instability of detector signal (~ 3%) corresponded to maximum device length of 16 cm. Because of limited temporal resolution, the actual microwave power and pulse duration are probably even higher and shorter, respectively, than the measured values.

Thus, in simulation and experiment, it was shown that it is possible to generate 3 cm wave length pulses with 150 MW power using the 4-ns electron beam.

6. SUMMARY

It was shown that, with no respect to the of space charge strength, the duration of linear stage of generation establishment in the X-band BWO can be as short as few nanoseconds if $I_b \gg I_{st}$. If no space charge is accounted in the simulation, this condition leads to intense first splash of microwave power with further self modulation (decaying for $I_b < 3.25 I_{st}$). For the parameters used in the actual experiment, the presence of space charge caused the increase of start current approximately by the factor of two. In this case, the efficiency as a function of current was rising until the self modulation occurred. The latter was rather non-sinusoidal and it appeared at the current level exceeding the value predicted without the account of the space charge by almost an order.

The simulation results agree with the experiment in which the possibility to generate stable microwave pulses with a power of ~150 MW with the use of a 4-ns electron beam was demonstrated. A compact high voltage generator was used capable of operation at a repetition rate of several hundreds p.p.s.. An increase of repetition rate of microwave pulses is possible if appropriate magnetic system is used. It would be interesting to obtain the same electron efficiency of the generator at lower magnetic field in order to decrease the energy consumption of magnetic system. A mobile version of the installation can be produced with the weight of ~200 kg which may be used as a transmitter in a nanosecond radar system.

7. REFERENCES

1. B.V. Bunkin et al, "Nanosecond Radar System Based on Repetitive Pulsed Relativistic BWO", in *Proc. of 9-th Intern. Conf. on High Power Particle Beams*, v. 1, pp. 195-202, 1992.
2. M. Skolnik, G. Andrews and J.P. Hansen, "Ultrawideband microwave-radar conceptual design", *IEEE AES Systems Magazine*, pp. 25-30, October 1995.
3. N.S. Ginzburg, S.P. Kuznetsov, and T.N. Fedoseeva, "The theory of transient processes in relativistic BWO", *Radiofizika (Sov.)*, v. 21, pp. 1037-1052, 1978.
4. I.K. Vikulov, A.S. Tager, "A method to study transient processes in the "O"-type BWO", *Radiotekhnika i elektronika (Sov.)*, v.12, No. 12, pp. 2146-2155, 1967.
5. L.D. Moreland, A.M. Roitman, E. Schamiloglu and R.W. Lemke, "Power and frequency measurements from uniform BWO as a function of length", *Abstr. Int. Conf. on Plasma Sci.*, Santa Fe, P-175, 1994.
6. N.M. Bykov, V.P. Gubanov, A.V. Gunin et al., "Relativistic BWO with high average power", *Journal of Technical Physics (Sov.)*, v. 59, No. 5, pp. 32-38, 1989.
7. N.S. Ginzburg, S.P. Kuznetsov, "Periodic and stochastic self-modulation regimes in distributed electron oscillators", in *Relativistic High-Frequency Electronics*. Gorky, USSR: Inst. Appl. Phys., Acad. Sci. USSR, pp.101-144, 1981.
8. G.N. Rapoport, "Non-linear theory of the "O"-type BWO with periodic slow wave structure", *Radiotekhnika i elektronika (Sov.)*, v. 9, No. 3, pp. 483-504, 1964.
9. G.N. Rapoport, "On the device of increase of BWO efficiency with the space charge parameters", *Radiotekhnika i elektronika (Sov.)*, v. 3, No. 2, pp. 255-261, 1958.
10. N.F. Kovalev, M.I. Petelin, M.D. Raizer and A.V. Smorgonsky, "O"-type devices based on stimulated Cherenkov and transit radiation of relativistic electrons", in *Relativistic High-Frequency Electronics*. Gorky, USSR: Inst. Appl. Phys., Acad. Sci. USSR, pp. 76-113, 1979.
11. V.P. Tarakanov, *User's Manual for Code KARAT*, Berkeley Research Associates, Inc., VA, 1992.

SESSION 5

Poster Session

Beam Focusing and Plasma Channel Formation in the PASOTRON™ HPM Source

Elmira S. Ponti, Dan M. Goebel, Robert L. Poeschel
Hughes Research Laboratories
3011 Malibu Canyon Rd. MS RL 61
Malibu, CA 90265

ABSTRACT

In the PASOTRON high power microwave source, electron beam focusing is achieved using a plasma channel (usually helium or xenon, ionized by beam impact) to neutralize the radial space charge forces within the beam so that the beam's own $\mathbf{J} \times \mathbf{B}$ forces will produce self focusing of the beam according to the Bennett effect. In order to take maximum advantage of this effect, the physics of the formation of the plasma channel and the resulting beam focusing has been studied and a simple computer model of this process is evolving based on the experimental results. A diagnostic tube was fabricated with a removable slow-wave structure to investigate the beam dynamics during the pulse. Two rows of probes extending down the length of the tube at 90° to each other are used to monitor the radial profile of the beam as it propagates as a function of time and axial distance, and a biased beam collector measures the total current arriving at the end of the tube. The dynamics of the plasma channel formation and the plasma density over time were then determined from these measurements and compared to the model. A small axial magnetic field (<250 Gauss) was also applied to assist the focusing mechanism with excellent results. The optimal range of background gas pressures and solenoid magnetic field as a function of beam current and voltage, as well as the dynamics of the beam focusing and plasma channel formation, will be presented.

Keywords: PASOTRON, microwave source, beam transport

1. INTRODUCTION

The PASOTRON is a novel family of microwave tubes that have been built as high power oscillators¹ and amplifiers, producing radiation in L, S, C and X-bands. The C-band tube, shown in Figure 1, was driven by an electron beam with energies of up to 135 kV, beam currents of up to 500 A, and pulsewidths in excess of 120 μsec . Spontaneously-generated RF power in the range of 1 to 5 MW was obtained, depending on the beam parameters and gas fill, and RF pulsewidths of over 100 μsec were achieved at up to 1-Hz pulse-repetition-rate. The electron-beam-to-microwave-radiation power-conversion efficiency for this type of device typically ranges from 15 to 25%¹. The PASOTRON has also been designed to utilize a helical the Slow-Wave Structure (SWS) for lower frequencies at which a rippled waveguide SWS would add too much size and weight to the system. A schematic of this helical SWS PASOTRON, as used in the L-Band system, is shown in Figure 2. This same type of system was used in these experiments to produce the electron beam, however the SWS was removed so that probes could be inserted along the length of the tube for diagnostic purposes.

PASOTRON sources do not require any external magnetic field for electron beam confinement. Instead the beam is confined using a plasma in the interaction region to neutralize the space charge of the electron beam so that the beam will tend to self pinch by the force of its own magnetic field. This lack of solenoid or large periodic permanent magnet arrangement reduces the overall size and weight of the microwave tube, as well as reducing the power supply requirement for a solenoid. In applications such as high power electronic countermeasures, in which size and weight are crucial considerations, this becomes a significant advantage. However, in order to further increase the device efficiency, beam energy recovery is desired. This cannot be done with the present configuration because a large portion of the beam intercepts the walls and SWS at the terminal end of the tube after having lost its energy to the microwave field. In order to make beam recovery feasible, an additional focusing mechanism would have to be implemented. We began by analyzing the profile and time evolution of the unmagnetized beam

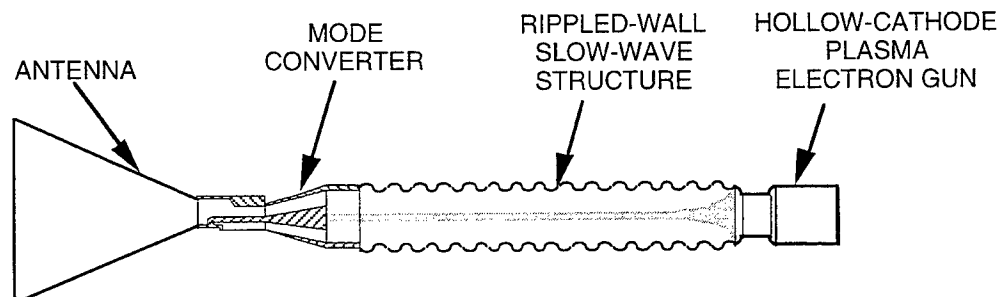


Figure 1: Schematic diagram of a rippled waveguide SWS C-Band PASOTRON Oscillator.

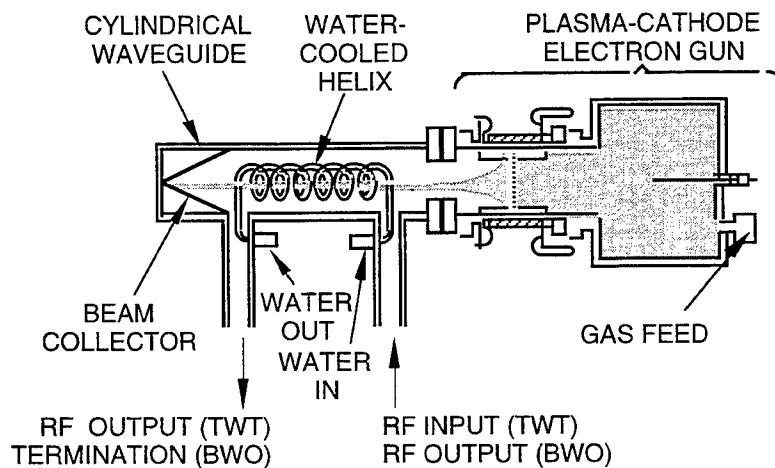
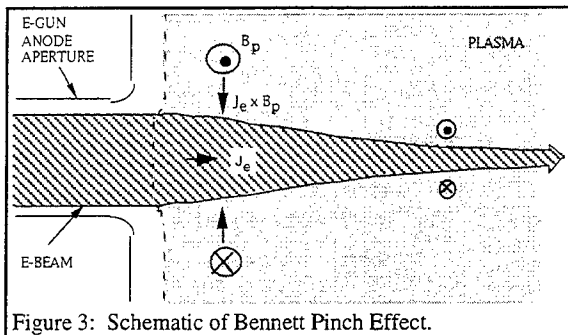


Figure 2: Schematic diagram of helical SWS PASOTRON oscillator.

and then added a small axial magnetic field (50 to 250 Gauss) in the form of a solenoid and again monitored the beam's profile and evolution.

2. EXPERIMENTAL CONFIGURATION

A high-current electron beam is generated by a Hollow Cathode Plasma (HCP) E-gun. Rather than use a $>1\text{kG}$ magnetic field to eliminate the rapid radial expansion of the electron beam, a PASOTRON balances these forces by the use of a background plasma (typically xenon) so that the electron beam's self-magnetic field can cause the beam radius to compress through a process commonly known as the Bennett Pinch Effect², as shown schematically in Fig. 3. The electron beam is injected into the neutral gas at pressures on the order of 10^{-5} Torr and ionizes the gas to form a plasma in which the electrostatic forces acting on the beam are largely neutralized. This condition permits the self-magnetic field of the electron beam to compresses the beam to an equilibrium diameter of less than 2 cm, as measured by witness plates placed at the entrance to the SWS. This pinch effect increases the beam current density by more than a factor of 10, and permits the high current E-beam to enter a relatively small diameter SWS without impacting its walls. Thus, the effect of the presence of the plasma is to balance the radial outward forces on the beam so that the beam propagates through the SWS. However, the plasma-channel transport is insufficient to keep the beam focused during RF generation when the beam bunching destabilizes the beam-plasma equilibrium.



Another problem with utilizing a plasma channel to assist a traditional magnetized beam transport system is that ions generated in the SWS diffuse toward the E-gun and are accelerated at high energy into the cathode structure, thereby damaging the cathode surface. This problem is eliminated by the use of a novel plasma-cathode electron gun³, which not only tolerates ion bombardment because the cathode is itself a plasma, but provides long pulse length operation and the capability of high average powers.

The configuration of the tube for this experiment is shown in Figure 4. Electrons generated within the hollow cathode by a plasma discharge are extracted and accelerated by a dc high-voltage applied between two grids to produce a large area, high-current density beam. The electron beam travels through a short drift section in which the beam diameter is compressed small enough to enter the SWS without interception. The spent electrons drift to the walls of the tube or are collected at the end of the tube by a graphite beam dump. The tube is attached to a vacuum system that is actively pumped to a base pressure in the 10^{-8} Torr range by a turbomolecular pump.

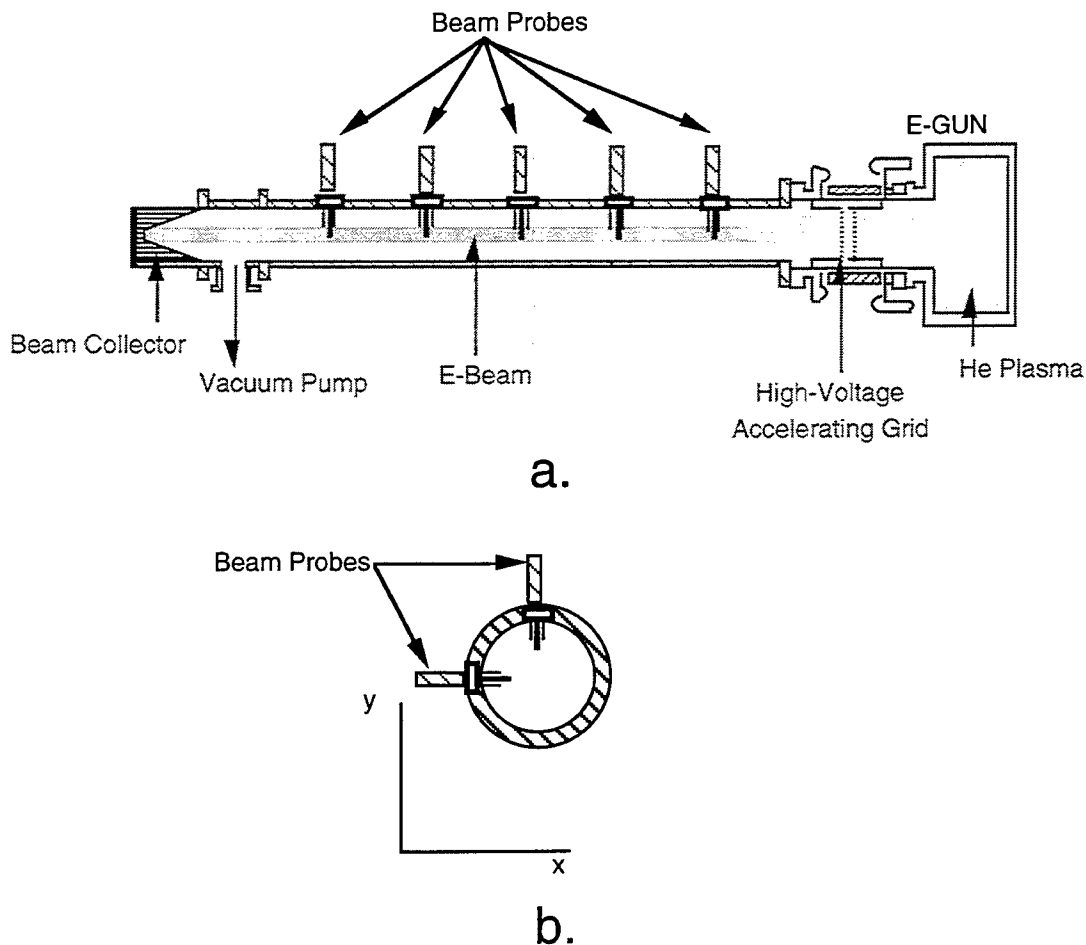


Figure 4: Schematic diagram of experimental configuration of tube: a) profile and b) view down axis of tube showing two rows of probes at 90° to each other.

2.1 Electron gun

Long electron-beam pulses are obtained from a Hollow Cathode Plasma (HCP) electron gun³. The gun overcomes the limitations of most high-power microwave tubes which employ either thermionic cathodes that produce limited current-density beams, or field emission cathodes that offer high current density but provide only short pulsewidths ($< 1 \mu\text{sec}$) because of plasma closure of the accelerating gap. The HCP electron gun provides both high-current density ($> 50 \text{ A/cm}^2$) and long-pulse operation without gap closure by generating a controlled plasma discharge which acts as the electron source. A low-pressure glow discharge generated inside the hollow cathode of the gun, shown in Fig. 5, produces a uniform and stable plasma front from which a high-current density beam is extracted. The cold-cathode discharge requires no filament heater power, and is relatively insensitive to vacuum conditions. Typical cathode materials used in the HCP E-gun are stainless-steel and aluminum, and the accelerator grids are made of molybdenum.

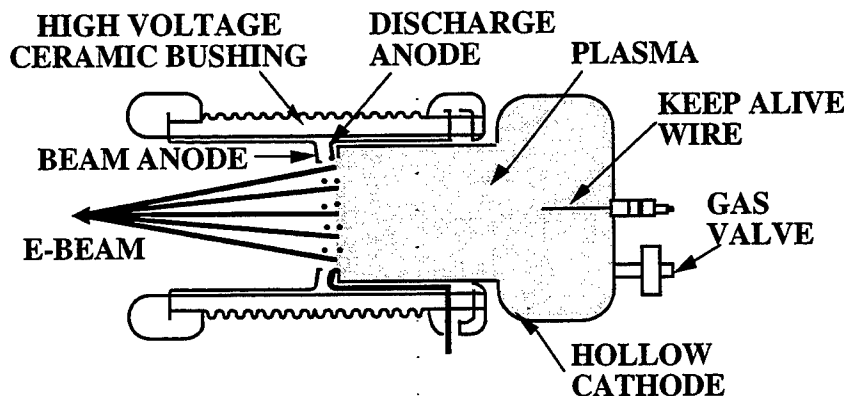


Figure 5: Schematic diagram of the Hollow-Cathode Plasma (HCP) E-gun.

To form the electron beam, a $\leq 100\text{-}\mu\text{sec}$ PFN is charged by a fiber-optically controlled power supply, and is switched into the plasma discharge system by an ignitron switch. A low current ($< 10 \text{ mA}$) "keep-alive" discharge is continuously maintained in the background gas to reduce the turn-on jitter during initiation of the cold-cathode discharge. The plasma density in the hollow cathode, and subsequently the beam current density, is controlled by the low-voltage ($< 5 \text{ kV}$), hollow-cathode discharge pulser. The anode of the discharge is the first grid of a high-perveance, multi-aperture electron accelerator. A dc high-voltage power supply connected between the grids accelerates electrons across the gap, while the low-voltage discharge pulser modulates the beam current to generate arbitrary pulse waveforms. The injection voltage of the electron beam is controlled by the dc voltage level and monitored by a precision high-voltage divider, while the beam current, pulsewidth, and pulse repetition frequency are independently controlled by the discharge pulser.

The gas pressure required to produce the glow discharge is in the range of 5 to 50 mTorr of helium. For high power microwave generation with a PASOTRON SWS, a transient helium gas-puff system is used to supply an adequate pressure in the hollow cathode to strike the glow discharge, and provide a reduced gas pressure in the SWS that enhances beam propagation and microwave generation. A simple SCR-controlled circuit is triggered prior to the ignitron switch to provide the current pulse for the fast gas-puff valve. The repetition rate of the system is presently limited to less than 10Hz by the recharge time on the gas puff valve circuit.

2.2 Probes and Photo Detectors

Ten apertures were built into the tube, five along the top and five along the side, as vacuum-tight feedthroughs for either the probes or the photo detectors. Both the probes and the photo detectors were interchangeable into any of these apertures. The probes consisted of .25mm dia. by 3mm long tungsten

wire at the end of a rod of a hollow copper tube which was insulated from any collection of ions or electrons by a glass sheath, as shown in Figure 6. The Cajon fitting permitted adjustment of the penetration depth of the probe tip from the wall to the center of the tube. A negative battery bias was used on the probes so that the measurement of highly energetic beam electrons would not be corrupted by the collection of plasma electrons. The photodetectors consist of photodiodes made by Hamamatsu and operate in the visible spectrum.

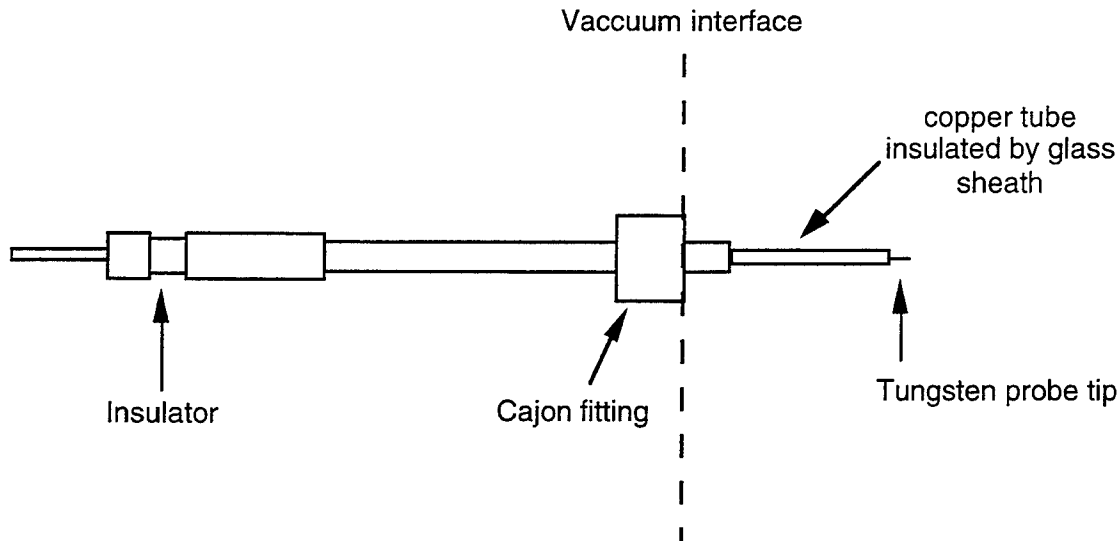


Figure 6: Schematic drawing of probe used as diagnostic for electron beam.

3. RESULTS

The parameters that were monitored were beam current, beam voltage, beam collector current, voltage on probes, applied axial magnetic field, and voltage output of photodetectors. These quantities were recorded versus time using fast A/D converters and LabView software to capture the variations within each 100 μ s pulse. The experiment was conducted on a single shot basis, as necessitated by the recharge time on the solenoid power supply.

3.1 Beam Propagation Measurements

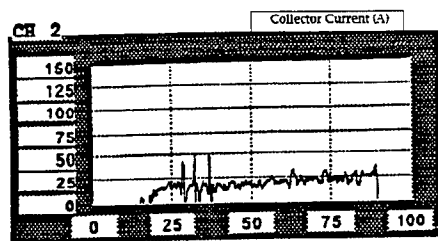
During operation with only the helium gas-puff (no xenon) at voltages under 50kV, the electron current that reaches the beam collector is typically less than half the beam current. Adding a xenon backfill, or operating at higher beam voltages, increases the beam transmission to the collector significantly. At a Beam voltage of 35kV and a current of about 100A, the collector current is shown in Figure 7 for several xenon background gas pressures with and without an applied magnetic field. As the gas pressure is increased without an applied field, the collected current increases but also becomes very noisy. When an axial magnetic field of about 200 Gauss is applied, nearly all of the current reaches the collector even at low xenon pressures. As the xenon pressure is then increased, the beam collector signal becomes more noisy, but the total collected current remains approximately constant regardless of pressure (within the normal operating range).

Figure 8 shows the amount of beam current reaching the beam collector at the end of the tube as the solenoid field is increased from no field to about 250 Gauss. With no external magnetic field applied, less than 10% of the beam current reaches the beam collector. As the magnetic field is increased, a maximum of 90% current collected occurs at about 200 Gauss. Thus, at a relatively small value of magnetic field, the current reaching the collector can be improved by over an order of magnitude, which could result in an increase in overall tube efficiency if a depressed collector configuration is used.

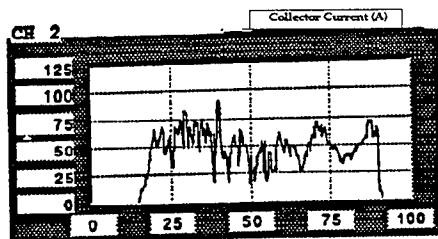
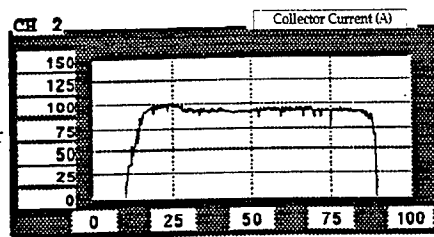
B Field Free

Xenon Pressure

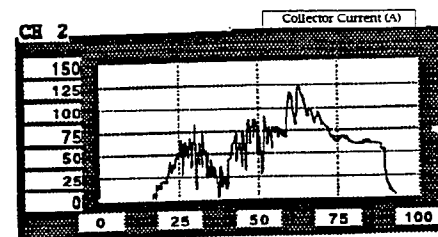
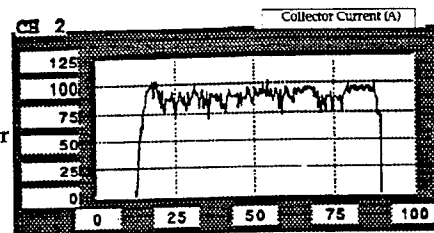
200 Gauss axial Field



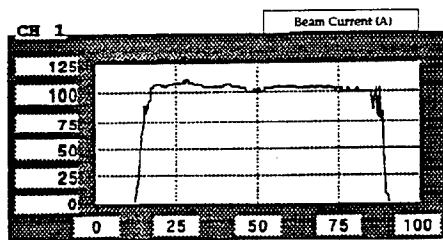
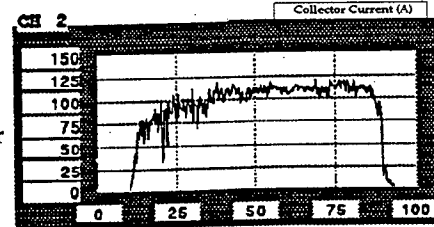
$P=1.3 \times 10^{-5}$ Torr



$P=2.1 \times 10^{-5}$ Torr



$P=3 \times 10^{-5}$ Torr



100A, 35kV

Figure 7: Electron Beam Collector Current data for various pressures of xenon shown with and without the effects of an axial magnetic field. All data is for beam conditions of approximately 100A and 35kV (representative beam waveform shown).

For the same conditions, Figure 9 shows the current collected by a probe that is located at 1cm radius from the center of the tube. This data is taken 35 μ s into the pulse, so that the beam has already focused and the radius has reached its quiescent value. Notice that the current collected by the probe with no externally applied magnetic field is significantly higher than with a field of >100 Gauss. Again the graph shows the beam to be focused the best at about 200 Gauss, above which the beam expands somewhat.

When a magnetic field greater than about 200 Gauss was applied the effects of an instability were observed for high values of beam current and background gas pressure. The effects of this were reduced current to the collector; large current collection on certain probes while none was collected on probes 90° to them; and light detected by certain photodetectors. This was determined to be a kink instability by the fact that probes orthogonal to each other would show maxima and minima in the current collected. At the onset of this instability, a decrease was observed in the collected current because the beam was impacting the walls of the tube.

With a beam current again of about 100A, the collector current was measured for a variety of xenon background gas pressures with and without an applied magnetic field. As shown in figure 9 when the gas pressure is increased without an applied field, the collected current increases but also becomes very noisy. When a magnetic field of about 200 Gauss is applied, nearly all of the current reaches the collector even at low xenon pressures. As the xenon pressure is then increased, the beam collector signal again becomes noisy, but the total collected current remains approximately constant regardless of pressure (within the normal operating range).

3.2 Model Developed from Experimental Data

A computer model of the time evolution and radius of the beam for a given axial has been developed. The results of the model's prediction of current collected on certain probes versus the experimentally determined values are shown in Figure 10. Probe #1 is located 14cm downstream of the accelerator grid (at the location of the entrance to the SWS if one was present), and probe #2 is located 10cm downstream of that. The current on the probes in the experimental data doesn't go to zero after the beam is focused, as shown in the prediction of the model, due to the onset of the kink instability. This model also accurately predicts the beam radius as a function of time and axial position, as shown in Figures 11 and 12, for given conditions of current and pressure. Figure 11 shows the time evolution and axial propagation of the beam with the locations of the walls of the tube, the beam collector, and the probes shown. For the initial 5 μ s of the pulse, the beam impacts all of the probes and a significant portion of it impacts the walls. By 6 μ s, the beam is focused enough that a significant portion reaches the beam collector, but the first probe still collects current until the plasma channel formation process is complete. By about 10 μ s the beam is essentially focused. Figure 12 shows the same electron trajectories in the presence of a SWS. For typical conditions in the absence of an externally applied magnetic field, the beam would focus to a small enough radius within 6 μ s to enter the SWS without impacting it. During the initial 6 μ s of a beam pulse, the beam front begins to impact ionize the xenon gas present throughout the tube. As the plasma density increases, the beam is forced to pinch to the equilibrium diameter. By 10 μ s into the pulse, the beam is essentially focused to its final value and remains at that radius for the duration of the pulse.. These times corresponded very well with the observed data (see Figure 10).

4. CONCLUSIONS

An experimental tube containing no SWS was built to study the dynamics of the electron beam in a PASOTRON ion-focused tube. Data was taken to determine the time and spacial evolution of the beam focusing mechanism. A magnetic field was then added to the tube in the form of a solenoid and it was found that for axial magnetic fields of about 200 Gauss the portion of the beam reaching the end of the tube was improved by more than an order of magnitude over having no magnetic field. Thus, in future versions of the PASOTRON tube, a depressed collector configuration may be implemented which would improve the overall device efficiency.

A computer model of the dynamics of the beam formation was then produced which agreed very well with the observed data. From this model, one can predict the beam's radius for at a certain position in the tube given the beam current and voltage, rate of rise of the current pulse, and background gas pressure. From this study we will be able to design more efficient tubes with this novel type of beam focusing mechanism in the future.

5. REFERENCES

1. D.M. Goebel, J.M. Butler, R.W. Schumacher, J. Santoru, and R.L. Eisehart, "High-Power Microwave Source Based on an Unmagnetized Backward-Wave Oscillator", IEEE Transactions on Plasma Science, **22**, No. 5, pp. 547-553 (1994).
2. W.H. Bennett, Phys. Rev., **45**, pg. 890 (1934).
3. D.M. Goebel, R.W. Schumacher, and R.M. Watkins, "Long-Pulse Plasma Cathode E-Gun", Conference on High Power Particle Beams, Washington, DC, May 25-29, 1992, pp. 1093-1098.

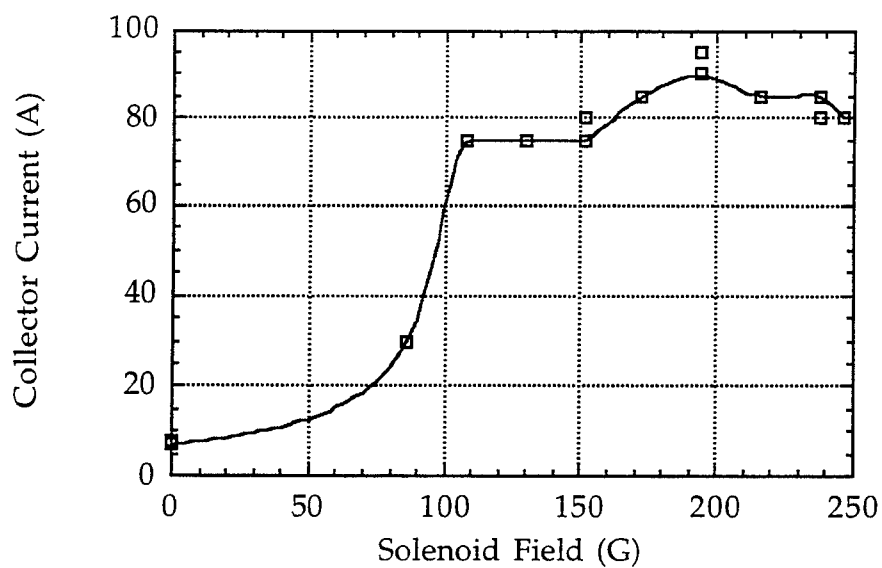


Figure 8: Current measured at beam collector 35 μ s into pulse as a function of applied solenoid field. The background plasma consisted of the helium puff only (no xenon) and the electron beam was 100A and 33kV.

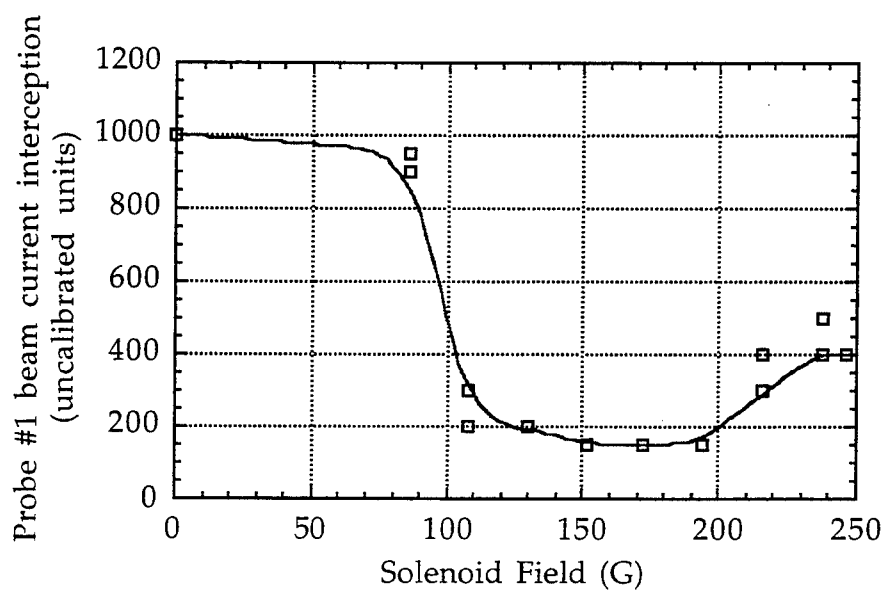


Figure 9: Current on probe closest to gun located at 1cm radius measured 35 μ s into pulse, as a function of applied solenoid field. The background plasma consisted of the helium puff only (no xenon) and the electron beam was 100A and 33kV.

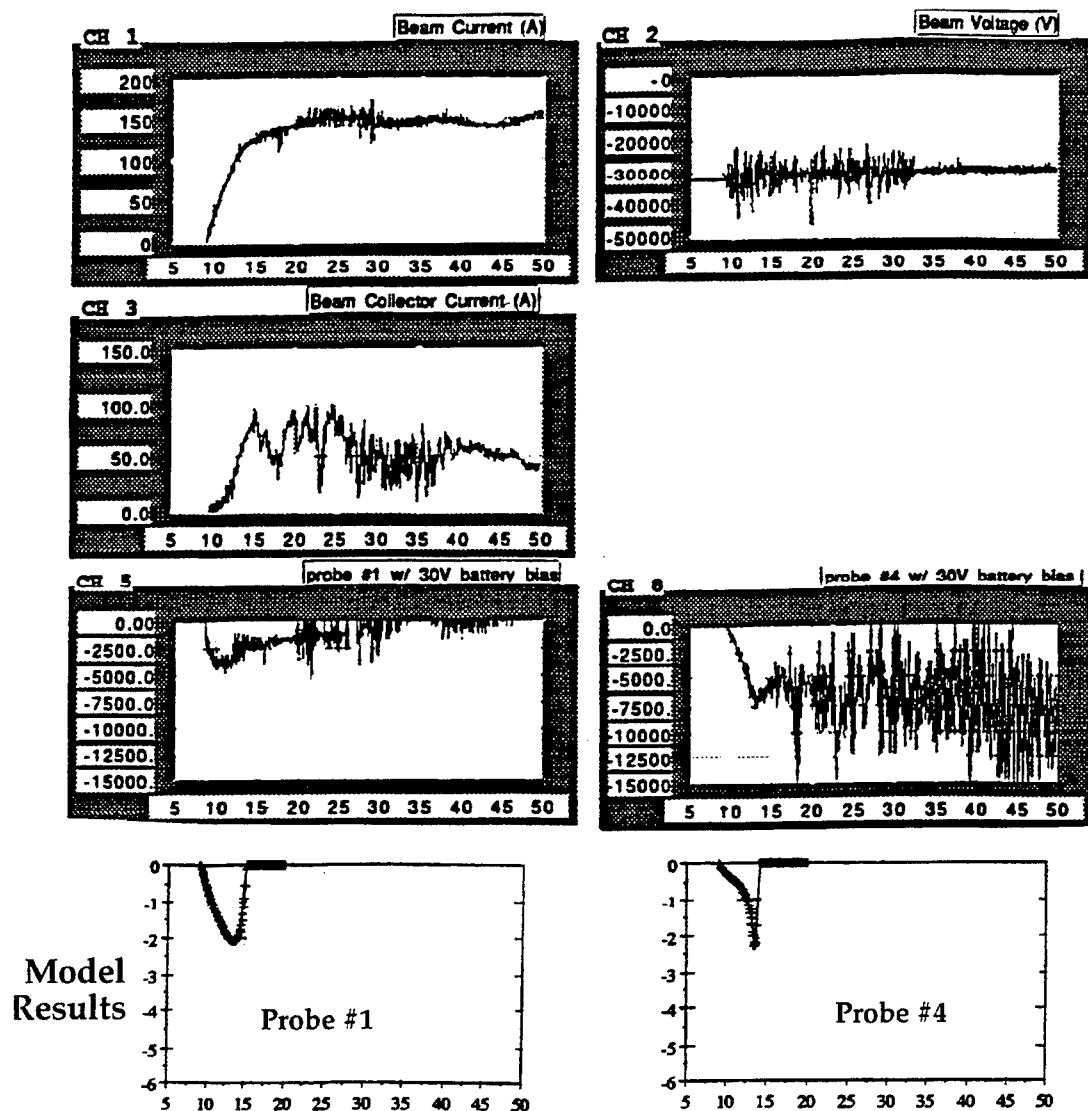


Figure 10: Measured data (channels are as labeled) and results of model showing the time evolution of the focusing of the beam. Note the strong correlation between the time at which the measured and modeled probes cease to collect current (i.e. the beam begins to focus). Data was taken with no axial magnetic field and a background gas of 5×10^{-5} Torr Xe.

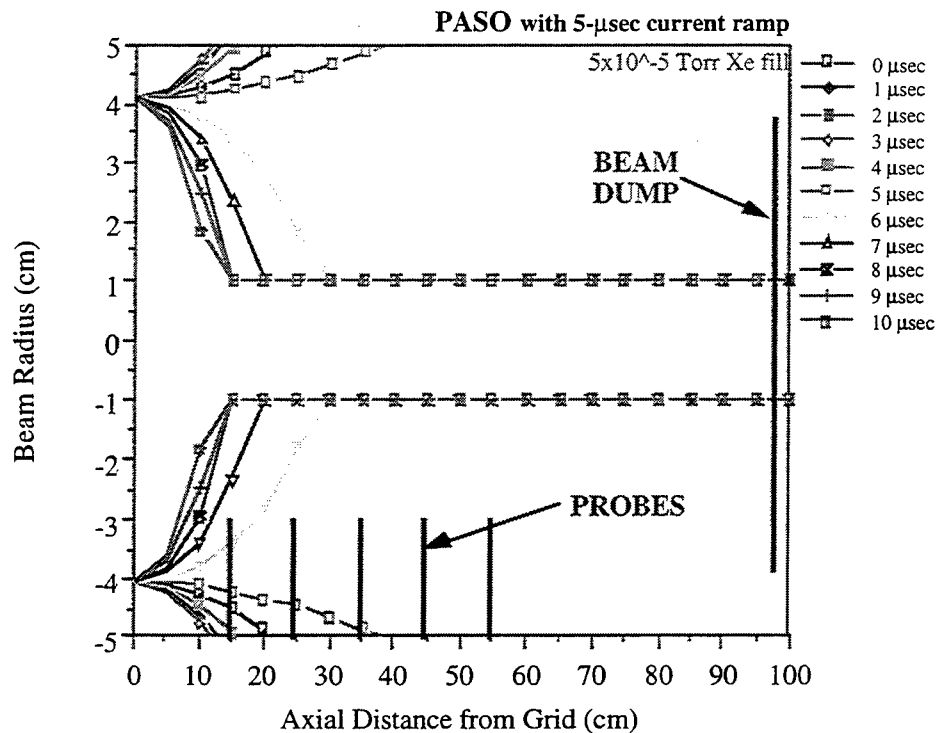


Figure 11: Results of model showing location of probes and beam collector relative to beam at given times for no externally applied magnetic field.

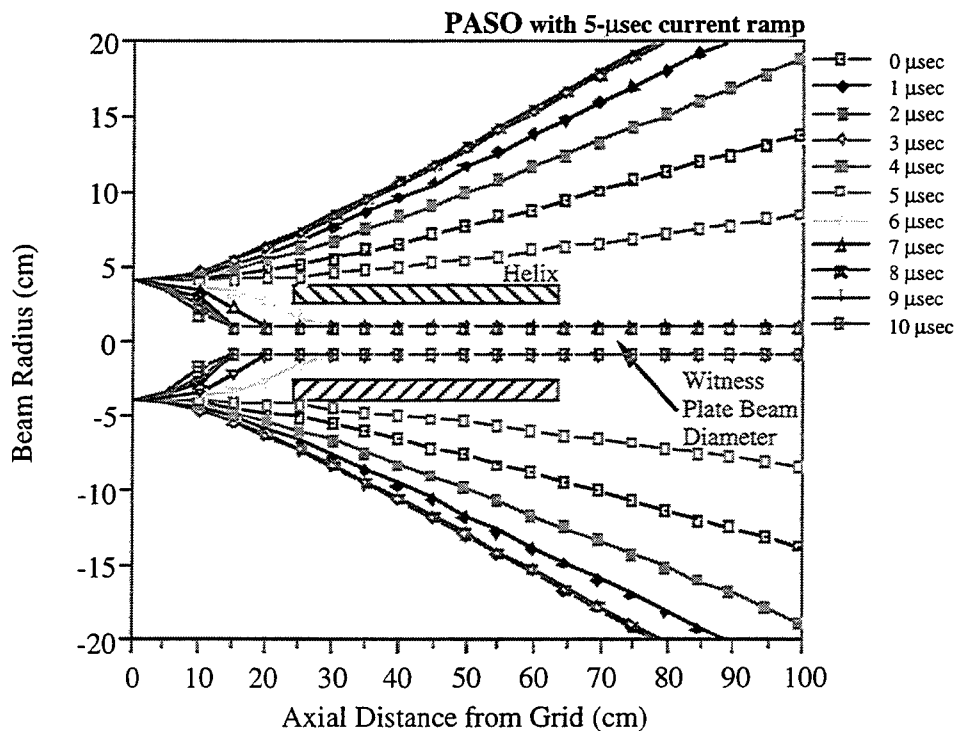


Figure 12: Results of model showing evolution of beam in time and radius as a function of axial distance for no applied magnetic field. Radius of typical helix SWS is shown for reference.

Pulse shortening in high-power backward wave oscillators

C. Grabowski, J. M. Gahl, E. Schamiloglu, and C. B. Fleddermann

Department of Electrical and Computer Engineering
University of New Mexico, Albuquerque, NM 87131

ABSTRACT

Pulse shortening is a phenomenon common to all high-power microwave devices. Whereas in electron beam driven sources the electron beam propagation in the device may be for several microseconds or more, the microwave pulse duration is typically no greater than ~100 ns. Specific reasons for pulse shortening may vary among devices, but all explanations of the phenomenon put forth involve the introduction of plasma into the interaction region near the walls and/or the degradation of the beam quality.

To gain a better understanding of pulse shortening in high power backward wave oscillators (BWO's), an investigation is being conducted at the University of New Mexico (UNM) on the UNM Long-Pulse BWO Experiment. Recent experiments have involved monitoring the beam current in the slow-wave structure (SWS) at different radii as a function of time. The current waveforms are correlated with the time histories of microwave pulses measured in separate experiments. The results reveal the appearance of electrons between SWS ripples at times corresponding to when the microwave signal peaks. A drop in the main beam current is observed shortly thereafter. Coatings of TiO_2 and Cr have been placed on the inner surface of the SWS in an effort to suppress electron emission. Initial results with the TiO_2 coatings have shown a measurable increase in microwave pulse width.

Keywords: pulse shortening, high power microwaves, backward wave oscillator, thin film coatings, multipactor

1. INTRODUCTION

A considerable amount of effort has been invested in experimental and theoretical studies of high power microwave devices driven by intense relativistic electron beams, beginning with the backward wave oscillator (BWO) in the early 1970's.¹ The first experiments in this area were conducted by Nation² and utilized a Blumlein to produce a 60 ns electron beam at energies of 200 ~ 500 keV to drive a BWO. Microwave pulses having peak powers of 10 MW and durations of 30 ns were obtained in these initial studies. Subsequent experiments involved injecting electron beams with higher energies and with longer pulse durations with the intent of obtaining higher peak and average powers.³ Gigawatt peak powers have now been achieved in a variety of different microwave devices;⁴⁻⁷ however, extending the pulse length to increase average power has been more difficult. As higher peak powers are produced, pulse widths tend to be limited to ≤ 100 ns irrespective of the duration of the electron beam pulse through the device.⁸⁻¹⁰

Several explanations, most centering around the undesirable introduction of plasma into the slow-wave structure (SWS), have been proposed to explain the phenomenon of pulse shortening in BWO's and related linear beam devices. Plasma in the vicinity of SWS walls and the beam can effectively "short out" the rippled or helical contours of the SWS⁸ or allow instabilities to develop in the electron beam.⁹ One source of unwanted plasma formation can be tied to cathode plasma expansion.^{8,10} As the cathode plasma expands transversely, the beam diameter expands with it. The increase in beam diameter then leads to electron bombardment of the anode, SWS, and other metal surfaces, which is then followed by plasma formation in these areas. Plasma formed at the collector may also travel back along magnetic field lines into the SWS,¹¹ or background gases and gases desorbed from the metal walls can be ionized by impact with beam electrons.¹²

The microwave fields generated in the device can even have adverse effects on device operation. These adverse effects can take the form of microwave breakdown, disruption of the electron beam which can then result in beam filamentation or beam electrons striking the SWS walls, or emission of electrons from SWS walls (multipactor).^{9,10-14} It has been suggested that this last effect, which may or may not be accompanied by plasma formation on the walls, leads to pulse shortening by producing an effective load for the microwaves in the SWS,¹² as the free electrons can then absorb the energy in the microwave fields. Benford and Price provide a more thorough discussion of these and other possible mechanisms involved in pulse shortening in Ref. 9.

Electron beam behavior and sources of plasma formation are the focus of the pulse shortening studies currently being conducted at the University of New Mexico on the UNM Long-Pulse BWO Experiment. Measurements made with a

current probe placed within the SWS suggest that beam disruption and emission of electrons and plasma from SWS walls are occurring in the presence of rf fields. When correlated with the microwave pulse waveforms obtained in separate experiments, peak electron emission is found to occur at approximately the same time at which microwave production begins to cease.

The application of various thin films to metal or dielectric surfaces which are subjected to high field stresses or electron bombardment has been shown to effectively suppress electron emission from those surfaces. During an earlier study at UNM with a quasi-DC, parallel-plate, high-voltage gap, metal and oxide films that were applied to the cathode effectively reduced field emission of electrons from the cathode surface and doubled the maximum field that could be sustained within the gap in high vacuum.¹⁵ Coatings of Ti, TiN, and Cr₂O₃, which have low secondary electron emission yields, have been shown to effectively suppress multipactor in cavities and on the rf windows of klystrons and accelerators.^{16,17} In an effort to further diagnose and suppress electron emission observed in the UNM Long Pulse BWO experiment, some of these coatings have been applied to the inner surfaces of the SWS in the experiment.

The following section of this paper will give a brief description of the UNM Long-Pulse BWO and the accelerator used to drive the BWO. Section 3 will outline the experiments that have been performed to identify the electron emission, including a description of the current probe and other diagnostic techniques that have been applied. Results from experiments performed both with and without the thin-film coatings on the SWS will be presented and discussed. Finally, some conclusions and plans for future work will be given in Section 4.

2. EXPERIMENTAL SETUP

2.1. BWO configuration

A modified Physics International Pulserad 110A electron beam accelerator is used to drive the UNM Long-Pulse BWO. The Pulserad 110A utilizes an 11-stage, 2.75 kJ Marx bank for its primary energy store. Originally, a 20 ns Blumlein followed the Marx bank in the Pulserad. In order to achieve long-pulse operation (500 ~ 600 ns), the Blumlein was replaced with a parallel LC network designed to convert the Marx bank, when erected, into a Type-A PFN.¹⁸ Several shunt resistors have also been placed across the accelerator output to reduce the output current and to provide better impedance matching with the electron beam diode.

A diagram showing the configuration of the BWO is given in Fig. 1. Cathode tips machined from graphite with annular knife-edge emitting surfaces (typically 20 mm diameter) are placed on the end of the cathode structure well within

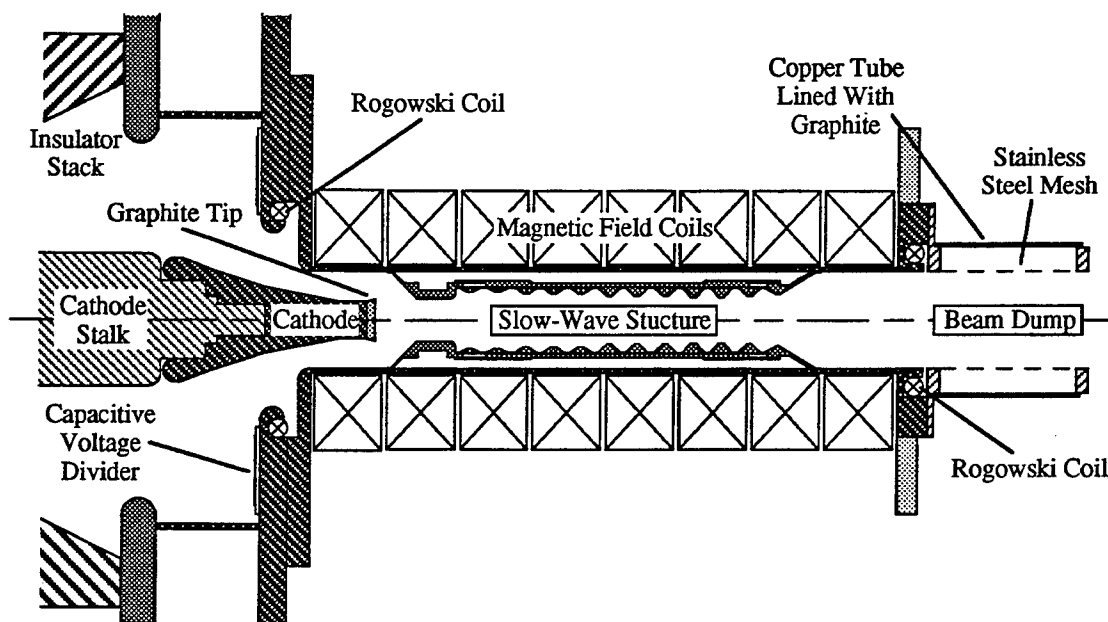


Figure 1 Cross-sectional diagram of the BWO.

the uniform region of the guiding magnetic field. Magnetic field strengths in most experiments range from 2 to 3 T. The anode-cathode (A-K) gap spacing for the diode can be varied by sliding the SWS back and forth in the waveguide in which it is placed.

The SWS itself has a modular construction in which each ripple is machined out of a ring of metal (stainless steel) and then slid into a tube which holds them in place. Typically a non-uniform ripple amplitude configuration, like that indicated in Fig. 1, is used. Studies conducted with the UNM Sinus-6 BWO have demonstrated that the initial shallow-ripple section of the SWS simply acts as a prebuncher for the electron beam.¹⁹ The prebunching section, which cannot generate microwave radiation by itself, significantly increases the efficiency of the energy extraction from the beam in the subsequent section which contains the deeper ripples.

The beam dump, or collector, at the end of the BWO is recessed from the waveguide wall behind a stainless steel mesh. The mesh, while opaque to the rf radiation, is transparent to the electrons. Thus, the collector plasma is formed (on the graphite-lined tube) outside the waveguide and away from the SWS. The grounded mesh also serves as a boundary to keep the plasma from drifting back into the waveguide.

2.2. Diagnostics

Voltage diagnostics on the accelerator and BWO consist of a resistive voltage divider, placed between the Marx bank and the LC network in the accelerator to monitor the Marx bank voltage, and a capacitive voltage divider, placed in vacuum near the cathode structure (Fig. 1) to monitor the cathode voltage. Two self-integrating Rogowski coils, placed around the cathode structure and just before the beam dump, monitor the current entering and exiting the SWS.

To monitor the microwave radiation from the experiment, a detector antenna, consisting of a short, open-ended section of WR-90 waveguide, is placed in the far-field region of the radiation pattern (150 cm from the radiating horn antenna aperture).

The waveguide can be positioned at various angles away from the axis of the horn antenna. The microwave signal picked up by the waveguide is attenuated and sent to a shielded room where it is then split into two signals using a power divider. One signal is sent to a crystal detector to make power measurements, and the other is mixed with a local oscillator signal to make frequency measurements.

The crystal detector and mixer outputs, as well as the signals from the current and voltage diagnostics, are recorded on Tektronix oscilloscopes. These waveforms are then transferred to a PC using LabVIEW®, where various calculations and analyses are performed and the data are plotted and saved to disk.

3. EXPERIMENTAL INVESTIGATION

Figure 2 shows a plot made by LabVIEW® of five typical microwave power waveforms obtained in the experiments. All waveforms are from experiments conducted with a cathode voltage of 350 kV, an A-K gap spacing of 2.5 cm, and a guiding magnetic field of 3 T. The time $t = 0$ represents the average time at which the cathode voltages in these experiments (and also those in Fig. 5) just begin to rise. Microwave pulse duration, measured at the base of the pulse, varies from 90 ns to 120 ns. As was mentioned in the previous section the electron beam current pulse is considerably longer, 500 ~ 600 ns. Often an increase in beam current, which is believed to be associated with gap closure, is observed, but this begins at 250 ns to 300 ns, well after microwave generation has ceased.

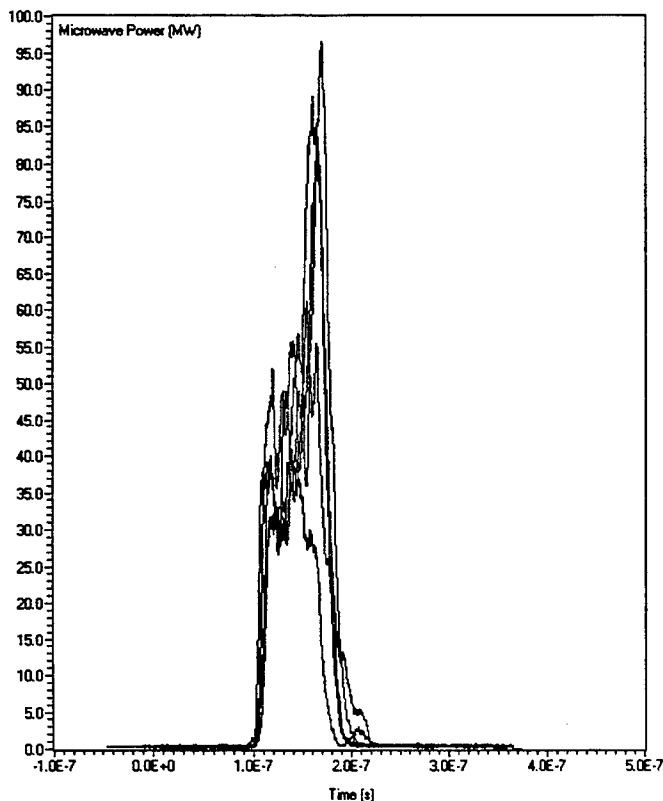


Figure 2 Microwave power waveforms obtained from experiments with $V_{\text{cath}} = 350$ kV, A-K gap = 2.5 cm, and $B = 3$ T. Five waveforms are shown.

A common element found among the many possible causes for microwave pulse shortening presented in Section 1 is the introduction of plasma into the SWS, often as a result of beam electrons striking metal surfaces. It was therefore deemed essential to monitor the behavior of the electron beam over time, and then to correlate its behavior with that of the microwave pulse.

3.1. Observations of beam current profile

To obtain a picture of the beam profile two current probes, which are similar to the one described by Korovin and Pegel in Ref. 20, were constructed. The probes, which are basically Faraday cups, consist of a stainless steel collector masked by two graphite disks, one with a radial slot in it and the other with 1 mm-diameter holes at different radii and spaced 30° apart. An illustration of one of the probes is shown in Fig. 3. By positioning the slot in the first disk over one of the holes in the second disk, only beam electrons at that particular radius are able to pass through and reach the collector. Thus, the radial current distribution is measured as a function of time. The second probe differs from the first only in that the $51\ \Omega$ termination resistance is not present, thereby enabling a bias to be placed on the collector.

The overall diameters of the probes are such that they can fit within the SWS tube between the ripples. Initial experiments were conducted with the first probe placed after the eighth ripple (Fig. 4a). These experiments were performed at cathode voltages of 350 and 500 kV with magnetic fields of 2 and 3 T. Current waveforms obtained from the probe are plotted out for each of the different radii from the 350 kV, 3 T experiments in Fig. 5. Again, $t = 0$ is the average time at which the cathode voltages in these experiments and those in Fig. 2 just begin to rise.

When compared with the microwave power waveforms in Fig. 2, several interesting observations can be made. Current in the beam is initially centered around a radius of 10 mm, as would be expected for a 20 mm diameter cathode. From Fig. 2, microwave generation is expected to begin at roughly 100 ns and then cease by 180 ~ 200 ns. During the middle of this time, however, currents appear at 12, 13, and 14 mm, well outside the initial beam boundary. It should be noted here that the radius of the SWS cutoff neck is 11.5 mm, and, furthermore, the radius of the ripple immediately in front of the probe is 12 mm (Fig. 4a). Current is also measured near the axis at this time. Then, at approximately 180 ns, as microwave production begins to cease, current in the main part of the beam, at radii of 10 and 11 mm, drops off rapidly.

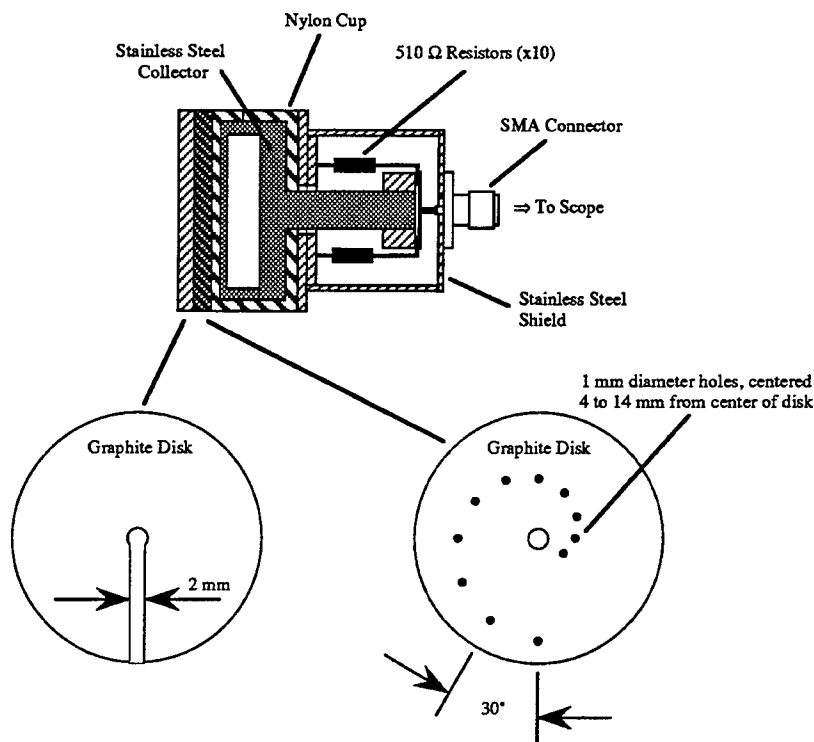


Figure 3 Diagram of current probe used to map the radial profile of the electron beam.

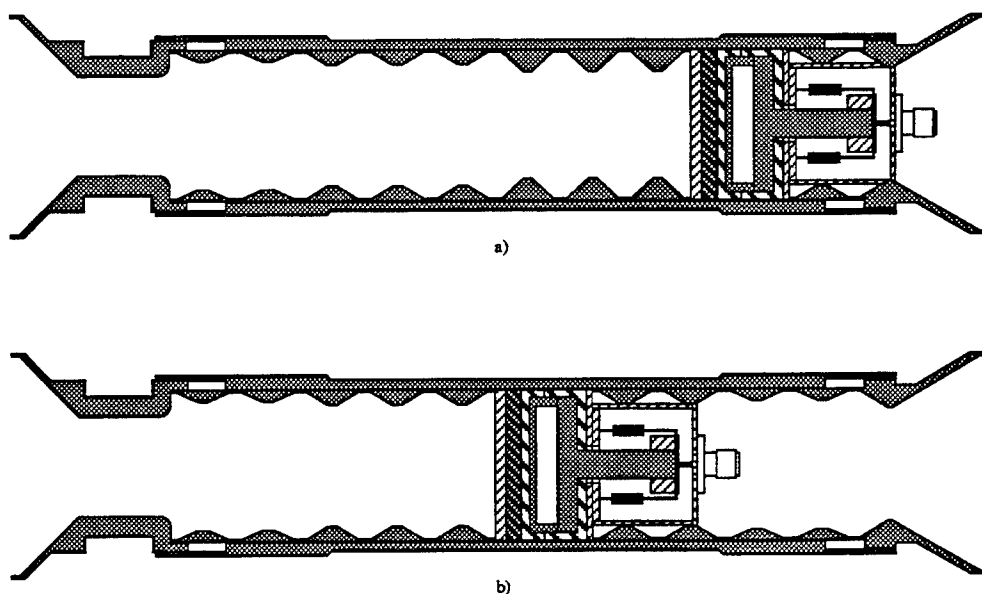


Figure 4 Placement of current probe in SWS: a) probe placed after 8th ripple, b) probe placed after 5th ripple, just after prebuncher section.

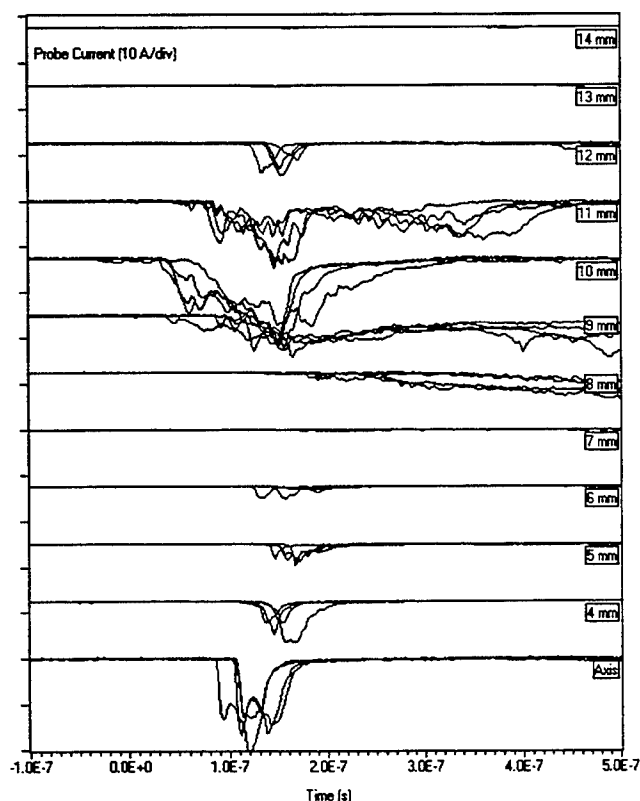


Figure 5 Current probe waveforms obtained from experiments having the same parameters as those of Fig. 2. Four waveforms are shown overlaid for each radial position.

A series of additional experiments were performed next with the probe moved further into the SWS, just after the prebuncher section, as shown in Fig. 4b.²¹ Currents at radii of 12 mm and greater were found to be negligible. Current in the main beam at 10 mm tended to decrease more slowly (and that beginning after 200 ns), while at 11 mm current slowly grew, a behavior which is characteristic of "normal" beam expansion.

In an open SWS tube if only the prebuncher section is present, no rf generation is expected based on the studies presented in Ref. 19. Thus, with the setup shown in Fig. 4b, no rf fields should be present to influence the electron beam. With the setup of Fig. 4a, although there are only three of the deeper amplitude ripples present, it is quite possible that some microwave generation is occurring. The observed behavior of the electron beam and the appearance of the electrons at radii of 12 mm and beyond then may be typical phenomena that occur in the presence of rf fields during BWO operation, when the probe is not closing off the SWS. Both phenomena have been suggested by the references listed in Section 1 as being possible factors contributing to pulse shortening.

In order to better characterize the electrons observed between the SWS ripples, the second probe was placed in the SWS at the position indicated by Fig. 4a, and a -200 V bias was placed on its collector. The initial current pulses appearing in the ripple shadows from 100 to 200 ns were observed again, but the remainder of the probe current waveform was remarkably flat.²¹

These observations with the biased probe suggest that the initial current pulses are comprised of very energetic electrons, while the later currents, which are not observed with the biased probe, are due to lower energy electrons. In that event, the initial pulse of electrons could be a result of field emission from the surface of the ripple immediately in front of the probe or secondary electron emission caused by beam electrons being deflected into the ripple by the rf fields. It is not likely that currents this close to the wall and recessed between the ripples are directly from beam electrons, as beam electrons would not only have to first be significantly deflected transversely into the shadow of the ripples, but then they would have to be strongly deflected again in the axial direction in order to travel through the apertures in the graphite disks of the probe. The later lower energy currents could be from plasma that is possibly formed when either the field emission or secondary electron emission processes are occurring.

3.2. Thin-film coatings on SWS walls

The sudden disappearance of the main beam current at 10 and 11 mm in Fig. 5, coupled with the fact that the currents between the ripples might be from energetic secondary electrons, suggest that rf disruption of the beam might be responsible for the microwave pulse shortening here. Conversely, it is also possible that considerable field emission from the SWS walls and the accompanying plasma formation might be producing an instability which is destroying the beam. To gain some insight into which, if either, of these scenarios might be relevant, as well as to identify the mechanism producing the electrons between the ripples, various thin-film coatings are being placed on the SWS walls and experiments are being conducted.

3.2.1 TiO₂ thin films

A series of experiments with a TiO₂ thin-film has already been conducted, and some of the results are shown in Figs. 6 and 7. TiO₂ was chosen as a result of the studies described in Ref. 15. In this work TiO₂ was found (after conditioning) to be one of the most effective thin-film materials for suppressing field emission of electrons from the cathode in a quasi-DC, parallel plate experiment. TiO₂ does, however, have a somewhat high secondary electron emission coefficient, and is therefore to be avoided when multipactoring is a concern.¹⁷ Thus, it seems to be an excellent material to use to try to identify whether the electrons emitted near the walls are from field emission or secondary electron emission.

As in the work of Ref. 15, the TiO₂ thin film was applied to the surfaces of the SWS ripples using an ion sputtering technique with a 2.5 cm diameter Kaufman gun. Ar/O₂ ion beams impacted a Ti target in an Ar/O₂ atmosphere. The sputtered Ti then reacted with the O₂ to form a TiO₂ film on the SWS ripples. The thickness of the sputtered film was approximately 1000 Å.

Microwave power waveforms from some of the first shots with the TiO₂ coated SWS are shown in Fig. 6. Peak power is slightly less here compared to the uncoated SWS results of Fig. 2, but the waveforms are very reproducible from one shot to the next. The power waveforms have also shifted closer to $t = 0$, but this is simply a result of the cathode voltages rising more abruptly at the beginning of the pulse in these experiments.

After these data were taken, the BWO was not operated for 2 1/2 weeks but was still left under vacuum. Approximately 65 shots were then fired to attempt to condition the coating, after which data from the

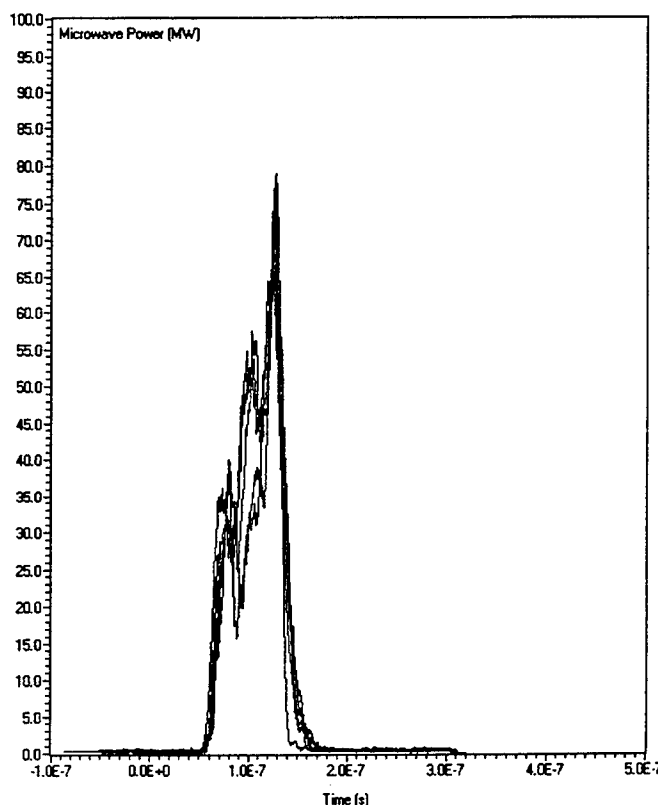


Figure 6 Microwave power waveforms obtained from initial experiments with TiO₂ coated SWS. Experimental parameters are $V_{\text{cath}} = 350$ kV, A-K gap = 2.5 cm, and $B = 3$ T. Five waveforms are shown.

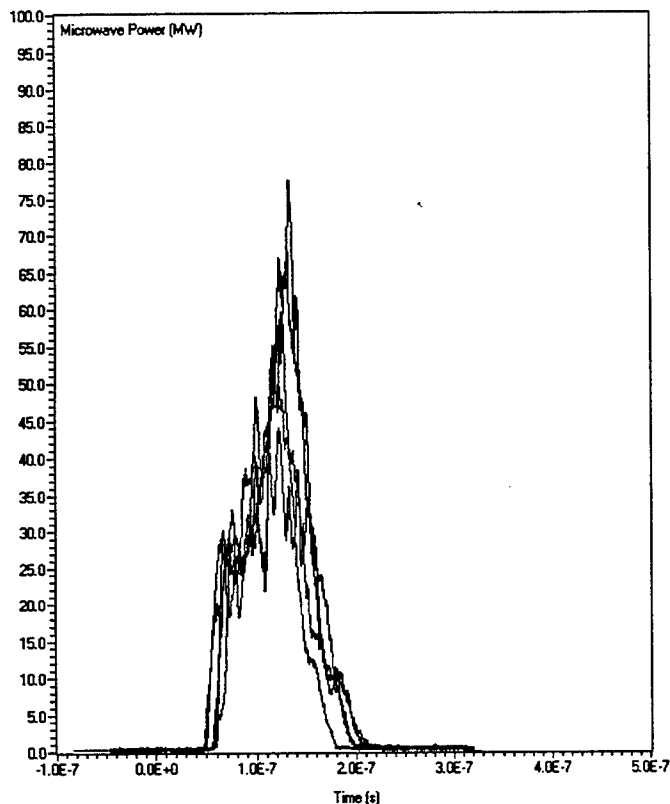


Figure 7 Microwave power waveforms obtained from experiments with TiO_2 coated SWS after conditioning. Experimental parameters are the same as for Fig. 6. Five waveforms are shown.

experiments were once again recorded. Power waveforms from five 350 kV, 3 T shots are shown in Fig. 7. Peak power has not increased at this point, but the pulse widths, measured at the base of the pulse, have increased to 140 ~ 170 ns, an increase of approximately 50 ns when compared with the waveforms in Figs. 2 and 6.

The SWS rings were removed from the experiment at this point and inspected. Significant damage was observed on the coatings, particularly on those on the deeper amplitude ripples. Damage was observed around the edges at the minimum radii, perhaps due to beam electrons scraping those edges, as well as on spots on the sides of the ripples, where breakdown or some sort of electron emission points might have been located.

At this point the SWS was reassembled with the second current probe inside it, in the configuration shown in Fig. 4a, and current profiles were observed at 11, 12, 13, and 14 mm with no collector bias and with a -200 V bias. Currents were again observed at 12, 13, and 14 mm, just as for the uncoated SWS case; however, it is not felt that these results conclusively identify that the currents must then be from secondary electron emission. The conditioning which was carried out by leaving the SWS in vacuum for an extended period of time and then firing numerous conditioning shots may have been reversed when the experiment was brought up to atmosphere again to inspect the rings and to insert the current probe. The need for a more non-invasive diagnostic, which would not require the BWO to be brought up to atmosphere or in any other way necessitate a change in the experimental configuration after conditioning, seems apparent.

3.2.2. Cr thin films

Following the last experiments with the TiO_2 thin films, the SWS rings were cleaned and a thin coating of Cr was placed on the rings. Cr was chosen for its low secondary electron emission coefficient, and because the coefficient has been shown to be relatively unaffected by the oxidation of the top surface of the film when exposed to atmosphere.¹⁷ The films were deposited using an electron beam evaporation technique in which an electron beam was used to heat a Cr target causing the Cr to sublime and then redeposit on the SWS ripples positioned above the target. Films approximately 1500 Å thick were evaporated onto the ripples.

At this time the initial experimental results are too preliminary to draw any substantial conclusions from them regarding the effect of the Cr film on the SWS inner surface. Experiments will proceed, though, in a manner similar to that for the TiO_2 coating experiments. The BWO will again be left under vacuum for a significant amount of time (approximately 2 1/2 weeks), at which point more measurements of microwave power will be made. Following the power measurements, tens of shots will be fired for further conditioning, after which power data will again be recorded and then compared with existing data.

4. CONCLUSIONS

The data gathered from both current probes has, for the first time, provided an indication of how the profile and behavior of the electron beam might vary in the SWS during microwave generation. In addition, the data demonstrate that electron emission and plasma formation are very likely occurring on the SWS walls during this time. The excellent correlation between the beam disruption and the wall emission observed in these experiments and the microwave pulse termination observed in previous experiments suggest that the first two processes are closely tied to pulse shortening.

It is not clear at this time whether the electron emission and plasma formation at the walls are a side effect of the beam disruption brought on by the rf fields, or whether the wall emission and plasma formation lead to beam disruption and pulse shortening. Coatings of TiO_2 and Cr have been placed on the SWS walls in an attempt to suppress the electron emission and plasma formation, as well as to identify its source. Results are still inconclusive at this point regarding the mechanism of the electron emission, field emission or secondary electron emission; however, a measurable extension of pulse width has been observed with the TiO_2 coating on the SWS after conditioning. Significant damage was also observed on the TiO_2 coating after these data were collected. Experiments are in progress with the Cr coating on the SWS.

As was mentioned in Section 3.2.2, the exposure of the coatings in the SWS to atmosphere after they have been conditioned may in some way reverse the benefits of the conditioning. The need for a more non-invasive diagnostic than the current probe, which would not require the BWO to be brought up to atmosphere after conditioning or in any other way necessitate a change in the experimental configuration, then seems apparent in order to obtain a better understanding of the processes that are actually occurring during microwave generation. To this end a Nd:YAG laser system (1064 nm) has been acquired and will be used to attempt to observe the evolution of the axially line-averaged plasma density between the electron beam and SWS walls. (Infrared lasers have been used in the past to measure plasma densities in ion diodes and plasma opening switches.²²) The plasma density measurements will then be correlated with the evolution of the microwave power output. Furthermore, this laser can be used to measure the spread in axial beam momentum, as in Ref. 23.

5. ACKNOWLEDGMENTS

The authors wish to thank B. Wroblewski for his help with the sputtering system and the application of the TiO_2 coating to the SWS ripple segments, as well as T. Cavazos for his help with the electron beam evaporation system and the application of the Cr film to the SWS ripples. This work is being supported through a High Energy Microwave Devices consortium funded by an AFOSR/DOD MURI grant and administered through Texas Tech University.

6. REFERENCES

- ¹ J. Benford and J. Swegle, *High Power Microwaves*, ch. 6, Artech House, Boston, 1992.
- ² J. A. Nation, "On the Coupling of an High-Current Relativistic Electron Beam to a Slow Wave Structure," *Appl. Phys. Lett.*, vol. 17, pp. 491-494, 1970.
- ³ Y. Carmel, J. Ivers, R. E. Kribel, and J. Nation, "Intense Coherent Cherenkov Radiation Due to the Interaction of a Relativistic Electron Beam With a Slow Wave Structure," *Phys. Rev. Lett.*, vol. 33, pp. 1278-1282, 1974.
- ⁴ Yu. F. Bondar, S. I. Zavorotnyi, A. L. Ipatov, N. I. Karbushev, N. F. Kovalev, O. T. Loza, G. P. Mkheidze, A. A. Ovchinnikov, A. A. Rukhadze, and L. E. Tsopp, "Measurements of RF Emission from a Carcinotron with a Relativistic Electron Beam," *Sov. J. Plasma Phys.*, vol. 9, p. 223, 1983.
- ⁵ S. P. Bugaev, V. I. Kanavets, A. I. Klimov, V. I. Koshelev, A. I. Slepikov, and V. A. Cherepenin, "Interaction of an Electron Beam and an Electromagnetic Field in a Multiwave 10^{10} W Cherenkov Generator," *Sov. J. Comm. Tech. Electr.*, vol. 32, pp. 79-87, 1987.
- ⁶ V. L. Granatstein, M. Herndon, P. Sprangle, Y. Carmel, and J. A. Nation, "Gigawatt Microwave Emission from an Intense Relativistic Electron Beam," *Plasma Phys.*, vol. 17, pp. 23-28, 1975.
- ⁷ K. J. Hendricks, P. D. Coleman, R. W. Lemke, M. J. Arman, and L. Bowers, "Extraction of 1 GW of rf Power from an Injection Locked Relativistic Klystron Oscillator," *Phys. Rev. Lett.*, vol. 76, pp. 154-157, 1996.
- ⁸ V. A. Burtsev, N. I. Zaitsev, N. F. Kovalev, I. S. Kulagin, A. G. Nikonov, M. I. Petelin, I. M. Roife, Yu. M. Savel'ev, and V. I. Engel'ko, "Generation of Microsecond Microwave Pulses by Relativistic Electron Beams," *Sov. Tech. Phys. Lett.*, vol. 9, pp. 617-618, 1983.
- ⁹ J. Benford, D. Price, and G. Benford, "Pulse Shortening in High Power Microwave Sources," to appear in the *Proceedings of Beams '96*, Prague, Czech Republic, June 1996.
- ¹⁰ S. N. Voronkov, O. T. Loza, and P. S. Strelkov, "Effect of the Cathode Plasma on the Operation of a Relativistic Carcinotron with Microsecond Pulse Length," *Plasma Phys. Rep.*, vol. 19, pp. 309-311, 1993.
- ¹¹ S. N. Voronkov, O. T. Loza, and P. S. Strelkov, "Limits on the Length of Radiation Pulses Generated by Microwave Oscillators Using Microsecond Relativistic Electron Beams," *Sov. J. Plasma Phys.*, vol. 17, pp. 439-442, 1991.
- ¹² A. S. El'chaninov, F. Ya. Zagulov, S. D. Korovin, G. A. Mesyats, and V. V. Rostov, "Limitation on the Length of High-Power Microwave Pulses in a Relativistic Carcinotron," *Sov. Tech. Phys. Lett.*, vol. 7, pp. 499-500, 1981.

- 13 S. P. Bugayev, M. P. Deychuli, V. I. Kanavets, A. I. Klimov, V. I. Koshelev, and V. A. Cherepenin, "Collapse of a Relativistic High-Current Electron Beam During Generation of High-Power Electromagnetic Radiation Pulses," *Radiotekh. Elektron.*, vol. 29, pp. 557-560, 1984.
- 14 J. R. M. Vaughn, "Multipactor," *IEEE Trans. Electron Devices*, vol. 35, pp. 1172-1180, 1988.
- 15 C. S. Mayberry, B. Wroblewski, E. Schamiloglu, and C. B. Fleddermann, "Suppression of Vacuum Breakdown Using Thin-Film Coatings," *J. Appl. Phys.*, vol. 76, pp. 4448-4450, 1994.
- 16 R. C. Talcott, "The Effects of Titanium Films on Secondary Electron Emission Phenomena in Resonant Cavities and at Dielectric Surfaces," *IRE Trans. Electron Devices*, vol. 9, pp. 405-410, 1962.
- 17 A. R. Nyaiesh, E. L. Garwin, F. K. King, and R. E. Kirby, "Properties of Thin Antimultipactor TiN and Cr₂O₃ Coatings for Klystron Windows," *J. Vac. Sci. Technol. A*, vol. 4, pp. 2356-2363, 1986.
- 18 D. B. Cummings, "Conversion of a Marx Generator to a Type-A Pulse Forming Network," IEEE Conference Record of the Twelfth Modulator Symposium, IEEE Cat. No. 76CH1045-4ED, 1976, pp. 142-146.
- 19 L. D. Moreland, E. Schamiloglu, R. W. Lemke, S. D. Korovin, V. V. Rostov, A. M. Roitman, K. J. Hendricks, and T. A. Spencer, "Efficiency Enhancement of High Power Vacuum BWO's Using Nonuniform Slow Wave Structures," *IEEE Trans. Plasma Sci.*, vol. 22, pp. 554-564, 1994.
- 20 S. D. Korovin and I. V. Pegel, "Structure of a High-Current Relativistic Electron Beam Formed in a Coaxial Magnetically Insulated Diode With an Edge-Type Cathode," *Sov. Phys. Tech. Phys.*, vol. 37, pp. 434-438, 1992.
- 21 C. Grabowski, J. M. Gahl, and E. Schamiloglu, "Electron Emission From Slow-Wave Structure Walls in a Long Pulse, High-Power Backward Wave Oscillator," submitted to *IEEE Trans. Plasma Sci.*, July 1996.
- 22 M. Tuszewski, W. J. Wagenaar, and M. P. Desjarlais, "Electron Density Measurements in a Magnetically Insulated Ion Diode," *J. Appl. Phys.*, vol. 77, pp. 6188-6193, 1995.
- 23 S. C. Chen and T. C. Marshall, "Thomson Backscattering From a Relativistic Electron Beam as a Diagnostic for Parallel Velocity Spread," *Phys. Rev. Lett.*, vol. 52, pp. 425-428, 1984.

Nonlinear study of mode locking in a quasi-optical gyrotron

Hao Wu and Alan H. McCurdy

University of Southern California, Department of Electrical Engineering/ Electrophysics
Los Angeles, California 90089-0271

ABSTRACT

Nonlinear, time-dependent multimode calculations have been carried out to study mode locking in quasi-optical gyrotron oscillators. The calculations are based on the rate equation model of modal growth and saturation. The slow-time formalism is used for particle motion and both the time varying electric and magnetic fields are included. It is found that radiation pulses of width 400 ps can be generated in nonlinear regime. The gyrotron features an open resonator of length 100 cm formed by a pair of spherical mirrors and a single pencil electron beam guided by external magnetic field in transverse direction to the axis of symmetry of the cavity. The strong current modulation is provided at frequency of 300 MHz, the nominal modal spacing between two odd modes in such a cavity. Eight odd modes are found to be locked to generate extremely short radiation pulses. Application for short pulse radiation in millimeter and submillimeter wavelength range include radar, plasma diagnosis, time domain metrology and communication systems. Parametric dependencies investigated include static magnetic field, beam current and beam voltage, as well as the drive signal amplitudes and frequencies. The work is geared towards support of a proof of principle experiment to generate high power radiation pulses of short duration via synchronous mode locking.

Keywords: quasi-optical gyrotron, mode locking, short pulse, millimeter wave radiation

1. INTRODUCTION

Operation of high power microwave oscillators at high frequencies typically involves the competition among many electromagnetic modes. This problem is seen in devices such as free electron lasers, gyrotrons, plasma based devices as well as the conventional slow wave devices such as traveling wave tubes. The physical mechanism for this mode competition lies in the nonlinear character of the electron beam from which the modes derives their energy. Modes compete with each other for energy. In solving the mode competition problem, much research has focused on suppression of unwanted modes for applications requiring extremely narrow spectral widths. However for some applications sharpness in the frequency spectrum is not important, it may be desired that the signal be short-pulse or frequency modulated. For these applications it may be possible to utilize the microwave oscillator in the overmoded state. In general, the output of the overmoded oscillator is most useful if it is periodic. To achieve periodicity it requires a coupling between the modes to lock them into a common frequency interval. Thus coherent output is obtained with a concomitant modulation in either the amplitude or frequency. The technique of mode locking has been highly successful in laser oscillators.¹⁻² This work is intended to demonstrate that mode locking in a quasi-optical gyrotron oscillator can result in high peak power, short-pulse radiation output.

There has been some theoretical and experimental work on mode locking of free-electron microwave and gyrotron devices. An early free electron laser (FEL) experiment³ utilized a pulsed electron beam and reported short pulse radiation output. However no tests of radiation output of as function of modulation parameters were reported. A general theoretical analysis of the nonstationary effects in FEL's⁴ predicted a wide range of behavior such as mode locking, phase locking and stochastic regimes. Recent FEL experiments reported self-mode locking⁵ and interpulse locking via an external cavity.⁶ Self-mode locked electron cyclotron masers were described using the quasi-linear rate equation model.⁷ A case of quasi-optical self-mode locking was reported and a path from single mode to stochastic behavior was described.⁴ Mode locking in a quasi-optical gyrotron using a time-dependent phase perturbation in the cavity was also considered.⁸ In this two-beam system the phase change was caused by one electron beam with a modulation imposed on the electron density while the other beam with no time dependence served as the gain medium. It was found that in this study that mode locking in the linear regime could not be obtained when only one beam was used for both the gain medium and the phase shifter.

Recent theoretical work has been done on mode locking a closed cavity gyrotron.⁹⁻¹¹ A quasi-linear theory, a fully nonlinear (slow-time scale) theory and MAGIC PIC code simulations have indicated the feasibility of mode locking a closed cavity gyrotron. A cavity composed of a radially tapered section and a straight section of waveguide is used to obtain an equidistant frequency spectrum. In the quasi-linear theory the best performance (mode locking with lowest required input

power) is obtained for a nonzero value of detuning. The FWHM of the optimal pulse is about 500 ps with a power of greater than twelve times of free-running time averaged power level. In the nonlinear (slow-time scale) theory, extremely short pulse radiation is obtained using large current modulation with an amplitude varying between zero and 2.0 A at the nominal modal frequency spacing between two modes. In MAGIC PIC simulations a train of narrow pulses (FWHM ~ 1 ns) is observed using a sinusoidal current density modulation with an amplitude of 5% of the dc current level varying at the frequency of modal spacing.

Here we demonstrate that mode locking in a quasi-optical gyrotron can be achieved using a single beam in nonlinear regime. Nonlinear slow-time scale multimode calculations indicate that a train of mode-locked millimeter wave pulses can be obtained using a strongly modulated electron beam in a quasi-optical gyrotron. The mode locking is synchronous in that an external modulation signal is applied to the gain medium (electron beam) to couple the modes. This method of mode locking is preferable since enhanced oscillator stability and pulse-to-pulse coherence may be achieved. Stable single-mode operation in quasi-optical gyrotrons has been focused on in previous studies.¹²⁻¹³ There are several reasons for considering the mode locking of a quasi-optical gyrotron device. First, short pulse or frequency modulated output may be desired. Second, unlike closed cavity gyrotrons, quasi-optical gyrotrons are not highly dispersive. The frequency spacing between modes in a quasi-optical gyrotron is equidistant. Hence it satisfies the prerequisite condition of mode locking automatically without altering the geometry of devices. Third, modes in quasi-optical gyrotrons are typically weakly coupled. This coupling usually allows multiple modes to oscillate in the free-running steady state. For all practical purposes, quasi-optical gyrotrons are overmoded. One might anticipate that mode locking could enhance the performance of such an overmoded device. It is expected that mode locking in such an oscillator will be similar to that observed in inhomogeneously broadened lasers. A set of slow-time scale nonlinear multimode equations for the electron momentum and the amplitude and phase of the electromagnetic field were derived and a vectorized time-dependent code was written based on those equations. Numerical results indicate that a quasi-optical gyrotron is appropriate for generating high peak power, subnanosecond pulse radiation at 150 GHz. Applications for short pulse radiation in the millimeter and submillimeter wavelength range include radar images of isolated targets, atmospheric sensing, Fourier transform spectroscopy, plasma diagnosis, communication systems and a variety of dynamic phenomena occurring on a very short time scale.

2. NONLINEAR MODE-LOCKING THEORY OF QUASI-OPTICAL GYROTRON

The basic structure of the quasi-optical gyrotron, shown in Fig. 1, consists of an open resonator of length L formed by a pair of spherical mirrors. The magnetic field B_0 is directed transverse to the axis of the open resonator. The electron beam propagates along the z axis and the axis of resonator coincides with the y axis. Therefore, the direction of the electron beam propagation is perpendicular to the radiation axis so that the coupling of the radiation is separated from collection of the electron beam. An alternative beam geometry is that of a sheet beam oriented along the y -direction. The electron beam used is a zero temperature, pencil one centered in the cavity with initial electron momentum perpendicular and parallel to the cavity longitudinal axis of p_{y0} and p_{z0} , respectively. Resonator fields are of small initial amplitudes and random phases. Strong coupling between the electrons and the modes will occur at frequencies near multiples of the relativistic electron cyclotron frequency.

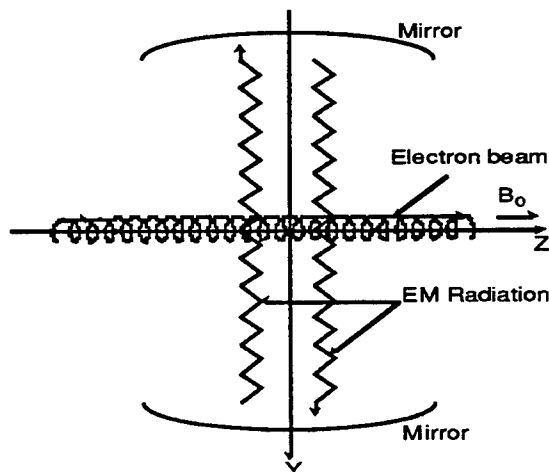


Fig. 1. Quasi-optical gyrotron configuration.

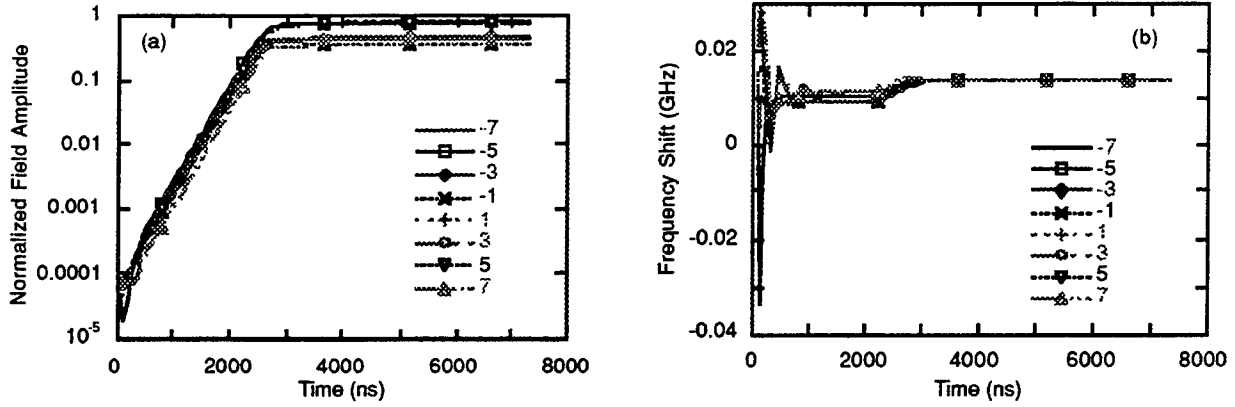


Fig. 2. Gyrotron modal evolution showing (a) normalized field amplitude and (b) oscillation frequency shift from the empty cavity resonant frequency. Curves are labeled by the axial mode index.

The analysis of the modal evolution relies on the slow time scale equations for electron momentum and the amplitude and phase of the electromagnetic field.¹⁴ The electric and magnetic fields are expanded in a sum of empty cavity modes:

$$\begin{aligned}\vec{E}(\vec{r}, t) &= \frac{1}{2} \sum_l A_l(t) e^{-z^2/w_0^2} e^{i(\omega_0 t + \tilde{\alpha}_l(t))} \sin(k_l y - \frac{1}{2}\pi) \vec{e}_x + \text{c.c.} \\ \vec{B}(\vec{r}, t) &= \frac{i}{2c} \sum_l A_l(t) e^{-z^2/w_0^2} e^{i(\omega_0 t + \tilde{\alpha}_l(t))} \cos(k_l y - \frac{1}{2}\pi) \vec{e}_z + \text{c.c.}\end{aligned}$$

where the modal amplitude $A_l(t)$ and the phase $\alpha_l(t)$ are assumed to vary slowly over a period of time $2L/c$, w_0 is the radiation waist radius and $\tilde{\alpha}_l = \alpha_l + (\omega_l - \omega_0)t$. The Lorentz force equations for the electron equations of motion are time averaged over all time scales faster $2\pi/(\omega_l - \Omega)$, where ω_l and $\Omega = |e|B_0/m\gamma$ are the field and relativistic cyclotron frequencies, respectively. We find the following equations governing the motion of the particles:

$$\begin{aligned}\frac{dp_{\perp}}{dz} &= -\frac{em\gamma}{p_z} e^{-z^2/w_0^2} \sum_n A_l J_n(Q) \sin(\theta - \tilde{\alpha}_l) \cos(k_l y_g - \frac{1+n}{2}\pi) \\ \frac{d\theta}{dz} &= \frac{em\gamma}{p_z} (n\Omega - \omega_0) + \frac{em\gamma}{p_{\perp} p_z} e^{-z^2/w_0^2} \sum_l A_l \frac{n J_n(Q)}{Q} (n \frac{p_{\perp}}{m\gamma c}) \cos(\theta - \tilde{\alpha}_l) \cos(k_l y_g - \frac{1+n}{2}\pi)\end{aligned}$$

where P_{\perp} is the magnitude of the transverse momentum, $\theta = n\Psi - \omega_0 t$ is the slowly varying relative phase between the electron and the electromagnetic wave, $\gamma = [1 + (P_{\perp}/mc)^2 + (p_z/mc)^2]^{1/2}$ is the relativistic factor, $\Omega_0 = |e|B_0/m\gamma_0$ is the non-relativistic cyclotron frequency, $Q = k_l/eB_0$ is a dimensionless quantity, (x_g, y_g) denote the guiding center position, l denotes mode number and n denotes harmonic number. The rate equations for the fields are derived in the usual way with the aid of Maxwell's equations and orthogonality of modes:

$$\frac{dA_1(t)}{dt} = -\frac{\omega_1 A_1}{2Q_T} + \frac{4I_0}{\pi \epsilon_0 w_0^2 L} \operatorname{Re} \int_{-\infty}^{\infty} \int_0^{\tau} \int_{-L_b/2}^{L_b/2} \int_0^{2\pi} \frac{p_{\perp}}{p_z} e^{-z/w_0^2} J_n(Q) e^{i(\theta - \tilde{\alpha}_1(t))} \cos(k_1 y_g - \frac{1+n}{2}\pi) \frac{d\phi_0}{2\pi} \frac{dy_0}{L_b} \frac{dt_0}{\tau} dz$$

$$\frac{d\tilde{\alpha}_1(t)}{dt} = \frac{\omega_1^2 - \omega_0^2}{2\omega_0} - \frac{\omega_1}{2Q_0} + \frac{1}{A_1} \frac{4I_0}{\pi \epsilon_0 w_0^2 L} \operatorname{Im} \int_{-\infty}^{\infty} \int_0^{\tau} \int_{-L_b/2}^{L_b/2} \int_0^{2\pi} \frac{p_{\perp}}{p_z} e^{-z/w_0^2} J_n(Q) e^{i(\theta - \tilde{\alpha}_1(t))} \cos(k_1 y_g - \frac{1+n}{2}\pi) \frac{d\phi_0}{2\pi} \frac{dy_0}{L_b} \frac{dt_0}{\tau} dz$$

where ω_1/Q_T is the phenomenological term for resonator losses due to boundary effects, Q_T and Q_0 are total and ohmic quality factors of the cavity, I_0 the dc beam current, τ the field period and L_b is the total sheet beam length.

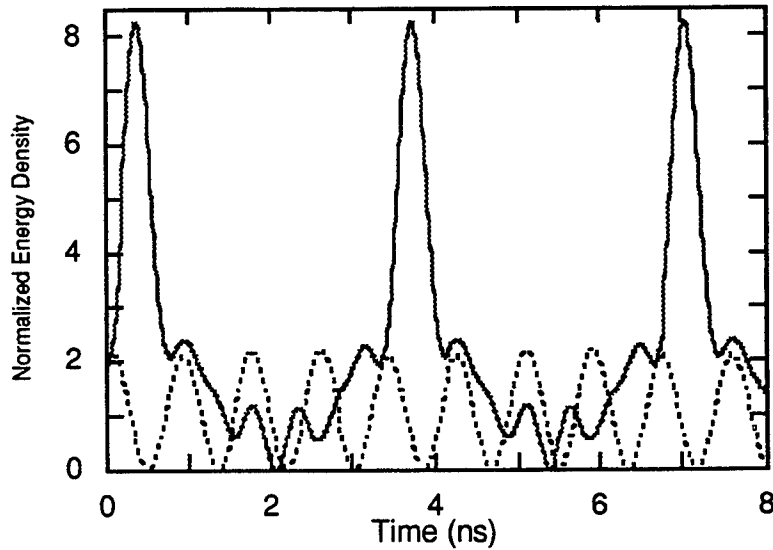


Fig. 3. Electromagnetic energy density vs. time for case corresponding to the case shown in Fig. 2 (solid line) and free-running case (dotted line).

The set of coupled equations is solved by solving for particle motion through the quasi-optical resonator while keeping the field amplitude fixed but allowing the phase to vary linearly in time. In other words, at a given instant time t , the fields are frozen and a set of electrons are integrated across the oscillator cavity. As the electrons pass through the cavity the field amplitude is kept fixed but the phase is modified by

$$\theta = \theta(t) + \frac{d\theta}{dt} \int \frac{dz}{v_z},$$

where z is the position of the electron and v_z is its axial velocity. After the electron integrations are completed, the electron kinetic energy change is computed and used in the field equations. The field equations are then incremented on time step and the electron integrations are again performed. This process is repeated until steady state is reached. Velocity modulation can

be included by making the axial velocity a function of the entrance time of a given particle into the cavity, though closed-cavity results indicate that velocity modulation may not generate better results than current density modulation. The particle motion must be determined for each value of t_0 over a time interval equal to the period of the radiation fields. Density modulation is easily included by making the dc beam current I_0 a function of time in the field equations. The particle equations used in this work are "slow-time scale" ones, which ignore physical phenomena occurring on a time scale of the field period or the electron cyclotron period. Thus the magnitude of the electron perpendicular momentum, the axial momentum and the relative phase between the electron and electromagnetic wave are the only particle variables computed. This saves an enormous amount of computational effort and is standard practice in this field of science. The field equations are "rate equations" in the sense that the electromagnetic fields are written as the product of a slowly varying phase term, and a rapidly varying term. The rapidly varying term is averaged away. This theory requires that the amplitudes and phases vary on a time scale which is slow compared to a period of the radiation field. The average is taken over electron entrance time t_0 , sheet beam position y_0 and electron initial gyrophase ϕ_0 . The input current is varied periodically in time with period L/c , or half of the field period. In other words, modulation is provided at twice of frequency spacing between two adjacent modes. Because the electron beam is centered at the cavity, only odd modes participate in energy interaction with beam. Therefore, the modulation frequency is the same as frequency difference between two adjacent odd modes.

3. NUMERICAL RESULTS

A time-dependent multimode code has been written based on above particle and rate equations. The code has been benchmarked against the published single mode results¹² for minimum starting oscillation current, oscillation efficiency and frequency shift and detuning. Also checks have been made to ensure that energy is conserved between the particles and fields. Fourth-order Runge-Kutta methods using Gill's constants have been used for the solution of both the particle and the field equations. This method has the desired accuracy and has been vectorized.

At time $t = 0$, all the modes are given an amplitude of 10^{-4} in normalized units and randomized phases. The following normalizations have been used in calculations:

$$\bar{t} = t \frac{c}{L}; \quad \bar{z} = \frac{z}{L}; \quad \bar{p} = \frac{p}{mc}; \quad \bar{A} = A \frac{eL}{mc^2}; \quad \bar{I} = I \frac{e}{\epsilon_0 mc^3}; \quad \bar{U} = U \frac{e}{mc^2},$$

where c is speed of light, L is cavity length, e is electron charge, m is electron mass, ϵ_0 is permittivity constant, and t , z , p , A , I and U are time, distance, momentum, electric field amplitude, current, and voltage, respectively.

The length between two cavity mirrors is set to be 100 cm and a power loss at the output mirror is assumed to be 2%. This corresponds to a total cavity quality factor $Q_T = 78540$ with operating frequency 150 GHz. In all calculations one single pencil electron beam has been used as both the gain medium from which the fields derive their energy and the phase shifter. The electron beam parameters are 60 KeV beam energy, p_{y0}/p_{z0} ratio 1.56 and w_0/λ ratio 4.8. The beam is located at $y = 0$, on the maximum of the field for modes with odd values of l and on the field null for modes with even values of l . It is observed that even modes are not excited by the pencil beam therefore only odd modes are considered in computation. The external axial magnetic field is constant 5.928 KG along z direction.

Modal growth and frequency shifts for eight modes have been studied under aforementioned parameters in multiple mode simulations. Figures 2 show the temporal evolution of eight modes from noise to the stationary state with large amplitude current density modulation. The beam current is given a square pulse modulation varying between 0 and 7.0 A at a frequency of 300 MHz. The duration of current pulse is 0.208 ns. The total simulation time was 7500 ns and Fig. 2 (a) shows that the steady state was reached after 3000 ns. The frequency shifts of all the modes are identical, slightly down shifted from empty cavity eigenfrequencies, as shown in Fig. 2 (b). The steady state response shown in Fig. 2 indicated that the gyrotron output energy is periodic in time. This does not guarantee large or narrow radiation pulses since the modal phases play a key role. Results similar to Fig. 2 were observed for a wide range of pulsed and sinusoidal modulations.

The instantaneous electric and magnetic energy density at the center of the cavity can be written as

$$E(t) = \sum_1 A_l(t) \cos(\omega_l t + \alpha_l) \sin\left(-\frac{1}{2}\pi\right)$$

$$B(t) = \sum_1 \frac{1}{c} A_l(t) \sin(\omega_l t + \alpha_l) \cos\left(-\frac{1}{2}\pi\right)$$

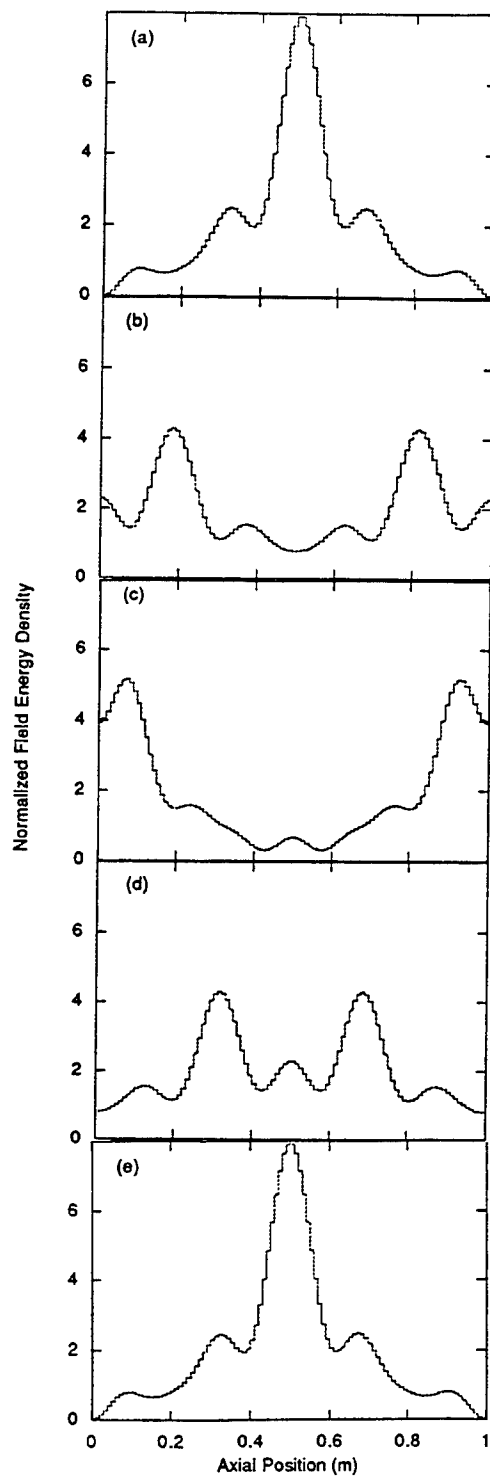


Fig. 4. Propagation of radiation pulse through the cavity. Axial field energy density profiles at times of (a) 0 ns, (b) 1.0 ns, (c) 1.9 ns, (d) 2.7 ns, and (e) 3.3 ns.

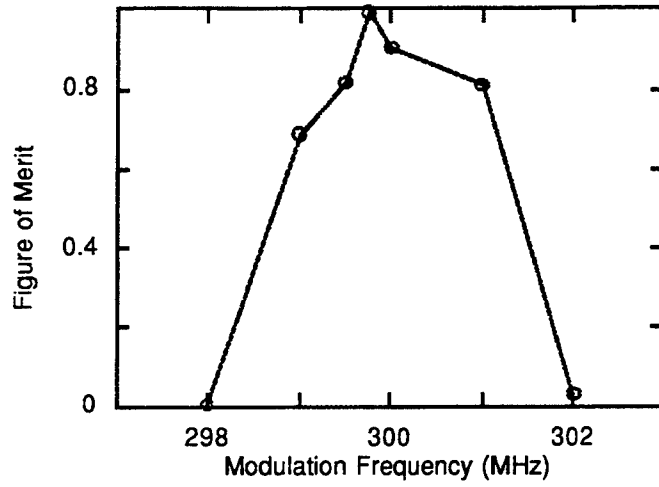


Fig. 5. Pulse formation at different modulation frequencies.

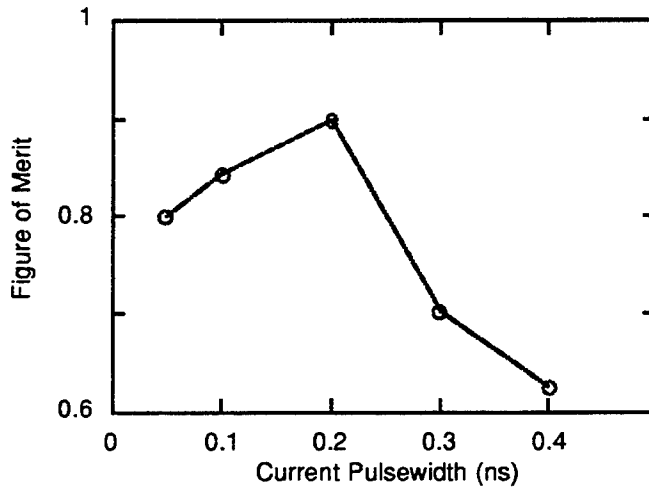


Fig. 6. Pulse formation at different current pulsewidths.

then the slow-varying envelope of total instantaneous energy density $W(t)$ is given by

$$W(t) = \frac{1}{2} \sum_{l,m} A_l(t) A_m(t) \cos((\omega_l^0 - \omega_m^0) t + (\Delta\omega_l - \Delta\omega_m) t + (\alpha_l - \alpha_m)) \cos(\frac{l-m}{2}\pi)$$

where A_l denotes the amplitude, ω_l^0 the eigenfrequency, $\Delta\omega_l$ the frequency shift, α_l the phase of mode l , and l and m are odd numbers from -7 to 7. The time domain behaviors for case with the same beam and cavity conditions as in Fig. 2 and a free-running case are shown in Fig. 3. The A_l , $\Delta\omega_l$ and α_l for Fig. 3 are computed from simulation data of last 1200 ns for each mode. The total instantaneous energy density output is normalized to the total average energy density ($1/2 \sum_l A_l^2$) of the

free-running case. It can be seen that the pulsing is at the modulation frequency of 300 MHz and has peak densities approximately eight times the average density of the free-running case. FWHM of radiation pulses is about 400 ps. The electronic efficiency is close to 10%. By contrast, the peak density which corresponds to the free-running case of Fig. 3 is much smaller with electronic efficiency of only 3%. It is found that only two modes are eventually obtained in the free-running case. The current used in the free-running case is a constant 0.6 A, which is very close to the averaged current used in modulation cases.

The radiation pulses are followed by several small trailing secondary peaks. This is due to the steady-state phases and amplitudes chosen by the modes. For the parameters chosen, the modal amplitude spectrum is not Gaussian and the phase separation is not exactly 0 or π . It is found that those modes close to carry frequency are weakly excited (with index -1 and 1) while modes away from central frequency but not far away are strongly excited (with index -5 and 5). We may use an amplitude filter to make modal amplitude spectrum close to Gaussian. The secondary pulses largely originate in nonoptimal phasing of the cavity modes. In general, the shorter the modulation pulsewidth is, the better the phase control of modes is. However, the modulation pulsewidth is limited by electron transit time, which is about 200 ps in this study.

The propagation of the radiation pulse in the cavity is shown in Fig. 4. The parameters are the same as in Fig. 2. The total instantaneous electromagnetic energy density (normalized to the time-averaged free-running energy density) is shown as a function of axial position in the cavity. The pulse bounce time is found to 6.67 ns, which is exactly twice of the modulation period. This is desired because fields can extract energy from the beam twice during one round trip. It can be seen clearly from the sequence 4(a) - 4(e) that two pulses traveling from center to mirrors, reflect back to center from the cavity mirrors. This pulse motion continues periodically in time. Two radiation pulses are seen in the cavity because the external magnetic field is perpendicular to cavity axis, therefore there is no preferred direction for radiation.

Figures 5 and 6 measure the quality of the radiation pulses by assigning a figure of merit, ζ , to each pulshape, where

$$\zeta = \frac{\bar{\epsilon}_p}{\bar{\epsilon}_T} \frac{\tau}{\Delta\tau} \frac{\bar{\epsilon}_p}{IV_{\text{beam}}\tau}.$$

$\bar{\epsilon}_p$ is the averaged energy delivered between the pulse half-power points and $\bar{\epsilon}_T$ is the averaged total energy delivered between the pulses. τ is the pulse peak-to-peak period and $\Delta\tau$ is the FWHM of the pulse. This figure of merit is high for high power, narrow pulses. It can be seen from Fig. 5 that optimal pulses are generated at a modulating frequency slightly below the nominal cavity modal spacing between two odd modes and the frequency range over which good pulses can be obtained is about 2 MHz. The pulses degrade severely outside this range. Fig. 6 indicates that optimal pulse formation is obtained with a current pulsewidth of 0.2 ns. Shorter pulses are observed to generate poorer results because they may be too short for energy to be transferred from beam to radiation pulses.

The mode locking dynamics are dependent on current pulse amplitude. For the case where 0.208 ns pulsewidth modulation is used, the starting oscillation current is above 4 A. Between 4 A and 8 A the steady-state amplitudes and growth rates are found to steadily increase as the current increases. Poor pulses are found in high current (above 8 A) cases where more modes are excited but the modal phases are not well controlled and the pulse shapes are inferior to those at low current.

It has been shown via nonlinear theory that radiation pulses of width 400 ps can be generated using one single beam in nonlinear regime in a quasi-optical gyrotron oscillator. The strong current modulation is provided at period of 300 MHz, the nominal modal spacing between two odd modes in such a cavity. Eight odd modes are found to be locked to generate extremely short radiation pulses. Further work is being done to tilt the cavity to have a preferential direction so that only one radiation pulse exists inside the cavity. Further work to investigate sinusoidal modulation and to include sheet beam in simulation is also under way.

4. ACKNOWLEDGMENTS

Computer support was provided by the National Science Foundation sponsored San Diego Supercomputer facility.

5. REFERENCES

1. S.E. Harris and O.P. McDuff, "Theory of FM laser oscillation," IEEE J. Quant. Electron., Vol. QE-1, pp. 245, September 1965.
2. P.W. Smith, "Mode-locking of lasers," Proc. IEEE, Vol. 58, pp. 1342-1359, September 1970.
3. D.A. Deacon, L.R. Elias, J.M.J. Madey, G.J. Ramian, H.A. Schwettman and T.I. Smith, "First operation of a free-electron laser," Phys. Rev. Lett., Vol. 38, pp. 892-894, April 1977.
4. Y.L. Bogomolov, V.L. Bratman, N.S. Ginzburg, M.I. Petelin and A.D. Yunakovsky, "Nonstationary generation in free electron lasers," Optics Comm., Vol. 36, pp. 209-212, February 1981.
5. K. Toyoda and Y. Kawamura, "Experimental study of free electron laser using cold relativistic electron beam," Laser and Particle Beams, Vol. 7, pp. 421-431, 1989.
6. D. Oepts, R.J. Bakker, D.A. Jaroszynski, A.F.G. van der Meer and P.W. van Amersfoort, "Induced and spontaneous interpulse phase locking in a free-electron laser," Phys. Rev. Lett., Vol. 68, pp. 3543-3546, 1992.
7. G.S. Nusinovish, "Theory of mode interaction in the gyrotron," Kfk Report No. 4111, August 1986.
8. W.M. Manheimer and M.E. Read, "Sub-nanosecond pulselength millimeter wave generation with a phase modulated quasi-optical gyrotron," Int. J. Electron., Vol. 61, pp. 1041-1048, 1986.
9. A.H. McCurdy, "Synchronous mode locking in a closed cavity electron cyclotron maser," J. Appl. Phys., Vol. 74, pp. 3576-3583, September 1993.
10. A.H. McCurdy, "Nonlinear theory of large-signal mode locking in a gyrotron oscillator," Appl. Phys. Lett., Vol. 66, pp. 1845-1847, April 1995.
11. H. Wu, R. Liou and A.H. McCurdy, "PIC code simulation of pulsed radiation in a tapered closed-cavity gyrotron," IEEE Trans. Plasma Sci., Vol. 24, June 1996.
12. T.M. Antonsen, Jr., B. Levush and W.M. Manheimer, "Stable single mode operation of a quasioptical gyrotron," Phys. Fluids, Vol. 2, pp. 419-426, February 1990.
13. B. Levush and T.M. Antonsen, Jr., "Mode competition and control in high-power gyrotron oscillators," IEEE Trans. Plasma Sci., Vol. 18, pp. 260-271, June 1990.
14. A. Bondeson, W.M. Manheimer and E. Ott, *Infrared and Millimeter Waves*, Vol. 9, pp. 309-340, Academic, New York, NY, 1983.

Multi-mode linear analysis of plasma Cerenkov masers driven by relativistic electron beams

M. Birau

Laboratoire de Physique des Milieux Ionisés
Centre National de la Recherche Scientifique
École Polytechnique 91128 Palaiseau Cedex (France)

ABSTRACT

A theoretical model of Cerenkov instability in the linear amplification regime of Plasma Cerenkov Masers has been improved. The novelty of the model consists in considering azimuthal dependence of the amplified electromagnetic field in the approach of finite thicknesses of annular electron beam and plasma in axial symmetric system. This assumption leads to a new topology of wave modes coupling and consequently, the spectrum of instability is found to be distributed over one or several frequency bands, according to initial parameters. This result gives the opportunity to foresee the emission spectrum for a giving experimental configuration. A special attention is paid to the field spatial dependence for different azimuthal modes.

Keywords: Plasma Cerenkov Maser, Relativistic electron beam, Multi-modes coupling, Field structure.

1. INTRODUCTION

The Plasma Cerenkov Maser (PCM) or Plasma Microwave Oscillator is an experimental device which as other electronic tubes is intended to the energy conversion from an electron beam to electromagnetic radiation. In the PCM, this radiation generation is permitted by the presence of a dense plasma column in the vicinity of the relativistic electron beam. The plasma enables new type of modes propagation in the waveguide which has the desirable property to have a phase velocity less than the speed of light in vacuum and therefore can be amplified by the electron beam.

The PCM driven by a relativistic electron beam (REB) has proved the ability to generate high-power microwaves. It was first done at the General Physics Institute of Moscow (GPI), and reported in 1982¹. In this first experiment, the solid beam passed through an annular plasma column. Since, calculations have shown that an annular electron beam would give a more efficient energy transfer from the beam to the generated wave². In 1994, measurements of the spectrum carried out at the GPI³ with a hollow beam have confirmed the wide band character of the PCM radiation predicted by theoretical investigations. The efficiency was of the order of 10 %.

In this paper, we shall investigate the process of microwave generation in the PCM within the framework of a linear theory. It should be noted that linear models of the interaction in the PCM have been already developed^{4, 5}. In both cases, axial symmetric models assume the interaction to be the result of a coupling only between plasma wave with the highest phase velocity mode of the plasma wave structure and the slow beam wave mode in an infinite magnetic field. In ⁴, the model considers a neglectable beam thickness so that, the structure of the slow modes due to the beam in the waveguide is reduced to a unique mode. In ⁵, this structure is reduced also to one mode, because here the beam density is assumed to be sufficiently weak. The lower phase velocity modes of the plasma column structure are shown to be sufficiently far from the slow beam mode and do not interact with it.

A linear analysis gives the opportunity to foresee the radiation spectrum for particular input physical parameters (beam and plasma radii and densities, energy of the electrons in the REB). Note however that because of non-linear processes the spectra obtained by such a way should be understood as "potentially amplifiable". This means that the dependence of the spectrum power density and of the linear growth rate on radiation frequency can be different. Moreover, "pure" non-linear processes can provide radiation at frequencies which are absent in the linear spectrum. Nevertheless, the linear spectrum is of interest to apprehend the radiation behaviour of the device.

Our model, as the previous ones, considers an infinite guiding magnetic field in the system infinite along the axis. However, it is an extension of the previous models in two directions. First, the finite beam thickness and the finite beam density are taken into account in the derivation of the dispersion relation. As a result, the modes structure due to the beam

presence in the cylindrical waveguide is getting complicated. Secondly, the model is able to consider the amplification of azimuthally depending modes.

In this framework, our first purpose is to investigate the coupling between the entire plasma mode structure and the entire beam mode structure due to the final radial geometry of the system and the non neglectable density of the beam and plasma for different azimuthal wavenumbers. The resulting new interactions will be discussed. The second purpose is to investigate the field structure in the interaction area for the amplified wave mode. The field structure inside the interaction area is indeed essential for the PCM efficiency because the amplified field in the interaction area is converted into a TEM wave in the vacuum area of the horn.

2. PCM LINEAR MODEL

A schematic of the PCM experimental setup is presented in Fig. 1: the hollow REB (1) propagates along the axis inside the hollow plasma column (2) in the interaction region. A strong longitudinal magnetic field is present all along the waveguide (3). Both REB and plasma are wasted on the collector (4). The radiation is emitted through the window (5) of the coaxial horn. We shall consider the interaction region supposed to be infinite in the longitudinal z direction. This assumption can be justified because the amplified radiation wavelength is shown to be much less than the interaction region length which is about 30 cm. The model considers the ions sufficiently heavy to be at rest. The density profile of the beam and plasma is supposed axissymmetric and rectangular along the radius.

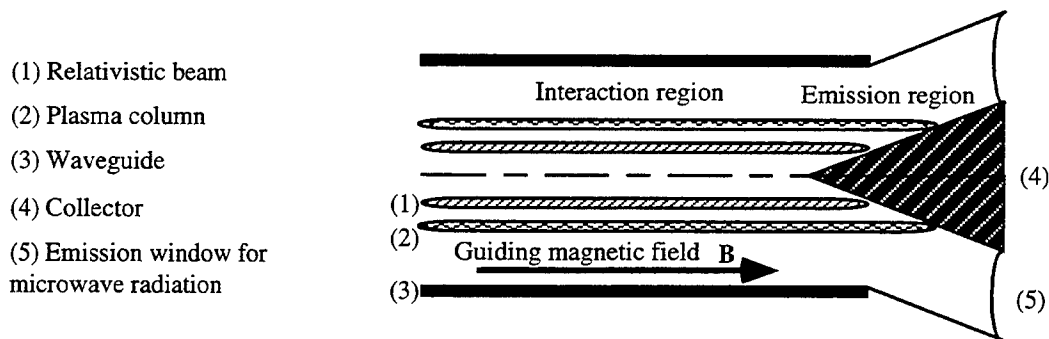


Fig. 1: Experimental setup scheme of the Plasma Cerenkov Maser

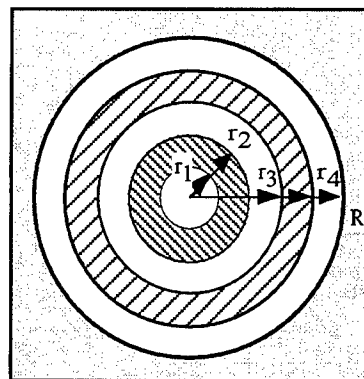


Fig. 2: Cross section of the system in the interaction region. r_1 - inner beam radius, r_2 - outer beam radius, r_3 - inner plasma radius, r_4 - outer plasma radius, R - waveguide radius. The beam and plasma densities are rectangular along the radius.

2.1 Derivation of the dispersion relation

The cross section of the system is presented in Fig. 2. The initial-value problem (without the wave) consists of a cold plasma characterised by its Langmuir frequency ω_p and of a cold monoenergetic beam propagating along the z axis with electron energy E and current I . The inner and outer radii of the columns will be denoted as r_1 and r_2 for the beam, r_3 and r_4 for plasma, R for the waveguide radius.

We assume the dependence of the field components to be:

$$f(r, \varphi, z, t, k, \omega) = f(r) e^{i(kz + l\varphi - \omega t)} \quad (1)$$

for each point defined by its cylindrical coordinates r, φ, z . As in ⁶, we linearize the equations of motion, continuity, and Faraday in Fourier-Laplace space, and find the conductivity tensor $\bar{\sigma}$ connecting the current density $\tilde{\mathbf{j}}$ and the electric field $\tilde{\mathbf{E}}$ according to $\tilde{\mathbf{j}}(\mathbf{k}, \omega) = \bar{\sigma}(\mathbf{k}, \omega) \tilde{\mathbf{E}}(\mathbf{k}, \omega)$. Using this expression and assuming the amplitude of the guiding magnetic field to be sufficiently strong, the dielectric tensor of the infinite medium is:

$$\bar{\epsilon} = \begin{pmatrix} 1 & 0 & 0 \\ 0 & 1 & 0 \\ 0 & 0 & \epsilon \end{pmatrix} \quad \text{where} \quad \begin{aligned} \epsilon &= \epsilon_v = 1 && \text{for vacuum} \\ \epsilon &= \epsilon_p = 1 - \frac{\omega_p^2}{\omega^2} && \text{for plasma} \\ \epsilon &= \epsilon_b = 1 - \frac{\omega_b^2}{\gamma_0^3 (\omega - k v_0)^2} && \text{for the beam.} \end{aligned} \quad (2)$$

The tensor of the infinite media can be applied in our case because the thickness of the plasma and the beam (of about 1.0 mm in both cases) is much larger than the corresponding Debye length. Including the dielectric tensor into the Faraday and Ampere linearized equations and using (1), we derive the following six equations governing the field structure in cylindrical coordinates.

$$\begin{aligned} E_r &= K^{-2} \left(-i k \frac{\partial E_z}{\partial r} + \frac{1}{r} \omega B_z \right) & , & \quad B_r = -K^{-2} \left(\frac{1}{r} \frac{\omega}{c^2} E_z + i k \frac{\partial B_z}{\partial r} \right) \\ E_\varphi &= K^{-2} \left(\frac{1}{r} k E_z + i \omega \frac{\partial B_z}{\partial r} \right) & , & \quad B_\varphi = -K^{-2} \left(\frac{i \omega}{c^2} \frac{\partial E_z}{\partial r} - \frac{1}{r} k B_z \right) \\ \frac{\partial^2 E_z}{\partial r^2} + \frac{1}{r} \frac{\partial E_z}{\partial r} + \left(\epsilon K^2 - \frac{l^2}{r^2} \right) E_z &= 0 & , & \quad \frac{\partial^2 B_z}{\partial r^2} + \frac{1}{r} \frac{\partial B_z}{\partial r} + \left(\epsilon K^2 - \frac{l^2}{r^2} \right) B_z = 0 \\ \text{where } K^2 &= k^2 - \frac{\omega^2}{c^2} \end{aligned} \quad (3)$$

E_z and B_z components are linearly independent. This enables us to define a basis of TM modes ($B_z = 0$) and TE modes ($E_z = 0$). We will focus our attention only on TM modes since the interaction requires a non-zero ($E_z v_z$) product. Due to the fact that the beam and plasma densities are rectangular along the radius, differential equations (3) can be integrated analytically. It should be emphasized that any other profile of plasma or beam density would make impossible an analytic solution of the problem. The integration of the differential equation leads to:

$$\begin{aligned} f(r) &= A J_l(\sqrt{-\epsilon K^2} r) + B Y_l(\sqrt{-\epsilon K^2} r) \quad \text{if } \epsilon K^2 < 0 \\ f(r) &= A I_l(\sqrt{\epsilon K^2} r) + B K_l(\sqrt{\epsilon K^2} r) \quad \text{if } \epsilon K^2 > 0 \end{aligned} \quad (4)$$

where J_l and Y_l are the Bessel functions of first and second kind of l order and I_l and K_l the corresponding modified Bessel functions. We see now that for each radius, (4) brings us to study the sign of the real quantity ϵK^2 in order to

determine the form of the solution. Each point (k, ω) of the Brillouin diagram corresponds to a given sign of ϵK^2 in vacuum, in plasma and in the beam. Hence, eight regions of the Brillouin diagram can be defined according to the sign of ϵK^2 in each medium. Each of these regions corresponds to a specific expression of the amplified field. As an example, and to illustrate the kind of solution we obtain, we present the radial dependence of the E_z component in a region where the value of ϵK^2 is positive in vacuum and negative in plasma and the beam. In the seven other regions, the field takes a similar form.

$$\begin{aligned}
 E_{z1}(r) &= A I_1(\sqrt{K^2} r) & \text{if } 0 \leq r \leq r_1 \\
 E_{z2}(r) &= B J_1(\sqrt{-\epsilon_b K^2} r) + C Y_1(\sqrt{-\epsilon_b K^2} r) & \text{if } r_1 \leq r \leq r_2 \\
 E_{z3}(r) &= D I_1(\sqrt{K^2} r) + E K_1(\sqrt{K^2} r) & \text{if } r_2 \leq r \leq r_3 \\
 E_{z4}(r) &= F J_1(\sqrt{-\epsilon_p K^2} r) + G Y_1(\sqrt{-\epsilon_p K^2} r) & \text{if } r_3 \leq r \leq r_4 \\
 E_{z5}(r) &= H I_1(\sqrt{K^2} r) + I E K_1(\sqrt{K^2} r) & \text{if } r_4 \leq r \leq R
 \end{aligned} \tag{5}$$

Here the index "p" or "b" of ϵ indicates the "beam" or "plasma" medium. (5) depends on 9 different constants A, B, C, D, E, F, G, H and I. The boundary conditions applied at each border of the beam, plasma and at the border of the waveguide form an algebraic linear system of 9 equations with 9 unknown quantities. Setting each determinant of the eight systems to zero yields the dispersion relation. It appears in the form of eight 9 by 9 determinants. The determinant corresponding to the region mentioned above is shown in (6).

$$\begin{vmatrix}
 I_1(\chi r_1) & -J_1(\mu \chi r_1) & -Y_1(\mu \chi r_1) & 0 & 0 & 0 & 0 & 0 & 0 \\
 -I_1'(\chi r_1) & \mu J_1'(\mu \chi r_1) & \mu Y_1'(\mu \chi r_1) & 0 & 0 & 0 & 0 & 0 & 0 \\
 0 & J_1(\mu \chi r_2) & Y_1(\mu \chi r_2) & -I_1(\chi r_2) & -K_1(\chi r_2) & 0 & 0 & 0 & 0 \\
 0 & \mu J_1'(\mu \chi r_2) & \mu Y_1'(\mu \chi r_2) & -I_1'(\chi r_2) & -K_1'(\chi r_2) & 0 & 0 & 0 & 0 \\
 0 & 0 & 0 & I_1(\chi r_3) & K_1(\chi r_3) & -J_1(v \chi r_3) & -Y_1(v \chi r_3) & 0 & 0 \\
 0 & 0 & 0 & I_1'(\chi r_3) & K_1'(\chi r_3) & -v J_1'(v \chi r_3) & -v Y_1'(v \chi r_3) & 0 & 0 \\
 0 & 0 & 0 & 0 & 0 & J_1(v \chi r_4) & Y_1(v \chi r_4) & -I_1(\chi r_4) & -K_1(\chi r_4) \\
 0 & 0 & 0 & 0 & 0 & v J_1'(v \chi r_4) & v Y_1'(v \chi r_4) & -I_1'(\chi r_4) & -K_1'(\chi r_4) \\
 0 & 0 & 0 & 0 & 0 & 0 & 0 & I_1(\chi R) & K_1(\chi R)
 \end{vmatrix} = 0 \tag{6}$$

Here, f' denotes the first derivative of any function f versus the radius, and:

$$\chi = \sqrt{K^2}, \quad \mu = \sqrt{-\epsilon_b}, \quad v = \sqrt{-\epsilon_p} \tag{7}$$

2.2 Results in real space: mono-coupling and multi-coupling of radial modes.

A search for the zeroes of $D(k, \omega) = 0$ was conducted numerically. For each k we find the frequencies ω that satisfy the dispersion relation. This method has the advantage of being simple and rigorous. The results are presented in Fig. 3 for $\omega_p = 3.0 \cdot 10^{11}$ rad/s and in Fig. 4 for $\omega_p = 5.0 \cdot 10^{11}$ rad/s. The values of all the parameters used in these calculations were defined for particular experimental conditions.

One can separate the wave modes in (3a) and (4a) diagrams in three groups: the beam modes are localised between the lines $\omega = kv_0 - \gamma^{3/2} \omega_b$ and $\omega = kv_0 + \gamma^{3/2} \omega_b$. Unlike the previous works^{4, 5}, we note that due to the non neglectable beam density and its finite thickness, the number of modes is infinite and despite their high density in the diagram, the first slow ones can be distinguished. Above the beam modes and above the line $\omega = kc$, there are common vacuum modes. They are just slightly shifted due to the presence of the beam and the plasma. Anyway, these modes do not participate in the process of interaction because they are characterised by a phase velocity highest than any slow beam mode. Below the beam structure and under the line $\omega = \omega_p$, the plasma mode structure is shown. All these modes have a phase velocity less than kv_0 which permit the interaction with the slow beam mode structure. The number of beam modes involved in the process of interaction depends on the physical parameters. In the case of Fig. 3, only the first slow beam mode interacts with the fastest plasma mode. As it is displayed in Fig. 3b, these modes are coupled for wavenumbers between a value very near 0 and k_1 ,

corresponding to the absence of the curves in the real diagram, the frequency becoming complex in this region. The point $k = k_1$ satisfies $dk/d\omega = 0$. The existence of the point $\omega = \omega_1$ defined by $d\omega/dk = 0$ shows that we deal with a convective instability. This instability is allowed by the negative sign of the longitudinal diagonal term of the dielectric tensor in plasma and the beam. The resulting instability spreads out over one uncommonly wide frequency band. This can be explained by considering the topology of the uncoupled modes. These ones are indeed very close to each other all along the instability wave numbers so that the instability takes place on a very large range. For a lower coupling, one could expect an island to appear between the two uncoupled modes in the instability region leading to a splitting of the instability in two different frequency bands. However, we did not observe such a splitting.

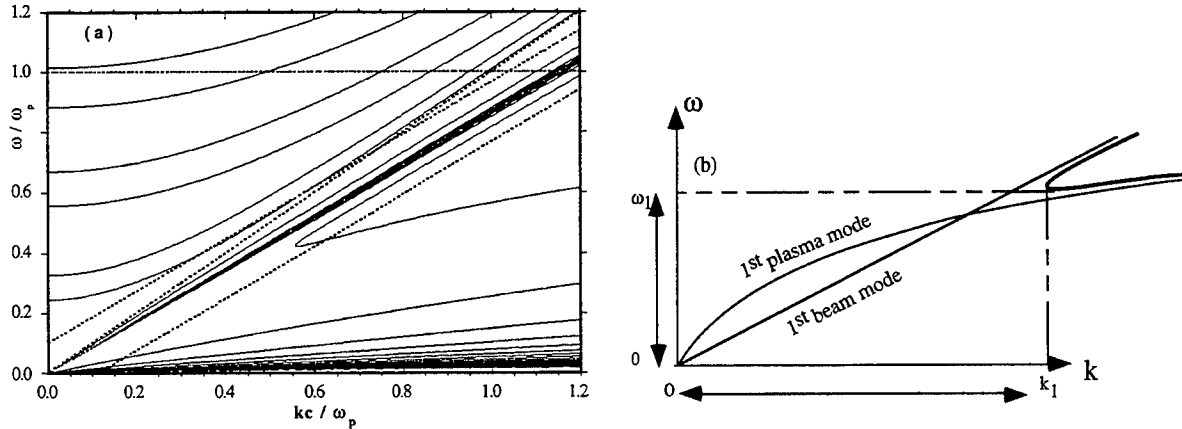


Fig. 3: (a) Solution of the dispersion relation for axisymmetric modes in real space. Here: $r_1 = 0.50$ cm ; $r_2 = 0.60$ cm ; $E = 511$ keV ; $I = 3.2$ kA ; $r_3 = 0.85$ cm ; $r_4 = 0.95$ cm ; $\omega_p = 3.0 \cdot 10^{11}$ rad/s ; $R = 1.80$ cm. Dashed lines represent the lines $\omega = \omega_p$, $\omega = kv_0 \pm \omega_b / \gamma^{3/2}$ and $\omega = kc$. (b): Superimposition diagram of the both coupled (heavy line) and uncoupled (thin lines) modes.

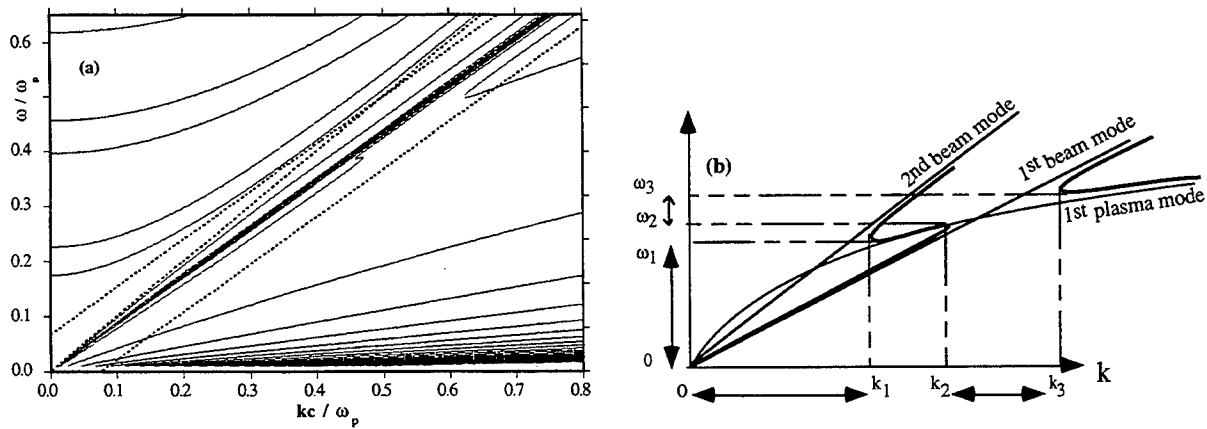


Fig. 4: (a) Solution of the dispersion relation in real space and (b) superimposition diagram of the both coupled and uncoupled modes. The parameters are the same as in Fig. 3, except for $\omega_p = 5.0 \cdot 10^{11}$ rad/s .

Instead of this, a multicoupling configuration takes place as shown in Fig. 4a obtained for a higher plasma density. The coupling topology is explained in Fig. 4b where three uncoupled modes have been superimposed with the dispersion relation itself: the fastest plasma mode and the two slowest beam modes. Four different regions of the Brillouin diagram can

be distinguished. Starting from low values of k and ω , the coupling begins between the first plasma mode and the second beam mode (k varying from 0 to k_1). Then for each real k between k_1 and k_2 , three real values of ω corresponding to each considered mode are present so that, in this range, the configuration is stable. Another instability due to the coupling of the same plasma mode with the first slow beam mode can be seen from k_2 to k_3 . Finally, for larger wavenumber values, the configuration is stable. Similar results have been obtained for non-zero azimuthal wavenumbers.

2.3 Linear growth rate of instability: mode competition

The analysis conducted for real (k, ω) informs us about the instability spectrum width without giving its amplitude. In order to estimate the consequences for the radiation spectrum we calculate the real wavenumber and the complex frequency which satisfies the differential equation (3). The distinction of the solutions based on εK^2 sign, which was necessary in real space, becomes here obsolete and we may write the solution:

$$f(r) = A J_1(\sqrt{-\varepsilon K^2} r) + B Y_1(\sqrt{-\varepsilon K^2} r) \quad (8)$$

where the argument of the Bessel functions J_1 and Y_1 is complex. Following the same analysis as in real space, one comes to the dispersion relation which has a similar form to the expression (11), and where the terms of the determinant are complex. With $\omega = \omega_r + i \omega_i$, one has to find three real roots k, ω_r, ω_i of the complex expression $D(k, \omega_r, \omega_i) = 0$. In the 2D real space (k, ω) analysis, it was possible to sweep systematically the Brillouin diagram. In the 3D volume, for calculation time reasons, this method can not be applied. To search for the roots, we have applied for fixed k the iterative Newton's method to the Taylor series expansion in ω of the dispersion function defined by $D(k, \omega) = 0$ ^{7, 8}.

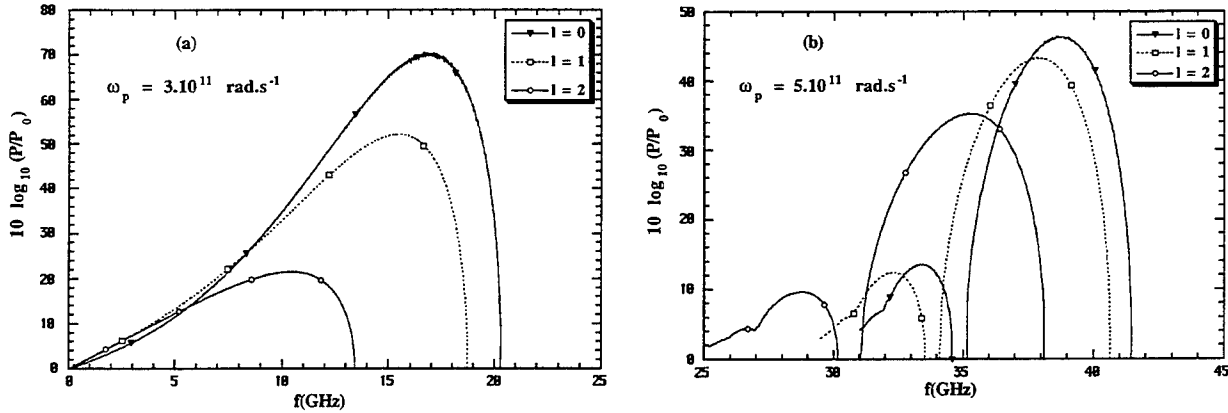


Fig. 5: Power growth rate of the instability versus frequency for $l = 0, l = 1$ and $l = 2$.

$r_1 = 0.50$ cm ; $r_2 = 0.60$ cm ; $E = 511$ keV ; $I = 3.2$ kA ; $r_3 = 0.85$ cm ; $r_4 = 0.95$ cm ; $R = 1.80$ cm ;

(a) $\omega_p = 3.0 \cdot 10^{11}$ rad/s ; (b) $\omega_p = 5.0 \cdot 10^{11}$ rad/s.

Figure 5 presents the result of calculations for three azimuthal wavenumbers and two plasma densities achievable in experiment. It represents the growth rate of the power expressed in dB after a run of 30 cm that corresponds to the length of the interaction region in the experiment. Note that there are few types of interactions in the figure. The main interaction is axisymmetric ($l = 0$) and is the result of the coupling between the fastest plasma mode and the slowest beam mode. This main interaction ($l = 0$) is displayed with the two first azimuthally depending interactions ($l = 1, l = 2$). Also, beside these three couplings and for each of them, radial secondary couplings may exist. These one involve slow beam modes of higher order (Fig. 4b).

The behaviour of the main coupling has been studied in respect to the plasma density³ and to the plasma-beam gap⁹ in the approach of neglectable plasma and beam thickness. Our result concerning this main coupling is very close to the previous studies one: for $\omega_p = 3.0 \cdot 10^{11}$ rad/s (Fig. 5a), the interaction is strong and spreads out on a frequency band departing

from zero. When the plasma density is increased ($\omega_p = 5.0 \cdot 10^{11}$ rad/s in Fig. 5b), the interaction is less and takes place on a more narrow band detached from zero. This has been foreseen in the analysis that we have carried out for real (k, ω) . Note also that the resulting instability is very much dependent on the beam-plasma gap⁹. In the case where the beam and plasma thicknesses are of the order of the gap between them, the approximation of neglectable beam and plasma thicknesses hardly corresponds to real experimental situation.

Let us now examine the secondary couplings. In Fig. 5a, only the first slow beam mode is involved in the interaction and the azimuthally depending couplings have a growth rate much less than the axisymmetric one. They take place from zero frequency in a more narrow band. In this linear approximation, we may suppose that each frequency of these azimuthally depending modes will be damped because of the mode competition with the axisymmetric one. However, strong non-linear wave-wave processes may contradict this statement. When plasma density is increased (Fig. 5b), each interaction characterised by its number l is accompanied by higher beam modes one. These couplings have a much less growth rate than the main radial one, but unlike the secondary azimuthal modes, their frequency do not overlap with the main interaction spectrum. In comparison with Fig. 5a, the difference in growth rate between the different azimuthal modes gets much less, especially between $l = 0$ and $l = 1$. This can be explained by the fact that each azimuthal coupling reaches its maximum for a different plasma density. Hence, with the used parameters, it seems possible to excite at least the first azimuthal depending mode.

3. FIELD STRUCTURE

From the previous analysis, the dispersion relation of the system is known, in other words, the complex frequencies ω able to propagate and grow for each real wavenumber k . Because of the wide spectrum band, the field structure depends on the wavenumber, and a particular field structure corresponds to each generated frequency of the spectrum. The total field structure is a superimposition of that corresponding to each frequency. However, the structure of the field corresponding to different frequencies are of the same nature, so the analysis is conducted with for one frequency. We have chosen the frequency with the topmost growth rate value. The assumptions made in our model with the Maxwell equations (3) lead to:

$$E_r = K^{-2} \left(-i k \frac{\partial E_z}{\partial r} \right), \quad E_\phi = K^{-2} \left(\frac{1}{r} k E_z \right), \quad B_r = -K^{-2} \left(\frac{1}{r} \frac{\omega}{c^2} E_z \right), \quad B_\phi = -K^{-2} \left(\frac{i}{c^2} \frac{\omega}{\partial r} E_z \right), \quad B_z = 0 \quad (9)$$

The dependence of each real field component along the radius includes two ingredients: its amplitude and, because of the complex character of the frequency, its phase $\alpha(r)$:

$$A_m = e^{\omega t} |A_m(r)| \cos(kz + l\phi - \omega t + \alpha_{am}(r)) \text{ where } A_m \text{ represents either } E_m \text{ or } B_m \text{ component, and } m = r, \phi \text{ or } z \quad (10)$$

We define the quantities $\alpha_\omega = \text{Arg}(\omega)$, $\alpha_{K^2} = \text{Arg}(K^2)$, so that the five radial phase dependencies can be reduced to two functions corresponding to E_r and E_z components:

$$\alpha_{br}(r) = -\alpha_{ez}(r) + \alpha_{K^2} \quad ; \quad \alpha_{b\phi}(r) = \alpha_{er}(r) + \alpha_\omega \quad ; \quad \alpha_{e\phi}(r) = \alpha_{ez}(r) + \alpha_\omega \quad (11)$$

Let us now focus our attention on the Poynting vector \mathbf{p} . Its components are defined by:

$$\mathbf{p} = \frac{\mathbf{E} \times \mathbf{B}}{\mu_0} = \frac{e^{2\omega_j t}}{2\mu_0} \begin{pmatrix} S_r \\ S_\phi \\ S_z \end{pmatrix} \text{ where}$$

$$\begin{aligned} S_r &= -|E_z(r)| |B_\phi(r)| [\cos(2(kz + l\phi - \omega t) + \alpha_{b\phi}(r) + \alpha_{ez}(r)) + \cos(\alpha_{b\phi}(r) - \alpha_{ez}(r))] \\ S_\phi &= |E_z(r)| |B_r(r)| [\cos(2(kz + l\phi - \omega t) + \alpha_{br}(r) + \alpha_{ez}(r)) + \cos(\alpha_{br}(r) - \alpha_{ez}(r))] \\ S_z &= |E_r(r)| |B_\phi(r)| [\cos(2(kz + l\phi - \omega t) + \alpha_{er}(r) + \alpha_{b\phi}(r)) + \cos(\alpha_{er}(r) - \alpha_{b\phi}(r))] \\ &\quad - |E_\phi(r)| |B_r(r)| [\cos(2(kz + l\phi - \omega t) + \alpha_{e\phi}(r) + \alpha_{br}(r)) + \cos(\alpha_{e\phi}(r) - \alpha_{br}(r))] \end{aligned} \quad (12)$$

Each component consists of two terms, both of them depending on the radius: an oscillatory term at the double frequency in time, and a temporally invariable term. The first one has a zero average value in time but permits to define the phase surface of each component. Choosing $l\phi - \omega t = 0$, we find the three surfaces:

$$z_r(r) = -\frac{\alpha_{b\phi}(r) + \alpha_{ez}(r) + \pi}{2k} ; \quad z_\phi(r) = -\frac{\alpha_{br}(r) + \alpha_{ez}(r)}{2k}$$

$$z_z(r) = \frac{1}{2k} \text{Atan} \left(\frac{|E_\phi| |B_r| \cos(\alpha_{e\phi}(r) + \alpha_{br}(r)) - |E_\phi| |B_r| \cos(\alpha_{er}(r) + \alpha_{b\phi}(r))}{|E_\phi| |B_r| \sin(\alpha_{e\phi}(r) + \alpha_{br}(r)) - |E_\phi| |B_r| \sin(\alpha_{er}(r) + \alpha_{b\phi}(r))} \right) \quad (13)$$

Note that on the surfaces defined above, the oscillatory term disappears.

Fig. 6, 7 and 8 represent E field amplitude and the Poynting vector components in r, ϕ and z directions versus the radius. We must emphasize that each dependence has been plotted along the corresponding phase surfaces defined previously. Each figure has been obtained for a frequency and a plasma density corresponding to the maximum growth rate of the instability. Naturally, though the process of kinetic energy transfer into radiation is localised in the beam crown, the raise of E_z there causes a proportional increase of all the field components throughout the radius, because of the radial boundary conditions.

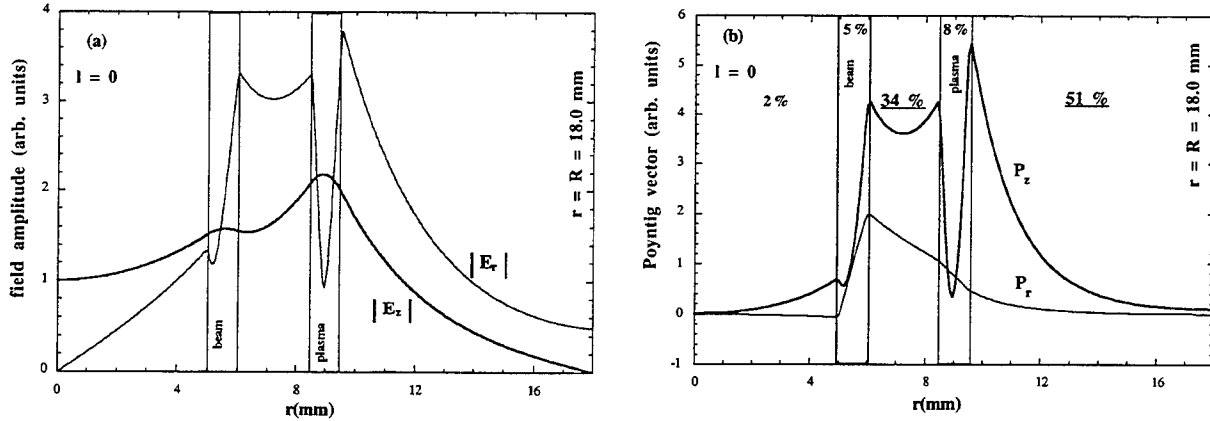


Fig. 6: Distribution of electric field amplitude (a), and Poynting vector components (b) along the radius for the axisymmetric modes.

Figure 6 represents the axisymmetric mode: the field dependence shows two maxima for the longitudinal component, and inversely a drop in the radial component in both plasma and REB. The phenomenon is more pronounced in plasma since its density is higher than that of the beam. Also, one can verify that the boundary condition on the metal border is strictly valid since the longitudinal component drops to zero at this radius. The power flux radial component can not be emitted because of the presence of the waveguide and one can verify that its value is zero at this boundary. The longitudinal component which describes the extractable power is almost zero inside the beam, reaches a high level between beam and plasma, has its maximum value at the outer boundary of plasma and decreases to a vanishing value at the metal wall.

We have displayed the percentage of the longitudinal power flow in each radial region. Note that because of the collector presence located at the end of the tube interaction region (Fig. 1), radiation is easily extracted only from the vacuum annulus between plasma and metal. Radiation from inside undergoes a very high attenuation when crossing plasma and possibly the beam, so that it is mostly reflected or absorbed. The amount inside the beam and plasma is quite impossible to extract and can be understood as natural losses of the device. In the vacuum zone located inside the beam, this value is neglectable. However, more than one third of the total power flux is localised between the beam and plasma columns and is not radiated, because of the experimental configuration of the exit. Moreover, this trapped energy increases the feed-back and can disturb severely both plasma and REB electrons distribution.

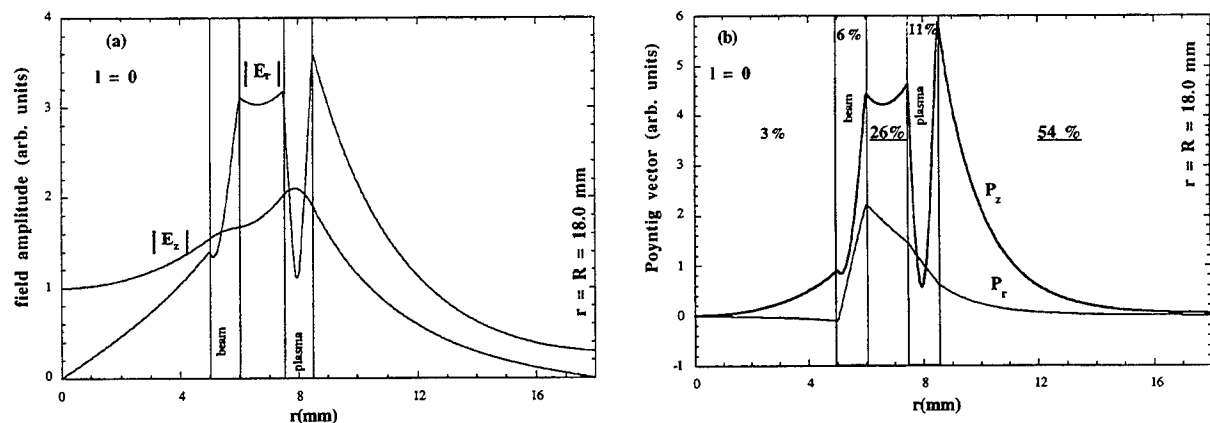


Fig. 7: Distribution of electric field amplitude and Poynting vector components for the axisymmetric modes in case of a little beam-plasma gap.

In Fig. 7, we have studied the effect of diminishing the gap between the beam and plasma with the hope that the power locked between the two media would strongly decrease. Despite the fact that the gap has been decreased almost two times, the distribution of energy remains did not change significantly. This means that the energy extraction from the PCM in Fig. 1 can not be improved by diminishing the beam-plasma gap.

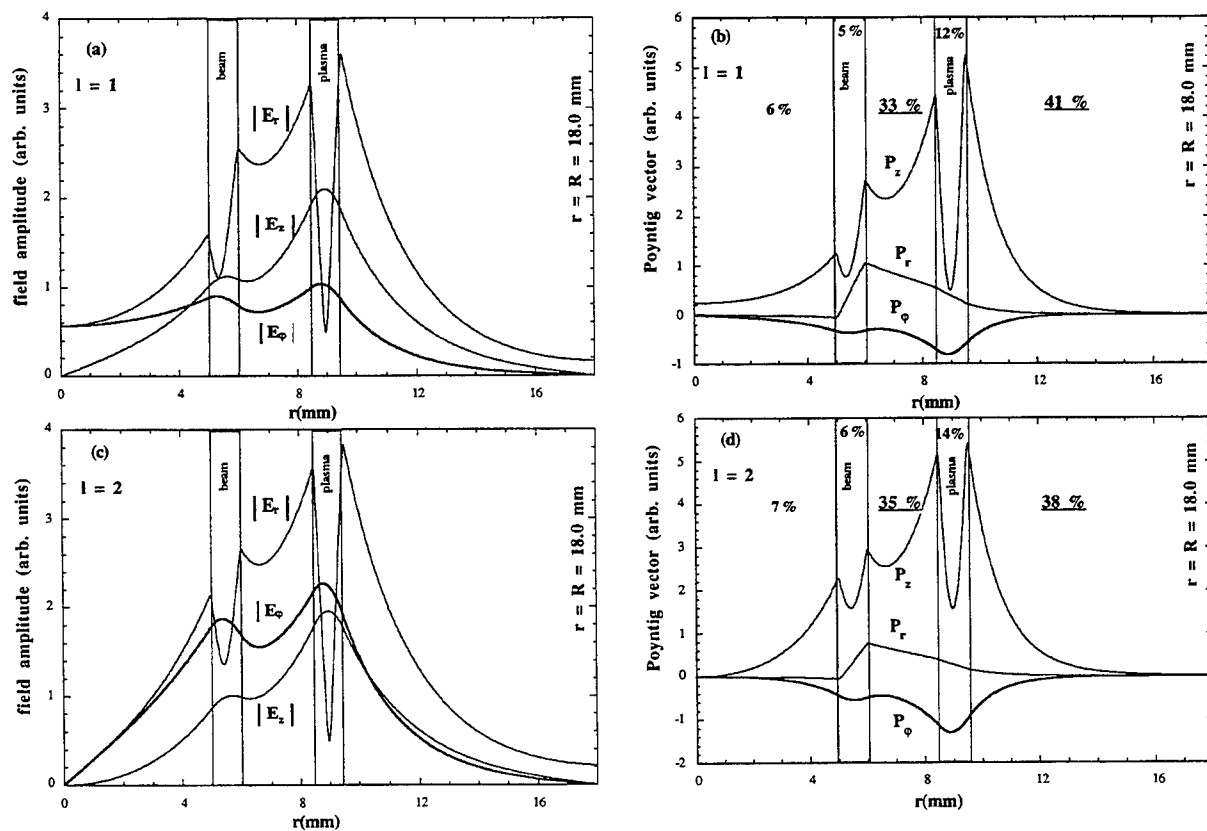


Fig. 8: Distribution of electric field amplitude (a, c) and Poynting vector components (b, d) along the radius for the first two non-axisymmetric modes ($l = 1, 2$).

In Fig. 8, we display the field and power dependencies for the first two azimuthal modes $l = 1, 2$. The field curves (Fig. 8a, c) show the profiles of E_r and E_z components similar to that of axisymmetric mode (except at the axis vicinity). E_ϕ component appears for $l = 1$ mode and is more pronounced in case of $l = 2$. The radial and longitudinal power flux are distributed as in Fig. (6b) with a less ratio of the longitudinal power flow outside the plasma. Note also the azimuthal component emergence absent in the axisymmetric case.

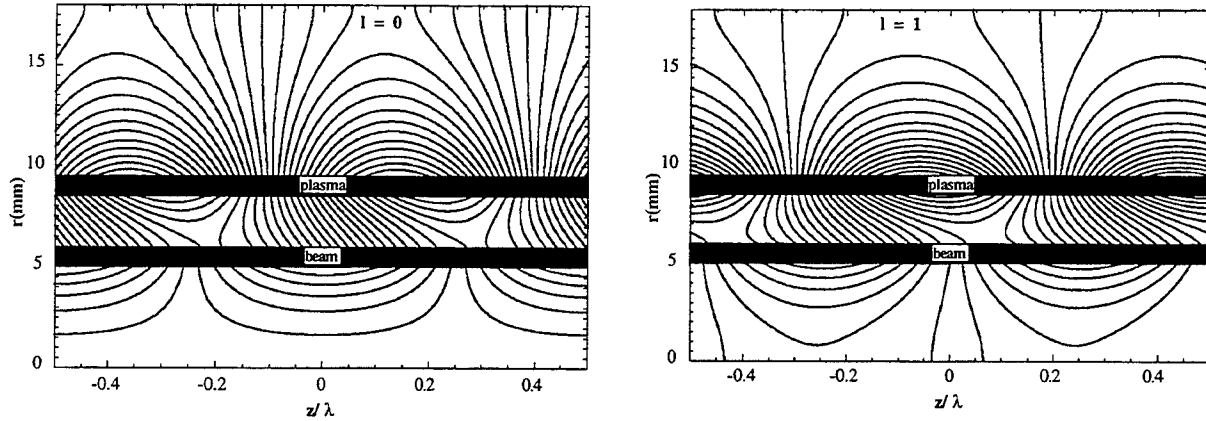


Fig. 9: Electric field lines of the amplified wave at the scale of a wavelength for the axisymmetric ($l = 0$) and the first non-axisymmetric ($l = 1$) mode. In both cases plasma density and the frequency correspond to the maximum growth rate of Cerenkov instability.

In Fig. 9, we present the field lines map at the scale of a wavelength in the interaction region for $l = 0$ and $l = 1$ modes. The axisymmetric case shows a classical profile of TM 01 mode inside the beam. However, the field lines are not strictly perpendicular to it. In the two other regions, because of the radial phase dependence, the field lines have a special configuration since some lines leaving plasma come back to it while others go up to the metal or the beam. We did not draw the field lines inside the beam and the plasma, because of their weak amplitude. Inside the beam and plasma, the electric field tends to a longitudinal orientation in accordance with Fig. 6, 7. The non axisymmetric map has been plotted with $\phi = 0$ and is similar to the first one.

4. CONCLUSION

We have presented an interaction model in the Plasma Cerenkov Maser in the framework of a linear theory. Few assumptions have been made to carry out the analysis.

- assumption of infinite media in the longitudinal direction ;
- assumption of infinite guiding magnetic field ;
- assumption of rectangular radial distribution of cold plasma and monoenergetic beam.

Beside the main interaction (axisymmetric interaction between the slowest beam mode and the fastest plasma mode) that had been studied before, we have considered secondary couplings of two kinds. Interactions between the fastest plasma wave and beam modes of higher order was demonstrated. These interactions have a little growth rate but may affect the radiation processes in the non-linear regime. Interactions depending on the azimuthal coordinate have a comparable growth rate with the axisymmetric one and have to be taken into account even at the linear stage, especially for a high plasma density. Finally, in the study of the field structure, we have pointed out the problem of power distribution versus the radius. A considerable part of energy appears to be trapped in the beam-plasma gap.

5. ACKNOWLEDGMENTS

The author thanks Jean-Max Buzzi and Oleg Loza for useful discussions. This work was in part supported by contract DGA-DRET n° 40-95-007-00.

6. REFERENCES

1. M. V. Kuzelev, F. H. Muhametzianov, M. S. Rabinovitch, A. A. Rukhadze, P. S. Strelkov, A. G. Shkvarunets, "Relativistic plasma microwave oscillator", *Zh. Eksp. Teor. Fiz.* **83**, 1358 (1982) [*Sov. Phys., JETP*, **56** (4), 780, (1982).]
2. J. S. De Groot, R. A. Stone, J. H. Rogers, "Plasma Cerenkov Maser", in Microwave and Particle Beam Sources and Propagation, Norman Rostoker, ed., *Proc.SPIE* 873, 37-50 (1988).
3. A. G. Shkvarunets, A. A. Rukhadze, P. S. Strelkov, "Wide-band relativistic plasma microwave oscillator" *Fiz. Plazmy* **20** (7, 8), 682 (1994) [*Plasma Physics Report*, **20** (7), 613 (1994).]
4. A.F. Alexandrov, M. V. Kuzelev, A. N. Khalikov, "Mechanisms for the nonelectrostatic interaction between an intense thin relativistic electron beam and an anisotropic plasma waveguide with a transverse density gradient", *Fiz. Plazmy* **14**, 455 (1988) [*Sov. J. Plasma Phys.*, **14** (4), 267 (1988).]
5. T. D. Pointon, J. S. De Groot, "Particle Simulations of Plasma and Dielectric Cerenkov masers", *Phys. Fluids*, **31** (4), April 1988.
6. A.F. Alexandrov, L. S. Bogdankevich, A. A. Rukhadze, "Principles of Plasma Electrodynamics", Springer Series in Electrophysics, **9**, Springer-Verlag, Berlin, Heidelberg, New York, Tokyo, (1984)
7. W. D. Jones, H. J. Doucet, J-M. Buzzi, "An introduction to the linear theories and methods of electrostatic waves in plasmas.", 287, Plenum Press, New York, (1985).
8. M. Abramowitz, I. A. Stegun, "Handbook of Mathematical Functions", Dover Publications, INC., New York, 18, (ninth edition, 1972).
9. M.V. Kuzelev, O. T. Loza, A.V. Ponomarev, A.A. Rukhadze, P.S. Strelkov, A.G. Shkvarunets, D.K. Ulyanov, "High-power tunable microwave oscillator, driven by REB in plasma", *Proceedings of the 11th International Conference on High-Power Particle Beams*, June 10-14, 1996, Prague, Czech Republic.

Analysis of an electromagnetically pumped free – electron – laser with a tapered guide magnetic field

Y. G. Liu, S. K. Zhang and C. L. Li

Department of Applied physics, National University of
Defense Technology, Changsha, Hunan, 410073, P. R. China

ABSTRACT

In this paper an electromagnetically pumped free – electron – laser (FEL) with a tapered guide magnetic field is investigated by solving the Vlasov – Maxwell equations. The linear and nonlinear dispersion relations are derived. The nonlinear dispersion relation is solved to obtain the growth rate of the FEL. The energy conversion efficiency is estimated. The results show that the growth rate and the energy conversion efficiency for this kind of FEL may be obviously enhanced by adding a tapered guide magnetic field properly.

Key words: electromagnetic pump, free – electron – laser, tapered guide magnetic field

1. INTRODUCTION

Electromagnetically pumped free – electron – lasers have been successfully investigated in theory by many authors¹⁻¹⁰, and some experimental reports on this subject have also appeared in the literature¹¹⁻¹³. The purpose of this paper is only to present some of our previous work done during the end of last decade. In Sec. 2, the linear and nonlinear dispersion relations are derived by solving the Vlasov – Maxwell equations. In Sec. 3, the growth rate and the energy conversion efficiency are formulated. Finally, some numerical results are given in Sec. 4.

2. BASIC EQUATION AND DISPERSION RELATIONS

Consider an intense current relativistic electron beam (REB) with velocity $\vec{V}_0 = V_0 \hat{e}_z$ propagating into the following electromagnetic field

$$\vec{E}_i = \frac{i}{\sqrt{2}} e_2 \frac{\omega_i B_i}{\kappa_i c} e^{i\phi_i} + C. C., \quad \vec{B}_i = \frac{1}{\sqrt{2}} e_2 B_i e^{i\phi_i} + C. C \quad (1)$$

where C.C. denotes the complex conjugate of the former term. Through Raman backscattering mechanism in this system coherent radiation of the FEL may be produced

$$\vec{E}_s = \frac{i}{\sqrt{2}} e_1 \frac{\omega_s B_s}{k_s c} e^{i\phi_s} + C. C., \quad \vec{B}_s = \frac{1}{\sqrt{2}} e_1 e^{i\phi_s} + C. C. \quad (2)$$

In Eqs. (1) and (2)

$$\phi_i = k_i z + \omega_i t, \quad \phi_s = k_s z - \omega_s t \quad (3)$$

$$e_{1,2} = \frac{1}{\sqrt{2}} (e_x \pm i e_y) \quad (4)$$

where ω_i, ω_s, k_i and k_s denote the angular frequencies and wavenumbers for the pump and the scattered waves, respectively.

In fact the radiation of FEL is the consequence of the coupling of the pump wave (ω_i, k_i) with the longitudinal electrostatic perturbation (ω, k) inherent in the REB. This is a typical three-wave parametric coupling process which should satisfy the resonance condition

$$\omega = \omega_s - \omega_i, \quad k = k_s + k_i \quad (5)$$

The longitudinal electrostatic wave can be written as

$$\vec{E} = E_0 e^{i\phi} \hat{e}_z + C. C \quad (6)$$

where

$$\phi = kz - \omega t \quad (7)$$

Now we describe the response of the electrons in the REB to the three waves by means of a distribution function

$$f = f_0 + f_i + f_s + f_E \quad (8)$$

where

$$f_0 = \frac{2}{\pi} \delta(P_\perp^2) \delta(P_z - P_0) \quad (9)$$

is the equilibrium distribution function for a cold REB, P and P_\perp are the components of the momentum \vec{P} in the perpendicular and the parallel (Z -axis) directions ($P_0 = \gamma_0 m_0 u_0$ with $\gamma_0 = (1 - \frac{u_0^2}{c^2})^{-1/2}$, m_0 being the electronic mass), and f_i, f_s and f_E are the responses of the

electrons to the pump wave (ω_i, k_i) , the scattered wave (ω_s, k_s) and the electrostatic wave (ω, k) , respectively. The total distribution function satisfies the Vlasov equation with $-e$ being the electron charge

$$\frac{\partial f}{\partial t} + \vec{v} \cdot \frac{\partial f}{\partial \vec{x}} - e[\vec{E} + \vec{E}_i + \vec{E}_s + \frac{1}{c}\vec{v} \times (\vec{B}_i + \vec{B}_s + \vec{B}_0)] \cdot \frac{\partial f}{\partial \vec{p}} = 0 \quad (10)$$

where we have considered adding a tapered guide magnetic field into the system

$$\vec{B}_0(Z) = B_0(1 - e^{-\alpha_0 Z})\vec{e}_z \quad (11)$$

in which $e^{-\alpha_0 Z} \ll 1$, α_0 is a constant.

Based on the equation of motion for electrons we can obtain

$$\dot{P}_\perp = e[-E_{ix} - E_{sx} + \frac{v_z}{c}(B_{iy} + B_{sy})]\cos\theta - e[E_{iy} + E_{sy} + \frac{v_z}{c}(B_{ix} + B_{sx})]\sin\theta \quad (12)$$

$$\begin{aligned} \dot{\theta} = & \omega_c - \delta\omega_c - \frac{e}{P_\perp}[E_{iy} + E_{sy} + \frac{v_z}{c}(B_{ix} + B_{sx})]\cos\theta \\ & - \frac{e}{P_\perp}[-E_{ix} - E_{sx} + \frac{v_z}{c}(B_{iy} + B_{sy})]\sin\theta \end{aligned} \quad (13)$$

where

$$\omega_c = \frac{eB_0}{\gamma m_0 c}, \Omega_0 = \frac{eB_0}{m_0 c}, \omega_0 = \frac{\Omega_0}{\gamma_0}, \delta\omega_c = \frac{eB_0}{\gamma m_0 c}e^{-\alpha_0 Z}$$

and $\gamma = (1 - \frac{v^2}{c^2})^{-1/2}$.

Then we write f_s and f_E in the combinations of their linear(L) and nonlinear(NL) parts

$$\begin{aligned} f_s &= f_s^L + f_s^{NL}, \\ f_E &= f_E^L + f_E^{NL} \end{aligned} \quad (14)$$

Substituting Eq. (14) into Eq. (10) and noticing Eq. (15), we may find the complicated expressions for f_s^L, f_s^{NL}, f_E^L and f_E^{NL} . The perturbation distribution function attributed to the tapered guide magnetic field may also be found

$$f_i = \frac{\omega_c[\frac{-e}{k_s c}(k_s v_z - \omega_s)\frac{\partial f_0}{\partial p_\perp} + \frac{ev_\perp}{c}\frac{\partial f_0}{\partial p_z}]B_{sx}}{(\omega_c + k_s v_z - \omega_s)[\omega_c - \omega_s + (k_s + i\alpha_0)v_z]}e^{i\beta\alpha_0 Z} \quad (15)$$

According to the relation of the current density

$$\vec{J} = -e \frac{n_0}{m_0} \int f \frac{\vec{P}}{\gamma} d^3 P \quad (16)$$

we may obtain \vec{J}^L and \vec{J}^{NL} from f^L and f^{NL} , respectively. Then substitute them into the Maxwell wave equation

$$\nabla^2 \vec{E}_{sum} - \frac{1}{c^2} \frac{\partial^2}{\partial t^2} \vec{E}_{sum} = \frac{4\pi}{c} \frac{\partial}{\partial t} \vec{J} + \nabla (\nabla \cdot \vec{E}_{sum}) \quad (17)$$

to find the linear and nonlinear dispersion relations, where

$$\vec{E}_{sum} = \vec{E} + \vec{E}_i + \vec{E}_s, \quad \vec{J} = \vec{J}^L + \vec{J}^{NL}$$

The resulting linear dispersion relations are

$$\omega_i^2 - k_i^2 c^2 + \frac{\omega_{pe}^2}{\gamma_0} \frac{k_i v_0 + \omega_i}{\omega_0 - k_i v_0 - \omega_i} = 0, \quad (18)$$

$$\omega_s^2 - k_s^2 c^2 - \frac{\omega_{pe}^2}{\gamma_0} \frac{k_s v_0 - \omega_s}{\omega_0 + k_s v_0 - \omega_s} = 0, \quad (19)$$

$$(k v_0 - \omega)^2 - \omega_{pe}^2 / \gamma_0^3 = 0 \quad (20)$$

and the nonlinear dispersion relation of the three-wave coupling process is

$$[(k v_0 - \omega)^2 - \frac{\omega_{pe}^2}{\gamma_0^3}] [D(\omega_s, k_s) + D_i] = \delta_{coupl} \quad (21)$$

where

$$D(\omega_s, k_s) = \omega_s^2 - k_s^2 c^2 - \frac{\omega_{pe}^2}{\gamma_0} \frac{k_s v_0 - \omega_s}{\omega_0 + k_s v_0 - \omega_s} \quad (22)$$

$$D_i = \frac{\omega_{pe}^2 \omega_0 (k_s v_0 - \omega_s) e^{-\alpha_0 L}}{\gamma_0 (\omega_0 + k_s v_0 - \omega_s) [\omega_0 - \omega_s + (k_s + i \alpha_0) v_0]} \quad (23)$$

$$\delta_{coupl} = \frac{\omega_{pe}^4 \Omega_i^2}{2 \gamma_0^4 k_i^2} \left[\frac{(k_i v_0 + \omega_i)(k_s v_0 - \omega_s)(k - \omega \frac{v_0}{c^2}) + \frac{\omega_0}{\gamma_0^2} (k_i \omega_s + k_s \omega_i)}{(k_s v_0 + \omega_0 - \omega_s)(k v_0 - \omega)(\omega_0 - k_i v_0 - \omega_i)} \right]^2 \quad (24)$$

in which L is the interaction length. If the term D_i is set to be zero, Eq. (21) is reduced to Eq. (25) in Ref. 9 for the case of adding a constant guide magnetic field into the system.

3. GROWTH RATE AND ENERGY CONVERSION EFFICIENCY

By making use of the linear dispersion relations (18)-(20) and the resonance condition (5), the right-hand side of Eq. (21) can be simplified

$$\delta_{\text{culp}} = 8\omega_{pe}^2 \Omega_i^2 \beta_i^2 / \gamma_0 \quad (25)$$

where $\beta_i = (\omega_i + k_i v_0) / (\omega_0 - k_i v_0 - \omega_i)$

On account of the nonlinear coupling between the scattered wave (ω_s, k_s) and the electrostatic wave (ω, k) in the presence of the pump wave (ω_r, k_i) the angular frequencies of the waves (ω, k) and (ω_s, k_s) get modified, therefore we may assume

$$\omega = \omega_r + \delta\omega, \omega_s = \omega_{sr} + \delta\omega \quad (26)$$

where $|\delta\omega| \ll \omega_r, \omega_{sr}$ and $\Gamma = \text{Im}(\delta\omega)$ denotes the growth rate. Putting Eq. (26) into Eq. (21), noticing $\omega_{pe} \ll \omega_s, \omega_i$ and $\omega_s \simeq 4\gamma_0^2 \omega_i$ for most normal cases, taking only the negative energy space - charge wave into account, we can simplify Eq. (21) to the form

$$\begin{aligned} \delta\omega (\delta\omega - 2\omega_{pe} / \gamma_0^{3/2}) (8\gamma_0^2 \omega_i \delta\omega + D_i) \\ = 8\omega_{pe}^2 \Omega_i^2 \beta_i^2 / \gamma_0 \end{aligned} \quad (27)$$

We define a critical value $\Omega_{\text{crit}} = (\omega_i \omega_{pe})^{1/2} / |\beta_i| \gamma^{3/4}$ to solve the simplified nonlinear dispersion relation for the strong pump limit $\Omega_i \gg \Omega_{\text{crit}}$. In this case, assuming reasonably $\gamma_0^2 \omega_i |\delta\omega| \gg |D_i|$, we can obtain $\delta\omega$ from Eq. (27)

$$\delta\omega = R_{st} + i\Gamma_{st} \quad (28)$$

where

$$R_{st} = -\frac{1}{2\gamma_0} (\omega_{pe}^2 \Omega_i^2 \beta_i^2 / \omega_i)^{1/3} [1 + \frac{(12-m)m}{36 + 2m^2}], \quad (29)$$

$$\Gamma_{st} = \text{Im}(\delta\omega) = \frac{\sqrt{3}}{2\gamma_0} (\omega_{pe}^2 \Omega_i^2 \beta_i^2 / \omega_i)^{1/3} [1 + \frac{m^2}{12(3+m)}], \quad (30)$$

$$m = \frac{\tilde{A}}{R_{sto}} \quad (31)$$

$$\tilde{A} = -\beta_i^2 \omega_{pe}^2 \omega_0 e^{-a_0 L} / 8\omega_i \gamma_0^3 (\omega_i + k_i v_0) \quad (32)$$

$$R_{sto} = -\frac{1}{2\gamma_0} (\omega_{pe}^2 \Omega_i^2 \beta_i^2 / \omega_i)^{1/3} \quad (33)$$

Comparing Eq. (30) with Eq. (34) in Ref. 9 we can see that the growth rate Γ_{st} of the FEL in the present case has been modified by a factor of $\triangle\Gamma = \Gamma_{sto} m^2 / 12(3+m)$, where $\Gamma_{sto} = \frac{\sqrt{3}}{2\gamma_0} (\omega_{pe}^2 \Omega_i^2 \beta_i^2 / \omega_i)^{1/3}$

Following Ref. 14 we can estimate the energy conversion efficiency η of the FEL for the strong pump limit. The resulting formula may be written as

$$\eta = \frac{\omega_{pe}}{2\gamma_0^{3/2}\omega_i} + \Delta\eta \quad (34)$$

where

$$\Delta\eta = R_{sto} \frac{(m-12)m}{2\omega_i(36+2m^2)} \quad (35)$$

From $m \ll 1$ and $R_{sto} < 0$ we can see that $\Delta\eta > 0$

4. NUMERICAL RESULTS

In order to evaluate the effect of the tapered guide magnetic field, we choose the following parameters

$$\gamma_0 = 2.57, \quad \omega_{pe}/\gamma_0\omega_i = 0.034, \quad \Omega_i/\gamma_0\omega_i = 0.004$$

to calculate the variations of $\Delta\eta$ and $\Delta\Gamma$ with the magnitude changing of the guide magnetic field. The results are shown in Fig.

1. We can see from this figure that properly adding a tapered guide magnetic field to the electromagetically pumped FEL may lead to obvious enhancement in the growth rate and the energy conversion efficiency.

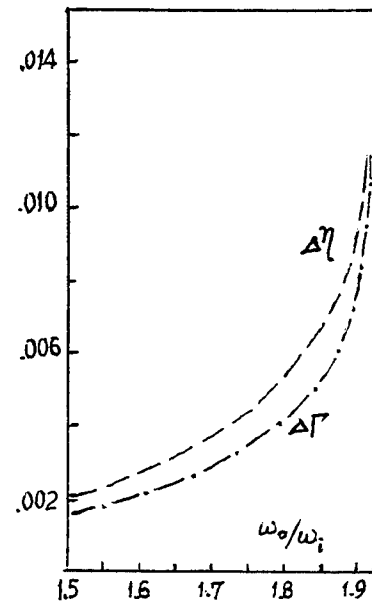


Fig.1 Variations of $\Delta\Gamma$ and $\Delta\eta$ with the changing of B_0

REFERENCES

1. H. P. Freund and R. A. Kehs, *phys. Rev.* , A34(1986), 2007
2. H. P. Freund, *IEEE J. Quantum Electron.* , QE – 23(1987), 1590
3. A. Goldring, L. Friedland , *Phys. Rev.* , A32(1985), 2879
4. V. K. Tripathi and C. S. Liu, *Phys Fluids*, B1(1989), 221
5. V. K. Tripathi and C. S. Liu , *Phys, Lett.* , A132(1988), 47
6. A. Sharma and V. K. Tripathi, *Phys. Fluids*, 31(1988), 3375
7. B. G. Danly et al. , *IEEE J. Quantum Electron.* , QR – 23(1989), 103
8. T. M. Tram et al. , *IEEE J. Quantum Electron.* , QE – 23(1989), 1578
9. B. L. Qian Y. G. Liu and C. L. Li, *ACTA OPTICA SINICA*, Vol. 9, No . 3 (1989), 225(in chinese)
10. B. L. Qian and Y. G. Liu, *ACTA PHYSICA SINICA (Overseas Edition)* Vol. 3, No. 5(1994), 345
11. Y. Carmel et al. , *Phys. Rev. Lett.* , 51(1983), 566
12. R. A. Kehs et al. , *phys. Rev. Lett.* , 60(1988), 229
13. R. A. Kehs et al. , *IEEE Trans. Plasma Sci.* PS – 18 (1990), 437
14. P. Sprangle, Cha – Mei Tang and W. Manheimer, *phys Rev.* A21(1980), 302

Electromagnetic oscillation generation in the virtual
cathode triode from the viewpoint of parametric interaction
of electrons with the variable field

V.P.Grigoryev, T.V.Koval

Institute of Nuclear Physics,
Politechnical University, Tomsk, Russia

ABSTRACT

This paper presents the investigation of the electromagnetic oscillation generation mechanism in the virtual cathode triode from the viewpoint of the parametric interaction of the electrons flow with the variable field. This field is realized due to the virtual cathode oscillations or the external effect. The electron motion dynamic, the transient state of the system, the saturation regime and the flow modulation are investigated. The power depends of the electromagnetic emission on the triode parameters for the different regimes parametric effect has been obtained.

INTRODUCTION

The development of the generators and amplifiers on the basis of a virtual cathode system necessitates the detailed studying a electron flow interaction mechanism with electromagnetic waves. At the time electron flow dynamics and emission mechanism were studied by the numerical simulation methods. Analytical investigations by the method of kinetic equation determine the spectral characteristics, the threshold parameters and the estimates of the emission power and efficiency. But the electron flow modulation under effect of the virtual cathode oscillations and the radiation field and the emission saturation mechanism were not investigated.

Present paper represents the results of theoretical investigation the electron flow modulation and the emission saturation in the virtual cathode systems from the viewpoint

parametric excitation of the electron oscillations in the non-linear system.

1. PARAMETRIC RESONANCE

We investigate a dynamics of a charged particle motion in the potential well

$$U = U_0 \frac{z^2}{z_0^2} \cos(1 - b \cos \omega t), \quad (1)$$

in which the parametric effect is connected with the oscillations of the potential well edges: $z_{VC} = z_0(1 + 0.5b \cos \omega t)$ or with the external field: $E \sim z U_0 b \cos \omega t$. Here z_0 is the anode-cathode spacing, b and ω are the amplitude and the frequency of the external effect. The relativistic particle motion in potential well (1) is described by equation

$$\ddot{z} + \Omega_0^2(1 - b \cos \omega t)z + 2\lambda_e \dot{z} - \gamma z^3 = 0, \quad (2)$$

Where $2\lambda_e$ is damping constant, that is caused by the emission, γ is the nonlinearity coefficient connected with relativistic effects and space charge field (for relativistic effects $\gamma = (\dot{z}/z)^2(\Omega_0/c)^2$, $\Omega_0^2 = 2eU_0/m_0/z_0^2$ is free electron oscillation frequency).

We investigate the case when the external effect frequency is $\Omega_0 = \omega q/2$, $q = 1, 2$. It corresponds to the excitation of the main two resonances: $\Omega_0 = \omega/2 + \Delta_1$ and $\Omega_0 = \omega + \Delta_2$ ($\Delta_{1,2} \ll \Omega_0, \omega$). The solution of the equation (2) is in terms of amplitude α and phase θ given by

$$z = \alpha \cos\left(\frac{\omega t}{2} + \theta\right), \quad \omega \approx 2\Omega_0, \quad (3)$$

$$z = \alpha \cos(\omega t + \theta) + \frac{b\alpha}{6} \cos \theta, \quad \omega \approx \Omega_0, \quad (4)$$

Here $\alpha(t)$ and $\psi(t) = q\omega/2 + \theta(t)$ are slowly varying in the time-scale compared to the Ω_0 time scale.

Substituting Eq.(3) and Eq.(4) into Eq.(2) and neglecting second time derivatives of α and θ , we obtain the equations describing the amplitude α and phase θ , the given by

$$\frac{d\alpha}{dt} = -\lambda_e \alpha - \alpha \frac{b^q \Omega_0}{4q} \sin 2\theta, \quad (5)$$

$$\frac{d\theta}{dt} = \Delta_q + \Gamma \Omega_0 \alpha^2 - \frac{b^q \Omega_0}{12} - \frac{b^q \Omega_0}{4q} \cos 2\theta, \quad (6)$$

where $\Gamma = (3/16)(\Omega_0/c)^2$, c is the light velocity.

The stationary amplitude α_{st} and phase θ_{st} are obtained from Eqs.(3)-(6)

$$\alpha_{st}^2 = \frac{1}{\Gamma \Omega_0} \left[-\Delta_q \pm \sqrt{\left(\frac{b^q \Omega_0}{4q} \right)^2 - \lambda_e^2 \Omega_0^2 + \frac{b(q-1)\Omega_0}{12}} \right] \quad (7)$$

$$\theta_{st} = \frac{1}{2} \arctg \left[\frac{\lambda_e}{\Delta_q + \Gamma \alpha_{st}^2 \Omega_0 - b^q \Omega_0 (q-1)/12} \right], \quad (8)$$

The steady-state regime of the stationary oscillations as follow from Eqs.(5)-(7) is realized for the external effect amplitude (depth modulation)

$$b^q > 4q \frac{\lambda_e}{\Omega_0}.$$

Note there are two stationary phases θ_{1st} and $\theta_{2st} = \theta_{1st} + \pi$. The time-dependent phases $\theta(t)$ for the different initial phases θ_0 are shown in Fig.1 (for resonance $\Omega_0 \approx \omega/2$) and Fig.2 (for resonance $\Omega_0 \approx \omega$). The used parameters here are: $\Delta_{1,2} = 0.2 \Omega_0$, $b=0.8$, $\Gamma \Omega_0^2 = 3/16$, $\lambda_e = 0.2 \Omega_0$. The transition time in of the steady state oscillations depend on the depth modulation, nonlinearity and frequency

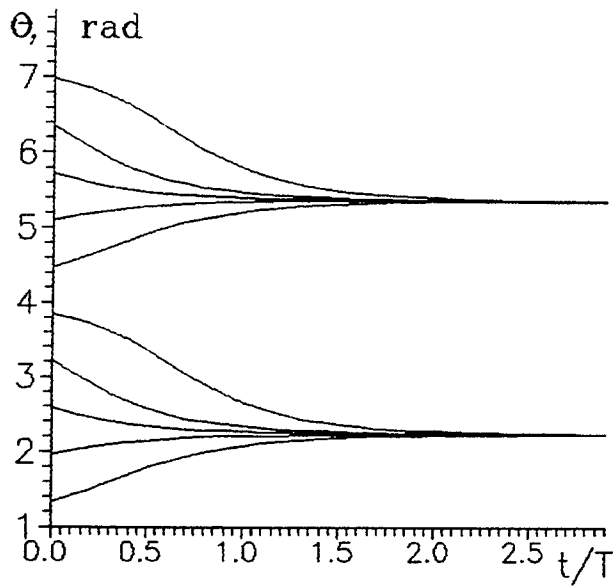


Fig.1.

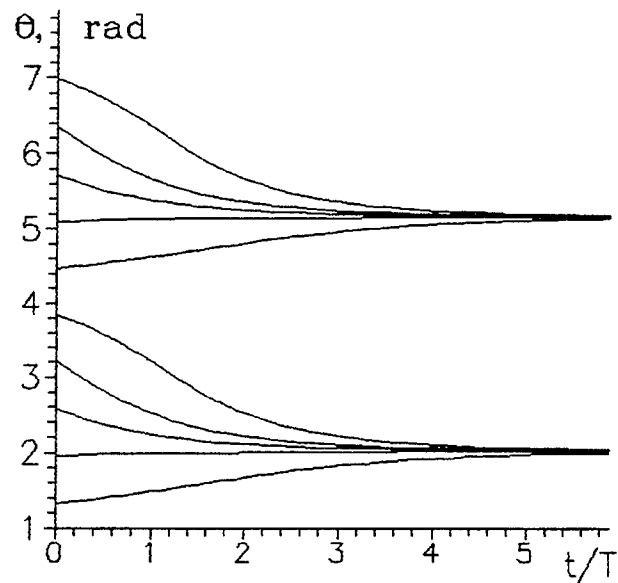


Fig.2.

tions depend on the depth modulation, nonlinearity and frequency detuning. As follow from Figs.1 and 2 the transition time is shorter for resonance $\Omega_0 \approx 2\omega$ then it is for resonance $\Omega_0 \approx \omega$ for equal depth modulation.

2. EMISSION POWER OF A CHARGED PARTICLE

We investigate a charged particle emission in a resonator. In this case the current density of the moving charge in cylindrical coordinates (r, ϕ, z) is expressed by

$$\vec{j}(r, t) = -ev_z \rho(r) \delta(z - z'(t)), \quad (9)$$

where $z(t) = z_0 - z$ is the coordinate of a particle, z is determined from Eqs.(3)-(4), $\rho(r)$ is charge density distribution on radii.

We use eigenmodes for determining of electromagnetic field. Also we take into the electromagnetic oscillations excitation on the multiple frequencies $l\psi$, $l=1, 2, \dots$. The emission average power within period $T = 2\pi/\omega_v$ on the frequencies near the eigenfrequencies of the resonator $\omega_v \approx l\psi$ is given by

$$\bar{P}_l = I_0 \hat{U}_0 \left(\frac{\alpha \psi r_e}{c z_0} \right)^2 G_l(k_z, k_\perp) \Phi_l(t), \quad (10)$$

where

$$G_l(k_z, k_\perp) = \frac{4 \varepsilon_m \Omega_0^2 z_0^2}{\pi R_c^2 h c} \frac{k_\perp^2}{k_z^2} \rho^2 \frac{J_l^2}{J_1^2(\mu_{0s})} \quad (11)$$

$$\rho = \int_{r_1}^{r_2} \rho_0(r) J_0(r k_\perp) r dr, \quad \int_{r_1}^{r_2} \rho_0(r) r dr = 1, \quad \varepsilon_m = \begin{cases} 1, & m=0 \\ 1/2, & m \neq 0 \end{cases}$$

$$J_l = \begin{cases} J_0(k_z \alpha) \cos(k_z z_0), & l=1 \\ J_1(k_z \alpha) \sin(k_z z_0), & l=2 \end{cases}, \quad I_0 = 17 \text{ kA}, \quad \hat{U}_0 = 511 \text{ kB}, \quad r_e = \frac{e^2}{m_0 c^2},$$

$$\Phi_l(t) = \frac{\lambda \Omega_0}{2(\lambda^2 + \dot{\theta}^2)}, \quad (12)$$

h and R_c are the high and the radii of the resonator, $k_\perp = \mu_{0s}/R_c$ and $k_z = \pi m/h$ are the transverse and longitudinal wave-numbers, $\omega/c = (k_\perp^2 + k_z^2)^{1/2}$, $\lambda = \omega_v/Q_v$, Q_v is the quality of the resonator, $v = \{s, m\}$.

From the expressions (10)-(12) follow that time-dependent of the charged particle emission power connected with the time-dependent $\theta(t)$. The maximum emission power take place in the steady-state regime ($\dot{\theta} = \alpha = 0$) and it do not depends from initial phase θ_0 .

The analysis of the geometrical function $G_l(k_z, k_\perp)$ show that the emission for $l=1$ take place on the modes with $k_z \ll k_\perp$ and the emission for $l=2$ take place on the modes with $k_z \approx k_\perp$.

3. COHERENT EMISSION POWER

The coherent emission power can be obtained by integrating currents and fields of N particles on initial phases θ_0 :

$$\bar{P}_{cl} = I_0 \hat{U}_0 \left(\frac{I}{I_0} \frac{2 \dot{\psi} \alpha}{c z_0} \right)^2 G_l(k_z, k_\perp) \Phi_l(t), \quad (13)$$

where

$$\Phi_I(t) = \frac{\lambda \Omega_0}{T} \int_0^{2\pi} \int_0^{2\pi} \int_0^T \frac{\rho(\theta_0) \rho(\theta'_0)}{\lambda^2 + \dot{\theta}^2} \sin \lambda \psi \sin \lambda \psi' d\theta_0 d\theta'_0 dt \quad (14)$$

The coherent emission power Eq.(10) as the emission power of the single charged particle Eq.(13) depend on slow time connected with the particles phase pulling to stationary phases $\theta_{st1,2}$. Because of the coulombian repulsion of the particle there are formed two electron bunches with regions phases: $\theta_{n1} \div \theta_{n2}$ and $\theta_{n1} + \pi \div \theta_{n2} + \pi$. Where $\theta_{n1,2}$ is defined by

$$\left(\frac{\theta_n}{\theta_{st}} \right)_1^2 = \frac{\theta_{st} \pm \pi [1 + \exp(2t\sqrt{H^2 - B^2})]}{\theta_{st} \pm \pi [1 - \exp(2t\sqrt{H^2 - B^2})]}, \quad (15)$$

where $H = \frac{b^q \Omega_0}{4q}$, $B = \Omega_0 - \omega + \Gamma z_0^2 \Omega_0 - (q-1) \frac{b^q \Omega_0}{12}$,

$t \leq t_n$, t_n is the time of bunch forming coinciding with the saturation time of the coherent emission.

For $\rho(\theta_0) = \text{const}$ function $\Phi(t)$ (Eq.(12)) is given by

$$\Phi_I = \frac{\Omega_0}{2\lambda} \left(\frac{\sin \Delta_-}{\Delta_-} \right)^2 \left(\frac{N_1^2}{N^2} + \frac{N_2^2}{N^2} + 2 \frac{N_1 N_2}{N^2} \cos \pi \right) \quad (16)$$

where $\Delta_- = l(\theta_{n1} - \theta_{n2})$. From analysis of the function Φ_I follow that there are two identical bunches for $N_1 \approx N_2$ and the coherent emission take place on the frequency $\omega \approx 2\Omega_0$ ($l=2$). In the real system the great nonuniformity of the electron flow is formed on the initial stage. In this case most of the particles are pulled to one phase and there is formed the main bunch ($N_1 \gg N_2$). The bunch oscillations correspond to gravity centre oscillations of the electron beam.

From analysis of the parametric interaction for the different frequencies of the external effect ($\Omega_0 \approx \omega/2$, $\Omega_0 \approx \omega$) follow that the emission power and frequency are insignificantly depend on external effect frequency in steady-state regime. The transition time depend on external effect frequency greatly.

Stabilization of synchronous frequency in system of strongly coupled microwave oscillators

Sergei S. Novikov, Sergei A. Maidanovskii, Stepan A. Sulakshin

Tomsk State University, Radiophysics Department
36, Lenin Ave., 634050, Tomsk, Russia

1. ABSTRACT

The present paper studies a way to improve the lock-in frequency stability in two coupled microwave sources. A case is considered where strong coupling between the oscillators is realized through a common load, with one of the devices having a high Q -factor oscillatory circuit. It has been shown both theoretically and experimentally that it is feasible in such systems to sufficiently enhance the stability of frequency generation, while retaining steadiness of operation of coherent modes typical for strongly coupled systems.

Also are considered symmetrical and non-symmetrical systems where the power addition or power subtraction modes operate. Effects of the common load on frequency and power characteristics are viewed.

Experimental results from low-power semi-conductor S -range oscillators are cited.

2. INTRODUCTION

An important characteristics of microwave sources is their frequency stability. One of the methods to improve this parameter is to incorporate high- Q cavities into resonance oscillatory circuits. Within the microwave range these resonators are section of the transmission line. The degree of coupling between the oscillator and the cavity determined the efficiency of steady-state operation. Strong coupling results in mode instability especially in multi-cavity systems, while for weak coupling the frequency stabilization region is narrow, which demands high precision of frequency selection. Powerful relativistic pulsers are especially unstable. Broad spectral bandwidth of the signal generated is due to non-steady processes occurring both in the power supply and HF circuits of the oscillators. This restricts the application prospects for relativistic devices.

An approach to increase the oscillation stability is based on the locking phenomenon. Within recent years a number of experimental have been performed¹⁻³, to study the parameters of locked operation of coupled relativistic oscillators. We proposed⁴⁻⁸ certain ways of designing coherent multi-oscillator systems. Those are based on strong coupling between the devices which is accomplished by direct junction of oscillators to the common load. It was demonstrated that such systems exhibit broad lock-in band, wide tuning range, low sensitivity of the lock-in mode to parameter variation, short time for the coherent mode to be established, simplicity of design and high efficiency of power addition.

From the general theory of locking it follows that the lock-in frequency of multi-device systems lies in the vicinity of internal oscillator frequencies and is affected by detuning of the latter the amplitude ratio and the coupling circuits parameters. This work investigates the impact the above factors produced on the frequency stability in a system of two microwave devices with different quality factors of their oscillatory circuits. We analyze here the dependence of power in the common load of symmetrical and non-symmetrical systems on detuning of oscillator frequencies.

3. EQUATION OF STEADY-STATE OPERATION

The concept of strong coupling was used in our work^{4,6} for the generalized theoretical model at two coupled oscillators. In practice it is implemented in a scheme of direct connection of the oscillators ($I_k(U_k)$, L_k , C_k) to the common load R by the transmission line sections of the lengths Θ_1 and Θ_2 (Fig. 1). The oscillatory circuit are tapped with the outer circuit by the matched transformers N .

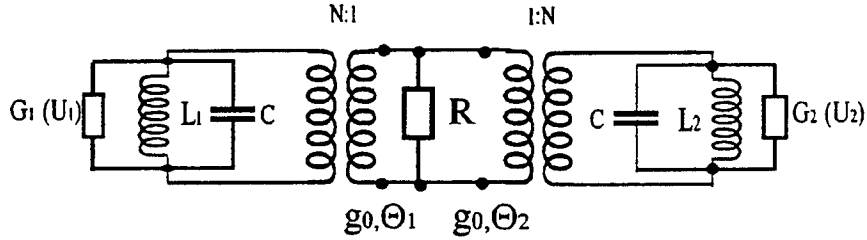


Fig. 1. System of two coupled oscillators.

The steady-state operation is described by the following system of normalized equations:

$$\begin{cases} \tilde{U}_1[-\tilde{G}_1(U_1) + \operatorname{Re} Y_{11}] + \tilde{U}_2[\operatorname{Re} Y_{12} \cos \Delta\varphi - \operatorname{Im} Y_{12} \sin \Delta\varphi] = 0 \\ \tilde{U}_2[-\tilde{G}_2(U_2) + \operatorname{Re} Y_{22}] + \tilde{U}_1[\operatorname{Re} Y_{12} \cos \Delta\varphi + \operatorname{Im} Y_{12} \sin \Delta\varphi] = 0 \end{cases} \quad (1a)$$

$$\begin{cases} \tilde{U}_1[\xi_1 + \operatorname{Im} Y_{11}] + \tilde{U}_2[\operatorname{Re} Y_{12} \sin \Delta\varphi + \operatorname{Im} Y_{12} \cos \Delta\varphi] = 0 \\ \tilde{U}_2[\xi_2 + \operatorname{Im} Y_{22}] + \tilde{U}_1[-\operatorname{Re} Y_{12} \sin \Delta\varphi + \operatorname{Im} Y_{12} \cos \Delta\varphi] = 0 \end{cases} \quad (1b)$$

where $\tilde{U}_k = U_k/U_0$ is the normalized amplitude; $\Delta\varphi = \varphi_2 - \varphi_1$ the phase difference of the locked oscillators; Y are the normalized parameters of the four-pole of the coupling; g_0 is the conductance of the transmission line section of the connector;

$\xi_k = \frac{C_k \omega_0 N^2}{g_0} \left(\frac{\omega_0^2 - \omega_k^2}{\omega_0^2} \right) \approx 2Q_k \frac{\Delta\omega_k}{\omega_0}$ is the generalized frequency detuning; C_k is the capacity of

the oscillatory circuits; ω_0 is the lock-in frequency; ω_k are the internal oscillator frequencies; and $\tilde{G}_k(U_k) = \tilde{G}_k(U_k) N^2/g_0$ are the normalized, averaged to the first harmonic conductances of the active elements.

The functions $G_k(U_k)$ describe non-linear properties of the active oscillator elements. For theoretical calculations one often uses a cubic approximation if the volt-ampere characteristics of the active elements. In the case where the oscillator load conductance is optimum, $g_{\text{opt.}} = g_0/N^2$, the function $G(U)$ is reduced to the following form⁶;

$$\tilde{G}(U) = 2 - \tilde{U}^2. \quad (2)$$

Then the amplitude U_0 corresponds to the optimal (with respect to power) operation. The Y -parameters of the four-pole are equal to:

$$\begin{aligned}
Y_{12} &= -[r(\cos \Theta_{\Sigma} - \cos \Theta) + j \sin \Theta_{\Sigma}]^{-1}, \\
Y_{11} &= Y_{12} [\cos \Theta_{\Sigma} + jr(\sin \Theta_{\Sigma} + \sin \Theta)], \\
Y_{22} &= Y_{12} [\cos \Theta_{\Sigma} + jr(\sin \Theta_{\Sigma} - \sin \Theta)],
\end{aligned} \tag{3}$$

where $r = 1/(2Rg_0)$, $\Theta_{\Sigma} = \Theta_1 + \Theta_2$ and $\Theta = \Theta_2 - \Theta_1$ is the non-symmetry parameter. For the sake of unambiguity let us assume $|\Theta| < \pi/2$.

The features of the locked-in oscillators (steady-state operation, frequency characteristics, locking band, etc.) are essentially determined by the coupling parameter Y_{12} . In case of a purely resistive coupling at the first type ($\Theta_{\Sigma} = 2n\pi$)

$$Y_{12} = -[r(1 - \cos \Theta)]^{-1} < 0 \tag{4}$$

and it is the oscillations close to the in-phase mode, $-\frac{\pi}{2} \leq \Delta\varphi \leq \frac{\pi}{2}$, that are steady^{6,9}. As follows from (4), the value of conductance of the coupling Y_{12} is much higher than g_0 . Indeed, given the matched common load ($r = 1$) and $\Theta = 30^\circ$, we have $Y_{12} = 7.5g_0$. Increase of the common load resistance R ($r < 1$) brings about a still tighter coupling. As concerns the non-symmetric parameter Θ , its decrease as shown elsewhere⁶, narrows the range of allowable values Θ_{Σ} (the tuning range), where the lock-in operation is steady. This requires a more precise tuning of the whole system. Therefore, for $\Theta_{\Sigma} = 2\pi n$ the scheme must be non-symmetrical ($\Theta \neq 0$).

In case of a purely resistive coupling of the second type ($\Theta_{\Sigma} = (2n + 1)\pi$)

$$Y_{12} = [r(1 + \cos \Theta)]^{-1} > 0 \tag{5}$$

and it is the oscillations close to the counter-phase, $\frac{\pi}{2} \leq \Delta\varphi \leq \frac{3}{2}\pi$, which are steady. For the symmetrical scheme ($\Theta = 0$) we have $Y_{12} = 0.5g_0$. It is evident that the coupling in this case is much looser. One may, nevertheless, make it tighter, given the directed mismatching of the common load ($r < 1$).

4. STABILIZATION OF LOCK-IN FREQUENCY

The lock-in frequency ω_0 is the solution of the complete system of equations (1). For qualitative estimation, however, we may confine ourselves to Eqs. (1b), which, including Eq. (3) for $\Theta_{\Sigma} = 2n\pi$, are reduced to the form

$$\begin{aligned}
\frac{\omega_0 - \omega_1}{\omega_0} &= \frac{1}{Q_1} \frac{r \sin \Theta - \left(\frac{U_2}{U_1}\right) \sin \Delta\varphi}{2r(1 - \cos \Theta)} \\
\frac{\omega_0 - \omega_2}{\omega_0} &= \frac{1}{Q_2} \frac{r \sin \Theta - \left(\frac{U_1}{U_2}\right) \sin \Delta\varphi}{2r(1 - \cos \Theta)}.
\end{aligned} \tag{6}$$

If the Q -factors of the oscillatory circuits are equal, then the lock-in frequency is derived as the arithmetic mean of the internal frequencies ω_k : $\omega_0 = (\omega_1 + \omega_2)/2$. Hence, instability of the internal frequencies ω_k causes that of the lock-in frequency of the same order. When the Q -factors are different, however, ω_0 lies closer to the internal frequency of that oscillator whose Q -factor is better. For instance, for $Q_1 \gg Q_2$ it is valid that $(\omega_0 - \omega_1) \ll (\omega_0 - \omega_2)$, i.e. there occurs stabilization of the lock-in frequency. From Eqs. (6) it directly follows that for $Q_1 \gg Q_2$ variation of the coupling circuits parameters does not significantly affect the frequency ω_0 . This is also true for $\Theta_\Sigma \neq 2n\pi$, because Eqs. (1b) are reduced to a form similar to Eqs. (6).

The effects of the oscillator parameters are made manifest by the presence of the amplitude ratio U_k incorporated into the right part of Eqs. (6). In order to estimate these effects let us rewrite one of the equations (1a) following (3) for $\Theta_\Sigma = 2n\pi$.

$$G_k(U_k) = Y_{12} \left[\frac{U_l}{U_k} \cos \Delta\varphi - 1 \right]. \quad (7)$$

From the latter equation there follows another important feature of the strongly coupled systems. In case of identical oscillator characteristics ($G_1(U_1) = G_2(U_2)$) there operates an equal amplitude mode ($U_2/U_1 = 1$). Having mutual deviation of characteristics $G_k(U_k)$, the strong coupling ($Y_{12} > 1$) provides the ratio U_l/U_k little varying from unity. That is to say, that the effects of oscillator characteristics on the lock-in frequency is lessened. Similar conclusions would also suit the case with $\Theta_\Sigma = (2n + 1)\pi$.

Increasing the Q -factor of the oscillating circuit of one device only does not sufficiently narrow the lock-in band. Deducing one equation of the Eqs. (6) from another for $U_2/U_1 = 1$ we obtain for $\Theta_\Sigma = 2n\pi$

$$\xi = \frac{r \sin \Theta - \sin \Delta\varphi}{r(1 - \cos \Theta)}, \quad (8)$$

where

$$\xi = \xi_1 - \xi_2 = 2 \left(\frac{Q_1 Q_2}{Q_1 + Q_2} \right) \frac{\omega_2 - \omega_1}{\omega_0} \quad (9)$$

– mutually generalized detuning.

In the case where the quality factors are equal ($Q_1 = Q_2 = Q$) Eq. (8) is reduced to the following:

$$\frac{\omega_2 - \omega_1}{\omega_0} = \frac{1}{Q} \frac{r \sin \Theta - \sin \Delta\varphi}{r(1 - \cos \Theta)} \quad (10)$$

and for $Q_1 \gg Q_2$

$$\frac{\omega_2 - \omega_1}{\omega_0} = \frac{1}{2Q_2} \frac{r \sin \Theta - \sin \Delta\varphi}{r(1 - \cos \Theta)}. \quad (11)$$

Comparison of Eqs. (11) and (10) shows that the range of allowable frequency detuning decreases no more than twice. As is obvious from (8), (10) and (11) the detuning band is broadened with tightening coupling, i.e. with decreasing r . Similar behavior is demonstrated by the scheme with $\Theta_\Sigma = (2n + 1)\pi$ for which the expression (8) has the form

$$\xi = -\frac{r \sin \Theta - \sin \Delta \varphi}{r(1 + \cos \Theta)}. \quad (12)$$

5. FREQUENCY-TO-POWER CHARACTERISTICS

The dependencies of power in the common load on frequency detuning characterize the stability of the lock-in operation and make it possible to estimate the limiting capabilities of the schemes and their response to variation of the circuit parameters.

The normalized value of power coming from each oscillator onto the common load R can be calculated following the formula

$$\tilde{P}_k = P_k / P_{k_{\max}} = \tilde{U}_k^2 \tilde{G}_k,$$

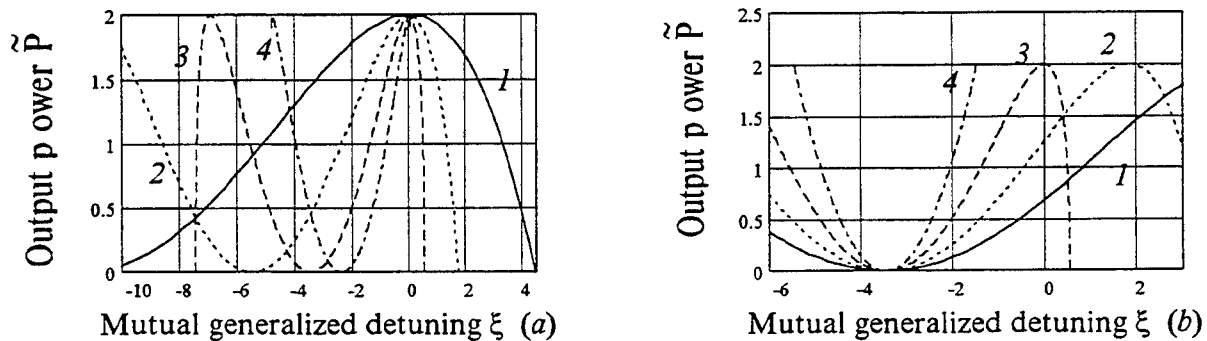
where \tilde{G}_k is the conductance transformed to the terminals of the oscillating circuits, \tilde{U}_k and \tilde{G}_k are determined from Eqs. (1), and $P_{k_{\max}}$ is the maximum power of the optimum load $g_{\text{opt.}}$. For the case of identical oscillators we obtain the expression for power \tilde{P} in the common load for the scheme with $\Theta_\Sigma = 2n\pi$

$$\tilde{P} = 2 \left[2 - \frac{1 - \cos \Delta \varphi}{r(1 - \cos \Theta)} \right] \left[\frac{1 - \cos \Delta \varphi}{r(1 - \cos \Theta)} \right] \quad (13)$$

and for the scheme with $\Theta_\Sigma = (2n + 1)\pi$

$$\tilde{P} = 2 \left[2 - \frac{1 + \cos \Delta \varphi}{r(1 + \cos \Theta)} \right] \left[\frac{1 + \cos \Delta \varphi}{r(1 + \cos \Theta)} \right]. \quad (14)$$

Shown in Fig. 2 are the frequency characteristics calculated through Eqs. (8), (12)-(14).



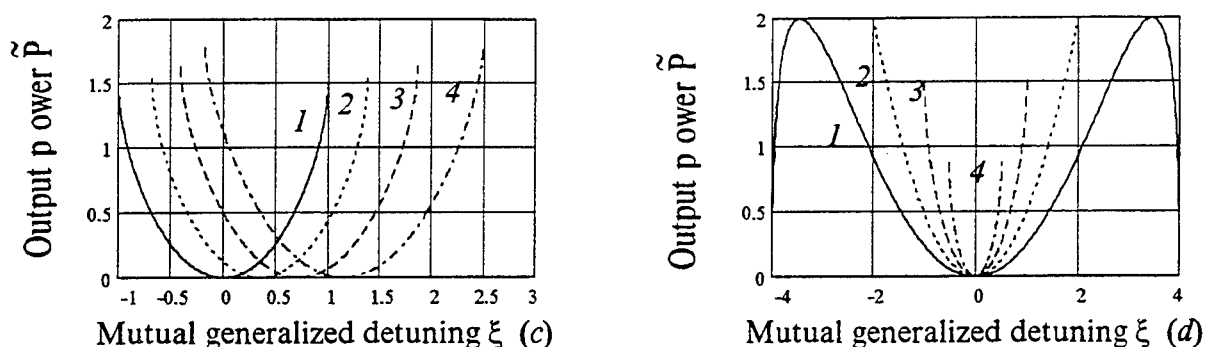


Fig. 2. Calculated power-to-frequency characteristics for system with power addition (a, b) and subtraction (c, d) in the common load:

- a – common load is matched ($R = 0.5\rho_0$), Θ is different: 1 – $\Theta = 20^\circ$; 2 – $\Theta = 40^\circ$; 3 – $\Theta = 60^\circ$; 4 – $\Theta = 80^\circ$;
b – $\Theta = 60^\circ$; R is different: 1 – $R = 0.5\rho_0$; 2 – $R = \rho_0$; 3 – $R = 0.5\rho_0$; 4 – $R = 0.25\rho_0$;
c – $R = 0.5\rho_0$, Θ is different: 1 – $\Theta = 0^\circ$; 2 – $\Theta = 20^\circ$; 3 – $\Theta = 40^\circ$; 4 – $\Theta = 60^\circ$;
d – $\Theta = 0^\circ$, R is different: 1 – $R = 2\rho_0$; 2 – $R = \rho_0$; 3 – $R = 0.5\rho_0$; 4 – $R = 0.25\rho_0$.

For the scheme with $\Theta_\Sigma = 2n\pi$ in case of the matched common load ($r = 1$)⁶ increase of the non-symmetry parameter Θ is accompanied by decrease of the lock-in band (Fig. 2a). The point of complete power addition $\tilde{P} = 2$ corresponds to the zero detuning $\xi = 0$ and the phase difference $\Delta\varphi = \Theta$. For negative detuning the zero point $\tilde{P} = 0$ corresponds to $\Delta\varphi = 0$. With growing common resistance R ($r < 1$) the lock-in band increases (Fig. 2b), which is related to the enhanced coupling conductance Y_{12} . It should be noted that the point of complete power addition is shifted to the region of positive detuning, without changing the characteristics profile.

For the scheme with $\Theta_\Sigma = (2n + 1)\pi$ in the middle of the lock-in frequency (Fig. 2c) there is the point of complete power subtraction $\Delta\varphi = \pi$. For the symmetry case ($\Theta = 0$) this occurs for the zero detuning irrespective of the load (Fig. 2d). It is important that mismatch of the load R to its increase ($r < 1$) results in significant broadening of the lock-in band. For instance, for $r = 0.25$ the band is by a factor of 4 broader than at $r = 1$. Note, that the power at the boundaries of the band can reach its maximum value $\tilde{P} = 2$.

If the latter scheme with the matched load ($r = 1$) is non-symmetrical ($\Theta \neq 0$) then the characteristics are merely shifted along the detuning axis and virtually do not change. The mutual generalized detuning used in the calculations is related to the frequency detuning $\Delta\omega = \omega_2 - \omega_1$ by the expression (9). For $Q_1 = Q_2 = Q$, we can make an estimate of Q through characteristic points of frequency dependencies. This point for non-symmetrical power addition corresponds to the zero power level for negative detuning, where $\Delta\varphi = 0$ (see Eq. (13)). For the symmetrical system we can choose a boundary point on the lock-in band, where, as is known⁴, the phase difference approximates 90° .

Of course, one can solve an inverse problem as well: to predict allowable detuning of internal oscillator frequencies using the known Q -factor for different parameters (non-symmetry, loads, etc.).

6. MODEL EXPERIMENT

In the model experiments we used semiconductor oscillators based on the Shottky transistors (*S*-band) and Gann diodes. Oscillators of the *S*-band based on transistors T (Fig. 3) were connected to each other and the common transmission line according to the scheme given in

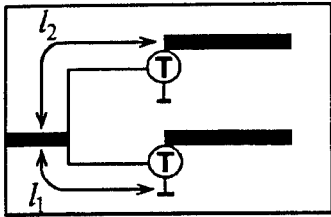
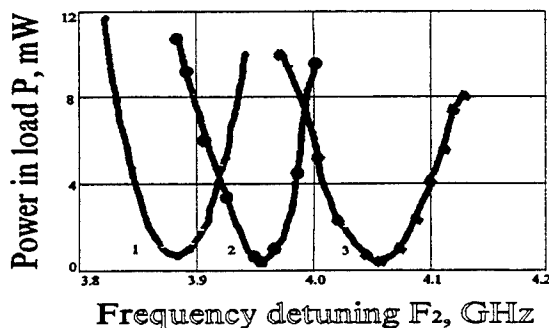


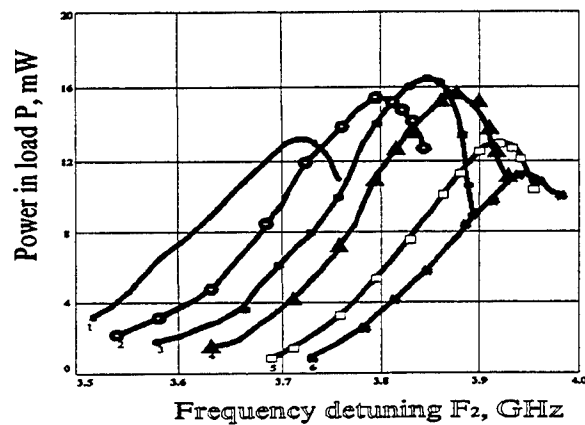
Fig. 3. Two oscillators system of *S*-band.

Fig. 2 by strip transmission lines l_1 and l_2 . These lines in the non-symmetrical system were selected such that $\Theta_1 + \Theta_2 = 360^\circ$; $\Theta_2 > \Theta_1$, and in the symmetrical scheme – $\Theta_1 + \Theta_2 = 180^\circ$; $\Theta_1 = \Theta_2$. The oscillator power were 6-8 mW in the detuning band 3-4 GHz. Here we present the experimental power-to-frequency characteristics for the case of the equal quality factor of the oscillating circuits measured in the lock-in band. The curves in Fig. 4b correspond to the non-symmetrical system ($\Theta \approx 55^\circ$) with the matched load $R = 1/(2g_0)$ ($r = 1$) for different frequencies f_1 of one of the oscillators, with other frequency f_2 being tuned. The region of frequencies f_1 (tuning range), where the typical profile of

dependencies is retained (see Fig. 2a), with complete power addition for $f_1 \approx f_2$, is large and exceeds 300 MHz. The lock-in band would be as wide as 250 MHz. This supports high steadiness of coherent state. It is to be noted that the left side of the calculated characteristics in the region of the second peak is not generally realized experimentally. The discussion of the fact is detailed elsewhere⁶. Characteristics of the symmetrical system (Fig. 4a) also conform with the theory. With the oscillator frequencies approximating each other, there occurs a virtually complete power subtraction. The lock-in band reaches 120 – 150 MHz. The behavior of this type is observed in the region of frequencies by far exceeding 300 MHz.



(a)



(b)

Fig. 4. Power-to-frequency characteristics for symmetrical (a) and non-symmetrical (b) systems with matched common load for different internal frequencies of oscillators:

(a) $\Theta \approx 0^\circ$; 1 – $f_1 = 3.88$ GHz; 2 – $f_1 = 3.95$ GHz; 3 – $f_1 = 4.05$ GHz.

(b) $\Theta \approx 55^\circ$; 1 – $f_1 = 3.7$ GHz; 2 – $f_1 = 3.78$ GHz; 3 – $f_1 = 3.83$ GHz; 4 – $f_1 = 3.86$ GHz; 5 – $f_1 = 3.9$ GHz; 6 – $f_1 = 3.93$ GHz.

Mismatch of the common load was realized by way of varying the wave conductance of the output line in the scheme of Fig. 3. Shown in Fig. 5 is the characteristics of the non-symmetrical

system for $R \approx 0.8/g_0$ ($r \approx 0.65$). As is evident from the figure, the lock-in band is widened up to 370 MHz ($\sim 10\%$). The zero detuning point being on the left slope of the curve, rather than in the maximum as is the case with the matched load. In the case of mismatch of symmetrical system the lock-in band grew as wide as 200 MHz with the minimum of power still corresponding to the zero detuning.

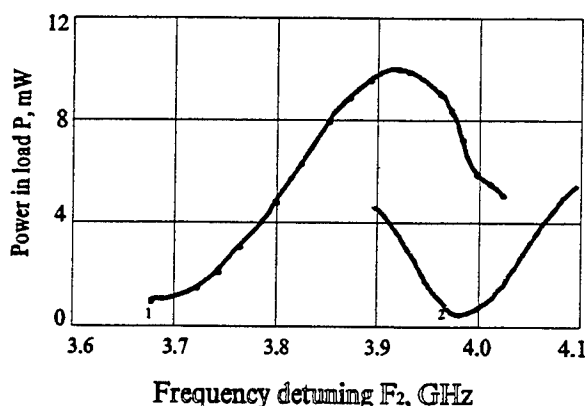


Fig. 5. Power-to-frequency characteristics for non-symmetrical (1) and symmetrical (2) systems with mismatch common load ($R \approx 0.8\rho_0$): 1 - $\Theta \approx 55^\circ$, $f_1 = 3.82$ GHz; 2 - $\Theta = 0$, $f_1 = 3.99$ GHz.

Thus, a directed mismatch of common loads in the coupling connectors of coherent systems may be of practical importance due to its ability to reduce requirements imposed on selection of internal oscillator frequencies, especially in a symmetrical scheme.

Of interest is the estimation of the Q -factor of oscillating circuits of transistor devices under loading. Deriving ξ from Eq. (8) for $\Theta = 55^\circ$ and $\Delta\varphi = 0$ and extrapolating the experimental plots in Fig. 4a to the detuning Δf_2 , where $P = 0$, we calculate Q through (9). This turns out to be $20 \div 25$. The same values can be derived calculating Q by the symmetrical system characteristics. Such values are typical of transistor oscillators of low power.

The schemes of power addition and subtraction described herein are characterized by a wide lock-in band and a large tuning range, and we consider them appropriate for composing coherent systems with any devices oscillating in a variety of frequency ranges.

A test of feasibility of frequency stabilization for a symmetrical system ($\Theta_1 = \Theta_2$) was also carried using the scheme of Fig. 3. The oscillating circuit of one of the cavities in this case was a high- Q multi-mode resonator ($Q_1 \gg Q_2$). The power-to-frequency characteristic (Fig. 6) was extracted during tuning of the internal frequency f_2 of the second oscillator. Along the abscissa we put variation of the lock-in-frequency Δf_0 . For the case of zero detuning the power on the common load is 50 dB lower than that on the lock-in band boundaries. The stabilization coefficient, determined as $K = \Delta f_2 / \Delta f_0$, approximates 100. The lock-in band has been narrowed and equals 80 MHz, which agrees with the theoretical estimates. Throughout the lock-in band there is only one steady-state coherent operating mode.

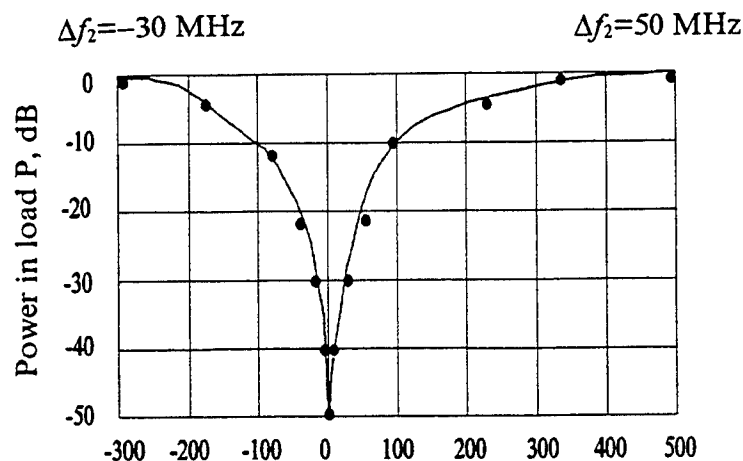


Fig. 6. Frequency detuning Δf_0 , KHz.

CONCLUSION

The research carried out presently is a continuation of our studies of strongly coupled coherent oscillator systems. These are characterized by a high steady state of coherent operation. The results reported in this paper demonstrate their novel properties. Incorporation of high- Q resonators into such systems allows us to significantly increase the frequency stability of oscillations without disturbing the steadiness of coherent operation. It has been shown that a directed mismatch of the common loads extends the lock-in bandwidth and further decreases limitations on selection of the internal oscillator frequency. The schemes of power addition and power subtraction described here may, from our standpoint, be used for conducting powerful microwave radiation sources.

ACKNOWLEDGMENTS

The work presented here was supported by the Russian Fund of Fundamental Researches.

REFERENCES

1. J. Benford et al., "Phase-locking of relativistic magnetrons", *SPIE*, Vol. 873, pp. 23-27 1988.
2. J.S. Levine, N. Aiello, J. Benford, and B. Harteneck, "Design and operation of a module of phase-locked relativistic magnetrons", *J. Appl. Phys.*, Vol. 70, No. 5, 1991.
3. J. Benford and J. Swegle, *High-Power Microwaves*, Artech House, Boston, 1992.
4. S.S. Novikov and A.S. Maidanovskii, "On the matched operation of synchronized generators with common load", *Radioteknika i Elektronika*, Vol. 28, No. 3, pp. 513-517, 1983.
5. S.S. Novikov and A.S. Maidanovskii, "The stability regime power's addition of four self-oscillators in non-symmetrical system", *Radioteknika i Elektronika*, Vol. 29, No. 1, pp. 88-92, 1984.
6. S.N. Vladimirov, A.S. Maidanovskii and S.S. Novikov, *The nonlinear oscillations of multifrequency autooscillators*. Tomsk University Publishing House, Tomsk, 1993.

7. S.S. Novikov, S.A. Sulakshin and S.A. Maidanovskii, "Receiving of superhigh powers in system of strongly coupled microwave oscillators", *Intense Microwave Pulse III, Proc. SPIE*, Vol. 2557, pp. 523-530, 1995.

8. G.G. Kanaev, S.S. Novikov, A.S. Sulakshin, S.A. Sulakshin, N.M. Filipenko "Coherent processes in the system of two connected relativistic magnetrons", *Pisma v Zh.T.F.*, Vol. 21, No. 20, pp. 51-54, 1995.

9. A.A. Dvornikov and G.M. Utkin, *Phase-locked oscillators of radiotransmitting systems*, Energiya, Moscow, 1980.

Intense microwave pulse production from vircators with inductive energy storage

A. G. Zherlitsyn, G. G. Kanaev, V. I. Tsvetkov

Institute of Nuclear Physics of Tomsk Polytechnical University
P. O. Box 25, Tomsk 634050, Russia

ABSTRACT

The high-voltage source has been developed for investigations of the vircator operation. It contains an inductive storage, electrically exploded opening switch, and separating spark gap. The inductive storage is made in the form of two inductively coupled coils; the primary coil provides fast current input from the pulsed current generator and the secondary coil, with the electrically exploded opening switch, forms the voltage pulse of parameters required for the microwave source operation. The microwave source is the vircator of triode configuration.

The results of the experiments performed are presented. At the primary voltage applied to the pulsed current generator of 40 kV and the stored energy of 12 kJ, the vircator voltage pulse is formed of 600 kV amplitude and 360 ns duration. The vircator current reaches the value of 13-14 kA. The stable microwave generation has been obtained in the S-band. The microwave power exceeds 300 MW and the microwave pulse duration is of 180-200 ns.

Keywords: inductive energy storage, electrically exploded opening switch, vircator triode, pulsed current generator

1. INTRODUCTION

The interest to using vircators with inductive energy storage as microwave sources is caused, first of all, by the fact that they are good candidates for compact pulsed sources of gigawatt radiation power level. Inductive energy storages are capable of higher density of stored energy comparing to capacitive storages. Vircators, in their turn, allow high-power microwave generation without external focusing magnetic fields requiring usually additional power supply of the same order as power supply for microwave device voltage sources. High energetic characteristics, simple design and low fabrication cost make vircators with inductive energy storage rather attractive.

In this report, the investigation results are presented for an S-band vircator of triode configuration¹ with an inductive energy storage.

2. CHOICE OF THE SCHEME

One of the simplest variants is the scheme where an inductive storage is a coil of fixed inductance value (Fig.1). High-voltage pulses are formed by an opening switch; typically, an electrically exploded opening switch (EEOS) is employed. An inductive storage is supplied from pulsed current generators which are low-voltage (1-10 kV) capacitive batteries or explosive generators.²

Earlier, the investigations of microwave generation in the vircator triode of the scheme shown in Fig.1 were carried out.³ As a result, the 600 kV peak voltage and 16 kA peak current pulses were obtained on the triode corresponding to electron beam kinetic power of up about 10 GW at the pulsed energy of ~2 kJ. However, the microwave radiated power was of ~100 MW that is much less than radiated power observed at the same peak values of voltage and current in the work¹ where the microwave pulse of about 1.2 GW was produced with the efficiency of 10-12%.

Additionally conducted studies resulted in the following summary. For efficient and stable microwave generation of gigawatt power level in a vircator triode, electron flows are required of 10^4 - 10^5 A current and 10^5 - 10^6 eV energy, and a voltage source should form the pulse of short rise-time (1-10 ns) and relatively "flat" top. In the scheme of Fig.1, peak values and rise-time of voltage and current pulses met these requirements, however, the voltage pulse shape was not optimal; there were sharp voltage peak and drop. It led to the generation process failure and did not allow obtaining high level of radiation power. One can get voltage change gentle making a voltage pulse longer by means of increasing inductance of the storage. At the same time, at increased inductance, it is necessary to employ high-voltage (hundreds of kilovolts) power supplies of inductive storage. The last requirement is conditioned by the facts that an EEOS works efficiently at energy injection time less than 10^{-5} s⁴, and stored

energy should be of tens kilojoules for high-power microwave generation in the triode. Hence, an inductive storage should be supplied from a high-voltage source with a high-impedance load. Those are either Marx generators or explosive generators of specific design⁵ combining short time of operation ($\sim 10^{-5}$ s) and ability to work with a high-impedance load at high voltages. As a result, the whole system becomes enormously complicated and not applicable practically.

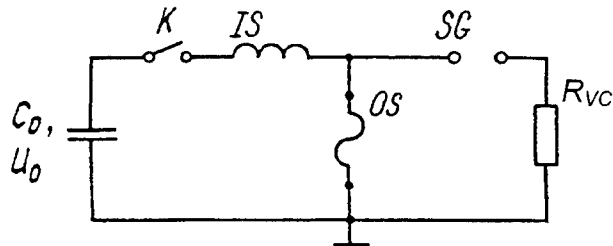


Fig.1. Microwave source (scheme 1). C_0 - power supply source; K - switch; IS - inductive storage; OS - electrically exploded opening switch; SG - spark gap; R_{vc} - high-current vircator diode.

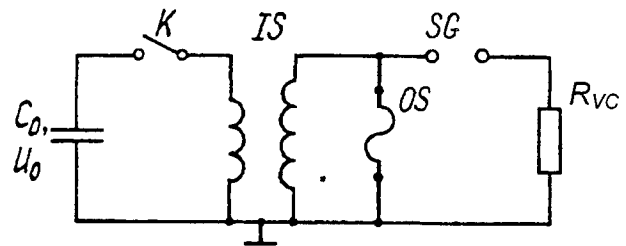


Fig.2. Microwave source (scheme 2). C_0 - power supply source; K - switch; IS - inductive storage; OS - electrically exploded opening switch; SG - spark gap; R_{vc} - high-current vircator diode.

One can increase a duration of a voltage pulse delivered to a vircator by means of another scheme using an EEOS and low-voltage power supplies which is shown in Fig.2. In this scheme, the inductive storage consists of two inductively-coupled coils. Parameters of the storage are the following. L_1 and L_2 are own coil inductances, M is the mutual inductance, $n = \sqrt{L_2/L_1}$ is the transformation coefficient, $k = M/\sqrt{L_1 L_2}$ is the coupling coefficient, $L_{1sc} = L_1(1 - k^2)$ is the inductance of the primary coil when the secondary coil is short circuited, $L_{2sc} = L_2(1 - k^2)$ is the inductance of the secondary coil when the primary coil is short circuited. Fast energy input (characteristic time of 10^{-5} s) to the EEOS from the power supply source occurs because of the fact that before EEOS explosion, the supply source is loaded by the inductance L_{1sc} . After EEOS explosion, the vircator, by means of the spark gap SG, is connected to the inductance L_{2sc} , and the vircator voltage pulse becomes longer. The last is valid if the condition $\pi\sqrt{L_1 C_0} \gg L_2(1 - k^2)/R_{vc}$ is satisfied.

The voltage pulse is formed in the following way. When the switch K is turned on, the current begins to flow through the EEOS, and it reaches maximum value $I_{EEOS} = (kU_0/n)\sqrt{C_0/L_{1sc}}$ at the moment $t_0 \approx (\pi/2)\sqrt{L_{1sc} C_0} \leq 10^{-5}$ s. EEOS parameters are choosed in such a way that wires are exploded at the moment t_0 , and the voltage $U_{sg} \approx L \Delta I/\Delta t$ (where ΔI is the current change through the EEOS during the time of explosion Δt) is applied to the spark gap SG. $L \approx L_{2sc}$ if $\pi\sqrt{L_1 C_0} \gg L_2(1 - k^2)/R_{vc}$.

At optimal EEOS parameters, the wires explosion time Δt may not exceed 10^{-7} s, and $\Delta I = I_{EEOS}$. When the spark gap voltage reaches the maximum U_{sg} , the breakdown occurs and the voltage appears on the vircator diode. Its value $U_{vc} = U_{sg}R_{vc}/(R_{vc} + R_{EEOS})$, where R_{vc} is the vircator impedance and R_{EEOS} is the EEOS impedance at the moment of its connection to the load. In this case, the rise-time of the vircator voltage pulse τ_r is determined by parasitic L_p and C_p of the spark gap and connecting cables, and the fall-time $\tau_f \approx L_{2sc}/R_{vc}$. Analysis of the voltage pulse formation using the scheme 1 and scheme 2 at the same parameters of the supply source, spark gap, and load, and the same time of energy injection into the EEOS shows that in the scheme 2, the pulse duration may be n^2 times larger than for the scheme 1.

In summary, using the inductive energy storage in the form of two inductively coupled coils, one can employ low-voltage supply sources, provide fast energy input to the EEOS and increase the voltage pulse duration. This makes possible to produce, with this storage, microwave radiation of high power level from the vircator triode.

3. MICROWAVE SOURCE DESIGN

Schematic of the source based on the scheme of Fig.2 is presented in Fig.3. It consists of the four main units: inductive storage I, commutation unit II, vacuum insulator III, and vircator IV.

The inductive storage I is made as two inductively coupled coils which are wound coaxially by copper foil. The primary coil is connected to the pulsed current generator and its switch 2. The secondary coil is connected to the commutation unit II. The paper-sheet insulation saturated with the transformer oil is used as the dielectric.

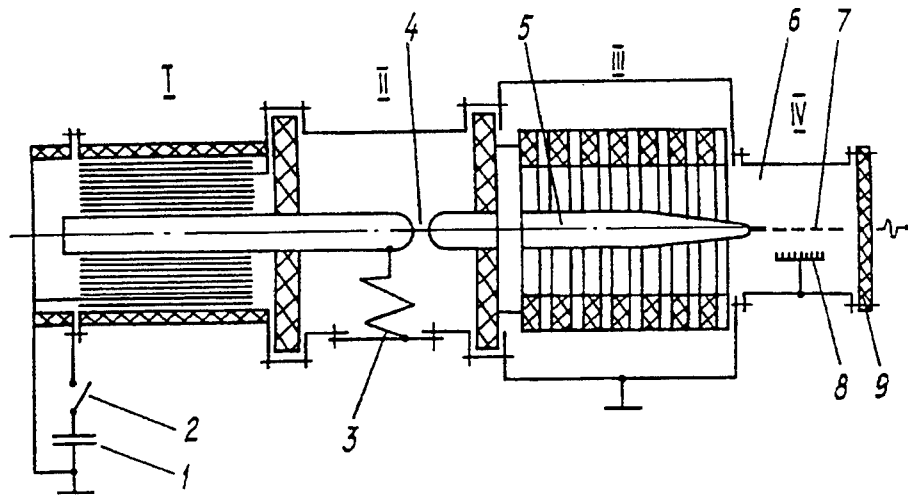


Fig.3. Microwave source design. 1 - pulsed current generator; 2 - switch; 3 - EEOS; 4 - spark gap; 5 - anode holder; 6 - vacuum chamber; 7 - mesh anode; 8 - cathode; 9 - microwave output window. I - inductive storage; II - commutation unit; III - vacuum insulator; IV - vircator triode.

The commutation unit II consists of the EEOS 3 and two-electrode spark gap 4. The EEOS is made as the set of parallel copper wires. A number of wires, their length and diameter are adjusted experimentally to optimize operation at various storage parameters.

The vacuum insulator III of coaxial type is made in the form of successively alternating dielectric and metal rings with forced distribution of the potential.

The vircator triode IV consists of the vacuum chamber 6, mesh anode 7 connected to the anode holder 5 and grounded multi-needle cathode 8. Microwave radiation is extracted through the dielectric window 9.

4. EXPERIMENTAL RESULTS

Experiments were conducted at the voltage on the pulsed current generator $U_0 = 45$ kV and stored energy $W_0 = 14$ kJ. Parameters of the inductive storage were: $L_1 = 6.6$ μ H, $L_2 = 40$ μ H, $k = 0.81$, $n = 2.5$. The time of energy injection into the EEOS $t_0 = 7$ μ s, maximum EEOS current $I_{EEOS} = 25.5$ kA. The time of EEOS wires explosion was evaluated by traces of EEOS current. In our experiments, $\Delta t = 0.2$ μ s. The voltage pulse rise-time depended on the spark gap operation regime. For example, when the gap between electrodes was varied from 3 mm to 12 mm at fixed gas pressure, it changed from 200 ns to 60 ns. In the vircator triode, the metal mesh of transparency $T = 0.6$ was used as the anode. Electrons were produced from the multi-needles field emission cathode of 80 cm² cross-section area. The anode-cathode gap was of 1.8 cm.

With these parameters, the high voltage pulse was formed of the amplitude $U_{VC} \approx 550$ kV. The vircator triode current fitted to Child-Langmuir law (taking anode transparency into account), and its amplitude value $I_{VC} \approx 11$ kA. From these voltage and current values, the diode impedance $R_{VC} \approx 50$ Ω so that the voltage pulse fall-time has to be no less than $\tau_f \approx L_{2SC} / R_{VC} = 260$ ns.

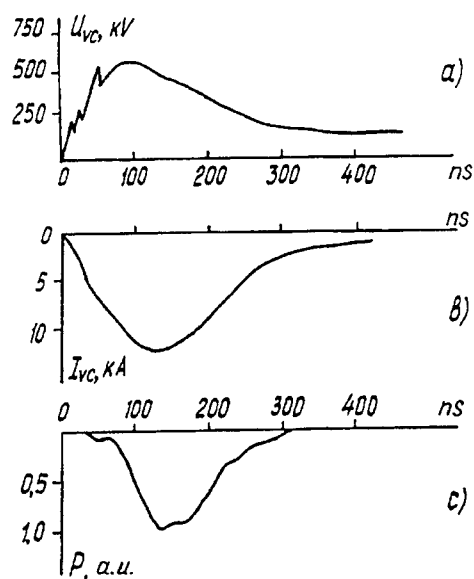


Fig.4. Typical oscillograms. a) - vircator triode voltage pulse; b) - current pulse; c) - microwave pulse ($P_{\max} = 400$ MW).

In Fig.4a,b, the traces of the vircator triode voltage and current pulses are presented. It is seen that the voltage pulse rise-time is of about 90 ns and the fall-time is of about 210 ns.

Microwave radiation from the triode occurred in the S-band. The output power was estimated on the base of far field radiation pattern measurements. In experiments, we observed stable generation of 300 MW power level. In some single shots, the radiation power was of the order of 400 MW. The typical oscillogram of microwave radiation power is presented in Fig.4c.

5. CONCLUSION

The analysis of microwave source schemes with inductive energy storage and the experimental investigations performed demonstrate that the storage in the form of two inductively coupled coils is much more efficient for microwave generation in vircators comparing to the single coil storage of fixed inductance.

6. REFERENCES

1. A. N. Didenko, V. P. Grigoryev, A. G. Zherlitsyn, "Generation of electromagnetic oscillations in systems with a virtual cathode," In *Plasma electronics (in Russian)*, pp. 112-131, Nauka, Kiev, 1989.
2. *Pulsed power systems physics and technique (in Russian)*, Ed., E. P. Velikhov, Energoatomizdat, Moscow, 1987.
3. E. I. Azarkevich, A. N. Didenko, A. G. Zherlitsyn *et al.*, "Electron beam and microwave radiation pulses generation by means of chemical explosives energy," (*in Russian*), *Teplofizika Vysokikh Temperatur*, Vol. 32, no. 1, pp. 127-132, 1994.
4. V. A. Burtsev, I. V. Kalinin, A. V. Luchinskii, *Electrical explosion of conductors and its application in electrophysical installations (in Russian)*, Energoatomizdat, Moscow, 1990.
5. A. A. Velikii, P. V. Dolgoplov, A. G. Zherlitsyn *et al.*, "Investigation of operation of helical explosive generators with axial initiation," (*in Russian*), Preprint of the Institute of Chemical Physics, Chernogolovka, 1989.

Narrow band microwave generation from virtual cathode oscillating inside a resonant cavity

Liu Jinliang, Zhang Yazhou, Li Chuanlu, Chen Guoqiang, and Tan Qimei

(Department of Applied Physics, National University of Defense Technology, Changsha 410073, Hunan, P. R. CHINA)

ABSTRACT

A narrow band microwave pulse has been obtained experimentally by using a resonant cavity surrounding virtual cathode oscillation(vircator). There are several separate dominant modes with different frequencies in a resonant cavity. Although, the coupled coefficient of radial extracting slot and Q value for each mode are not the same, but to tune the virtual cathode oscillation by varying the diode voltage, so that its dominant frequency of free-running virtual cathode oscillation is near the passband of every mode in the resonant cavity, respectively, the several narrow band microwave pulses with different frequencies can be obtained. In our experiments, a cylindrical resonant cavity is used with the microwave power being extracted radially through circumferential a slot into rectangular waveguide, and the two narrow band single microwave pulses with different frequencies are observed. The resonant points of the cavity at 4.16GHz and 5.13GHz are selected. The measured frequencies of microwave are 4.14GHz and 5.09GHz with peak power of 1~4MW, 3dB bandwidth is 0.36% and 0.53 % of the central frequency, respectively.

Keywords: Microwave pulse, Virtual cathode oscillation, Resonant cavity, 3dB bandwidth.

1. INTRODUCTION

A typical free-running virtual cathode oscillator includes an electron beam injected into an open-ended waveguide, with the beam current exceeding the space-charge-limiting current. It has been reported that this device can produce gigawatt power level with total energy of 850J in a single pulse¹. The mechanical simplicity and high output peak powers of vircators make this type of microwave source has been widely investigated. The central frequency of vircator can be written by

$$f = (4.77 / d) \ln[\gamma_0 + (\gamma_0^2 - 1)^{1/2}] \quad (1)$$

where d is the anode to cathode gap in cm, $\gamma_0 = V_d/0.511 + 1$, V_d is diode voltage in MV. The emitted frequencies increase with increasing diode voltage V_d . The electrons are supplied by

an electron beam diode with a field-emission cathode for pulse lengths range from tens to hundreds of nanoseconds. The diode voltage is affected by the impedance match between the formed pulse line and the diode. Any mismatch between the two will produce a variation of voltage. The diode voltage variation can be significant with short pulse, simply because as the pulse gets shorter, the rise and fall time become a larger fraction of the voltage pulse. Consequently, the frequency of the free-running vircator is considerably instable, the 3dB bandwidth in single pulse is usually 5%~10% of the centre frequency.

Most of the applications require not only high output power but also frequency stability. The direct way that stabilize the frequency of a free-running vircator is to surround it with a resonant cavity and allow the vircator to lock to a cavity mode. As long as the cavity mode has an electric field component that couples to the oscillating vircator cathode, feedback occurs between the two. This feedback results in microwave producing over a narrow frequency band corresponding to the excited cavity mode. The use of a resonant cavity surrounding the vircator to achieve frequency locked operation has been investigated experimentally in Los Alamos National Laboratory²⁻³. In their experiment the 3dB bandwidth is less than 1% during 100ns single pulses and is about 0.3% during 1μs single pulses. This paper presents the experimental results that two narrow band single microwave pulse with different frequencies, which are achieved by changing diode voltage, are obtained by using a resonant cavity surrounding the vircator.

2. EXPERIMENTAL APPARATUS AND DIAGNOSTICS

This experiment uses a resonant cavity surrounding the oscillation virtual cathode to obtain single microwave pulse of stable frequency. A microwave resonant cavity has two important

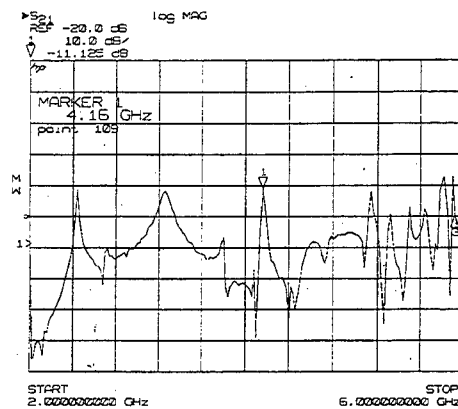


Fig.1 The curve of resonant property of the cavity

properties that are particularly useful in this application. First, it is frequency selective, a cavity has several narrow band resonant points with different, when the dominant frequency of free-running oscillation frequency is near the passband of a suitable mode in the microwave resonant cavity, the frequency of microwave pulses can be locked to the frequency of a resonant point and narrow bandwidth microwave pulses are obtained. Second, microwave energy can be effectively and usefully coupled out of a resonant cavity. To know resonant property of our cavity, a short E-probe is used to excite microwave signal in the cavity. The curve of resonant property of the cavity is shown in Fig 1, which is measured by HP8510C microwave network analyzer. The cavity has several resonant points in Fig.1. Although, there is a maximum Q value and narrow bandwidth at the resonant point with 2.7GHz. However our 81-7M-01 intense relativistic electron beam accelerator⁴ (IREBA) operation is unstable at 2.7GHz of the vircator. In addition, the frequency band of rectangular waveguide connected with the resonant cavity is 3.95~5.85GHz. For these two reasons the frequencies of the resonant points are selected at 4.16GHz and 5.13 GHz.

The cylindrical resonant cavity configuration is shown in Fig.2. The vircator is driven by a 1MV, 100kA and 100ns 81-7M-01 IREB accelerator. The electron beam is formed by a diode consisting of a field-emission cathode and anode. The annular cathode has 48cm inner diameter and 64cm outer diameter with a velvet on the front surface, and the anode is

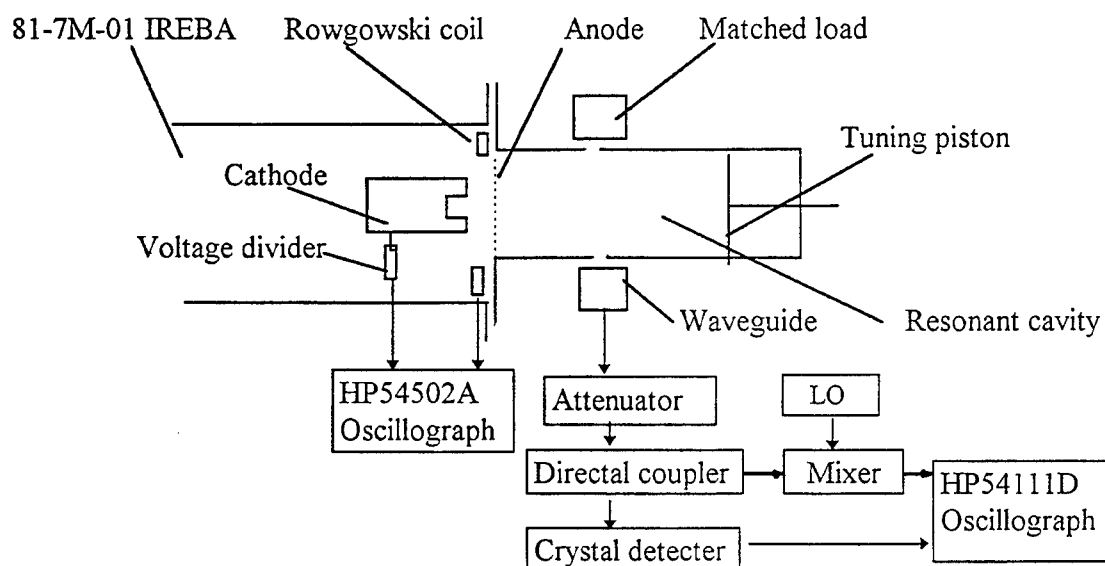


Fig.2. The schematic of the experimental apparatus and signal measurement block diagram

stainless steel wire screen. The anode-cathode aperture is 1.1 cm. We employed a cylindrical copper-plated steel cavity whose inner diameter is 93cm and length is tuning from 75cm to 164cm. The cavity has two rectangular slots located circumferentially at 180° intervals. The microwave pulse is extracted from one the rectangular aperture and then propagates into rectangular waveguide, the other aperture connect with matched load. In our experiment, the cavity length is 164cm and operated at TM_{211} mode with 5.13GHz and TM_{112} mode with 27GHz respectively. Transverse magnetic modes possess an axial electric field that strongly couples to the oscillating virtual cathode's electric field. In addition, the TM modes have a circumferential magnetic field at the wall. This configuration has the important advantage of coupling the microwave power from the cavity by exciting the dominant TE_{10} mode in the rectangular output waveguide. This allows an unambiguous measurement of output power using conventional waveguide diagnostics because that mode of propagation in the waveguide is well characterized. The microwave output power from vircator is coupled into BG-48 rectangular waveguide(C-band) by rectangular coupled slot of the cavity. The vacuum in the diode and cavity region is 8×10^{-5} Torr. Only the microwave in the C-band are measured in the experiments.

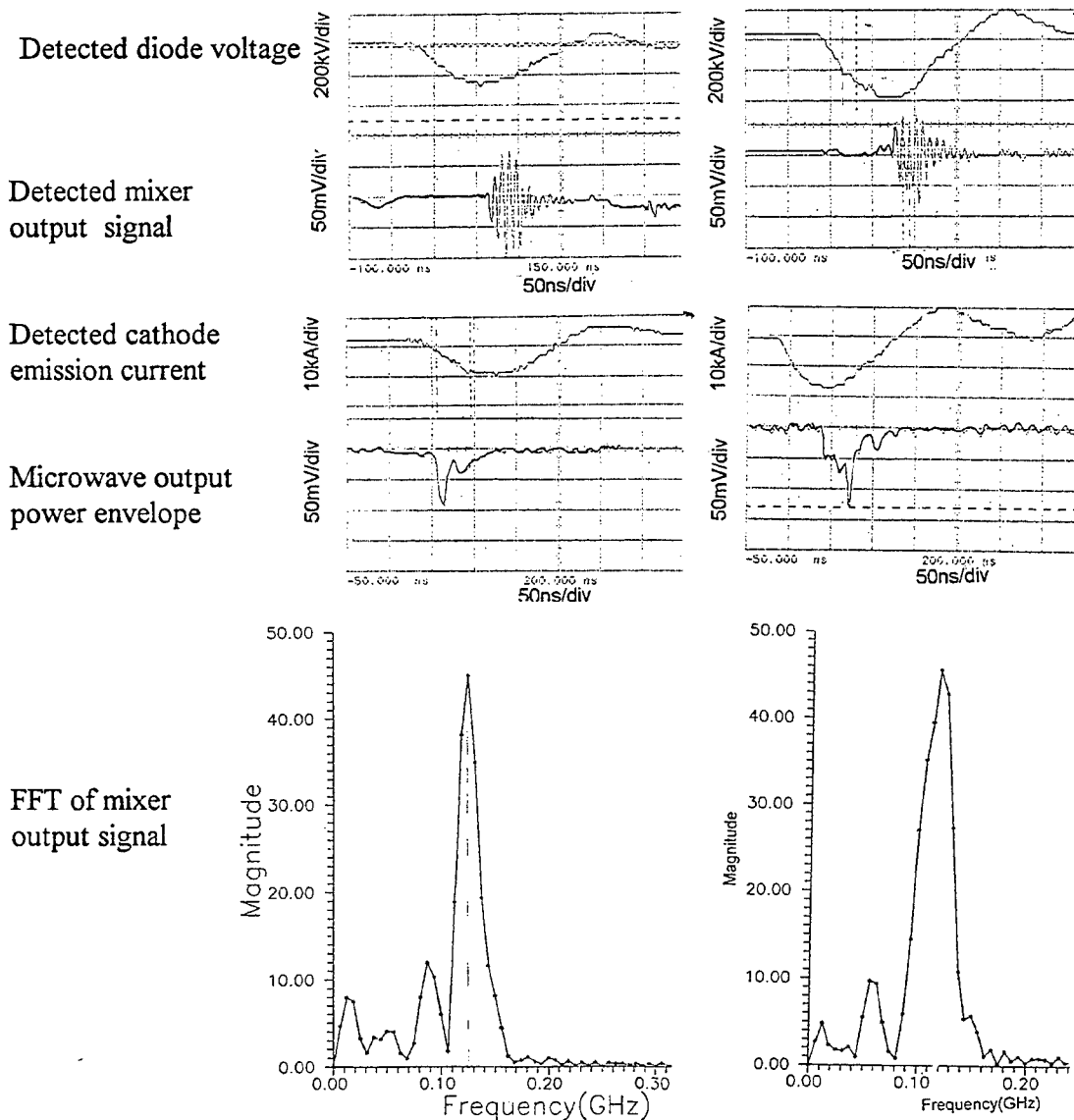
Experiment diagnostics are divided into the beam measurement and microwave measurement. the signal measurement block diagram is shown in Fig.2. Beam measurement includes one Rowgowski coil and resistance voltage divider. The Rowgowski coil measures the cathode emission current and the divider measures the diode voltage, the measured signals of current and voltage are observed by HP54502A oscilloscope. The microwave output power is coupled into the rectangular waveguide through radial extracted aperture. Microwave power in the waveguide is divided into two parts after travelled through 1M semirigid cable, coaxial attenuator and power splitter. One power inputs to the calibrated crystal detector for absolute power measurement, the other travels into the mixer with a local oscillator (LO) for measuring the microwave frequency. The attenuator, coupling coefficient of rectangular aperture, crystal detector and mixer system are calibrated by using 50ns, 4GHz standard single microwave pulse. The resonant cavity Q is measure by HP8510C microwave network analyzer.

3. EXPERIMENTAL RESULTS

At ± 40 KV and ± 25 KV Marx charging voltage, 1.1cm diode-cathode gap and $\phi 30\text{cm} \times \phi 45\text{cm}$ annular velvet emitting area, the diode voltage and cathode emission current for a typical shot are shown in Fig.3. In all four waveforms, the total width of the current and voltage pulse is about 180ns. The microwave output power is extracted radially from the cavity through a coupled rectangular slot and propagates into BG-48 rectangular waveguide as shown in Fig. 1. Typical microwave output power envelope, mixer output signal and FFT of mixer output signal are shown in Fig.3.

According to the Fig.3, Fig.1, Eq.(1) and the factor of calibrated crystal detector. The following parameters are obtained:

Frequency of resonant point	4.16 GHz	5.13GHz
Q value of resonant point	140	96
Detected diode peak voltage	250kV	410kV



(a) LO= 4.00GHz (b) LO=4.97GHz
 (a) at 4.14 GHz dominant frequency (b) at 5.09GHz dominant frequency
 Fig.3. The typical waveforms of measurement signals and FFT of mixer output signals

Detected cathode emission peak current	11kA	17kA
Calculated frequency of the vircator	4.13GHz	5.18GHz
Detected frequency of microwave	4.14GHz	5.09GHz
Detected microwave output peak power	3.64MW	3.98MW
3dB bandwidth of microwave signal	15MHz (0.36%)	27mhz(0.53%)

In our experiment, the anode-cathode gap (d) is 1.1cm, when the measured diode voltages are 250 KV and 410KV, the frequencies calculated from the Eq.(1) for the vircator are 4.13GHz and 5.18GHz, which resemble the frequency of resonant points, 4.16GHz and 5.13GHz. From many experiment, when the frequencies of output microwave and calculated frequencies of vircator are both close to the frequencies of resonant points, a good mixer output signal can be obtained and 3dB bandwidth will be narrow. Our experiment results are in agreement with theoretical predictions.

In the Fig.3, it is clear that higher diode voltage results higher microwave output power and wider width of microwave pulse. If d is kept constant, higher diode voltage leads to stronger oscillation of the vircator and higher microwave output peak power. Moreover, higher microwave output peak power causes longer the time of releasing energy from the cavity, so the width of microwave pulse becomes wider.

From above mentioned parameters, we know that 3dB bandwidth at 4.14 GHz is more narrow than at 5.09GHz. There are two reasons for this, first, Q value of resonant point at 4.16 GHz is greater than at 5.13GHz, second, the frequency of free-running vircator is closer to the frequency of resonant point at 4.16 GHz than at 5.13GHz. This experiment clearly indicates that Q value of the resonant cavity is higher and the frequency of free-running vircator is nearer to frequency of resonant point, it will result in the 3dB bandwidth of microwave output signal is more narrow. However, as the accelerator of driving the vircator is a little unstable, if the Q value of resonant cavity is too high, it is difficult that the frequency of free-running vircator approaches the frequency of resonant point.

4.CONCLUSION

The frequency stabilization of vircator is achieved by surrounding the vircator with a resonant microwave cavity. The oscillation frequency of the vircator can be locked to the TM_{112} mode with 4.14GHz and the TM_{211} with 5.09GHz, and the 3dB bandwidth is 0.36% and 0.53%, respectively. The microwave output peak power is about 4 MW.

REFERENCES

1. G.A. Huttlin et al, Intense microwave and particle beams II, Howard E. Brandt, pp.147, 1991.
2. M. V. Fazio, R.F. heberling, and J. K. Wright, "Narrow band microwave generation from an oscillating virtual cathode in a resonant cavity," J. Appl. Phys. 65(3), pp. 1321-1327, Feb. 1989.
3. M. V. Fazio, B. L. Freeman et al, "A microsecond-pulse-length, frequency stabilized virtual cathode oscillator using a resonant cavity," IEEE Trans. On Plasma Science, Vol. PS-20, No.3, pp. 305-311, June 1992.
4. Li Chuanlu et al, "The 81-7M-01 intense reativistic electron beam accelerator," Journal of National University of Defense Technology. Vol.15, pp.1-10, June 1993.

Single pulse analysis with a 35GHz optical sampler

A. Ghis, M. Cuzin, M.C. Gentet, P. Ouvrier-Buffet, M. Nail*, Ph. Gibert*, D. Husson*, L. Armengaud**, M. Lalande**, B. Jecko**.

CEA LETI, 17 rue des Martyrs, 38041 Grenoble Cedex 9, France

*CEA-DAM, CE Limeil Valenton, 94195 Villeneuve St Georges Cedex, France

**IRCOM, Université de Limoges, 87060 Limoges Cedex, France.

ABSTRACT

A compact optical sampler has been developed for the imaging of single-shot optical or electrical pulses. The analyzed duration is 400ps, and the temporal sampling rate is 4ps (250GSa/s). The spectral density of the input signal is restored in the resulting data until 35GHz.

The device consists of a 50 Ohms propagation microstrip structure, lined by periodically arranged ultra-fast photoconductive switches. When illuminated, these switches short the propagation line to storing capacitors. To operate the device, the input signal is injected onto the line; when the signal to analyze is displayed along the line, facing the optical gates, these gates are switched on, and the storing capacitors collect an amount of charges related to the voltage present on the line.

When an optical or X-ray pulse is on analysis, the electrical signal injected into the propagation line is delivered by a CdTe very fast detector.

This device has been operated with a femtosecond laser.

The analysis of a single pulse through the optical sampler results in an amplitude versus time curve, exhibiting temporal characteristics very close to those measured with a classical sampling head (repetitive signal) and much shorter than those measured with single shot existing analyzer.

KEYWORDS : ULTRA-FAST - SINGLE-SHOT ANALYSIS - SAMPLING - OPTICAL - PULSE

1. INTRODUCTION

As a part of the French high power laser project called Megajoule, picosecond diagnostics are being worked out. Running the expected experiments will need the analysis of the very short X-ray pulses¹ emitted from the irradiated target. In the same way, the on-line control of each of the 240 convergent beams will be operated through ultra fast sensors delivering the bunch spatial dimensions, including duration (length). The final objective of this study^{2,3} is to deliver diagnostic means to catch single events lasting from 10ps to 100ps and to restore the evolution of its energy during the analyzed period. The events may range from X-rays to visible light radiation, or any purely electrical pulse, so long as a synchronous optical pulse can be supplied.

The principle of the optical sampling is the spreading of the pulse along a propagation line⁴, and the spatial simultaneous sampling of the instant voltage at a hundred of points. In this paper, we will first present each of the functional steps necessary to the complete operation, describe the concerned parts of the device and their specific characterizations. Then we will consider the whole device, describe the operating mode, present the results obtained and compare the performances with those of other existing single shot signal recorders.

2. RADIATION TO ELECTROMAGNETIC PULSE CONVERSION

First of all, if the pulse to be caught is a radiation, it has to be converted into an electrical pulse. A very fast CdTe coaxial photosensor has been developed for this operation.

The CdTe thin film is elaborated by chemical vapor deposition onto a thin ring of sapphire⁵. In this case, the radiation considered is low energy X-rays, so the thickness of the film has been optimized at 0.6 μ m. Gold concentric contact pads are deposited onto the CdTe film. The external diameter of the sapphire ring is 1.8mm, and the inner diameter is 350 μ m (figure 1). The ring is then slipped around the aim of a 50 Ω /50GHz coaxial cable, connected with 50GHz jack.

The rise-time of this sensor, biased through a fast PPL bias tee, has been measured with the TEK-SD32 sampling head of the CSA803 oscilloscope. It is as short as 7.8ps (the sampling head itself provides a rise time of 7ps) (figure 2) . The electrical image of the considered pulse is thus available for been measured by optical sampling.

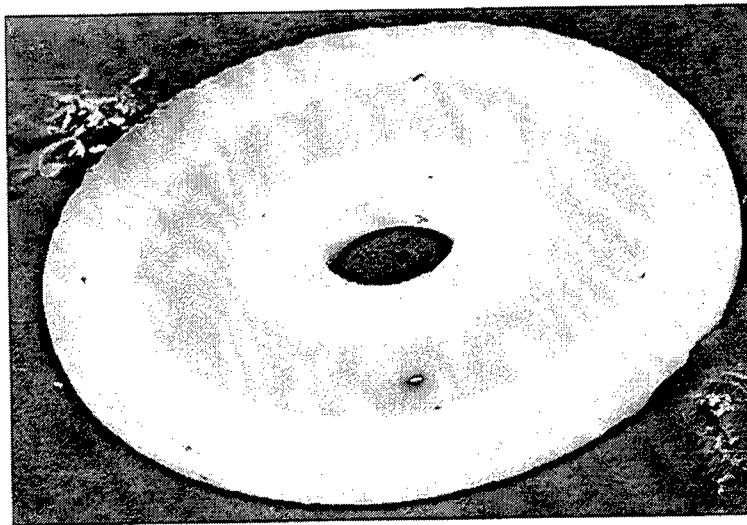
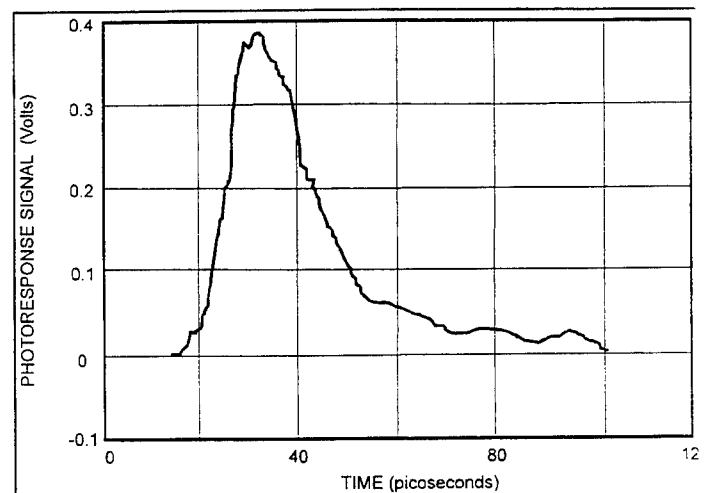


*figure 1 : Coaxial CdTe detector ring of ceramic covered with CdTe thin film, and concentric gold contacts.
The central hole is 350 μ m in diameter, the total ring is 1.8mm in diameter.*

figure 2 : Photoresponse of the CdTe Coaxial detector to a 450fs/532nm laser pulse. DC bias : 50V

rise time : 7.8ps; fwhm : 15.3ps

The response has been measured by temporal sampling of the repetitive (10Hz) signal with a 50GHz scope.



3. SPATIAL SAMPLING

The electrical signal is then injected onto a 50Ω propagation line. Depending on the wave velocity in such a structure, the temporal variations of the intensity are available as a spatial variations of the pulse intensity along the line. At any instant after the beginning of the propagation on the line, each element of the line is polarized by a voltage related to the initial shape of the pulse. The line is 48mm long. It is lined by 100 periodically spaced sampling gates, with a pitch of $465\mu\text{m}$ (see figure 3).

If all the gates are activated simultaneously, the part of the signal laying at the sampling instant in front of the 100 gates is 400ps wide, and the equivalent sampling step is 4ps. The gates are photoconducting resistors. They are connected one side to the propagating line, the other to storage capacitors, via 100 microstrip lines. These lines are called sampling lines.

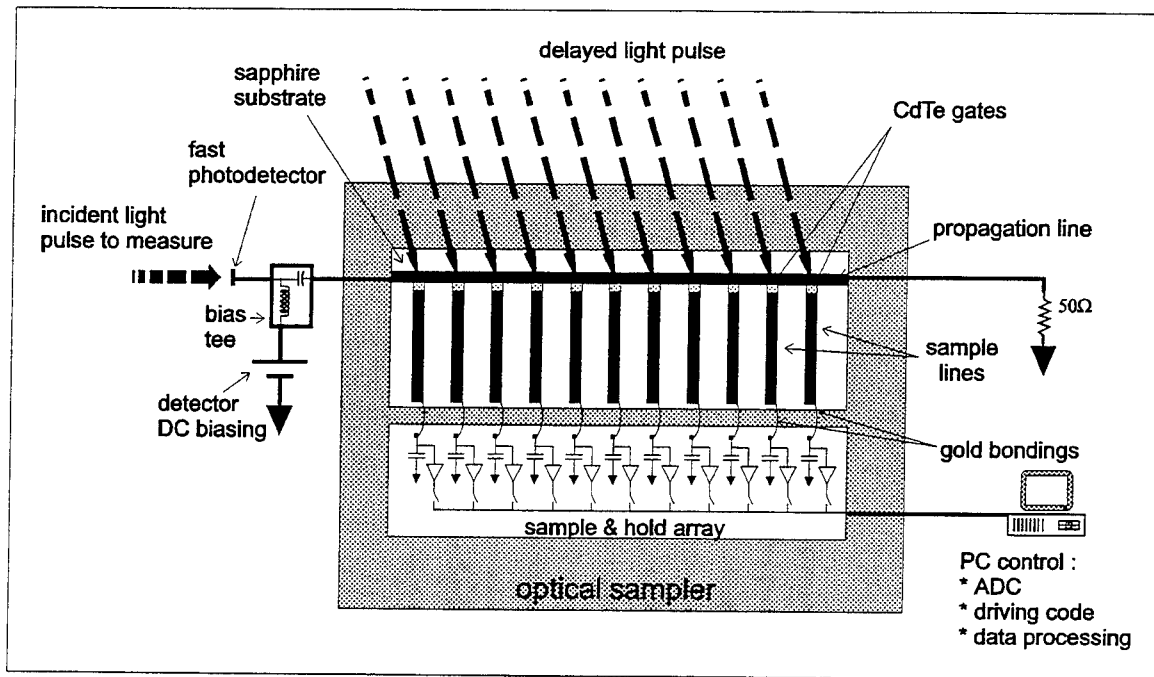


figure 3 : general synoptic scheme of the optical sampler and its environment

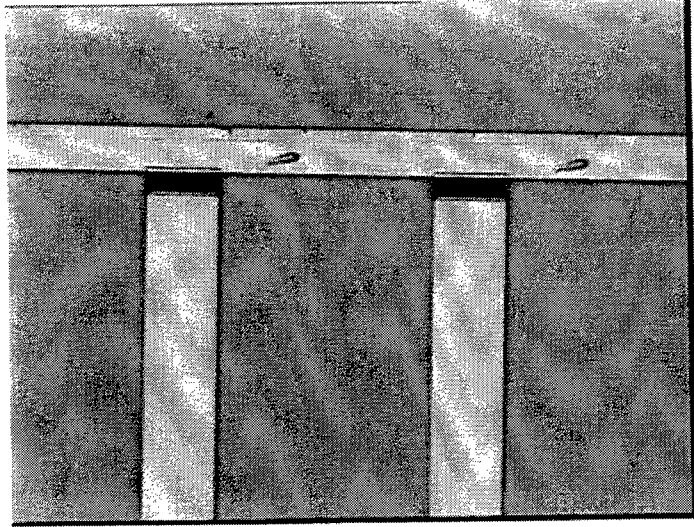
To sample the signal which propagates along the line, a very short laser pulse is applied simultaneously onto the 100 gates. A charge quantity proportional to the instantaneous voltage facing the gate is injected through the CdTe toward the sampling lines. As long as the laser pulse is shorter than the return time of the bunch of charge to the gate, the stored data are the image of the spread pulse. If the optical pulse is longer than 4ps, an averaging effect between sampling points is obtained.

4. SAMPLING GATES

The sensor material is CdTe deposited at low temperature by molecular beam epitaxy (MBE) on a 2" sapphire substrate⁶. The thickness of the film is $1\mu\text{m}$, the 100 rectangular gates are $120\mu\text{m}$ long and $30\mu\text{m}$ large (figure 4). The key criterion

for these pads is the steepness of their response. A second range criterion is the ratio of resistance when illuminated to resistance in the dark.

figure 4 : photo of two CdTe sampling gates. They are $120\mu\text{m}$ long and $40\mu\text{m}$ large, covered over $5\mu\text{m}$ each side by the gold lines, thus remaining $30\mu\text{m}$ of photoresistive width. It is seen on the photo a part of the propagation line ($72\mu\text{m}$ large), and the departure of the sampling lines ($120\mu\text{m}$ large).



After complete processing, the measurement of the rise time and recombination time of the CdTe pads is not directly achievable. Some experiments make it possible to approach them : when the propagation line is DC biased, the illumination of one of the CdTe gates generates on the line a negative pulse, which is the CdTe response. The measurement of this pulse may be done at the end of the propagation line, but the initial characteristics of the pulse will be altered by the traveling along the line and through the connectors, even if the gate nearest the end of the line is used. We could also observe the pulse generated by a CdTe gate sampled by one of its neighboring gates. This is obtained with two laser beams focused on two close gates, and delayed one from the other of an adjustable time. This experiment minimizes the distortion of the significant pulse before its measurement. Operating this way, and considering that both gates are similar, we obtain an autocorrelation of the response of a CdTe gate. The result of this experiment is presented figure 5 . This curve allows us to consider that the typical recombination time of the CdTe gate is close to 1ps.

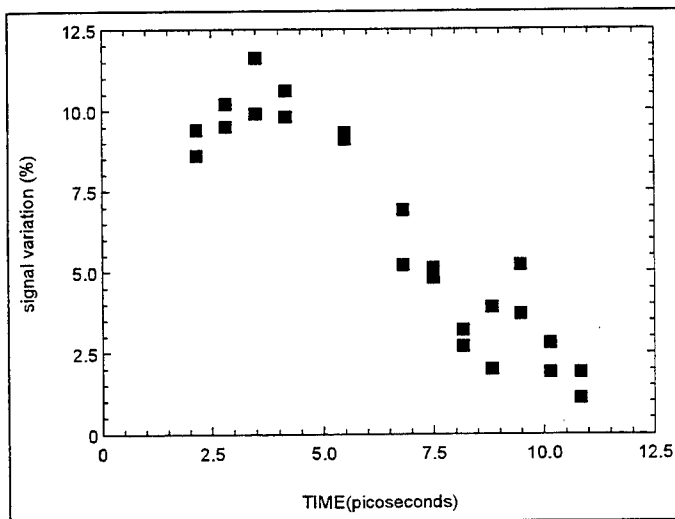


figure 5 : Autocorrelation of the photoresponse of the sampling gate. The pulse generated by one gate is sampled by the neighboring gates with a variable time delay. The data reported is the relative variation of the signal measured through gate 65 depending whether the gate 70 has been previously irradiated or no. The X coordinate is the delay between measurements (arbitrary origin).

The dark resistance is about $10^{10}\Omega$. The illumination of a single gate by a 450fs laser pulse, with an incident energy of 1nJ at a wavelength of 532nm reduces the resistance of the pad to a value close to $5k\Omega$.

5. PROPAGATION AND SAMPLING LINES

5.1. Lines description

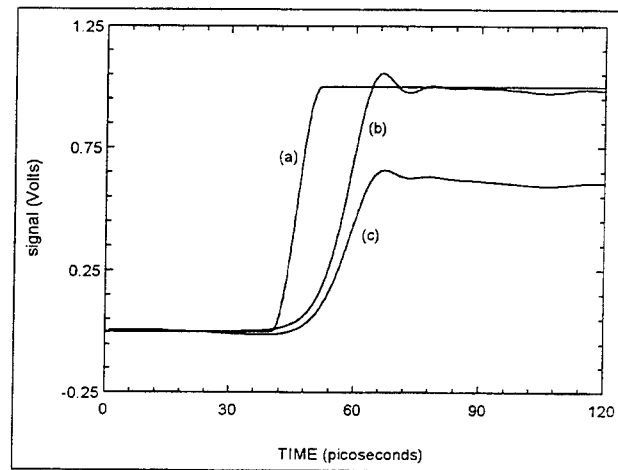
The propagation line is microstrip type, and made of a gold ribbon deposited onto the sapphire substrate. The thickness of the substrate is as small as $72\mu\text{m}$, in order to reduce high frequencies radiation and the consecutive distortion of the propagation signal. The width of the line has been calculated to provide a dynamic impedance of 50Ω ; the line is $72\mu\text{m}$ large. The thickness of the gold layer is $1\mu\text{m}$, to avoid skin effects while minimizing the on-line DC resistance. The sampling lines are elaborated from the same gold layer. They are $120\mu\text{m}$ large and 7mm.

5.2 line modeling

An electromagnetic full-wave computer code^{7,8} has been used to model the pulse propagation along the 48mm of the propagation line. The smooth of the initial edge of a sharp step has been calculated (figure 6), first considering that ohmic losses are null, then with realistic ohmic losses. The results of the calculation exhibits a diminution of the signal amplitude by a factor of two due to the only resistance. The initial rise time of the step is widened from 7ps to 12.5ps. The calculated transmission spectrum of the line is drawn on figure 8.

figure 6 : Modeling : Comparison of the amplitude and shape of a voltage step before and after its propagation along the 48mm of the line. The calculation has been done with and without considering ohmic losses.

(a): injected voltage step;
(b) : resulting voltage step without ohmic losses;
(c) : resulting voltage step with ohmic losses.



5.2. Line bandwidth measurements

The DC resistance of the propagation line, measured through the two ending connectors is 28Ω . In the same way, the transmission parameter S_{21} has been measured with a 60GHz Wiltron network analyzer (figure 7). From the DC transmission level, the frequency at which the transmission is lowered by 3dB is 35GHz.

It appears that there are very sharp absorption resonances every 8GHz in the transmission parameter⁹. This is due to the sampling lines along the propagation line; they are capacitively coupled, and the typical resonant frequency of these lines, calculated from their width and length, is 8GHz. This perturbation does slightly interfere when a single pulse propagates along the line. It absorbs a part of the pulse spectrum, and feeds it back to the propagation line with a 120ps delay.

The evaluation of the transmission spectrum for a pulse is achieved by propagating a pulse along the line, and calculate ratio of the frequency spectrum of the transmitted pulse to the spectrum of the injected pulse. To generate a pulse with a

frequency spectrum wide enough to let us evaluate high frequencies transmission, we took advantage of the speed of the sampling gates. They do generate on the line faster pulse than our fast diodes. We activated the last gate, and caught the emitted signal once at the first end, and once at the opposite end of the line. We are thus free from the eventual irreproducibility of the gate photoresponse. The resulting transmission spectrum is given on figure 8. The perturbation due to the sampling line are noticeable. The global bandwidth at -3dB of the propagation line is confirmed to be 35GHz.

figure 7 : Transmission spectrum (S_{21} parameter) of the propagation line obtained with a network analyzer.

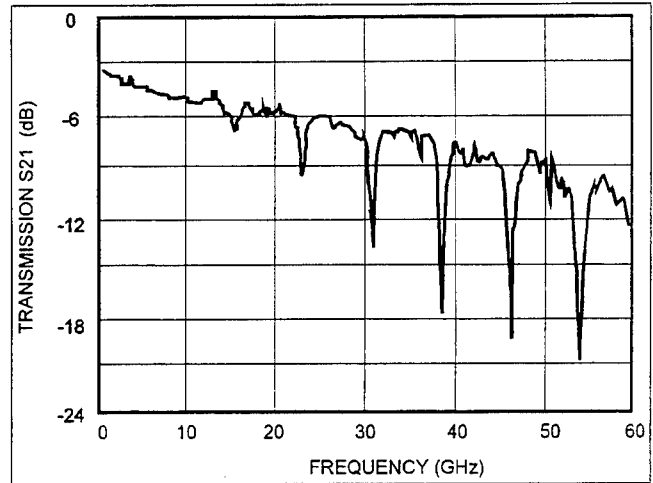
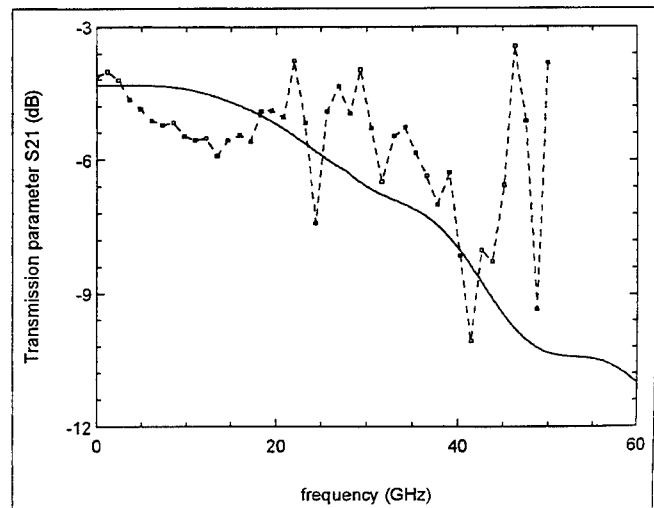


figure 8 : Comparison between calculated (continuous line) an measured (dashed line) pulse transmission spectrum of the propagation line. the measured points are obtained by Fourier transformation of a pulse temporal attenuation.



6. READ OUT ELECTRONICS AND PACKAGING

The 100 sampling lines are connected via gold wire bondings to an sample-and-hold multiplexer array EGG Reticon with 128 channels (see figure 9). This circuit is implanted close to the sapphire substrate supporting the gates and lines. It performs the storing of the charge samples in capacitors of 15pF, and the serialization of the analog equivalent voltages when reading out. An on-site amplifier sends them sequentially towards the remote control and acquisition board. The acquisition and analog to digital conversion of the serial data are performed by a Datal in-board PC card. The 12 bits encoded data are then processed by a Labview device operating program¹⁰.

*figure 9 : photo of the packaged device.
foreground : sapphire substrate, with the
propagation line and the sampling lines
array, middle ground : the sample-and-
hold array circuit, with inputs bonded to
the sampling lines, background : driving
electronics. Contacts are taken by the
50GHz connectors at each end of the
propagation line.*

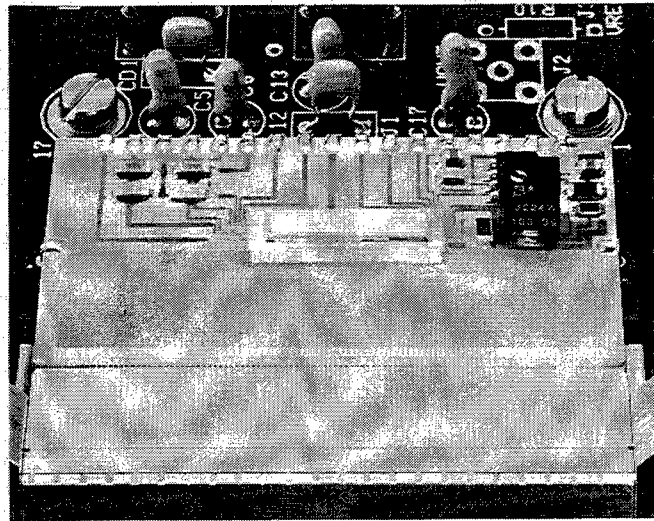
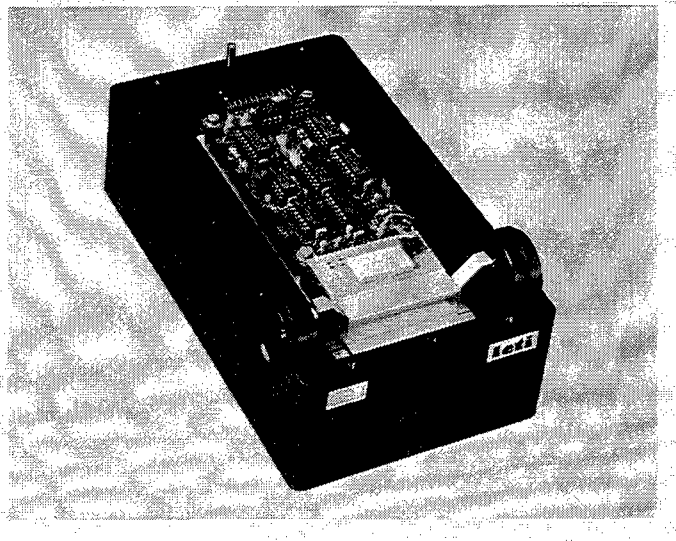


*figure 10 : photo of the packaged device.
The sapphire, the sample-and-hold
circuit, and the close driving and
input/output electronics are in a compact
and handy case. The cover has been
removed for picture.
dimensions : 195mmX112mmX76mm.*



The complete acquisition system encodes an initial charge quantity ranging between $\pm 500\text{fCb}$ into a ± 2000 digital value (12 bits). Particular attention has been paid to minimize electromagnetic perturbations of the transmitted analog signal. The final sensitivity is 10fCb , corresponding to 150mV (DC) on the propagation line, when the sampling is operated by a 450fs pulse with 1nJ deposited on the sampling gate.

The optical sampler is packaged in a remote box (figure 10) with a rectangular window facing the array of photoconductive gates, two 50GHz connectors to inject the signal onto the propagation line through any of its ends, and low frequency dialog lines to the computer. It is battery supplied.

7. ACQUISITION AND DATA PROCESSING

The optical sampler is operated through a Labview sequence. The background offset of the charge acquisition chain is first registered, and subtracted from any further registered data.

Then, to calibrate the measurement system, a DC voltage is applied to the propagation line, and an acquisition is performed, triggered by a laser pulse identical - in shape, time duration and energy - with the pulse that will be used for the single shot signal sampling. The information thus registered is the transfer function of the peculiar experiment, as it takes into account both the individual discrepancy in the CdTe gates' photoresponses, as well as the energy distribution (often quasi-gaussian distribution) on the gates alignment.

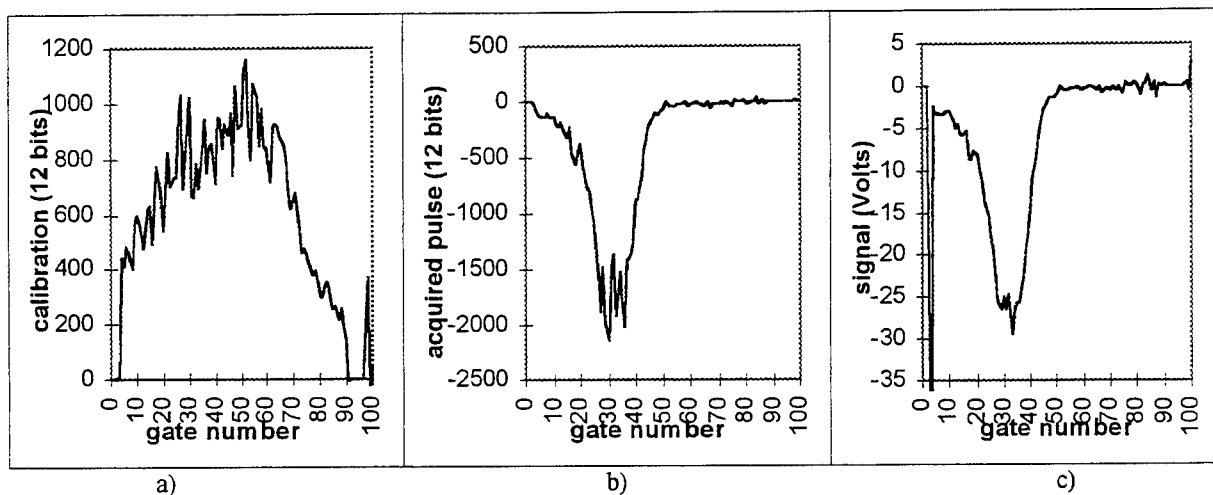


figure 10 : data processing : a) calibration curve acquired with a DC voltage on the line. b) acquired pulse without taking into account the calibration data. c) resulting calibrated measurement. This pulse has been generated and measured with a 40ps laser pulse.

After the actual signal acquisition has been operated, the data processing sequence calculates, for each of the 100 values acquired, the average voltages that were facing each of the gates during the sampling period (figure 10). The voltages are obtained by referring the data to the transfer function and to the DC voltage that had been applied for the calibration.

8. SINGLE SHOT SIGNAL ACQUISITION

The optical sampler performances are evaluated by their reliability in the description of the signal on test.

The temporal characteristics of the restored signal cannot be compared directly with those of the signal on test as no tool is available to qualify it. The fastest recording tool is a 50GHz sampling head for a scope operating on a repetitive signal (250kSa/s).

We choose as reference the result obtained with the 50GHz sampling scope. We measured an electrical pulse generated by the CdTe coaxial detector presented in §2. It was biased with 50V through a bias tee, and irradiated by a 450fs repetitive (10Hz) laser pulse. We compare in table 1 the rise time, the full width at mid-height (FWHM), and the fall time of this pulse, when measured with the 35GHz optical sampler, the previous version of the device³, which exhibited a 18GHz bandwidth, and when measured with a classical single shot analog recorder.

instrument/method	restored rise time	restored FWHM	restored fall time
reference (repetitive signal) 50GHz sampling TEK CSA803/SD32	10,5ps	23,1ps	28ps
optical sampler 35GHz (beginning of line)	12ps	31ps	27ps
optical sampler 35GHz (middle of line)	15ps	31ps	28ps
optical sampler 35GHz (end of line)	16ps	30ps	31ps
optical sampler 18GHz ³	19ps	36ps	
single shot 7GHz IN7000 Intertecnic	53ps	73ps	

table 1 : Comparison between temporal data resulting from the measurement of a similar pulse with various instruments and methods.

We did report in this table the temporal values obtained with the optical sampler for different delays between the injection of the signal to the propagation line and the sampling time. The propagating signal is distorted by its traveling along the line, and the time constants of the restored waveform are slightly enlarged. However, the measurements taken with the optical sampler are very close to the reference, even if the sampling occurs after a long propagation. The gain in reliability achieved by enlarging the bandwidth of the optical sampler from 18GHz to 35GHz is clear, and these two versions of the sampler are much more accurate than commercially available analog samplers.

9. CONCLUSION

The implementation of ultra-fast measurements, as it involves optical triggering, may look complex. In fact, the femtosecond X-ray or high power laser experiments, which are producing these types of very short pulses, often provide optical facilities.

Because of the very short response time of the photoconductive material used, the spatial sampling of a very short electrical pulse has been possible. Associated with a large transmission frequency spectrum propagation device and with a charge sensitive array circuit, we realized a measurement system, compact and preformant. Signals up to 35GHz can be described in amplitude versus time with a 4ps sampling mode, and during 400ps. As long as pure electrical measurements can only deal with frequencies lower than some 10 gigahertz, devices such as the optical sampler do bring a serious increase in reliability in the temporal analysis of the involved phenomena.

10. REFERENCES

1. J.P. Garçonnet, J. L. Bourgade, M. Nail, D. Schirmann, M. Cuzin. " Ultrafast photoconductive detectors for burn time and bangtime measurements on Phébus". Rev. Sci. Instrum. vol. 63 (10) p.4871 (1992).
2. V. Gerbe, J. Lajzerowicz, M. Cuzin, L. Armengaud, M. Lalande, B. Jecko, M. Nail, Ph. Gibert, J. L. Bourgade, D. Schirmann. "Realisation and characterisation of an electrical single pulse ultra-fast optosampler" SPIE vol. 2273 p 150 (1994).
3. M. Nail, Ph. Gibert, J. L. Micquel, M. Cuzin, M. C. Gentet, V. Gerbe, J. Laszerowicz, P. Rouviere, L. Armengaud, M. Lalande, B. Jecko. "Electrical single pulse optoelectronic sampling of Xray photodetector signal". Nucl. Instr. and Met. in Phys. Res., to be published 1996.
4. E. Rossa. "Picosecond diagnostics", Opt. Eng, vol. 4 (8), p 2357 (1995).
5. M. Nuss, D. Kisker, P. Smith, T. Harvey. "Efficient generation of 480fs electrical pulses on transmission lines by photoconductive switching in metalorganic chemical vapor deposited CdTe", Appl. Phys. Lett. vol. 54 (1) 1989.
6. S. Yoo, B. Roderick, S. Sivananthan, J. P. Faurie, P. A. Montano. "Low temperature performance of an MBE grown CdTe X-ray photodetector detector", SPIE vol 2519, p87 (1995)
7. L. Armengaud, M. Lalande, N. Breuil, B. Jecko, A. Ghis, M. Cuzin, M. Nail, Ph. Gibert. " Optoelectronic sampler : modelling and characterisation"; SPIE 's Annual Meeting Denver96, 4-9 Aug 1996, Intl Conf. Millimeter Waves and Applications III, vol. 2842-35.
8. L. Armengaud, L. Lalande, B. Jecko, N. Breuil, B. Barthelemy, M. Cuzin. " Electromagnetic analysis of optoelectronic devices applied to the study of a sampler and an autocorrelator ", IEEE trans. Microwaves Theory and Techniques, accepted for publication in July 1996.
9. C. Shu, E. Yang, D. Auston. "Propagation characteristics of picosecond electrical pulses on a periodically loaded coplanar waveguide", IEEE trans. Microwaves Theory and Techniques, vol. 39 (6) 1991.
10. Labview. National Instruments Co. Austin TX78730-9824.

Addendum

The following papers were announced for publication in this proceedings but have been withdrawn or are unavailable.

- [2843-17] **Numerical simulation of the electron-beam pinch in virtual cathode triode**
V. P. Grigoryev, T. V. Koval, N. I. Sablin, Tomsk Polytechnical Univ. (Russia)
- [2843-19] **Investigations of phase-locking process in system of strongly coupled relativistic magnetrons**
A. S. Sulakshin, N. M. Filipenko, G. G. Kanaev, Tomsk Polytechnical Univ. (Russia); S. S. Novikov, S. A. Sulakshin, Tomsk State Univ. (Russia)
- [2843-21] **Possibility of high-power microwave applications for technological purposes**
A. S. Sulakshin, Tomsk Polytechnical Univ. (Russia)
- [2843-25] **Stochatron: microwave oscillator based on the virtual cathode and realizing the regime of stochastic resonance**
A. E. Dubinov, K. E. Mikheyev, V. D. Selemir, A. V. Sudovtsov, Russian Federal Nuclear Ctr.
- [2843-26] **Vircator powering from energy-inductive storage device with semiconductor opening switch**
A. E. Dubinov, D. L. Gladilin, V. G. Kornilov, V. D. Selemir, V. S. Zhdanov, Russian Federal Nuclear Ctr.
- [2843-30] **Cyclotron absorption in relativistic BWO at low-focusing magnetic field**
A. N. Vlasov, Moscow State Univ. (Russia); Y. C. Carmel, T. M. Antonsen, Jr., V. L. Granatstein, Univ. of Maryland/College Park
- [2843-33] **Self-synchronization of a turbulent electron flux near a virtual cathode**
A. E. Dubinov, V. D. Selemir, N. V. Stepanov, V. E. Vatrugin, Russian Federal Nuclear Ctr.
- [2843-34] **Basic research on microwave plasmas and their applications**
S. Liu, Univ. of Electronic Science and Technology (China)
- [2843-45] **Studies of harmonic multiplying gyrotron oscillators and amplifiers**
H. Z. Guo, G. S. Nusinovich, M. Walter, J. Rodgers, S. Chen, V. L. Granatstein, Univ. of Maryland/College Park
- [2843-48] **Generation of high-power microwave radiation by excitation of plasma resonator**
A. E. Dubinov, A. L. Babkin, V. I. Chelpanov, S. Galkin, V. G. Kornilov, V. D. Selemir, V. S. Zhdanov, Russian Federal Nuclear Ctr.
- [2843-49] **Beam-plasma processor relevant to high-power wideband plasma-filled microwave sources**
M. A. Zavjalov, L. A. Mitin, V. I. Perevodchikov, A. L. Shapiro, All-Russian Electrotechnical Institute

- [2843-50] **Generation peculiarities of electromagnetic radiation produced by a virtual cathode moving with faster-than-light velocity**
A. E. Dubinov, V. D. Selemir, N. V. Stepanov, A. V. Sudovtsov, Russian Federal Nuclear Ctr.
- [2843-51] **Experimental simulation of pulse-repetitive-phased multielement antenna array based on vircators**
B. Alyokhin, A. E. Dubinov, V. D. Selemir, O. Shamro, K. Shibalko, N. V. Stepanov, Russian Federal Nuclear Ctr.
- [2843-52] **Vircator with plasma anode**
A. E. Dubinov, A. L. Babkin, V. I. Chelpanov, V. G. Kornilov, V. D. Selemir, V. S. Zhdanov, Russian Federal Nuclear Ctr.
- [2843-53] **Investigations on the pulse sharpening of the ferrite transmission line**
J. Yan, F. Paoloni, M. Lesha, Univ. of Wollongong (Australia)
- [2843-55] **Coaxial vircator with radially diverging beam**
A. E. Dubinov, E. Dubinov, I. Konovalov, V. D. Selemir, Russian Federal Nuclear Ctr.
- [2843-60] **Formation of nanosecond and subnanosecond electron beams for high-power microwave generation**
M. I. Yalandin, V. G. Shpak, M. R. Ulmaskulov, S. A. Shunailov, Institute of Electrophysics (Russia); I. V. Pegel, Institute of High-Current Electronics (Russia)

Author Index

Agee, Forrest J., 144, 172
 Alyokhin, B., Addendum
 Antonsen, Thomas M., Jr., Addendum
 Armengaud, Lydie, 314
 Babkin, A. L., Addendum, 117
 Birau, Michel, 269
 Blankenship, Earl, 144
 Bliokh, Yu. P., 208
 Botton, M., 57, 101
 Brandt, Howard E., 96, 183
 Calico, Steve E., 144
 Carmel, Yuval C., Addendum
 Carroll, James J., 172
 Cavecy, Kenneth H., 188
 Chelpanov, V. I., Addendum, 117
 Chen, Guoqiang, 307
 Chen, S., Addendum
 Chen, Xiaodong, 47
 Chernin, David P., 160
 Clark, M. Collins, 144
 Cohen, I., 101
 Coleman, Phillip D., 14
 Copeland, Richard P., 172
 Cuzin, Marc, 314
 Dickens, James C., 153
 Ding, Wu, 110
 Dubinov, Alexander E., Addendum
 Dubinov, E., Addendum
 Elliott, J., 153
 Englert, Thad J., 166
 Esterson, M., 47
 Fainberg, Ya. B., 208
 Feicht, Jon R., 69
 Filipenko, Nikolai M., Addendum
 Fleddermann, Charles B., 251
 Gahl, John M., 251
 Galkin, S., Addendum
 Galstjan, Eugene A., 117
 Gentet, Marie-Claude, 314
 Ghis, Anne, 314
 Gibert, Philippe, 314
 Gilgenbach, Ronald M., 24, 38, 160
 Gladilin, D. L., Addendum
 Glotova, M. Y., 134
 Goebel, Dan M., 69, 240
 Grabowski, Chris, 251
 Granatstein, Victor L., Addendum
 Grigoryev, V. P., Addendum, 287
 Gubanov, V. P., 228
 Guo, Hezhong Z., Addendum
 Hatfield, Lynn L., 153, 172
 Haworth, Mike D., 144, 166
 Hendricks, Kyle J., 14, 24, 144, 166
 Hochman, Jonathan M., 38
 Husson, Daniel, 314
 Huttlin, George A., 90

Jasper, Louis J., 80
 Jaynes, Reginald L., 38
 Jecko, Bernard, 314
 Jerby, Eli, 30
 Judy, Daniel C., 90
 Kanaev, Gennadii G., Addendum, 303
 Kazanskiy, Lev N., 117
 Khomenko, Alex I., 117
 Kishek, R., 160
 Kononov, I., Addendum
 Kornilov, V. G., Addendum, 117
 Korovin, Sergei D., 228
 Koval, T. V., Addendum, 287
 Kristiansen, Magne, 153, 172
 Krompholz, Hermann, 153
 Lalande, Michèle, 314
 Lash, J. S., 38
 Lau, Y. Y., 14, 38, 160
 Lazard, Carl J., 90
 Lazarev, Yuri N., 123, 197
 Lehr, F. Mark, 166
 Lei, Li, 30
 Leibovitz, Chaim, 101
 Lemke, Raymond W., 144
 Leopold, J., 101
 Lesha, M., Addendum
 Li, Chuanlu, 280, 307
 Lindsay, Peter A., 47
 Litz, Marc S., 90
 Liu, Jinliang, 307
 Liu, Shenggang, Addendum
 Liu, Yong Gui, 280
 Luginsland, John W., 14, 38
 Maidanovskii, Sergei A., 293
 Mankowski, John J., 172
 Martin, T. H., 172
 Masterson, Keith D., 188
 McCurdy, Alan H., 260
 Mikheyev, K. E., Addendum
 Miller, R. Bruce, 2
 Mitin, L. A., Addendum, 208
 Nail, Maurice, 314
 Novikov, Sergei S., Addendum, 293
 Novotny, David R., 188
 Nusinovich, Gregory S., Addendum
 Ouvrier-Bufferet, Patrice, 314
 Paoloni, F., Addendum
 Pegel, Igor V., Addendum, 228
 Perevodchikov, Vladimir I., Addendum, 208
 Petrov, Peter V., 123, 197
 Poeschel, Robert L., 240
 Ponti, Elmira S., 69, 240
 Ralph, Dale L., 144
 Rintamaki, J. I., 38
 Rodgers, J., Addendum
 Rosenberg, Avner, 57, 101
 Rostov, V. V., 228

Sablin, N. I., Addendum
Schamiloglu, Edl, 251
Schnitzer, Itzhak, 57, 101
Scholfeld, David W., 172
Selemir, V. D., Addendum, 117
Shamro, O., Addendum
Shapiro, A. L., Addendum, 208
Shepelev, Andrew V., 134
Shibalko, K., Addendum
Shiffler, Donald A., 166
Shlapakovskii, Anatolii S., 137
Shpak, Valery G., Addendum
Shunailov, Sergey A., Addendum
Shvartsburg, Alexandre V., 134
Šoln, Josip Z., 219
Spencer, Thomas A., 24, 38, 144
Stepanov, N. V., Addendum
Stepchenko, A. S., 228
Stump, Mark D., 24
Sudovtsov, A. V., Addendum
Sulakshin, Alexander S., Addendum
Sulakshin, Stepan A., Addendum, 293
Tan, Qimei, 307
Totmeninov, E. M., 228
Tran, George T., 80
Tsvetkov, V. I., 303
Ulmaskulov, Marat R., Addendum
Vatrunin, V. E., Addendum
Vlasov, Alexander N., Addendum
Walter, M., Addendum
Watkins, Ron M., 69
Wu, Hao, 260
Yalandin, Michael I., Addendum
Yan, Jianping, Addendum
Zavjalov, M. A., Addendum, 208
Zhang, S. K., 280
Zhang, Yazhou, 307
Zhdanov, V. S., Addendum, 117
Zherlitsyn, Alexey G., 303